# SULFUR TOLERANCE OF Pd/Au ALLOY MEMBRANES FOR HYDROGEN SEPARATION FROM COAL GAS

By

**Chao-Huang (Mike) Chen**

A PhD thesis

Submitted to the faculty of the

**Worcester Polytechnic Institute**

In fulfillment of the requirement for the

Degree of Doctor of Philosophy

In Chemical Engineering

By

_____

September 2011

**APPROVED BY:**

_____ _____

Dr. Yi Hua Ma, Advisor Dr. David DiBiasio, Head of Department

_____ _____

Dr. Satya Shivkumar, Committee Member Dr. Jianyu Liang, Committee Member

_____

Dr. Nikoloas Kazantzis, Committee Member

*for my family*

# Acknowledgements

To be able to complete the dissertation, there are too many people I need to give my thanks to. Firstly to my advisor Prof. Yi Hua Ma, thank you for the guidance through these years. The insightful advice that you provided during the discussions allowed me explore the problems in a more comprehensive way. I'm especially thankful for your patience when disagreements occurred during the discussions. I would also like to thank you for all the opportunities that you gave me. The opportunities to attend and present the work at conferences allowed me to build confidence in research and to see other research in the fields, which always gave me inspiration for my research. The opportunities to perform experiments at ORNL provided me the chance to use the most advanced instruments that I would not normally have access to and to discuss the research problems with many experts in different fields. In addition, I also thank you for the lesson that you taugh in addition to your expertise. As a role model, you probably worked harder than everyone else in the lab and the great effort you put kept the lab always funded which allowed us to be more concentrated on our research. What I've learned from you for the past years was comprehensive, which allowed me to become an independent researcher (I am still learning).

To my committee members: Prof. Shivkumar, Prof. Liang, and Prof. Kazantzis thank you for the advice and insightful suggestions. The insight given from your expertises added valuable dimension to my research.

Thanks go to the U.S. Department of Energy for the financial support including Award No. DE-FG26-04NT42194, DE-FC26-07NT43058 (supported by the University Coal Research Program), and DE-FE0004895. In addition, the research at the Oak Ridge National Laboratory's High Temperature Materials Laboratory was sponsored by the U. S. Department of Energy, Office of Energy Efficiency and Renewable Energy, Vehicle Technologies Program.

I am very grateful to all of my colleagues in the lab. Dr. Ivan Mardilovich, Dr. Federico Guazzone, Dr. Jacopo Catalano, Dr. M. Engin Ayturk, Dr. Rajkumar Bhandari, Dr. Natalie Pomerantz, Dr. Samingprai Sutheerawat, Alpna Saini, Alex Augustine, Reyyan Koc and Pei-Shan Yen, thank you for all the help that you ever provided. All the discussions that we had really gave me a lot of inspiration for my work. Thank you all not only being my colleagues but also my friends, and I really enjoyed the time that we hang out together. I am really lucky and honored to work with you guys.

I would like to give my thanks to Doug White and Jack Ferraro for the technical help and support. The help that you provided to build and troubleshoot my system, and the SEM and XRD was definitely crucial to my work. To Paula Moravek, thank you for always being able to get the items that I asked for. To Felicia Vidito and Tiffany Royale thank you for all the administrative support with me bothering you all the time asking for help. To the entire Chemical Engineering Department, all of you make my experience at WPI more pleasant.

Thanks go to Dr. E. Andrew Payzant and Dr. Harry Meyer III for the help in conducting the HT-XRD and XPS experiments druing my stay at Oak Ridge. The expertise and advice that you provided were really benefitical to my research. Thanks Dr.

Boquan Li for the help with the SEM sample preparation and Don Pellegrino for the help with the atomic adsorption spectroscopy.

Thanks to Kung-Chuan, Chung-Nien, Jason, Daniel, Lance, Wendi, Tsai, and all of my friends here and in Taiwan, your encouragement along the way keep me moving on.

To my family, dad, Yu-Wen, and especially my dearest mom, thank you for your great support and understanding throughout these years, without which I would not be able to complete my study here.

And finally to Hsinyi, there is no word or sentence that I can find to express my feeling to you. The love, support, patience, and understanding that you showed throughout these years doubles the joys at the happiest times and let me survive the darkest moments. To have you and baby Irene is truly the most beautiful blessing in my life.

# Abstract

This work provides a detailed characterization study on $H_2S$ poisoning of Pd and Pd/Au alloy composite membranes to obtain fundamental understandings of sulfur poisoning phenomena and preparation of sulfur tolerant membranes. The enhancement of the sulfur tolerance by alloying Pd with Au has been confirmed by both permeation test and microstructure analysis (SEM and XRD). While pure Pd membranes exhibited the permeance decline in the presence of $H_2S$ due to both sulfur adsorption and bulk $Pd_4S$ formation, Pd/Au alloy membranes showed the permeance loss merely resulted from the surface sulfur adsorption without bulk sulfide formation up to 55 ppm $H_2S$.

The XPS study confirmed that the $H_2S$ adsorption on the Pd/Au alloy surfaces was dissociative, and both surface Au and Pd sulfides were formed with the preferential Au-S bonding. The adsorption type of sulfur on the Pd/Au alloy surfaces was monolayer with a limited coverage, which increased with decreasing temperature. The permeance loss of Pd/Au membranes was essentially fully recoverable in $H_2$, and the integrity of the membranes remained unaltered after the poisoning/recovery tests. Increasing Au composition in the Pd/Au membranes increased the sulfur tolerance. A Pd/Au alloy membrane of 16.7 wt% Au exhibited a permeance over 50% of its original value in the presence of 5 ppm $H_2S$ at 400°C, while a Pd membrane showed 85% permeance loss.

The Pd/Au alloy membranes were fabricated by the Au displacement deposition, which had an empirical reaction order of 3.2 determined by the AAS. The HT-XRD study verified that the formed Pd/Au alloy layers were thermally stable up to 500°C.

# Executive Summary

The fabrication of Pd/Au alloy (non-homogenous) composite membranes and the characterization of $H_2S$ poisoning and recovery of Pd and Pd/Au alloy composite membranes were studied for obtaining a fundamental understanding of sulfur poisoning phenomena and preparation of sulfur tolerant membranes. The fabrication of Pd/Au alloy composite membranes was carried out by the electroless deposition of Pd followed by the Au displacement deposition on the tubular porous metal supports (0.1 $\mu$m media grade, 24 $cm^2$ effective area). Prior to the deposition, the supports were oxidized in air at 700 – 800ºC and plated with Pd/Ag barrier layers for intermetallic diffusion protection, and graded with $Al_2O_3$ slurry to reduce the surface pore size. After the Pd and Au deposition, the membranes were heat-treated at 500 – 550ºC for 48 hours to form stable Pd/Au alloy layer on the top of the membranes. The Au weight fraction in the Pd/Au alloy membranes was controlled by the number of Au displacement deposition loops with the multi-layer structure. Pd and Pd/Au coupons were also prepared with the similar preparation method on 316L porous stainless steel plates (0.1 $\mu$m media grade, 1 cm x 1 cm x 1 mm) for the detailed microstructure study.

The factors affecting the Au displacement of Pd as well as the kinetics of the Au displacement plating was investigated. Pre-treating the Pd surface with acid to remove the non-conducting contaminants was important for the Au displacement reaction, which had an empirical reaction order of 3.2 with respect to Au ion concentration. Approximately 0.5 – 0.6 $\mu$m thick Au layer was deposited once a complete coverage on

the Pd surface by the Au deposit was attained. Increasing the Au ion concentration, acidity, and temperature of the displacement bath resulted in a faster Au displacement deposition rate.

The annealing conditions for forming Pd/Au alloy were studied by both *ex-situ* XRD and the *in-situ* High Temperature X-ray Diffraction methods. The Pd/Au inter-diffusion occurred at the temperature as low as 322°C. However, the inter-diffusion rate decreased significantly (by 2 – 3 orders of magnitude) as the annealing proceeded due to the strongly composition-dependent diffusion rate of Pd and Au, resulting in the formation of thermally stable non-homogenous Pd/Au alloy layers. For forming a stable Pd/Au alloy top layer for sulfur resistance, annealing the Pd/Au bi-layers (~10 wt% Au) at above 500°C for ~ 48 hours was sufficient. The *in-situ* HTXRD study also revealed the mechanism and the kinetics of the Pd/Au alloy formation. The kinetics of the Pd/Au alloy formation was obtained by the quantitative analyses of the HTXRD data at 450 - 600ºC based on the Avrami model, which indicated that the transformation was a one-dimensional diffusion controlled process. The estimated activation energy for the Pd/Au alloy formation was 248 kJ/mol, and in good agreement with the literature value.

The characterization of the Pd/Au alloy membranes in $H_2$ showed that the Pd/Au alloy membranes followed Sieverts' law at 250 – 450°C and gave comparable $H_2$ permeance compared to the pure Pd membranes. The $H_2$ permeance of the Pd/Au membranes was stable at elevated temperatures up to 500ºC due to the formed thermally stable Pd/Au alloy layer. The Pd/Au membrane of approximately 5 wt% Au exhibited the highest $H_2$ permeance with the lowest activation energy. Further increase of the Au

composition caused the decrease of permeance as well as the increase of activation energy.

The $H_2S$ poisoning tests showed that the Pd membrane experienced a two-stage permeance decline upon the exposure to a 55 ppm $H_2S/H_2$ mixture at 400°C, which were due to (i) surface site blocking by the dissociative adsorption of $H_2S$, and (ii) bulk sulfidation of Pd with the formation of $Pd_4S$. The formation of bulk $Pd_4S$ with the formation of pinholes was confirmed by the micro-structural (XRD and SEM) analysis, and the exposure conditions for forming $Pd_4S$ observed in the study agreed with the thermodynamic prediction. The formation of pinholes was due to the large stress in the Pd lattice caused by the incorporation of sulfur formed as $Pd_4S$. The extent of the Pd sulfidation increased with decreasing temperature and the growth of the $Pd_4S$ layer was one-dimensional phase boundary controlled based on the Avrami analysis. The X-ray photoelectron spectroscopy (XPS) analysis suggested the two potential Pd sulfide species, PdS and $Pd_4S$ that possibly bonded on the top surface and in the sub-layers of Pd respectively. The permeance loss of Pd membranes was found be to partially recoverable in $H_2$. The partial permeance recovery was due to the restoration of Pd from $Pd_4S$. However, a fixed amount of surface sulfide was still present on the Pd after the recovery as evidenced by the XPS study.

On the other hand, the Pd/Au membranes exhibited the resistance to bulk sulfidation upon exposure to the $H_2S/H_2$ mixtures up to 55 ppm in the temperature range of 350 – 500°C, and underwent no significant structural changes caused by the bulk sulfide formation after the exposures evidenced by XRD and SEM. The permeance decline of the Pd/Au alloy membrane upon the $H_2S$ exposures resulted mainly from the

surface site-blocking by adsorbed sulfur, which caused the decrease of the effective area for the $H_2$ adsorption without altering the $H_2$ transport mechanism. The presence of surface sulfide was confirmed by the XPS analysis, and the deconvolution of the XPS sulfur peak suggested the preferential Au-S bonding, which resulted in the significant reduction of the Pd-S bonding compared to the poisoned Pd membranes.

The permeance loss of the Pd/Au alloy membranes was essentially fully recoverable, which was potentially due to more reduction of the Pd-S bonding compared to Au-S bonding after recovering in $H_2$. The un-recovered Au-S bonding increased the overall surface coverage enabling the nearly complete reduction of the Pd-S bonding due to the decrease of the Pd-S binding energy at high overall sulfur coverage. The adsorption of sulfur on the Pd/Au surface was monolayer adsorption with limited surface coverage, which caused less permeance loss and more permeance recovery of the Pd/Au membranes at higher temperatures due to the exothermic nature of the $H_2S$ adsorption. The length of the $H_2S$ exposure showed no effect on the degree of permeance decline at a fixed temperature substantiated that the permeance loss was resulted from the $H_2S$ adsorption on the membrane surface. Finally, increasing the Au composition in the Pd/Au membranes reduced the permeance loss in the presence of $H_2S$. However, by taking the effect of the Au composition on the $H_2$ permeance into account, the optimum Au composition with the highest relative $H_2$ permeance (to Pd foil) in the presence of $H_2S$ was within 10 – 30 wt%.

# Table of Contents

# List of Figures

# List of Tables

# 1. Introduction

Hydrogen plays an important role in modern industries due to its diverse usage in numerous applications. For examples, hydrogen is extensively used in different refining processes, such as hydrodealkylation, hydrodesulfurization, and hydrocracking to refine crude oils by the petrochemical industry. In chemical plants, hydrogen is used largely to produce ammonia, methanol, hydrochloric acid, and other chemicals. In addition, hydrogen is used as a reducing agent to refine metal ores, as a carrier gas in electronic industry, as a reducing atmosphere in glass and ceramic production, as a protective atmosphere in nuclear fuel plants, and as a hydrogenation agent in food industry.

Another major application with growing importance of hydrogen today is to be used as an energy carrier. For being an energy carrier, hydrogen has the highest combustion energy release per unit of weight of any commonly occurring material and is emission free. Due to the advantages, hydrogen is used as a fuel for rockets and internal combustion engines in some specially designed vehicles in Europe. In addition, hydrogen can power fuel cells providing electricity for human needs in most aspects, including transportation (i.e. fuel cell powered vehicles) and industrial needs. Since only water is produced when generating energy form hydrogen, the use of hydrogen as an energy carrier in long term reduces the emissions of greenhouse gases thereby possibly mitigates the global climate change. As a result, hydrogen become the major energy carrier in the future can be foreseen.

Hydrogen can be made from diverse resources ranged from fossil fuels, nuclear power to renewable resources (e.g. solar, wind, and bio method). Due to the growing global climate change concerns as mentioned previously, the clean and renewable processes are preferable such as electrolysis, thermochemical conversion of biomass, photolytic and fermentative micro-organism systems, photo-electrochemical systems, and high-temperature chemical cycle water splitting). However, most of these technologies are still at the research and development stage and not practical yet for industrial scale production. As a result, extracting $H_2$ from relatively abundant fossil fuels (e.g. steaming reforming of natural gas, and coal gasification) is most economical and widely used processes for large scale production of $H_2$ today. It will continue to be so until the maturity of the clean and sustainable $H_2$ production techniques has been achieved. To minimize the environmental impacts, the carbon capture and sequestration is necessary for such processes due to the $CO_2$ emissions from the reactions.

Although steam reforming of natural gas is the dominant process for industrial hydrogen production today, utilizing coal to produce hydrogen (i.e. coal gasification) is potentially the most preferable process in the near future since coal is the most abundant and widely dispersed fossil fuel on the globe. In addition, the hydrogen produced from coal is more cost effective compared to natural gas (Agnew 2004). Usually, the $H_2$ concentration in the syngas produced from the coal gasification process can be further increased by a water-gas shift (WGS) reaction along with $CO_2$ as the main by-product. Coal gasification process can also be used in an integrated gasification combined cycle (IGCC) to simultaneously produce $H_2$ and generate electricity from turbines powered by the syngas.

Higher efficiency and cost effectiveness of the $H_2$ production can be achieved by applying Pd-based membranes (membrane reactor) in the above-mentioned processes to extract high purity $H_2$ during the $H_2$ production reaction with fossil fuels. For example, the wet scrubbing and pressure swing adsorption (PSA) are the most widely used method to extract $H_2$ out of the steam reforming product gas stream, which requires high temperatures and pressures to obtain high conversions. By the use of Pd-based membrane reactors, the $H_2$ production from the reaction and high purity hydrogen extraction through the $H_2$ selective Pd-based membrane occurred simultaneously resulting in an increase of the conversion. As a result, the necessary reaction temperature to achieve certain conversion is lower with a membrane reactor. Shu et al. (1995) found that the conversion of a methane steam reforming reaction was 1.4 times higher in the Pd/Ag alloy membrane reactor than that in the non-membrane system. Similar improvement in efficiency and cost effectiveness in coal gasification process by the use of Pd-based membrane reactors was also reported (Criscuoli 2000; Barbieri, 2005). In addition to higher conversion, the high concentration $CO_2$ under high pressure in the retentate as $H_2$ is being extracted by the Pd-based membranes reduces the cost of carbon capture by eliminating the pressurizing stage required for carbon sequestration (Bredesen, 2004).

Currently, asymmetric composite Pd-based membranes on porous metal supports prepared by electroless deposition are considered to be the most suitable for industrial scale $H_2$ production in the abovementioned processes. While metal supports provide the mechanical strength and simplicity of module construction, electroless plating technique provide the good quality and uniformity of the deposited film on complex shapes and simplicity of large scale production. Efforts in enhancing of thermal stability and

decreasing the thickness of dense Pd-based $H_2$ selective layer made such composite Pd-based membranes more industrial attractive due to the reduction of palladium cost and high hydrogen permeance (Mardilovich et al., 2000; Ma et al., 2000, 2004, 2007; Guazzone 2006; Ayturk 2006, 2007) . However, the poor chemical stability of palladium in the presence of impurities, especially $H_2S$, restricted the use of Pd-based membranes in the practical applications. Sulfur is one of the major impurities in fossil fuels, especially in coal. As a result, producing $H_2$ from such fossil fuels usually produces sulfur containing by-products. For example, $H_2S$ is a typical by-product in syngas along with hydrogen, CO and $CO_2$ and other impurities.

Even a small quantity of $H_2S$ (a few ppm) could cause a large decrease in hydrogen permeance of a Pd foil (McKinley, 1967). When exposed to higher concentrations of $H_2S$, not only the performance (i.e. $H_2$ permeance) but also the structure of Pd membranes were degenerated (Chen and Ma, 2010; Mundschau et al., 2006; Kulprathipanja et al., 2005; Edlund and Pledger, 1993; Kajiwara et al., 1999) with the formation of pinholes, cracks or even rupture of the Pd layer, cause the membrane to lose the ability to separate $H_2$ from other non-dissociative gases. As a result, sulfur causes severe and irreversible damage of Pd membranes resulting in the reduction of $H_2$ permeability and membrane deterioration.

The loss of permeance mainly resulted from the decrease of the $H_2$ adsorption caused by the adsorbed sulfur on the Pd surface. Due to the high affinity of Pd to sulfur, $H_2S$ could dissociatively adsorb on the Pd surface. The adsorbed sulfur blocked the adsorption sites on the Pd surface and generated an energy barrier where each adsorbed sulfur effectively blocked 4 to 13 sites for the $H_2$ adsorption (Bruke and Madix, 1990;

Gravil and Toulhoat, 1999; Lang, 1985). In addition, the adsorbed sulfur could incorporate with Pd to form bulk sulfide depending on the $H_2S$ exposure conditions (i.e. temperature, time and $H_2S$ concentration). When bulk sulfide formed, the sulfide layer acted as a mass transfer barrier with a lower $H_2$ permeability (Kulprathipanja et al., 2005; Morreale et al., 2007). Furthermore, the formation of bulk sulfide generated large stress in the Pd lattices due to the large difference in the lattice constants between pure Pd and palladium sulfide. As a result, the formation of pinholes, cracks or even rupture of the Pd membranes occurred (Kajiwara, 1999).

Several approaches, such as varying the crystal structure (nano-structure or amorphous) (Bryden and Ying, 2002), have been investigated recently to enhance the resistance to sulfur poisoning of Pd membranes (Gao et al., 2004). However, the most promising approach to enhance the sulfur resistance was to alloy Pd with other elements, thereby altering its electronic, chemical properties and reactivity (Rodriguez, 1996).

Although most efforts have been placed in Pd/Cu alloy membranes for higher sulfur resistance (Kulprathipanja et al., 2005; Pomerantz and Ma 2009; Morreale et al., 2004; Kamakoti et al., 2005), Pd/Au alloy membranes have received increasing attention recently due to their two-fold beneficial characteristics. Pd/Au alloy membranes showed higher $H_2$ permeability than pure Pd membranes in the Au content range below 20 wt%, which resulted from the higher solubility of $H_2$ in Pd/Au alloys although there was a quite large discrepancy on how much increase of the permeability (McKinley, 1967; Gryaznov, 2000; Sieverts, 1915; Sonwane et al., 2006 a,b) . Pd/Au alloys have also shown higher sulfur resistance compared to other Pd alloys. McKinley (1967) observed a flux decline of 10% on a $Pd_{60}Au_{40}$ alloy foil in the presence of 4.5 ppm $H_2S$ at 350ºC, while a decline of 95%

was observed on a $Pd_{60}Cu_{40}$ alloy foil under the same conditions. Way et al. (2008) also observed a 38% permeance decline on a $Pd_{85}Au_{15}$ alloy membrane in the presence of 5 ppm $H_2S$ at 400ºC, while a 71% permeance drop was observed on a $Pd_{94}Cu_6$ FCC phase membrane. In the literature, limited research has been done regarding the $H_2S$ poisoning of Pd/Au alloy membranes, especially in the Au content range below 20 wt%. No systematic data were available regarding the relation between sulfur resistance and Au content in the Pd/Au alloy membrane.

One simple and efficient way of Au deposition is the galvanic displacement method, which does not require external sources of current, reducing agent and complexing agent (Okinaka, 1990; Parker, 1974; El-Shazly and Baker, 1982; Coutts and Revesz, 1966). The plating technique solely requires simple plating equipment and is environmentally friendly. Forming Pd/Au alloy on the top layer of the membrane by the displacement plating technique (and annealing) allows the membrane to have sulfur tolerance, while overall low Au content minimizes the use of the high cost Au.

The main objective of this research was to obtain the fundamental understanding involved in the synthesis, the $H_2$ permeation characteristics, the effect of $H_2S$ on Pd and Pd/Au alloy composite membranes synthesized by the electroless deposition technique on porous metal supports. In summary, the specific objectives of this research were:

- To understand the factors affecting the displacement plating of Au and the kinetics of Au displacement plating.
- To understand the kinetics of the Pd/Au alloy phase transformation and the annealing conditions required to fabricate Pd/Au alloy membranes.

- To understand and characterize the hydrogen transport mechanism through Pd/Au membranes, and to understand the effect of the Au content on the hydrogen permeation.
- To understand the permeation characteristics of Pd and Pd/Au membranes during $H_2S$ poisoning and recovery in $H_2$
- To understand how the morphology and crystal structure of Pd and Pd/Au alloy membranes were affected by $H_2S$ poisoning
- To understand how exposure temperature, exposure time, and $H_2S$ concentration affect the degree of $H_2S$ poisoning.
- To understand the effects of the Au content in the membrane on the degree of $H_2S$ poisoning.
- To understand how $H_2S$ bonds to the surface of Pd and Pd/Au alloy membranes

# 2. Literature Review

## 2.1 Pd – H System

The permeability of transition metals to hydrogen was first discovered by Deville (1864) with the experiments on platinum and iron. Not much time after, the phenomenon of the diffusion of hydrogen through palladium was discovered by Graham (1866). Since then, palladium gained large interests because of its high permeability and adsorption ability to hydrogen. Hydrogen atom with its atomic diameter of 1.558 Å is considered to form interstitial solid solution with palladium according to the Hagger's rule (Pollock, 1993). According to the Hagger's rule, an element forms interstitial solid solution with palladium if its atomic diameter is less than 1.62 Å. The adsorption and permeation mechanism of palladium to hydrogen was proposed by Alefeld and Volkl (1978) that hydrogen atoms occupy interstitial sites within the Pd lattice causing the lattice to expand and jump between the interstitial sites.

Figure 2.1 is the Pd-H phase diagram, which was plotted with the atomic H/Pd ratio (n) as a function of hydrogen pressure at different temperatures. Hydrogen adsorption isotherms are shown in the plot, where the relations between hydrogen solubility and temperature and pressure are stated. It should be noted that the construction of isotherms varied with the technique development. Lewis (1967) constructed the isotherms by measuring weight, while Frieske and Wicke (1973) achieved more accurate isotherms with the use of magnetic susceptibility. Dilatometric method was applied by Latyshev and Gur'yanov (1988) to obtain the isotherms.

In addition, a miscibility gap of two Pd-H phases is observed in the phase diagram under the dotted line region as shown in Figure 2.1. The two Pd-H phases are α phase with a smaller H content and lattice parameter and β phase with a larger H content and lattice parameter. These two phases both have FCC crystal structures and co-exist under a certain (critical) temperature. Frieske and Wicke (1973) measured the critical temperature of the phase transition to be 291°C. Latyshev and Gur'yanov (1988) determined the critical temperature of 299°C with the critical atomic H/Pd ratio of 0.292 and the critical pressure of 21.5 bars.

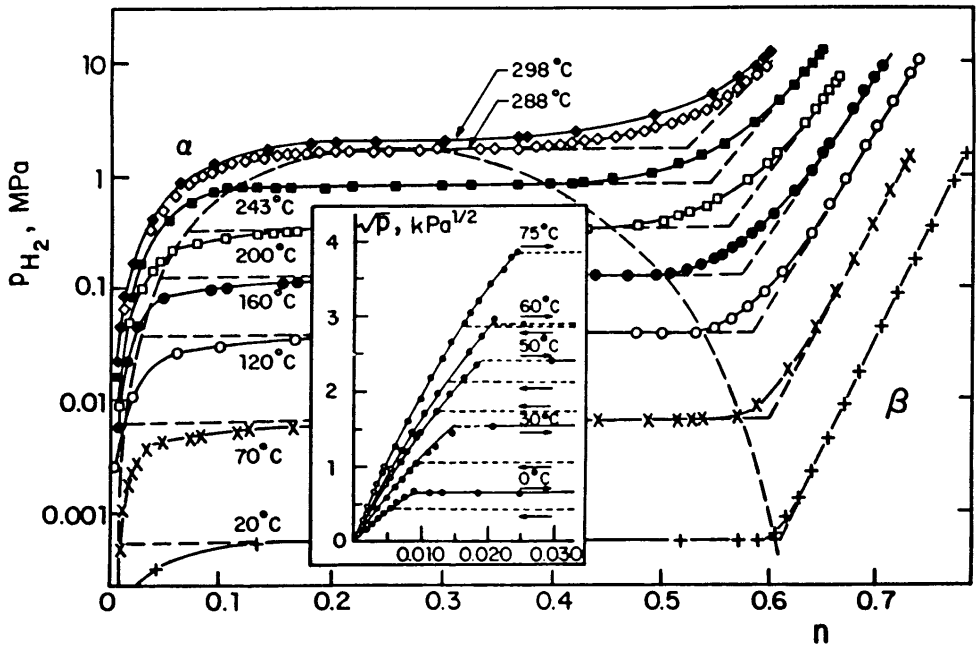


Figure 2.1. Pd – H phase diagram (Figure taken from Shu et al., 1991, adapted from Frieske and Wicke, 1973, and Wicke and Nernst, 1964[1].

[1] The figure was done by Shu et al. (1991, whih was adapted from Frieske and Wicke, 1973 and Wicke and Nernst, 1964. Values of the y-axis in the insert were mistakenly listed as 10, 20, 30, and 40 by Shu et al. (1991) and corrected by Guazzone (2006) based on the data in Wicke and Nerst's work (1964).

The detail mechanism of phase transformation of these two phases due to the hydrogen content was studied by Alefeld and Volkl (1978). Hydrogen occupying interstitial sites within Pd in the α phase caused the lattice parameter to increase from 3.891 Å to 3.894 Å. At the saturation point of the α phase, the lattice parameter underwent a non-continuous jump to 4.026 Å marking the miscibility gap. It should be noted that the phase transition studied by Alefeld and Volkl (1978) was at room temperature.

Such an α ↔ β phase transformation caused significant lattice deformation for the release of strain in lattice, which was termed as hydrogen embrittlement by Lewis (1967). The hydrogen embrittlement could cause the deterioration of Pd structure resulting in the dramatic decline of hydrogen selective separating ability of Pd. In order to avoid the undesired hydrogen embrittlement, operating Pd membranes with careful control of the temperature and pressure outside the two phase region is necessary. Alternatively, the hydrogen embrittlement phenomenon could be moderated by alloying with other metals into Pd, such as Ag, Cu, Au, Y and etc. since the critical temperature and pressure for the two phase region changes after alloying.

At the low atomic H/Pd ratio ($n_{H/Pd}$) range, isotherms show that the atomic H/Pd ratio in Pd is proportional to the square root of the hydrogen pressure as shown in the inset of Figure 2.1. The proportionality constant is known as the Sieverts' constant and is shown in Equation 2.1, where $P_{H2}$ is hydrogen pressure in atmosphere, $K_s$ is the Sieverts' constant in $atm^{0.5}$, and $n_{H/Pd}$ is the atomic H/Pd ratio in Pd. The linear dependence is only observed at low concentrations of hydrogen in Pd and when the surface interactions of hydrogen and Pd are at equilibrium.

$$P_{H_2}^{0.5} = K_s \cdot n_{H/Pd} \tag{2.1}$$

## 2.2 Mechanism of Hydrogen Transfer in Pd Membranes

Hydrogen transport through Pd is mainly governed by the solution diffusion mechanism among the multi-step processes, which are defined as follows (Shu et al., 1991):

(1) Diffusion of $H_2$ in gas phase from the bulk gas to the Pd surface

(2) Dissociative chemisorption of $H_2$ on the Pd surface

(3) Dissolution of H from the Pd surface to the bulk metal

(4) Diffusion of H through the Pd lattice

(5) Transition of H from the Pd bulk metal to the surface

(6) Recombination and desorption of $H_2$ from the Pd surface

(7) Diffusion of $H_2$ from the Pd surface to the bulk gas

In step (4), H atoms diffuse through the Pd lattice by "jumping" between the octahedral interstitial sites of the FCC Pd lattice (Alefeld and Volkl, 1978) as shown schematically in Figure 2.2.

Step (2), the dissociative chemisorption of hydrogen on Pd, results in the gaseous hydrogen to be attached on the Pd surface as hydrogen atoms. This process initiates the transportation of hydrogen through the dense Pd layer. Hydrogen flux adsorbed on the surface at a dynamic equilibrium is expressed as the difference between adsorption and desorption rates as shown in Equation 2.2.

$$J_{H_2} = k_d \cdot \theta^2 - k_a \cdot P_{H_2}(1-\theta)^2 \tag{2.2}$$

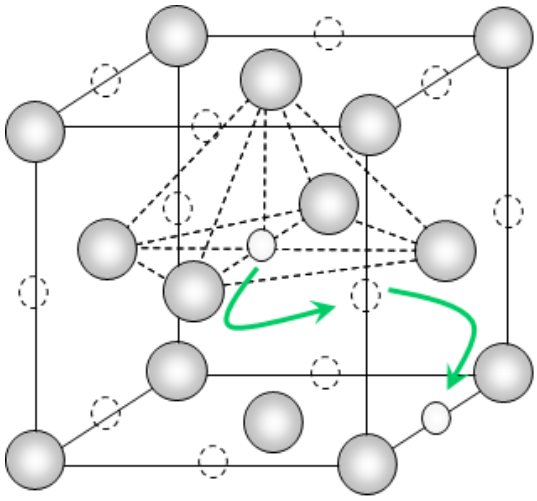

Figure 2.2. Pd unit cell with a H atom jumping between interstitial sites: Pd - grey, H - white, interstitial sites – dotted (The figure was plotted by Pomerantz, 2010).

In Equation 2.2., $J_{H_2}$ is hydrogen flux adsorbed on the Pd surface with the unit of $m^3/(m^2*h)$, and $k_a$, $k_d$ are the rate constants of adsorption with the unit of $m^3/(m^2*h*atm)$ and desorption with the unit of $m^3/(m^2*h)$ respectively, and $\theta$ is the fractional surface coverage.

The dissociatively adsorbed hydrogen atoms on Pd surface are then dissolved into Pd lattice though the interstitial sites (The step (3)). The flux of the dissolved hydrogen into bulk Pd at a dynamic equilibrium is then expressed as the difference between the rates of the surface hydrogen entering and exiting the Pd lattice, as shown in Equation 2.3.

$$J_{H_2} = -k_o n_{H/Pd} \cdot (1-\theta) + k_i \cdot (1-n_{H/Pd}) \cdot \theta \qquad (2.3)$$

Where $k_i$, $k_0$ are the rate constants of dissolution and reverse step with the unit of $m^3/(m^2*h)$.

The step (4), the diffusion of hydrogen in bulk Pd, is assumed to be the rate-limiting step. This assumption is valid for a clean Pd film with a thickness greater than 1 μm and operated above 400°C (Ward and Dao, 1999). One dimensional diffusion is also assumed and the diffusion flux is expressed by the Fick's law of diffusion at steady state as shown in Equation 2.4 (after integrating).

$$J_{H_2} = -\frac{D}{l} \cdot \left(C_{H,2} - C_{H,1}\right) \tag{2.4}$$

Where $D$ is the diffusion coefficient of H atom in Pd, $m^2/h$, $l$ is the thickness of Pd layer in m, and $C$ is the hydrogen concentration in $mol/m^3$. The concentration of hydrogen in Pd is expressed as the product of the atomic H/Pd ratio ($n_{H/Pd}$) and the hydrogen solubility constant ($\kappa$) in Pd with the same units as the concentration as shown in Equation 2.5.

$$C_H = \kappa \cdot n_{H/Pd} \tag{2.5}$$

Substitution of Equation 2.5 into Equation 2.4 yields Equation 2.6:

$$J_{H_2} = -\frac{D \cdot \kappa}{l}\left(n_{H/Pd,2} - n_{H/Pd,1}\right) \tag{2.6}$$

Since the bulk diffusion of hydrogen is assumed to be the rate limiting step (i.e. the diffusion rate is substantially smaller than the surface adsorption and dissolution rate), both sorption and dissolution is considered to be at an equilibrium state. As a result, the adsorption rate equals to desorption rate, and dissolution rate equals to the rate of its

reverse step. Therefore, the overall rates of adsorption and dissolution (Equations 2.2 and 2.3) are equal to zero and can be expressed as Equation 2.7. It should be noted that the atomic H/Pd ratio is very small and could be neglected ($n_{H/Pd} << 1$) in the second term in Equation 2.3.

$$-k_a P_{H_2} \cdot (1-\theta)^2 + k_d \theta^2 = -k_o n_{H/Pd} \cdot (1-\theta) + k_i \cdot \theta = 0 \tag{2.7}$$

The atomic H/Pd ratio, $n_{H/Pd}$, in Equation 2.7 is solved and expressed in Equation 2.8 as a proportion to square root of the hydrogen pressure. The expression provides the mathematic relation of the isotherms at the low atomic H/Pd ratio ($n_{H/Pd}$) range as shown in the inset of Figure 2.1. In addition, the expression also indicates that the Sieverts' constant, $K_s$, is actually the equilibrium constant for the hydrogen dissolution in terms of rate constants of adsorption and dissolution as shown in Equation 2.9.

$$n_{H/Pd} = \frac{k_i \cdot k_a^{0.5}}{k_o \cdot k_d^{0.5}} P_{H_2}^{0.5} \tag{2.8}$$

$$K_s = \frac{k_o \cdot k_d^{0.5}}{k_i \cdot k_a^{0.5}} \tag{2.9}$$

By substituting Equation 2.8 and Equation 2.9 into Equation 2.6, Sieverts' Law is derived as expressed in Equation 2.10. The physical meaning of Sieverts' Law is that the permeating hydrogen flux through a Pd layer is linearly dependent on the difference of the square root of the pressures between the Pd layer at a given temperature. According to the assumptions made in the derivation of the hydrogen permeation process, Sieverts' Law is only valid at low concentrations of hydrogen in the bulk Pd and when diffusion through Pd is the rate limiting step of the hydrogen permeation.

$$J_{H_2} = \frac{D \cdot \kappa}{K_s \cdot l}\left(P_{H_2,2}^{0.5} - P_{H_2,1}^{0.5}\right) \tag{2.10}$$

In Equation 2.10, the term ($D^*\kappa / K_s$) is defined as permeability, $Q$, with the unit in mol*m/(m$^2$*h*atm$^{0.5}$), which is expressed as the product of diffusivity, $D$ in m$^2$/h and solubility, $S$ ($S = \kappa / K_s$) in mol/(m$^3$*atm$^{0.5}$). Since the diffusion coefficient, $D$, and the equilibrium (Sieverts') constant, $K_s$, are dependent on temperature, they can be expressed as a function of temperature in the Arrhenius relation as shown in Equation 2.11 and Equation 2.12.

$$D = D_o \cdot \exp\left(\frac{-E_D}{R \cdot T}\right) \tag{2.11}$$

$$S = S_o \cdot \exp\left(\frac{\Delta H}{R \cdot T}\right) \tag{2.12}$$

Where $E_D$ is the activation energy for hydrogen diffusion in kJ/mol and $\Delta H$ is the enthalpy of hydrogen dissolution with the same unit. $R$ is the universal gas constant in J/(mol*K) and $T$ is the temperature in K. Since the permeability, $Q$, is the product of the solubility and the diffusion coefficients, similar temperature dependent expression for permeability is derived as shown in Equation 2.13. $Q_o$, which is the product of $D_o$ and $S_o$, is defined as permeability, and $E_Q$, the activation energy for permeation, equals to the sum of the activation energy for hydrogen diffusion and the enthalpy of dissolution in kJ/mol.

$$Q = D \cdot S = Q_o \cdot \exp\left(\frac{-E_Q}{R \cdot T}\right) \tag{2.13}$$

Expressing Equation 2.10 in terms of permeability, *Q*, gives Equation 2.14., where *Q(T)* is expressed as Equation 2.13.

$$J_{H_2} = \frac{Q(T)}{l}\left(P_{H_2,2}^{0.5} - P_{H_2,1}^{0.5}\right) \tag{2.14}$$

Permeance, *F*, defined as Equation 2.15 with unit mol/($m^2$*h*$atm^{0.5}$) is more convenient to describe the permeation characteristic of a membrane in most practical cases, where the membrane thickness is not certain. While the permeability is independent of membrane thickness, the permeance (*F*) is inversely proportional to the membrane thickness.

$$F = \frac{Q}{l} \tag{2.15}$$

Sieverts' equation (Equation 2.10 or 2.14) is derived based on several assumptions as mentioned previously. In cases that the assumptions become invalid, the Sieverts' Law becomes invalid and the *n* value, the exponent of the pressure, deviates from 0.5. For example, if the atomic H/Pd ratio, $n_{H/Pd}$, is too high to be neglected in Equation 2.3 due to the high hydrogen pressure in the gas phase, the Sievert's equation, therefore becomes not valid.

Another example is that when the assumption that the solid diffusion of hydrogen atom in the Pd layer is the rate-limiting step is no longer valid. Since this causes the

adsorption and dissolution steps being not at equilibrium, Equation 2.7 is not valid and the Sievert's equation is no longer valid. One circumstance that causes the rate limiting step being not the diffusion is when the Pd layer is very thin. In case of very thin Pd layer, the diffusion rate might be close to or even faster than adsorption rate causing adsorption to become the rate limiting step. Since the adsorption hydrogen flux is dependent on the hydrogen pressure rather than the square root of the hydrogen pressure, the *n*-value deviates from 0.5 and becomes close to 1.

Ward and Dao (1999) proposed a hydrogen permeation mechanism to determine the minimum thickness of Pd film that the deviation of the *n*-value occurred due to the change of rate limiting step for hydrogen transport from diffusion to adsorption. The calculation from their model showed that when the thickness was below 1 $\mu$m, the rate limiting step of hydrogen transport through the Pd film was not the diffusion and the *n*-values deviated from 0.5. Several researchers have reported their results to be in good agreements with the model proposed by Ward and Dao (1999). Zhao et al. (1998, 2000) observed deviations of *n*-values from 0.5 on the Pd membranes of thicknesses less than 1 μm. Wu et al. (2000) also reported an *n*-value of 1for the Pd membrane of thickness of 0.3 – 0.4 $\mu$m. However, several researchers also found the deviation of *n*-value for thicker Pd membranes. Tong and Matsumura (2004) and Tong et al (2005a) measured *n*-values of 1 for a 6 $\mu$m thick and a 3 μm thick Pd membrane. They also reported that the activation energy for hydrogen permeation of the reported Pd membranes were higher (16 - 18 kJ/mol) and reasoned that the surface adsorption was the rate-limiting step.

In addition to the thickness of Pd film, the impurities such as CO or $H_2S$ adsorbed on the Pd surface can also possibly cause the rate limiting step to change from diffusion

to adsorption and the deviation of *n*-values from 0.5. The adsorption of impurity molecules not only reduces active sites but also increases the energy barrier for hydrogen dissociative adsorption, resulting in the significant decrease of hydrogen adsorption rate and hydrogen permeance. Peden et al. (1986) studied the effects of the presence of $H_2S$ on $H_2$ permeating through Pd. They found that the rate-limiting step for hydrogen transport through Pd became the surface adsorption when the adsorbed sulfur layer was larger than 0.4 monolayer (ML). Guazzone et al. (2006) observed that the *n*-value varied from 0.67 to 0.53 of a pure Pd membrane when heating from 300 to 500$^{o}$C. The *n*-value variation was attributed to the removal of contaminants from the membrane surface upon heating.

Another assumption made when deriving the Sieverts' equation is that the hydrogen diffuses only through the Pd lattice. When the Pd film is not dense (i.e. significant amount of cracks and pinholes presented in the Pd film), the Sieverts' equation is no longer valid due to that hydrogen also transports through the cracks and pinholes. The hydrogen flux transport through cracks and pinholes is the sum of Knudsen diffusion and viscous flow dependent on pressure difference. This model is known as the dusty-gas model (Mason and Malinauskas, 1983), and is expressed in Equation 2.16.

$$J = \left(F_k + F_v \cdot P_{avg}\right) \cdot \Delta P = \left\{ \frac{2}{3}\sqrt{\frac{8}{\pi}} \frac{\varepsilon \mu_k r}{l\sqrt{RTM}} + \frac{1}{8} \cdot \frac{\varepsilon \mu_v r^2}{l \eta RT} \cdot P_{avg} \right\} \cdot \Delta P \qquad (2.16)$$

Guazzone et al. (2006) studied the relation between the *n*-values and the ideal $H_2$/He selectivities of the Pd membranes. According to the results, when the selectivity was below 15 – 20, the *n*-values were close to 1 due to the predominance of the Knudsen

diffusion and viscous flow of hydrogen. On the other hand, the transport of hydrogen follows Sievert's equation when the selectivity was above 400.

In the case of composite membranes, significant mass transfer resistance of the support also caused the *n*-value to vary. Henis and Tripodi (1981) used the mass transfer resistance concept to model the mass transfer rate of a component *i* though a composite membrane. The permeating flux for a component *i* through a membrane layer can generally be expressed as Equation 2.17, where $J_i$ is the permeating flux for component *i*, $Q_i$ is the permeability of component *i* through the layer, $\Delta P_i$ is the pressure difference between the layer and *l* is the thickness of the layer.

$$J_i = Q_i \Delta P_i / l = \Delta P_i / R_i \tag{2.17}$$

By making an analog to an electrical circuit with the permeating flux being equivalent to the electrical current and the pressure difference being equivalent to the electrical potential, the conceptual resistance for component *i* to permeate through a membrane layer is expressed as Equation 2.19.

$$R_i = l / Q_i \tag{2.18}$$

For a composite membrane consisting of several layers, the total resistance for component *i* to transport can be expressed as the sum of resistance of each layer as shown in Equation 2.20.

$$R_{tot} = \frac{l_{tot}}{Q_{tot}} = R_1 + R_2 + R_3 + ..... = \frac{l_1}{Q_1} + \frac{l_2}{Q_2} + \frac{l_3}{Q_3} + ..... \tag{2.19}$$

In case of hydrogen permeating through a dense Pd composite membrane, the driving force for hydrogen to transfer through the dense Pd layer is the pressure difference in half power rather than pressure difference. As a result, the mass transfer resistance of a dense Pd layer becomes a function of pressure as shown in Equation 2.20. It should be noted that the notation 2, 3, was referred to the other layers in the composite Pd membrane depending on the structure of the composite membrane (e.g. $Q_2$ and $l_2$ were the permeability and the thickness of the intermetallic barrier and $Q_3$ and $l_3$ were the permeability and the thickness of the porous support.)

$$R_{tot} = R_{Pd} + R_2 + R_3 + ..... = \frac{l_{Pd}}{Q_{Pd}(P_{H,2}^{0.5} - P_{H,1}^{0.5})} + \frac{l_2}{Q_2} + \frac{l_3}{Q_3} + ..... \quad (2.20)$$

According to Equation 2.20, small thickness or high permeability of a layer contributes negligible mass transfer resistance for hydrogen transport in composite Pd membrane. Typically, the mass transfer resistance of a porous support, which has extremely high permeability compare to the dense selective layer, is negligible (Guazzone, 2006). As a result, hydrogen transport through the Pd composite membranes follows Sieverts' equation and *n*-values are close to 0.5. However, in case of significant mass transfer resistance from the support, *n*-values deviate from 0.5. Collins and Way (1993) reported an *n*-value of 0.573 on the palladium alumina composite membrane and attributed the deviating *n*-value to the high support resistance.

## 2.3 Porous Supports, Supports Modification, and Intermetallic Diffusion Barrier

Today, the main trend of hydrogen permeation membranes is the composite membranes, which consist of a selective dense metal layer and a porous support. The composite membranes are capable of achieving thin selective layer with robust mechanical strength resulting in high permeation flux and low Pd membrane cost with wide applications compared to metal-foil membranes.

Porous metal, ceramic, and Vycor glass are usually used as the porous support depending on the application. Ceramics are widely used as porous supports for preparing Pd composite membranes (Uemiya et al., 1991b; Uemiya et al., 1997; Zhao et al., 1998). One advantage of ceramic supports is the easy control of the pore size. As a result, ceramic supports usually have smaller pore size and narrow pore size distribution. In addition, ceramics show high thermal stability. No inter-diffusion between ceramic supports and hydrogen selective metal layer occurs at high temperatures. Vycor glasses also have the advantages of small and uniform surface pore size and high thermal stability. Therefore, they were also widely used as supports (Uemiya et al., 1991a; Yeung et al., 1995). Bryden and Ying (1995) observed that the average pore size of the Vycor glass was 40 Å and high thermal stability of the Vycor glass up to 600$^{o}$C. However, the large difference in thermal expansion characteristics between the ceramic or Vycor glass supports and hydrogen selective metal layers might cause the deformation and cracking of the membranes during thermal cycling. Furthermore, since ceramics and Vycor glasses are usually brittle and fragile, it is difficult to handle the sealing and welding for scaling

up the hydrogen permeation applications when using the Pd composite membranes prepared on those supports.

In contrast, porous metal supports such as porous stainless steel (PSS), porous Inconel or Hastelloy supports, have similar thermal expansion characteristics to the hydrogen selective metal layers. As a result, less strain is generated between the hydrogen selective layers and the porous metal supports during the thermal cycling. In addition, due to the high ductility of metal, porous metal supports are easier to handle for large scale gas permeation applications. Therefore, porous metal supports are getting increasing attention for fabricating Pd based composite membranes (Shu et at., 1993a; Mardilovich et al., 1998). However, there are a couple of challenges when using porous metal supports. One is the poor control of the pore size and pore size distribution. Usually, porous metal supports have larger pore size and wider pore size distribution. Mardilovich et al. (2002) estimated that the thickness required to obtain a dense Pd layer is roughly three times the diameter of the largest pore on the PSS support surface. Since smaller thickness of hydrogen selective layer is preferred due to not only lower cost but also higher hydrogen permeance, modification of the porous supports to reduce the pore size is necessary. Developments in modification of the porous supports will be discussed later in the section.

Another drawback of the porous metal supports is that the intermetallic diffusion between the hydrogen selective metal layers and porous metal supports occurs at elevated temperatures, causing the decrease of hydrogen permeance. A diffusion barrier layer between hydrogen selective metal layers and porous metal supports is required to avoid such intermetallic diffusion from occurring. Efforts have been devoted by several

researchers in the past to develop the diffusion barrier on the porous metal supports and the development will be discussed in detailed later in this section.

In addition to porous ceramics (alumina), Vycor glasses, and porous metals, other porous materials have also been reported as the supports for hydrogen permeating Pd based membranes. Wu et al. (2000) used porous $TiO_2$ as supports for preparing Pd membranes. $TiO_2$ was selected for its photo-catalytic properties for the Photo-Catalytic Deposition (PCD) activation process, which involved UV light irradiation reaction. Tong et al. (2004a, b, 2005b) used micro-fabricated silicon as supports for preparing Pd/Cu, Pd/Ag alloy membranes. Silicon wafer is easy to be micro-fabricated to gain uniform pore size (in this case, pore size was 5 $\mu$m in diameter). Starkov et al. (2005) also used electro-chemical etched silicon wafers as porous supports for preparing Pd/Ag alloy membranes. The electro-chemical etching process resulted in 23 - 72% porosity on Si wafer, which correspond to pore size of 0.9 - 4.5 $\mu$m in diameter. Buxbaum and Kinney (1996) used niobium and tantalum as non-porous supports, which are also selective to hydrogen with even higher permeabilities than Pd. However, Nb and Ta don't have the catalytic activity for hydrogen dissociation and need to be coated with a Pd layer on the surface for selective-permeating $H_2$. Another disadvantage of Nb and Ta was the poor chemical stability, which were affected by the surface contaminates such as CO more than Pd. In addition, the critical temperatures for hydrogen embrittlement of Nb and Ta are even higher than Pd (350°C for Ta and 420°C for Nb) resulting in an even smaller operation window for those membranes. Edlund and McCarthy (1995) also prepared Pd membranes on non-porous supports with high selectivity to hydrogen. Instead of niobium

and tantalum, they used vanadium as supports. However, the intermetallic diffusion of Pd and V at 700$^{o}$C caused the failure of the hydrogen permeation test.

In order to decrease the pore size as well as the thickness of dense hydrogen selective layers on porous supports, several surface modifications have been reported in the literature. Filling the large pores is the most widely used approach and the resultant supports are usually termed as asymmetric supports. Li et al. (1996) modified the $\alpha$–alumina supports with a thin $\gamma$–alumina layer by the sol-gel calcination process, resulting in the average pore size of 5 nm and a dense Pd layer of 1 $\mu$m. Uemiya et al. (1991b), Jayaraman et al (1995a,b), and Xomeritakis et al. (1996) used similar $\gamma$ phase alumina / $\alpha$ phase alumina asymmetric supports for Pd-based membranes preparation.

Nam and Lee (2000) pretreated PSS supports with Ni powder to obtain smoother surfaces for further Pd deposition and the resultant dense Pd alloy layers were less than 2 μm. Wang et al. (2004) used zirconium oxide ($ZrO_2$) powder to modify the PSS supports. The resultant Pd membrane was 10 $\mu$m with a hydrogen permeance of 17.6 $m^3/(m^3*h*atm^{0.5})$ and a $H_2$/Ar selectivity of 1500 at 500°C. Guazzone (2005) modified the support surface by putting alumina powder with successively smaller particle sizes. The resultant membrane was 6 μm thick with a permeance of 39 $m^3/(m^2*h*atm^{0.5})$ and an ideal $H_2$/He selectivity of 800 at 500°C. The modification also improved the thermal stability of the membrane with the observation of the stable permeance at 500°C for 1000 hours. Similarly, Gao et al. (2005) deposited a thin $ZrO_2$ layer to modify the surface and to act as the intermetallic diffusion barrier at the same time. They dipped the supports in $ZrOCl_2.8H_2O$ sol-gel followed by the heat treatment at 500$^{o}$C for 6 hours to form a $ZrO_2$

layer on the PSS supports. The resultant 10 $\mu$m thick Pd/Cu (54wt% Cu) membrane showed a stable permeance of 0.89 $m^3/(m^2*h*atm)$ at 753K.

Tong and Matsumura (2004) immersed the PSS supports into $Al(OH)_3$ solution with ultrasonic vibration and vacuum suction from the inside of the tube. The surface pore size of the support was decreased significantly after the modification, and the resultant dense membrane was 6 $\mu$m thick. Before testing, the membrane was heat treated at 500$^o$C for 3 hours in hydrogen to recover the support pores by the evaporation of the water from the $Al(OH)_3$. As a result, the mass transfer resistance due to the modification was decreased. A hydrogen permeance of 23 $m^3/(m^2*h*atm)$ with the selectivity of infinite at 500°C was reported. Tong et al. (2005a) used the similar approach to prepare a 3 $\mu$m Pd membrane on PSS with a permeance of 36 $m^3/(m^2*h*atm)$ and an infinite selectivity at 500°C which was stable for 200 hours of testing. Ayturk (2007) also modified the PSS supports by the use of $Al(OH)_3$ solution and denser alumina hydroxide slurry was applied. The method was reported to provide effective fabrication of smoother support surfaces, resulting in thinner and more uniform membranes.

If the pore size is too small, however, it may significantly increase the mass transfer resistance of porous supports resulting in the increase of the overall mass transfer resistance for hydrogen permeation. Mardilovich et al. (2002) estimated that a porosity less than 0.2 on the supports caused significant mass transfer resistance contribution from the supports. It should be note that the small porosity reported by Mardilovich et al. (2002) was resulted from the support oxidation at high temperatures. The increase in the *n*-value due to mass transfer resistance observed by Collins and Way (1993) occurred when the surface pore diameter was less than 10 nm on porous ceramic supports.

In addition, the adhesion between the hydrogen selective layer and support may be poor if the surface of the support is too smooth due to the pore size being too small. The deposited Pd or Pd/Ag film on the extremely smooth silicon wafers can be easily peered off (Klette and Bredesen, 2005). The phenomenon is an indication of poor adhesion between the selective layers and the extremely smooth support surface.

As mentioned earlier, the intermetallic diffusion between hydrogen selective metal layers and porous metal supports deteriorated the performance of the composite membranes at elevated temperatures. Bryden and Ying (2002) observed the decline of hydrogen permeance of Pd membranes increased as the iron content increased at 200$^{o}$C. Gryaznov et al. (1993) reported the 50% decline of the Pd/Ru alloy membrane permeance after 1000 hours at 800ºC due to the diffusion of the elements in the metal support into the selective layer. The temperature where the intermetallic diffusion occurs is roughly the half of the metal melting point in Kelvin, which is termed as Tamman temperature. At the Tamman temperature, the mobility of metal atoms increases significantly due to thermal vibration resulting in the diffusion into the adjacent metal. Edlund and McCarthy (1995) observed that hydrogen accelerated the intermetallic diffusion process between Pd and V at 700$^{o}$C.

Several studies have shown that putting a thin layer of high melting point materials as intermetallic diffusion barriers between the selective metal layers and the metal supports prevented such intermetallic diffusion effectively. Gryaznov et al. (1993) introduced a thin layer of high melting point metals and metal oxides, such as tungsten, tantalum oxide, magnesia, alumina, and zirconia, between the selective layers and the supports to obtain high thermally stable membranes. However, too thick the layer of the

intermetallic diffusion layer caused the decline of the permeance (Gryaznov et al., 1993). Gryaznov et al. (1993) found that a 1.2 $\mu$m layer of alumina caused an 8% decrease and a 0.08 μm layer of molybdenum caused a 30 % decrease in hydrogen permeance.

Edlund and McCarthy (1995) pressed a thin layer of aluminum oxide that had been calcined at 800$^{o}$C for 12 hours between the Pd layers and vanadium supports to prevent intermetallic diffusion. The permeance of the membrane was stable at 700°C for 80 hours, while a similar membrane but without the alumina layer showed a sharp permeance decline at the same temperature. Shu et al. (1996) examined 0.1 $\mu$m TiN as an intermetallic diffusion barrier between PSS supports and Pd/Ag layers. They reported that with a 0.1 $\mu$m TiN layer, the membrane showed thermal stability at temperature as high as 973K according to Auger electron depth profiling analysis. Nam and Li (2001) deposited a silica layer by sol-gel followed by calcination at 1073K for 5 hours between Pd/Cu layers and Ni modified PSS supports. They reported the improved membrane remained the same structure after 40 days at 723K.

Ma et al. (2000) introduced an oxide layer prepared by in-situ oxidation of PSS as the intermetallic diffusion barrier between the selective layer and PSS supports. They oxidized PSS supports at 900°C for four hours to produce an oxide layer rich in stable $Cr_2O_3$ and found the hydrogen permeance of the resultant Pd membrane to be stable for 1000 hours at 350°C. Ma et al. (2004) observed that a higher oxidation temperature yielded a thicker oxide layer with little effect on the mean pore size indicating that the oxidation did not constrict the internal pore system. Engwall et al. (2003) determined the mass transport resistance of the oxidized support. They reported that the contribution of the oxidized support (oxidized at 600$^{o}$C) to the total membrane pressure drop was 1.9%,

indicating negligible effect of the oxidation layer formed at high temperature on the support resistance to mass transfer. In addition to the oxide layer, Ma et al. (2007) also deposited a porous Pd/Ag barrier layer between the support and the dense layer as an intermetallic diffusion barrier. They reported a stable hydrogen permeance of 15.6 $m^3/(m^2*h*atm^{0.5})$ at 500°C for 500 hours on the 24 $\mu$m thick (including the Pd/Ag barrier layer) Pd membrane.

## 2.4 Pd alloy

There are several advantages to alloy Pd with other elements for fabricating the hydrogen selective membranes. Firstly, the operational temperature window can be increased by alloying Pd with other elements due to the critical temperature for hydrogen embrittlement can be decreased after alloying. In addition, the hydrogen permeability and chemical stability can be enhanced by alloying Pd with other elements.

The relative hydrogen permeability of binary Pd alloys to pure Pd foil at 350 and $500^oC$ is given in Figure 2.3. Several alloys such as Pd/Y, Pd/Ce, Pd/Ag, and Pd/Au exhibited higher hydrogen permeability than pure Pd. Some ternary alloys also showed higher permeability than pure Pd. $Pd_{93.5}Ru_{0.5}In_{6.0}$ and $Pd_{80}Ag_{19}Rh_1$ showed 2.8 and 2.6 times higher hydrogen permeability than pure Pd (Gryaznov et al., 2000).

Among Pd alloys, Pd/Ag and Pd/Cu are most studied due to the low cost of the elements. In addition, these alloys enhanced the membrane properties in either hydrogen permeability or chemical stability. Recently, alloying Pd with Au was getting increasing attention since Pd/Au alloys potentially enhanced both hydrogen permeability and chemical stability of the membranes.

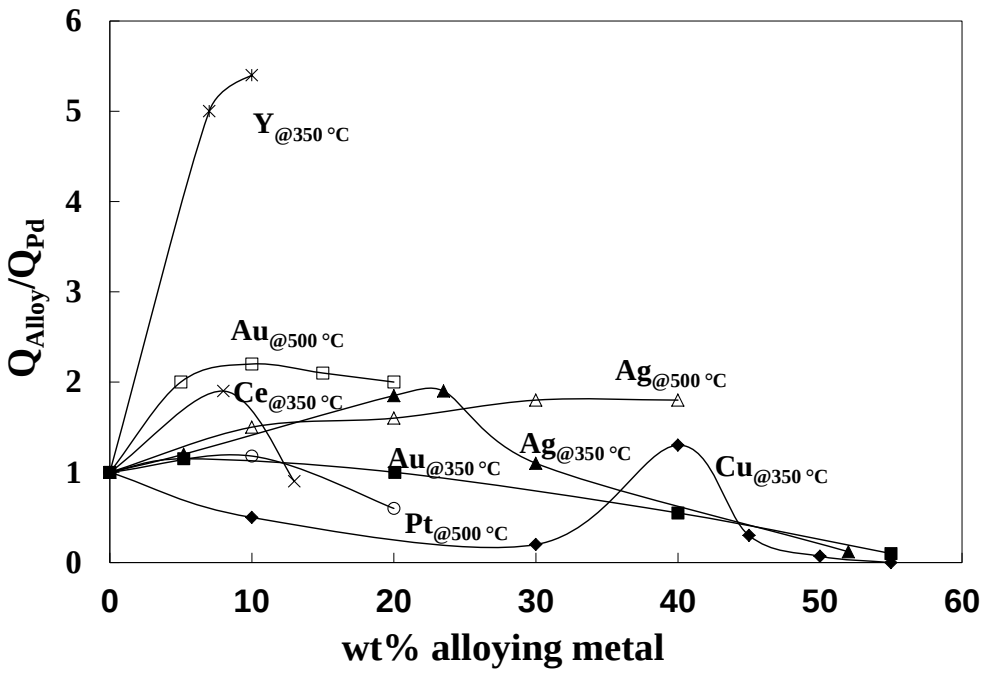


Figure 2.3. Permeability of Pd alloys to pure Pd as a function of alloying metal composition.[2]

In addition to minimize the hydrogen embrittlement (Hunter, 1960), the most significant advantage to alloy Pd with Ag is the increase of hydrogen permeability (McKinley, 1969). The hydrogen permeability of Pd/Ag alloy could be 1.7 - 2.0 times higher than pure Pd within the Ag composition of 10 - 30wt% (McKinley, 1969; Knapton, 1977; Holleck, 1970; Gryzanov et al., 2000). The high hydrogen permeability of the Pd/Ag alloy was resulted from the high solubility of H atom. Sieverts et al. (1915) and Holleck (1970) reported that the solubility of H atom in Pd/Ag showed a maximum value within Ag composition of 20 - 30wt%. Due to the beneficial characteristics, composite Pd/Ag alloy membranes for the hydrogen separation were extensively studied (Uemiya et al., 1991b; Shu et al., 1993a; Athahyde et al., 1994).

[2] Data at 350ºC adapted from Knapton, 1977, data at 500ºC taken from Gryaznov, 2000

Pd/Cu alloys also exhibited excellent ability to prevent hydrogen embrittlement at elevated temperatures in addition to its low cost. Karpova and Tverdoskii (1959) observed that the critical temperature for the $\alpha$-$\beta$ phase transition of Pd/Cu alloy with 40wt% Cu was below 25$^{o}$C. Another advantage of Pd/Cu alloys (FCC) was the high sulfur resistance (Morreale et al., 2004; Gao et al, 2004; Kulprathipanja et al., 2005; Pomerantz and Ma 2009). One drawback to alloy Pd with Cu is the decrease of hydrogen permeability except for a peak permeability at 40 wt% Cu as shown in Figure 2.3. Pd/Cu alloys possess both BCC and FCC phases depending on Cu composition. Peak hydrogen permeability of Pd/Cu alloy at 40 wt% Cu was resulted from significantly high hydrogen diffusivity in BCC phase (Subramanian and Laughlin, 1991; Kamakoti and Sholl, 2003; Kamakoti et al., 2005). Pomerantz and Ma (2011) fabricated the composite Pd membranes with a sub-micron FCC Pd/Cu alloy layer on the surface which potentially exhibited higher sulfur resistance and minimized the permeability reduction caused by the Cu alloying at the same time. Due to the ability to reduce the hydrogen embrittlement and the sulfur poisoning, composite Pd/Cu alloy membranes, therefore, were also widely studied (Uemiya et al., 1991a; Nam and Lee, 2001; Roa et al., 2003; Tong et al., 2004; Pomerantz and Ma 2009, 2011).

Because of the higher cost of Au, Pd/Au alloy membranes for hydrogen separation were less studied in the past compared to Pd/Ag or Pd/Cu alloy membranes. However, due to the two-fold beneficial characteristics of Pd/Au alloys in terms of higher permeability and enhanced chemical stability, Pd/Au alloy membranes have received increasing attention recently.

Pd/Au alloys exhibit higher hydrogen permeability than pure Pd within the Au composition of 5 – 20 wt% as shown in Figure 2.3. Similar to Pd/Ag alloys, higher hydrogen permeability was resulted from higher hydrogen solubility in Pd/Au alloys. Figure 2.4 shows the hydrogen solubility in Pd/Au alloys as a function of Au composition. A maximum hydrogen solubility can be seen in the Au composition range between 20 – 40 wt% Au. Since permeability is the product of solubility and diffusivity, by considering that the hydrogen diffusivity in Pd/Au alloys decreased as increasing Au composition (Sonwane et al., 2006a, b), a shift of the peak hydrogen permeability of Pd/Au alloys from peak solubility as a function of Au composition is expected.

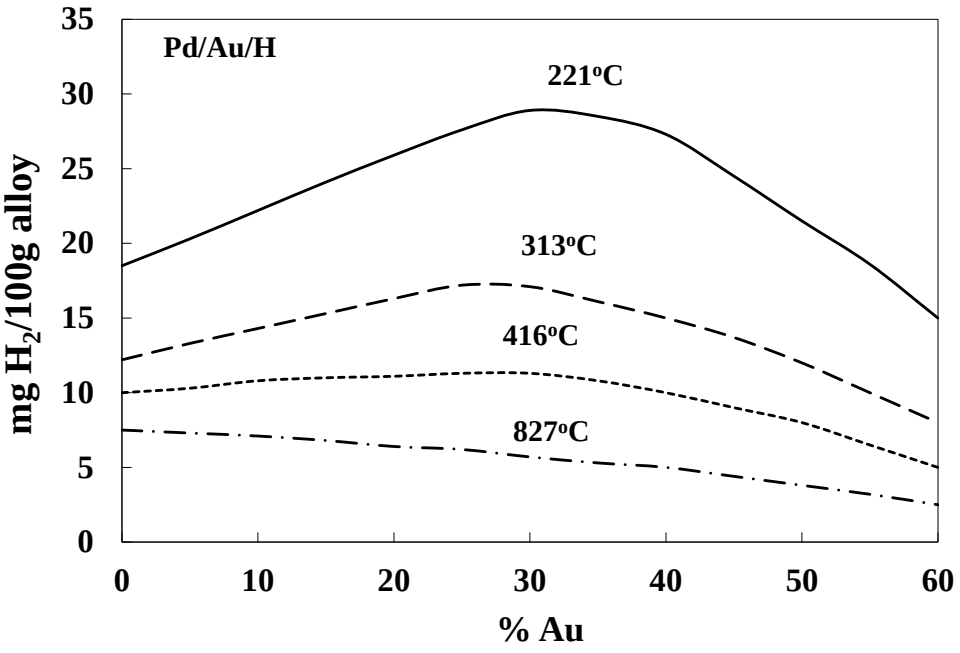


Figure 2.4. Solubility of H in Pd/Au alloys at 1 atm (Adapted from Sieverts et al., 1915).

Sonwane et al. (2006a, b) modeled the hydrogen permeability of Pd/Au alloys. They used density functional theory (DFT) and kinetic Monte Carlo simulations (KMC)

to investigate the solubility, diffusivity, and permeability of hydrogen in Pd/Au alloys over the temperature range of 400 - 1200K. According to their calculation, hydrogen solubilities were higher than pure Pd within Au composition of 10 – 30 wt%. They attributed the higher solubility to the strong biding sites for hydrogen atoms in Pd/Au alloys. In addition, by taking hydrogen diffusivity into account, they predicted a maximum hydrogen permeability at Au composition of 12 wt%, which was 4.8 times of pure Pd.

The hydrogen permeability of Pd/Au alloy is lower than Pd as Au composition was above 20 wt%, and continues to decrease as increasing Au composition as shown in Figure 2.3. According to the Pd-Au phase diagram as shown in Figure 2.5, Pd and Au form disordered FCC Pd/Au alloys where Pd or Au atoms randomly occupy the lattice positions in most temperature and composition range below melting point. However, in certain temperature and composition range, ordered structures (super lattice) including PdAu, $PdAu_3$, and $Pd_3Au$ formed where the lattice positions for Pd and Au atoms are fixed. Since these ordered structures have the same FCC structure as disordered alloys with only a slight change in unit size, the properties of the ordered structure alloys are considered to be very similar to the disordered alloys. Indeed, the smooth and continuous hydrogen permeability change as a function of Au composition indicated that the hydrogen permeability is only a function of Au composition with the crystal structure (ordered or disordered) showing no effect.

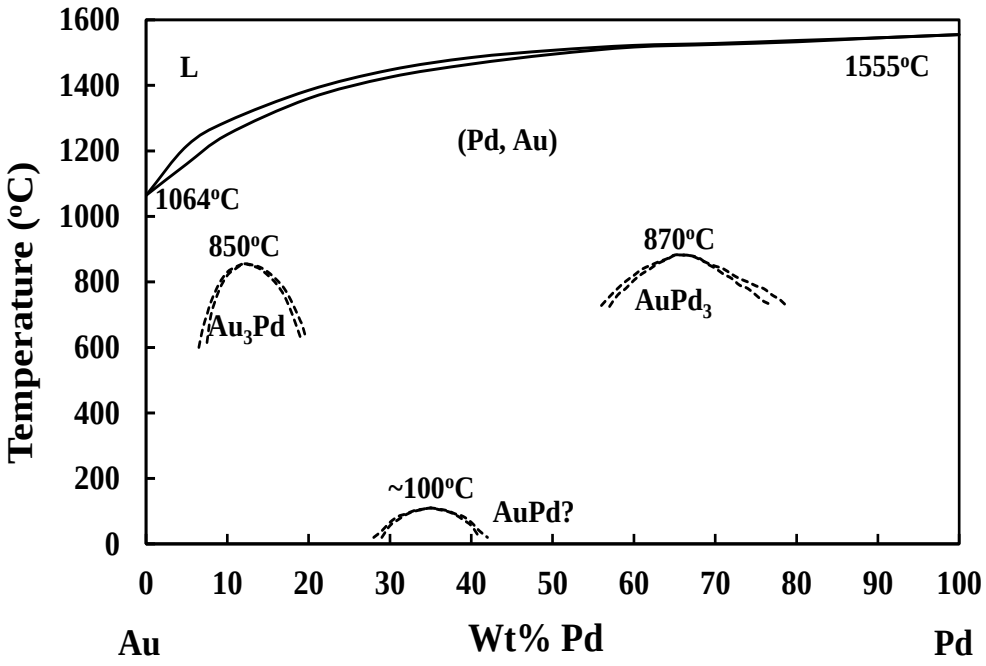


Figure 2.5. Phase diagram of Pd/Au (Adapted from H. Okamoto, T.B. Massalski, 1987).

There are conflicting results regarding the effect of Au content on the hydrogen solubility and permeability in the literature. Grashoff et al. (1983) reported significantly low solubilities in Pd/Au alloys, while others have found the opposite results (Grayznov et al., 2000; Sonwane et al, 2006a, b). McKinley (1966) showed that Pd/Au alloys showed only a slightly higher hydrogen permeability than pure Pd within 5 – 20 wt% Au range at 350$^{o}$C. On the other hand, Gryaznov et al. (2000) reported that the Pd/Au alloys within the same Au composition range exhibited hydrogen permeabilities 2 times higher than pure Pd at 500$^{o}$C. The discrepancy could be due to the non-uniform Au distribution in the Pd/Au alloys tested in the cited literature. More discussion will be provided later in *Section 6.3.1*.

In addition to enhancing the hydrogen permeability, Pd/Au alloys also exhibited high resistance to poisoning by impurities such as $H_2S$ (McKinley, 1967). Among all poisoning impurities, sulfur compounds show the most severe poisoning effect on Pd-based membranes and the detailed discussion will be given in *Section 2.6*.

Other Pd alloys were also studied in the past for fabricating hydrogen selective membranes. Nam and Lee (2000) prepared Pd/Ni alloy membranes on PSS supports. They reported that the Pd/Ni alloy membranes showed not only no hydrogen embrittlement, but also a better hydrogen perm-selectivity at temperature of 623 - 823K. Bryden and Ying (1998) prepared nano-structured Pd/Fe alloy membranes. They reported that no $\alpha$-$\beta$ phase transformation occurred and rapid adsorption of hydrogen at room temperature of Pd/Fe alloy membranes. The hydrogen solubility decreased with increasing Fe content. In addition, they reported the stability of the grain structure of Pd/Fe alloys up to 400$^{o}$C with no growth in the grain size. Itoh et al. (1995, 1998) prepared amorphous $Pd_{(1-x)}Si_{(x)}$ membranes for hydrogen separation. They reported that the amorphous Pd/Si alloy showed a higher hydrogen permeability than crystallized ones and a resistance to the hydrogen embrittlement at the testing temperatures of 50 - 300$^{o}$C. The amorphous Pd/Si alloy ribbons were prepared by rapid quenching from the melts with the use of a single roller spinning technique. The prepared Pd/Si ribbons had an average thickness of 40 $\mu$m.

## 2.5 Composite Pd-based Membrane Fabrication Techniques

For fabricating Pd and Pd alloy composite membranes, several deposition techniques have been proposed, such as sputtering, chemical vapor deposition, pyrolysis,

electroplating, electro-less plating. The characteristics of each deposition technique are discussed in this section.

### *2.5.1 Sputtering*

During the sputtering deposition, the energized plasma ions hit the target of the desired deposition element causing the atoms to leave the target and deposit on the support. Plasma, which is composed of elections and gas ions, is formed by the low pressure gas in the high electromagnetic field. Sputtering deposition technique produces high quality thin film with extremely good control of film composition, crystalline structure, grain size and phase. However, high vacuum environment and extremely clean and smooth surface of the supports are required for the sputtering deposition, resulting in high cost of equipment and complicated process. In addition, the deposition technique is difficult to apply on the supports of complex shape (e.g. tubular). As a result, it is undesirable for industrial applications.

Athahyde et al. (1994) prepared Pd/Ag alloy membranes with 24 at% Ag by the sputtering deposition with the alloy target of the same composition (76 at% Pd+24 at% Ag). The Pd/Ag alloy layers of 0.025 – 0.1 $\mu$m were deposited on the porous polymer supports pre-modified with a poly dimethylsiloxane layer. Athahyde et al. (1994) reported the permeance of a 0.05 $\mu$m Pd/Ag membrane was 0.5 $m^3/(m^2*h*atm)$ at 25ºC. The long term stability and selectivity test with a 50/50 mol% $H_2/CO_2$ mixture was also performed. A stable hydrogen permeance over a 1200 hour testing period was reported. However, the selectivity decreased from 100 to 50, resulting in $H_2$ purity in the permeate stream decreased from 99% to 98%.

Bryden and Ying (1995) used DC magnetron sputtering to prepare ultra-thin Pd membranes on porous Vycor glass supports. The thickness of the Pd layers ranged from 0.5 - 5 $\mu$m. They observed the significant formation of pinholes and cracks after testing at 200$^{o}$C in $H_2$, which they reasoned to be due to the hydrogen embrittlement. They also observed the significant grain growth (by two orders of magnitude) of the Pd layer after testing at 200$^{o}$C, which they attributed to the presence of large interface between the substrate and the film.

Jayaraman et al. (1995a,b) deposited Pd on the polished and γ-alumina modified porous α-alumina supports by radio frequency (RF) magnetron sputtering. Less than 0.5 $\mu$m thick dense Pd layers were fabricated. However, no gas permeation data of the prepared membranes were reported. Jayaraman and Lin (1995a,b) prepared Pd/Ag alloy membranes with 25 wt% Ag by the same sputtering technique on the similar ceramic supports. The deposited Pd/Ag layers had thicknesses ranged from 0.25 – 0.5 $\mu$m. The hydrogen permeance of 2.3 $m^3/(m^2*h*atm)$ with a $H_2/N_2$ selectivity of 6 at 400°C on a 0.35 $\mu$m thick Pd/Ag membrane was reported. The extremely low selectivity was reasoned to be the result of pinholes formation in the Pd/Ag layer.

Zhao et al. (2000) deposited Pd-Ag alloy by sputtering with a Pd/Ag alloy (24 wt% Ag) target on the α-alumina supports pre-modified with γ-alumina sol-gel. The resultant Pd/Ag membrane had the thickness less than 1 μm. The $H_2/N_2$ selectivity of 1000 at 411$^{o}$C was reported without providing the hydrogen permeance.

Tong et al (2004a) deposited Pd-Cu alloy on the micro-machined silicon support by the dual-sputtering, where two metal targets were used and deposited simultaneous on the support. An extremely thin layer of Ti was deposited on the Si supports before the Pd

and Cu deposition to enhance the adhesion. The 0.2 - 0.75 $\mu$m Pd/Cu alloy membrane with 23 wt% Cu showed a $H_2$ permeance of 129 $m^3/(m^2*h*atm)$ and a $H_2$/He selectivity of 500 at 725K. Tong et al. (2004b) fabricated Pd/Ag membranes on micro-fabricated silicon support by the same technique. The micro-fabricated Si supports had uniform pore size of 5μm. Tong et al. (2005b) later reported the gas permeation data of the prepared Pd/Ag membranes. The 0.5 $\mu$m Pd/Ag alloy membrane with 23 wt% Ag exhibited a $H_2$ permeance of 322 $m^3/(m^2*h*atm)$ with a $H_2$/He selectivity of 1500 at 723K.

### *2.5.2 Chemical Vapor Deposition*

Chemical vapor deposition (CVD) technique involves chemical reaction during the plating process. The basic principle of CVD is the decomposition or reduction of the desired element containing compounds (usually is gaseous) on the support surface. The reactions occur at support surface with the energy provided through the support by different means (e.g. by heating the support). After decomposition, the solid element was deposited on the support surface while other compounds (usually is gaseous) diffused away from the support. Different means of providing energy, such as plasma, laser, etc., resulted in different kinds of CVD, such as Plasma-enhanced CVD (PECVD) or Laser-Enhanced CVD (LECVD). CVD is capable to deposit single metal or alloy with nice quality in a small thickness. However, the process involves numbers of steps including the diffusion of gaseous compounds to the support surface and decomposition reactions. As a result, numerous variables need to be considered, such as the flux rate, and partial pressure of the compound, substrate temperature, etc. Such tedious and complicated procedure, therefore, is unpractical for industrial applications.

Yan et al. (1994) deposited Pd on the porous α-alumina supports with the metal-organic chemical vapor deposition (MOCVD) technique with the metal source of palladium acetate. A hydrogen permeance of 80 $m^3/(m^2*h*atm)$ with a $H_2/N_2$ selectivity of 1000 on a 2 μm thick Pd membrane prepared was reported.

Xomeritakis et al. (1996) used counter-diffusion CVD to prepare thin Pd membranes on the γ-modified α-alumina supports. Palladium chloride vapor and hydrogen were used as the Pd precursor. 0.5 - 1 $\mu$m thick Pd membranes were prepared, and hydrogen permeances of 4 - 8.1 $m^3/(m^2*h*atm)$ at temperature from 350 - 450$^oC$ with a selectivity from 50 to 1000 was reported. In addition, the activation energy for hydrogen permeation of the prepared membranes was 38kJ/mol. They attributed these high activation energies to the rate limiting step of hydrogen transport though the submicron Pd membrane being the surface adsorption.

Uemiya et al. (1997) deposited Pd, Ru and Pt on the alumina supports by the CVD technique. They estimated that the effective thickness of Pd membrane was 5 μm by considering not only the gravimetric change but also the fact that the deposit was into the pores under the surface. A hydrogen permeance of 11 $m^3/(m^2*h*atm^{0.5})$ and a $H_2/N_2$ selectivity of 240 were measured on the Pd membrane at 400°C. They reported that the Pd membrane prepared by the CVD showed 1.6 times higher hydrogen flux in comparison to the Pd membrane previously prepared by the electroless plating (Uemiya et al., 1991a). They attributed the higher flux observed on the Pd membrane prepared by the CVD to a different permeation mechanism, which consisted of both the solution-diffusion and surface diffusion of spillover hydrogen on the deposited Pd in the pores.

Itoh et al. (2005) prepared a 2 – 4 $\mu$m Pd membrane on the tubular alumina support with forced flow CVD. The pressure difference between the tubular support caused by the forced flow resulted in the preferential deposition of Pd on the walls of support pores. The preferential deposition plugged the pinholes effectively, resulting in a thinner membrane. The membrane showed a hydrogen permeance of 102 $m^3/m^2*h*atm^{0.5}$ and a $H_2/N_2$ selectivity of 5000 at 300°C.

Similar to CVD, the spray pyrolysis plating technique also involves the decomposition of metal-salt solution. The metal containing solution droplets are sprayed into a high temperature flame (usually hydrogen-oxygen flame), where the droplets of the gaseous metal containing solution are pyrolyzed (decomposed) near the support. It results in the deposition of the metal atoms decomposed from the solution on the support surface.

Li et al. (1993) fabricated Pd/Ag membranes on alumina hollow fibers by the spray pyrolysis of palladium nitrite and silver nitrite solutions in a $H_2$-$O_2$ flame. A lower Ag content on the deposit (4 wt%) than that in the solution (10 - 40wt%) was reported. They reasoned it to be the evaporation of more Ag from the substrate at high temperature during the pyrolysis. A uniform Pd/Ag alloy deposit was obtained when the support temperature was above 970ºC, where Pd/Ag alloying took place. A 24 wt% Ag Pd/Ag alloy membrane with the thickness of 1.5 - 2 $\mu$m was prepared with the spray pyrolysis plating, and the membrane showed a hydrogen permeance of 8 $m^3/(m^2*h*atm)$ and a $H_2/N_2$ selectivity of 24 at 500ºC.

### *2.5.3 Electro Plating*

Electroplating is essentially an electrolysis process. The anode is usually, but not necessarily, made of the metal desired for deposition, while the cathode is the support to be deposit. The electrodes are immersed in the electrolyte solution (mostly aqueous) composed of metal ions desired for deposition. The other sides of the electrodes are connected to a low voltage DC power supply, resulting in an electronic circuit. During the electroplating, electrons move from the DC power supply to the cathode and continuing through the electrolyte solution reaching the anode then back to the DC power supply. While electrons move towards the anode in the solution, the metal ions with positive charges move toward the cathode and deposit on it. During the electrolysis process, the metal ions are reduced to atoms at cathode while the metal atoms at anode keep being oxidized as ions into solution. The plating methods also provide alloy deposition capability. More than two metal ions could be introduced in the electrolyte solution for simultaneous deposition. A complexing agent is required to minimize the electrochemical potential between the metal ions since the electro plating rate depends on the reduction potential of the metal ion.

Nam and Lee (1999, 2000) fabricated Pd/Ni alloy membranes on the mesoporous stainless steel (SUS) by electroplating technique with suction (vacuum) at the other side of the SUS supports. Prior to the electro plating, the support was pre-treated with Ni powder and CuCN solution followed by sintering at 800$^{o}$C for 5 hours to obtain smoother surface and better adhesion between deposit layers and the supports. The deposit layer was characterized to be Pd/Ni alloy. However, the disordered crystalline structure was also identified and a further heat treatment at 723 K for 1 hour was required for obtaining

the poly-crystalline structure. With this technique, Pd/Ni dense membranes with the thickness less than 2 $\mu$m layer were prepared. The gas permeation results showed that the Pd/Ni membranes showed a $H_2$ permeance of 158 $m^3/(m^2*h*atm)$ and a $H_2/N_2$ selectivity of 3000 at 723 K. Nam et al. (2001) fabricated Pd/Cu alloy membranes by the same plating technique. A new membrane structure was also introduced with a thin silica layer between the support layer and Pd/Cu alloy as an intermetallic diffusion barrier. A hydrogen permeance of 68 $m^3/(m^2*h*atm)$ with a selectivity as high as 70000 at 732K was reported for the 2 μm thick Pd/Cu composite membrane prepared. Lee et al. (2003) prepared Pd membranes by the same plating method on the silica modified SUS supports. They failed to report the gas permeance data of the Pd membranes because of the significant leak resulted from the formation of pinholes during the testing in $H_2$ at the elevated temperatures.

Bryden and Ying (1998) prepared nano-structured Pd/Fe alloy membranes on PSS supports by pulsed electrodeposition technique. Pt coated Ti was used as anode while porous PSS was used as cathode. $PdCl_2$ and $FeSO_4 \cdot 7H_2O$ solutions were used as Pd and Fe ion sources in the electrolyte at the temperature of 25 - 80$^oC$. The deposit was characterized to be the FCC Pd/Fe alloy phase with grain size ranged from 10 – 40 nm in diameter and Fe content form 0 – 40 at%. They reported that the Pd/Fe alloy film of Fe content more than 20 at% showed a thermal stability without significant grain growth at the temperature up to 400$^oC$. In addition, no α-β phase transformation occurred at room temperature of the Pd/Fe alloy film. Bryden and Ying (2002) fabricated Pd/Fe alloy membranes with the same pulse electroplating method. They reported that the hydrogen permeance decreased as the Fe content increased due to that hydrogen adsorption

decreased with increasing Fe content. The 6 $\mu$m thick membrane with 7 at% Fe showed a hydrogen permeance of 4.7 $m^3/(m^2*h*atm)$ and a $H_2$/He selectivity of 35 at 200$^o$C. The Pd/Fe membranes were further characterized for the sulfur and carbon monoxide resistance at the same temperature, and the characterization results will be provided later in *section 2.6*.

### *2.5.4 Electroless Plating*

Electroless plating, similar to electroplating, also involves the oxidation-reduction reactions in the plating process. However, in the electroless plating, the reaction requires no external electric power but needs a reducing agent in the bath. Therefore, electroless plating is also known as "chemical plating". In addition, the oxidation-reduction reaction in the electroless plating usually occurs on the deposited metal surface, therefore, it is also termed as "autocatalytic plating".

The electroless plating has advantages over other plating techniques for fabricating Pd and Pd alloy composite membranes. First of all, easy procedure and simple equipment are needed for the plating, resulting in low cost of the plating technique. Furthermore, no need of external current and conductivity of the supports widen the selection of supports and applications. In addition, it is possible to produce uniform deposit layer on complicated shapes by the electroless plating.

A typical plating bath consists of a source of metal ions, a reducing agent, a complexing agent and/or a stabilizer (Mallory and Hajdu, 1990). $Pd(NH_3)_4Cl_2$, $PdCl_2$, and Pd acetate are generally used as a source of Pd ions. Ethylenediamine tetraacetic acid (EDTA), ethylenediamine (EDA), ammonia ($NH_3$) is usually added in the bath as a

complexing agent to prevent precipitation. For the reducing agent, hydrazine, hypophosphite, trimethylamine borane, formaldehyde is commonly used.

Rhoda and Madison (1959) developed the electroless plating bath for Pd deposition for the first time with hydrazine as the reducing agent. In addition to hydrazine, the other major component in the bath were $Pd(NH_3)_4Cl_2$ and $Na_2EDTA$. Kawagoshi (1977) added thiourea in the bath to improve the solution stability.

Sergienko (1968) developed another electroless plating bath for Pd with hypophosphite as the reducing agent. The bath also contained palladium chloride and EDTA. Pealstein et al. (1969) developed a more stable hypophosphite-based bath with ammonia as the complexing agent. Zayats et al. (1973) further improved the stability of the hypophosphite ammonia bath by adding thiosulfate. Hough et al. (1981) developed a Pd electroless plating bath with trimethylamine borane as the reducing agent. Abys (1984) developed a Pd plating bath with formaldehyde as the reducing agent in the low pH range.

Today, the most suitable reducing agent for Pd electroless plating bath is considered to be hydrazine. The hypophosphite and amine boron-based bathes resulted in co-deposition of phosphorous and boron, respectively (Pealstein et al. 1969, 1974). The formaldehyde-based bath results in a low Pd plating rate due to its weak reducing ability. As a result, the plating bathes for Pd plating today are mainly based on the hydrazine-based bathes (Rhoda 1959, Kawagoshi 1977) with small variations. Modern Pd plating bath contains $Pd(NH_3)_4Cl_2$ as the Pd ion source, $Na_2EDTA$ and $NH_3$ as the complexing agent/ buffer solution, and hydrazine as the reducing agent. The pH of the bath is between 9 and 12 and the plating temperature is 50 - 70$^oC$.

The reaction between $Pd(NH_3)_4Cl_2$ and hydrazine is expressed in Equation 2.21 (Mallory and Hajdu, 1990).

$$2Pd(NH_3)_4^{2+} + N_2H_4 + 4OH^- \rightarrow 2Pd + 8NH_3 + N_2 + 4H_2O \quad (2.21)$$

Yeung et al. (1999) reported the kinetics of Pd electroless plating in hydrazine-based bath, including the effect of Pd ion, hydrazine, and ammonia concentration on the plating rate and deposit quality. Larger concentrations of hydrazine and Pd ions resulted in higher deposition rates with larger Pd grain size in morphology and more bath precipitation. In contrast, larger concentrations of ammonia resulted in more stable plating baths but slower deposition rate with smaller Pd grain size. In conclusion, the grain size of the deposit Pd layer was a function of plating rate, which was a function of Pd ion, reducing agent, and ammonia concentration. Cheng and Yeung (2001) reported similar kinetics of electroless Pd plating in the hypophosphite-based bathes.

Prior to electroless plating, the supports are required to be seeded with Pd nuclei. The seeding process is termed as sensitization/activation and the most widely used sensitization/activation procedure (Uemiya 1991a,b; Shu et al., 1993a, 1996; Mardilovich et al., 1998, 2002) is done by several sequential immersions into $SnCl_2$/HCl and $PdCl_2$/HCl bathes. The reduction of $Pd^{2+}$ by $Sn^{2+}$ is expressed in Equation 2.22.

$$Sn^{2+} + Pd^{2+} \rightarrow Sn^{4+} + Pd^0 \quad (2.22)$$

More Pd nuclei pre-seeded on the support surface resulted in more uniform deposit. However, too thick an activation layer lessened the adhesion of the plated layers (Mardilovich et al., 1998).

The above-mentioned Sn-Pd based activation and hydrazine based electrolessplating bathes have been used extensively by many researchers to fabricate Pd based composite membranes for hydrogen permeation. Uemiya et al. (1991a) fabricated Pd, Pd/Cu, and Pd/Ag alloy membranes by the electroless plating on the porous glass tubes. The Pd/Ag and Pd/Cu alloy membranes were prepared by plating Pd and Ag or Cu in sequence followed by the heat treatment at 773K for 12 hours in Ar. They observed that the hydrogen permeation was inversely proportional to the Pd thickness, and obtained a hydrogen permeance of 15.2 $m^3/(m^2*h*atm)$ on the 13 μm thick Pd membrane at 773K. A dramatic decrease of $H_2/N_2$ selectivity at 573K was observed, which they attributed to the formation of cracks and pinholes due to the hydrogen embrittlement. In contrast, the 21.3 μm Pd/Ag (7wt% Ag) and the 18.9 μm Pd/Cu (6.2wt% Cu) membranes showed high $H_2/N_2$ selectivity at temperatures of 473 - 573K with lower hydrogen permeances (Pd>Pd/Ag>Pd/Cu). Uemiya et al. (1991b) further characterized the 5.8 μm Pd/Ag alloy membranes (23 - 26wt% Ag) prepared on the porous tubular ceramic supports. They reported a hydrogen permeance of 46.3 $m^3/(m^2*h*atm)$ at 773K while that of a commercial Pd/Ag membrane of 150 $\mu$m at the same temperature was only 1.4 $m^3/(m^2*h*atm)$. In addition, they reported that the Pd/Ag membrane with 23wt% Ag showed the highest hydrogen permeance.

Shu et al. (1991) modeled and designed the Pd membrane reactors by taking into account the factors affecting hydrogen permeability after extensively reviewing the plating techniques for fabricating Pd and Pd alloy membranes. Shu et al. (1995) prepared a 10.4 $\mu$m Pd/Ag membrane of 5.1 wt% Ag on the PSS supports by successive plating of Pd and Ag followed by a heat treatment at 550$^o$C to form Pd/Ag alloy. The membrane

was characterized during a methane steam reforming reaction with $Ni/Al_2O_3$ catalysts. They reported that the methane conversion was highly enhanced as a result of the product hydrogen permeating thorough the Pd/Ag membrane. As a specific case, with a total pressure of 136 kPa and steam-methane molar ratio of 3 at 500$^oC$, the methane conversion was 1.4 times higher than that in the non-membrane system.

Mardilovich et al. (1998) fabricated defect-free Pd membranes on the PSS supports by electroless plating with the hydrazine-based bathes. A hydrogen permeance of 8 $m^3/(m^2*h*atm^{0.5})$ with an ideal $H_2/N_2$ selectivity more than 5000 at 350$^oC$ was reported. In addition, the long term stability of the membrane at 350$^oC$ for 1100 hours was reported. Furthermore, the permeating fluxes of non-permeable gases, such as $N_2$, He, was quantitatively determined as the combination of Knudsen diffusion and viscous flow. The permeation of the non-permeable gases was attributed to the gaps created at high temperatures in the dense Pd layer.

Investigations on improving the conventional electroless plating procedure including the activation and electroless plating procedure have been carried out by several researchers. Li et al. (1996) modified the activation process by using $Pd^{2+}$ modified γ-AlOOH sol-gel to activate ceramic supports followed by the calcination at 550$^oC$ and the reduction of Pd atom at 400$^oC$ in $H_2$. They reported the improved activation process resulted in a higher electroless plating rate, no residual of tin impurities in the Pd layer, and no peeling off of the Pd layer.

Zhao et al. (1998) used $Pd^{2+}$ modified bohemite sol-gel to activate ceramic supports. The process not only activated the supports but also blocked the larger pores of the substrate. The activated supports were further electroless plated with Pd with vacuum.

The prepared membrane was 1 $\mu$m thick and showed a permeance of 87 $m^3/(m^2*h*atm)$ at 450°C with a $H_2/N_2$ selectivity of 23. Zhao et al. (2000) used the similar plating procedure to fabricate Pd/ceramic membranes. The resultant membrane had a thickness less than 1 $\mu$m, and exhibited a hydrogen permeance of 1.3 $m^3/(m^2*h*atm)$ at 314°C with a $H_2/N_2$ selectivity of 130.

Paglieri et al. (1999) activated the supports by pre-deposition of palladium acetate followed by the reduction of Pd atom at 500°C in $H_2$ to eliminate the residual tin in the Pd layer. They reported a higher stability of the membrane prepared by the activation process in comparison to the conventional method. They reasoned that the residual tin remained in the Pd layer prepared by the conventional method caused the deterioration of the membrane structure during characterization at elevated temperatures.

Wu et al. (2000) activated the supports by using the photocatalytic deposition (PCD). A porous $TiO_2$ support was immersed in the palladium chloride solution and irradiated with UV light to form Pd nuclei followed by the electroless deposition. The resultant membrane had a thickness of 0.3 – 0.4 $\mu$m, and showed a hydrogen permeance 56.2 $m^3/(m^2*h*atm)$ with an ideal $H_2/N_2$ selectivity of 1140 at 500ºC. The long term testing showed a decrease in permeance from 25.9 to 21.3 $m^3/(m^2*h*atm)$ at 400ºC over a 160 hour period. They reasoned that the decline in permeance at 400°C was due to the rearrangement of the Pd lattice.

Yeung et al. (1995) developed an electroless plating procedure combined with osmosis. Osmotic pressure was created by placing concentrated salt solutions (3M $CaCl_2$ in the study) inside the porous Vycor glass tube while the plating solution was at the outside of the tube. The osmotic pressure caused water from the plating solution to

diffuse through the support, resulting in a higher plating rate. They reported that the Pd layer prepared by the method showed a higher luster, density, and smaller grain size in comparison to the conventional plating.

Li et al. (1998) prepared a 10 $\mu$m Pd membranes on the PSS support with electroless plating combined with an osmotic pressure resulted from a 3M NaCl solution inside the support. A permeance of 17.4 $m^3/(m^2*h*atm^{0.5})$ and an ideal $H_2/N_2$ selectivity of 1000 at 480°C were reported with a long term stability for 250 hours at 400°C. Li et al. (1999) used the osmosis combined electroless plating technique to repair the Pd/α-alumina membranes with defects (pinholes). They reported that the Pd/α-alumina membranes became gas tight after plating with osmosis without gaining too much thickness. They reasoned that when applying osmosis pressure, the plating solution moved through the pinholes on the membranes. As a result, Pd was extensively deposited on the wall of the pinholes. Li et al. (2000a) reported that after two repair cycles, the thickness of the membrane increased from 7.6 to 10.3 $\mu$m, and the hydrogen permeance decreased from 129 to 58.1 $m^3/(m^2*h*atm^{0.5})$ at 467°C with the $H_2/N_2$ selectivity increased from 10 and to 970.

Souleimanova et al. (1999) studied the effect of osmosis during the electroless plating on the morphology of Pd deposit. They reported that by applying osmosis during plating, finer and more uniformly distributed Pd grains as well as smaller thickness of the dense layer were obtained. Souleimanova et al. (2000) reported that even finer Pd grains were obtained by increasing sucrose solution concentration up to 9M, which caused a lager osmotic flux. Souleimanova et al. (2001) reported that the hydrogen permeance of the Pd membrane prepared with osmosis increased with increasing surose solution

concentration. Specifically, the composite Pd/Vycor membranes prepared with a sucrose solution of 9M showed a hydrogen permeance of 40 $m^3/(m^2*h*atm^{0.5})$ at 500$^oC$. They attributed the higher permeance to the smaller thickness and Pd grain size prepared with higher sucrose concentration.

Souleimanova et al. (2002) reported that by the electroless plating with osmosis, a 8 μm Pd membrane was prepared and the resultant membrane showed a hydrogen permeance of 40 $m^3/(m^2*h*atm^{0.5})$ at 500°C. On the other hand, the Pd membrane prepared by the conventional plating had 18 μm in thickness and showed a hydrogen permeance of 16 $m^3/(m^2*h*atm^{0.5})$ at 500°C. In addition, a lower activation energy for hydrogen permeation (18.8 kJ/mol) was observed on the membrane fabricated with osmosis in comparison to the one prepared by the conventional method (21.6 kJ/mol). The lower activation energy was attributed to the smaller Pd grain size in the membrane. Furthermore, they reported that the Pd membrane prepared with osmosis remained gas tight after 15 thermal cycles between room temperature and 500°C, while the Pd membrane fabricated by the conventional method started to crack after 4 cycles.

Zhao et al. (1998, 2000) prepared Pd membranes on ceramic supports by electroless plating with vacuum on the other side of the support, which also created a flux of plating solution crossing the support though the pores. The resultant Pd deposits were reported as more compact than those prepared conventionally.

Ilias et al. (2007) added surfactants into the plating solution to remove the bobbles formed during the plating including cationic, anionic, and non-ionic. They observed that with the non-ionic surfactant in the plating bath, the plating rate increased about 10%

with more uniform deposit morphology. Further, the surfactant with almost neutral HLB (hydrophilic-lipophilic balance) showed strongest capability of removing gas bobbles.

For alloy deposition by the electroless plating technique, the most widely used method is to deposit the elements in sequence followed by the heat treatment to form alloy (Uemiya et al. 1991b; Keuler et al. 1999; Lin and Chang, 2004). Another approach to prepare alloy layer by the electroless plating is the co-deposition. Although the deposit by the co-deposition is still not the alloy, different elements deposited are surrounded by each other resulting in the less heat treatment required for the alloy formation than sequential deposition.

Shu et al. (1993a) co-deposited Pd and Ag on the activated PSS supports with the hydrazine-based bathes. The co-deposition was performed by keeping the total metal concentration constant in the bath. The phases of the deposit were identified as Pd and Ag separately, and a heat treatment at 400$^{o}$C for 150 minutes resulted in the formation of Pd/Ag alloy. Furthermore, they observed the preferential deposition of Ag during the co-deposition, which passivated the further Pd deposition. They reasoned that it was due to the more catholic nature of Ag. Pre-deposition of Pd prior to Pd/Ag co-deposition was suggested to eliminate the passivity and to increase the plating rate. The Pd/Ag deposit by co-deposition showed 53 - 56 wt% Ag in content.

Cheng and Yeung (1999) studied the kinetics of Pd and Ag co-deposition on the porous Vycor supports with the hydrazine-based bath. They studied the effects of the hydrazine and ammonia concentration in the bath on the co-deposition. Preferential Ag deposition was also observed. In addition, they observed that with lower total metal ion concentration in the bath (5mM), the deposit composition is close to the bath

composition. Higher hydrazine concentration and lower ammonia concentration resulted in more Pd deposit. They developed a kinetic model for Pd, Ag and Pd/Ag plating with hydrazine based bath, which was in good agreement with the experimental data. After annealing at 400$^{o}$C and 500$^{o}$C, the Pd/Ag alloy membranes were tested for its hydrogen permeation at 350$^{o}$C. The membranes pre-annealed at 400$^{o}$C and 500$^{o}$C showed hydrogen permeance of 2.6 $m^3/(m^2*h*atm^{0.5})$ and 3.8 $m^3/(m^2*h*atm^{0.5})$, respectively, which was about 1.4 - 1.7 times higher than pure Pd membranes with the same thickness.

Chen et al. (2004) reported that the morphology of the deposit was strongly affected by the Ag content during the Pd and Ag co-deposition. The increase of the Ag content increased the dendritic structure of the deposit, which was resulted from the large difference between the deposition rate and growth mode of Pd, and Ag.

## 2.6 Sulfur Poisoning of Pd

### *2.6.1 S-Pd Interactions*

Sulfur is a major poisoning compound to the catalysts consisted of transition metals such as Ni, Pd or Pt, which causes the deactivation and the reduction of selectivity of the catalysts (Hughes, 1984; Butt and Petersen, 1988; Barbier et al, 1990). Research have shown that even small amount of $H_2S$ caused the deactivation of Pd catalysts (Feuerriegel and Klose, 1998; Gelin et al., 2003) as well as the deterioration of the performance of Pd membranes (McKinley, 1967; Edlund et al, 1993; Kajiwara et al., 1999).

A number of research have been carried out to study the issue of sulfur poisoning in terms of sulfur adsorption and sulfur-metal interaction (McCarty and Wise, 1980;

Oudar, 1980a, Bartholomew et al., 1982, Biswas et al., 1988, Barbier, 1990). McCarty and Wise (1980) observed a half sulfur coverage on Ni surface at temperature of 373 - 873K with extremely low $H_2S$ partial pressure of 1 – 10 ppb, which indicated the extremely high sulfur affinity of the metal. They also reported that the surface-adsorbed sulfur was energetically stable at the testing condition (i.e. low $H_2S$ concentration), resulting in a high surface sulfur coverage without the dissolution of sulfur into the bulk.

Sulfur poisoning is mainly resulted from the surface sulfur adsorption rather than the bulk metal sulfide formation. Bartholomew et al. (1982) reported that Ni catalysts were poisoned by only a few ppm $H_2S$ at 450 - 550°C, while the required $H_2S$ concentration for bulk Ni sulfide formation was of 100 – 1000 ppm in the same temperature range according to the equilibrium Ni-S phase diagram (Rosenqvist, 1954).

The adsorption of sulfur compounds on the metal surface is dissociative, resulting in the formation of surface sulfides (Bartholomew et al., 1982). Surface sulfides are much easier to form and stable in a wider range of conditions compared to bulk sulfides. Absolute Gibb's free energies ($\Delta G_0$) for the formation of bulk sulfides were at least 40 kJ/mol lower than those of surface sulfides (Bartholomew et al., 1982). This indicated that much higher sulfur concentration is required to form bulk sulfides than forming surface sulfides. The threshold concentrations for forming surface and bulk sulfides could be different by three orders of magnitude. In addition to high sulfur concentration, the formation of bulk sulfides also requires the dissolution and segregation of adsorbed the sulfur molecules, which requires extra energy allowing sufficient diffusion (Oudar et al., 1980b).

Although the surface adsorption is mainly responsible for the sulfur poisoning phenomenon, the thermodynamic properties of bulk sulfides are still important for studying the poisoning phenomenon. For example, the equilibrium phase diagrams, such as Pd-S as shown in Figure 2.6, provide the information of possible sulfide species under different poisoning conditions. In addition, the free energies of metal sulfide formation data assess the potential difficulty to form a sulfide from a specific metal. The expression of the free energy for a metal sulfide formation is given in Equation 2.23 with the reaction given in Equation 2.24. In general, if a metal has a higher absolute value of the free energy of sulfide formation, that metal is potentially more sulfur resistant since higher sulfur concentrations are required to form a sulfide (for both either bulk and surface).

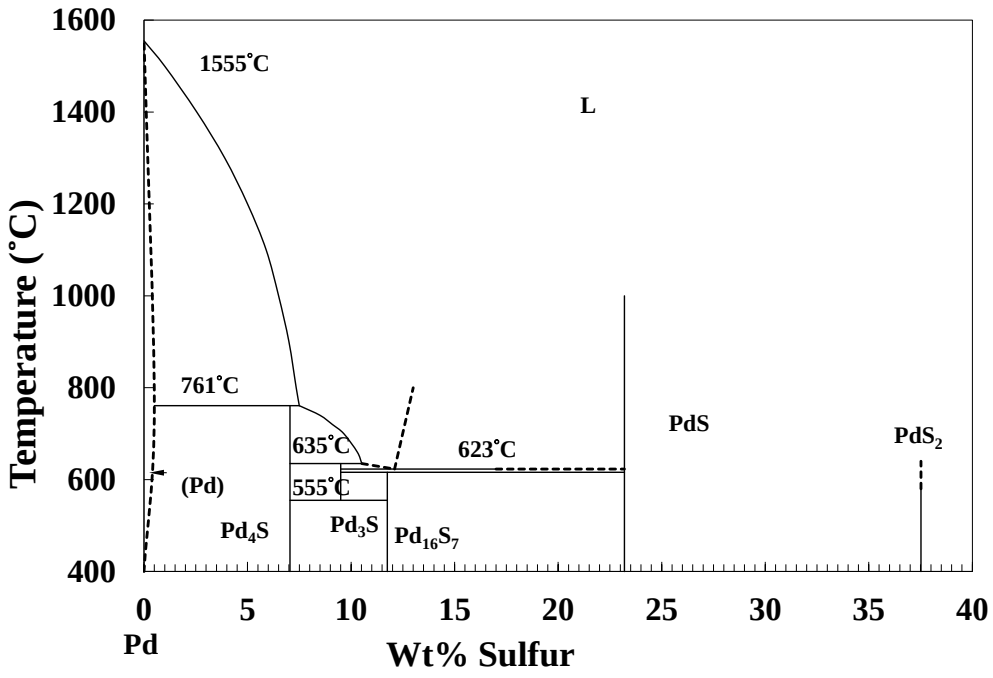


Figure 2.6. Pd-S phase diagram (Taylor, 1985).

$$\Delta G_0 = RT \ln\left(\frac{P_{H_2S}}{P_{H_2}}\right) = \Delta H - T\Delta S \quad (2.23)$$

$$(x/y)M + H_2S \leftrightarrow (1/y)M_xS_y + H_2 \quad (2.24)$$

Since adsorption of sulfur containing compounds on metal surfaces involves metal-sulfur bonding, the adsorption was considered to be essentially irreversible (Bartholomew et al., 1982). However, the regeneration of the sulfur-poisoned metals has been shown by a number of researchers. Barbier et al. (1985) reported that $H_2S$ adsorption on metals was partially irreversible by examining desorption of $H_2S$ of the $Pt/Al_2O_3$ catalysts at 500$^oC$ in $H_2$. The quantity of irreversible sulfur was determined after 30 hours under $H_2$ at 500$^oC$, and was found to be independent of poisoning conditions. By a heat treatment (at 300°C) in oxygen followed by the hydrogen reduction under the mild conditions (at 200°C), Mathieu and Primet (1983) reported that the full regeneration of the sulfur-poisoned $Pt/Al_2O_3$ catalysts was possible. Hughes (1984) also reported that the catalytic activity of Ni catalysts was fully regained when the sulfur concentration in the feed is reduced below the critical level. Generally speaking, the metals of high electronic affinities are considered to be easier to be regenerated after being sulfur – poisoned due to that the metal-sulfur bonds formed are more covalent (Barbier et al., 1985). It should be noted that when forming metal-sulfur bonds, electrons transfer from metals to sulfur due to the higher electronic affinity of sulfur than metals. The electron affinity of S is 2.08ev, while the electron affinities of Pd, Cu, Au, Pt, and Ni are 0.56, 1.24, 2.32, 2.13, and 1.16 ev, respectively.

The heat of adsorption ($\Delta H_{ad}$) is generally expressed as the difference between the activation energy of adsorption and desorption as shown in Equation 2.25. For the

dissociative adsorption of sulfur compounds (e.g. $H_2S$) on metals, the activation energy of sulfur adsorption is negligible, resulting in the heat of adsorption being equal to the activation energy of desorption (Barbier et al., 1990).

$$\Delta H_{ad} = E_a - E_d \tag{2.25}$$

Oudar et al. (1980a) applied Van't Hoff equation (as shown in Equation 2.26) on the $H_2S$ adsorption isotherms of different metals at different temperatures to obtain the heat of sulfur adsorption on different metals. The binding energies of S-metals were further calculated by the use of the heat of sulfur adsorption obtained and Equation 2.27, where X is the binding energy and D is the dissociation energy of 1 mole $S_2$ (422 kJ/mol). The S-metal binding energies calculated by Oudar et al. (1980a) ranged from 326 to 485 kJ/mol for the investigated metals including Ag, Cu, Pt, Fe, Ni, Mo, and Cr. However, no Pd-S isotherm has been reported in the literature.

$$\left.\frac{\partial \log\left(P_{H_2S} \big/ P_{H_2}\right)}{\partial T}\right|_{\theta} = \frac{-\Delta H_{\theta}}{RT^2} \tag{2.26}$$

$$\Delta H_{ad} = X - D/2 \tag{2.27}$$

The comparison of the heat of sulfur adsorption among metals requires taking the sulfur coverage into account since the binding energy of S-metal is a function of surface sulfur coverage. McCarty et al. (1983) reported that the $-\Delta H$ decreased from 122 to 26 kJ/mol while the sulfur coverage increased from 0.1 to 0.6 on Pt. This also suggested that the sulfur affinity of a metal decreased as the surface sulfur coverage was increased.

Saleh (1970) investigated the $H_2S$ adsorption on Pd at temperatures ranging from -80 to 250ºC. The dissociative adsorption of $H_2S$ on Pd was confirmed at temperatures as low as -80°C by the observation of a slight hydrogen desorption (1 μl/min) after heating the Pd film up to 0 - 70°C. In addition, the adsorption reaction became negligible when a monolayer (ML) coverage of sulfur was attained. Saleh (1970) also reported no hydrogen desorption when admitting $H_2S$ on the $H_2$ pre-adsorbed Pd. Since the binding energy of Pd-S and Pd-H, and the heat of adsorption for $H_2$ and $H_2S$ were comparable, he attributed the phenomenon to no displacement reaction between sulfur bonding and hydrogen bonding.

Saleh (1970) further calculated the activation energy for $H_2S$ adsorption by the use of the adsorption rates at temperatures ranging from 25 to 250ºC. He reported that the activation energy for $H_2S$ adsorption is proportional to the inverse of $X^3$ as expressed in Equation 2.28.

$$E_{a,x} = 87.8 - \frac{160.3}{X} \pm 6.3 \qquad (2.28)$$

Equation 2.28 showed that the activation energy of $H_2S$ adsorption was a function of the amount of absorbed S, which includes the amount of sulfur on the surface and in the bulk. At $X \leqq 1.8$, the activation energy of adsorption ($E_a$) was ~ 0. It should be noted that the minimum activation energy value is zero and there is no physical meaning for the negative activation energy values. Prior to the attainment of a monolayer of sulfur on the surface (X = 1.35), Equation 2.28 supported the statement of Barbier et al. (1990) that the

[3] $X = V_s/V_m$ where $V_s$ is the volume of $H_2S$ adsorbed and $V_m$ is the volume of a krypton monolayer on the Pd film. When X = 1.35, surface sulfur coverage (θ) = 1 monolayer (ML) (Saleh et al., 1961).

activation energy for the adsorption of sulfur on metals was negligible. As X was increased above 1.8, the activation energy of adsorption became non-negligible and kept increasing with increasing X to a limiting value of 87.8 kJ/mol. Saleh (1970) attributed the increase of the activation energy of adsorption with increasing X (above 1.8) to the result of the bulk sulfide formation. The result also indicated that above full surface coverage (1 ML), further adsorbed $H_2S$ started dissoluting into the bulk Pd.

Similar phenomenon was observed by the theoretical simulation performed by Alfonso (2006), who utilized density functional theory (DFT) to model the sulfur adsorption on Pd (1 1 1). He reported that above the critical sulfur coverage of 0.75 ML, the incorporation (dissolution) of sulfur into subsurface of Pd became energetically favorable rather than continuous adsorption on the surface. The sulfur in the subsurface of Pd was considered as precursors for the bulk sulfide formation.

Alfonso et al. (2005a) theoretically studied the molecular (physical) and dissociative adsorption of $H_2S$ on Pd (1 1 1) by the use of gradient-corrected density functional theory (DFT). The reaction pathway and energy profile for the $H_2S$ decomposition to S and H on the Pd surface was proposed as shown in Equation 2.29.

$$H_2S_{(g)} \rightarrow H_2S_{(ad)} \rightarrow SH_{(ad)} + H_{(ad)} \rightarrow S_{(ad)} + H_{(ad)} \quad (2.29)$$

The preferential binding sites and binding energies for $H_2S$, SH, and S to Pd were investigated at different sulfur coverages from 0.06 to 0.33 ML. They reported that $H_2S$ molecules were preferentially bonded to the top sites of Pd alloy, while HS and S were preferably bonded to the bridge sites and the hollow sites, respectively. The order of the binding energy value was S-Pd > SH-Pd > $H_2S$-Pd, suggesting that Pd-S was the most

stable species while Pd-$H_2S$ was the least stable species. In addition, they reported that although both molecular and dissociative adsorption of $H_2S$ were exothermic, the former one had no activation barrier while the latter had low activation barriers. They concluded that the adsorbed $H_2S$ molecules were not stable and would undergo dissociative adsorption on a Pd (1 1 1) surface.

Alfonso (2005b) further investigated the S-Pd interaction as a function of sulfur coverage on Pd (1 1 1) by the use of DFT. He reported that at low coverages (< 0.5 ML), the atomic S bonded with Pd in the hollow sites was more energetically stable. However, at high coverages (> 0.5 ML), the preferential adsorption sites changed to the top surface and $S_2$ became more stable due to significant S-S interactions. The results suggested that as the sulfur coverage was increased, the strength of Pd-S bonding decreased.

### *2.6.2 Structure of Adsorbed S on Pd and Effect of Sulfur on Hydrogen Adsorption*

A number of studies have been carried out to understand the structure of adsorbed S on Pd surface with $H_2S$ or $S_2$ as adsorbate gases (Speller et al., 1999; Maca et al., 1985; Dhank et al., 1998; Patterson and Lambert, 1987; Boemermann et al., 1996) and the effects of adsorbed sulfur on Pd surfaces on $H_2$ adsorption (Rodriguez et al., 1998; Peden et al., 1986; Burke and Madix, 1990; Gravil and Toulhoat, 1999; Wilke and Scheffler, 1995).

For understanding the surface structure of sulfur-adsorbed Pd in the literature, it is worth mentioning some notational conventions for classifying a surface layer. If a surface structure (2-D) (including the lattice parameter) is identical to that of a parallel plane (2-D) in bulk, such surface structure is notated as (1*1). In some circumstances (i.e. the surface reconstruction or the surface adsorption), the surface structures have unit cells

that are integral multiples of the bulk unit cells. A (2*2) notation is used to describe a surface structure with the unit cells having the lattice parameters twice those of the bulk. In addition, (2*2) can be equivalently designed as $(2^{0.5}*2^{0.5})R45^{o}$, which means that the surface structure has the lattice parameters that are $2^{0.5}$ multiple of those in the bulk with a rotation through $45^{o}$ with respect to the bulk (Cottam and Tilley, 1989). The surface structures described above are shown in Figure 2.7.

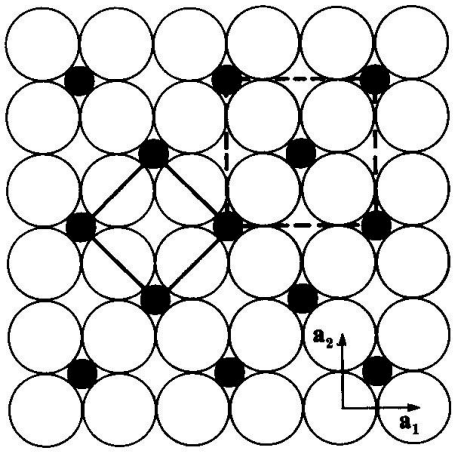


Figure 2.7. Schematic of equivalent surface structures: (2*2) (square marked in dotted line) and $(2^{0.5}*2^{0.5})R45^{o}$(square marked in solid lines). $a_1$ and $a_2$ are the lattice parameters of the bulk unit cells. Open circles represent bulk lattice atoms and solid circles represent surface lattice atoms or adsorbed atoms (Cottam and Tilley, 1989).

Speller et al. (1999) investigated and modeled the surface structure of sulfur adsorbed Pd (1 1 1) by the use of LEED (low energy electron diffraction), STM (scanning tunneling microscopy), XPS (X-ray photoelectron spectroscopy), and FLAPW (fully potential linearized augmented plane waves) calculation technique. They reported the $(3^{0.5}*3^{0.5})R30^{o}$ surface structure of Pd after exposure to $H_2S$ at room temperature. The same surface S-Pd structure has also been observed by other researchers (Maca et al. 1985; Dhank et al., 1998; Patterson and Lambert, 1987). In addition to $(3^{0.5}*3^{0.5})R30^{o}$,

$(7^{0.5}*7^{0.5})R19^{o}$, (2*2) stripes, (2*2) triangles (very little), and disordered structures were also observed on the S adsorbed Pd (1 1 1). Upon heating from 370 to 700K, the dominative structure on the S adsorbed Pd surface changed from $(3^{0.5}*3^{0.5})R30^{o}$ to $(7^{0.5}*7^{0.5})R19^{o}$.

Speller et al. (1999) further compared the surface structures between sulfur-adsorbed Pd and the Pd with sulfur segregated to surface from bulk at 700K. In addition to the dominative $(7^{0.5}*7^{0.5})R19^{o}$ structure, the sulfur-adsorbed Pd showed more (2*2) stripe structures while the sulfur-segregated Pd had more (2*2) triangular islands structures. The formation of island structure was explained by a random walk model in which the sulfur atoms moved randomly across the Pd surface until all sulfur atoms became immobile with maximum number of bonds formed. No clear model was proposed for the stripe structures. In addition, they observed the smooth steps composed of Pd atom layers on the clean Pd (1 1 1) were roughened after adsorbing sulfur, while the same steps were decorated with (2*2) stripes in the segregation case. The above-mentioned structures are shown in Figure 2.8 and Figure 2.9.

Speller et al. (1999) further investigated the atomic sulfur positions in the $(7^{0.5}*7^{0.5})R19^{o}$ structure in different models by the use of FLAPW calculation. One sulfur atom in a unit cell model was quantitatively in agreement with the segregation structure, and the sulfur atom was bonded at the FCC hollow sites in Pd. For the S adsorption, they proposed a mix layer with 2 sulfur atoms in a unit cell, one at the FCC sties and the other at the HCP sites.

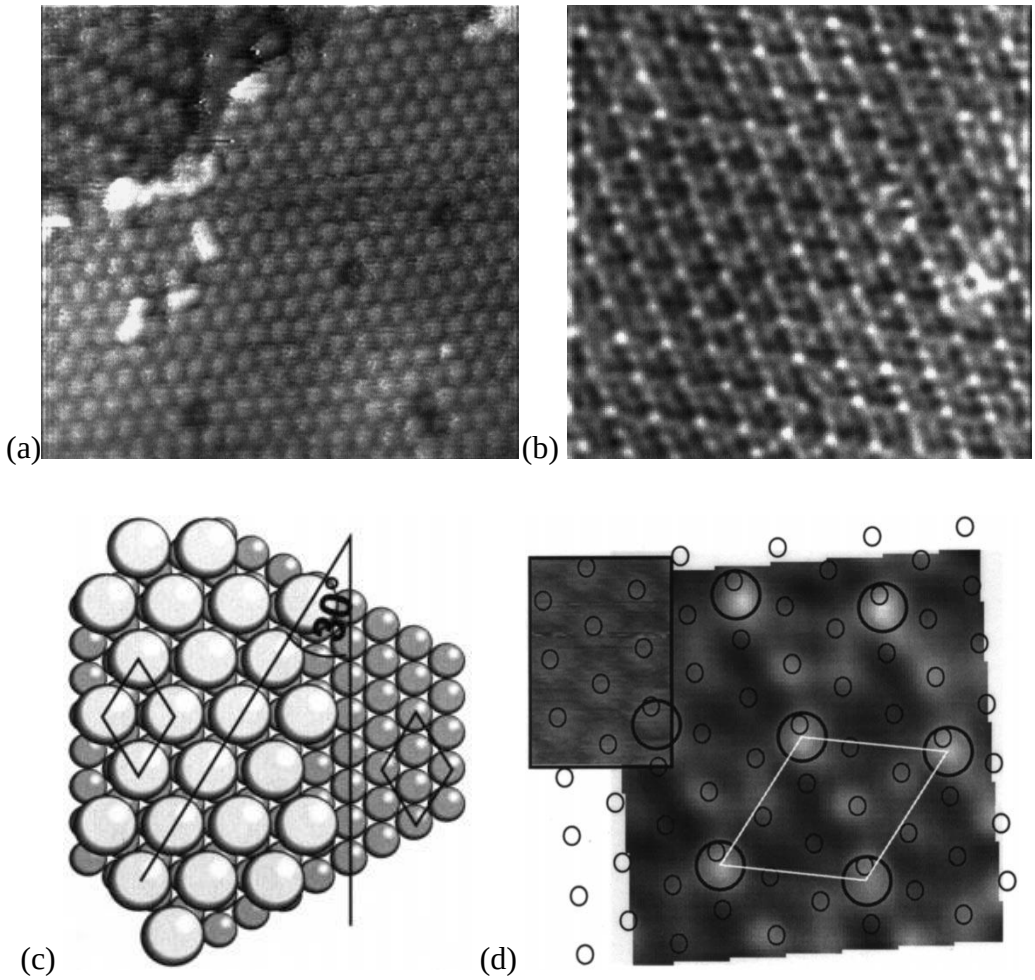


Figure 2.8 (a) STM topography of $(3^{0.5}*3^{0.5})R30^{o}$ (100 Å x 100 Å), (b) STM topography of $(7^{0.5}*7^{0.5})R19^{o}$ (80 Å x 80 Å), (c) model of $(3^{0.5}*3^{0.5})R30^{o}$, and (d) model of $(7^{0.5}*7^{0.5})R19^{o}$ on the STM image with the insert being the clean Pd (1 1 1) (Speller et al., 1999).

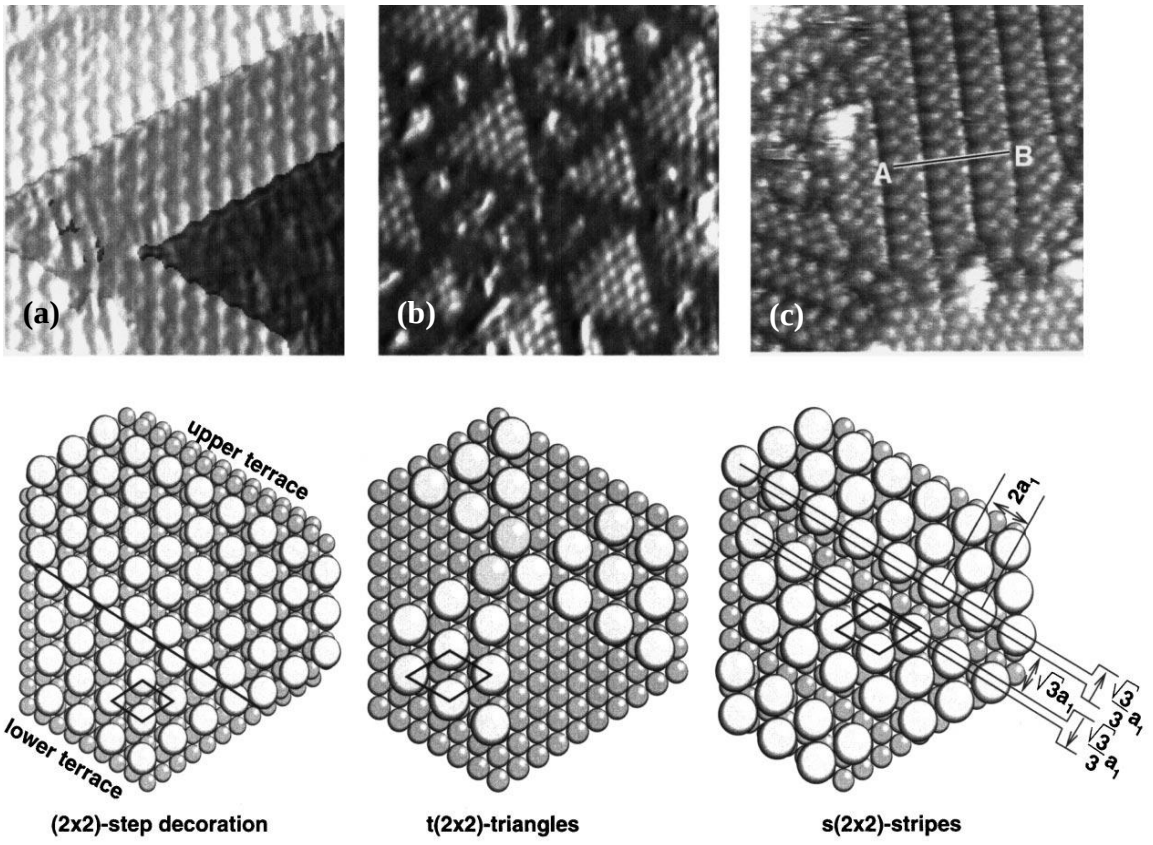


Figure 2.9. STM topographies and models of the three different (2*2) structures. (a) Steps on Pd after segregation (80 Å x 80 Å), (b) 2D triangular islands (120 Å x 120 Å), and (c) 2D stripes (90 Å x 90 Å) (Speller et al., 1999).

Dhanak et al. (1998) also studied sulfur adsorption on Pd (1 1 1) using similar surface characterization techniques. They also observed the $(3^{0.5}*3^{0.5})R30^{o}$ structure at a lower temperature of 320K and the $(7^{0.5}*7^{0.5})R19^{o}$ structure at a higher temperature of 500K. They suggested that the sulfur adsorption position in the $(3^{0.5}*3^{0.5})R30^{o}$ structure was at the FCC threefold hollow sites which was in agreement with the observation of Maca et al.(1985). For $(7^{0.5}*7^{0.5})R19^{o}$ structure, mixed layers of S-Pd model was proposed.

Patterson and Lambert (1987) studied the sulfur adsorption on Pd (1 1 1) with $S_2$ as the adsorbate gas. The $(7^{0.5}*7^{0.5})R19^{o}$ structure was observed with an incident $S_2$ flux

of $1*10^{-19}$ molecules/$m^2$. They also reported that the mechanism of the bulk sulfide formation with $(7^{0.5}*7^{0.5})R19^{o}$ structures was a function of temperature at high incident $S_2$ fluxes. At 550K, the sulfides were formed by the nucleation and growth of 3-D sulfide crystalline. At 300K, sulfides were formed layer by layer, while at 100K, only a single layer of elemental bulk sulfide was formed.

Rodriguez et al. (1998) used synchrotron based high resolution photoemission spectroscopy and *ab initio* calculations to study the electronic properties changes of Pd after dissociative adsorption of $S_2$. They reported that the formation of Pd-S bonds included large positive binding energies shifts in the core and valence levels of Pd. After chemisorption of sulfur on Pd surfaces, there was a substantial decrease in the electron density near the Fermi level and a simultaneous drop in the electron amount of its 4d orbital. As a result, the adsorbed sulfur atoms affected the surface properties of Pd resulting in the decrease of the dissociation ability to hydrogen of Pd.

The effect of adsorbed sulfur on Pd surfaces on $H_2$ adsorption was mainly considered to be the geometric blocking of the adsorption sites by adsorbed sulfur atoms. Burke and Madix (1990) investigated the influence of the adsorbed sulfur on the adsorption and desorption of hydrogen on Pd (1 0 0)[4] by performing the temperature programmed desorption (TPD) experiments. They observed that the saturation coverage of hydrogen decreased linearly with increasing sulfur coverage, and no hydrogen could be adsorbed above a sulfur coverage of 0.28 ML. The phenomenon suggested the direct site blocking effect by adsorbed sulfur atoms with each sulfur atom blocking 3.7 sites for hydrogen adsorption. In addition, they reported that the sticking coefficient decreased

[4] Pd has FCC structure, which does not show (1 0 0) or (1 1 0) planes (Cullity and Stock, 2001). Such planes mentioned in the present study that was quoted from the literatures are referred to surfaces, not planes of unit cells.

from 1 on the clean Pd with the addition of sulfur to 0.05 at a sulfur coverage of 0.25 ML. The decrease of the sticking coefficient was found to be in a manner consistent with the number of sites for hydrogen adsorption blocked per sulfur atom. However, they also indicated that the S-H interaction was more complicated than pure site blocking according to the $H_2$ desorption kinetics. The activation energy of hydrogen desorption was found to decrease from 85 kJ/mol on the clean Pd (1 0 0) to 49 kJ/mol on the sulfur-covered Pd surface with a coverage of 0.15 ML caused by the compensation effect. They explained that the compensation effect was resulted from either lower mobility of H on S adsorbed Pd surface or the activation barrier for hydrogen desorption caused by the adsorbed sulfur.

The sticking coefficient (or probability) mentioned earlier was defined as the fraction of molecules colliding with the surface that was adsorbed. As shown in Equation 2.30, the rate of the dissociative adsorption of hydrogen on palladium expressed in terms of sticking coefficient, $s(\theta)$ and the rate of hydrogen molecules bombardment, $\Gamma(T)$ (Ward and Dao, 1999). While the sticking coefficient is dependent on coverage, the rate of hydrogen bombardment is a function of temperature.

$$J_{H_2} = 2 \cdot s(\theta) \cdot \Gamma(T) \tag{2.30}$$

A clean Pd surface had a hydrogen sticking coefficient of 1 (Ward and Dao, 1999), meaning that all the hydrogen molecules that collided with the Pd surface would adsorbed on it. In the presence of impurities such as sulfur which also adsorbed on the surface sites, the sticking coefficient decreased as increasing impurity coverage to zero eventually.

Gravil and Toulhoat (1999) performed the first principles calculation to investigate the adsorption of hydrogen on the sulfur adsorbed Pd (1 1 1). They concluded that the sulfur poisoning effect on hydrogen adsorption was essentially structural effect although it was more complex than simple site blocking. Firstly, they reported that adsorbed sulfur atoms reduced the adsorption sites for hydrogen with each sulfur atom blocking 4 sites. Secondly, the adsorbed sulfur atoms reduced the mobility of the adsorbed hydrogen atoms and increased the diffusion barrier for the adsorbed hydrogen atoms around adsorbed sulfur atoms. As a result, each sulfur atoms effectively block 13 adsorption sites. They observed that no hydrogen adsorption occurred at a sulfur coverage above 0.33 ML.

Similarly, Lang et al. (1985) addressed the role of electronegative atoms, such as sulfur as a poison for the adsorption of electron acceptor such as $H_2$ on Pd. The adsorbed poisoning atoms acted as an "electronic block" in a region of 3.2 - 3.7 Å surrounding the adsorption sites resulting in geometric blocking of hydrogen in the region.

Wilke and Scheffler (1995) explained the effect of adsorbed sulfur on Pd surfaces on hydrogen adsorption in terms of adsorption energy. They performed DFT calculations to investigate hydrogen adsorption on S adsorbed Pd (1 0 0) surfaces with different sulfur coverage of 0 ML (clean surface), 0.25 ML, and 0.5 ML. They observed that the $H_2$ adsorption energy on clean Pd surfaces was the highest and decreased as the sulfur coverage was increased. It should be noted that higher adsorption energy means that the adsorption was more energetically stable. In addition, the $H_2$ adsorption sites varied from FCC hollow sites to the subsurface sites as the sulfur coverage was increased from 0 to 0.5 ML. According to the calculations, at the sulfur coverage of 0.25 ML, the decrease of

the $H_2$ adsorption energy was not sufficient to entirely "block" hydrogen adsorption sites on the Pd surface and the $H_2$ dissociative adsorption remained exothermic. It should be noted that the term "block" referred to a substantial reduction of binding energy of Pd-H, resulting in the unstable hydrogen adsorption. The partial blockage of hydrogen adsorption at low sulfur coverage (0.25 ML) was caused by the energy barriers formed by the sulfur in the reaction pathways for hydrogen dissociation. On the other hand, at a high sulfur coverage (>0.5 ML), a repulsive H-S interaction would block hydrogen adsorption entirely from the adsorption sites.

Actually, Wilke and Scheffler (1995) confirmed that the hydrogen dissociation path was non-activated (no activation barrier) on Pd (1 0 0) surface by obtaining the 2-D six-dimensional potential energy surface (PES) of $H_2$ dissociation and adsorption on clean Pd (1 0 0) surfaces. They suggested two limiting possibilities for the variation of the PES of the $H_2$ dissociation on Pd after the sulfur adsorption. Firstly, sulfur mainly modified the region of the H adsorption geometry in the PES, thus, the hydrogen bond property changed (adsorption energy changed). Secondly, sulfur changed the path or/and its energetic, thus the hydrogen dissociation path changed to an activated process, which had an energy barrier hindering the hydrogen dissociation.

In addition to affecting the dissociative adsorption of hydrogen, adsorbed sulfur also caused the transport mechanism of hydrogen to change. Peden et al. (1986) studied the dissociative adsorption kinetics of hydrogen on both clean and sulfur-adsorbed Pd (1 1 0) surfaces in an ultra-high vacuum at 100°C. They observed that the hydrogen adsorption rate decreased significantly at sulfur coverage greater than 0.4 ML and that the rate of adsorption was proportional to the hydrogen pressure. The substantial reduction of

the sticking coefficient to the order of $10^{-6}$ was also observed at sulfur coverage great than 0.4 ML. As a result, they concluded that the rate limiting step of hydrogen transport through the Pd layer changed from bulk diffusion to surface adsorption at sulfur coverage higher than 0.4 ML. In addition, they reported that the activation energy for hydrogen adsorption decreased from 22.7 kJ/mol on clean Pd to 14.3 kJ/mol on sulfur-adsorbed Pd, suggesting the presence of activation barriers for hydrogen dissociative adsorption. The decrease of activation energy for hydrogen adsorption after the sulfur adsorption was in agreement with the observation of Burke and Madix (1990).

Antoniazzi et al. (1989) reported that the rate limiting step for hydrogen transport through Pd foils would change from bulk diffusion to hydrogen surface recombination when Pd surface was covered with sulfur or carbon. They reported that the hydrogen recombination coefficient (Kr) derived from the permeation data as well as the sticking coefficient, increased by a factor of $10^4$ as sulfur coverage decreased from 0.14 to 0.06 at 625K. The hydrogen permeation through clean Pd in diffusion-limited regime with high $H_2$ incident fluxes and in surface recombination-limited regime with low $H_2$ incident fluxes was reported. They reported that the hydrogen permeance in surface recombination-limited regime could be smaller by 4 orders of magnitude than that in diffusion-limited regime. In case of sulfur-covered Pd, they reported that increasing the surface coverage resulted in the diffusion-limited permeation regime shifting into higher incident $H_2$ flux range. Since the activation energy for hydrogen permeation was insensitive to the surface sulfur coverage, they attributed the change in hydrogen recombination coefficient ($K_r$) to the reduction in the number of adsorption sites. This

implied that the poisoning was due to the blocking of the adsorption sites with each sulfur atoms blocked more than one adsorption site.

### *2.6.3 Effect of Sulfur on Membrane Performance and Methods for Improvement of its Performance*

Hurbert and Konecny (1961) investigated the effect of $H_2S$ on the rate of hydrogen diffusion though a Pd foil. They reported an ~ 84% reduction in $H_2$ flux of a 24 μm Pd foil membrane in the presence of 50 ppm $H_2S$ in $H_2$ at 350°C within ~ 120 minutes. They attributed the reduction in $H_2$ flux to the formation of a grey film on the Pd foil membrane, and the formation of the gray film appeared to be irreversible. McKinley (1967) reported an instantaneous 60% decline of hydrogen permeance of a 1mm thick Pd foil at 350°C upon exposing to a 4.5 ppm $H_2S/H_2$, and the reduction in permeance increased to 70% after 2 days exposure. They also reported that the Pd foils after the exposure lost its luster and appeared slight dull. However, they reported that the poisoning effect was reversible by observing the full permeance restoration of the sulfur-poisoned Pd foils in pure $H_2$ over a period of 2 days. They reasoned that the poisoning was caused by the $H_2S$ adsorption rather than the chemical attack or sulfide formation.

Mundschau et al. (2006) observed not only the decline of $H_2$ permeance of the 10 $\mu$m Pd foil upon feeding a 20 ppm $H_2S$ balanced with 60% $H_2$-He mixture at 320$^{\circ}$C for over 100 hours, but also the formation of numerous pinholes on the membrane after the exposure. Kulprathipanja et al. (2005) reported the failure of a 4 $\mu$m Pd/ceramic composite membrane with the loss of selectivity upon exposing to a 115 ppm $H_2S$ in a 50% $H_2$-$N_2$ mixture within 2 hours at 450$^{\circ}$C due to the formation of numerous pinholes. Edlund and Pledger (1993) reported the rapid failure (within seconds) of the $Pd/SiO_2/V$

composite membrane by a catastrophic ruptures with the formation of pinholes and cracks upon exposure to pure $H_2S$ of 115 psia at 700°C. Kajiwara et al. (1999) also reported the formation of cracks on the composite Pd membranes after exposing to $H_2S$. They exposed a Pd/porous alumina composite membrane to 6200 ppmv $H_2S/H_2$ at 400ºC, and observed a significant increase of both hydrogen and nitrogen flux within 1 hour. After the testing, they observed numerous pinholes and cracks formed on the Pd membrane, which were responsible for the increase of both hydrogen and nitrogen fluxes. The formation of pinholes and cracks on the Pd membrane was attributed by them to the formation of Pd sulfide ($Pd_4S$) in the Pd layer. The formation of $Pd_4S$ generated large stress in the Pd lattice because of the large difference in lattice constants between Pd and $Pd_4S$. The relaxation of the stress caused the formation of pinholes and cracks.

As shown in the literature stated previously, the sulfur poisoning effect of $H_2S$ to Pd membrane included not only the surface site blocking by adsorption but also sulfidation of Pd (i.e. Formation of $Pd_4S$). Morreale et al. (2007) determined the growth rates of $Pd_4S$ layer formed on a 100 μm Pd foil in a 1000 ppm $H_2S$-10%He-$H_2$ gas mixture by gravimetric methods at 623 - 908K. In addition, they predicted the hydrogen flux through the Pd layer with the $Pd_4S$ layer formed during the exposure by the sequential resistance model through a multi-layered membrane. Density functional theory was employed by the authors to estimate the hydrogen permeability of $Pd_4S$. Good agreements were reported by the authors between the activation energies for hydrogen permeation predicted by the model and the experimental data of 30.9 kJ/mol. However, the permeabilities (*n*-value of 0.5) obtained through the experiments were approximately

7 times greater than the model prediction. The discrepancy was attributed to the numerous cracks formed in the $Pd_4S$ layer due to the structure change.

Iyoha et al. (2007) investigated the effect of $H_2S$ to $H_2$ partial pressure ratio on the sulfidation of Pd and $Pd_{70}Cu_{30}$ membranes. The formation of $Pd_4S$ was determined to be a function of the $P_{H2S}/P_{H2}$ value and the membrane components activity values, which were determined by thermodynamics calculations (Barin et al. 1993). Iyoha et al. (2007) reported that the Pd membrane resisted the sulfidation when exposed to the $P_{H2S}/P_{H2}$ value below the equilibrium value predicted for $Pd_4S$ formation, and experienced sulfidation above the equilibrium value. However, deviations from the predicted values were reported on the $Pd_{70}Cu_{30}$ membranes, which they attributed to the copper segregation to the membrane surface.

In order to enhance the resistant to sulfur poisoning of Pd membranes, several methods have been proposed in the literature, including varying the crystal structure of Pd layers and alloying Pd with other elements (Gao et al., 2004).

Nano-structured Pd based membranes have been shown to enhance hydrogen permeability, resistance to hydrogen embrittlement, and sulfur resistance (Bryden and Ying, 2002). Bryden and Ying (2002) reported that the nano-structured Pd/Fe membrane showed a less decline of hydrogen flux (~80%) than that of polycrystalline structured Pd/Fe membrane (~95%) in the presence of 51.9 ppm $H_2S$ at 200$^oC$ over 140 minutes. It should be noted that the nano-structure referred to that the grain size was smaller than 30 nm while the polycrystalline structure had grain size over 100 nm. Since sulfur atoms favorably adsorb on high coordination number sites but not grain boundaries (Biswas et al., 1988), the better sulfur resistance of the nano-structured membranes was attributed by

the authors to the fact that the nanostructures have more grain boundary areas than the polycrystalline structures.

Amorphous Pd based membranes also showed a higher hydrogen solubility, permeability, and resistance to hydrogen embrittlement than polycrystalline Pd based membranes (Itoh et al., 1995, 1998). Although no sulfur resistance data have been reported up to date, the amorphous membranes have a high potential to show high sulfur resistance due to the extremely high defect and dislocation ratio in amorphous metals. However, the high tendency for small grains to grow at elevated temperatures limited the practical applications for the nanostructured or amorphous membranes. Bryden and Ying (2002) reported that after annealing at 400$^{o}$C, the sulfur resistance of the Pd/Fe membranes decreased due to the grain growth.

Alloying Pd with other elements also potentially enhances sulfur resistance due to that electronic, chemical properties and reactivity of Pd are significantly different after alloying. Bimetallic catalysts have been extensively reported to enhance the activity, selectivity, and poisoning resistance over monometallic catalysts due to the "ensemble" (geometric) and "ligand" (electronic) effect by adding a second metal (Rodriguez, 1996; Mazzone et al., 2008). The ensemble effect, referred to the addition of a second metal, may block certain sites reducing or eliminating the formation of inhibiting species, while the ligand effect referred to the formation of new metal-metal bonds, may modify the electronic structure resulting in the different activity for reactant.

In order to search for proper elements for forming higher sulfur resistance Pd alloys, the thermodynamics of bulk sulfide formation should be considered firstly although resistance to formation of bulk sulfide is not sufficient for reducing sulfur

poisoning. The higher absolute value of the free energy ($\Delta G_0$) of the sulfide formation implied higher sulfur resistance due to the fact that the threshold $H_2S$ concentration for forming sulfide was higher (Mundschau 2006). Operating the membranes under the equilibrium $H_2S$ concentration showed resistance to the formation of bulk sulfides (Iyoha et al. 2007).

Among different Pd alloys, Pd/Cu alloys have been studied extensively for sulfur resistance. As mentioned in *section 2.4*, Pd and Cu form FCC and BCC alloy according to Cu composition. Although showing high hydrogen permeability and chemical stability in the environments containing CO, $CH_3OH$, $CO_2$, and $H_2O$. (Han et al., 2002; Gao et al., 2004), BCC PdCu alloy showed poor sulfur resistance. McKinley (1967) reported a 95% decline of hydrogen permeance in the presence of 4.5 ppm $H_2S/H_2$ on a BCC $Pd_{60}Cu_{40}$ alloy foil at 350°C.

Morreale et al. (2004) investigated the sulfur resistance of the Pd/Cu alloy foils of different Cu composition and phase by feeding 1000 ppm $H_2S/H_2$ up to 620 kPa at the temperatures of 603 - 1123K. They reported that the FCC Pd/Cu alloys showed sulfur resistance with little decline in hydrogen permeance in the presence of 1000 ppm $H_2S$. The Pd/Cu alloy with mixed FCC-BCC phase showed partial sulfur resistance, while the BCC Pd/Cu alloy of 40 wt% Cu showed a permeance decline of 99% at 340°C and 80% at 440°C. The smaller permeance decline at 440°C was attributed to more FCC phase transformation in the 40 wt% Cu Pd/Cu alloy than at higher temperatures. They also reported that it was the $H_2S$ concentration that determined the degree of poisoning, rather than the time of exposure. However, the testing time was not reported. O'Brien et al. (2010) tested the 25 μm $Pd_{47}Cu_{53}$ BCC Pd/Cu alloy foil in the presence of 1000 ppm $H_2S$

at 350°C, and reported that the hydrogen flux was undetectable within 5 minutes of exposure. Post XPS characterization of the Pd/Cu foil showed the formation of the Pd-Cu-S terminal layer within 3 nm from the surface of the Pd/Cu alloy foil. The sulfide layer was considered by the authors to be either inactive for hydrogen dissociation or impermeable to hydrogen atoms.

Kulprathipanja et al. (2005) investigated the sulfur poisoning effect on both surface morphology and gas permeation characteristics of both Pd and Pd/Cu alloy membranes. They reported that the $H_2$ permeance of Pd/Cu alloy membranes decreased to a steady state value in the presence of $H_2S/H_2$ with $H_2S$ concentrations less than 250 ppm at 723K. They reasoned the phenomenon to be the sites blocking effect of sulfur. Higher $H_2S/H_2$ caused a complete sulfur adsorption layer forming a mass transfer barrier for hydrogen to penetrate. The exposure to even higher $H_2S/H_2$ concentrations at the same temperature resulted in the formation of numerous pinholes causing the failure of the membranes. They attributed the formation of pinholes to the formation of Pd and Cu sulfide which caused the expansion of the lattice and the rearrangement of the film structure. The authors also concluded that the $H_2S$ concentration was the factor causing the membrane failure, rather than exposure time. The $H_2S$ concentration caused pure Pd membranes to fail was 100 ppm and that for Pd/Cu alloy membranes was 300 ppm. The authors also reported that in the presence of steam at lower temperatures, the sulfidation of the membrane was aggravated. Kulprathipanja et al. (2005) also reported that in the presence of sulfur, Cu segregated to the surface due to the stronger interaction between sulfur and copper resulting in the surface phase varied from BCC to FCC, therefore, less hydrogen permeation.

Pomerantz and Ma (2009) investigated the performance and log-term stability of the composite Pd membranes with a Pd/Cu top layer in the presence of $H_2S$ in the temperature range of 350 - 500°C. They reported an 80% reduction in $H_2$ permeance of the Pd/Cu membrane in a ~50 ppm $H_2S/H_2$ gas mixture at 500°C, and attributed the permeance loss to the surface sulfide formation which blocked the adsorption sites. The hydrogen permeance was recovered mostly in $H_2$ with the amount recovered and the rate of recovery increased with increasing temperature which was attributed to the exothermic adsorption of $H_2S$ on the metals. In addition, they reported that the amount of irreducible surface sulfides increased with increasing exposure time and decreasing temperature. The authors also reported that the He leak decreased after the $H_2S$ exposure and attributed it to the sulfur segregation to grain boundaries and defects, which were the pathways for non-permeable gases. Most recently, Pomerantz and Ma (2011) fabricated the composite Pd membranes with a sub-micron FCC Pd-Cu alloy layer on the surface. The resultant membranes exhibited similar $H_2$ permeance compared to Pd membranes with the same thickness. Pomerantz (2010) also reported that the composite membranes with a sub-micron FCC Pd/Cu alloy layer on the surface exhibited a good sulfur resistance in the presence of $H_2S$ up to 5 ppm at 400 – 500°C.

Pt is another potential candidate to alloy with Pd for improving sulfur resistance. Pure Pt membranes have been studied as membrane reactors for converting $H_2S$ to $H_2$ and $S_2$ due to its high chemical stability even in the presence of $H_2S$ at high temperatures (Edlund and Pledger, 1993). Pt membranes also showed the ability to limit coke formation (Edlund and Pledger, 1994). Kajiwara, et al. (1999) studied the sulfur resistance of Pt membranes in the presence of 6200 ppm $H_2S$ at 400°C. They reported

that the structure of the Pt membrane remained unaltered, while the formation of numerous pinholes was observed on a Pd membrane after the same test. The authors, therefore, concluded that Pt was more sulfur resistant than Pd structurally, which they attributed to the less lattice expansion of Pt after sulfur adsorption. However, a reduction of 94% in hydrogen permeance of the Pt membrane was reported during the $H_2S$ exposure. This indicated that the sulfur adsorbed on the Pt surface and blocked the adsorption sites although Edlund and Pledger (1994) have proposed that platinum sulfide compounds were not stable above 225°C.

In the catalysts field, researchers have reported that Ru and Rh showed higher sulfur resistance (Ryu et al, 1999; Acoya et al, 1991). Ryu et al. (1999) examined the $H_2S$ resistance of a series of $Pd/Al_2O_3$ catalysts with different amount of Rh and Ru. They characterized the activity of the bimetallic catalysts in the catalytic methane combustion reaction before and after exposure to $H_2S$ in an oxygen-rich atmosphere (100 ppm $H_2S$/Air at 500$^oC$) for 5 hours. They observed that the Ru/Pd bimetallic catalysts showed the most enhanced activity in catalytic methane combustion reaction even after the catalysts being poisoned by $H_2S$. They reported that $Ru/Pd/Al_2O_3$ showed the lowest temperature required for a 90% conversion ($T_{90}$) among the catalysts tested. In addition, $Ru/Pd/Al_2O_3$ also showed the smallest difference in $T_{90}$ values before and after being sulfur-poisoned. The results indicated high resistance to $H_2S$ poisoning of the $Ru/Pd/Al_2O_3$ catalysts.

Au is another candidate of a great potential for forming alloy with Pd in order to enhance the sulfur resistance. In the catalysts field, Pd/Au alloys have shown high resistance to various poisonous impurities. Sarkany et al. (2002) reported that the Pd/Au

alloy catalysts showed better selectivity in acetylene hydrogenation reaction than the Pd catalysts due to the fact that less carbon adsorbed on it (i.e. less site blocking). Mazzone et al. (2008) theoretically studied the interaction between CO and the Pd/Au alloy. They reported that the binding energy of the CO-Pd/Au alloy bond decreased with increasing Au composition in the Pd/Au alloy in both one and two CO molecules adsorption models. This implied that the adsorption of CO on the Pd/Au alloy surface was less stable than on the Pd surface.

Vnerzia et al. (2003) reported higher sulfur resistance of the Pd/Au catalysts than Pd catalysts. They investigated the performance of the Pd/Au catalysts in the hydrodesulfurization of dibenzothiophene and thiophene and observed no decrease in catalytic activity, suggesting the high sulfur resistance of the Pd/Au catalysts. They also confirmed the sulfide phase ($Pd_4S$) on the Pd catalysts after the hydrodesulfurization of thiophene while the Pd/Au catalysts showed no sulfide formation after the same reaction. The high sulfur resistance of Pd/Au was reasoned by the authors to be the electronic and ensemble size effect after adding Au into Pd. Pawelec et al. (2004) also reported that the Pd/Au alloy catalysts were resistant to sulfur poisoning. The Pd/Au catalysts supported on γ-alumina were tested for the hydrogenation of naphthalene and toluene in the presence of dibenzothiophene (DBT) (Concentration up to 113 ppm) in the temperature range of 498 - 548K. They reported the naphthalene hydrogenation occurred concurrently with hydrodesulfurization of DBT, and no decrease in catalytic activity was observed on any of the Pd/Au catalysts.

Very few research have studied the Pd/Au alloy membranes for hydrogen separation as well as the sulfur resistance in the literature. McKinley (1967) reported that

a $Pd_{60}Au_{40}$ alloy showed the best sulfur resistance among all the Pd-based alloy foils tested including Pd, $Pd_{73}Ag_{27}$, and $Pd_{60}Cu_{40.}$ In the presence of 4.5 ppm $H_2S$ at 350$^oC$, the $Pd_{60}Au_{40}$ alloy foil showed a small decline of 10% in hydrogen flux over a period of 2 days. Under the same testing conditions, the percentages of hydrogen permeance decline were 70% for the Pd foil, 95% for the $Pd_{60}Cu_{40}$ alloy foil, and >99% for $Pd_{73}Ag_{27}$ alloy foil. In the presence of 20 ppm $H_2S$, the $Pd_{60}Au_{40}$ alloy foil showed a 56% decline in the hydrogen flux at the same temperature. The full recovery of the hydrogen permeance was possible after exposing to $H_2$ for 2 days after the $H_2S$ exposures. No other gold compositions were tested.

Until very recently, Way et al. (2008) characterized the sulfur resistance of the composite Pd/Au alloy membranes of Au content ranging from 5 to 45 wt% in the presence of $H_2S$ at 400$^oC$. They fabricated the composite Pd/Au alloy membranes by electroless depositing Pd and Au sequentially with the ammonia hydroxide-based bathes on the $ZrO_2$ modified PSS supports followed by the heat treatments at temperature above 200$^oC$ to 1200$^oC$. They reported the inhomogeneous Pd/Au alloy layer due to the segregation of Au to the surface. A bulk 20 at% Au Pd/Au alloy membrane was found to be 58 at% Au at the surface. For the sulfur resistance characterization, they reported a 38% permeance decline of the $Pd_{85}Au_{15}$ alloy membrane in the presence of 5 ppm $H_2S$ at 400$^oC$, while a 71% permeance loss was observed on a $Pd_{94}Cu_6$ FCC phase membrane. They attributed the high sulfur resistance of Pd/Au to the lower sulfur-Pd/Au alloy binding energy when compared to Pd and the Pd/Cu alloys. They also tested a $Pd_{90}Au_{10}$ composite membrane in a simulated water gas shift (WGS) gas mixture (51% $H_2$, 26%$CO_2$, 21% $H_2O$, and 2% CO) at 400$^oC$, and operated at a 76% hydrogen recovery of

total gases which was nearly the same as the hydrogen flux seen with exposure to a pure $H_2$ gas having similar hydrogen partial pressure in the simulated WGS gas mixture, indicating the highly chemical stability of the Pd/Au membrane.

Chen and Ma (2010) investigated the performance of the composite Pd/Au (8wt% Au) alloy membrane in the 54.8 ppm $H_2S/H_2$ gas mixtures at 350 – 500°C. The authors reported that the Pd/Au alloy membrane exhibited the resistance to form bulk sulfide under the testing conditions by showing no continuous permeance decline during the $H_2S$ exposure. No significant He leak increase and the morphological change after the $H_2S$ tests further substantiated the lack of bulk sulfide formation on the Pd/Au membranes. The permeance loss of the Pd/Au membrane was attributed by the authors to the dissociative adoption of the $H_2S$ on the surface which decreased with increasing temperature and was recoverable.

# 3. Experimental

## 3.1 Membrane synthesis

### *3.1.1 Porous metal supports*

Four types of substrates including porous stainless steel 316L (PSS) plates, porous Hastelloy plates, porous Inconel tubular supports, and porous Hastelloy tubular supports were used in this study. All the porous metal substrates were with the media grades ranging from 0.1 - 0.5 $\mu$m, and were purchased from either Mott Metallurgical, Inc. or Chand Eisenmann Metallurgical, Inc. A 0.5 $\mu$m media grade of a porous substrate is defined when the support rejects 95% of particles with a diameter of 0.5 $\mu$m or greater. However, previous work by Mardilovich et al. (2002) has shown that the pore sizes determined by mercury porosymmetry analysis were significantly larger than the support grade. The compositions of the metal substrates used in the study were listed in Table 3.1.

The PSS and Hastelloy plates (coupons) were prepared by cutting sheets of either 316L PSS or Hastelloy into 1 x 1 $cm^2$ or 1 x 1.5 $cm^2$ pieces (the thickness of coupons were 0.1 cm). The coupons were used to investigate the plating and annealing conditions.

On the other hand, the porous tubular supports (Inconel or Hastelloy) were used for permeation experiments. The dimensions of the tubular supports were 1.27 cm in outer diameter and 6 cm long with a wall thickness of 0.16 cm. The porous tubular supports were welded to non-porous 316L SS tubes with the same outer diameter at both ends with a blind cap on one end. The assemblies were then used for membrane

preparation and permeation testing. Typical coupon and tubular supports are shown in Table 3.1.

Table 3.1. Chemical composition (wt%) of porous metal support[5]

| Element | 316L SS | Inconel 625 | Hastelloy C-22 |
|---|---|---|---|
| Al | | < 0.4 | |
| C | < 0.03 | < 0.01 | < 0.01 |
| Cr | 16 – 18.5 | 20 - 23 | 20 – 22.5 |
| Co | | < 1 | < 2.5 |
| Fe | balance | < 5 | 2 - 6 |
| Ni | 10 - 14 | balance | balance |
| Mo | 2 - 3 | 8 - 10 | 12.5 – 14.5 |
| Mn | < 2 | < 0.5 | < 0.5 |
| Si | < 1 | < 0.5 | < 0. 08 |
| P | < 0.045 | < 0.015 | < 0.02 |
| S | < 0.03 | < 0.015 | < 0.02 |
| Ta | | < 0.05 | |
| Ti | | < 0.4 | |
| W | | | 2.5 – 3.5 |
| V | | | <0.35 |

[5] www.azom.com; www.csialloys.com

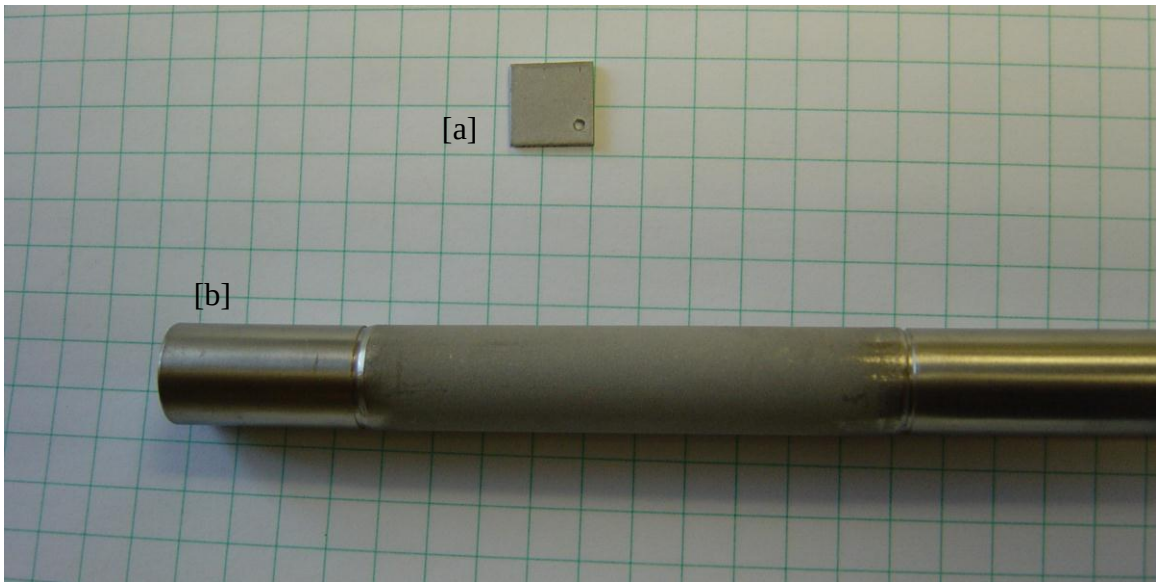


Figure 3.1. [a] Coupon (porous plate) and [b]Tubular supports.

### *3.1.2 Pretreatment of porous metal supports*

Cleaning of the metal supports was the first step of the membrane synthesis. The alkaline cleaning solution (the compositions were summarized in Table 3.2) and the cleaning procedure reported by Mardilovich et al (1998) were adopted in the study. The cleaning process starts with the immersion of the metal supports in an alkaline ultrasonic bath for at least 30 minutes at 60°C to remove any dirt, grease and oil. Following the alkaline bath, the metal supports were rinsed with pressurized tap water until the support surface was pH-neutral. A strip of a pH indicator was used to check the pH of the support surface by contacting it on the surface of the metal supports during the rinsing process. Usually, it takes an hour for the metal supports to become pH-neutral. After reaching pH-neutral, the metal supports were immersed for 5 minutes in ultrasonic deionized (DI) water and isopropanol bath for the final rising and facilitating the drying before drying in the oven for over 2 hours at 120 - 140$^{o}$C. The DI water mentioned here and in the rest of

the entire thesis was with an electrical-resistivity of 18.2 MΩ-cm, which was produced by the Thermo Scientific Barnstead E-pure water filtration system.

Table 3.2 Composition of the alkaline solution

| Component, purity | Amount | Merchant |
|---|---|---|
| $NaPO_4 \cdot 12H_2O$, 98 wt% | 45 g/l | Alfa Aesar |
| $Na_2CO_3$, 99.5 wt% | 65 g/l | Alfa Aesar |
| NaOH, 97 wt% | 45 g/l | Alfa Aesar |
| Industrial detergent | 5 ml/l | Alconox |

After cleaning, the metal supports were oxidized at 700 - 800 ºC in stagnant air for 12 hours to form an oxide layer on the surface. This oxide layer acts as an intermetallic diffusion barrier layer between the support metals (i.e. Fe, Ni, Cr) and the $H_2$ selective Pd or Pd alloy layer (Ma et al., 2000). A Lindberg (Blue M732) oven was used for the oxidation of supports with a heating and cooling rate of 10ºC/min. The mass of the supports was measured before and after oxidation and the He flux of the tubular supports was measured before and after oxidation.

In the case of tubular supports, some were further modified with other pretreatment steps after oxidation. The modifications will be described in detail in *Section 3.1.5.*

### *3.1.3 Support activation*

In order to initiating the autocatalytic electroless plating, seeding the support surface with Pd nuclei by activation was necessary. The formation of Pd nuclei was described in Equation 2.22.

The activation procedure and chemical recipes (as shown in Table 3.3) reported by Mardilovich et al (1998) was used in the study.

Table 3.3 Composition of activation solutions

| Component, purity | Amount | Merchant |
|---|---|---|
| $SnCl_2 \bullet 2H_2O$, 98 wt% | 1 g/l | Aldrich |
| $PdCl_2$, 99.9 wt% | 65 g/l | Alfa Aesar |
| HCl, 37 wt% | 1 ml/l | Merck |

In order to have a thoroughly wet and fresh surface, the supports were immersed in DI water for 1 - 3 minutes, immersed in 1 M HCl for 30 seconds, and then immersed in DI water for 15 minutes before the activation process. The activation procedure consisted of immersing the supports in the $SnCl_2$ solution for 5 minutes, DI water for 2 minutes, fresh DI water for 3 minutes, the $PdCl_2$ solution for 5 minutes, 0.01 M HCl for 2 minutes and then fresh DI water for 3 minutes. It usually took about 3 - 6 cycles to complete the activation process when the entire support surfaces turned into dark color. The purpose of immersing the supports in DI water and 0.01 M HCl in between the $SnCl_2$ and the $PdCl_2$ solutions was to prevent the hydrolysis of the $Sn^{2+}$ and $Pd^{2+}$ ions which would form hydroxyl-chlorides on the supports.

### *3.1.4 Electroless plating*

Both autocatalytic electroless plating and the displacement (immersion) electroless plating methods were used in the study. While the former was used for plating Pd and Ag, the latter was used for depositing Au. The compositions and the conditions of plating solutions used in the study are given in Table 3.4. It should be noted that the term

"electroless plating" usually referred to the autocatalytic plating, however, the general term of electroless plating included both autocatalytic and displacement reduction deposition (El-Shazly and Baker, 1982; Okinaka,1990). In order to define these two ways of electroless plating, the term "electroless plating" referred to the specific autocatalytic plating and the term "displacement plating" or "galvanic displacement plating" referred to the displacement (immersion) plating in the entire thesis.

Table 3.4 Plating bath compositions and conditions

| Component, purity/Condition | Pd bath | Ag bath | Au bath | Merchant |
|---|---|---|---|---|
| $Pd(NH_3)_4Cl_2 \cdot H_2O$, 99wt% | 4 g/l | - | - | Alfa Aesar |
| $AgNO_3$, 99wt% | - | 0.519 g/l | - | Aldrich |
| $Na_2EDTA \cdot 2H_2O$, 99wt% | 40.1g/l | 40.1g/l | - | Aldrich |
| $NH_4OH$ (28%), 28wt% | 198 ml/l | 198 ml/l | - | Merck |
| $H_2NNH_2$ (1 M), 98.5wt% | 5.6 ml/l | 5.6 ml/l | - | Alfa Aesar |
| $Na \cdot Au(Cl)_4 \cdot 2H_2O$, 99wt% | - | - | 2 – 5 mM | Alfa Aesar |
| pH | 10 - 11 | 10 - 11 | 2 - 4 | |
| Temperature (°C) | 60 | 60 | R.T. - 60 | |

Before plating, the supports (with an activated layer) were immersed in DI water for 1 - 3 minutes, immersed in 1 M HCl for 30 seconds, and then immersed in DI water for 10 minutes to obtain a thoroughly wet and fresh surface. It should be noted that this was only required for the dried activated-supports. Typical Pd plating procedure consisted of several successive immersions of the supports in the plating solution at 60ºC for 90 minutes with the hydrazine added just before the support was immersed. The heating of the plating solution was done by placing the plating solutions in a heated water bath. In between the Pd plating bathes, the support was immersed in DI water at 60ºC for

5 minutes before immersion in a fresh Pd plating solution. Usually, 5 rounds of Pd plating were performed on a well-activated support. The membrane would be rinsed with DI water and dried at 120 - 140ºC for at least 2 hours. The mass of the supports was measured before and after plating and the He flux of the tubular supports was measured before and after plating. Ag deposition was conducted in a similar way of Pd plating and only carried out for forming Pd/Ag barrier layer in the study, which will be described in *Section 3.1.5*.

The average thickness of the plated films was estimated gravimetrically according to Equation 3.1

$$z = \frac{\Delta m}{A \cdot \rho} \cdot 10000 \tag{3.1}$$

where z is the film thickness in μm, Δm is the weight gain in g, A is the plated area in $cm^2$ and ρ is the density of the plated film in $g/cm^3$.

In the case of the tubular supports, after the support was "liquid dense", a vacuum was applied inside the tube by attaching the tube side to an aspirator or vacuum pump for further plating. "Liquid dense" referred to a state of plating supports when no plating solution can penetrate through the porous support (i.e. no solution was found inside the tube) during the typical Pd plating. The purpose of applying vacuum is to minimize the Pd required to entirely seal the porous support (to gas dense). When applying vacuum, the strength of vacuum was increased gradually from ~ 8, ~16 to 27 in Hg. A vacuum was increased only when the support was liquid dense during plating at the previous vacuum level. Pd was deposited on the tubular support until gas dense (i.e. no He flow

was measured at $\Delta P$= 2.5 atm., the maximum value of the He permeation testing rig). In practical, the membrane was deemed dense if the membrane had a He flow rate of less than 0.03 sccm at $\Delta P$ = 2.5 atm.

In the case of Au plating, the galvanic displacement plating was carried out according to several previous work (Parker et al., 1974; El-Shazly and Baker, 1982). Before plating, the Pd-deposited supports were immersed in DI water for 1 - 3 minutes, immersed in 1 M HCl for 5 minutes, and then immersed in DI water for 5 minutes. It was found that the immersion in HCl was important for the displacement reaction which would be described in detail in *Chapter 4*. After the immersions in HCl and DI water, the Pd-deposited supports were then immersed in the Au plating solution for 120 – 180 minutes. Due to the nature of the displacement plating, the displacement reaction would essentially cease when the surface was entirely covered by the deposited Au layer resulting in roughly a 0.5 μm thick Au layer. The application of gravimetrical method for thickness estimation (as shown in Equation 3.1) was extremely difficult due to the fact that the weight change after displacement plating was the combination of mass of Au deposited and mass of Pd dissolved.

### *3.1.5 Support grading and Pd/Ag barrier*

As mentioned previously in *Section 3.1.2*, some membranes prepared on tubular supports were further modified after oxidation. In order to decrease the pores size as well as the pore size distribution of the support for minimizing the thickness of dense Pd layer, the supports were graded with $Al_2O_3$ slurries prior to plating. The compositions of the slurries used in the study are summarized in Table 3.5.

Table 3.5 Components of $Al_2O_3$ slurry

| Component, purity | Slurry A | Slurry B | Slurry C | Merchant |
|---|---|---|---|---|
| 5 μm $Al_2O_3$, 99.95wt% | 1 g/l | - | - | Alfa Aesar |
| 3 μm $Al_2O_3$, 99.95wt% | 0.5 g/l | - | - | Alfa Aesar |
| 1 μm $Al_2O_3$, 99.95wt% | - | 1 g/l | - | Alfa Aesar |
| 0.3 μm $Al_2O_3$, 99.95wt% | - | 0.4g/l | 1 g/l | Alfa Aesar |
| 0.01-0.02 μm $Al_2O_3$, 99.95wt% | - | 0.05 g/l | 0.05 g/l | Alfa Aesar |
| HCl (1M), 36wt% | 0.5ml/l | 0.5ml/l | 0.5ml/l | Merck |

Prior to grading, the support was attached to a vacuum of ~ 8 in Hg and immersed in DI water for 5 minutes followed by the immersion in 1 M HCl for 5 seconds and then in DI water for another 5 minutes. For most of the membranes prepared in the study, the support was then immersed in the slurry B for 10 seconds. The vacuum was increased to 27 in Hg immediately after the support was taken out of the slurry and placed in DI water for 5 minutes. A vacuum of 27 in Hg was kept while taking the support out of DI water and drying in air for several seconds before the final drying in the oven at 120 - 140ºC for at least 2 hours.

For membranes C-14, C-15, and C-16, the grading was carried out by immersing the supports in slurry A, B, and C consecutively under the vacuum for 40, 20, and 10 seconds respectively while the procedures before and after grading remained unchanged.

After grading, the support was deposited with "Pd glue "to seal the $Al_2O_3$ particles within the pores of the support. The Pd glue was a thin Pd layer which was deposited under a vacuum of ~8 in Hg until the plating solution was depleted (roughly 3 - 5 minutes) after one activation loop under the same vacuum.

On top of the Pd glue layer, consecutive Pd and Ag layers were deposited in order to further decrease the pore size of the support. This porous Pd/Ag layer also functioned

as an additional intermetallic diffusion barrier (Ayturk et al., 2006). The deposition of Pd/Ag barrier layer was conducted according to Ma et al. (2007). After activation (3 loops), Pd was deposited for 30 minutes with a concentration of 0.33 ml/l of 1 M hydrazine, Ag for 60 minutes with 0.58 ml/l of 1 M hydrazine, Pd for 60 minutes with 0.38 ml/l of 1 M hydrazine, Ag for 60 minutes with 0.58 ml/l of 1 M hydrazine, and Pd for 60 minutes with 0.58 ml/l of 1 M hydrazine. The resultant Pd/Ag barrier layer was lightly sanded by hand with 2400 grit SiC paper and cleaned in an ultrasonic isopropanol bath.

### *3.1.6 Annealing and polishing*

For some membranes tested in the study, a method of annealing and polishing sequential layers was applied during the final rounds of Pd deposition to mitigate leak growth during the testing at elevated temperatures. After the membrane was liquid dense and a certain number of rounds of Pd plating, the membrane was annealed at 550ºC for 12 hours in a furnace in which He was purged on both the shell and tube sides of the membrane.

Following the annealing, the membrane was mechanically treated with a lathe with 600 and then 1200 grit SiC sandpaper and cleaned in an ultrasonic DI water and isopropanol. Another layer of Pd was then deposited on top of the polished membrane surface. The sequence of annealing, polishing, and plating was repeated 2 – 3 times until the membrane was dense. The mass and He leak of the membrane was monitored in between all of the steps.

## 3.2 Membrane characterization

### *3.2.1 He leak measurement (at Room Temperature)*

Starting from bare support, the He flux of the tubular support was measured after every step during the membrane fabrication until the membrane was dense. A shell-and-tube type stainless steel module was employed for the He flux measurement with a pressure difference up to 2.5 atm. Since the range of He flux was within 4 – 5 orders of magnitude difference during the entire membrane fabrication from bare support to dense, three different flow meters were utilized to measure different ranges of the He volumetric flow rate. For high flow rates in the initial stages of the membrane fabrication, a GCA Wet Test Flow Meter from Precision Scientific was used. The Wet flow meter was able to measure the flow rate up to 13 l/min.

An Alltech 4068 digital flow meter was utilized during the middle stages of the preparation for flow rates of 2 – 300 ml/min. In the final stages of membrane fabrication where membrane was close to dense, a bubble flow meter was used for flow rates smaller than 2 ml/min.

### *3.2.2 Permeation-testing apparatus*

Figure 3.2 shows the experimental apparatus used in the study for testing the performance (i.e. $H_2$ permeance and selectivity) of the membranes in pure $H_2$ or $H_2S/H_2$ mixtures. The permeation-testing module, as shown in the broken-line rectangle area in Figure 3.2, was designed based on the work of Mardilovich et al. (1998). This shell-and-tube permeation-testing module consisted of a 316L SS tubular casing with a 1” outer diameter (O.D). and length of 15 - 20”. The testing membranes were placed inside the

casings with the non-porous parts attached to the casings by the use of reducing units and a removable graphite ferrule. The connecting reducing units were modified by attaching a 1/8" tubing to allow the gas to flow in the shell side (retentate). The other end of the casing was connected to a ¼" tube to allow feed gas to enter the casings. All the tubings and fittings were made of 316L SS and purchased from Swagelok Inc. The permeation-testing module was mounted vertically into the tubular ceramic-fiber furnace made by Watlow Inc. The ends of the module outside the furnace were wrapped with insulation strips to minimize the heat loss during testing at elevated temperatures. The temperature of the module was monitored by Omega type-k thermocouples and controlled by a Eurotherm 2116 temperature controller connected to the furnace heater.

The feed gas of industrial grade (99.5%) $H_2$ or He purchased from ABCO flows through the shell side of the membrane with a needle valve adjusting the flow rate. The retentate gas flow is measured by a digital mass flow meter purchased from MKS (0 – 1000 sccm) before exiting to the vent while the permeate flow rate was measured by digital mass flow meters at the tube side of the membrane. For measuring the permeate $H_2$ flow rate, a MKS mass flow meter for $H_2$ (0 – 1000 sccm) was used. In the case of extremely high $H_2$ flow rate, the wet flow meter was utilized with the correction of the water vapor pressure effect. For measuring permeate He flow rate, a MKS mass flow meter for He (0 – 20 sccm) was used. A bubble flow meter was used for very small He flow rates below the detection limit of the mass flow meter.

The shell side pressure is regulated by a Veriflo pressure regulator (0 – 250 psi) supplied from Parker Instrumentation and measured by a pressure transducer made by MKS (0 – 250 psi), while the tube side pressure was kept at ambiance pressure (~ 1atm)

and monitored by a MKS pressure transducer (0 – 50 psi). A ballast volume of 3.8 liters supplied from Swaglok Inc was installed before the module to ease the transition between $H_2$ and He. A low pressure (~ 1atm) He sweep gas flow (purge) at 1 atm at the tube side regulated with a needle valve was also used to ease the transition between $H_2$ and He. In addition, the He sweep gas was also used to prevent the membrane from oxidizing during the start-up/shut-down operation while heating/cooling the testing module between room temperature and elevated temperatures, but not used during the permeation tests.

In the case of $H_2S/H_2$ gas mixture feed, the gas flow was regulated by a mass flow controller purchased from MKS (0 – 1000 sccm) before entering the module and the feed pressure was controlled by a back pressure regulator (with gauge; 0 – 100 psi) made by SGD Inc at outlet of the retentate side. The $H_2S/H_2$ mixtures were made by either Airgas or ABCO and had an analytical accuracy of ± 2%. A gas mixer was used to produce different $H_2S$ concentrations by mixing pure $H_2$ with $H_2S/H_2$ gas mixture of know concentration. As depicted in Figure 3.3, the gas mixer itself was made of 316L SS tubing packed with stainless steel filings and of the same dimensions of the shell casing used for permeation experiments. A $H_2$ and a $H_2S/H_2$ mix gas flow each controlled by a mass flow controller (Brooks 5850E, 0 – 600 sccm for $H_2$; MKS, 0 – 1000 sccm for $H_2S/H_2$) entered the mixer from the two opposite sides to allow cross current mixing where the two gas streams met. The packed stainless steel filings caused further turbulence for better mixing when the gas stream passed through before exiting the mixer. It should be noted that all the O-rings present in valves in the entire testing apparatus were switched to Kelzar from the standard Viton for sulfur resistance.

A SCB-68 data acquisition system box supplied by National Instruments and LabView 6.1 software was used to continuously acquire the parameters including temperature, pressure, and flow rates and store in the computer during the entire course of characterization.

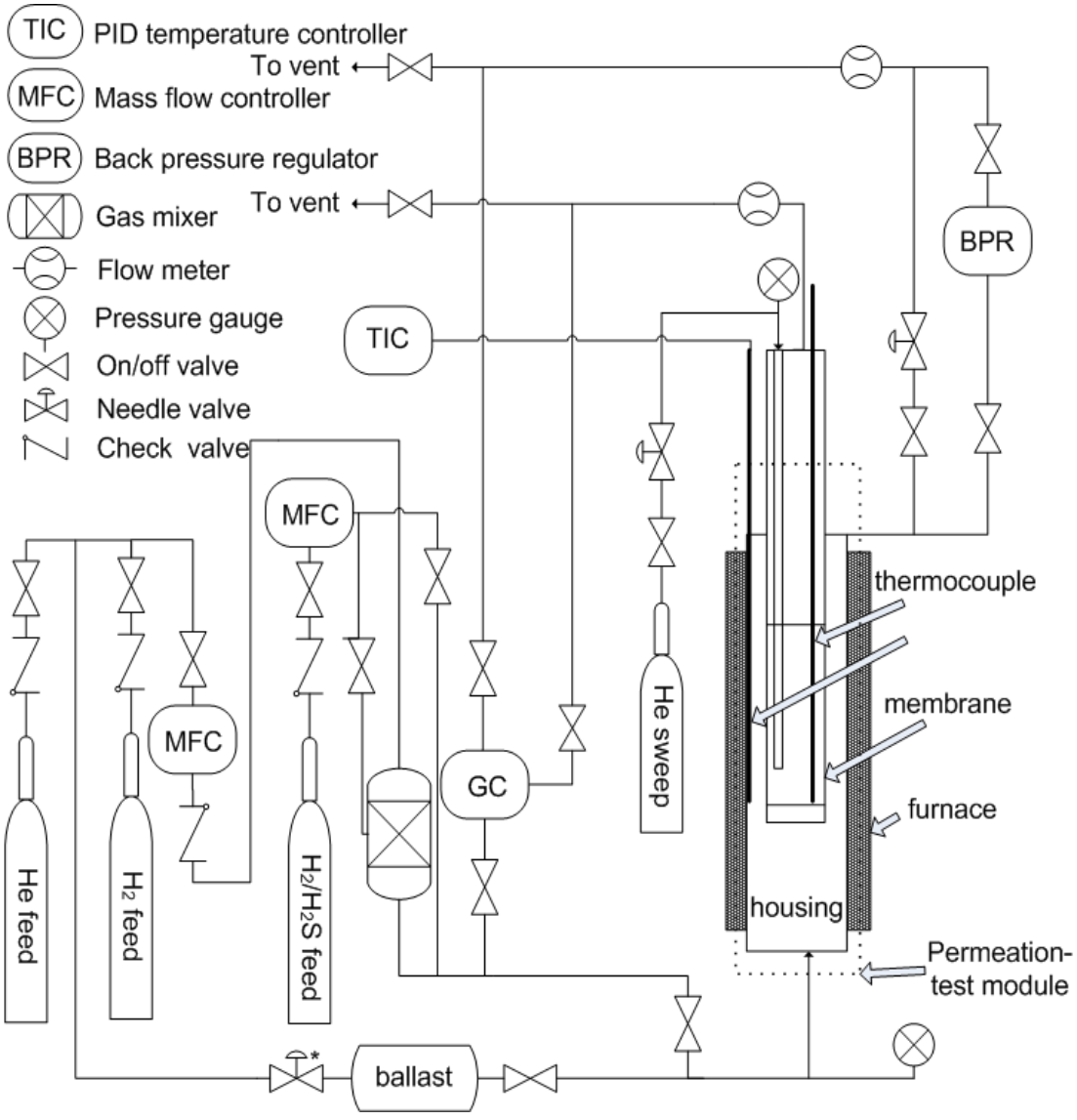


Figure 3.2. Experimental apparatus for testing permeance and sulfur tolerance

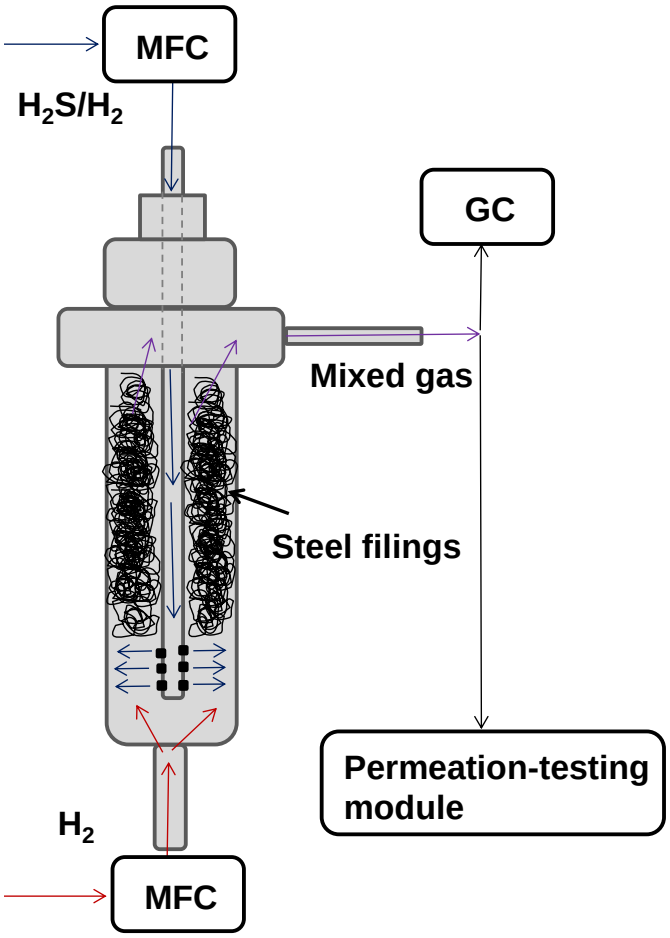


Figure 3.3. Mixer apparatus.

### *3.2.3 Characterization protocol*

After the membrane containing module and all the connecting tubing and thermocouples were properly installed, the system was purged with He at both shell and tube sides for 1 - 3 hours to remove air and humidity originally presented in the system. During the purge, the shell side pressure was maintained at 2 atm with the tube side pressure being the ambiance pressure of ~1 atm. Following the purge, the temperature was raised above the critical temperature for α-β phase transformation at a rate of 0.5 - 1ºC/min. Upon attainment of the target testing temperature, the He leak was measured at

$\Delta P$ = 1 atm ($P_{feed}$ = 2 atm, $P_{permeate}$ = 1 atm) by shutting off the He sweep flow at the tube side before switching to $H_2$ of the same feed pressure (2 atm).

After the $H_2$ flux stabilized, the feed pressure was changed from 1.2 to 4 atm with an increment of 0.2 – 0.4 atm and the corresponding $H_2$ fluxes were measured. The tube side pressure was kept at 1 atm during the entire characterization. The $H_2$ fluxes measured under different pressure differences were then used to calculate the permeance with a linear regression in accordance with Sieverts' Law (Equation 2.14). After the permeance measurement, the He leak of the membrane at $\Delta P$ = 1 atm ($P_{feed}$ = 2 atm, $P_{permeate}$ = 1 atm) was measured again at the same temperature by switching $H_2$ to He. A He sweep at tube side was turned on when switching $H_2$ to He to ease the transition. The He leak measured after the $H_2$ permeance measurement was used to calculate the ideal selectivity of the membrane, which was the ratio of $H_2$ to He flux through the membrane at $\Delta P$=1 atm ($P_{feed}$ = 2 atm, $P_{permeate}$ = 1 atm).

The same procedure for $H_2$ permeance and He leak measurement was performed at other temperatures in the range of 250 - 500ºC. When changing the temperature of the system, He was flushed at both shell and tube side and a temperature ramping rate of 0.5 - 1ºC/min was used. The permeance calculated at different temperatures was used to determine activation energy of permeation of the membrane by the use of Arrhenius relation.

The sulfur poisoning tests were performed by flowing $H_2S/H_2$ mixture of known concentration to the membrane after the membrane reached a steady state permeance in $H_2$ at a fixed temperature. The pressure of $H_2S/H_2$ mixture feed was kept the same (2 atm) as the $H_2$ feed before switching the gas and remained unchanged during entire the

exposure experiment. After reaching the desired exposure time, $H_2S/H_2$ gas feed was cut off and $H_2$ was reintroduced to the membrane for the permeance recovery. Once again, the feed pressure was kept the same between $H_2S/H_2$ mixture and $H_2$ gas feed. The He leak at $\Delta P$ =1 atm ($P_{feed}$ = 2 atm, $P_{permeate}$ = 1 atm) was also measured after the recovery in $H_2$. The same procedure for the $H_2S$ poisoning test was repeated at other temperatures as needed.

## 3.3 Instrumental analysis

### *3.3.1 SEM and EDX*

The surface and cross-sectional morphology characterizations were mainly carried out with the Amray 1610 Turbo scanning electron microscope (SEM). The SEM was also equipped with a Princeton Gamma-Tech (PGT) Avalon energy dispersive X-ray (EDX) light element detector and a RBA-1610 5MC type Robinson retractable backscattered electron detector for qualitative and quantitative elemental analysis. The Spirit software (PGT Corporation) was utilized for both image and chemical compositions analysis. The spatial resolution for SEM-EDX was between 0.8 – 1.2 $\mu$m for an accelerating voltage of 20 keV and the penetration depth was about 1 $\mu$m for the samples (consisted of primarily Pd) investigated (Goldstein et al., 2003). Another SEM employed in the study was the JEOL 840 SEM. The SEM was equipped with both Secondary Electron Imaging (SEI) and Backscattered Electron Imaging (BEI) for morphology image acquisition and Kevex EDX Spectroscopy system for chemical analysis.

The samples for cross-sectional analysis were prepared by cutting with a SiC saw blade and mounting in phenolic powder with a Smithells II mounting press. The mounted

samples were then ground with SiC papers of increasing grain fineness (decreasing particle size) from 120 to 2400 grit with the Metaserv 2000 grinder-polisher. The samples were further polished with either the 1 $\mu$m diamond suspension (made by Buehler) by the use of Vibromet I automatic polisher or the 1 $\mu$m and 0.05 $\mu$m $\alpha$-$Al_2O_3$ slurries by the use of the polisher powered by the Eplus AC adjustable speed controller. Following the polishing, the samples were painted with carbon paint and sputter coated using a gold/palladium target to avoid charging.

### *3.3.2 XRD*

The general phase identification analysis was conducted by using a Rigaku Geigerflex X-Ray diffractometer (XRD) equipped with a CuK$\alpha$ radiation source ($\lambda$ = 1.54 Å), and a curved crystal monochromator. A JADE software was utilized for data analysis.

The time-resolved, *in-situ* HT-XRD characterizations of phase evolution were performed at the High Temperature Materials Laboratories (HTML) at Oak Ridge National Laboratories (ORNL). For non-isothermal phase transformation study, the Scintag PAD-X vertical $\theta/\theta$ diffractometer was used, which was equipped with a 2kW Cu X-ray tube, a Buehler HDK 2.3 furnace, and an *m*Braun linear position sensitive detector (LPSD). The PANalytical X'Pert Pro $\theta/\theta$ MPD/X-ray diffractometer equipped with a Cu K$\alpha$ radiation source operated at 45 kV and 40 mA, an Anton Paar XRK-900 furnace, and a PANalytical X'celerator real-time multiple-strip detector was adopted for isothermal phase transformation analysis. All *in-situ* HT-XRD characterizations, including the sample heating/cooling stage, were conducted in an ultra-high purity He atmosphere with a pressure slightly higher than the ambiance pressure. For the non-isothermal analysis

performed on the Scintag diffractometer, the temperature was firstly increased to approximately 265°C at a rate of 60ºC/min followed by a rate of 8-9 ºC/min to ~662°C while collecting the diffraction data. For the isothermal characterization performed on the PANalytical diffractometer, the temperature was increased to the target annealing temperature at a rate of 50ºC/min.

The quantitative analysis of the diffraction data was carried out with the software X'Pert Highscore Plus using a Le-Bail fit and a flat background. The weight fractions were calculated by the direct comparison method of the integrated peak intensities (Cullity and Stock, 2001).

### *3.3.3 XPS*

The near surface chemical analysis was performed at the High Temperature Material Laboratory (HTML) at Oak Ridge National Laboratory (ORNL), Tennessee. A Thermo Scientific K-alpha X-ray photoelectron spectroscopy equipped with a monochromatized aluminum source operated at 200 W was employed. The pass energy used for high resolution spectra (narrow scans) was 50 eV. The analysis area was approximately 200 x 400 μm and the maximum information depth was approximately 10 nm. The peak-fitting and quantitative analysis of the XPS data was performed by the use of Advantage 4.38 software from Thermo Scientific with a Smart-type background.

### *3.3.4 Gas Chromatography*

A SRI 8610C gas chromatograph (GC) equipped with a flame photometric detector (FPD) was employed to measure the composition of retentate gas flow during the $H_2S$ exposure/recovery experiments. Figure 3.4 is the schematic representation of a FPD detector. A photomultiplier tube (PMT) amplified the photon signal reaching the

detector resulting in a measurement accuracy of $H_2S$ down to 200 ppb. The column used for $H_2S$ composition measurements was a 1/32" MXT stainless steel capillary tube. The GC was also equipped with a thermal conductivity detector (TCD) to measure the composition of various gases such as $H_2O$, CO and $CO_2$.

The conditions for $H_2S$ detection were optimized for maximizing the signal (i.e. peak sharpness and height). The air and hydrogen gases used for fueling the FPD were flowed at pressures of 2 - 4 and 30 - 35 psia, respectively depending on the detecting $H_2S$ concentration range. The carrier gas, He, was flowed to the GC at a pressure of 19 - 20 psia. The oven temperature was set at 50ºC and the FPD temperature was set at 150ºC. A 10-way automatic actuator valve took samples from the flow to the GC by opening the valve to the loop at 0.1 minutes and closing the valve to the loop at 0.3 minutes. The residence time of the $H_2S$ was roughly 1.7 - 1.8 minutes at the stated conditions. The calibration of the GC is described in detail in Appendix A.

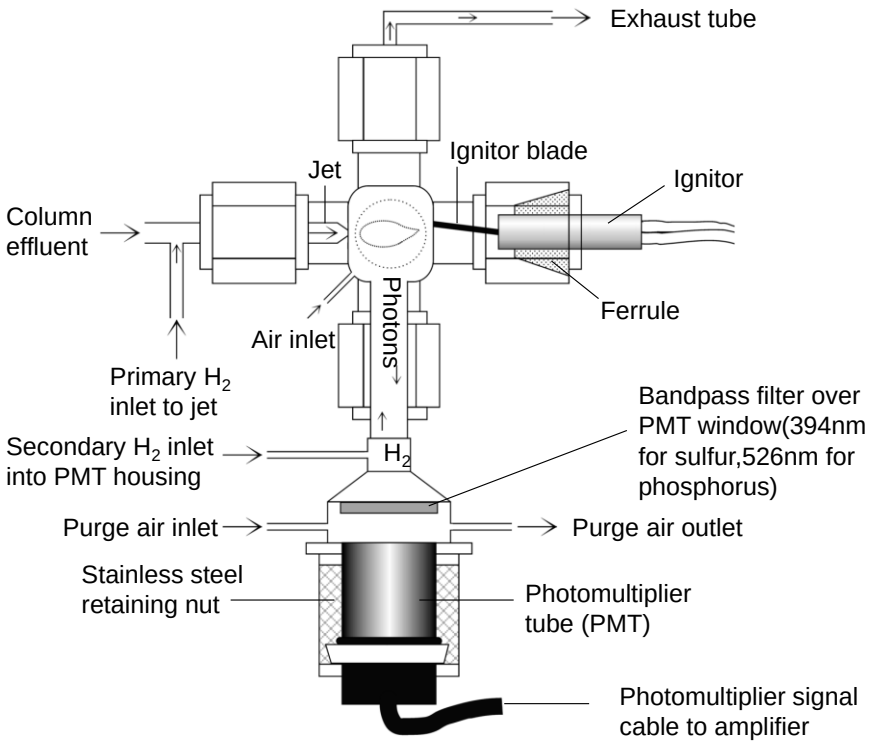


Figure 3.4 Schematic of the FPD detector.

### *3.3.5. Atomic Adsorption Spectroscopy (AAS)*

Perkin Elmer AAnalyst 300 atomic adsorption spectrometer was employed to determine the Pd and Au ion concentration in the plating baths during the Au displacement deposition. The AA spectrometer was equipped with a six lamp turret for either hollow cathode lamps (HCL) or electrode discharge lamps (EDL), HGA-850 Graphite Furnace System and AS800 Autosampler. An air/acetylene gas mixture was used to fuel the flame. HCL were used for both Au and Pd detection. The Au HCL was operated at a slit width of 0.7 *n*m and a wavelength of 242.8 *n*m, while the Pd HCL was run at a slit width of 0.2 *n*m and a wavelength of 244.8 *n*m. The AA Winlabs Software was used to run and calibrate the spectrometer.

The calibration curves for both Pd and Au were constructed prior to the characterization by diluting the Pd and Au stock standard solutions (the concentration for both Pd and Au were 1000 ± 4 mg/l) purchased from Fluka Analytical. The calibration is described in detail in Appendix B. For the characterization, the aliquot of 0.25 ml in volume was taken from the plating bathes at different time intervals for both Pd and Au analysis. A Finnpipette automatic pipette made by Labsystems with a range of 100 – 1000 $\mu$l was used to take the samples. The aliquots were diluted in 5 wt% HCl with the dilution factor of 100 so that both Pd and Au concentrations of the aliquots were within the calibration curves.

# 4. Galvanic displacement deposition of Au on Pd

## 4.1 Introduction

The displacement plating reaction is essentially an electrochemical reaction involving a pair of two half-reactions (i.e. reduction and oxidation). The metal of a higher standard electrode potential is reduced to atom, while the other metal of a lower electrode potential is oxidized (displaced) to ion during the reaction. The displacement reaction occurs spontaneously due to the electrode potential difference of the metals, which is analogical to a galvanic cell. The difference in electrode potentials of the two electrodes is referred to as electro-motive force (EMF). Therefore, no external electrical power or reducing agent is required.

The displacement plating is usually done by immersing the support metal (of a lower electrode potential) into the electrolyte solution containing the metal ions which is desired to be deposited. The displacement reaction, in principle, either completely cease or proceed at an immeasurable slow rate once the base metal surface is effectively covered by a layer of the deposited metal (i.e. EMF $\approx$ 0). As a result, the deposit layer produced by the displacement plating is usually very thin (within a couple of microns). Since noble metals such as Au and Ag usually have high electrode potentials, the displacement plating technique is suitable for depositing a thin layer of noble metal on top of a less noble metal. The electronic industries use the displacement plating technique extensively to deposit Au wire on the integrated circuit (usually on the Si substrates) ((El-shazly and Baker, 1982; Honma and Watanabe, 2002).

If the EMF is too small, the displacement reaction rate is significantly slow due to the small driving force. However, if the EMF is too big, the vigorous reaction results in the powdery and non-adherent deposit layer due to the rapid precipitation. The standard electrode potentials of $Pd^{2+}$ and $Au^{3+}$ are given in Equation 4.1 and 4.2. The Moderate difference in the electrode potentials results in the Au displacement plating on Pd surface a practical process. Complexing agents change the electrode potentials of metals in the electrolyte since the electrode potentials depend primarily on the concentration of free ions in the solution. In the study, chlorine ions ($Cl^-$) were used as the complexing agent in the plating bath. The electrode potentials of $Pd^{2+}$ and $Au^{3+}$ decrease nearly equivalently after forming chlorine complexes (as shown in Equation 4.3 and 4.4) in the solution retaining the suitability of the plating method.

$$Pd^{2+} + 2e^- = Pd^0, E_0 = 0.98v \quad (4.1)$$

$$Au^{3+} + 3e^- = Au^0, E_0 = 1.52v \quad (4.2)$$

$$Pd(Cl)_4^{2-} + 2e^- = Pd^0 + 4Cl^-, E_0 = 0.62v \quad (4.3)$$

$$Au(Cl)_4^- + 3e^- = Au^0 + 4Cl^-, E_0 = 1.00v \quad (4.4)$$

The main objective of this chapter was to investigate the factors affecting the galvanic displacement plating of Au on Pd, including the surface condition of Pd, Au ion concentration, temperature, pH, and agitation of the plating bath. In addition, the kinetics of the Au displacement plating on Pd was also studied. The fundamental understanding obtained from the results was important for depositing Au layers of good quality for the Pd/Au membranes fabrication.

## 4.2 Experimental

The Pd-deposited coupons were prepared for studying the factors affecting the Au displacement plating. The coupons were made of 316L PSS plates (0.1 μm media grade) and had dimensions of 1 cm x 1 cm x 0.1 cm. The coupons were cleaned and oxidized at 800°C for 12 hours followed by the activation and the Pd deposition by the electroless plating to have approximately 10 μm in thickness. The bath used for the Au displacement plating was sodium tetrachloroaurate ($Na{\cdot}Au(Cl)_4{\cdot}2H_2O$) solution. The compositions and the conditions used for the displacement plating are given in Table 4.1.

The membrane, C-14, was used to study the kinetics of the Au displacement plating at room temperature (~25°C). The membrane was made on a 0.1 $\mu$m media grade Hastelloy C-22 support with a dimension of 1.27 cm outer diameter and 6 cm length. After oxidizing at 800°C for 12 hours, membrane C-14 was graded with $\alpha$-$Al_2O_3$ slurries followed by the Pd/Ag barrier layers deposition. Roughly 30 μm of the dense Pd layer was deposited on top of the Pd/Ag layer prior to the kinetics study. The plating bath volume to surface ratio was 4.1 cm. The plating bath of 3 mM Au ions was stirred at an agitation speed of 400 rpm for minimizing the diffusion transfer barrier for Au ions in the bath. The compositions of the displacement solution were determined by atomic absorption spectroscopy, as described in *Section* 3.*3.5*.

Table 4.1. Au displacement plating bath compositions and conditions

| Component, purity/Condition | Au bath |
|---|---|
| $Na{\cdot}Au(Cl)_4{\cdot}2H_2O$, 99wt% | 2 – 12 mM |
| pH | 2 - 5 |
| Temperature (°C) | R.T. - 60 |

## 4.3 Results and Discussion

### *4.3.1 Effect of the surface conditions of the Pd deposits*

In order to examine the influence of surface condition of the Pd layers on the Au displacement reaction, the Pd-plated coupons were pre-immersed in different solutions including water, 0.01M HCl, and acetone before the Au displacement plating. The Pd samples were firstly immersed in the above-mentioned solutions for 3 minutes then in DI water for 5 minutes. Following the pre-immersions, the Pd samples were immersed in the displacement plating bath of 3 mM Au ions for 10 and 20 minutes at room temperature.

Figure 4.1 shows the Au weight fraction determined by both the EDX and XRD methods of the Au displacement plated samples that were pre-immersed in the different solutions. The EDX elemental analysis was performed by several area scans at a magnification of 1000X, while the Au weight fraction determined by the XRD method was conducted by the use of the direct comparison method (Cullity and Stock, 2001) on the Au (1 1 1 ) and Pd (1 1 1) peaks. The same trend of the results was observed in Figure 4.1 between the EDX and XRD analysis although the EDX analysis showed higher Au contents than the XRD results. This was due to that the penetration depth of the X-ray in the EDX analysis was ~1 μm while that in the XRD analysis was ~3 $\mu$m. As a result, the smaller penetration depth of the EDX technique resulted in higher relative Au fraction. Since the XRD technique provided relative more bulk information than the EDX method, the Au weight fractions reported in the rest of the section were based on the XRD method unless specifically indicated. It should be noted that the Au weight fractions reported were not the entire bulk Au weight fraction due to the penetration depth of the X-ray as

mentioned. Nevertheless, the results still provided the understanding of the influence of the factors that affected the Au displacement of Pd qualitatively.

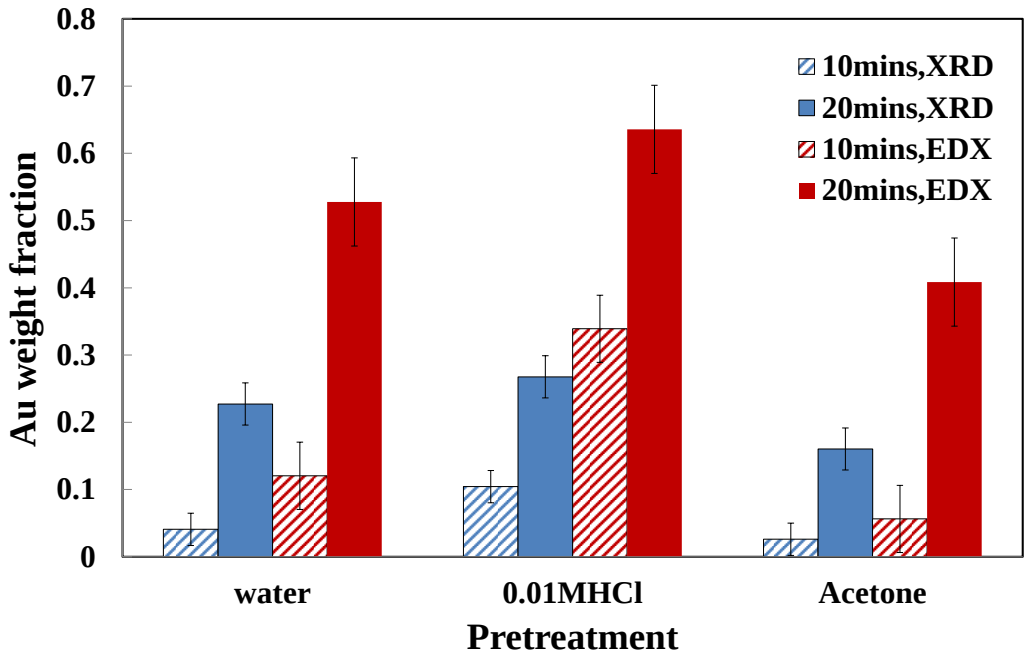


Figure 4.1. The effect of pre-treatments on the Au displacement of Pd.

As seen in Figure 4.1, the samples pre-immersed in the 0.01M HCl solution showed the most Au deposited while the ones pretreated in acetone showed the least Au deposited after either 10 or 20 minutes plating. The results suggested that the Pd surface condition was important to the Au displacement reaction. Any no-conducting film on the surface, such as organic and oxide contaminants would effectively prohibit the displacement reaction, consequently prevent the immersion deposition (Parker et al., 1974). The displacement reaction required the contact of Pd surface with Au ion, which resembled to an adsorption process. As a result, the reaction rate was a function of available sites on the surface. Increasing the sites covered (either by deposited Au or contaminants) decreased the reaction rate, thereby the displacement rate. The results also

indicated that pre-immersing Pd in acid to remove the contaminants increased the efficiency of the Au displacement reaction.

Figure 4.2 shows the Au weight fraction (determined by the XRD method) of the samples pre-immersed in 0.01, 0.1, and 1 M HCl for 3 minutes followed by the 10 minutes plating in the 3 mM Au bathes. The higher pre-treatment HCl concentrations resulted in more Au deposited for the same plating time as seen in Figure 4.2. In addition to higher HCl concentration, increasing pre-immersion time in acid also gave rise to more Au deposited for the same plating time. Figure 4.3 shows the Au weight fraction of the samples pre-immersed in 1 M HCl for 1, 2, and 3 minutes followed by the 10 minutes plating in the 3 mM Au bathes. The Au weight fraction increased with increasing pre-immersing time in the 1 M HCl solution. Increasing either pre-treatment HCl concentrations or pre-treatment time resulted in more surface contaminants being removed, thereby more efficient Au displacement deposition. The results also suggested that pre-treatment HCl concentration exhibited a stronger influence on the contaminants removal and Au displacement reaction than the pre-treatment time in the HCl solutions.

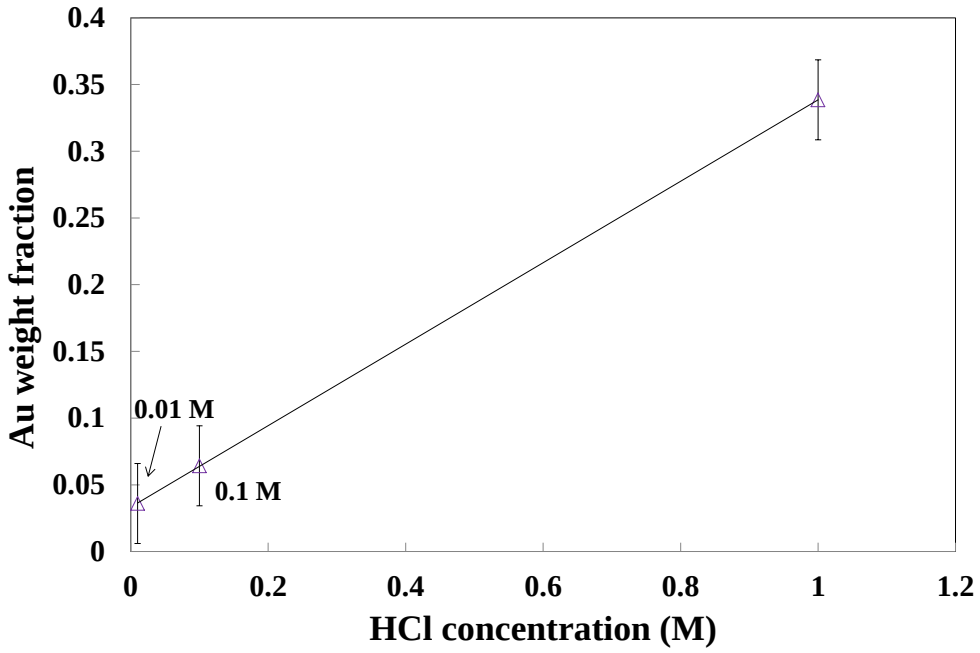


Figure 4.2. The effect of pre-treatment acid concentration on the Au displacement of Pd.

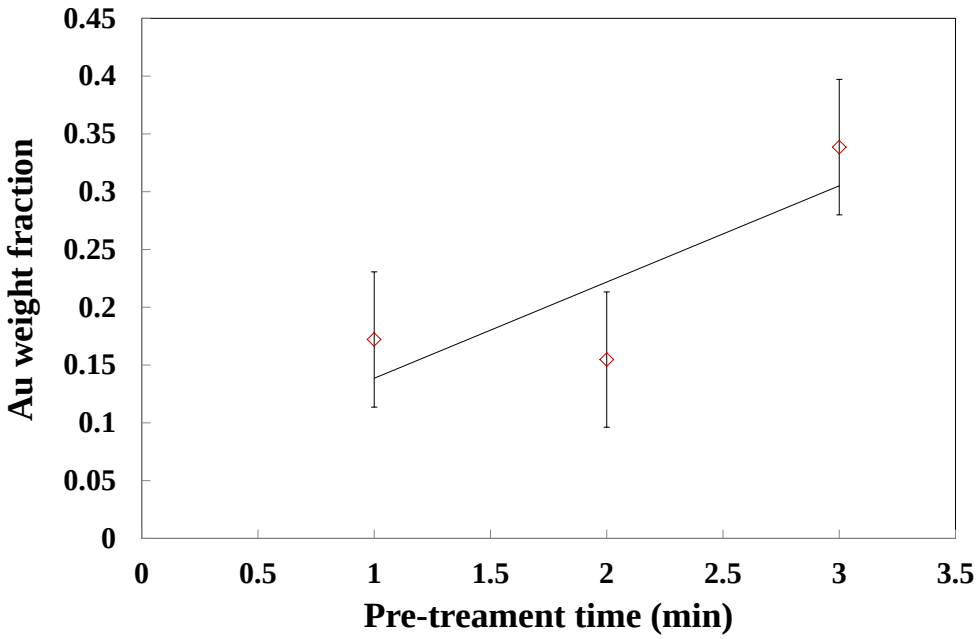


Figure 4.3. The effect of pre-treatment time acid on the Au displacement of Pd.

In addition to the effect of surface contaminants, the influence of surface roughness of the Pd sample on the Au displacement of Pd was also examined. Figure 4.4 compared the Au weight fraction of the Au-plated samples with and without pre-polishing the coupons. The polishing of the PSS coupon (0.1 μm grade) was performed by using the 800 grit SiC sand papers until the shine surface was achieved. After the Pd plating, the Au displacement plating was performed for 30 minutes in the 3 mM Au bathes. As shown in Figure 4.4, the un-polished sample with a rougher surface showed more Au deposited compared to the polished sample with a smoother surface under the same plating conditions. More surface area on the rougher surface sample resulted in more Au deposition for the fixed plating time. The preferred Au nucleation at the surface defects such as cleavages and slips with extra nucleation at the defects (Coutts and Revesz, 1966) also accounted for the more Au deposition on the porous sample with a rougher surface. Larger final thicknesses of the Au deposit layer on the rougher and porous surfaces by the displacement plating were also reported in the literature (El-shazly and Baker, 1982).

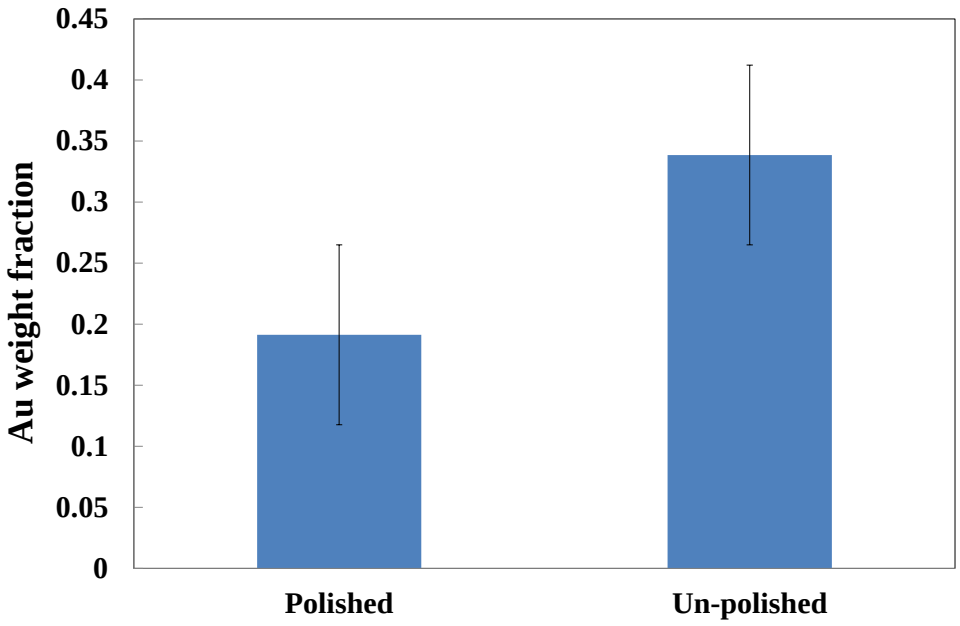


Figure 4.4. The effect of the surface roughness of the Pd layer on Au displacement deposition.

Finally, for applying the displacement plating method on the composite Pd/PSS samples, dense Pd layers that fully covered the PSS supports were necessary. Due to the extremely low reduction potentials of the support metals (e.g. $Cr^{3+}$ = Cr, $E_0$= - 0.74*v*; $Ni^{2+}$ = Ni, $E_0$ = - 0.26*v*; $Fe^{2+}$ = Fe, $E_0$ = - 0.44*v*), the uncovered spots would undergo vigorous displacement reaction while immersing into the Au displacement bathes. As mentioned previously, the Au deposits from such rapid reaction were powdery and poorly adhered to the surface resulting in the continuous attacking of Au ions on the support similar to a corrosion process. In the study, at least 10 μm thick Pd layers were found to be necessary to prevent the continuous corrosion of the support metals from occurring.

### *4.3.2 Effect of Au ion concentration, temperature, and pH of the plating bath*

Figure 4.5 displays the amount of Au deposited determined by the XRD method as a function of time in the two different Au ion concentration bathes. The 2 and 3 mM Au ion bathes were used for the Au displacement plating for 10, 20, and 30 minutes at room temperature. Linear increase of the Au deposition with time was observed in both the Au ion concentration bathes. This indicated that a dense Au layer has not yet formed under the plating conditions within the plating time of 30 minutes since the displacement reaction would cease or proceed at an immeasurably slow rate once the base metal surface is effectively covered by a layer of the deposited metal.

In addition, the higher Au ion concentration also resulted in a higher deposition rate as evidenced by the higher slope in Figure 4.5. The phenomenon could be explained by the Nernst equation (as expressed in Equation 4.5) with the general expression for the complete Au displacement reaction of Pd (as shown in Equation 4.6). The Nernst equation determines the electrode potential ($E$) of the complete reaction under non-standard conditions. It should be noted that the standard conditions refer to that the concentration of the solute is 1M at 25°C under a pressure of 1 atmosphere (in case of gas electrode).

$$E = E_0 - \frac{RT}{nF} \ln \frac{[Pd^{2+}]^3}{[Au^{3+}]^2} \tag{4.5}$$

$$2Au^{3+} + 3Pd^{0} = 2Au^{0} + 3Pd^{2+}, E_0 = 0.54v \tag{4.6}$$

In the Nernst equation (as shown in Equation 4.5), $E_0$ is the standard electrode potential of the reaction, $R$ is the universal gas constant, $T$ is the temperature, $n$ is the

number of the moles of electrons transferred, and *F* is the Faraday constant. The nature logarithm term is actually the equilibrium constant (*K*) of the reaction. According to Equation 4.5, increasing the Au ion concentration increased the electrode potential (*E*) of the Au displacement of Pd, which was the driving force for the reaction. Consequently, a higher Au displacement rate would be observed in a higher Au ion concentration bath due to the higher driving force.

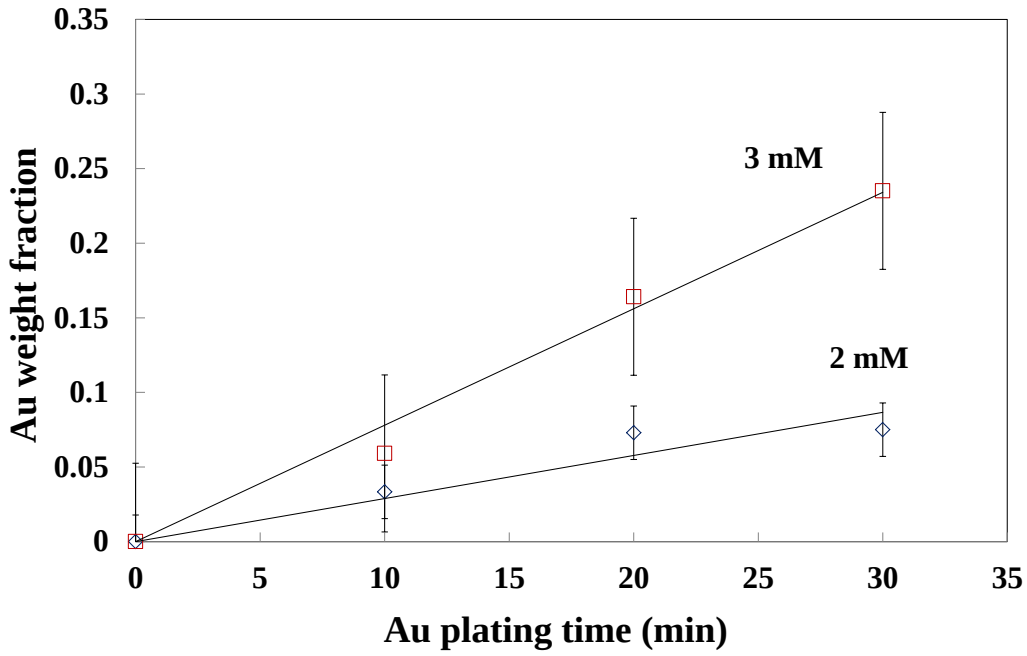


Figure 4.5. The Au displacement of Pd as a function of time in different Au ion concentration bathes.

El-Shazly and Baker (1982) concluded that the Au ion concentration showed no significant effect on gold deposition rate from the results of Au displacement plating of nickel. The completion of the reaction under the plating conditions used by the authors might account for the results observed. The Au ion concentrations used by El-Shazly and Baker (1982) were 2 to 8 g/l (10 to 40 mM) and the plating lasted for 1 – 2 hours. Much

higher Au ion concentration and longer plating time were adopted by the authors, which possibly resulted in the completion of the displacement reaction. Once the displacement reaction was completed, no difference in the amount Au deposited would be observed since the identical maximum amount of Au was deposited. Figure 4.6 shows the effect of the Au ion concentration on the Au displacement of Pd. The Au weight fraction of the samples after 30 minutes plating increased with increasing Au ion concentration to an asymptotical value above 9 mM as seen in Figure 4.6. The high and identical Au amount deposited above 9 mM implied that the dense Au layer that fully covered the Pd surface has formed at the concentration within 30 minutes plating.

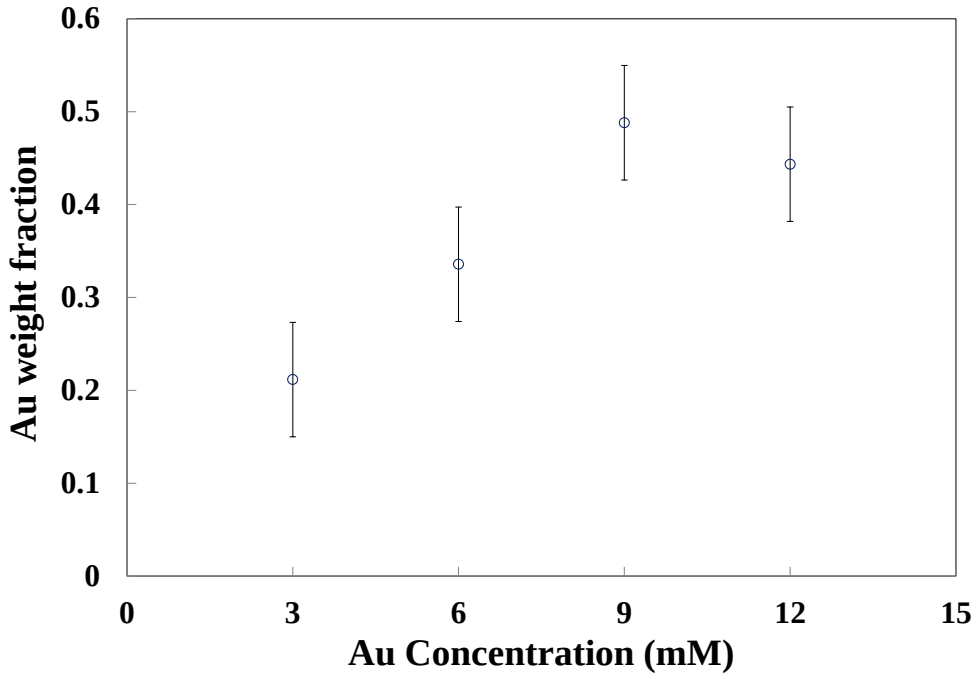


Figure 4.6. The effect of Au ion concentration on the Au displacement of Pd.

Figure 4.7 shows the effect of the temperature on the amount of Au deposited through the displacement reaction. The Au plating was performed in 3 mM Au ion concentration bathes for 20 minutes at room temperature (~25°C), 40, and 60°C, and the

Au fractions of the deposited samples were determined by the XRD method. As seen in Figure 4.7, the Au fraction, thereby the amount of Au deposited, increased with increasing temperature. The Nernst equation as shown in Equation 4.5, once again, could be used to understand the effect of temperature on the Au displacement of Pd. In the case of the Au displacement of Pd, the concentration of Pd ion was much smaller than the Au ion concentration in the bath resulting in the negative value of the nature logarithm term in Equation 4.5. As a result, the electrode potential of the reaction increases as the temperature was increased. The higher electrode potential of the reaction (or EMF) indicated higher driving force for the reaction, consequently higher displacement (or deposition) rate. El-Shazly and Baker (1982) reported similar temperature-dependence of the Au displacement plating on the electroless plated Ni ceramic substrates over the temperature range of 25 - 85°C. Higher Au deposition rates were reported at higher temperatures. The non-linear increase of the Au deposition with increasing temperature was also observed by the authors. An increase of the slope after 40°C and further increase of the slope after 80°C were reported.

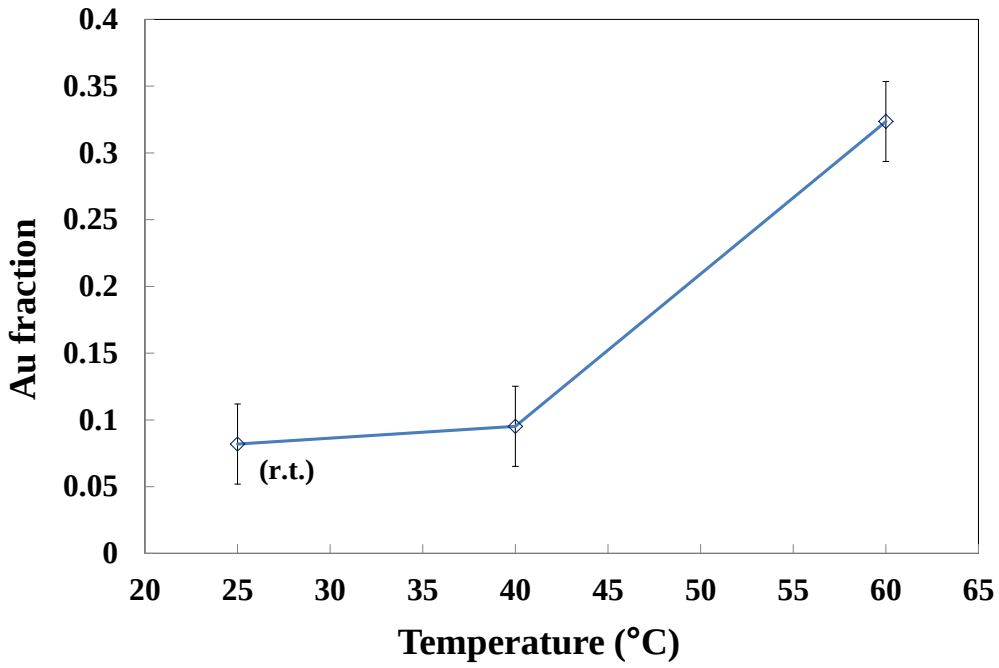


Figure 4.7. The effect of temperature on the Au displacement of Pd.

Figure 4.8 exhibits the Au displacement deposition as a function of pH of the plating bath. The Au plating was conducted in the 3 mM Au plating bath for 20 minutes and the Au fractions of the samples were determined by the XRD method. The original pH value of the 3 mM $Na_2.Au(Cl)_4.2H_2O$ solution was ~3, and was altered by adding 1 M HCl or NaOH solution. As observed in Figure 4.8, more Au was deposited for the fixed time when the pH of the bath was lower. Most reduction reactions of metal ions occur in the acid aqueous solutions[6] with $H^+$ from water involving in the reaction (at the reactant side). Therefore, the concentration of $H^+$ also affects the electrode potential of the reaction according to the Nernst equation (as shown in Equation 4.5). When the pH of the bath decreased, the increase of the $H^+$ concentration resulted in the increase of the electrode potential of the Au displacement reaction of Pd, thereby the Au deposition rate.

[6]http://bilbo.chm.uri.edu/CHM112/tables/redpottable.htm

The displacement reaction is essentially a corrosion process since the mechanism of the displacement plating involved both the reduction of Au ions and the oxidation of Pd atoms. Higher metal oxidation rates were usually observed in the lower pH environments (e.g. Faster rust rate of iron in acid rain).

Figure 4.8 also displays that the Au deposition rate decreased slightly when the pH value was below 2.5. The phenomenon was caused by the electrode potential of the displacement reaction being too high caused by the high $H^+$ concentrations in the low pH bathes. As mentioned previously, if the EMF is too big, the vigorous reaction resulted in the powdery and non-adherent deposit layer due to the rapid precipitation. Indeed, slight precipitations were observed in the plating bathes of the pH value of 1.6.

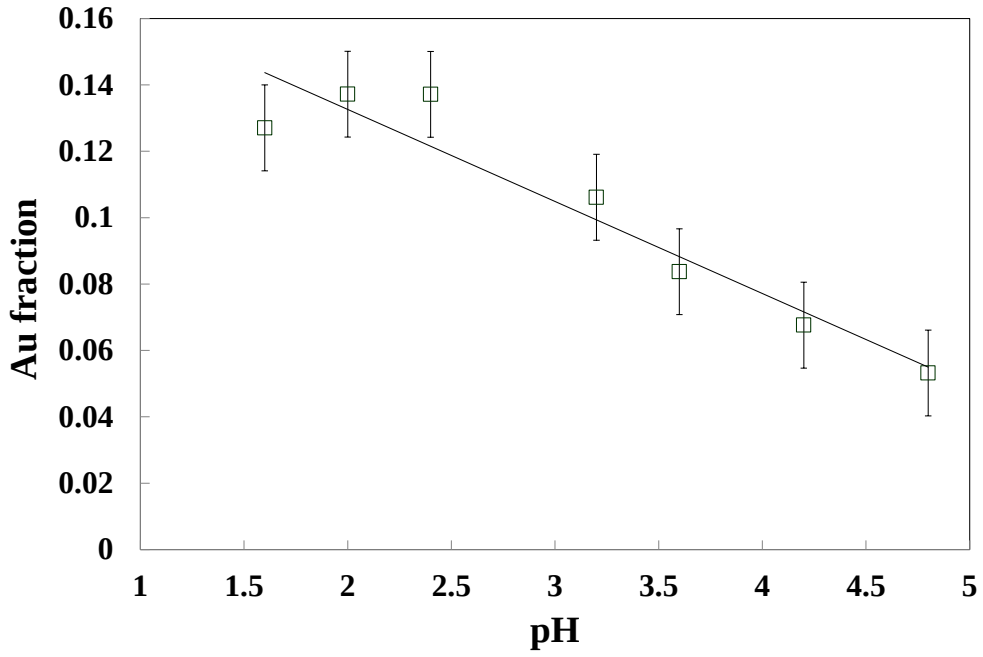


Figure 4.8. The effect of pH on the Au displacement of Pd.

### *4.3.3 Effect of bath agitation on of Au displacement of Pd*

In order to investigate the influence of bath agitation on the morphology of the Au deposits by the displacement plating technique, the Pd coupons were plated with Au in the 3 mM Au bathes for 30 minutes with the bath agitation speeds of 0 – 600 rpm.

Figure 4.9 shows the surface morphologies of the Au deposits plated with different bath agitation speeds. Non-uniform cluster size of the Au deposit was observed on the sample plated without the bath agitation as shown in Figure 4.9(a). In addition, the non-uniform coverage of the Au deposits was also observed with some portions of the Pd surface not covered by the Au deposits. Increasing the bath agitation speed to 100 rpm showed no significant effect on the non-uniformity of the cluster size and the coverage of the Au deposits as shown in Figure 4.9(b). The largest cluster size of the Au deposit was in the range of 1 – 2 $\mu$m in diameter with the bath agitation speeds up to 100 rpm.

In contrast, the cluster size as well as the non-uniformity of the cluster size of the Au deposits reduced significantly with the bath agitation speed of 200 rpm as shown in Figure 4.9 (c). The largest cluster size of the Au deposit was in the range of 0.3 – 0.5 $\mu$m in diameter. In addition, the Au deposits were also more uniformly covered the Pd surface. The reduction in Au cluster size and the increase in the uniformity of the Au cluster size and the coverage were due to the reduction of the diffusion resistance for Au ion in the bath caused by the bath agitation. As a result, more Au nuclei were deposited on the Pd surface more evenly occupying more surface sites. In addition, more even growth on each nucleus was also achieved. Further increasing the bath agitation speed up to 600 rpm showed no apparent further decrease in the Au cluster size and the increase in the uniformity of the Au cluster size and the Au coverage as shown in Figure 4.9(d), (e),

and (f). This suggested that the diffusion resistance of Au ion in the plating bath was potentially minimized with a bath agitation speed above 200 rpm.

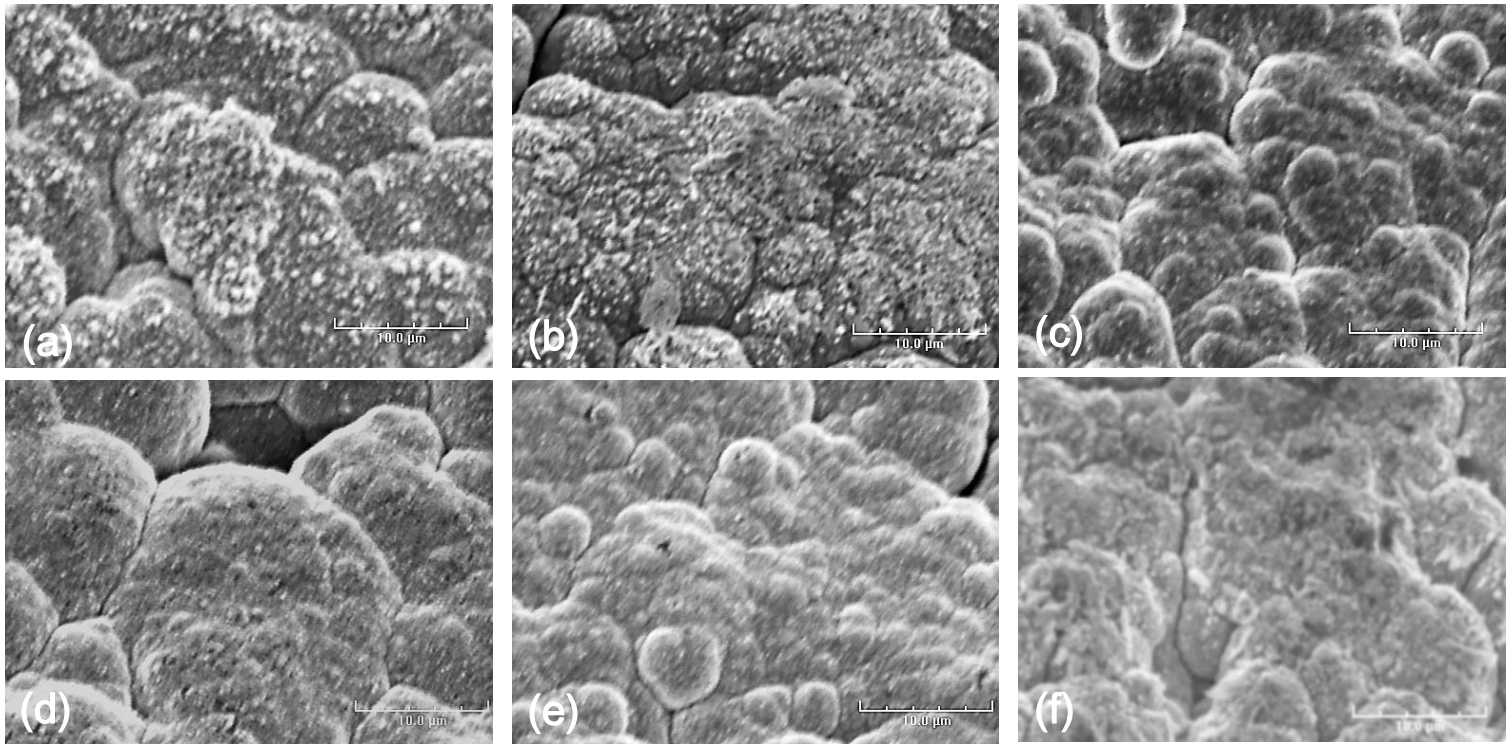


Figure 4.9. SEI surface micrographs of the Au displacement deposited samples with the bath agitation speeds of (a) 0 rpm, (b) 100 rpm, (c) 200 rpm, (d) 400 rpm, (e) 500 rpm, and (d) 600 rpm (Magnification: 3kX).

Figure 4.10 shows the Au weight fraction of the samples deposited with different bath agitation speeds. The Au weight fraction increased slightly with the increase of the bath agitation speed up to 200 rpm. Further increasing the bath agitation speed above 400 rpm resulted in a more apparent increase in the Au weight fraction. The result suggested that in order to minimize the diffusion resistance in the plating bath, the bath agitation speed above 400 rpm was necessary.

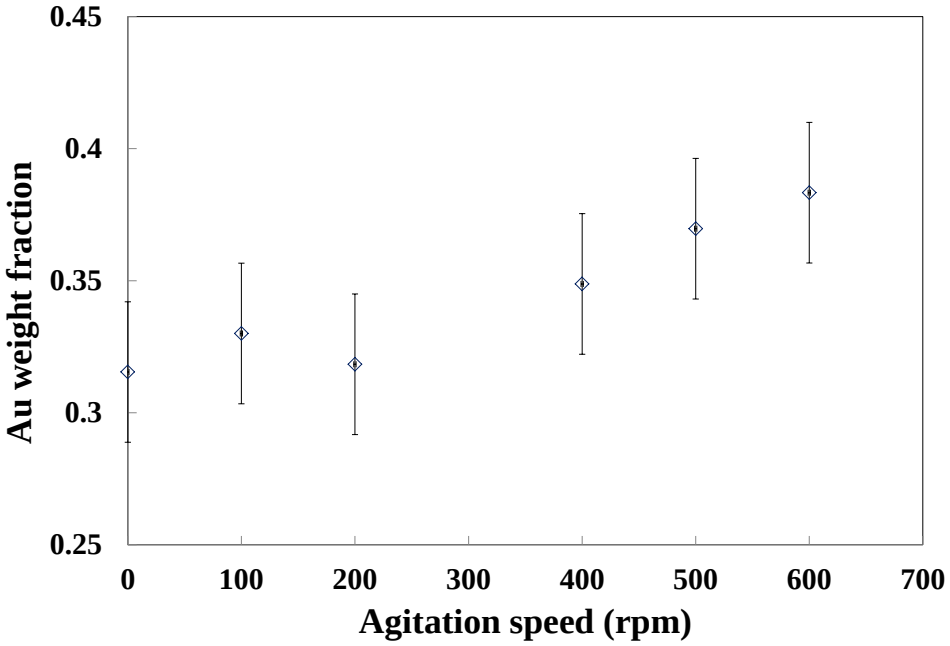


Figure 4.10. The effect of agitation speed on the Au displacement of Pd.

### *4.3.4 Kinetics of Au displacement plating on Pd*

For studying the kinetics of the Au displacement plating on Pd, a typical Au displacement solution of 3 mM Au ions at room temperature was used. The plating bath volume to surface ratio was 4.1 cm (The surface area of the membrane was 24 $cm^2$ and the volume of the displacement solution was 100 $cm^3$). According to the study of the bath

agitation influence on the Au displacement of Pd, the mass transfer barrier in the bath was significantly reduced at bath agitation speeds above 400 rpm as stated previously. In addition, previous study on the Pd displacement of Cu with similar volume to surface ratio (3.9 – 4.3cm) indicated that the diffusion barrier for metal ion in the bath was minimized at bath agitation speeds above 400 rpm (Pomerantz, 2010). As a result, a bath agitation speed of 400 rpm was used for minimizing the diffusion transfer barrier for Au ions in the bath for the kinetics study.

Figure 4.11 shows the concentration of the Au and Pd ions in the displacement bath as a function of time. The concentration of Au ions decreased from the initial concentration of 3 mM with increasing plating time, while the concentration of Pd ions increased from 0 as the plating time was increased. The decrease/increase was linear for the first 30 - 50 minutes and proceeded to slow down reaching an asymptotical value after 2 hours indicating that the displacement nearly ceased due to the formation of the Au layer on top of the Pd surface.

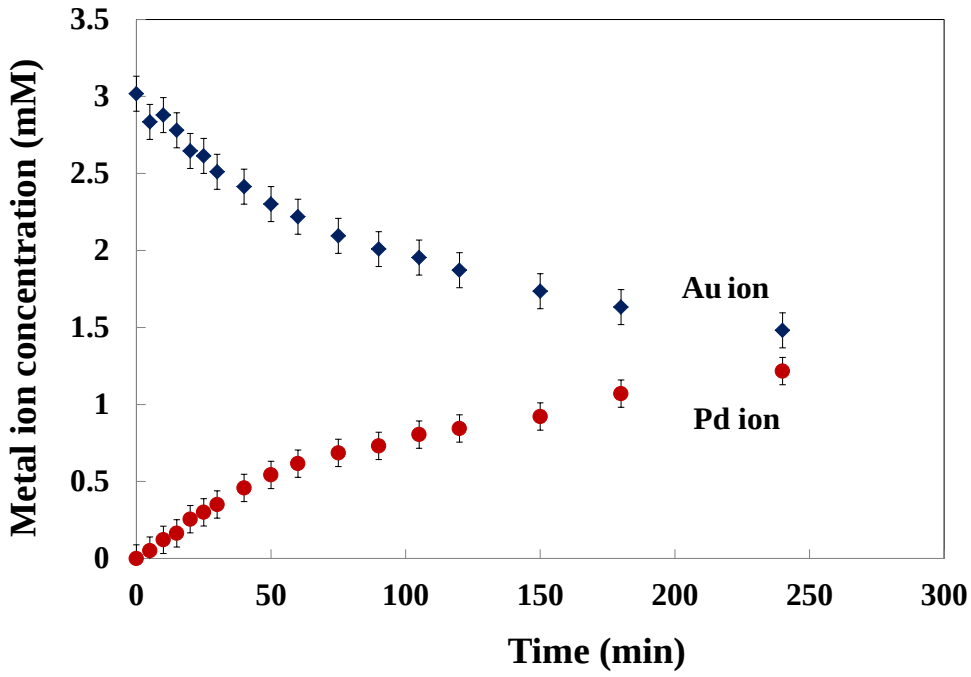


Figure 4.11. The Au and Pd ion concentration in the displacement bath as a function of time (The bath was stirred at an agitation speed of 400 rpm).

Figure 4.12 shows the amount of Au and Pd ions reacted (i.e. reduced or displaced) during the displacement reaction as a function of time. The amount of reacted Au and Pd ions were calculated according to the concentration change of both metal ions as shown in Figure 4.11 and the volume of the plating solution (100 ml). The predicted amounts of Au ion reduced based on the amount of Pd ion displaced and the overall displacement reaction were also plotted in Figure 4.12. Both the amounts of the reduced Au ions and the displaced Pd ions increased with increasing time reaching an asymptotical value.

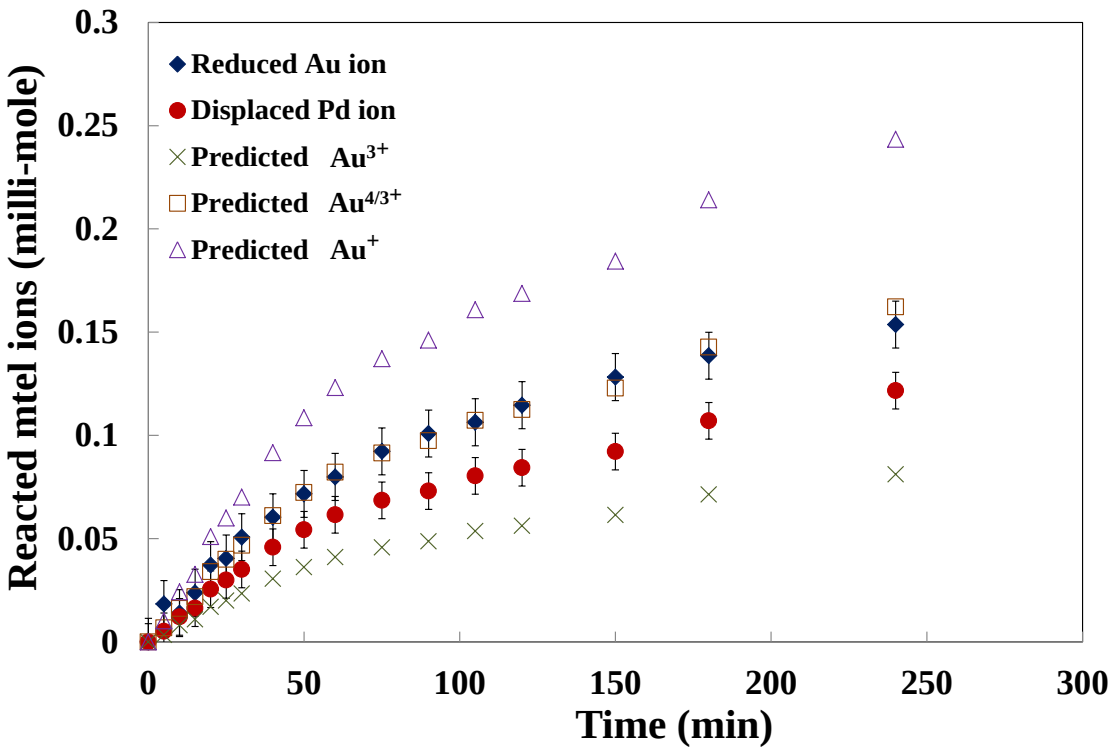


Figure 4.12. The amount of Au ions reduced and Pd ions displaced as a function of time. (The predicted $Au^{3+}$ ions were calculated assuming the reduction of $Au^{3+}$ took place, while the predicted $Au^{+}$ ions were calculated assuming the reduction of $Au^{+}$ occurred. The predicted $Au^{4/3+}$ ions were calculated assuming reduction of both $Au^{3+}$ and $Au^{+}$ took place. All the calculations were based on the amount of displaced $Pd^{2+}$ ions.)

Considering the complete reaction expressed in Equation 4.7 occurred during the Au displacement of Pd with the reduction of $Au^{3+}$ ions occurred, 2/3 $Au^{3+}$ ions were reduced per displaced $Pd^{2+}$ ion according to the complete reaction. The predicted $Au^{3+}$ ions based on the amount of the displaced $Pd^{2+}$ were significantly lower than the experimental data as shown in Figure 4.12.

$$Pd(Cl)_4^{2-} + 2e^- \rightarrow Pd^0 + 4Cl^- \quad E_0 = 0.62\,V$$

$$+\ Au(Cl)_4^- + 3e^- \rightarrow Au^0 + 4Cl^- \quad E_0 = 1.00\,V \qquad (4.7)$$

$$2Au(Cl)_4^- + 3Pd^0 + 4Cl^- \rightarrow 2Au^0 + 3Pd(Cl)_4^{2-} \quad E_0 = 0.38\,V$$

The possible transformation of $Au^{3+}$ to $Au^+$ in acid (as expressed in Equation 4.8) gave rise to that the deposition of Au but was also possibly resulted from the reduction of $Au^+$ (as expressed in Equation 4.9). If the reduction of $Au^+$ ions occurred during the Au displacement of Pd according to the complete reaction expressed as Equation 4.10, two $Au^+$ ions were reduced per displaced $Pd^{2+}$ ion. As seen in Figure 4.12, the predicted $Au^+$ ions based on the amount of the displaced $Pd^{2+}$ were significantly higher than the experimental observation. Neither case fit with the experimental results, suggesting the possibility for different reaction mechanism for the Au reduction. Considering that both the reduction reactions of $Au^{3+}$ and $Au^+$ ions occurred during the displacement reaction, one displaced $Pd^{2+}$ would effectively cause 4/3 Au ions to be reduced. The amount of Au ions predicted based on the amount of the displaced $Pd^{2+}$ by this model fit with the experimental data perfectly as seen in Figure 4.12. The results suggested that two reduction reactions of Au ions in two different oxidation states (i.e. $Au^{3+}$ and $Au^+$) took place simultaneously while Pd atoms were oxidized to $Pd^{2+}$ during the displacement reaction.

$$Au^{3+} + 2e^- = Au^+, E_0 = 1.36v \qquad (4.8)$$

$$Au^+ + e^- = Au^0, E_0 = 1.83v \qquad (4.9)$$

$$Pd(Cl)_4^{2-} + 2e^- \rightarrow Pd^0 + 4Cl^- \quad E_0 = 0.62\ V$$

$$+ Au(Cl)_2^- + e^- \rightarrow Au^0 + 2Cl^- \quad E_0 = 1.15\ V \qquad (4.10)$$

$$2Au(Cl)_2^- + Pd^0 \rightarrow 2Au^0 + Pd(Cl)_4^{2-} \quad E_0 = 0.53\ V$$

Figure 4.13 shows the conversion, *x*, as a function of time for the Au displacement of Pd. The conversion was defined as Equation 4.11, where $C_0$ is the initial $Au^{3+}$ ion concentration (e.g. in the study, $C_0$ was 3 mM).

$$x = \frac{C_0 - C}{C_0} \qquad (4.11)$$

As seen in Figure 4.13, the displacement rate was linear for the first 30 -50 minutes. After 4 hour reaction, a conversion of 50 % was achieved. The linear Au displacement plating rate within the first 30 - 50 minutes was calculated to be 0.4 $\mu$m/h, while the average Au deposition rate within 4 hour displacement was 0.16 $\mu$m/h. The total thickness of Au deposited until the displacement reaction essentially ceased was approximately 0.6 $\mu$m. It should be noted that it was very difficult to estimate the amount of the deposited Au, therefore, the thickness of the Au layer by the gravimetric method (as expressed in Equation 3.1) due to the fact that the displacement deposition involved both the deposition of Au (weight gain) and dissolution of Pd (weight loss). On the other hand, the use of AAS monitoring Au ion concentration enabled the estimation of the Au deposition rate for the determination of the respective thicknesses as a function of time.

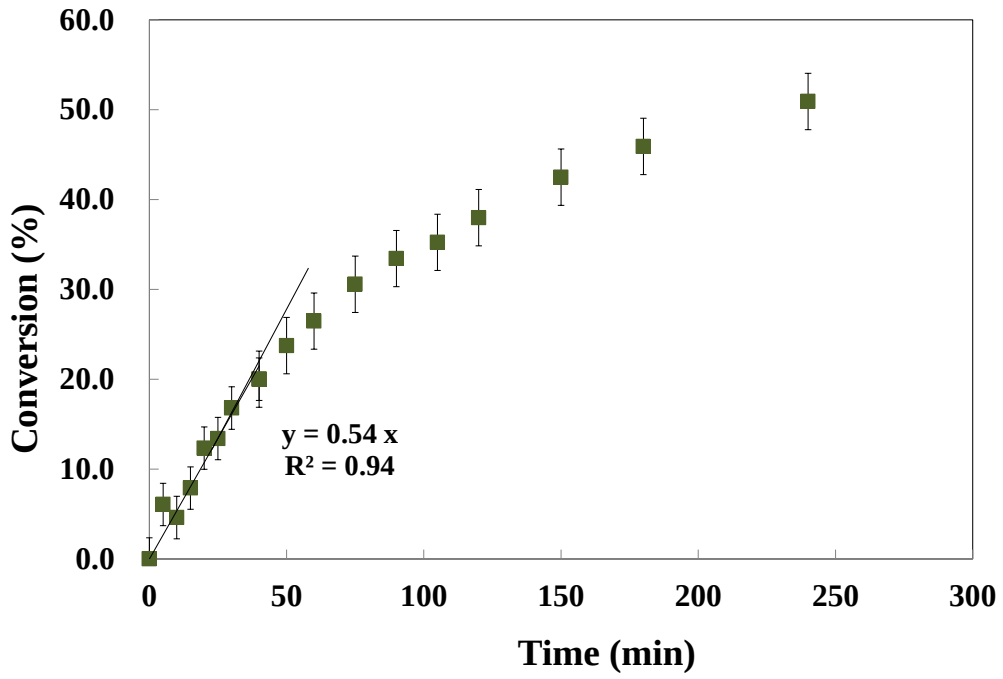


Figure 4.13. Conversion as a function of time (The initial Au ion concentration was 3mM and the bath was stirred at an agitation speed of 400 rpm).

For estimating the rate constant, *k*, and the reaction order, $\alpha$, of the Au displacement reaction of Pd, the empirical rate equation with respect to the Au ion concentration was used as shown in Equation 4.12. The rate equation was based on the complete displacement reaction shown in Equation 4.6.

$$r = -\frac{d\left[Au^{3+}\right]}{dt} = k\left[Au^{3+}\right]^{\alpha} \tag{4.12}$$

By the use of the conversion, *x*, as defined in Equation 4.11, integrating Equation 4.12 with the assumption of $\alpha \neq 1$ yielded the conversion as a function of time as expressed in Equation 4.13.

$$x = 1 - \left[(\alpha - 1) C_0^{\alpha-1} k \cdot t + 1\right]^{\frac{1}{1-\alpha}} \quad (4.13)$$

By the use a non-linear regression of the experimental data (See Figure 4.13), the rate constant *k*, and the reaction order, $\alpha$, can be calculated by Equation 4.13. The value of $\alpha$ and $k$ calculated by the use of Equation 4.13 was 3.2 and 2628 $min^{-1}*M^{-2.2}$, respectively.

Figure 4.14 shows the fit of experimental data with the non-linear regression of Equation 4.13. As observed in Figure 4.14, the non-linear regression fitted the experimental data quite well. The result also suggested that the Au displacement reaction of Pd was approximately a third-order reaction ($\alpha$ = 3.2).

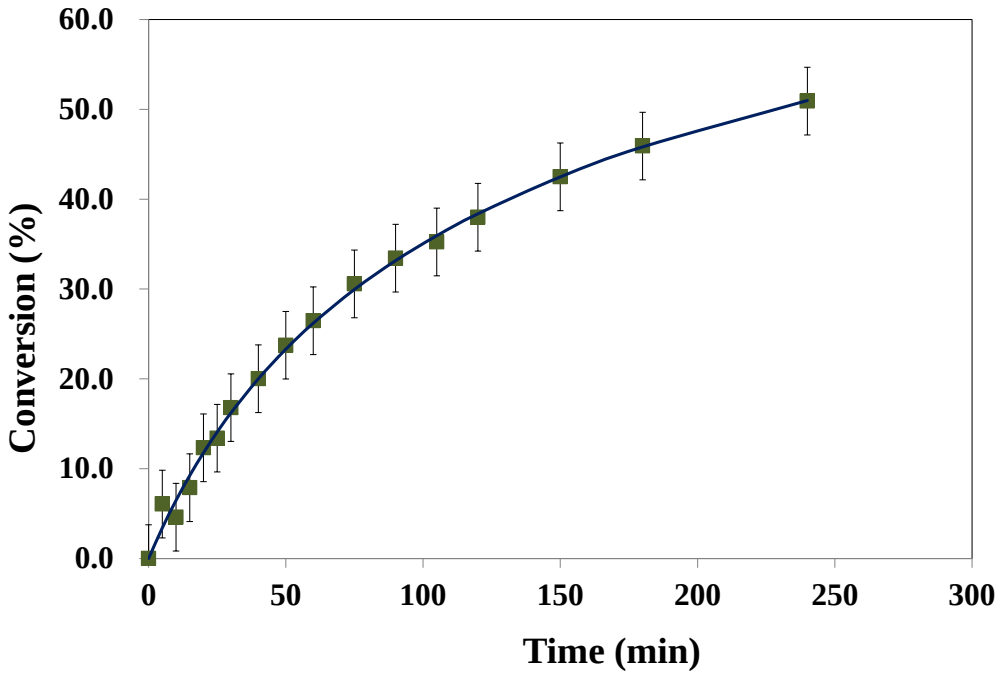


Figure 4.14. The non-linear regression for the Au displacement of Pd with initial Au ion concentration of 3 mM.

For the kinetics and the reaction order of the displacement reaction, Coutts and Revesz (1966) reported an empirical equation for nucleation kinetics in the Au displacement deposition on Si supports, which was second order with respect to the available site on the surface as shown in Equation 4.14.

$$\frac{dN_t}{dt} = \frac{(N - N_t)^2}{k} \tag{4.14}$$

Where $N$ is the density of nuclei extrapolated to infinite deposition time, and $N_t$ is the density of nuclei at time *t*. According to Equation 4.14, $N$ was considered as the maximum number of sites available for Au nucleation on Si surface, and at time *t*, the available sites for Au nucleation was ($N$ - $N_t$). The nucleation mechanism was resembled as an adsorption process by Coutts and Revesz (1966). An adsorption process is usually a first-order reaction with respect to the available sites. However, the second-order reaction model was proposed by Coutts and Revesz (1966) from the experimental data. The authors attributed it to the two processes involved in the displacement nucleation which were the formation of the Au nuclei and the dissolution of the Si atoms.

Pomerantz (2010) reported that the reaction order with respect to the Pd ion concentration was roughly 1 in the Pd displacement of Cu reaction with the 0.56 mM initial Pd ion concentration. According to the Pd displacement of Cu reaction as expressed in Equation 4.15, one Cu atom was displaced when one Pd ion was reduced.

$$Pd^{2+} + Cu^0 = Pd^0 + Cu^{2+}, E_0 = 0.61v \tag{4.15}$$

While resembling a displacement reaction to an adsorption process in a simple decomposition case (i.e. A+S(s) = AS; A: reactant in gas or liquid phase, S: available sites on the surface), the reaction order was 1 with respect to the reactant when the adsorption/desorption was the rate-limiting step or low reactant concentration in the reaction-controlled process. Since the initial Pd ion concentration used by Pomerantz (2010) was very small (0.56 mM), the Pd displacement of Cu was most likely the reaction-controlled process.

However, in the case of the Au displacement of Pd in the current study, the high reaction order of 3.2 with respect to Au ion concentration was observed, which indicated that reaction mechanism was more complicated and could not be assumed to be a simple decomposition adsorption process. Indeed, according to the Au displacement of Pd reaction as shown in Equation 4.6, the reaction involved two Au ions to displace three Pd atoms, which could be considered as a multi-molecular reaction. In addition, there was possibly another displacement reaction with $Au^{+}$ to displace Pd atom as mentioned earlier (see Equation 4.10). As a result, the mechanism of the Au displacement of Pd was complicated, which possessed a high reaction order.

## 4.4 Conclusions

Surface condition of Pd layer was found to be important for the Au displacement plating reaction. Pre-treating the Pd surface with acid to remove the non-conducting contaminants increased the Au displacement efficiency. The rough surface of the Pd layer on the porous support resulted in more Au deposition.

Due to the electrochemical nature of the displacement plating, increasing the Au ion concentration, acidity, and temperature of the displacement bath resulted in a faster Au displacement deposition rate. Agitating the Au plating bath at a speed above 400 rpm resulted in a smaller size and a narrow size distribution of the deposited Au clusters which evenly covered on the Pd surface. In addition, a slight increase of the Au deposition rate was also observed with the bath agitation speed above 400 rpm which was due to the minimization of the diffusional resistance within the plating bathes.

The Au displacement reaction of Pd was empirically found to have a reaction order of 3.2 with respect to Au ion concentration, which suggested a complicated reaction mechanism. Approximately 0.5 – 0.6 $\mu$m thick Au layer was deposited after 3 - 4 hours plating. The limiting thickness of the deposited Au layer by the displacement plating method can be used as a guideline to fabricate the Pd/Au alloy membranes of a desired Au composition. The Au composition can be increased by the multi—Au layers deposition by the displacement plating method with a thin Pd layer (0.5 – 1 $\mu$m) deposited in between the Au layers.

# 5. Solid-State Transformation of Pd/Au Alloy Bi-layers

## 5.1 Introduction

The Pd electroless deposition along with the Au displacement plating produced the sequential Pd and Au bi-layer structures. Therefore, a heat treatment (annealing) of the deposited Pd/Au bi-layers was necessary in order to form the Pd/Au alloy layers on the membranes. The annealing for the alloy formation on the hydrogen-selective composite membranes was usually conducted in the inert (i.e. He, $N_2$, Ar) or reducing (i.e. $H_2$) atmospheres in the moderate temperature range (500 - 600°C) due to the chemical and thermal stability of the membrane materials (Ayturk et al 2008; Pomerantz et al. 2010). A very recent study (Shi et al. 2010) reported that the formation of a 3 $\mu$m homogeneous Pd/Au alloy with 7 at% (12.2 wt%) required approximately a week at 600°C in $H_2$. For the purpose of enhancing the $H_2S$ resistance of the membranes, the formation of a Pd/Au alloy layer at the top of the membrane was sufficient and more practical since the formation of homogeneous alloy requires more amounts of Au and extremely long annealing time. Therefore, an optimum annealing condition in terms of temperature and time for the formation of the Pd/Au alloy layer at the top of the membrane should be determined.

In addition to the determination of the optimum annealing conditions for the formation of the Pd/Au alloy, the understanding of the kinetics of the Pd/Au alloy phase transformation from the two pure metal phases (i.e. Pd and Au) was also valuable for

both the fabrication and the permeance characteristics of the Pd/Au alloy membranes. In addition, according to the Pd-Au phase diagram as shown in Figure 5.1, Pd and Au possibly form the ordered-structures FCC Pd/Au alloys including $Pd_3Au$ and $PdAu_3$ in certain compositions in the moderate temperature range (450 - 600°C). As a result, the understanding of the mechanism for the Pd-rich disordered FCC Pd/Au alloy (Au wt%< 20) phase transformation was also important. Unfortunately, no studies on the in depth investigation of the kinetics as well as the mechanism for the Pd/Au alloying have been reported in the literature. While the *ex-situ* methods are sufficient to determine the possible optimum annealing conditions for the formation of the Pd/Au alloy, an *in-situ* method is required to investigate the kinetics as well as the mechanism of the Pd/Au alloy transformation.

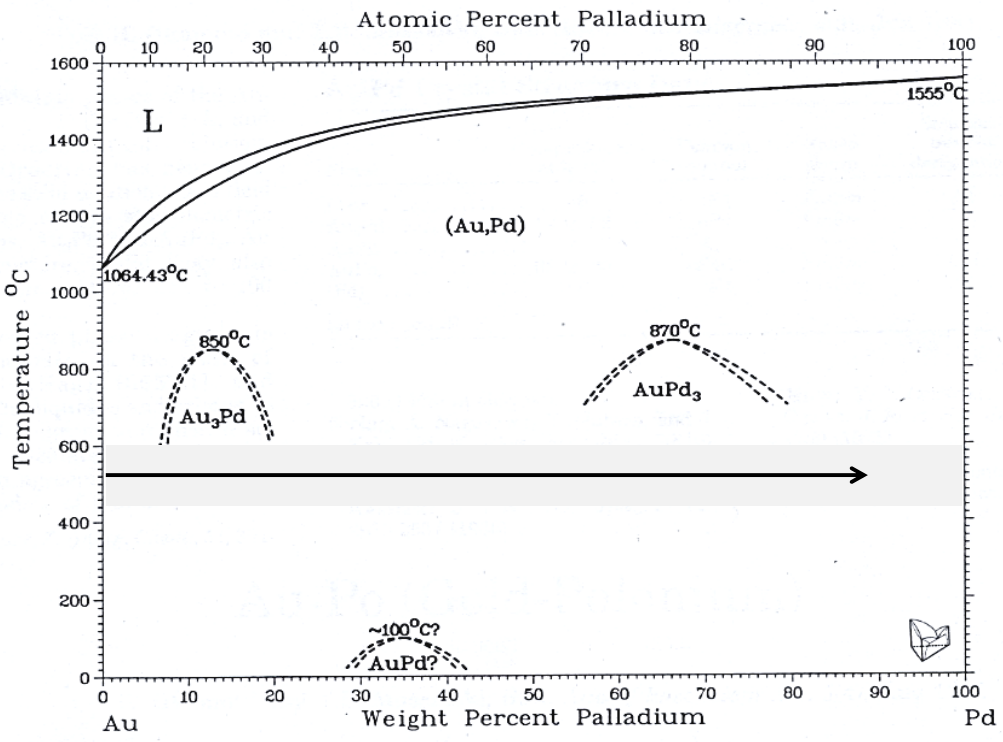


Figure 5.1. Pd-Au phase diagram (H. Okamoto, T.B. Massalski, 1987). The gray area indicates the temperature range tested in this work.

Time-resolved, high temperature X-ray diffraction analysis (HTXRD) is one of the promising approaches for the *in-situ* study of the phase transformation in solids. The *in-situ* studies by the use of the HTXRD technique regarding the product phase transformation from the parent phases in thin films have been carried out by several researchers (Choi et al., 2005; Hancock and Sharp, 1972; Kim et al. 2005, 2008; Ayturk et al., 2008; Pomerantz, 2010). Among the cited research, Ayturk et al. (2008) studied the isothermal Pd/Ag alloy formation from the Pd/Ag bi-layers and Pomerantz et al. (2010) investigated the isothermal FCC Pd/Cu alloy formation from the Pd/Cu bi-layers. Both studies obtained qualitative and quantitative information for the alloy membrane

fabrication and permeance characteristics by understanding the kinetics and the mechanism of the alloys formation through the *in-situ* HTXRD analysis.

The main objective of this chapter was to determine the annealing conditions required to form Pd/Au alloy from the deposited Pd/Au bi-layers by both the *ex-situ* (XRD and SEM) and the *in-situ* (HTXRD) analysis. The influence of annealing time and temperature on the Pd/Au alloying was investigated. In addition, the kinetics and the mechanism of the formation of the Pd-rich disordered FCC Pd/Au alloy was investigated by the use of the time-resolved *in situ* HT-XRD. The information obtained was crucial for the fabrication of the Pd/Au alloy membranes with sulfur resistance.

## 5.2 Experimental

The Pd-Au bi-layer samples tested in this chapter were prepared on the 0.1 $\mu$m grade PSS coupons (1cm x 1cm or 1cm x 1.5cm). After oxidizing at 800°C for 12 hours in air, the PSS coupons were electroless-plated with Pd (to approximately 10 $\mu$m) followed by the Au displacement deposition described in *Section 3.3.5*. The properties and the annealing conditions of the samples are given in Table 5.1.

Table 5.1. The coupons and the annealing conditions tested in this chapter

| Annealing condition | | Pd thickness (μm) | Wt% Au | Characterization method |
|---|---|---|---|---|
| T (°C) | atm | | | |
| 400 | $H_2$ | 8.5 | 8.7 | *ex-situ* XRD |
| 450 | $H_2$ | 7.9 | 9.3 | *ex-situ* XRD |
| 500 | $H_2$ | 8.2 | 8.9 | *ex-situ* XRD |
| 550 | $H_2$ | 8.7 | 8.5 | *ex-situ* XRD |
| 190 - 530 | He | 8.9 | 7.7 | *in-situ* HTXRD |
| 450 | He | 9.0 | 7.7 | *in-situ* HTXRD |
| 500 | He | 10.0 | 6.5 | *in-situ* HTXRD |
| 550 | He | 9.6 | 6.7 | *in-situ* HTXRD |
| 600 | He | 9.5 | 7.8 | *in-situ* HTXRD |

The detailed methods for the *in-situ* HTXRD analysis including non-isothermal and isothermal conditions were given in *Section 3.3.2*. It should be noted that when performing the Scintag PAD-X diffractometer, the actual temperature on the Pd/Au sample surfaces was not directly measured since the readout temperature was measured at the bottom of the Pt strip heater by a thermocouple. A significant temperature gradient might possibly exist between the bottom of the Pt strip and the surface of the Pd/Au samples (the thickness of the Pd/Au bi-layer coupon was ~0.1 cm). Therefore, a temperature calibration was required to estimate the surface temperature from the readout temperature (King et al. 1997; Ayturk et al., 2008). The temperature calibration was usually performed by using the thermal expansion of the tested metal. The detailed calibration method on the Scintag PAD-X diffractometer can be found in the work of Ayturk (2007) with the Pd-Ag/porous Hastelloy samples. In this study, the lattice thermal

expansion of Pd was used in the readout temperature of 25 - 750°C, and the resultant calibration is shown in Figure 5.2.

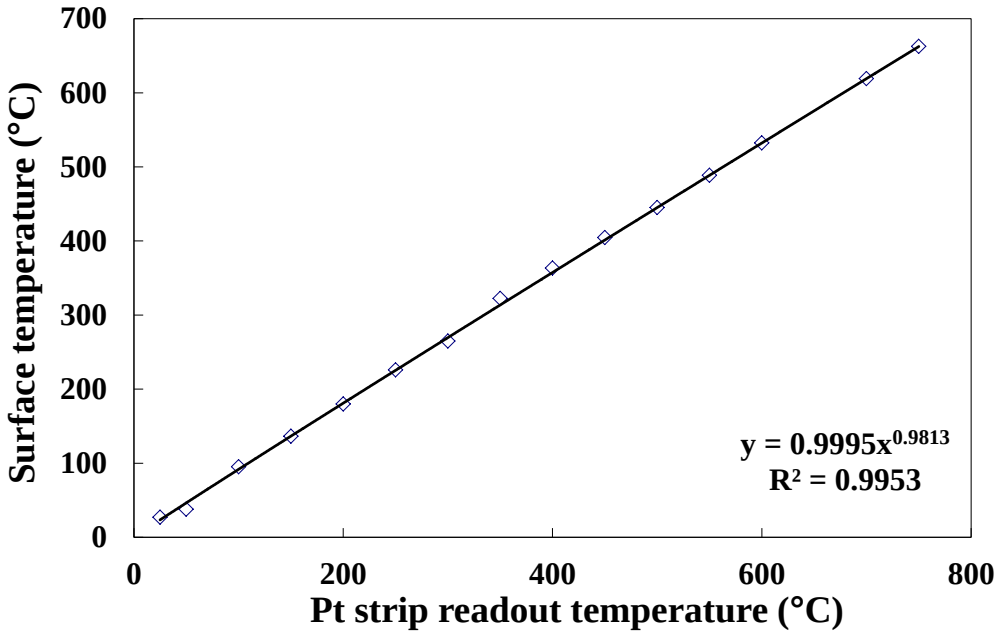


Figure 5.2. Temperature calibration of the Scintag PAD-X diffractometer for the Pd/Au samples based on the linear expansion of Pd (1 1 1).

For the *ex-situ* annealing studies in $H_2$, the Pd/Au bi-layer coupons were placed on the stainless steel sample holder and inserted into the stainless steel shell casing inside the furnace. The BLUE M tube furnace of model TF55035A with a programmable PID temperature control (maximum temperature of the furnace was 1100ºC) was used. Helium was used to purge the housing during the heating/cooling stages between room temperature and the target annealing temperatures, while $H_2$ was flowing through the housing during the annealing period. The heating/cooling rate of 10°C/min was used.

It should be noted that the information gathered from the XRD did not include the entire Pd/Au bi-layer (approximately 10 $\mu$m) due to the limited penetrating ability of the

diffracted X-ray. The maximum depth ($t$) of the X-ray diffraction detected by the XRD diffractometer was determined by Equation 5.1 (Cullity and Stock, 2001)

$$G_x = \frac{I_{D(x=t)}}{I_{D(x=0)}} = \exp\left\{-\frac{2\mu x}{\sin\theta}\right\} = \frac{1}{1000} \tag{5.1}$$

Where $G_x$ is the fraction of X-ray intensity diffracted at a distance ($x$) below the surface to that diffracted at the surface (i.e. $x$ = 0), and $\mu$ is the linear absorption coefficient of the material with the X-ray source being Cu k$\alpha$. The maximum depth ($t$) was defined when the fraction was 0.001. In practice, the signal was negligible when the fraction was smaller than 0.01. The penetration depth of X-ray (taken at $G_x$ = 0.01) in the Pd/Au bi-layer samples ranged from 3.5 to 6 $\mu$m depending on the Au concentration according to Equation 5.1 as shown in Figure 5.3. It should be noted that the calculation was based on the diffraction at (1 1 1) plane.

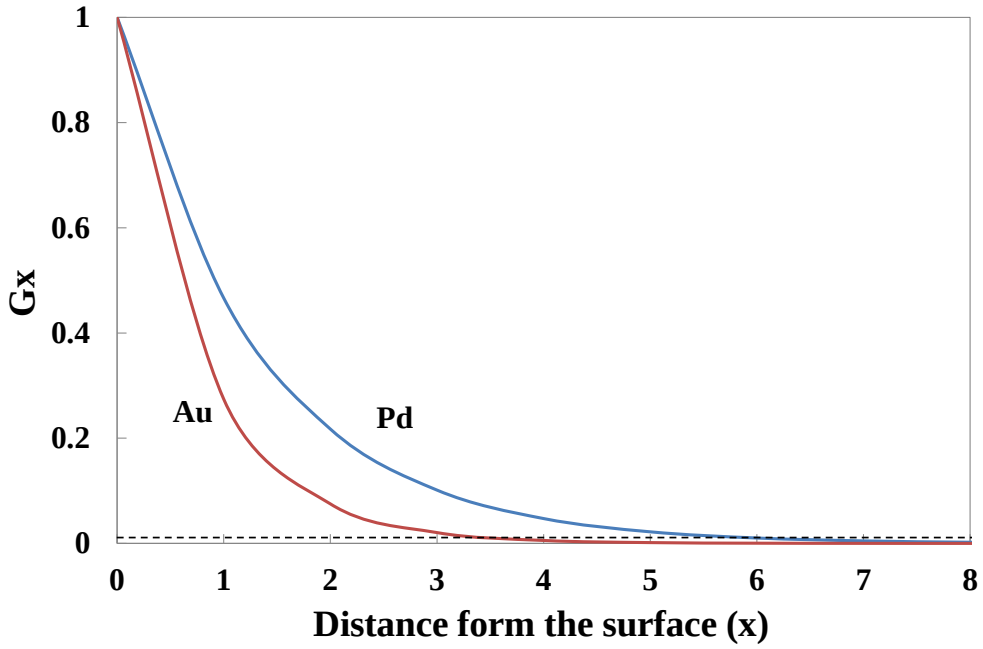


Figure 5.3. Fraction of the diffracted intensity ($G_x$) as a function of the distance from the surface (x) for Pd and Au from the (1 1 1) plane of the FCC structure. The penetration depth was estimated at $G_x$ = 0.01(the dotted line).

## 5.3 Results and Discussion

### *5.3.1 The Pd/Au Alloy Formation (ex-situ analysis)*

In order to investigate the effect of annealing temperature and time on the formation of FCC Pd/Au alloy, the Pd/Au bi-layer samples were annealed in $H_2$ under different annealing conditions. Figure 5.4 shows the X-Ray Diffraction (XRD) patterns of the Pd/Au bi-layer coupons before and after annealing for the different lengths of time in the temperature range of 400 - 550$^{o}$C. The XRD pattern of the Pd/Au bi-layer coupon before annealing (labeled as as-deposited) showed distinct peaks for Pd at $2\theta$ of 40.35$^{o}$,

47.05°, 68.55° and Au at 2$\theta$ of 38.45°, 44.75°, 67.1° diffracted from the planes (1 1 1) to (2 2 0). This verified the Pd/Au bi-layer structure on the coupons.

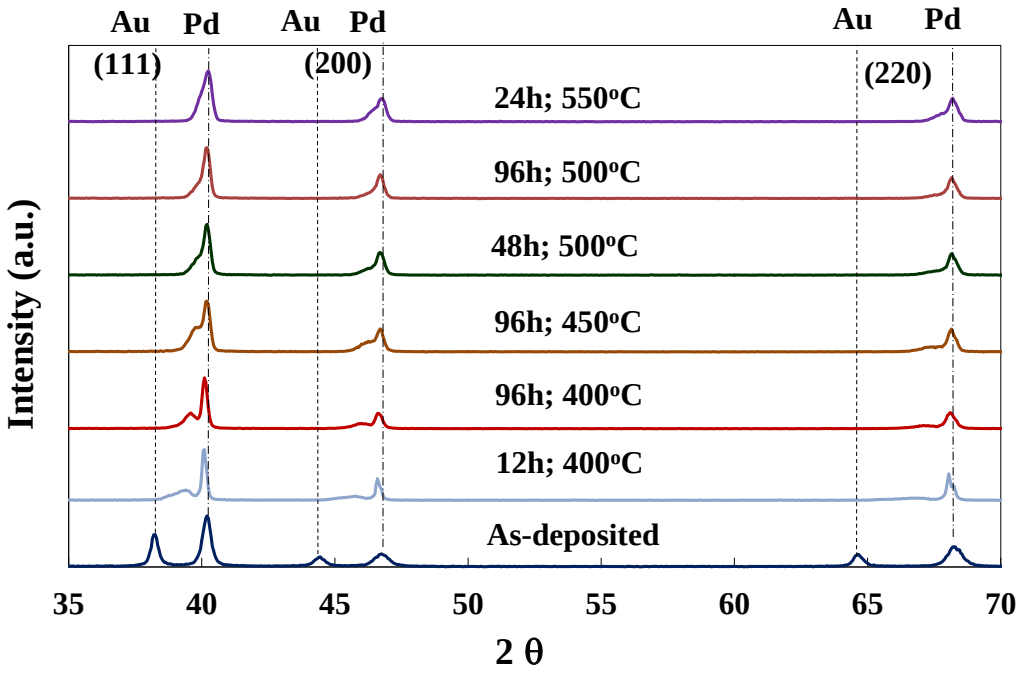


Figure 5.4. XRD patterns of the Pd/Au bi-layer samples before/after annealing in $H_2$ under different conditions (The XRD pattern before annealing labeled as as-deposited).

Following the annealing, the XRD pattern of the coupon annealed at 400°C for 12 hours showed the disappearance of pure Au peaks along with the appearance of peaks in between the Pd and Au peak positions which indicated the formation of a FCC Pd/Au alloy. The formation of the Pd/Au alloy caused by the Pd/Au inter-diffusion throughout the entire Au layer under such mild annealing condition was due to the extremely small thickness of the Au layer. However, the existence of the apparent Pd peaks even after 96 hours annealing at the same temperature (Figure 5.4) suggested that the formed Pd/Au alloy layer was not as thick as the X-ray penetration depth (3.5 - 6 $\mu$m) although a higher

alloy peak intensity was observed due to more Pd/Au inter-diffusion. The result also implied that the Pd/Au inter-diffusion rate decreased as the annealing proceeded. It is also worthy to mention that the width of the Pd peaks decreased after annealing as compared to the as-deposited one (Figure 5.4), which was caused by the increase of the Pd grain size due to the grain growth at elvated temperatures.

The XRD pattern of the coupon annealed at 450°C for 96 hours was very similar to the one annealed for 96 hours at 400°C with the exception of the larger intensity of the alloy peaks and the shift of the alloy peak positions towards more closely to the Pd peaks. This indicated the formation of a thicker and more Pd-rich Pd/Au alloy layer caused by more Pd/Au inter-diffusion at 450°C although the existence of the apparent Pd peaks still suggested a relatively thin Pd/Au alloy layer.

According to the Vegard's law, the lattice parameter of an alloy without a miscibility gap had a linear relationship with the alloy composition. The lattice parameter of the Pd/Au alloy as a function of the Au composition was reported by Maeland (1964) as shown in Figure 5.5. Since Pd, Au, and Pd/Au alloy had the same FCC structure, the crystal having larger lattice parameters produced the diffraction lines at lower $2\theta$ positions. As a result, the fact that $2\theta$ position of the formed Pd/Au alloy moved toward Pd peaks indicated that the formed Pd/Au alloy was more Pd-rich. According to Figure 5.5, the Au fraction in the formed Pd/Au alloy after annealing at 400°C for 12 hours was approximately 40 wt% based on the $2\theta$ position in the XRD pattern (See Figure 5.4). The Au contents were roughly 32 and 22 wt% after 96 hours annealing at 400 and 450°C, respectively.

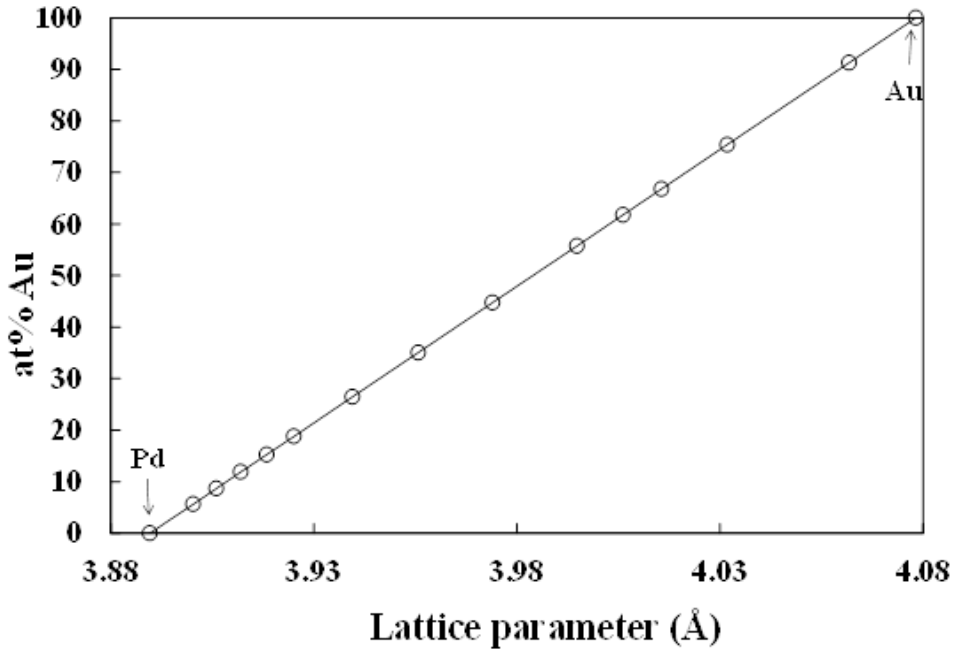


Figure 5.5. Lattice parameter of Pd/Au alloy as a function of Au composition (Maeland, 1964).

As also seen in Figure 5.4, the XRD pattern of the coupon annealed at 500°C for 48 hours showed only the peaks for the Pd/Au alloy without the presence of the Pd and Au peaks, indicating that the formed Pd/Au alloy layer was at least as thick as the XRD penetration depth. The positions of the Pd/Au alloy peaks were very close to those of pure Pd peaks, indicating the alloy formed was highly Pd-rich. The Au fraction in the formed Pd/Au alloy was approximately 16 wt% according to the Vegard's law. However, the un-symmetrical peak shapes observed in all the planes (especially in the higher planes, i.e. plane (2 0 0), (2 2 0)), still suggested the possible existence of an Au gradient on the surface. By comparing the XRD pattern annealed at 500°C for 48 and 96 hours as shown in Figure 5.4, increasing the annealing time to 96 hours did not significantly increase the degree of Pd/Au inter-diffusion and Pd/Au alloy formation. Annealing at the

higher temperature of 550°C for a shorter time period of 24 hours resulted in a similar Pd/Au alloy formation as the ones annealed at 500°C for time longer than 48 hours as evidenced by the XRD pattern shown in Figure 5.4. This indicated that a similar degree of Pd/Au inter-diffusion and alloy formation could be achieved at a higher temperature for a shorter length of annealing time. The result suggested that the annealing temperature had a stronger influence on the Pd/Au inter-diffusion and the formation of Pd/Au alloy than the annealing time.

The cross-sectional SEM analyses including EDX were performed on the annealed Pd/Au bi-layer samples to verify the existence of the Au gradient. Figure 5.6(a) is the cross-sectional micrograph of the Pd/Au bi-layer supported on the oxidized PSS support after annealing at 450°C for 96 hours and Figure 5.6(b) is the corresponding EDX line scan.

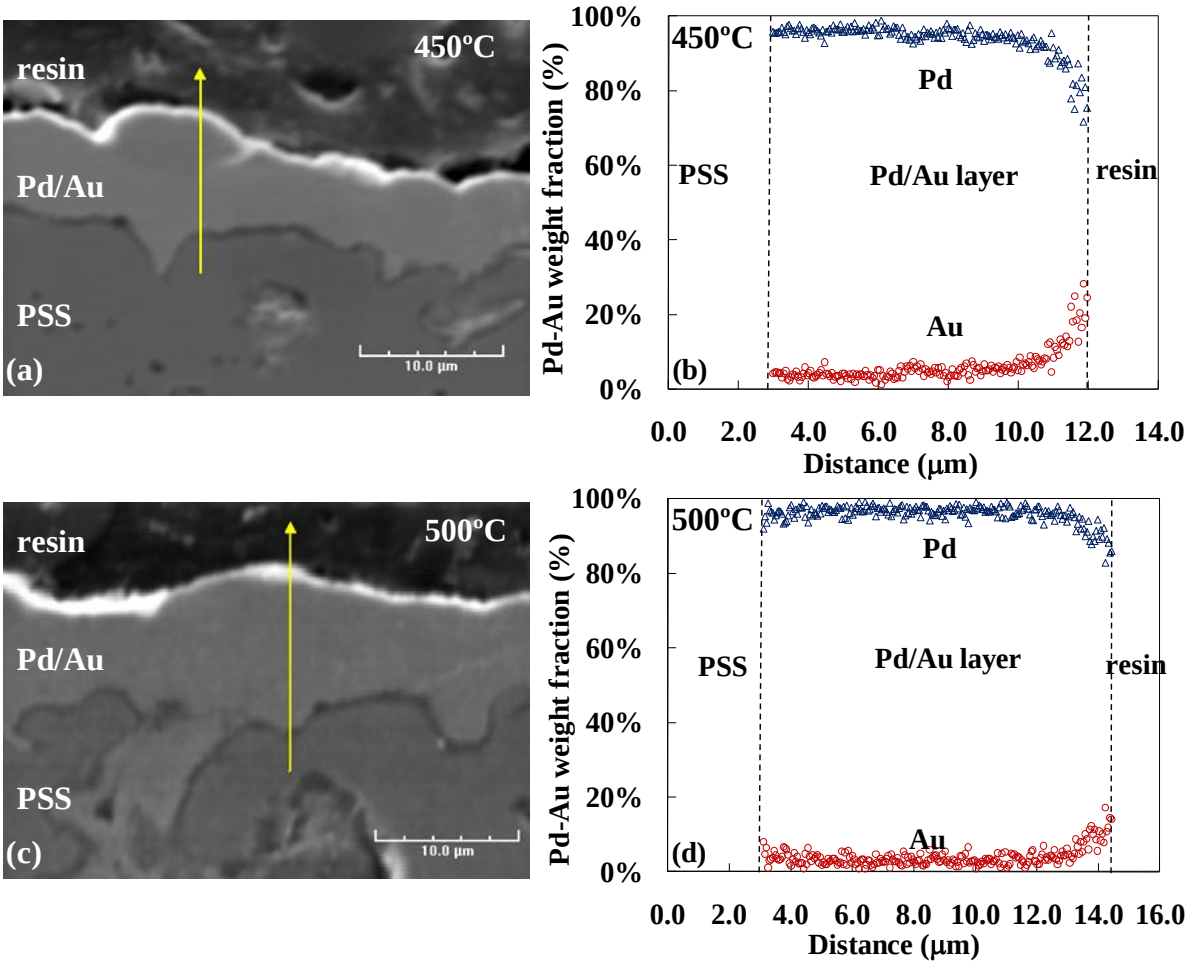


Figure 5.6. (a) Secondary-electron imaging (SEI) cross-sectional micrograph, (b) corresponding energy dispersive X-ray spectroscopy (EDS) line scan, (c) SEI cross-sectional micrograph, and (d) corresponding energy dispersive X-ray spectroscopy (EDS) line scan of the Pd/Au bi-layers annealed at 450°C and 500°C for 96 h in $H_2$, respectively.

In Figure 5.6(a), the 0.5 – 0.7 $\mu$m dark layer between the Pd/Au layer and PSS support was the metal oxide intermetallic diffusion barrier layer, and the arrow indicates the direction of the EDS line scan. The thickness of this Pd/Au bi-layer sample was roughly 9 $\mu$m. The dotted lines in Figure 5.6(b) represented the interfaces of the Pd/Au layer between the support and mounting resin. An apparent Au gradient was seen from

the surface of the Pd/Au bi-layer with the highest Au concentration of ~30 wt% at the surface of the Pd/Au bi-layer (the interface between the Pd/Au layer and the mounting resin). The cross-sectional micrograph and the corresponding EDX line scan of the Pd/Au bi-layer after annealing at 500°C for 96 hours are shown in Figure 5.6(c) and (d), respectively. In this sample, the thickness of the Pd/Au bi-layer was roughly 11 $\mu$m, and an Au gradient at the surface of the Pd/Au layer could also be seen. However, the Au concentration at the surface of the Pd/Au bi-layer sample was lower, roughly 18 wt%. Since the Pd/Au bi-layer samples had very similar compositions before the annealing, the lower Au content at the surface observed after the annealing at 500°C indicated that the higher annealing temperature resulted in more Pd/Au inter-diffusion which was in agreement with the XRD results. The results also indicated that a homogenous alloy had not formed throughout the entire Pd/Au layer even after annealing at 500°C for as long as 96 hours. Yet, annealing the Pd/Au bi-layers at 500°C for a reasonable amount of time was sufficient to form a Pd/Au alloy top layer with a sufficient thickness to obtain potentially higher $H_2$ permeance and sulfur resistance.

Most Pd/Au inter-diffusion occurred in the early stage of the annealing as evidenced by the surface Au fraction as a function of annealing time shown in Figure 5.7. The Au fractions were estimated by the EDX elemental analysis performed by several area scans at a magnification of 1000X. As shown in Figure 5.7, surface Au weight fractions decreased most rapidly in the first 12 hours of the annealing at all temperatures. Further increasing the annealing time resulted in a non-significant decrease in surface Au fraction especially at higher annealing temperatures (>500°C). This indicated that the Pd-Au inter-diffusion rate was the highest at the beginning of the annealing and decreased

with annealing time due to the decrease of the driving force (i.e. the decrease of the concentration gradient).

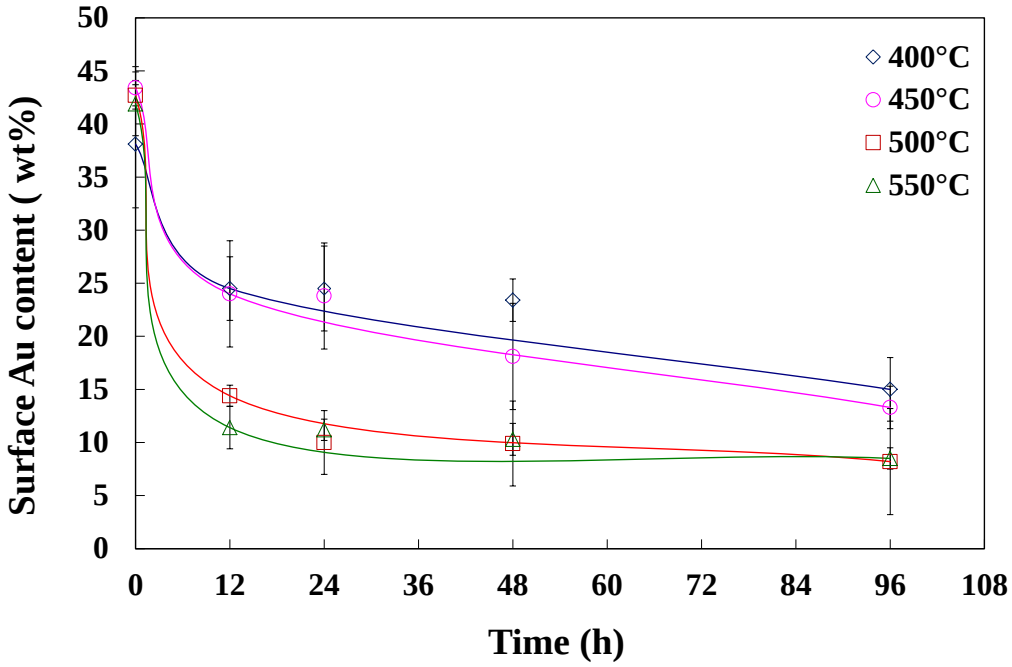


Figure 5.7. Surface Au fraction (detected by EDX) as functions of annealing time.

Figure 5.8 shows the surface Au weight fraction as a function of the annealing temperature after annealing for 96 hours. The surface Au weight fractions decreased with increasing annealing temperatures due to more Pd/Au inter-diffusion at higher temperatures, which agreed with the XRD results. In addition, no significant difference in the surface Au weight fractions was observed while the annealing temperature was above 500$^{o}$C. This suggested that annealing at 500$^{o}$C was sufficient to form the Pd/Au alloy on the top layer although higher annealing temperatures further reduced the annealing time for the formation of the alloy with similar composition.

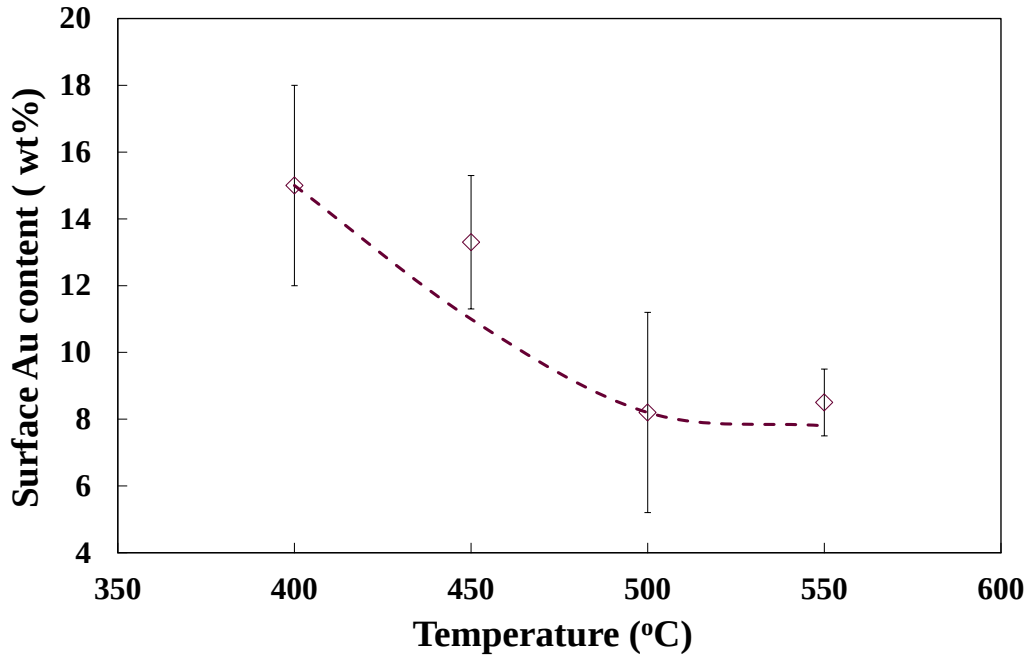


Figure 5.8. Surface Au fraction (detected by EDX) as a function of annealing temperature.

Figure 5.9 displays the SEM micrographs of the Pd/Au bi-layer samples annealed for 96 hours at different temperatures. The as-deposted sample as shown in Figure 5.9(a) showed a number of Au clusters on the surface. Following the annealing at all temperatures, the cluster structure on the surfaces of the Pd/Au bi-layer samples became less apparent due to the fusion of Au during the annealing. In addition, the grain size of Pd also increased during the annealing as stated previously (See Figure 5.4). The results suggested that the annealing caused not only the Pd/Au inter-diffuion but also the morphology change of the deposited layers due to the rearrangement of the atoms. The degree of morphology change caused by the fusion and grain growth increased with incresing temperturture as expected due to higher atomic mobilities at higher temperatures. As shown in Figure 5.9, at the annealing temperature above 500$^{o}$C, the

morphology of the Pd/Au bi-layers was siginificant rounder and flater with a number of pinholes caused by the intense grain growth.

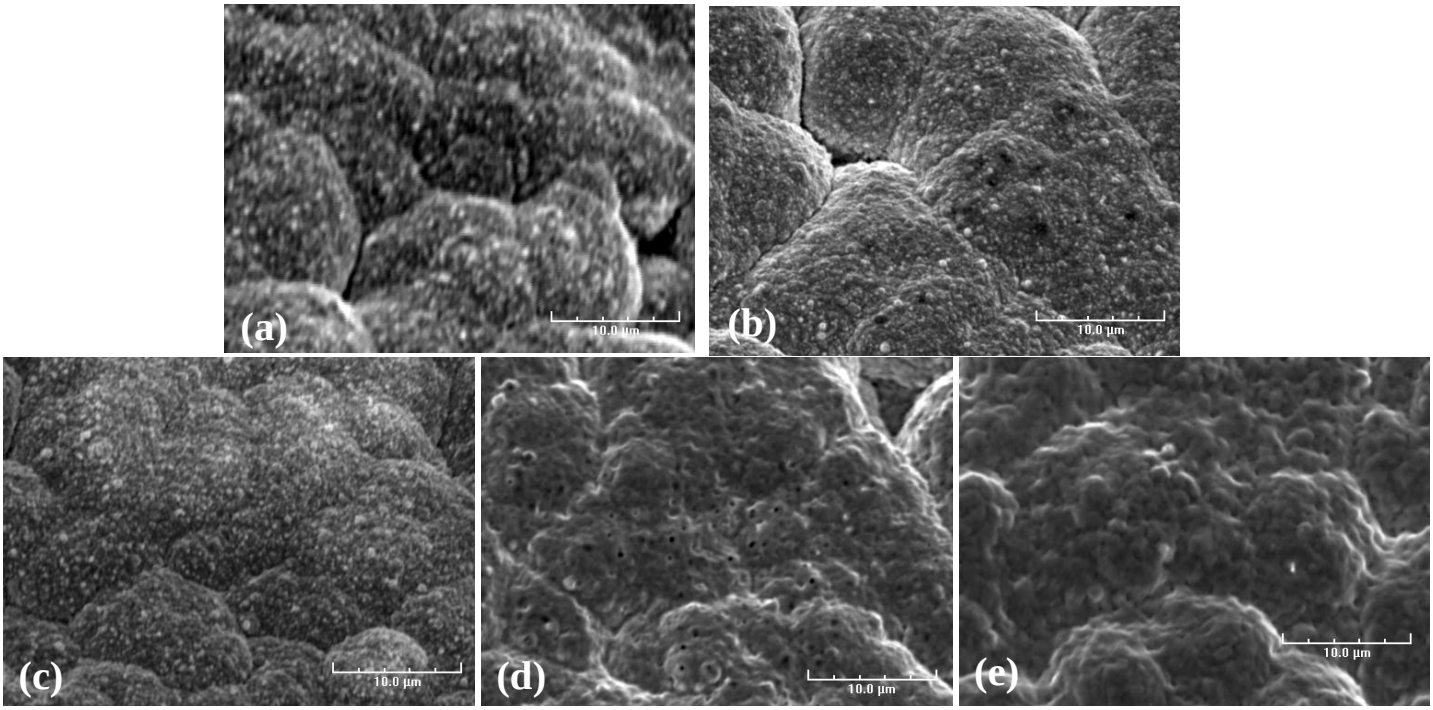


Figure 5.9. Surface SEM micrographs at 3000x of the Pd/Au bi-layer samples those were (a) as-deposited, and annealed for 96 hours at (b) 400$^{o}$C, (c) 450$^{o}$C, (d) 500$^{o}$C, and (e) 550$^{o}$C.

The extent of morphology change due to the fusion and grain growth also increased with the increasing annealing time as evidenced by the evolution of the surface morphology of the Pd/Au bi-layer samples annealed at 500$^{o}$C shown in Figure 5.10. The cluster structure became less apparent as the annealing time was increased. At the end of the 96 hours annealing, surface grains merged together due to the high extent of grain growth, resulting in a flat surface with several pinholes.

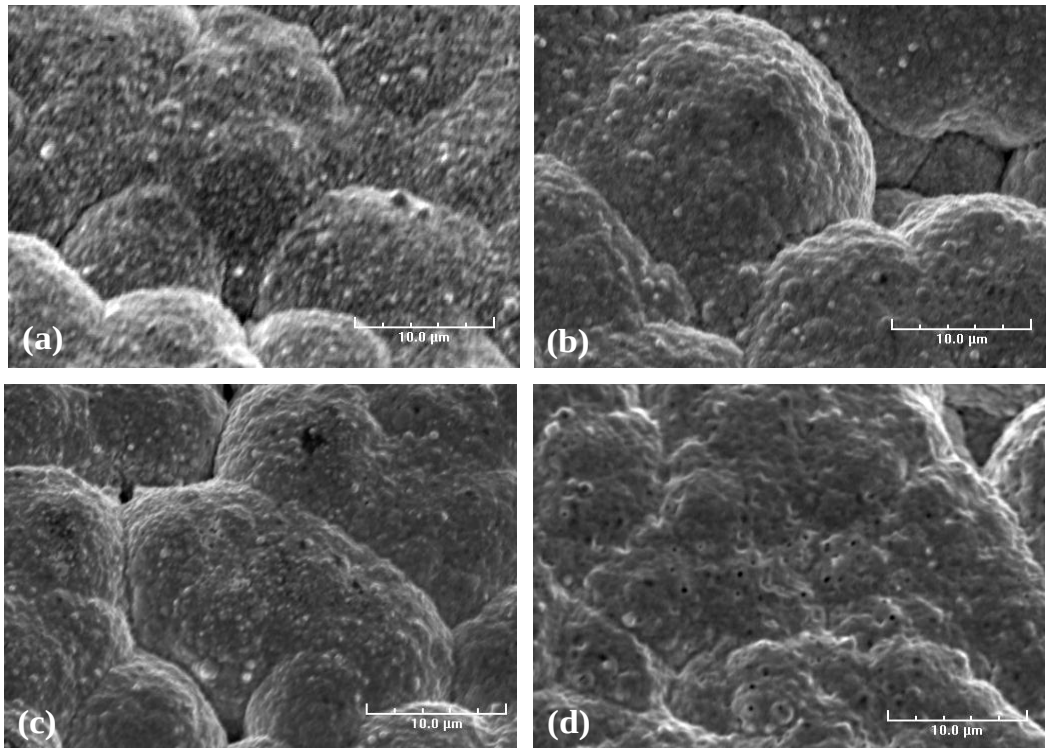


Figure 5.10. Surface SEM micrographs at 3000x of the Pd/Au bi-layer samples that were (a) as-deposited, and annealed at 500°C for (b) 24, (c) 48, and (d) 96 hours.

### *5.3.2 Time-resolved in-situ HT-XRD*

The non-isothermal annealing of the Pd/Au bi-layer in helium was first investigated by the *in-situ* HTXRD in order to determine the temperature that the formation of the Pd/Au alloy started to occur. The Pd/Au bi layer was first heated from room temperature (~25°C) to approximately 265°C with a rapid heating rate (60°C/min) followed by a ramping rate of 9°C/min to 662°C. Figure 5.11 shows the XRD patterns of the Pd/Au bi-layer sample during the non-isothermal annealing process. The peaks of the pure Pd and Au phases from the planes (1 1 1) and (2 0 0) at room temperature were shown in the first XRD pattern in Figure 5.11. Upon heating, a shift of both Pd and Au

peaks to lower values of $2\theta$ was observed due to the thermal expansion of the lattice (As shown in the second XRD pattern in Figure 5.11).

As observed in Figure 5.11, the Au-rich Pd/Au alloy peaks close to Au peaks (as a shoulder) started to appear at approximately 322°C caused by the noticeable amount of the Pd/Au inter-diffusion at the temperature. Along with the increase of Pd/Au alloy peaks intensity, the Au peaks were decreasing in intensity as the temperature was further increased and disappeared at roughly 558°C. This indicated that the Pd/Au inter-diffusion occurred throughout the entire Au layer in forming the Pd/Au alloy. As the temperature was further increased, the Pd/Au alloy peaks were not only larger in intensity but also moving toward Pd peaks indicating the formation of more Pd-rich alloy.

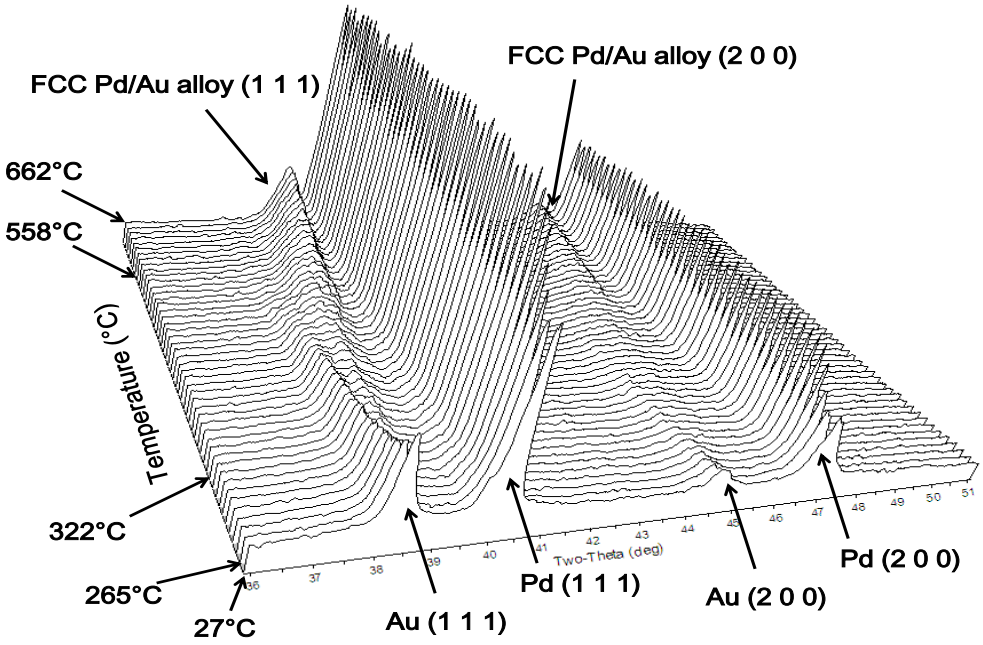


Figure 5.11. *In-Situ* HTXRD scans for non-isothermal annealing of the Pd/Au bi layer.

The occurrence of the Pd/Au inter-diffusion at such mild annealing condition (at the temperature as low as 322°C, and the entire duration of the non-isothermal annealing test was within 50 minutes) was due to the small thickness of the Au layer. Boyko et al. (1968) have reported that the inter-diffusion coefficient of the extremely thin Pd/Au bi-layers (10 – 15 nm) was greater than bulk value by 5 – 7 orders of magnitude. Recent study on the Au displacement plating of Pd nanowires by Teng et al. (2007) indicated that the Pd/Au alloy formed right after the plating due to the extremely high diffusion rate of atoms caused by the extremely high surface to volume ratio on the nano-structure (Gleiter, 1992; Mori et al., 1991). Moreover, the grain boundary diffusion possibly became predominant when the high density of the grain boundary (small grain size), defects, vacancies, and dislocations were present in the interface of the bi-layers. The grain boundary diffusion was much faster than the bulk (lattice) diffusion (usually by 2 - 4 orders of magnitude) due to the fact that the overall area for diffusion was noticeably increased. In addition, while the bulk diffusion required more thermal energy, the grain boundary diffusion occurred at lower temperatures. The PSS support and the plating techniques adopted in the study produced rough deposit layers with small clusters (See Figure 5.9(a)), which contained high density of the grain boundary. As a result, higher Pd/Au inter-diffusion rate occurred under mild annealing conditions was expected.

During the annealing, the Au peak intensity reduced substantially and became asymmetrical due to the Pd/Au alloy formation, and shifted towards the Pd peak which remained, sharp, symmetric and showed no shift of the peak position. The phenomenon was also observed in the previous discussion on *ex-situ* and the *in-situ* isothermal annealing which would be described shortly. The phenomenon indicated that the

diffusion of Pd into the Au film was much faster than the Au diffusing into the bulk of Pd. Similar Pd/Au inter-diffusion phenomenon also reported by Murakami et al. (1976), who further concluded that the diffusional asymmetry indicated a strongly concentration-dependent inter-diffusion coefficient of the Pd/Au inter-diffusion.

DeBonte et al. (1974, 1975) studied the inter-diffusion of Pd/Au bi-layers in the temperature range of 200 – 389°C by the construction of the concentration profile of Pd and Au in the Au and Pd layer after annealing. They reported that the diffusion of Pd into Au was mainly the grain boundary diffusion while the bulk diffusion of Au into Pd was more predominant. This provided the possible explanation for the observation that the diffusion of Pd into Au was faster than the diffusion of Au into Pd since the grain boundary diffusion was much faster than the bulk diffusion although Au had a higher self-diffusion coefficient (Okkerse, 1956; Makin et al., 1957) than Pd (Peterson, 1964).

The HTXRD scans for the isothermal annealing of the Pd/Au bi-layer coupons in helium at 450, 500, 550, and 600ºC were shown in Figure 5.12. The first XRD pattern in each HTXRD data set was scanned at room temperature before the annealing process, and the existence of only Pd and Au phases on the samples was verified. The peak shift of both the Pd and Au of all the planes to a lower value of $2\theta$ in the beginning of annealing process at elevated temperatures (As shown in the second XRD patterns in Figure 5.12) was due to the thermal expansion of the lattice as described earlier. Almost instantaneous appearance of the Pd/Au alloy phase and the disappearance of the pure Au phase upon attainment of the annealing temperatures of 450 - 600°C were also observed in Figure 5.12. This was due to the fact that the Pd/Au inter-diffusion and the alloy

formation had already started below the target annealing temperatures according to the non-isothermal annealing study described previously as shown in Figure 5.12.

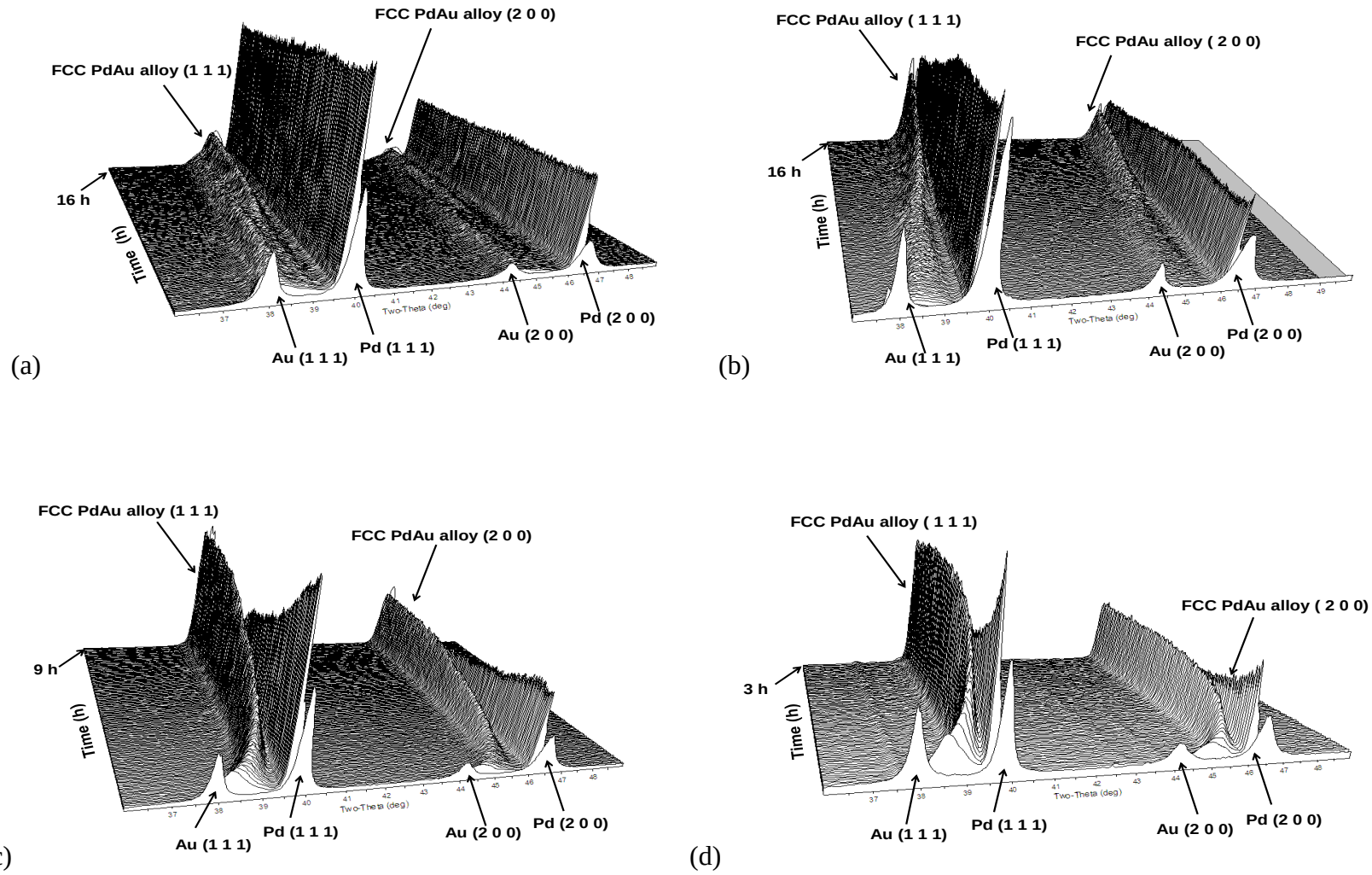


Figure 5.12. *In-Situ* HTXRD scans for isothermal annealing of the Pd/Au bi layers at (a) 450°C, (b) 500°C, (c) 550°C, and (d) 600°C.

The annealing temperature, however, affected the Pd/Au alloy formation. As seen in Figure 5.12(a), two Pd/Au alloy peaks appeared during the annealing at 450ºC suggesting two Pd/Au alloy species. The Au rich Pd/Au alloy (the one close to the Au peak) was larger in the initial stage of the annealing while the Pd rich Pd/Au alloy became predominant with increasing peak intensity in the latter period of the annealing. Although no apparent two Pd/Au alloy peaks, the very broad and poorly-defined Pd/Au alloy peaks in the initial annealing stage at 500ºC (Figure 5.12(b)) suggested the possible existence of more than one Pd/Au alloy species at the stage. As time progressed further, the Pd/Au alloy peak became much narrow and better-defined in shape and close to the Pd peaks indicating that single Pd-rich Pd/Au alloy remained in the sample.

Annealing at even higher temperatures of 550 and 600ºC was very similar as shown in Figure 5.12(c), (d). The formed Pd/Au alloy peaks passed through the two alloy peaks area and very rapidly moved toward Pd peaks from the beginning of the annealing process. No apparent two alloy peaks were observed, however, a slightly broader and less-defined peak in the initial annealing stage still implied the multi Pd/Au alloy species although the period was very short. The Pd/Au alloy peaks also increased faster in intensity with the apparent decrease in the Pd peak intensity. This indicated that the inter-diffusion of Pd and Au and the formation of the Pd/Au alloy were relatively rapid at these temperatures.

The Au contents in the formed Pd/Au alloys were estimated based on the $2\theta$ positions of the alloy peaks at the end of the isothermal annealing and the use of the Vegard's law (See Figure 5.5). The Au fraction were 65 and 38 wt% after the annealing at 450°C ( It should be noted that there were two Pd/Au alloy peaks formed at 450°C as

mentioned previously), 17 wt% after the annealing at 500°C, 16 wt% at 550°C, and 14 wt% at 600°C.

In order to understand the Pd/Au alloy formation phenomenon observed at different annealing temperatures, one must review the Pd-Au phase diagram. As seen in the Pd-Au phase diagram (See Figure 5.1), Pd and Au exhibited complete solubility in the solid phase over the entire composition range (i.e. there is no miscibility gap). Pd, Au, and Pd/Au alloys all had the FCC phase, which varied only in composition but not in the crystal structure. Therefore, Pd and Au form the substitutional solid solution with an arbitrary composition with Pd and Au in random positions in the lattice similar to the Pd-Ag binary system. However, in the temperature range tested (450 - 600°C), there were two ordered-structure (super-lattice) regions in the Pd-Au binary system, namely $PdAu_3$ ($T_c$ = 850°C) and $Pd_3Au$ ($T_c$ = 870°C) where Pd and Au atoms occupied the fixed positions in the lattice. The super-lattice structure formed in the Pd-Au binary system is known as $L1_2$ or $Cu_3AuI$ type with 75% Pd (or Au) occupied at corner sites and 25% Au (or Pd) occupied at face site in the lattice. As a result, in addition to the random solid solution, $Pd_xAu_y$, two ordered Pd/Au alloys, $PdAu_3$ and $Pd_3Au$, could form during the annealing depending on the Au composition.

The overall bulk compositions of the prepared Pd/Au bi-layers in the study were within the range of disordered Pd-rich Pd/Au alloy ($Pd_xAu_y$, x>>y). The formation of the disordered Pd-rich Pd/Au alloy was postulated as shown in the schematic representation in Figure 5.13. Since the ordered structures including $PdAu_3$ and $Pd_3Au$ were more energetically stable than disordered alloy, they are preferably formed as Au diffused into the Pd layer during the initial stage of annealing. As the annealing progressed, the

ordered Pd-rich alloy, $Pd_3Au$ became more predominant than $PdAu_3$ due to the composition gradient. As time further progressed, the driving force from the composition gradient transferred the ordered $Pd_3Au$ into the disordered Pd-rich $Pd_xAu_y$ alloy. Since there was only a very slight change in the size of the unit cell on ordering, and none in its shape and crystal structure, there would be practically no changes in the positions of the diffraction lines. The transition between ordered $Pd_3Au$ and disordered Pd rich $Pd_xAu_y$ was continuous and smooth rather than an abrupt change with a new peak appearing in the XRD pattern as seen in the FCC-BCC transition in the Pd-Cu binary system (Pomerantz et al., 2010).

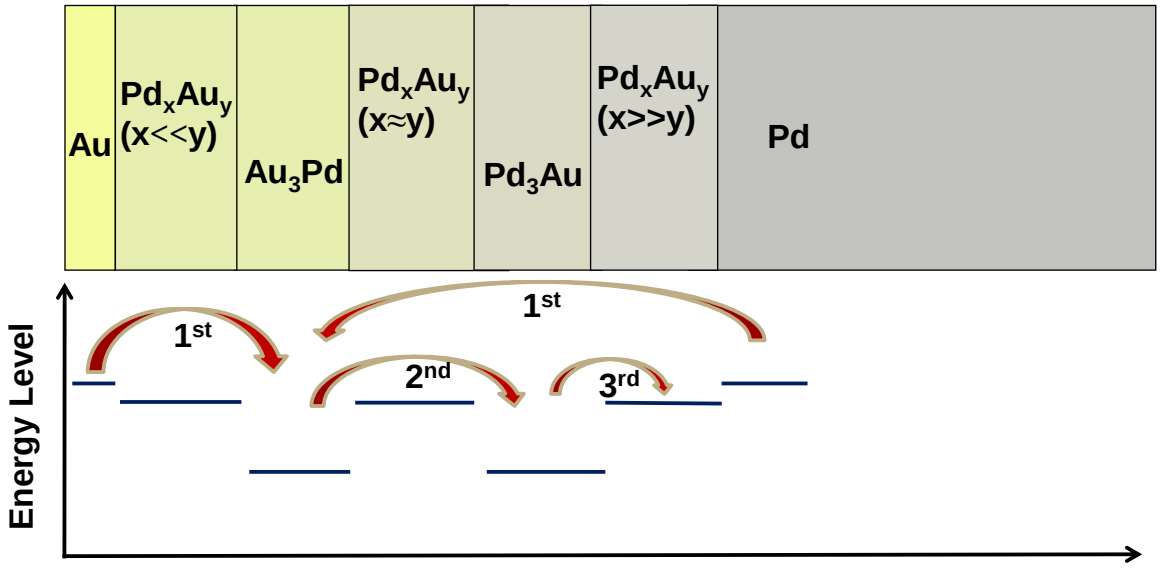


Figure 5.13. Schematic representation of forming disordered Pd-rich Pd/Au alloy ($Pd_xAu_y$, x>>y).

The existence of both ordered and disordered Pd/Au alloys provided the explanation for different Pd/Au alloying phenomenon observed at different temperatures. At 450°C, the Pd/Au alloys formed were still in the ordered structure regions at the end

of the entire annealing process of 16 hours due to the insufficient energy provided for the Pd-Au inter-diffusion at the temperature. On the other hand, at higher annealing temperatures of above 550°C, the transition through the ordered structure regions were so rapid that the ordered structures could be ignored. In addition, the degree of order decreased with increasing temperature since the ordered structure only appeared under the critical temperature ($T_c$). Annealing at higher temperatures (closer to the $T_c$), the alloying phenomenon would be similar to the formation of random solid solution due to the less degree of order, while annealing at lower temperatures, the ordered structure would be more apparent due to the high degree of order. The shapes of the ordered structure regions and the distance between them in the Pd-Au phase diagram provided another way of understanding the different alloying phenomenon caused by the annealing temperature. The distance between the two ordered structures were closer at lower temperatures as seen in Figure 5.1. As a result, the ordered structures would be more predominant at lower temperatures since the transition between ordered structures was easier due to the smaller gap between them, while larger gap between ordered structures at higher temperature resulted in a more disorder solid solution phenomenon. Nevertheless, the result suggested that the annealing temperature should be at least 500°C in order to form Pd-rich Pd/Au alloy within reasonable annealing time, which was in a good agreement with the *ex-situ* XRD analysis.

Although the X-ray diffraction lines would be practically identical between ordered and disordered structure as mentioned earlier, ordered structures also produced extra diffraction lines, known as “super-lattice lines”, due to the fixed position of each participating atom. It should be noted that the diffraction lines observed on both

disordered and ordered structures were known as "fundamental lines". All the super-lattice lines are much weaker than the fundamental lines since their structure factors involved the difference, rather than the sum. An approximate estimate of relative intensity of the super-lattice lines to fundamental lines could be made by comparing their relative structure factor $|F|^2$ values by ignoring the multiplicity factor and Lorentz-polarization factor. For example, the intensity of the fully ordered $Pd_3Au$ and $PdAu_3$ could be estimated by the following equations:

$$\frac{I_s}{I_f} = \frac{|F|_s^2}{|F|_f^2} = \frac{(f_{Au} - f_{Pd})^2}{(f_{Au} + 3f_{Pd})^2}, \langle Pd_3Au \rangle \tag{5.2}$$

$$\frac{I_s}{I_f} = \frac{|F|_s^2}{|F|_f^2} = \frac{(f_{Au} - f_{Pd})^2}{(3f_{Au} + f_{Pd})^2}, \langle PdAu_3 \rangle \tag{5.3}$$

Where $I_s$ and $I_f$ are the intensity of the super-lattice lines and fundamental lines, respectively. $f_i$ is the form factor of atom $i$ ($i$ = Pd or Au). At low $2\theta$ where $(\sin\theta)/\lambda \approx 0$, the form factor, $f_i$, roughly equals to the atomic number, $Z_i$. Since the atomic numbers of gold and palladium are 79 and 46, respectively. The intensity of super-lattice lines of ordered $Pd_3Au$ was roughly 2% of the fundamental lines and that of $PdAu_3$ was 1% of the fundamental lines. Such weak peaks were therefore difficult to be observed in the XRD patterns.

Figure 5.14 displays the weight fraction of all the phases as a function of time during annealing at 450 - 600ºC. According to the previous discussion, five phases were possibly to co-exist during annealing, which were Au, $PdAu_3$, $Pd_3Au$, Pd-rich $Pd_xAu_y$, and Pd. However, since the Pd-rich $Pd_xAu_y$ phase was transformed from the ordered

$Pd_3Au$ phase and the transition between these two phases were continuous and impossible to distinguish, these two phases were analyzed as one single phase of $Pd_3Au$-FCC PdAu during the weight fraction analysis. As seen in Figure 5.14, the pure Au phase decreased sharply in the beginning of the annealing while the pure Pd phase gradually decreased. As mentioned previously, this was due to the small quantity of Au being present in the bi-layers and the much higher Pd diffusion rate into the Au layer.

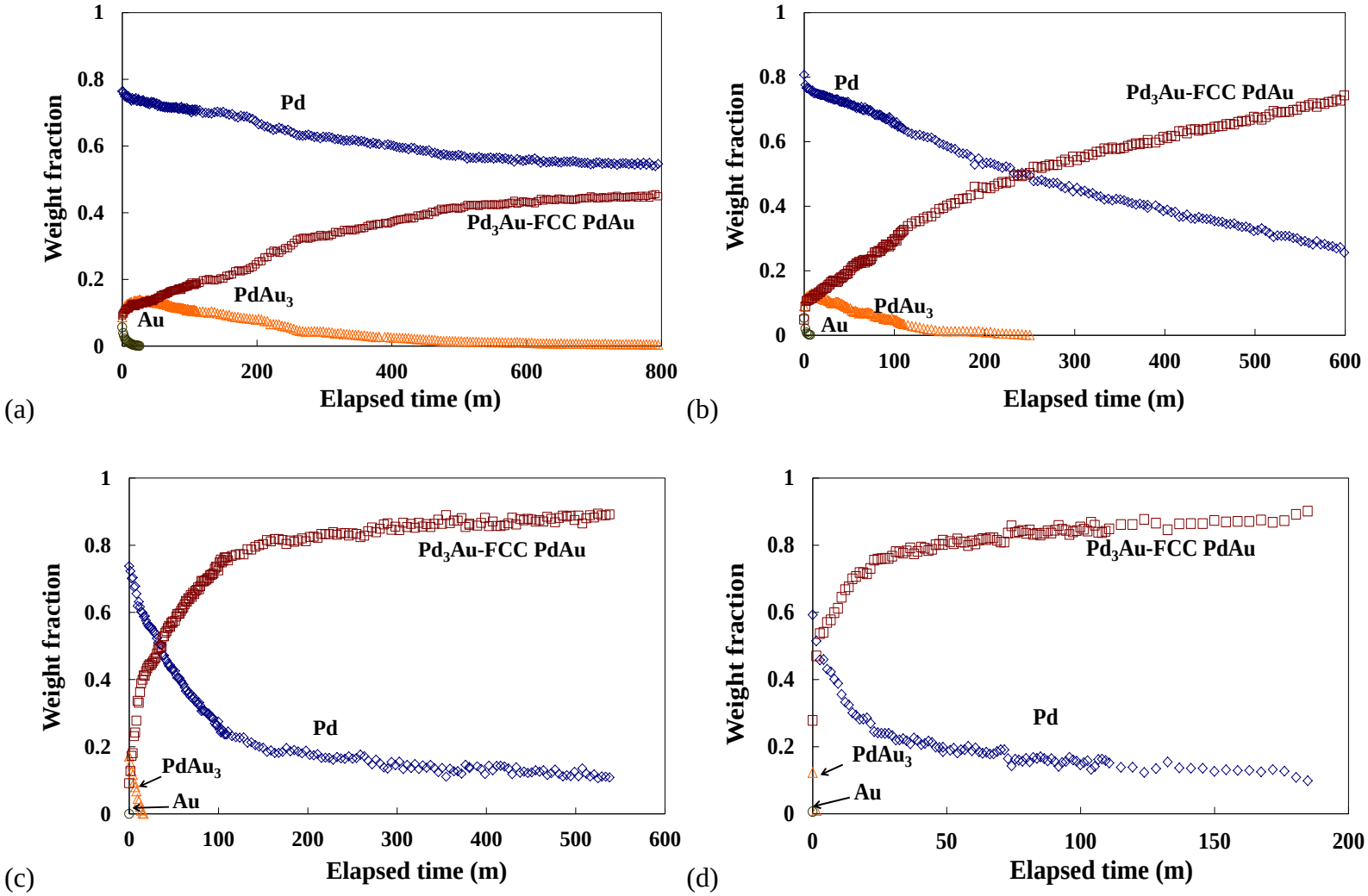


Figure 5.14. Weight fraction of the Pd-Au phases as a function of time during annealing in He at (a) 450°C, (b) 500°C, (c) 550°C, and (d) 600°C.

Unlike the $Pd_3Au$-FCC PdAu phase that continuously increased during the entire annealing process, the $PdAu_3$ phase showed maxima in weight fraction in the early stage of annealing since it was an intermediate alloy. A maximum value of roughly 15 wt% of the $PdAu_3$ phase could be seen at all the annealing temperatures from 450 to 600°C, while the duration of the $PdAu_3$ phase decreased with increasing temperature. Annealing at 450°C, the $PdAu_3$ phase reached the maximum at roughly 30 minutes and became barely detectable after 450 minutes while the $PdAu_3$ phase appeared at 125 minutes with the maximum at 10 minutes at 500°C. Annealing at higher temperatures above 550°C, the $PdAu_3$ phase reached the maximum value almost instantaneous at the onset of the annealing and disappeared in a few minutes. Higher diffusion rate at higher temperatures shortened the duration of intermediate $PdAu_3$ phase as well as the pure Au phase.

Figure 5.14 also showed that the diffusion and phase transformation rate decreased significantly with increasing annealing time, which was consistent with the observations from the *ex-situ* study. Take the sample annealed at 550ºC as an example (Figure 5.14(c)), the weight fraction of the Pd phase decreased from 75 to 25 wt% with the disordered FCC Pd/Au alloy phase increasing from 15 to 80 wt% during the first 100 minutes of the annealing. However, the fractions of the Pd and the disordered Pd/Au phase varied by only ~10 wt% over the next 400 minutes.

The decrease in the diffusion and phase transformation rate with time was due to the decrease in the concentration gradient, the driving force for the diffusion. In addition, as mentioned earlier, the asymmetric inter-diffusion of Pd and Au indicated a strongly concentration-dependent inter-diffusion coefficient. Indeed, the Pd/Au inter-diffusion coefficient varied by nearly 3 orders of magnitude depending on the composition

(Murakami et al., 1976). The maximum value of the inter-diffusion coefficient was at 0 Pd wt% while the minimum value was in the range of 50 – 90 wt% Pd. Moreover, as annealing proceeded, the grains grew in addition to the inter-diffusion as mentioned previously, which resulted in the decrease of the density of grain boundary. Therefore, the grain boundary diffusion became less and less predominant while the process was gradually controlled by the bulk diffusion which had a much smaller diffusion as the annealing proceeded. As a result, after the initial rapid Pd/Au inter-diffusion (mostly Pd diffusion into Au) due to the structure of the as-deposited and high composition gradient, the inter-diffusion rate as well as the phase transformation rate dropped significantly caused by the above-mentioned reasons. The decrease in the inter-diffusion rate with time was more apparent at higher annealing temperatures, which was also readily understood by the causes just mentioned. Finally, the Pd phases were still seen after the annealing under all the annealing conditions which indicated the small thickness of the formed Pd/Au alloy layer.

Figure 5.15 shows the corresponding surface morphologies of the Pd/Au bi-layers after the aforementioned isothermal annealing under different conditions. As shown in Figure 5.15(a) – (c), after annealing at 450, 500, and 550°C (the annealing time was 16, 16, and 9 hours, respectively), larger grain sizes were observed due to the grain growth and compared to the as-deposited sample as shown in Figure 5.9(a). Significant grain coarsening was observed at the annealing temperature above 500$^{o}$C. The results were in agreement with the obsevration from the *ex-situ* study. The grain coarsening observed once again suggested that the Pd/Au inter-diffusion gradually became bulk diffusion control due to the reduction of the grain boundary density. Figure 5.15(d) shows the

surface morphology of the sample after annealing at 600°C for 11 hours. The Pd/Au bi-layer collapsed after roughly 6 hours annealing as evidenced by the peaks representing the support metals (e.g. Fe) appeared in the XRD pattern. The collapse was possibly due to the extremely high stress generated at 600°C. It should be noted that the *in-situ* XRD data discussed previously were taken for the first 3 hours of the annealing when the the integraty of the sample strucutre was still unchanged.

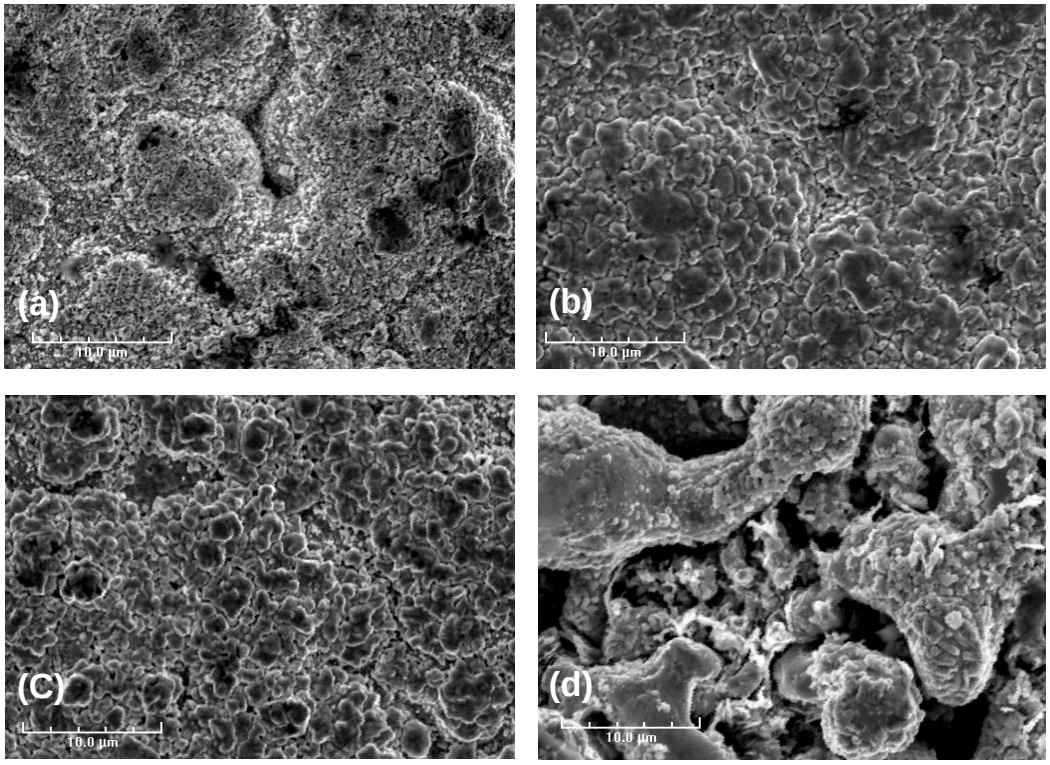


Figure 5.15. Surface micrographs at 3000x for the samples annealed in ultra-high purity helium at (a) 450 ºC for 16 hours, (b) 500ºC for 16 hours, (c) 550ºC for 9 hours, and (d) 600ºC for 11 hours.

In addtion to larger grains, some pores were also observed on the surface of the smaples (Figure 5.15(a) – (c)). The rearrangement of the atom during the grain growth accounted for the formation of pinholes. In addition, the Kirkendall effect (Kirkendall et al., 1939), which occurred when two metals inter-diffused with different rates, also

possibly caused the pinhole formation. The Kirkendall porosity has been observed in several research papers regarding the binary metal inter-diffusion (Van Dal et al. 2000; Ayturk, 2007). In the current study, since Pd potentially diffused into the Au layer faster than Au diffusing into the Pd layer especially in the initial stage of the annealing as mentioned earlier, the pinholes might form due to the Kirkendall effect.

The Au fractions were estimated by the EDX elemental analysis performed by several area scans at a magnification of 1000X. The results showed that approximately 25 wt% Au on the surface after annealing at 450°C, while 8 – 10 wt% Au was observed on the surfaces after annealing at 500 and 550°C. Very little Au was detected on the sample after annealing at 600°C due mainly to the collapse of the Pd/Au bi-layer.

Figure 5.16 shows the cross-sectional micrographs and corresponding EDX line scans of the Pd/Au bi-layers after the aforementioned isothermal annealing. The cross-sectional micrographs of the samples after annealing at 450 - 550°C (Figure 5.16(a), (c), and (e)) showed that the thickness of the Pd/Au layer ranged from 5.1 – 10 $\mu$m and the metal oxide inter-diffusion barrier layer was within 0.3 – 1.4 $\mu$m. The metal oxide layer was the dark layer between the Pd/Au layer and the PSS support in the cross sectional micrographs. A small amount of Pd was observed in the PSS after the annealing at 550°C as shown inside the circle in Figure 5.16(e) which implied the occurrence of slight intermetallic diffusion between Pd and the PSS. The cross-sectional micrograph of the sample after annealing at 600°C for 11 hours was shown in Figure 5.16(g). The range of the Pd/Au layer was difficult to define due to the collapse of the film as mentioned previously. Noticeable intermetallic diffusion between the Pd and the PSS support was also observed.

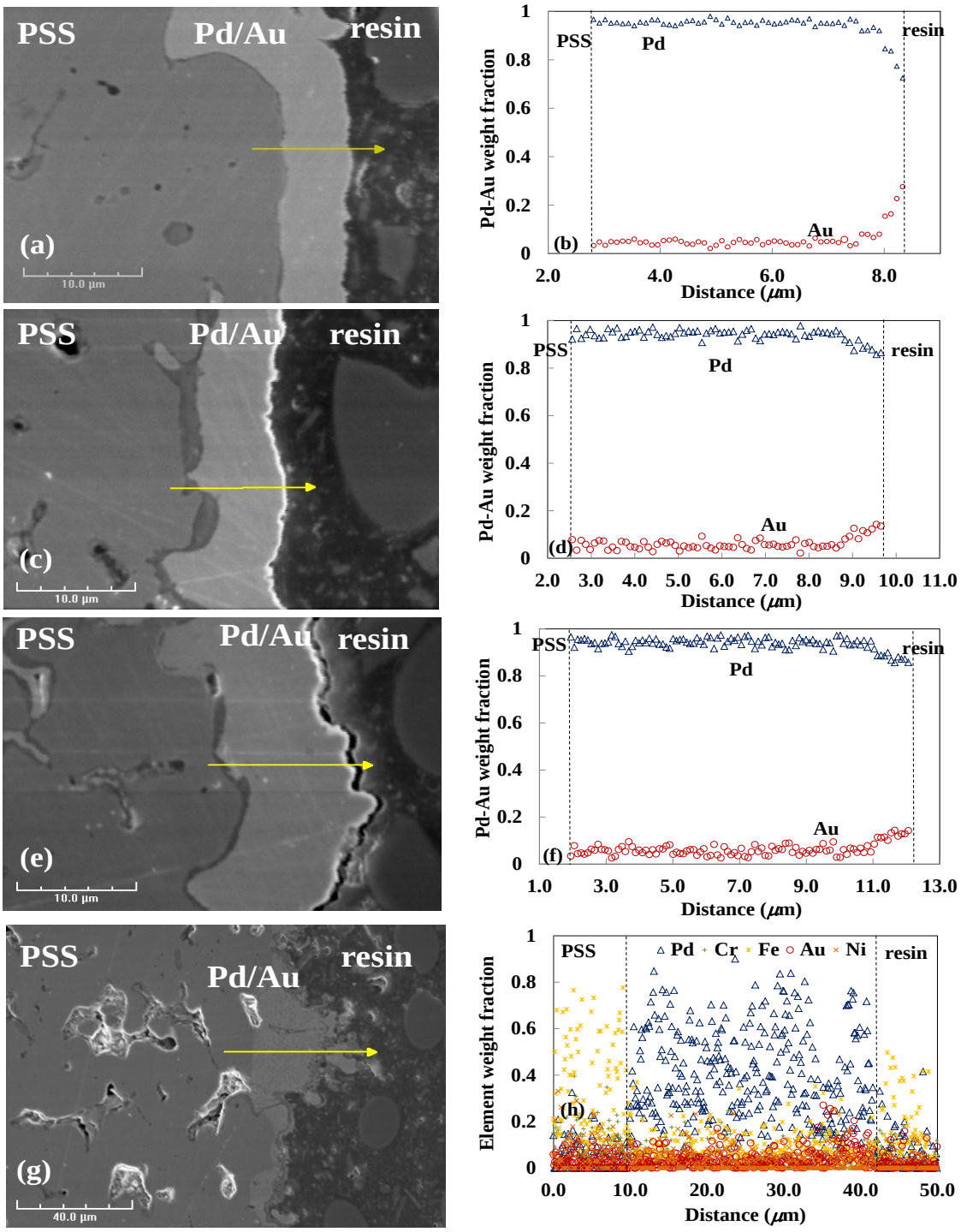


Figure 5.16. Cross sectional micrographs for the samples annealed in ultra-high purity helium at (a) 450 ºC for 16 hours, (b) 500ºC for 16 hours, (c) 550ºC for 9 hours, and (d) 600ºC for 11 hours ((a)-(c) were taken at a magnification of 3kx while (d) was taken at 1kx).

The corresponding EDX line scans of the samples in terms of Pd-Au weight fraction after annealing at 450 - 550°C were shown in Figure 5.16(b), (d), and (f). The dotted lines in the EDX line scans represented the interfaces of the Pd/Au layer between the support and mounting resin. Apparent Au gradients were seen from the surface of the Pd/Au bi-layer on all three samples. The surface Au concentration on the samples after annealing at 450, 500, and 550°C were approximately 27, 14 and 13 wt%. The depths of the Au were approximately 1, 1.5, and 1.8 $\mu$m on the samples after annealing at 450, 500, and 550°C, respectively. The results were consistent with the observation from the *ex-situ* study (See Figure 5.6). Figure 5.16(h) shows the EDX line scan of the sample after annealing at 600°C. Due to the collapse of the Pd/Au layer and the serious intermetallic diffusion between Pd and the PSS support, Pd as well as support metals (i.e. Fe, Cr) were observed almost throughout the entire scan.

Small penetration depths of Au observed after annealing were in agreement with the *in-situ* XRD study where Pd peaks remained on the XRD patterns after annealing. Murakami et al. (1976) reported that very little penetration of Au has reached the bulk of Pd while Pd diffused significantly into Au while annealing the Pd/Au bi-layers. The results accompanied with *in-situ* XRD study discussed earlier, showed that the Pd/Au inter-diffusion took place with a very high rate initially and the diffusion rate decreased significantly as the annealing proceeded. This implied that the formed Pd/Au alloy layers were thermally stable without noticeable compositional change at elevated temperatures that were equal or lower the annealing temperatures.

### *5.3.3 Kinetic analysis*

A kinetic study of the Pd/Au alloy phase growth provided the understandings of the Pd/Au alloying reaction mechanism as well as the reaction rate constants and activation energy of the reaction. One of the most successful and widely used solid-state reaction models was the Avrami model, which was also known as Kolmogorov-Johnson-Mehl-Avrami (Kolmogorov, 1937; Avrami, 1939, 1940, 1941; Johnson, 1939; Anderson and Mehl, 1945). The Avrami model was essentially a nuclei growth model which stated that during the isothermal phase transformation, the new phase appeared as nuclei initially and started to grow continuously from nuclei until the growing nuclei impinging onto each other. There are several assumptions made in the model which were: (1) the nucleation of the new phase occurred independently and randomly in the previous phase, (2) the growth rate did not depend on the extent of transformation, and (3) the nuclei grew at the same rate in all direction. The model can be expressed by Equation 5.4

$$\alpha = 1 - \exp\left\{-(kt)^n\right\} \tag{5.4}$$

or linearized form as shown in Equation 5.5:

$$\ln\left[-\ln(1-\alpha)\right] = n\ln k + n\ln t \tag{5.5}$$

Where $\alpha$ is the fraction of the new phase, $n$ is the Avrami exponent, $k$ is the reaction rate constant, and $t$ is time. $n$ is not only strongly dependent on nuclei growth geometry but also related to the reaction mechanism and nucleation rate. The reaction rate constant, $k$, on the other hand, is dependent on temperature due to the fact that the size of the nuclei, the number of nucleation sites, and the nuclei growth rate are strongly temperature dependent.

According to the linearized form of the Avrami equation (as shown in Equation 5.5), the Avrami exponent, *n*, and the rate constant, *k*, can be estimated by plotting ln[-ln(1-α)] as a function of ln*t*. Figure 5.17 shows the Avrami plot of the disordered FCC Pd/Au alloy phase growth at three different annealing temperatures of 500 ºC, 550ºC, and 600ºC. It should be noted that since the major interest of the study was to understand the formation of the disordered Pd-rich FCC Pd/Au alloy, the isothermal annealing data at 450°C were not used due to the fact that only the ordered $Pd_3Au$ alloy was formed at the end of the annealing at the temperature (See Figure 5.12(a)). The good linear fit of the data in the plot indicated that the Avrami model was able to describe the growth of the Pd/Au alloy in the testing temperature range.

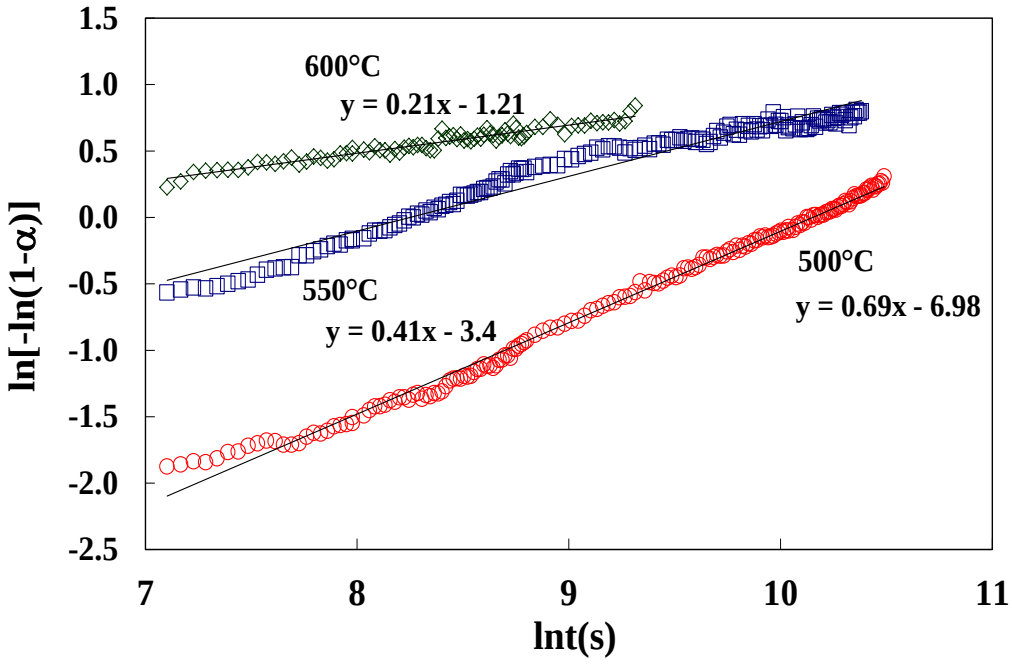


Figure 5.17. Avrami model plots for the isothermal annealing at different temperatures.

The estimated Avrami exponents, *n*, as well as the rate constant, *k*, at different temperatures are listed in Table 5.2. As shown in Table 5.2, the *n* values were in the range of 0.2 – 0.7 and consistently decreased with increasing temperature.

Table 5.2. Kinetic parameters for the Pd/Au alloy formation from a bi-layer.

| temperature (ºC) | k (1/s) | n |
|---|---|---|
| 500 | $3.89*10^{-5}$ | 0.69 |
| 550 | $2.61*10^{-4}$ | 0.42 |
| 600 | $3.30*10^{-3}$ | 0.21 |

Figure 5.18 shows the fit of the experimental data to the Avrami model. As expected, the experimental data of the Pd/Au alloy formation fitted the model quite well within the testing temperature range. Once again, the result suggested that the formation of Pd/Au alloy from the Pd and Au bi-layers followed the Avrami model.

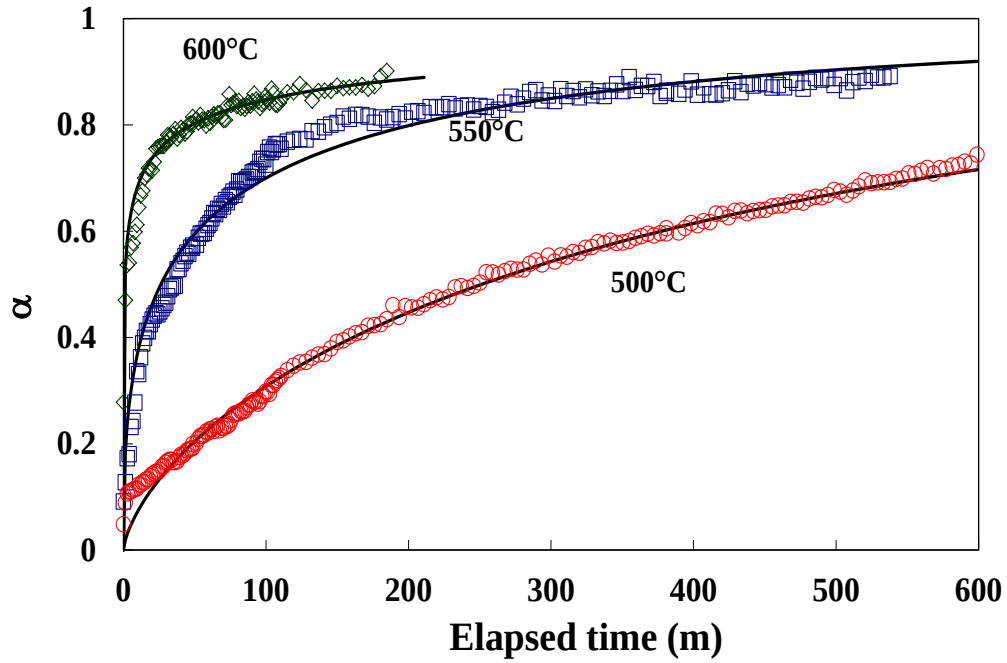


Figure 5.18. Weight fraction of the disordered Pd-rich Fcc Pd/Au alloy as a function of time. The solid lines were calculated according to the Avrami model.

As stated previously, the *n* values depended strongly on the nuclei growth geometry and were usually integrals. According to Christian (1965), the growth would be three dimensional or sphere-like if $3 \leqq n \leqq 4$, two dimensional or plate-like if $2 \leqq n \leqq 3$, and one dimensional or rod-like if $1 \leqq n \leqq 2$. However, anomalous *n* values (especially lower than one were commonly seen in numerous solid state transformation systems since *n* values were also related to the reaction mechanism and nucleation rate. Hulbert (1969) further mathematically interpreted the Avrami exponents by considering different reaction mechanisms and nucleation rates conditions (i.e. varying boundary conditions), and expanded the range of the *n* values from 0.5 to 4. According to his model, the *n* values of 0.2 – 0.7 obtained in this study indicated that the Pd/Au alloy phase was formed through a one-dimensional diffusion controlled process. The one-dimensional diffusion

controlled growth indicated that the Pd/Au alloy layer thickened as a thin plate with complete edge impingement during the formation, and the rate-limiting step was the diffusion of Pd and Au while the nucleation step was instantaneous.

Although the Avrami analysis suggested that the formation of the Pd/Au was diffusion-controlled, the process was more complicated than the simple diffusion-controlled mechanism. In an ideal diffusion-controlled solid-state reaction with the assumption of constant interface area, the transformation should also follow the parabolic rate law, i.e. the fraction of the phase transformed was propotional to reaction time in half power ($\alpha = kt^{0.5}$). However, the parabolic law analysis of the Pd/Au alloy tranforamtion data showed a noticeable deviation from the linear linear square root proportionality with the exponent constants ranged from 0.17 – 0.52 in the temperature range of 500 – 600°C. The small exponent constants (0.125 - 0.3) has been explained in terms of electronic defects, of which concentration was time-dependant, acting as intermediate (Bamford, 1969). That is, the nucleation did not take place randomly but preferably at the defect area, such as grain boundries, vacancies, and dislocations…etc. and the interface area was not constant. The non-randomly and non-continuously distributed nucleation also possibly resulted in the very small *n* values obtained in the Pd/Au alloy system during the Avrami analysis as stated previously.

In comparison to other Pd-based binary alloy formation from bi-layers in the same temperature range of 500 - 600°C, Pd/Ag (Ayturk et al., 2008) also exhibited low temperature-dependent Avrami exponents ($0.3 < n < 0.8$) which was due to the one-dimensional diffusion-controlled mechanism. The authors also reported the poor fit with the parabolic rate law analysis, which they attributed to the perferentail heterogeneous

nucleation on the defects. Pd/Cu (Pomerantz et al., 2010), on the other hand, exhibited the athermal *n* values of 1 suggesting one-dimensional phase boundary controlled mechanism. Similar mechanisms were observed in Pd/Ag and Pd/Au systems. This was due most likely to the fact that both Pd/Ag and Pd/Au binary systems have the complete solid-phase miscibility where only compositional changes occurred. It should be noted that although there are two short-range order compounds, $Pd_3Au$ and $PdAu_3$, in the Pd/Au binary system, the alloy structures were identical in the entire composition range. In the case of Pd/Cu system, the bcc phase was a miscibility gap in the FCC phase and both compositional and structural changes occurred.

While the Avrami exponents of the Pd/Ag system increased with the increasing temperature (Ayturk et al., 2008), a decrease of the *n* values of the Pd/Au was found as the temperature was increased. Both cases have been seen in previous solid-state reaction studies. Kim et al. (2005) reported the increase of the *n* values ($0.3 < n < 0.8$) with temperature in the formation of $CuInSe_2$ from InSe/CuSe. The increase of the nucleation rate due to overcoming the nucleation barrier at higher temperatures was believed to cause such a temperature dependence. On the other hand, the formation of Anatase ($TiO_2$) (Choi et al., 2005) and decomposition of $BaCO_3$ (Hancock and Sharp, 1972) exhibited the decreasing Avrami exponents with increasing temperature. No clear explanations have been provided to the phenomenon by the authors.

The very low *n* values and very rapid initial increase in the product (e.g. alloy) weight fraction suggested the diffusion-controlled process (Bamford, 1969). In such processes, the rate-limiting step was diffusion rate of the reactant species and the nucleation step was usually completed very rapidly. Indeed, the alloying formation was

essentially the diffusion phenomenon. In the case of the Pd/Au alloy formation, the nucleation step was either close to or even completed before the attainment of the target isothermal annealing temperature, especially for the high target annealing temperature according to the non-isothermal study. The smaller *n* values observed at higher temperatures in the Pd/Au alloy formation might be due to the smaller duration of the nucleation step at higher temperatures.

The rate constants shown in Table 5.2 increased with increasing temperature which was reasonable due to the fact that the transformation was diffusion-controlled. The span of the rate constants at 500 – 600°C was over two orders of magnitude, suggesting that the transformation was highly sensitive to temperature. That is, the transformation rate could be largely varied by just a small change in temperature.

The rate constants shown in Table 5.2 could be further used to estimate the apparent activation energy for the Pd/Au alloy formation by employing the Arrhenius equation as shown in Equation 5.6.

$$k = A \exp\left[-\frac{Ea}{RT}\right] \tag{5.6}$$

Where *k* is the rate constant with the unit of 1/s, A is the pre-exponential factor, and *Ea* is the apparent activation energy in kJ/mol, *R* is the universal gas constant and *T* is temperature in °K. Figure 5.19 shows the regression of the temperature-dependent rate constants in the Arrhenius plot. The apparent activation energy for the Pd/Au alloy formation by the Avrami model was estimated to be 248 kJ/mol. Neukam (1970) reported an activation energy of 173.1 kJ/mol for the Pd/Au inter-diffusion based on the inter-diffusion coefficients measured on the bulk Au-17 at% Pd bi-layer in the temperature range of 600 - 1000°C. DeBonte et al. (1974, 1975) reported an activation energy of 86.5

kJ/mol for the grain boundary diffusion of Pd in Au and an activation energy of 57.7 kJ/mol for the grain boundary diffusion of Au in Pd. The reported activation energies was based on the diffusivities of the Au- 10 at% Pd bi-layer in the temperature range of 200 - 389°C. Lower activation energies usually indicated higher diffusivities. Indeed, the diffusion coefficient (grain boundary) reported by DeBonte et al. (1974, 1975) were greater than the value reported by Neukam (1970) by 2 - 4 orders of magnitude.

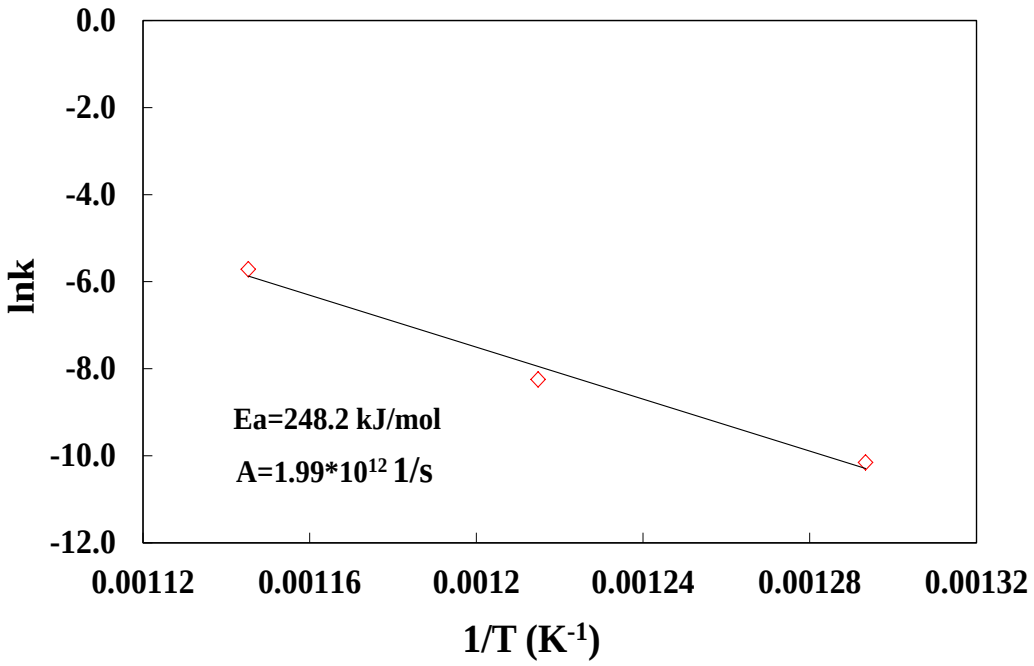


Figure 5.19. Arrhenius plot for the rate constants of the Pd/Au alloying formation estimated by the Avrami equation. The activation energy and the pre-exponential factor estimated was also indicated in the plot.

The activation energy calculated from the Avrami rate constants in the study was closer to the value for the bulk diffusion than those for the grain boundary diffusion. As mentioned previously, although the grain boundary diffusion was possibly predominant

in the initial stage of the Pd/Au inter-diffusion, the bulk diffusion gradually became the predominant diffusion mechanism with time due to the significant grain growth and coarsening. Since the disordered Pd-rich FCC Pd/Au alloy was the final product phase which formed in the relatively later stage of the annealing, the fact that the activation energy for the alloy formation was closer to the activation energy for the bulk diffusion was quite reasonable. The result suggested that the formation of the Pd/Au alloy phase was a bulk diffusion-controlled process. Ayturk et al. (2008) and Pomerantz et al. (2010) had also observed activation energies for the Pd/Ag and Pd/Cu alloy formation which corresponded to bulk diffusion rather than grain boundary diffusion while annealing the Pd/Ag and Pd/Cu bi-layers in $H_2$ in the temperature range of 500 - 600°C.

Pomerantz et al. (2010) reported that the grain size of the bi-layer affected the diffusion mechanism by reviewing several studies regarding the Pd/Cu inter-diffusion (Bitler et al., 1985, Chow et al., 1998, Al-Kassab et al., 1995). Reducing the grain size increased the grain boundary diffusion regime. Although the deposited Pd/Cu bi-layers usually tended to show grain boundary diffusion (Bitler et al., 1985, Chow et al., 1998), Pomerantz et al. (2010) reasoned that the larger Pd gain size prepared by the electroless deposition and significant grain growth and the lattice expansion under the $H_2$ atmosphere favored the bulk diffusion of Cu into Pd rather than grain boundary diffusion.

The reported activation energies the for self-diffusion of Pd and Au were 267.12 kJ/mol in the temperature range of 1450 - 1500°C (Peterson, 1964) and 165.5 – 175.1 kJ/mol in the temperature range of 600 - 1048°C (Okkerse, 1956; Makin et al., 1957). The activation energies for the Pd/Au inter-diffusion including the calculated value in the current study and the value reported by Neukam (1970) fell into the range of self-

diffusion of Pd and Au. While the Au - 17 at% Pd bi-layer had an activation energy of 173.1 kJ/mol (Neukam 1970) which was close to that of Au self-diffusion, the calculated activation energy in the study was 248.2 kJ/mol which was close to that of Pd self-diffusion. This suggested that the activation energy calculated from the rate constants corresponded to that of the diffusion of a low Au content Pd/Au alloy. Indeed, the bulk Au compositions of the Pd/Au bi-layers were approximately 10 wt%.

## 5.4 Conclusions

By conducting both *ex-situ* and the *in-situ* XRD characterizations, the annealing conditions for forming the Pd/Au alloy as well as the mechanism and kinetics of the alloy formation were revealed. The mechanism for the formation of disordered Pd-rich FCC Pd/Au alloy was proposed. Since two ordered structures, $PdAu_3$ and $Pd_3Au$, existed in the composition and temperature range studied, the ordered structures were formed as intermediate product during the annealing process.

The kinetics of the Pd/Au alloy formation was obtained by the quantitative analyses of the *in-situ* time-resolved HTXRD data. The results showed that the Pd/Au alloy formation fitted quite well with the Avrami model. The small Avrami exponents obtained ($0.2 < n < 0.7$) indicated the transformation was a one-dimensional diffusion controlled process. The activation energy for the Pd/Au alloy formation estimated by the Avrami rate constants and the Arrhenius relation was 248 kJ/mol. This value suggested that the bulk diffusion was the predominant mechanism rather than the grain boundary diffusion.

The Pd/Au inter-diffusion could occur under mild annealing condition (T = 322°C) according to the non-isothermal study due to the structure of the as-deposited film (i.e. thin layer and small grain size). However, the inter-diffusion rate decreased significantly as the annealing proceeded due to the strongly composition-dependent diffusion rate of Pd and Au and the significant grain growth.

The diffusion of Au into Pd was far slower than the diffusion of Pd into Au layer resulting in a very small penetration of Au into the Pd layer with a gradient even after long annealing time (96 hours). The results suggested that the formed Pd/Au alloy layers

were thermally stable without noticeable compositional change at elevated temperatures that were equal or lower the annealing temperatures. Finally, the results suggested that annealing the Pd/Au bi-layers (~10 wt% Au) at above 500°C for a reasonable amount of time (< 48 hours) was sufficient to form a stable Pd/Au alloy top layer with a sufficient thickness to obtain potentially higher $H_2$ permeance and sulfur resistance.

# 6. $H_2$ transport in Pd/Au membranes

## 6.1 Introduction

For the purpose of enhancing the $H_2S$ resistance of the membranes, the formation of a Pd/Au alloy layer at the top of the membrane was sufficient since the sulfur poisoning was essentially the surface phenomenon as described in *Section 2.6.1*. In addition, the extremely long annealing time at high temperatures required to form a homogeneous Pd/Au layer from the Pd/Au bi layers (Shi et. al. 2010) made the fabrication of the homogeneous Pd/Au alloy membranes unpractical.

As shown in *Chapters 4* and *5*, the sequential Pd and Au deposition by the electroless and the displacement plating followed by the annealing in the mid-range temperatures (500 – 600°C) within a reasonable time could produce the stable Pd/Au alloy top layer on the membranes. While there were a few research reported regarding the $H_2$ permeabilities of the homogeneous Pd/Au foils (McKinley, 1967; Gryaznov, 2000; Gade. et. al., 2010), the $H_2$ permeation characteristics of the composite Pd/Au membranes with Au gradients near the surfaces were not found in the literature.

The main objective of this chapter was to investigate the $H_2$ permeation characteristics of the composite Pd/Au membranes (with Au gradients near the surface) prepared by the electroless and galvanic displacement deposition. In addition, the $H_2$ permeabilities of the Pd/Au foils were also discussed.

## 6.2 Experimental

The properties of the membranes characterized in this chapter are listed in Table 6.1. Except for membrane C-16, all the membranes were prepared on 0.1 $\mu$m grade Inconel tubular supports purchased from Mott Metallurgical, Inc. The membranes prepared on the Inconel supports were oxidized at 700ºC for 12 hours in air for forming the intermetallic diffusion barrier. Following the oxidation, the membranes were graded with the $Al_2O_3$ slurry (slurry B as indicated in *Section 3.1.5*) and sealed with the "Pd glue" as described in *Section 3.1.5*. Membrane C-16, on the other hand, was prepared on a 0.1 μm Hastelloy C-22 support purchased from Chand Eisenmann, Inc. Polishing of the bare support by the 600 and 800 grit SiC sand papers was performed on membrane 16 before the 12 hours oxidation at 800ºC. The grading of membrane C-16 was conducted with the three different $Al_2O_3$ slurries (slurry A, B, C as indicated in *Section 3.1.5*) followed by the sealing with the Pd glue.

A Pd/Ag barrier was deposited on all the membranes followed by a slight sanding with a 2400 grit sand paper as described in *Section 3.1.5*. Followed the Pd/Ag barrier layer deposition, a dense Pd layer was deposited on all the membranes by the electroless plating method. Membranes C-07, C-09, C-11, and C-12 were pre-annealed in He for 12 hours followed by the polishing with 600 and 1200 grit sand papers for 3 times during the final rounds of Pd deposition to mitigate leak growth.

Membranes C-07, C-09, C-11, C-12, and C-16 were characterized first as Pd membranes in $H_2$ and He at elevated temperatures prior to the Au deposition. The Au deposition was performed by the displacement plating. Since the thickness of the Au layer deposited by the displacement plating was approximately 0.5 $\mu$m according to

*Chapter 4*. Higher Au content Pd/Au membranes (i.e. membranes C-11, C-12, and C-16) were prepared by sequentially depositing different number of Au layers on the membranes (i.e. 2 to 3 Au layers). Between Au layers, a thin Pd layer (0.5 – 0.8 $\mu$m) was deposited for the Au displacement plating. A heat treatment in $H_2$ at 500°C for at least 48 hours (until the $H_2$ permeance stabilized) was conducted on the as-deposited membranes for forming the Pd/Au alloy top layer (according to *Chapter 5*) before the gas permeation characterization. The permeation characterizations of the membranes were performed in the system described in *Section 3.3.2*.

Table 6.1. Membranes tested in this chapter

| Membrane | Intermetallic diffusion | grading | Pd/Ag barrier | Pd layer (μm) | Au layer (μm)[7] | wt% Au |
|---|---|---|---|---|---|---|
| C-04 | air/700ºC/12 h | $Al_2O_3$ slurry+Pd glue | 2.1 | 15.5 | 0.5 | 8 |
| C-07 | air/700ºC/12 h | $Al_2O_3$ slurry+Pd glue | 5.9 | 7.7 | 0.5 | 5.6 |
| C-09 | air/700ºC/12 h | $Al_2O_3$ slurry+Pd glue | 4.1 | 14.2 | 0.5 | 4.2 |
| C-11 | air/700ºC/12 h | $Al_2O_3$ slurry+Pd glue | 3.8 | 12.9 | 1.0 | 8.7 |
| C-12 | air/700ºC/12 h | $Al_2O_3$ slurry+Pd glue | 2.9 | 12.6 | 1.5 | 12.3 |
| C-16 | air/800ºC/12 h | $Al_2O_3$ slurry+Pd glue | 0.6 | 10.0 | 1.5 | 16.7 |

## 6.3 $H_2$ transport through Pd/Au films

Figure 6.1 shows the relative hydrogen permeability of the Pd/Au alloy to pure Pd foil as a function of Au composition at 350 and 500°C reported in the literature (McKinley, 1966; Gryaznov et. al., 2000). The peak hydrogen permeabilities in the small

[7] The thickness of Au layer was estimated by the number of the Au displacement deposition, according to the results described in *Chapter 4*, one displacement plating resulted in an approximately 0.5 $\mu$m Au layer.

Au composition range (approximately 10 wt%) were observed at both temperatures. As discussed in *Section 2.4*, the enhancement of the hydrogen permeability was due to the increase of the $H_2$ solubility in the small Au composition range.

The theoretical calculation of the hydrogen permeabilities of the Pd/Au alloys at 350 and 500°C by Catalano (2011)[8] based on the thermodynamic data were also shown in Figure 6.1. The calculation was conducted based on the model proposed by Ward and Dao (1999), which took into account all the steps involved for the hydrogen transport thought the hydrogen selective layer (e.g. Pd/Au in this case) including dissociative adsorption, surface to bulk, bulk diffusion, bulk to surface, molecular desorption. The $H_2$ adsorption, solubility, and diffusivity data in the Pd/Au alloys (Okamoto and Massalski, 1985; Maestas and Flanagan, 1973; Maeland and Flanagan, 1965; Mealand and Flanagan, 1967) were then used to solve the $H_2$ flux through all the transporting steps (Catalano, 2011). The detailed calculation procedure could be found in the previous work of Catalano et. al. (2010). As shown in Figure 6.1, the results of the theoretical calculations (Catalano, 2011) appeared to agree with the experimental results reported by McKinley (1966) better. A maximum $H_2$ permeability between 5 – 20 wt% Au of roughly 15 % higher than Pd was observed on both the experimental work of McKinley (1966) and the theoretical calculation of Catalano (2011). It should be noted that it was difficult to determine the exact Au composition for the maximum $H_2$ permeability due to the insufficient data points in the range.

The $H_2$ permeability of the 45 wt% Au Pd/Au alloy predicted by the theoretical calculation (Catalano, 2011) was off the curve as shown in Figure 6.1. This was due to the sudden decrease of the $H_2$ diffusivity in the Pd/Au alloy with the Au composition

[8] Un-published results

greater than 40 wt% reported in the literature (Maestas and Flanagan, 1973), which was used in the calculation by Catalano (2011). Nevertheless, the theoriatical calculation done by Catalano (2011) fit the experimental work of McKinley (1966) quite well in the general trend in the large Au composition range of 0 – 55wt%.

The theoretical calculation (Catalano, 2011) also suggested that the enhancement of the hydrogen permeability by the addition of Au was more apparent at lower temperatures (Figure 6.1). Since the increase of the $H_2$ permeability in the Pd/Au alloy was due to the increase of the $H_2$ solubility, the fact that the $H_2$ solubility decreased with increasing temperature (Sieverts et al., 1915; Figure 2.4) resulted in less increase in $H_2$ permeability at higher temperatures. It should be noted that although the diffusivity increased with increasing temperature, the diffusivity was less temperature sensitive compared to the solubility.

The reason for the discrepancy observed between the results reported by Gryaznov et al. (2000) and the theoretical calculations was unclear. Possible inhomogeneous Au distribution through the Pd/Au foils tested by the authors could cause the discrepancy. It has been shown in the literature that Au tended to segregate to the surface due to the reduction of surface energy by Au (Anton et. al., 1993; Way et. al. 2008). The surface segregation of Au possibly increased the inhomogeneity of the Pd/Au foils. In addition, the fabrication technique also showed the influence on the $H_2$ permeability of the Pd/Au foils (Gade et al., 2010). The authors reported that the Pd/Au foils prepared by the sputtering showed higher $H_2$ permeabilities than the ones prepared by the cold-work with the same Au composition. The authors reasoned that the less stable orientation in the cold-worked Pd/Au foils (2 0 0) promoted the Au segregation to the

surface. However, no detailed preparation and characterization of the Pd/Au foils were provided in the work of Gryaznov et al. (2000).

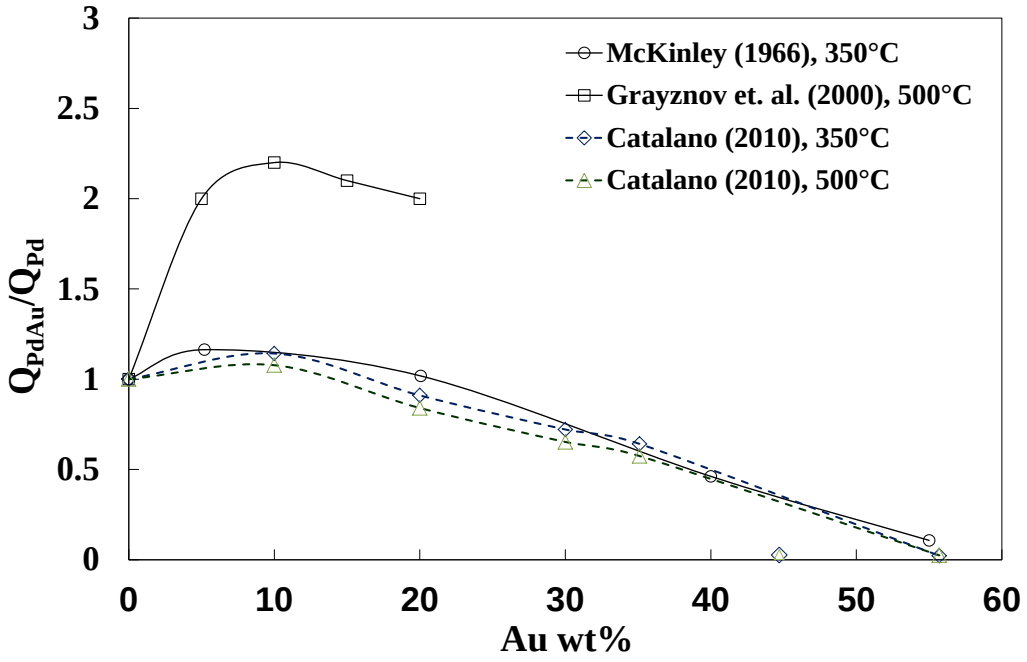


Figure 6.1. Permeability as a function of Cu content for Pd/Cu foils.

## 6.4 Results and Discussion

### *6.4.1 $H_2$ permeation of non-homogeneous Pd/Au alloy composite membranes*

Prior to the Au deposition, membranes C-07, C-09, C-11, C-12, and C-16 were first characterized as Pd membranes in the temperature range of 250 – 450°C for approximately 500, 200, 300, 200, and 140 hours, respectively. After the characterization, membranes C-07, C-09, C-11, C-12, and C-16 were then deposited with Au and characterized at 250 – 500°C for another ~350, 200, 150, 150, and 180 hours, respectively.

Membrane C-04 was first prepared on a green (new) support and tested in pure $H_2$ and He at temperatures up to 550°C for ~1100 hours. However, the accidental loss of $H_2$ supply at the elapsed testing time of 950 hours at 550°C for ~18 hours caused the oxidation of the membrane with the appearance of the membrane turning from shinning silver to dull darkish. It has been shown in the literature that the bulk oxidation of Pd occurred above 200°C in the presence of oxygen (Su et al, 1998; Lam and Boudart, 1977). Therefore, membrane C-04 has been polished with silicon carbide (grit 800) sand papers by hand to remove the oxide layer and re-deposited with Pd and Au for repairing, and tested again at elevated temperatures up to 550°C in pure $H_2$ and He for another 800 hours. After having developed a significant He leak, membrane C-04 was re-deposited for the second time by the same polishing method and re-plated with Pd and Au. Membrane C-04 was then annealed at 500°C for more than 48 hours, followed by the characterization in pure $H_2$ and He for ~800 hours in the temperature range of 250 – 500°C.

Figure 6.2 are the Sieverts' plots for membranes C-04, C-07, C-09, C-11, C-12, and C-16 at 350°C. The good fit of the $H_2$ flux data of all the membranes with the Sieverts' regression indicating that the $H_2$ transport through all the PdAu composite membranes followed Sieverts' law. The results suggested that the rate-limiting step of the $H_2$ permeation through the composite Pd/Au membranes was one dimensional diffusion of atomic hydrogen through the Pd/Au alloy layer.

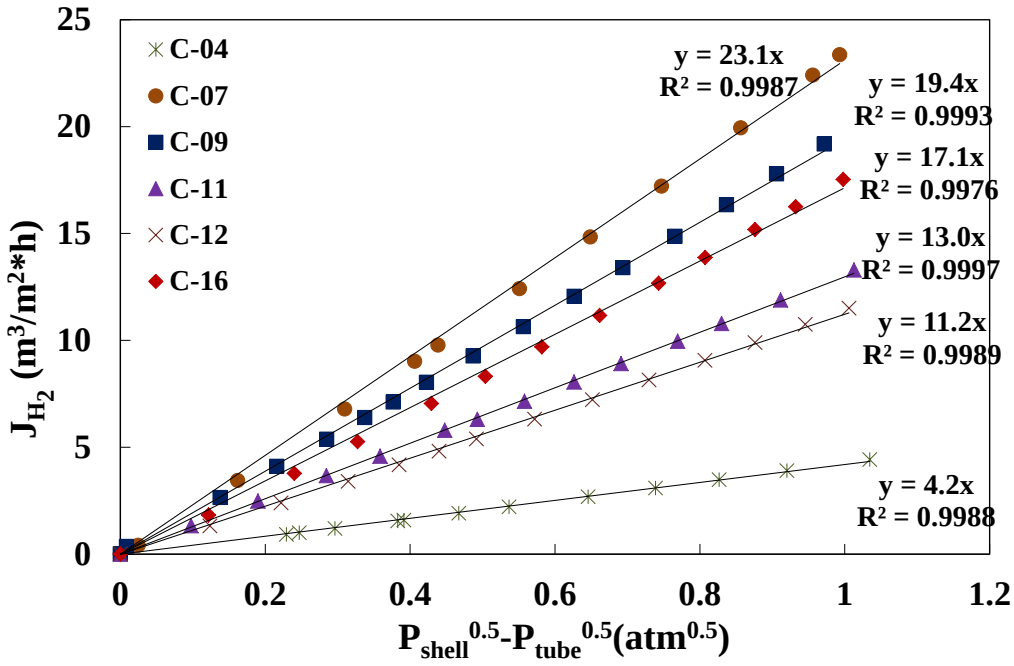


Figure 6.2. Sieverts' law regression for membranes C-04, C-07, C-09, C-11, C-12, and C-16 at 350°C.

The $H_2$ permeance at 350°C (and at other temperatures) calculated according to the Sieverts' regression for membranes C-04, C-07, C-09, C-11, C-12, and C-16 were summarized in Table 6.2. The $H_2$ permeance of all the tested membranes (except membrane C-04) before the Au deposition (i.e. as Pd membranes) were also included in Table 6.2. The relative permeance of the tested Pd/Au membranes to a free-standing Pd foil (Guazzone, 2006; Ayturk, 2007) with the same thickness of each membrane were different at a fixed temperature. The variation in the relative permeance of the Pd/Au composite membranes to the free standing Pd foils suggested the influence of the Au addition to the $H_2$ permeance since the Au composition in each membrane was different. Further discussion on the effect of Au composition on the $H_2$ permeation will be provided

in *Section 6.4.3* by also taking the support resistance into account since the support resistance also affected the relative permeance of the composite membranes to foils.

Table 6.2. Performance of membranes C-04, C-07, C-09, C-11, C-12, and C-16.

| membrane | Thickness ($\mu$m) | Au content (wt%) | Temperature (ºC) | $F_{H2}$ ($m^3/m^2*h*atm^{0.5}$) | % of Pd foil | $J_{H2}/J_{He}$ ($\Delta$p=1atm) | Ea (kJ/mol) |
|---|---|---|---|---|---|---|---|
| C-04 | 18.3 | 5-8 | 450 | 5.9 | 23 | 88 (at 400°C, ~800h) | 13.5 |
| | | | 400 | 4.5 | 24 | | |
| | | | 350 | 4.2 | 24 | | |
| | | | 250 | 2.5 | 26 | | |
| C-07 | 14.1 | 5.4 | 450 | 34.7 | 89 | 1300 (at 450°C, ~340h) | 12.9 |
| | | | 350 | 30.3 | 105 | | |
| | | | 250 | 25.4 | 107 | | |
| $C\text{-}07_{(Pd)}$ | 12.7 | --- | 450 | 31.8 | 86 | 5900 (at 250°C, ~500h) | 14.3 |
| | | | 350 | 21.9 | 90 | | |
| | | | 250 | 12.8 | 94 | | |
| C-09 | 18.8 | 4.2 | 450 | 26.8 | 107 | 4500 (at 450°C, ~200h) | 11.7 |
| | | | 350 | 19.4 | 118 | | |
| | | | 250 | 12.7 | 138 | | |
| $C\text{-}09_{(Pd)}$ | 17.7 | --- | 450 | 27.7 | 57 | 600 (at 250°C, ~200h) | 13.5 |
| | | | 350 | 19.0 | 59 | | |
| | | | 250 | 11.7 | 62 | | |
| C-11 | 17.7 | 8.5 | 450 | 19.0 | 72 | 4300 (at 350°C, ~150h) | 14.3 |
| | | | 400 | 16.0 | 73 | | |
| | | | 350 | 13.0 | 74 | | |
| $C\text{-}11_{(Pd)}$ | 16.9 | --- | 450 | 21.1 | 76 | 4700 (at 350°C, ~300h) | 13.8 |
| | | | 400 | 17.8 | 78 | | |
| | | | 350 | 14.6 | 80 | | |
| C-12 | 17.0 | 12.3 | 450 | 15.8 | 57 | 900 (at 350°C, ~150h) | 12.7 |
| | | | 400 | 13.4 | 59 | | |
| | | | 350 | 11.2 | 62 | | |
| $C\text{-}12_{(Pd)}$ | 15.8 | --- | 450 | 18.5 | 62 | >10000 (at 350°C, ~130h) | 11.0 |
| | | | 400 | 16.5 | 67 | | |
| | | | 350 | 13.8 | 70 | | |
| C-16 | 12.0 | 16.7 | 450 | 24.5 | 63 | >10000 (at 350°C, ~170h) | 13.3 |
| | | | 400 | 20.7 | 65 | | |
| | | | 350 | 17.1 | 67 | | |
| $C\text{-}16_{(Pd)}$ | 7.0 | --- | 450 | 38.9 | 58 | 900 (at 400°C, ~130h) | 11.0 |
| | | | 400 | 33.8 | 61 | | |
| | | | 350 | 29.0 | 66 | | |

However, the extremely low permeance as well as the relative permeance to a free standing Pd foil of membrane C-04 was unlikely merely due to the addition of Au and the support resistance. Indeed, the unusually low $H_2$ permeance of membrane C-04 was later confirmed by the intermetallic diffusion of the support (Inconel) elements (i.e. Ni, Cr) into the Pd-Au layer as evidenced by the EDX line scan of membrane C-04 after the characterization (including the $H_2S$ tests) as shown in Figure 6.4(b). The EDX line scan as well as the cross section micrograph characterization of all the tested membranes will be discussed later in *Section 6.4.2*. The intermetallic diffusion of support metal (e.g. Fe, Ni, Cr) into the $H_2$-selective layer has been well-documented for causing the low permeance of composite Pd-based/porous-metal-support membranes (Gryaznov et al., 1993; Ayturk et al., 2006). The long term test (cumulatively ~450 hours) of membrane C-04 at 550°C during the first two tests was believed to cause the intermetallic diffusion of Ni and Cr into the Pd/Au layer. In the entire duration of the final characterization, membrane C-04 showed stable $H_2$ permeance up to the highest testing temperature of 500°C, indicating that there was no further significant structural or compositional change.

Table 6.2 also shows the ideal selectivities ($J_{H2}/J_{He}$, $\Delta p$ = 1atm) of membranes C-04, C-07, C-09, C-11, C-12, and C-16 at the end of characterization. Except membrane C-04, all the tested membranes showed fairly good ideal selectivities. Since the He leak of membrane C-04 was not particularly large (~0.6 sccm at 400°C after 800 hours testing), the unusually low selectivity of membrane C-04 was a result of the abnormally low $H_2$ permeance caused by the intermetallic diffusion as discussed previously. As a result, it was believed that there were no abnormally large pinholes/defects in membrane C-04 and such a small He leak should not have any significant impact on $H_2$ permeance

and *n*-value (Guazzone et al., 2006). Nevertheless, all the tested membranes showed reasonably good He leak stability during the entire course of the characterization.

Figure 6.3 shows the Arrhenius dependence of the $H_2$ permeance on temperature for membranes C-04, C-07, C-09, C-11, C-12, and C-16. The permeance was calculated with the Sieverts' regression in the temperature range of 250 - 450$^{o}$C for all the membranes. The activation energies estimated for membranes C-04, C-07, C-09, C-11, C-12, and C-16 were also given in Table 6.2. The activation energies observed on the membranes were within the range of the composite Pd-based membranes reported in the literature (Guazzone, 2006). The activation energy of a free standing Pd foil for hydrogen permeation was 14.9 - 15.6 kJ/mol (Guazzone, 2006; Ayturk, 2007), slightly smaller activation energies were usually measured on the composite Pd membranes due to the mass transfer resistance from the porous supports (Guazzone, 2006). The addition of Au could also affect the activation energy of the membrane since the $H_2$ permeation was affected by the addition of Au as mentioned earlier. However, it was difficult to conclude the influence of Au on the activation energy based on the activation energies measured (Figure 6.3) since the Au composition was not the only factor affecting the activation energy of a composite membrane. The comparison in activation energy before and after the Au deposition on each tested membrane could show the influence of Au composition on the activation energy. Further discussion will be given in *Section 6.4.3*.

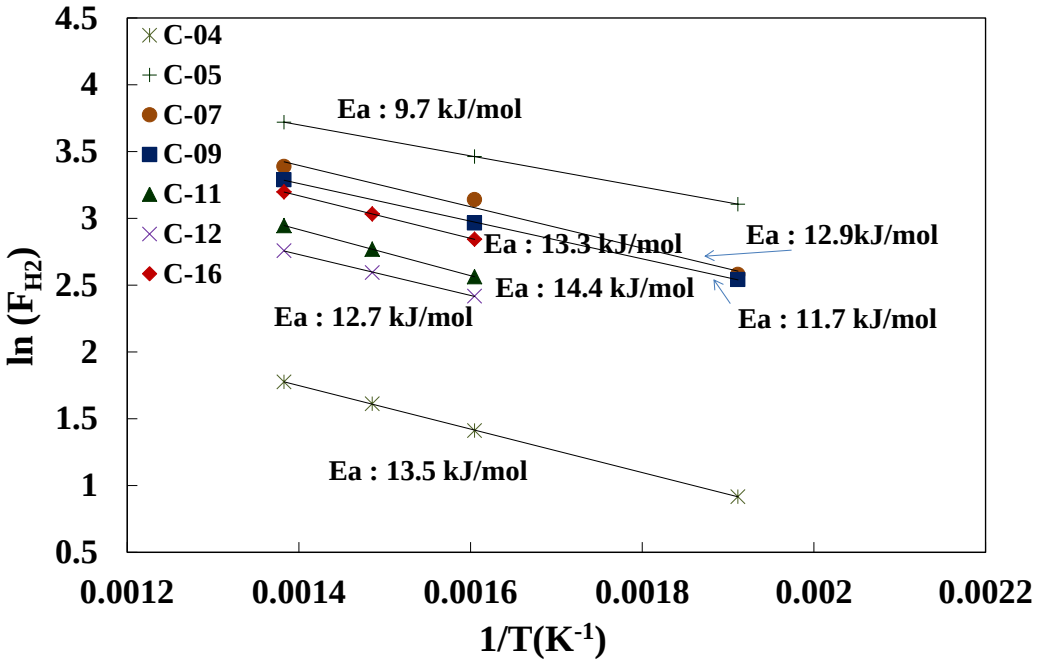


Figure 6.3. Arrhenius plot for $H_2$ permeance of membranes C-04, C-07, C-09, C-11, C-12, and C-16. The estimated activation energies for $H_2$ permeation were also listed in the plot.

### *6.4.2 Cross-sectional analysis*

Figure 6.4(a) and (b) show the cross-sectional SEI micrograph and corresponding EDX line scans of membrane C-04. According to the cross-sectional micrograph (Figure 6.4(a)), the thickness of the dense Pd/Au layer was 7 – 9 $\mu$m. An Au gradient existed at the top 2 – 3 $\mu$m thick layer with the highest Au content of ~13 wt% at the surface. The oxygen and aluminum observed in the support region (below 3 $\mu$m mark) of the EDX line scan (Figure 6.4(b)) confirmed the existence of the oxidized layer and the $Al_2O_3$ grading layer. The randomly scattered oxygen in the entire Pd/Au layer (3 $\mu$m - 12 $\mu$m) was from the background noise and the surface contaminations of the SEM sample during the sample preparation.

As shown in the insert in Figure 6.4(b), the cross-sectional analysis confirmed the diffusion of Ni into the Pd/Au layer within ~5 $\mu$m from the support (up to the position at the distance of ~8 $\mu$m) with the highest Ni composition of ~14 wt% at the interface between the dense Pd/Au layer and the support. In addition, the diffusion of Cr into the selective layer within ~1 $\mu$m from the support (up to the position at the distance of ~4 $\mu$m) with the highest Cr composition of ~8wt% at the interface between the dense layer the support was also seen in Figure 6.4(b). The result confirmed that the unusual low $H_2$ permeance of membrane C-04 was the result of inter-metallic diffusion of the support metal into the Pd/Au layer as described in *Section 6.4.1*.

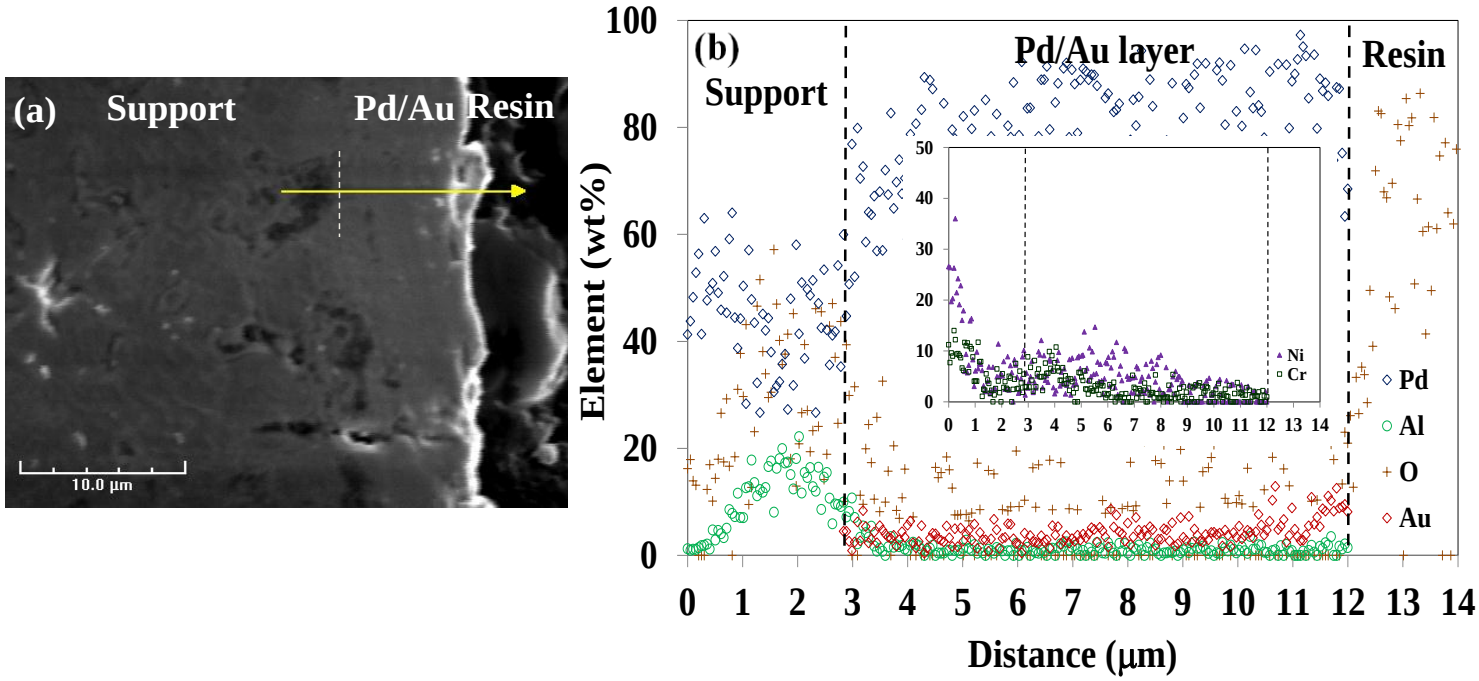


Figure 6.4. (a) Secondary-electron imaging (SEI) cross-sectional micrograph, and (b) corresponding energy dispersive X-ray spectroscopy (EDX) line scan (the insert is the Ni and Cr composition) of membrane C-04 after the characterization (including the $H_2S$ testing).

Figure 6.5 - Figure 6.9 show the cross-sectional SEI micrographs and corresponding EDX line scans of membranes C-07, C-09, C-11, C-12, and C-16 respectively. Instead of displaying the compositional profiles of all the elements, the relative Pd-Au weight fraction profiles were shown in the EDX line scan since the major interests in this chapter was to examine the uniformity of Au composition throughout the dense layer. As seen in the EDX line scans, Au gradients existed in all the membranes indicating the inhomogeneous Pd/Au alloy formed on all the Pd/Au membranes. The surface (highest) Au fractions detected were as approximately 18, 14, 24, 34, and 46 wt% on membranes C-07, C-09, C-11, C-12, and C-16. The trend observed in the EDX analysis agreed with the bulk Au content estimated gravimetrically (See Table 6.1). The penetration depths of Au were within 3 – 4 $\mu$m from the surfaces of the membranes resulting in the layer beneath the Au gradient layer were pure Pd layers. The average thicknesses of the Au gradient (Pd/Au) and Pd layer and the surface Au weight fraction of the membranes were summarized in Table 6.3.

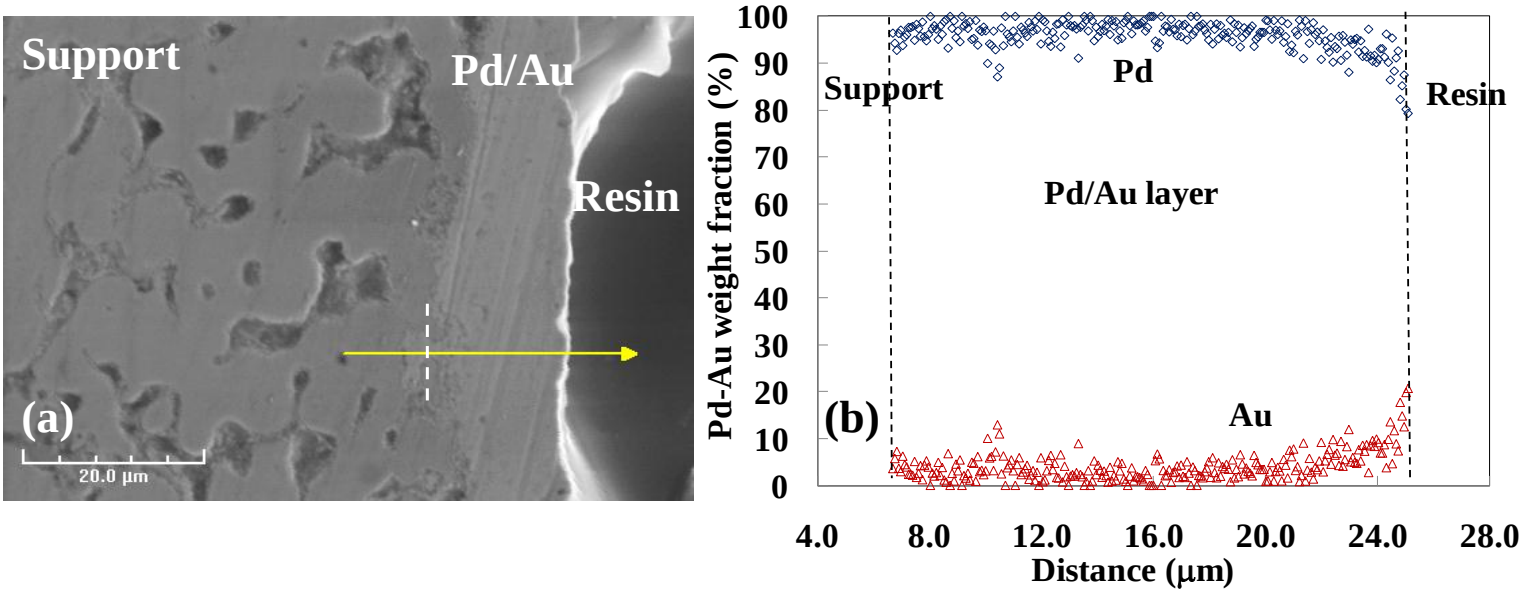


Figure 6.5. (a) Secondary-electron imaging (SEI) cross-sectional micrograph, and (b) corresponding energy dispersive X-ray spectroscopy (EDX) line scan of membrane C-07 after the characterization.

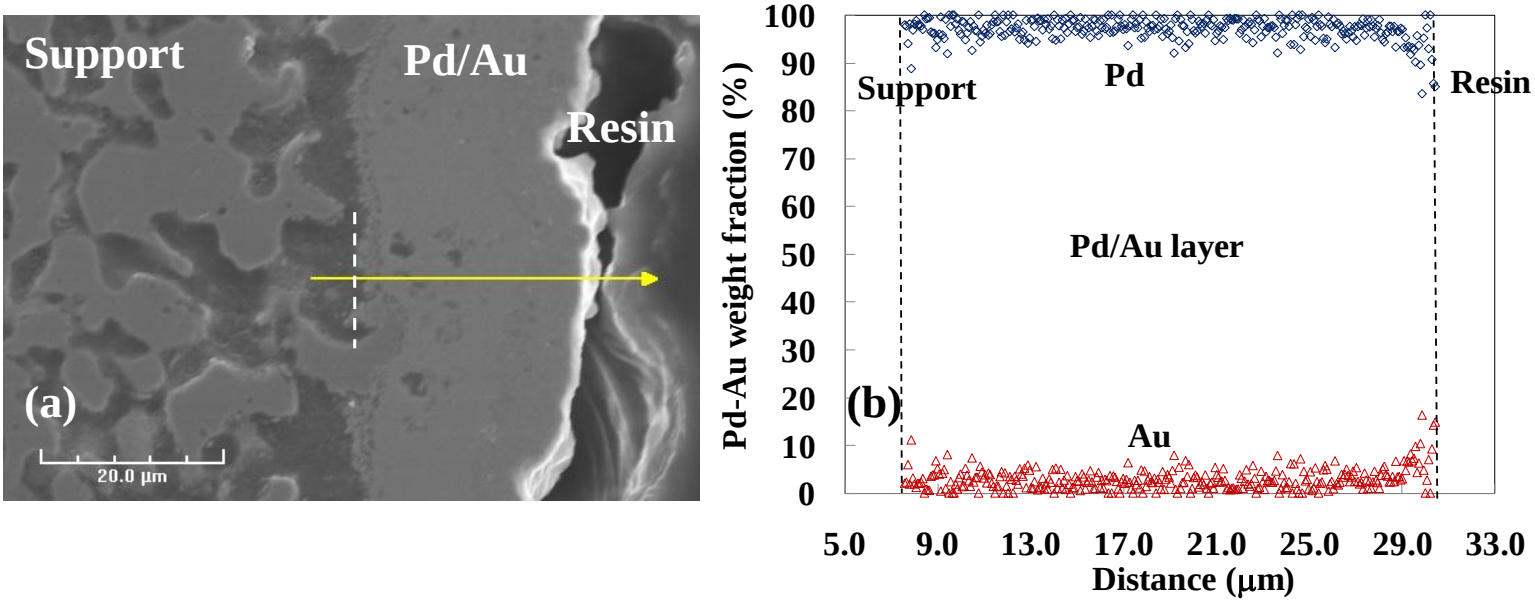


Figure 6.6. (a) Secondary-electron imaging (SEI) cross-sectional micrograph, and (b) corresponding energy dispersive X-ray spectroscopy (EDS) line scan (the insert is the Ni and Cr composition) of membrane C-09 after the testing (including the $H_2S$ testing)..

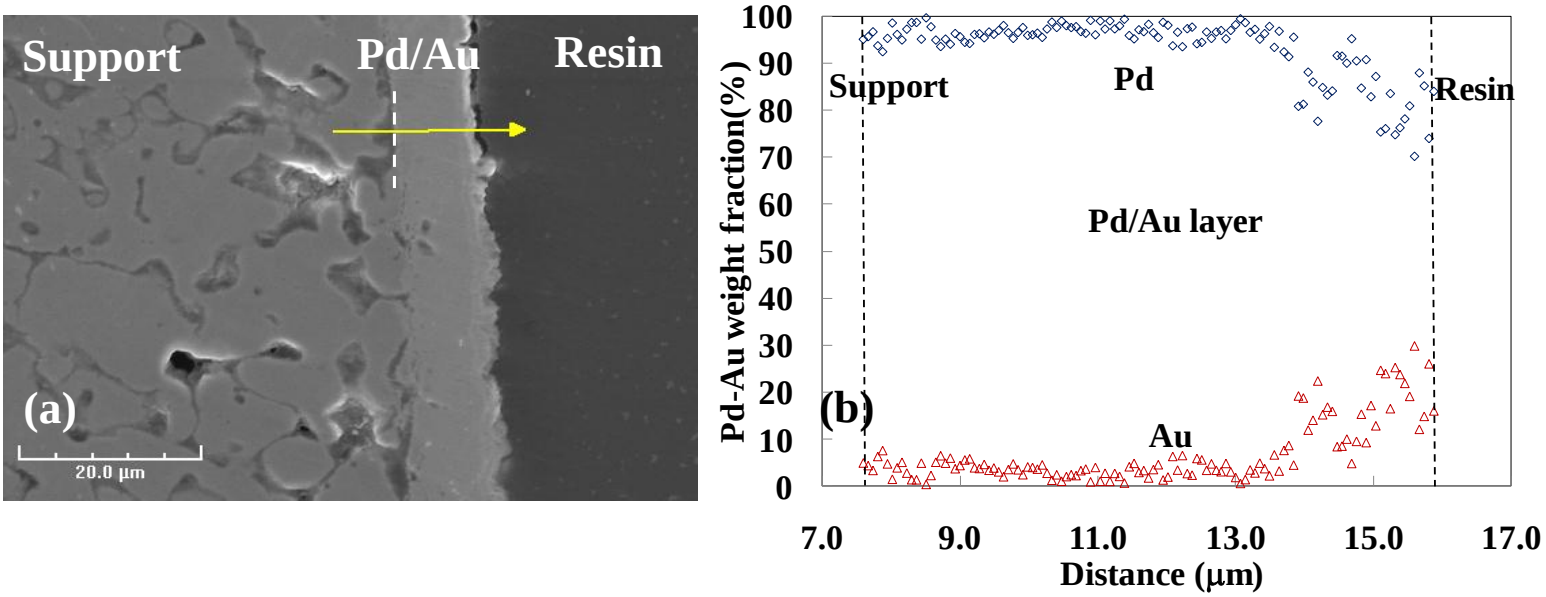


Figure 6.7. (a) Secondary-electron imaging (SEI) cross-sectional micrograph, and (b) corresponding energy dispersive X-ray spectroscopy (EDX) line scan of membrane C-11 after the characterization (including the $H_2S$ testing)..

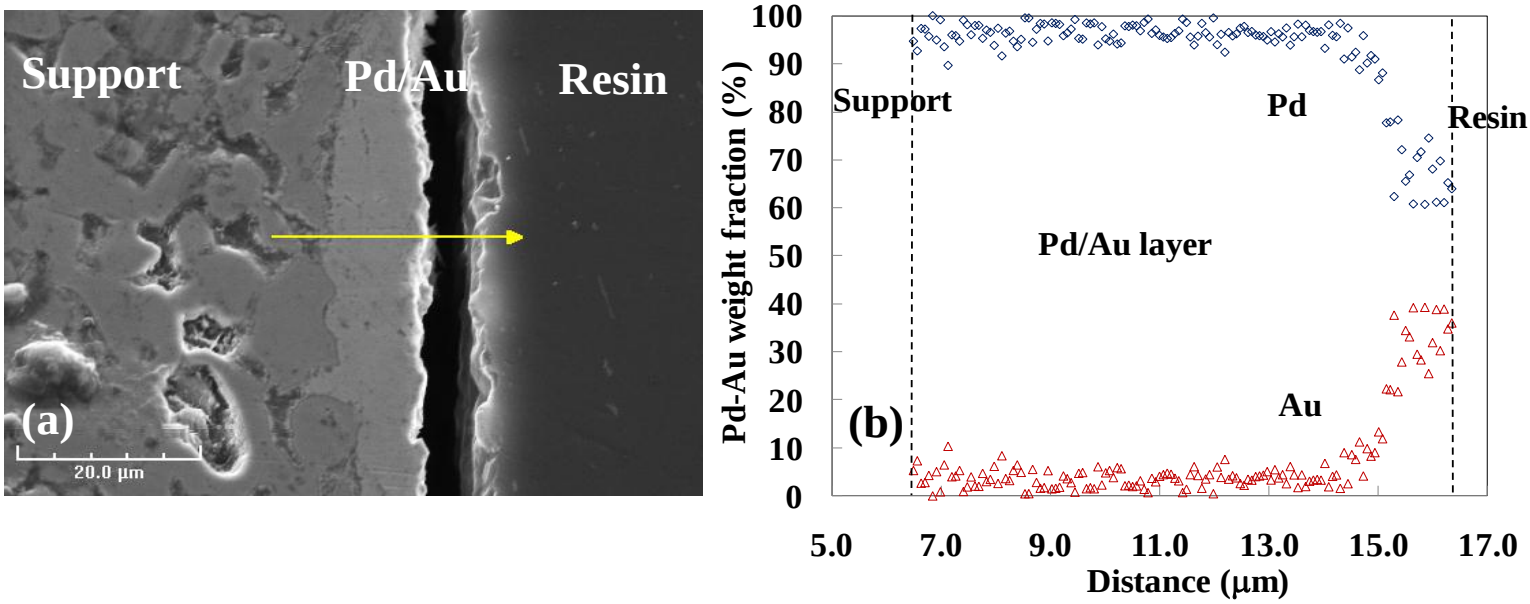


Figure 6.8. (a) Secondary-electron imaging (SEI) cross-sectional micrograph, and (b) corresponding energy dispersive X-ray spectroscopy (EDX) line scan of membrane C-12 after the characterization (including the $H_2S$ testing)..

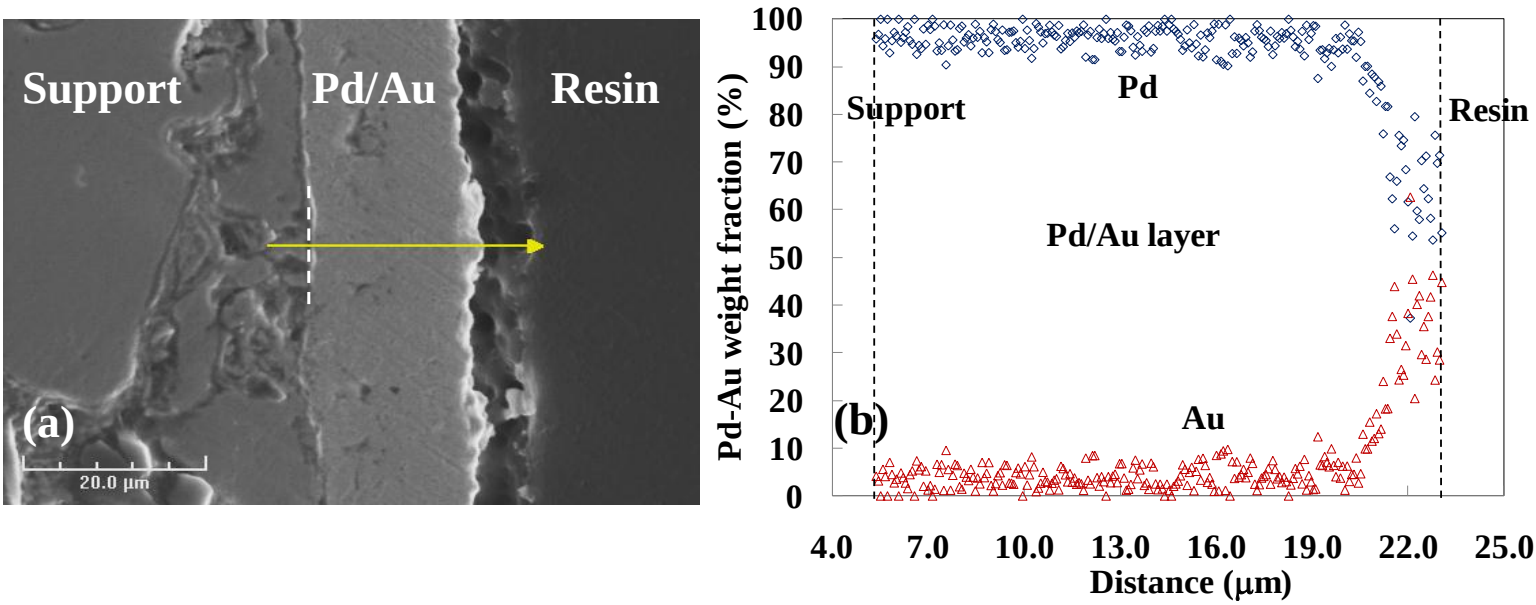


Figure 6.9. (a) Secondary-electron imaging (SEI) cross-sectional micrograph, and (b) corresponding energy dispersive X-ray spectroscopy (EDX) line scan of membrane C-16 after the characterization (including the $H_2S$ testing).

Table 6.3. The thickness of the Au gradient and Pd layer and the surface Au composition detected by cross sectional EDX line scan of membranes C-07, C-09, C-11, C-12, and C-16.

| Membrane | Thickness ( µm) | | Surface Au composition (wt%) |
|---|---|---|---|
| | Pd layer | Au gradient layer | |
| C-07 | 14.1 | 3.9 | 18.2 |
| C-09 | 20.3 | 3.3 | 14.3 |
| C-11 | 6.7 | 3.1 | 24.1 |
| C-12 | 13.5 | 3.4 | 34.2 |
| C-16 | 15.3 | 3.5 | 46.4 |

The Pd/Au alloy layers formed on the surface were considered to be very stable due to the significant reduction of the Pd-Au diffusion rate (by 2 – 3 orders) once the Pd/Au alloy formed as discussed in *Chapter 5*. The stable $H_2$ permeance of the Pd/Au membranes after the Pd/Au alloy formation also substantiated the formation of the stable

Pd/Au layer. Figure 6.10. is the $H_2$ permeance history of membrane C-16 after the Au deposition including the annealing stage at 500°C. Before the $H_2$ characterization over the temperature range of 350 - 450°C, membrane C-16 was annealed at 500°C in He and $H_2$ for approximately 60 hours in order to form a Pd/Au alloy layer on top of the membrane. The stable $H_2$ permeance at 500°C during the annealing stage after switching from He was observed. This suggested that the formation of Pd/Au alloy reached the equilibrium value at 500°C within the first few hours. Indeed, according to the isothermal Pd/Au alloying study, the majority of the Pd/Au inter-diffusion and alloy formation occurred and reached to the equilibrium value within the first 10 - 12 hours as discussed in *Chapter 5*. Furthermore, the non-isothermal annealing study (*Section 5.3.2*) also indicated that the formation of the Pd/Au alloy occurred below 500°C. As a result, the formation of the Pd/Au alloy on membrane C-16 took place even during the temperature increasing period. The stable $H_2$ permeance during the characterization at 350 - 450°C followed by the annealing at 500°C indicated the stable structure and composition of membrane C-16 (Figure 6.10.).

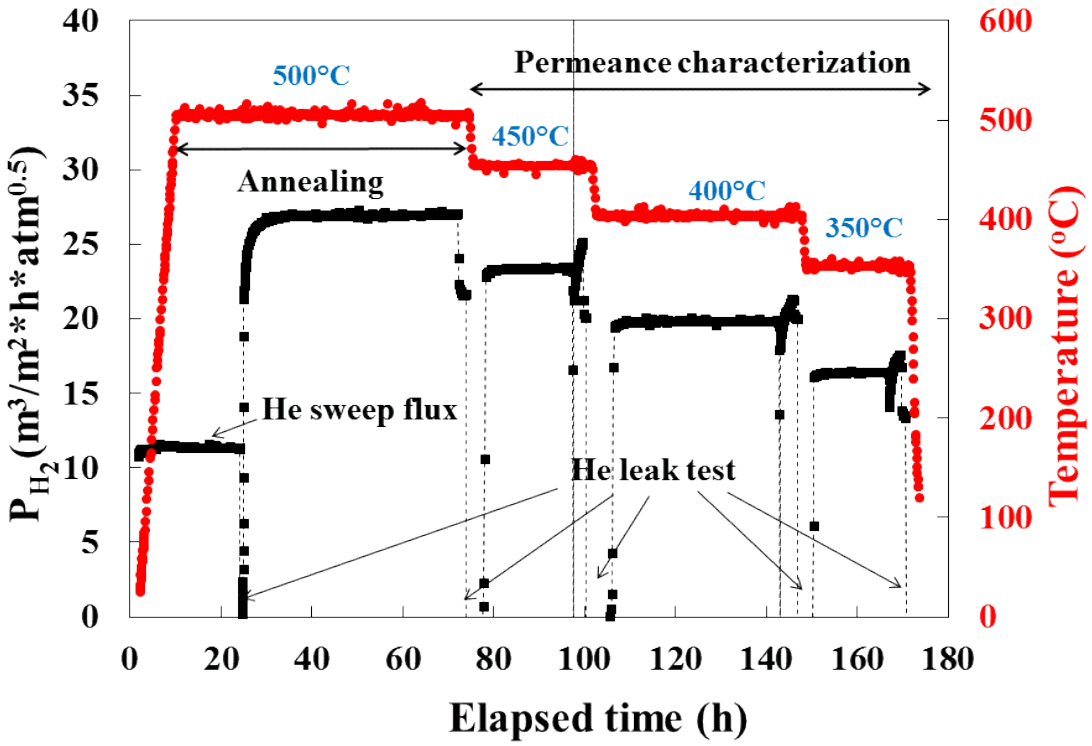


Figure 6.10. $H_2$ characterization history of membrane C-16.

### *6.4.3 $H_2$ transport through non-homogenous Pd/Au layers*

The influence of the Au addition on the $H_2$ permeation from the experimental observation of membranes C-07, C-09, C-11, C-12 and C-16 was examined by comparing the $H_2$ permeabilities between the Pd film and the Pd/Au alloy (non-homogenous) layers of the different membranes. By the use of the He flux data of the porous supports (at room temperature) and the $H_2$ flux data of the Pd/Au composite membranes (at elevated temperatures) with the dusty-gas model (Mason and Malinauskas, 1983, see Equation 2.16), the permeance of the Pd/Au layers were estimated. The method was essentially to estimate the actual pressure drop between the Pd/Au layers (Guazzone, 2006) and the detailed description of the method is provided in

Appendix C. The permeabilities of the Pd/Au layers were then estimated by multiplying the estimated permeance and the thickness (See Table 6.2) of the Pd/Au layers.

Table 6.4 (the 2nd and 3rd column) shows the relative $H_2$ permeabilities of the Pd/Au alloy layers to the Pd foil at 450 and 350°C calculated based on the aforementioned method with the flux data (both He and $H_2$) of membranes C-07, C-09, C-11, C-12, and C-16. The permeability of Pd foil reported by Guazzone (2006) and Ayturk (2007) was used for the comparison. However, the use of the constant $H_2$ permeability value of the Pd foil for the comparison on different membranes could be misleading in this case. This is because the "Pd layer" also included the Pd/Ag barrier layer in this study and the thickness of the Pd/Ag layer was different on each membrane (See Table 6.1). In addition, the thicknesses of the Pd layers in the composite membranes were not as uniform as the free standing Pd foils, which also caused the deviation of the permeability value. Indeed, as also shown in Table 6.4 (the 4th and 5th column), the estimated $H_2$ permeabilities of the Pd layers (i.e. before the Au deposition, see Table 6.2) in the composite membranes were different on different membranes and were not the same as those reported in the literature (Guazzone, 2006; Ayturk, 2007). The estimation of the $H_2$ permeabilities of the Pd layers in the composite membranes was done by the same method used for estimating the permeabilities of the Pd/Au layers in the membrane as described in the previous paragraph.

Therefore, in order to better examine the influence of the Au addition on the $H_2$ permeation, the relative $H_2$ permeability of the Pd/Au alloy layer to the Pd layer (i.e. before the Au deposition) estimated on each membrane was used which was also shown in Table 6.4 (the 6th and 7th column). For better observation of the effect of Au content on

the relative $H_2$ permeability, the results were expressed in the graphical representation as shown in Figure 6.11. As seen in Figure 6.11, it clearly showed that the relative $H_2$ permeability showed a maximum value at low Au wt% range (~5wt% Au) and decreased with increasing Au composition being similar to that of the homogenous Pd/Au foils (See Figure 6.1). Furthermore, higher relative $H_2$ permeabilities of the Pd/Au layers were observed at the lower temperature (i.e. 350°C), which was due to the increase of the $H_2$ solubility with decreasing temperatures as discussed in *Section 6.3*.

Table 6.4. The relative $H_2$ permeabilities of the Pd/Au alloy layers to Pd foils[9].

| Membrane | $Q_{Pd/Au}/Q_{Pd\ (litt.)}$ | | $Q_{Pd\ (exp.)}/Q_{Pd\ (litt.)}$ | | $Q_{Pd/Au}/Q_{Pd\ (exp.)}$ | |
|---|---|---|---|---|---|---|
| | 450°C | 350°C | 450°C | 350°C | 450°C | 350°C |
| C-07 (5.4 wt% Au) | 1.13 | 1.22 | 1.10 | 1.13 | 0.97 | 1.09 |
| C-09 (4.1 wt% Au) | 0.94 | 1.08 | 0.98 | 0.97 | 1.02 | 1.11 |
| C-11 (8.3 wt% Au) | 0.74 | 0.76 | 0.79 | 0.82 | 0.94 | 0.93 |
| C-12 (12.4 wt% Au) | 0.56 | 0.60 | 0.65 | 0.73 | 0.86 | 0.83 |
| C-16 (16.7 wt% Au) | 0.64 | 0.68 | 0.59 | 0.66 | 1.08 | 1.02 |

[9] The $H_2$ permeability of Pd, $Q_{pd(litt.)}$ was taken from the work of Guazzone (2006) and Ayturk (2007), while $Q_{pd(exp.)}$ was calculated from the composite membranes tested.

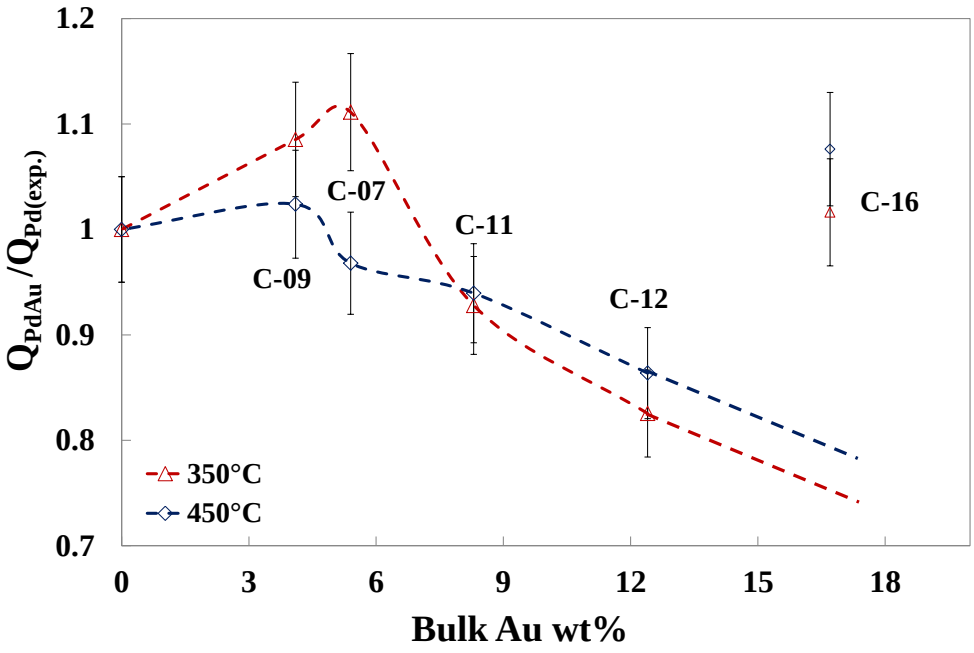


Figure 6.11. Relative $H_2$ permeability of the Pd/Au alloy layer to Pd layer as a function of bulk Au weight in the Pd/Au alloy membranes.

As also shown in Table 6.4 and Figure 6.11, the relative permeability of membrane C-16 appeared to be higher than expected and deviated from the trend that the permeability continuously decreased with increasing Au composition. Since membrane C-16 exhibited an excellent selectivity during the entire characterization (See Table 6.2), the unreasonable high permeability observed on membrane C-16 was unlikely due to the leak on the membrane. The discrepancy, however, was most likely due to the uncertainty of the thickness estimated gravimetrically during the Pd deposition. It has been confirmed that the support metals (i.e. Ni and Cr) could easily react with ammonia, which was a major component in the Pd plating solution (See Table 3.4). $Ni(OH)_2$ and $Cr(OH)_3$ precipitates would form in ammonia and $Ni(OH)_2$ could dissolve in excess ammonia

forming $[Ni(NH_3)_6]^{2+}$ solution (blue in colour)[10]. The batch of the porous support (Hastelloy C-22 provide by Chand Eisenmann Metallurgical) used for fabricating membrane C-16 had very large pores (~ 50 $\mu$m) and pore size distribution both in the pores and on the support surface[11]. During the Pd deposition of membrane C-16, blue solution and particles from the tube side of the support was observed from time to time, indicating the occurrence of the reaction between support metals and plating solution. As a result, the gravimetrically-estimated Pd thickness on membrane C-16, which was used for estimating the Pd permeability, was expected to give larger errors.

Figure 6.12 shows the relative activation energy of the Pd/Au layers to the Pd layers (i.e. before Au deposition, see Table 6.2) in the composite membranes as a function of Au composition from the $H_2$ characterization of membranes C-07, C-09, C-11, C-12, and C-16. The activation energy of the Pd/Au layer and the Pd layer was estimated by the permeance of the Pd/Au layer and Pd layer at 250 – 450°C. The estimation of the permeance of the Pd/Au and the Pd layer on the composite membranes was with the method described previously. As observed in Figure 6.12, the relative activation of the Pd/Au layer decreased first at low Au composition range where the increase of relative permeability of the Pd/Au layer was observed. Further increasing the Au composition resulted in the increase of the relative activation of the Pd/Au layer while the relative permeability of the Pd/Au alloy was decreasing (See Table 6.4). The activation energy for $H_2$ permeation was the sum of the activation energy for diffusion and the heat of dissolution (See Equation 2.13). The decrease of the relative activation energy of the Pd/Au at low Au concentrations, where the $H_2$ solubility was higher, was resulted from

[10] http://www.public.asu.edu/~jpbirk/qual/qualanal/catprop.html
[11] DOE DE-FC26-07NT43058 14th quarterly report.

the smaller heat of dissolution. The increase of the relative activation energy with increasing Au composition at the higher Au composition range was caused by the increase of both the heat of the dissolution and the activation energy of diffusion with the decrease of both the $H_2$ solubility and diffusivity. It should be noted that while the permeability of membrane C-16 deviated from the trend due to the uncertainty of the Pd thickness estimation (See Table 6.4), the relative activation energy estimated agreed with the trend fairly well. This was because the thickness was not required while estimating the activation energy from the permeance data of the Pd/Au and the Pd layer.

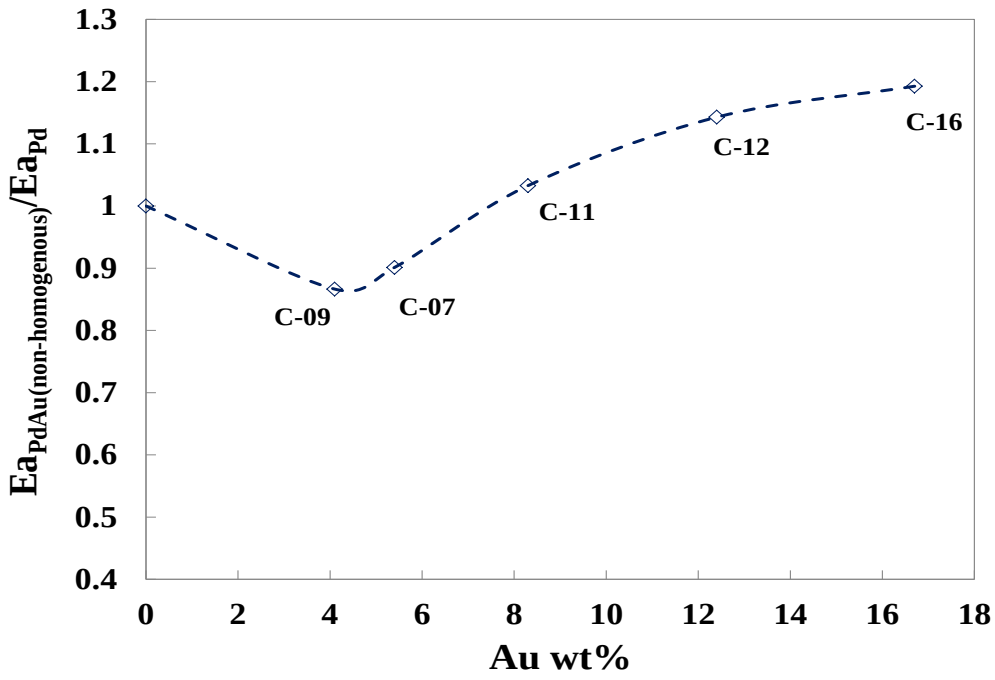


Figure 6.12. Relative activation energy for $H_2$ permeation of the Pd/Au alloy (non-homogenous) layer to Pd as a function of bulk Au weight in the Pd/Au alloy.

According to the transfer resistance model (Henis and Tripodi, 1981), the overall effective permeability of the non-homogenous layer can be estimated by the sum of the resistance from each layer comprising the entire layer. The resistance of a layer equals to

the thickness of the layer divided by the permeability of the layer (See Equation 2.19). As the total resistance equals to the sum of the resistance from each layer, the total permeability of a series of layers with different permeabilities and thickness was expressed in Equation 6.1, where *l* is the thickness and *Q* is the permeability.

$$Q_{tot} = \frac{l_{tot}}{\frac{l_1}{Q_1} + \frac{l_2}{Q_2} + ..... + \frac{l_n}{Q_n}} \tag{6.1}$$

As shown in the cross-sectional EDX line scan analysis of the Pd/Au membranes tested in the study (see Figure 6.5 - Figure 6.9), the non-homogenous Pd/Au alloy layer could be divided into two layers: pure Pd layer and the Au gradient layer. Therefore, the overall $H_2$ permeability of the non-homogenous Pd/Au layers can be expressed in terms of the mass transfer resistance from the pure Pd and the Au gradient layer as shown in Equation 6.2.

$$Q_{overall-PdAu} = \frac{l_{Pd} + l_{Au\ gradient}}{\frac{l_{Pd}}{Q_{Pd}} + \frac{l_{Au\ gradient}}{Q_{Au\ gradient}}} \tag{6.2}$$

Ideally, the effective permeability of the Au gradient layer could be estimated from the experimental observation of the overall relative permeability of the entire non-homogenous Pd/Au layers to Pd (See Table 6.4) by using Equation 6.2. The thicknesses of the Pd and the Pd/Au layers in the membranes tested were determined by the cross-sectional SEM analysis and shown in Table 6.3. Since the relative permeability to Pd was used, the $H_2$ permeability of the Pd layer was taken as one.

Figure 6.13 shows the effective $H_2$ permeability of the Au gradient layer as a function of the bulk Au composition at 350°C estimated by the aforementioned method. The effective $H_2$ permeability of the Au gradient layer calculated by the theoretical calculation was also shown in Figure 6.13.

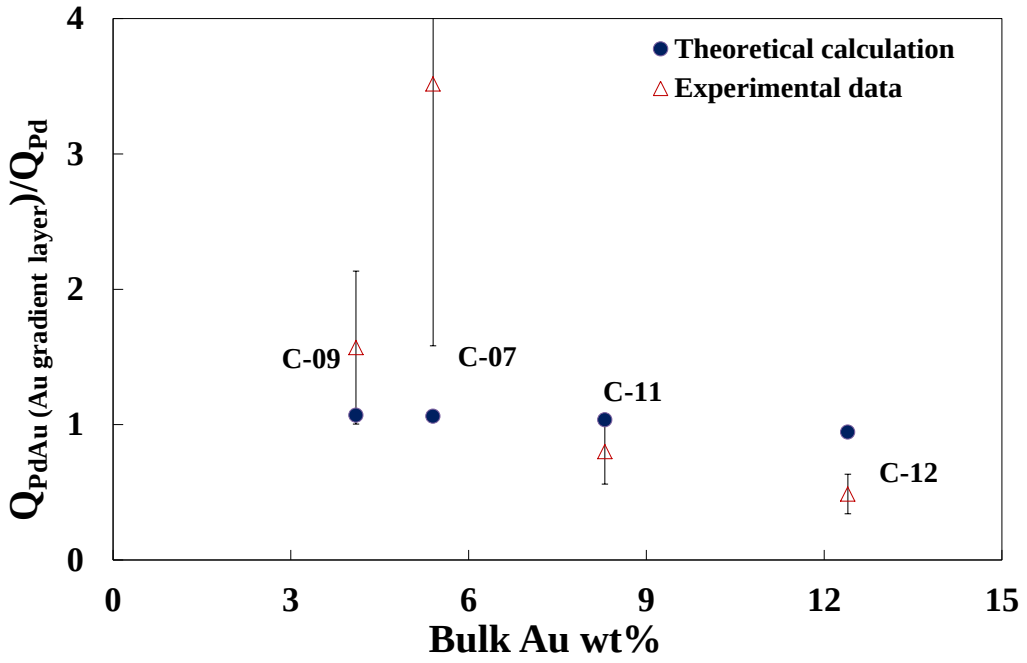


Figure 6.13. Relative $H_2$ permeability of the Au gradient layer (in the non-homogenous Pd/Au alloy layer) to Pd as a function of bulk Au weight in the Pd/Au alloy.

For theoretically estimating the permeability of the Au gradient layer, the relative permeability of the Pd/Au alloy (homogenous) to Pd as a function of Au wt% was calculated based on the thermodynamic data (Catalano 2011) was used (See *Section 6.3*). The empirical polynomial regression of the relative permeability of the Pd/Au alloy to Pd by the theoretical calculation (Catalano 2011) at 350°C is shown in Equation 6.3 (It should be noted that the regression is valid between the Au composition between 0 – 55 wt%).

$$Q_{PdAu} = 0.000009 \cdot (wt\%\ Au)^3 - 0.0011 \cdot (wt\%\ Au)^2 + 0.0166 \cdot (wt\%\ Au) + 1 \qquad (6.3)$$

Since the Au composition is a function of distance (x) in the Au gradient layer, the effective permeability of the Au gradient layer was estimated by the integral form of Equation 6.1 as expressed in Equation 6.4, where permeability is a function of the distance in the Au gradient layer. One reasonable approximation was made that the Au gradient in the Au gradient layer was linear from 0 to the surface Au wt% according to the observation from the cross-section analysis (See Figure 6.5 - Figure 6.9). As a result, the Au composition was then a linear function of the thickness in the Au gradient layer with the slope equaling to the surface Au composition divided by the thickness of the Au gradient layer.

$$Q_{Au\ gradient} = \frac{x}{\int_x \frac{dx}{Q(wt\%\ Au(x))}} \qquad (6.4)$$

As observed in Figure 6.13, significant discrepancy between the results from the experimental observation and the theoretical calculation was observed. Although both theoretical calculation and the experimental data showed higher permeability than Pd at low Au composition of 4 – 5 wt% Au and decreased continuously with increasing Au composition, the extents were much smaller from the theoretical calculation. The discrepancy could be due to the large error of the permeability of the Au gradient layer estimated from the experimental data. The error bars of the experimental data (20 – 70%) shown in Figure 6.13 were determined by assuming a reasonable 5% error while determining the overall permeability of the entire non-homogenous layer ( $Q_{overall-PdAu}$ ) by

the experiments. When estimating a denominator term inside another denominator (as $Q_{Au\ gradient}$ in Equation 6.2), the error is usually multiplied. In addition, the thickness of the Pd/Au layer and Pd layer in the membranes as well as the Au composition used for the estimation were based on the cross-sectional EDX analysis, which was a semi-quantitative method. The possible error between the measured and the actual thickness and Au concentration would also result in the noticeable error in the determination of the effective permeability.

Figure 6.14 shows the effective $H_2$ permeability of the entire non-homogenous Pd/Au layer as a function of the bulk Au composition at 350°C from the experimental data (See Table 6.4) and the theoretical calculation. The theoretical calculation was performed by the use of the resistance model shown in Equation 6.2 with the effective permeability of the Au gradient layer by the use of the permeability of the homogenous Pd/Au alloy with Equation 6.3 and 6.4 as described previously. The effective permeability of the Au gradient layer from the theoretical calculation was also shown in Figure 6.14. While both the theoretical calculation and experimental data showed the similar trend, the discrepancy in the extent of permeability variation affected by the Au addition was observed. Once again, the possible error in determining the permeability of the Pd/Au alloy layers by the experiments could account for the discrepancy between the experimental data and the theoretical calculation. It should be noted that a 5% error was assumed on the experimental data shown in Figure 6.14.

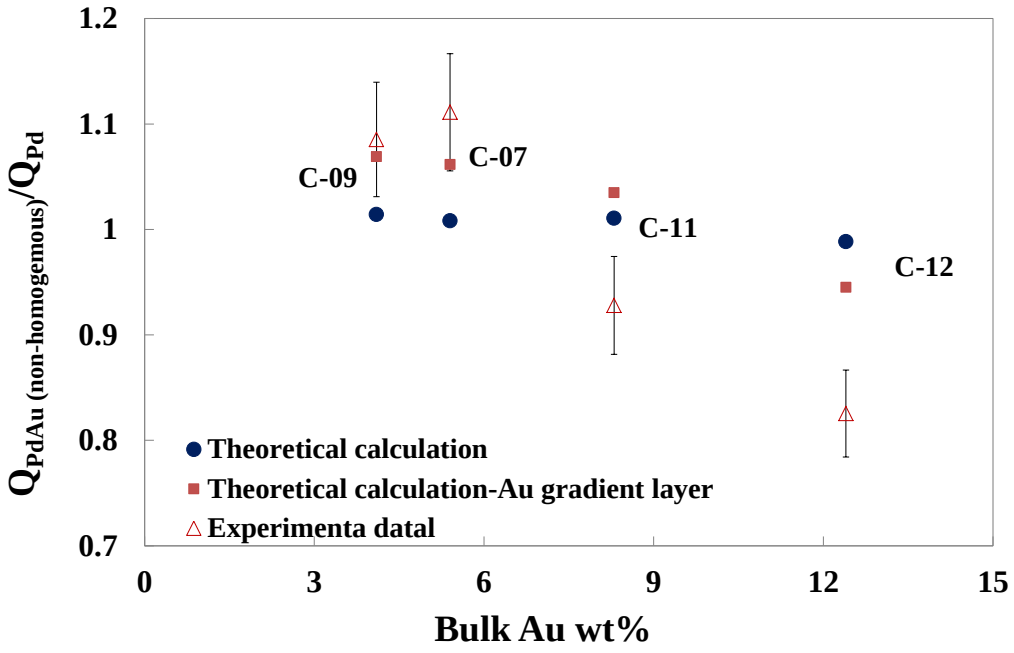


Figure 6.14. Relative $H_2$ permeability of the non-homogenous Pd/Au alloy layer to Pd as a function of bulk Au weight in the Pd/Au alloy.

Figure 6.14 also shows that the permeabilities of the entire Pd/Au alloy layers estimated by the theoretical calculation were less sensitive to the Au composition compared to those of the Au gradient layers. This was due to that the thickness of the Au gradient layer in the entire non-homogenous Pd/Au alloy layer was small compared to the Pd layer (See Table 6.3). While estimating the effective permeability of the overall Pd/Au alloy layer by the transfer resistance model (Henis and Tripodi, 1981) as shown in Equation 6.2, the contribution from the Au gradient layer was much less compared to the Pd layer. As a result, the effective permeability of the overall Pd/Au alloy estimated was very close to that of pure Pd layer (~1).

## 6.5 Conclusions

The $H_2$ permeation characteristics of the composite Pd/Au alloy (non-homogenous) membranes prepared by the Au displacement deposition followed by the annealing were investigated. The Pd/Au composite membranes (of the bulk Au wt% up to 16.7 wt% , ~ 46 wt% Au at surface) followed Sieverts' law at 250 – 450°C with the $H_2$ feed pressure up to 4 atm. The Pd/Au alloy layers on the prepared composite membranes were non-homogenous composed of a relative thin Au gradient layer on the surface and a pure Pd layer under the Au gradient layer. The Pd/Au alloy layers formed were thermally stable and the $H_2$ permeance of the Pd/Au membranes was stable at elevated temperatures up to 500ºC. Although the $H_2$ permeabilities of the non-homogenous Pd/Au alloy layers predicted from the theoretical calculation showed a significant deviation from the experimental data, the trend of influence on the $H_2$ permeability by the addition of Au agreed with each other from both the theoretical calculation and experimental observation. The $H_2$ permeability was enhanced at low Au weight fraction and diminished with further increasing the Au composition.

# 7. Effect of $H_2S$ on the Performance of Pd and Pd/Au Membranes

## 7.1 Introduction

In the catalysts field, Pd/Au alloys have exhibited high sulfur tolerance (Vnerzia et al., 2003; Pawelec et al., 2004). However, as mentioned in *Section 2.6.3*, there was little research done regarding sulfur poisoning of the hydrogen-selective Pd/Au alloy membranes in the literature (McKinley, 1967; Way et al., 2008) especially in the Au content range below 20 wt% where $H_2$ permeability potentially could be enhanced. No systematic data were available regarding the effect of temperature, exposure time, $H_2S$ concentration, and the Au content on the $H_2$ permeation characteristics of Pd/Au alloy membranes in the presence of $H_2S$. In addition, the permeance recovery characteristics of Pd/Au alloy membranes after $H_2S$ poisoning was rarely investigated.

The main objective of this chapter was to investigate the performance of the Pd/Au membranes prepared by the electroless and galvanic displacement plating techniques in $H_2S/H_2$ mixtures with the $H_2S$ concentration up to approximately 55 ppm at 350 - 500°C. The recovering property of the Pd/Au membranes in pure $H_2$ after the $H_2S$ exposure was also investigated. In addition, the influence of temperature, exposure time, $H_2S$ concentration, and Au content on $H_2S$ poisoning and recovery characteristics of the Pd/Au alloy membranes were studied. Similar poisoning and recovery characterizations were also conducted on the Pd membranes for comparison purpose.

## 7.2 Experimental

The properties of the membranes characterized in this chapter are listed in Table 7.1. Membrane C-06, C-06R and C-10 were Pd membranes while other membranes listed in Table 7.1 including C-04, C-09, C-11, C-12, and C-16 were Pd/Au membranes.

The detailed preparation of the Pd/Au membranes including membranes C-04, C09, C-11, C-12, and C-16 was described in Chapter 6. The Pd membrane C-06 was prepared on a 0.1 μm grade Inconel tubular supports purchased from Mott Metallurgical, Inc. After the oxidization at 700ºC for 12 hours in air, the membrane was graded with the $Al_2O_3$ slurry (slurry B as indicated in *Section 3.1.5*) and sealed with the "Pd glue" as described in *Section 3.1.5*. Following the $Al_2O_3$ grading, a Pd/Ag barrier was deposited on the membranes followed by a slight sanding with a 2400 grit sand paper as described in *Section 3.1.5*. The Pd layer was then deposited on the membrane by the electroless plating method until dense. After the characterization, membrane C-06 was repaired with additional plating of 3.3 $\mu$m Pd. The repaired Pd membrane was referred to as membrane C-06R.

The permeation characterizations of the membranes both with and without the presence of $H_2S$ were performed in the system described in *Section 3.3.2*.

Table 7.1. Membranes tested in this chapter

| Membrane | Intermetallic diffusion | grading | Pd/Ag barrier | Pd layer (μm) | Au layer (μm)[12] | wt% Au |
|---|---|---|---|---|---|---|
| C-04 | air/700ºC/12 h | $Al_2O_3$ slurry+Pd glue | 2.1 | 15.5 | 0.5 | 8 |
| C-06 | air/700ºC/12 h | $Al_2O_3$ slurry+Pd glue | 3.6 | 7 | 0 | 0 |
| C-06R | air/700ºC/12 h | $Al_2O_3$ slurry+Pd glue | 3.6 | 10.3 | 0 | 0 |
| C-09 | air/700ºC/12 h | $Al_2O_3$ slurry+Pd glue | 4.1 | 14.2 | 0.5 | 4.2 |
| C-10 | air/700ºC/12 h | $Al_2O_3$ slurry+Pd glue | 5.3 | 10.7 | 0 | 0 |
| C-11 | air/700ºC/12 h | $Al_2O_3$ slurry+Pd glue | 3.8 | 12.9 | 1.0 | 8.5 |
| C-12 | air/700ºC/12 h | $Al_2O_3$ slurry+Pd glue | 2.9 | 12.6 | 1.5 | 12.3 |
| C-16 | air/800ºC/12 h | $Al_2O_3$ slurry+Pd glue | 0.6 | 10.0 | 1.5 | 16.7 |

## 7.3 Results and Discussion

### *7.3.1 $H_2$ permeance*

The membranes for the $H_2S$ tests were first characterized in $H_2$. The characterizations of the Pd/Au membranes including membranes C04, C-09, C-11, C-12, and C-16 in pure $H_2$ were described in *Chapter 6*. In this section, the $H_2$ permeating characteristics of the Pd membranes, C-06, C-06R and C-10 are discussed. Membranes C-06, C-06R, and C-10 were characterized in pure $H_2$ and He for over 300, 115, and 230 hours, respectively. The characterization was performed in the temperature range of 250 – 500°C, which was within the suitable operation temperature range of the water-gas shift reaction.

Figure 7.1 shows that membrane C-06 followed Sieverts' law in the testing temperature and pressure range. This verified that the rate-limiting step for $H_2$ transport

[12] The thickness of Au layer was estimated number of Au displacement deposition, according to the results described in *Chapter 4*, one displacement plating resulted in an approximately 0.5 μm Au layer.

through the composite Pd membrane was the one dimensional diffusion of atomic hydrogen through the dense Pd layer (See *Section 2.2*). As seen in Figure 7.1, the $H_2$ permeance of membrane C-06 was 19.5 $m^3/(m^2*h*atm^{0.5})$ at 300°C and increased with increasing temperature to 50.8 $m^3/(m^2*h*atm^{0.5})$ at 500°C. The permeance values were equivalent to free-standing Pd foils with a thickness of 10.9 – 12.5 $\mu$m (Guazzone, 2006; Ayturk, 2007). The gravimetrically estimated thickness of the $H_2$-selective layer of membrane C-06 was approximately 11 $\mu$m including the Pd/Ag barrier layer. The result indicated that the $H_2$ permeance of membrane C-06 was very close to that of a free-standing Pd foil of roughly the same thickness.

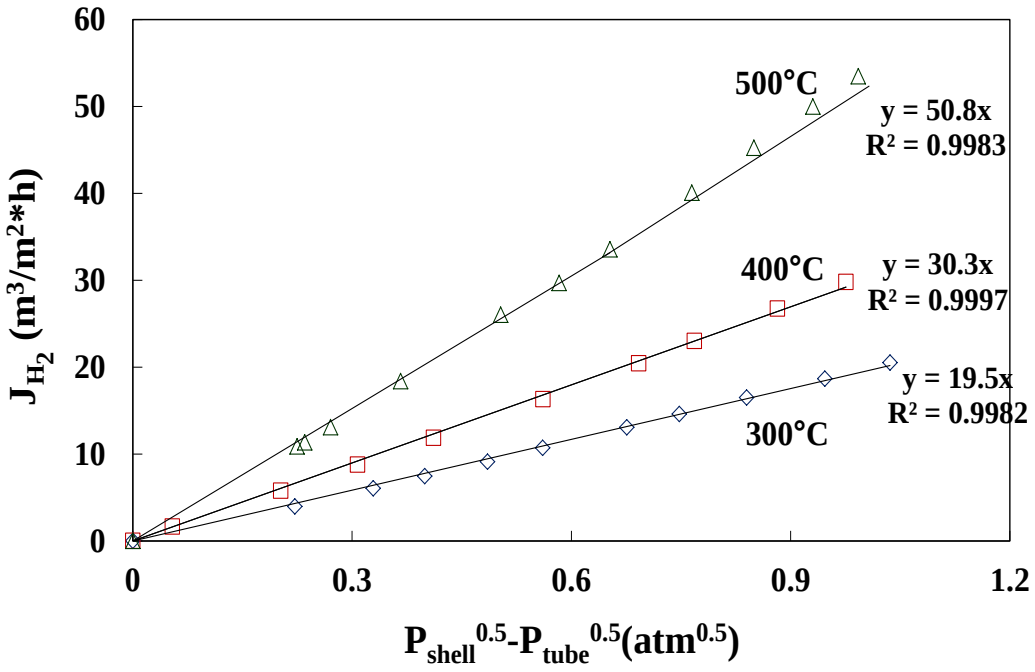


Figure 7.1. Sieverts' law regression for membrane C-06 at 300 - 500°C.

The He leak of membrane C-06 increased from 0.25 to ~ 9 sccm during the 120 hours testing at 500°C. As a result, membrane C-06 was re-plated with Pd. Membrane C-06R was prepared by an additional plating of 3.3 $\mu$m Pd on membrane C-06, resulting in

the total thickness of the $H_2$ selective layer to be ~14 $\mu$m. Membrane C-06R exhibited a $H_2$ permeance of 24 $m^3/(m^2*h*atm^{0.5})$ at 400°C using the $H_2$ flux from a single measurement of pressure difference of 1 atm ($P_{feed}$ = 2 atm, $P_{permeate}$ = 1 atm) by assuming Sieverts' law. A 16 $\mu$m thick free-standing Pd foil would produce a similar $H_2$ permeance at 400°C (Ayturk, 2007). The ideal selectivity ($J_{H2}/J_{He}$, $\Delta p$ = 1atm) was theoretically infinite for membrane C-06R after 115 hours of characterization at 400°C before the $H_2S$ testing.

Figure 7.2 is the Sieverts' law regression for membrane C-10 at 350 - 450°C. Once again, the results showed that membrane C-10 followed Sieverts' law quite well suggesting the diffusion controlled mechanism for the $H_2$ transport. The $H_2$ permeance of membrane C-10 was 25.6 $m^3/(m^2*h*atm^{0.5})$ at 350°C and increased with increasing temperature to 34.7 $m^3/(m^2*h*atm^{0.5})$ at 450°C. The permeance values were equivalent to a free-standing Pd foil with a thickness of 12.1 – 13.6 $\mu$m (Guazzone, 2006; Ayturk, 2007). However, the gravimetrically estimated thickness of the $H_2$-selective layer of membrane C-10 was approximately 16 $\mu$m including the Pd/Ag barrier layer. The slight discrepancy could possibly be resulted from the errors in determining the membrane thickness gravimetrically. The ideal selectivity ($J_{H2}/J_{He}$, $\Delta p$ = 1atm) was theoretically infinite for membrane C-10 after roughly 230 hours characterization at 400°C before the $H_2S$ testing.

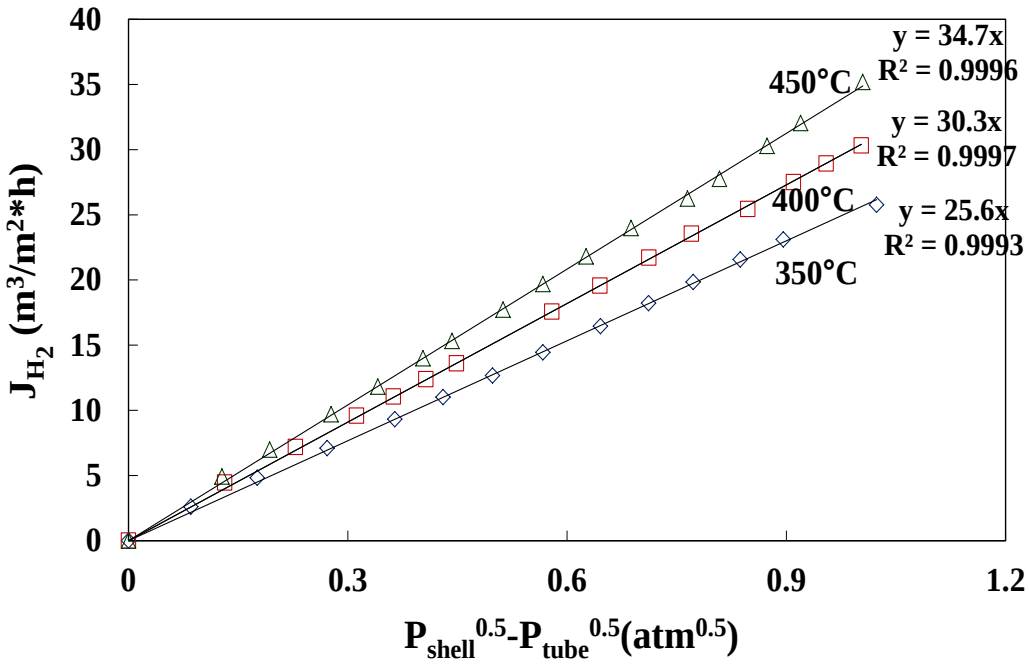


Figure 7.2. Sieverts' law regression for membrane C-10 at 350 - 450°C.

Figure 7.3 shows the Arrhenius dependence of the $H_2$ permeance on temperature for membranes C-06, C-06R and C-10. While the permeance of membranes C-06 and C-10 were calculated with the linear regression of the Sieverts' plots (See Figure 7.1 and Figure 7.2), the permeance of membrane C-06R were calculated by the hydrogen flux from a single pressure difference of 1 atmosphere ($P_{feed}$ = 2 atm , $P_{permeate}$ = 1 atm) assuming Sieverts' law at 250 - 450°C. The activation energies for the $H_2$ permeation of membranes C-06, C-06R and C-10 were 17.2, 12.8 and 11.7 kJ/mol, respectively. The activation energies of membrane C-06R and C-10 were within the typical values for the composite Pd membranes (Guazzone, 2006). Although the activation energy of a free standing Pd foil for hydrogen permeation was 14.9 - 15.6 kJ/mol (Guazzone, 2006; Ayturk, 2007), the activation energies of composite Pd membranes were usually within 8 - 12 kJ/mol due to the mass transfer resistance from the porous supports especially with

the support modification (e.g. grading) (Guazzone, 2006). Mardilovich et al. (1998) reported an activation energy of 16.4 kJ/mol for the Pd/PSS composite membrane, which was very close to the Pd foil. This was most likely due to that the porous support used by the authors had a 0.5 $\mu$m grade and was not graded, resulting in insignificant mass transfer resistance from the support. The supports used in this study, however, had a smaller grade of 0.1 $\mu$m and were graded with $Al_2O_3$.

The high activation energy of membrane C-06 (17.2 kJ/mol) was most likely resulted from the possible over-estimated hydrogen permeance at 500$^o$C. As mentioned previously, the He leak of membrane C-06 increased considerably during the test at 500$^o$C due to the pinhole formation on the membrane. The pinholes also allowed $H_2$ to permeate through by Knudsen diffusion and viscous flow (*Section 2.2*), resulting in the over-estimation of hydrogen permeance at 500$^o$C. In fact, the activation energy of membrane C-06 estimated from the permeance values at 300 and 400$^o$C was 13.7 kJ/mole, which was very close to that of membrane C-06R.

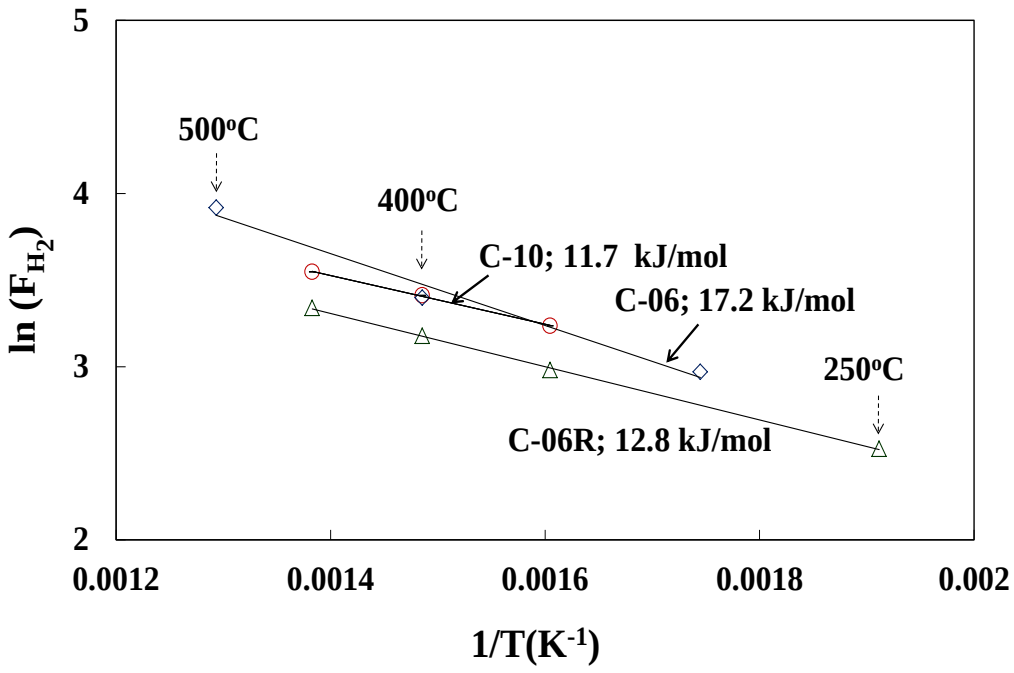


Figure 7.3. Arrhenius plot for $H_2$ permeance of membranes C-06, C-06R, and C-10. The estimated activation energies for $H_2$ permeation were also listed in the plot.

### *7.3.2 Effect of $H_2S$ exposure on the performance of Pd membrane*

Figure 7.4 shows the relative $H_2$ permeance ($F_{H2}/F_{0H2}$) of membrane C-06R as a function of time at 400°C upon exposure to a 55 ppm $H_2S/H_2$ mixture and the subsequent recovery in $H_2$. The relative $H_2$ permeance ($F_{H2}/F_{0H2}$) shown in Figure 7.4 was the ratio of permeance ($F_{H2}$) to the original permeance ($F_{0H2}$) before the $H_2S$ exposure at the testing temperature. The $H_2S$ concentration was chosen in accordance with the U.S. Department of Energy (DOE) guideline (Hydrogen from coal program, 2009).

As shown in Figure 7.4, upon exposing to a 55 ppm $H_2S/H_2$ mixture, the permeance of membrane C-06R decreased instantaneously to approximately 25 % of the original value. Following the sudden decline, the permeance continued to decline over the 24 hours period until it reached the steady state value by a total loss of 93% of the

original permeance. This suggested that the sulfur poisoning mechanism on the Pd membranes was most likely more than just surface site blocking by the adsorption of sulfur under the testing condition. While the initial sudden permeance decline was caused by the surface site blocking, the following continuous permeance decline was resulted from the bulk sulfidation of Pd (i.e. the formation of bulk sulfide, $Pd_4S$). Since the $H_2$ permeability of $Pd_4S$ was smaller than that of Pd by 2 orders of magnitude (Morreale, 2007), the $H_2$ permeance declined continuously with increasing $Pd_4S$ thickness as the poisoning progressed.

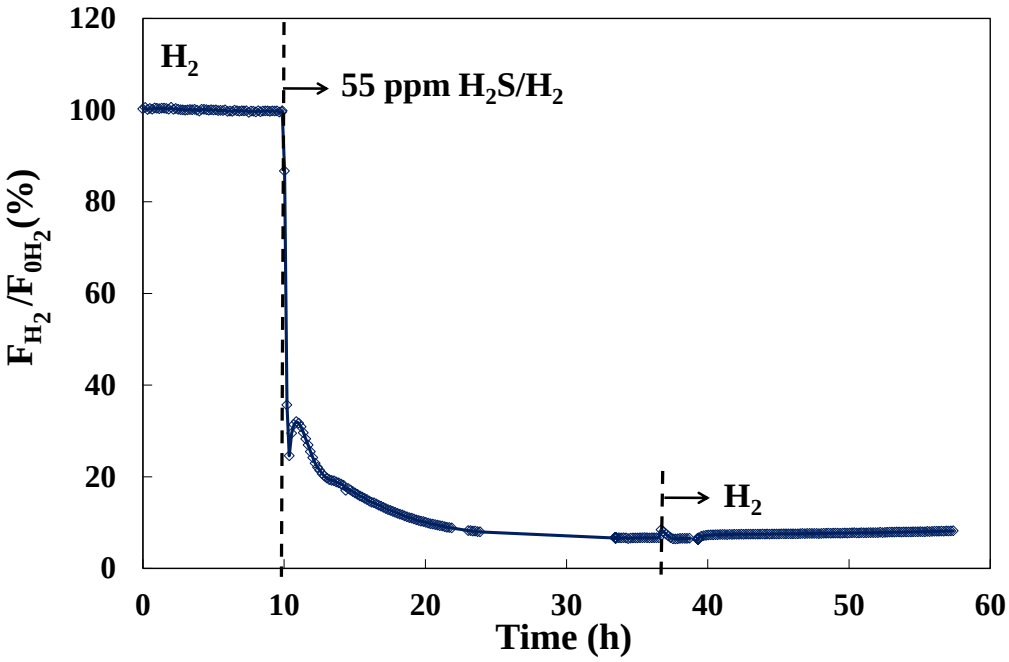


Figure 7.4. The poisoning of membrane C-06R in a 55 ppm $H_2S/H_2$ mixture and the recovery in $H_2$ at 400°C.

Indeed, the $Pd_4S$ phase is stable under the testing condition according to the thermodynamic calculations (Mundschau et al., 2006; Iyoha et al., 2007). The coupon study performed under the same poisoning condition also confirmed the formation of

$Pd_4S$ phase. More results of the coupon study regarding the $H_2S$ poisoning will be discussed in *Chapter 8*. Mundschau et al. (2006) in a recent study observed a similar $H_2$ permeance decline pattern while exposing a Pd foil membrane to a 20 ppm $H_2S$-60 mol% $H_2$-He mixture at 320°C for approximately 120 hours. The testing condition was also within the stable $Pd_4S$ region, and the authors also confirmed the formation of 5 – 10 μm thick $Pd_4S$ layer after the testing.

Figure 7.4 also shows that upon introducing pure $H_2$ to membrane C-06R after the poisoning, very little permeance increase was observed for as long as 20 hours. This indicted that reversing the $Pd_4S$ formation reaction was nearly impossible under the recovery condition. Thermodynamically, the stability of $Pd_4S$ sulfide decreases with increasing temperature which suggested that recovering the membranes at higher temperatures could potentially recover the permeance. Indeed, the poisoned Pd coupons showed the recovery of the Pd phase from the $Pd_4S$ phase after recovering in $H_2$ at 500°C for 48 hours (More discussions will be given in *Chapter 8*). However, the recovery at higher temperatures was not performed on membrane C-06R due to the integrity of the membrane structure was destroyed which will be further discussed in the following.

McKinley (1967) reported the full restoration of the Pd foil membrane in pure $H_2$ after exposing to a 4.5 ppm $H_2S/H_2$ mixture at 350°C for 4 days. However, the recovery conditions (i.e. temperature and time) were not specified. The author reasoned that the poisoning was caused by the adsorption of $H_2S$ rather than the sulfide formation under their testing conditions. According to the thermodynamic prediction (Mundschau et al., 2006; Iyoha et al., 2007), $Pd_4S$ was stable and would form under the testing condition used by McKinley (1967). In addition, McKinley (1967) also reported that the Pd foil lost

its luster after the poisoning. As a result, the permeance restoration of the Pd membrane observed by McKinley (1967) was most likely due to the reverse reaction of the $Pd_4S$ formation rather than just the desorption of the $H_2S$.

The He leak of membrane C-06R measured at the end of the recovery was ~10 ml/min. The large increase of the He leak suggested that the structure of the Pd layer was deteriorated due to the formation of bulk $Pd_4S$. As a significant amount of sulfur dissoluted into the Pd lattice, large stress was generated due to the difference in the lattice constant between Pd and $Pd_4S$, which caused the deterioration of the membrane structure. The formation of pinholes or even cracks on the Pd layers after $H_2S$ exposure has been observed by several researchers (Kajiwara et al., 1999; Kulprathipanja et al., 2005; Mundschau et al., 2006).

The performance of the Pd membrane in the presence of small $H_2S$ concentrations was also investigated. Figure 7.5 shows the relative $H_2$ permeance ($F_{H2}/F_{0H2}$) of membrane C-10 as a function of time at 400°C upon exposure to a 0.2 ppm $H_2S/H_2$ mixture and the subsequent recovery in $H_2$. The $H_2S$ concentration in the retentate (at the outlet of the shell side) monitored by the GC during the testing and recovery was also plotted in Figure 7.5 (the right-hand side *y*-axis).

As shown in Figure 7.5, upon the exposure to the 0.2 ppm $H_2S/H_2$ mixture, the permeance of membrane C-10 decreased gradually to a steady state value of approximately 52 % of the original permeance. The gradual permeance decline was caused by the increase of the $H_2S$ concentration rather than the bulk sulfide formation as mentioned earlier (See Figure 7.4). This is because the $Pd_4S$ sulfide phase was not stable with 0.2 ppm $H_2S$ at 400°C according to the thermodynamic calculations (Mundschau et

al., 2006; Iyoha et al., 2007). As a result, the permeance loss of membrane C-10 in 0.2 ppm $H_2S$ was mainly caused by ~ 50% of the surface site being blocked by sulfur rather than the bulk sulfide formation.

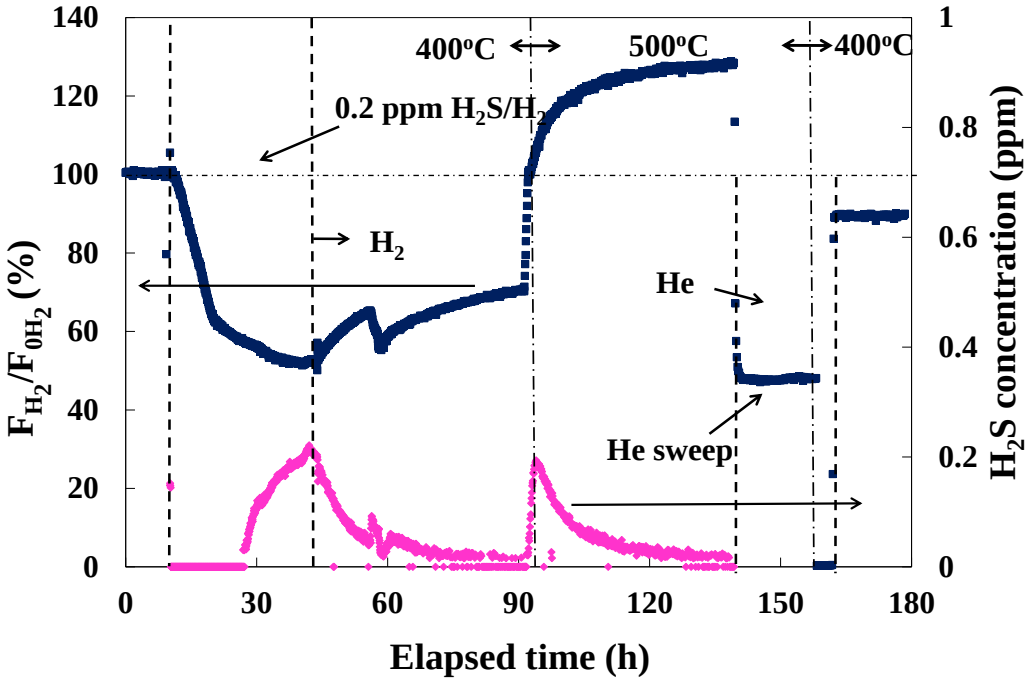


Figure 7.5. The poisoning of membrane C-10 in a 0.2 ppm $H_2S/H_2$ mixture and the recovery in $H_2$ at 400°C.

The $H_2S$ concentration in the mixed gas feed to the membrane was diluted initially since the tubing and the reactor were made of stainless steel which also potentially adsorbed $H_2S$. As the amount of sulfur adsorbed by the system walls approached the equilibrium value with time, the $H_2S$ concentration that reached the membrane surface increased back to the set value gradually causing the permeance to decline gradually. As observed in Figure 7.5, the fact that the $H_2S$ concentration in the retentate was un-detectable for approximately 15 hours upon the $H_2S$ introduction and increased gradually to ~ 2 ppm substantiated the hypothesis. The result also implied that

the Pd membrane started to loss $H_2$ permeance in the presence of an extremely small amount of $H_2S$ (< 0.2 ppm).

As shown in Figure 7.5, the permeance of membrane C-10 could be recovered to some extent (~ 67% of the original value) at the same poisoning temperature of 400°C. The recovery of the permeance was resulted from the desorption of the adsorbed sulfur as evidenced by the $H_2S$ concentration detected by the GC during the recovery. Further recovery at 500°C resulted in more $H_2S$ desorption and consequently more permeance recovery as shown in Figure 7.5. After the recovery at 500°C, the permeance of membrane C-10 recovered to 89% of the original value before the $H_2S$ exposure. It should be noted that the recovery at 500°C was continued until the $H_2S$ concentration became un-detectable along with the attainment of the stable $H_2$ permeance (usually within 30 – 60 hours). The result suggested that there were certain amount of adsorbed sulfur was bonded with Pd with higher binding energies and could not desorb under the recovery condition. The binding energy of the adsorbed sulfur increased with decreasing sulfur coverage due to the reduction of the sulfur-sulfur repulsive force (Alfonso, 2005b). As a result, there was sulfur bonded with Pd with higher binding energies than others. This also explained why the rate of permeance recovery and sulfur desorption decreased as the recovery progressed as observed in Figure 7.5. More detailed discussion regarding the permeance recovery phenomenon will be given in *Section 7.3.3*.

After testing in the 0.2 ppm $H_2S$ and the recovery, membrane C-10 was characterized in higher $H_2S$ concentration mixtures. Figure 7.6 shows the relative $H_2$ permeance of membrane C-10 and the $H_2S$ concentration in the retentate as a function of time at 400°C upon exposure to a 1 ppm $H_2S/H_2$ mixture and the subsequent recovery in

$H_2$. A sudden decline in permeance to a steady state value of ~ 20% of the initial permeance upon the introduction of the 1 ppm $H_2S/H_2$ mixture was observed. It should be noted that the initial permeance before the 1 ppm $H_2S$ was not the original permeance before any $H_2S$ exposure since the permeance did not recover to the original value after the 0.2 ppm $H_2S$ test as mentioned previously. Since the $Pd_4S$ sulfide phase was not stable with 1 ppm $H_2S$ at 400°C according to the thermodynamic calculations (Mundschau et al., 2006; Iyoha et al., 2007), the 80% permeance loss of membrane C-10 in 1 ppm $H_2S$ was mainly resulted from the surface site blocking by the adsorbed sulfur.

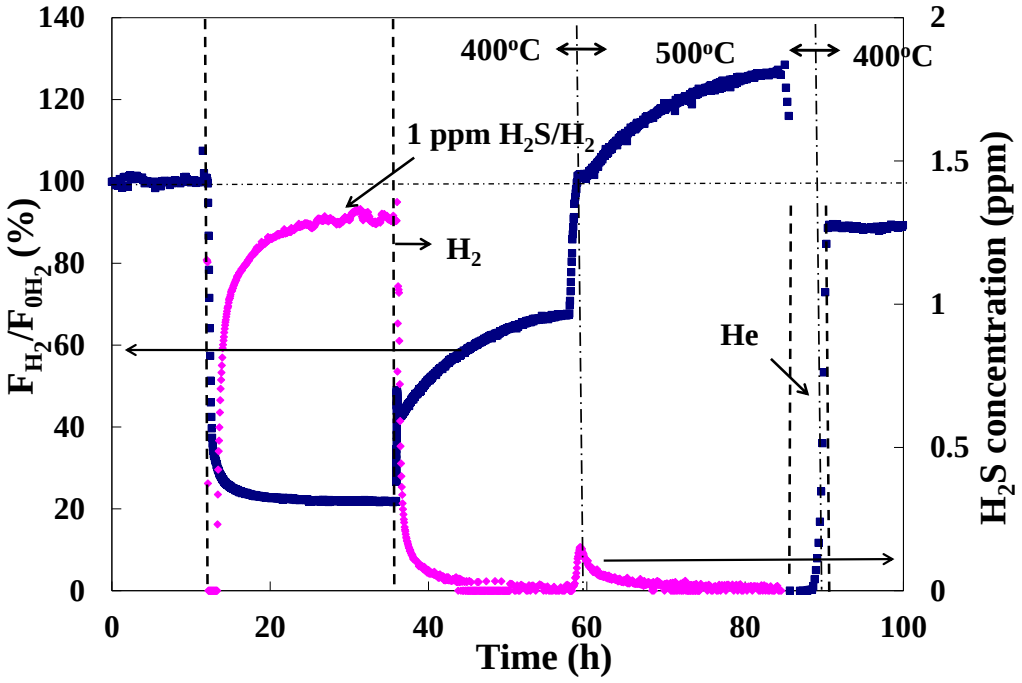


Figure 7.6. The poisoning of membrane C-10 in a 1 ppm $H_2S/H_2$ mixture and the recovery in $H_2$ at 400°C.

As observed in Figure 7.6, the $H_2S$ concentration in the retentate was undetectable within the first 30 minutes upon the $H_2S$ exposure which was due to the $H_2S$ adsorption of the system walls as mentioned earlier. However, the effect of $H_2S$ dilution caused by

the adsorption of the system on the membrane permeance was less apparent compared to the 0.2 ppm $H_2S$ exposure. This was because the time required for the system to reach the equilibrium adsorption was less while feeding a higher $H_2S$ concentration. In addition, a higher $H_2S$ concentration value in the retentate of approximately 1.3 ppm than the set concentration of 1 ppm was observed during the $H_2S$ exposure (Figure 7.6). This was resulted from the decrease of $H_2$ in the retentate due to the $H_2$ permeation through the membrane. The phenomenon was expected to be more apparent on the membranes with higher permeance.

Figure 7.6 also shows that after recovery in $H_2$ at 400 and 500°C, the permeance of membrane C-10 was recovered to ~ 88% of the initial value before the 1 ppm $H_2S$ exposure due to the desorption of the adsorbed sulfur. Once again, the un-recovered permeance loss under the recovery condition was caused by the sulfur bonded with Pd with higher binding energies.

Figure 7.7 shows the relative $H_2$ permeance of membrane C-10 and the $H_2S$ concentration in the retentate as a function of time at 400°C upon exposure to a 10 ppm $H_2S/H_2$ mixture and the subsequent recovery in $H_2$. Immediately after the introduction of 10 ppm $H_2S$, a sudden decline in permeance to a steady state value of ~ 14% of the initial permeance before the 10 ppm $H_2S$ exposure was observed. The rapid decline was due to the fact that the time required for the system to reach the equilibrium adsorption for the relative high $H_2S$ concentration was negligible.

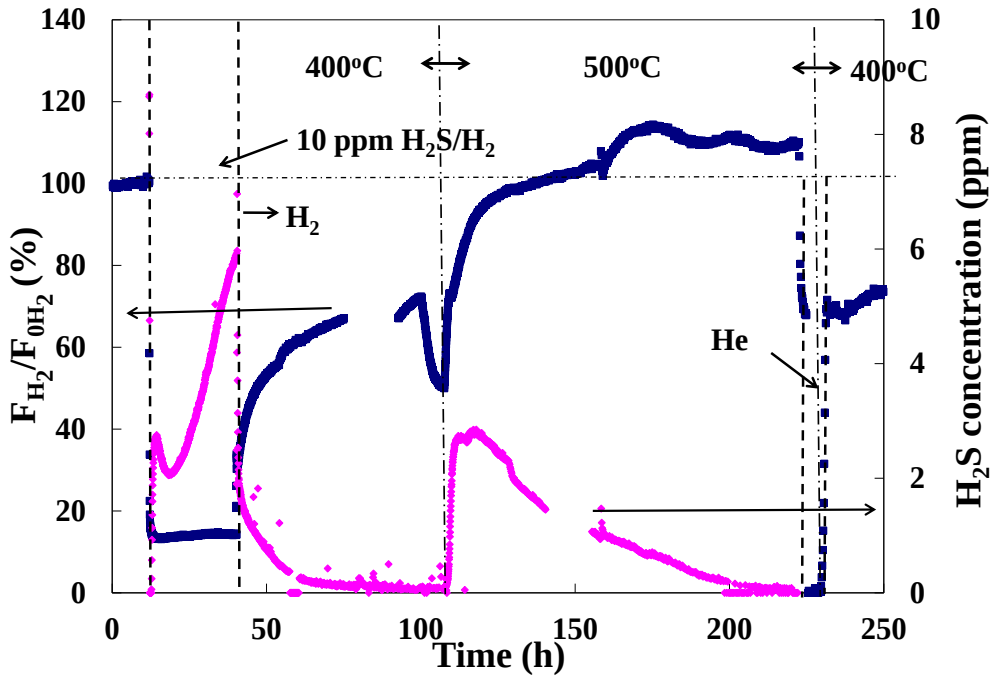


Figure 7.7. The poisoning of membrane C-10 in a 10 ppm $H_2S/H_2$ mixture and the recovery in $H_2$ at 400°C.

According to the thermodynamic prediction (Mundschau et al., 2006; Iyoha et al., 2007), 10 ppm $H_2S$ cause the bulk $Pd_4S$ sulfide to form at 400°C. The coupon study (which will be discussed in *Chapter 8*) also confirmed the formation of $Pd_4S$ phase while exposing to the 10 ppm $H_2S$ at 400°C. In addition, once the adsorption reached the equilibrium (in a short length of time), the $H_2S$ concentration in the retentate also reached a steady state value slightly higher than the feed concentration as seen in Figure 7.6. However, as observed in Figure 7.7, the un-steady and lower $H_2S$ concentration in the retentate during the entire $H_2S$ exposure compared to the feed concentration of 10 ppm suggested the continuous sulfur adsorption by the Pd membrane during the exposure. The continuous adsorption of sulfur was due to the formation of bulk $Pd_4S$. The increase of $H_2S$ concentration in the retentate suggested the rate of sulfur adsorption, and

consequently the rate of $Pd_4S$ formation decreased with time which agreed with the coupon study in *Chapter 8*. Although the bulk $Pd_4S$ sulfide most likely formed in 10 ppm $H_2S$ at 400°C, no continuous permeance decline was observed (Figure 7.7) as compared to the result of 55 ppm exposure (See Figure 7.4). This was most probably due to that the $Pd_4S$ scale formed was too small under the testing condition, resulting in the insignificant permeance decline.

After the recovery in $H_2$ at 400 and 500°C, the permeance of membrane C-10 was recovered to ~ 77% of the initial value before the 10 ppm $H_2S$ exposure as shown in Figure 7.7. The recovery of the permeance was resulted from the desorption of the adsorbed sulfur due to the reverse reaction of the $Pd_4S$ formation. The reverse reaction of the $Pd_4S$ formation was also confirmed by the coupon study (See *Chapter 8*). However, due to the bulk sulfide formation, sulfur in the subsurface of the Pd layer bonded with an even higher binding energy (Alfonso, 2006) caused more un-recovered permeance loss under the recovery condition.

Figure 7.8 shows the percentage of irrecoverable permeance of membrane C-10 as a function of $H_2S$ concentration from 0.2 – 40 ppm. The percentage of irrecoverable permeance was the ratio of the recovered permeance after the poisoning to the original permeance before any $H_2S$ exposure. It should be noted that the sequence of the poisoning and recovery tests was carried out in the order of increasing $H_2S$ concentration (i.e. the first poisoning test was with 0.2 ppm $H_2S$ and the last test was with 40 ppm $H_2S$).

As shown in Figure 7.8, the irreversible permeance loss increased from roughly 10% with 0.2 ppm $H_2S$ to approximately 20% with 1 ppm $H_2S$ and remained the same value with the $H_2S$ concentration up to 5 ppm. It has been reported in the literature

(Barbier et al., 1985) that the amount of irreversibly adsorbed sulfur on the metal catalysts ($Pt/Al_2O_3$) did not change with the poisoning sulfur concentration. It should be noted that the recovery condition used by the authors was at 500°C in $H_2$ for 30 hours. The results of the sulfur poisoning of the Pd membrane indicated that the equilibrium sulfur adsorption which accounted for the irrecoverable permeance was attained with approximately 1 ppm $H_2S$. The 20% permeance loss corresponded to approximately 0.05 ML (monolayer) assuming that each adsorbed sulfur blocks 4 $H_2$ adsorption sites (Burke and Madix, 1990).

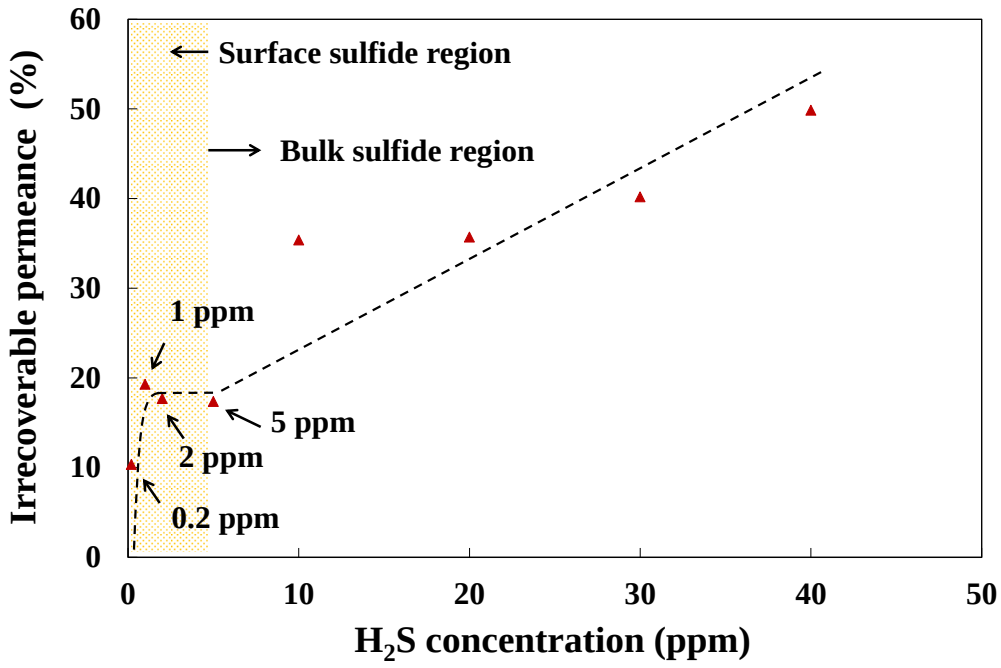


Figure 7.8. Percentage of irrecoverable permeance of membrane C-10 at 400°C as function of $H_2S$ concentration (The dotted area indicated the unstable sulfide region according to the thermodynamic calculation (Mundschau et al., 2006)).

As the $H_2S$ concentration was increased beyond 5 ppm, the irrecoverable permeance appeared to increase with increasing $H_2S$ concentration. This was probably due to the fact that the formation of bulk sulfide increased the amount of sulfur in the

sub-layer of Pd with high binding energy. Since the bulk sulfide increased with increasing $H_2S$ concentration, more sulfur boned with higher binding energies increased with increasing $H_2S$ concentration. It should be noted that according to the thermodynamic calculation (Mundschau et al., 2006), the stable $Pd_4S$ phase formed when the $H_2S$ concentration was higher than approximately 3 ppm at 400°C.

The He leak and the ideal $H_2$/He selectivity of membrane C-10 at 400°C as a function of the elapsed time during the $H_2S$ testing was plotted in Figure 7.9. The He leak was measured at the end of each $H_2S$ testing including the recovery at 500°C with a pressure difference of 1 atm ($P_{feed}$ = 2 atm, $P_{permeate}$ = 1 atm). As observed in Figure 7.9, below 2 ppm of $H_2S$, the He leak was small (< 0.06 sccm) after the exposure and increased insignificantly with increasing $H_2S$ concentration. However, as the $H_2S$ concentration was greater than 15 ppm, the He leak became more noticeable and increased rapidly with increasing $H_2S$ concentration. Since the bulk $Pd_4S$ would form with the $H_2S$ concentration greater than roughly 3 ppm at 400°C (Mundschau et al., 2006), the large He leak observed in the concentration range was due to the formation of bulk sulfide which deteriorated the membrane structure as mentioned previously.

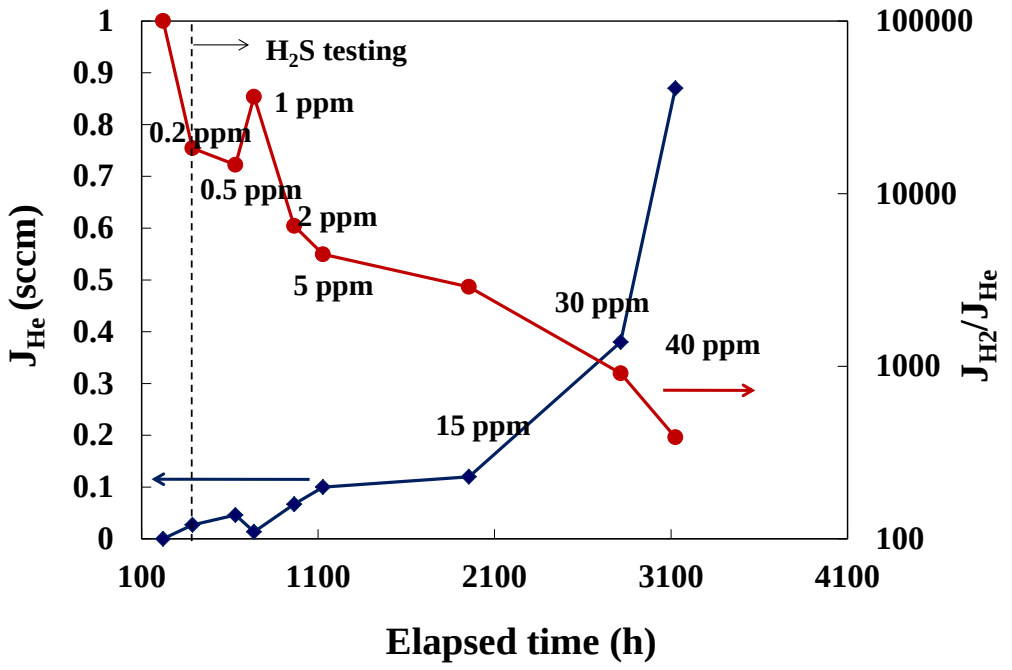


Figure 7.9. The He leak flux and the ideal selectivity history (measured as $\Delta p$ = 1atm, $P_{feed}$ = 2 atm, $P_{permeate}$ = 1 atm) of membrane C-10 during the $H_2S$ testing.

### *7.3.3 Effect of $H_2S$ exposure on the performance of Pd/Au membrane*

Figure 7.10 shows the relative $H_2$ permeance ($F_{H2}/F_{0H2}$) of membrane C-04 (~8 wt% Au) as a function of time at 400°C upon exposure to a 55 ppm $H_2S/H_2$ mixture and the subsequent recovery in $H_2$. A sharp decline in $H_2$ permeance by approximately 85% was observed on membrane C-04 within minutes upon the $H_2S$ exposure. However, the permeance reached a steady state value immediately and remained unchanged for the entire exposing duration of 4 hours. This suggested that the permeance decline of membrane C-04 was resulted from only the surface site blocking without bulk sulfidation. This is due to the fact that the formation of the bulk sulfide caused the continuous permeance decline due to the thickening of the sulfide layer of low $H_2$ permeability (See Figure 7.4).

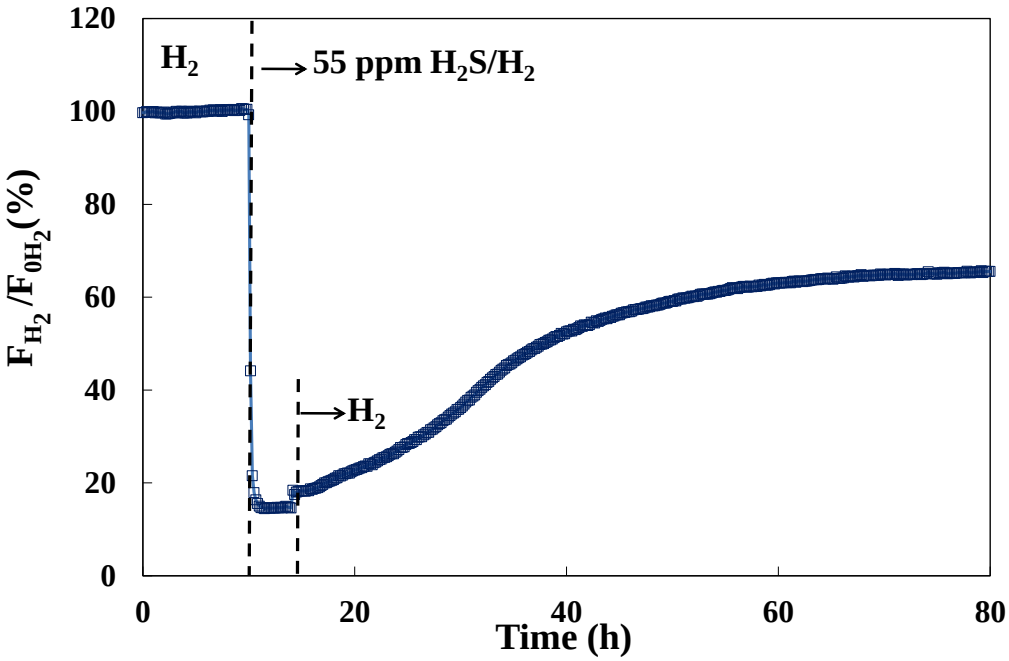


Figure 7.10. The poisoning of membrane C-04 in a 55 ppm $H_2S/H_2$ mixture and the recovery in $H_2$ at 400°C.

The ideal $H_2$/He selectivity of membrane C-04 at 500°C before and after the $H_2S$ testing at 400°C was 142 with a He leak of 0.87 sccm and 139 with a He leak of 0.94 sccm, respectively. No significant change in the $H_2$/He selectivity indicated that the change in the structure of membrane C-04 caused by the $H_2S$ exposure was minimum, substantiating the fact that no bulk sulfide was formed. In fact, the He leak and the ideal selectivities of membrane C-04 during the entire $H_2S$ poisoning/recovery test of approximately 3000 hours were very similar. The He leak at 500°C oscillated between 0.8 - 1.0 sccm resulting in the ideal selectivities within 110 - 250. In addition, the results of the sulfur poisoning experiments on the Pd/Au coupons also confirmed the lack of bulk sulfide formation on the Pd/Au layers after the $H_2S$ exposures under the similar testing conditions. The detailed sulfur poisoning study on the coupons will be given in *Chapter 8*.

As mentioned in *Section 2.6.2*, the surface site blocking effect by adsorbed sulfur referred not only to the simple geometric blocking of adsorption sites but also the electronic blocking effect, due to the adsorbed sulfur generating an energy barrier for $H_2$ dissociative adsorption and diffusion. As a result, each adsorbed sulfur effectively blocks 4 to 13 sites for $H_2$ adsorption (Burke and Madix, 1990; Gravil and Toulhoat, 1999; Lang et al., 1985). Based on the percentage of the observed permeance loss, the sulfur coverage on membrane C-04 was approximately between 0.07 – 0.21 ML (monolayer). In fact, 0.3 – 0.5 ML sulfur coverage was sufficient to block all the $H_2$ adsorption sites on the Pd surface according to previous studies (Burke and Madix, 1990; Gravil and Toulhoat, 1999; Wilke and Scheffler, 1995). The results also suggested that, the time required to reach the adsorption equilibrium between $H_2S$ and the Pd/Au alloy surface was very short, within only a few minutes.

Figure 7.10 also shows that the permeance loss of membrane C-04 after the $H_2S$ exposure could be recovered. A steady state value of approximately 65% of the original permeance was recovered in pure $H_2$ at the poisoning temperature of 400°C. This indicated that the bonding between the adsorbed sulfur and the Pd/Au alloy surface was partially reversible since the $H_2$ permeance recovery was associated with desorption of the adsorbed sulfur. Upon the pure $H_2$ introduction, the gas-solid equilibrium of the $H_2S$ dissociative adsorption shifted due to the decrease of the $H_2S$ concentration in the gas phase, resulting in the desorption of adsorbed sulfur and the recovery of the $H_2$ permeance. The variation of the permeance recovery rate (slope) as shown in Figure 7.10 suggested that the desorption rate of the adsorbed sulfur varied along the recovery process. After an instantaneous increase of ~4% in permeance, a linear recovery to ~52%

of the original permeance within 24 hours took place followed by an a much slower rate approaching asymptotically to the steady state value of ~65% of the original permeance.

The possible reason for the variation of the desorption rate of the adsorbed sulfur was that the adsorbed sulfur was bonded to the Pd/Au alloy surface with different binding energies. It has been shown by the theoretical calculations that the binding energy of sulfur to Pd decreased as the sulfur coverage was increased (from 5.07 ev/ S atom at 0.11 ML to 3.29 ev/S atom at 1 ML) due to the increase of the repulsive force between sulfur atoms with increasing sulfur coverage (Alfonso, 2005b). As the sulfur coverage decreased during the recovery, the binding energy between sulfur and Pd increased, resulting in the lower desorption and permeance recovery rate. A similar phenomenon of stage-wise permeance recovery has also been observed in Pd/Cu alloy membranes (Pomerantz and Ma, 2009). In addition, the linear permeance recovery rate was found to be temperature dependent. Since the permeance recovery was primarily associated with the desorption of sulfur from the membrane surface, the activation energy for desorption of the adsorbed sulfur was estimated to be 94 kJ/mol based on the linear permeance recovery rate in the temperature range of 350 - 500$^{\circ}$C. The value was within the chemisorption regime and consistent with the dissociative (chemical) adsorption mechanism of $H_2S$.

In order to verify if the unrecovered permeance was the result of the irreversible sulfur on the surface of membrane C-04, further recovery in $H_2$ was performed on membrane C-04 at the higher temperature of 500$^{\circ}$C and the result is shown in relative permeance in Figure 7.11.

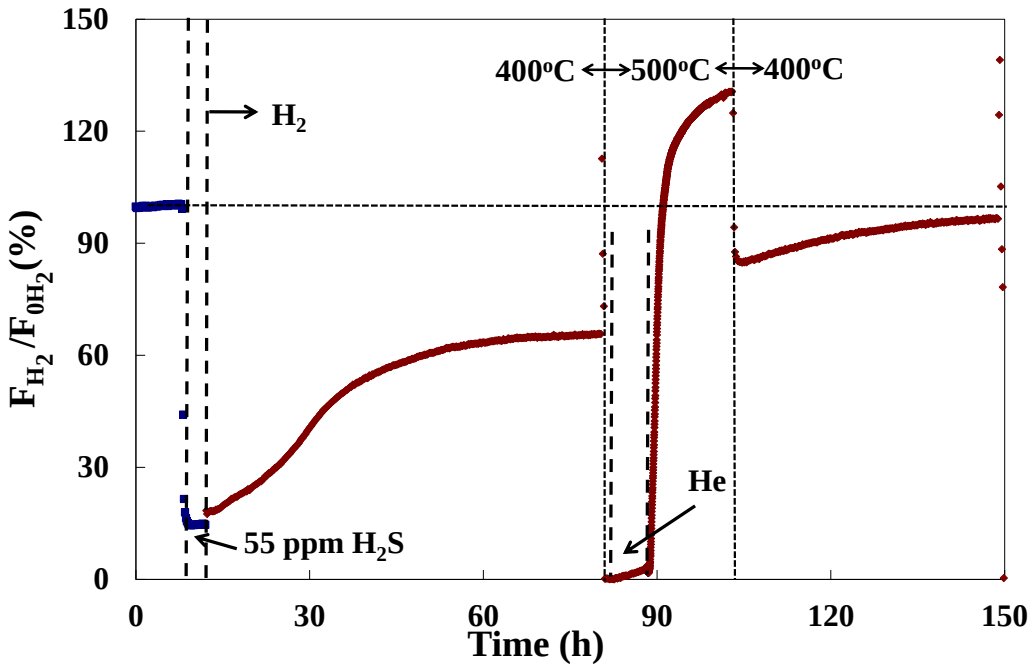


Figure 7.11. The recovery of $H_2$ permeance of membrane C-04 in pure $H_2$ at 400°C and 500°C (Membrane C-04 was poisoned at 400°C).

As seen in Figure 7.11, after increasing the temperature to 500°C for approximately 24 hours (including roughly 5 hours in He for the leak measurement), the permeance of membrane C-04 was nearly fully recovered to over 97% of its original permeance at 400°C. Since the dissociative adsorption of $H_2S$ on metals was exothermic, desorption of adsorbed sulfur became more favorable due to the shifting of equilibrium toward gas phase at higher temperatures resulting in more permeance recovery. In addition, more energy was provided to the membrane surface at higher temperatures to desorb the adsorbed sulfur with higher binding energies. A very small portion of the permeance (less than 3%) was still not recoverable after 24 hours at 500°C, indicating the existence of a small portion of adsorbed sulfur with even higher binding energies. Nevertheless, the results suggested that the poisoning of the Pd/Au alloy membrane was

caused by only the surface site blocking poisoning mechanism without bulk sulfidation in a 55 ppm $H_2S/H_2$ mixture, and ~100% recovery was possible. The full permeance restorations of the Pd/Au alloy ($Pd_{60}Au_{40}$) foils in $H_2$ have also been reported by McKinley (1967) after exposing to 4 - 6600 ppm $H_2S/H_2$ mixtures. The author also reasoned that the permeance loss during the $H_2S$ exposure was caused by the surface site blocking due to the adsorption of $H_2S$ rather than the bulk sulfide formation.

### *7.3.4 Effect of the temperature of $H_2S$ exposure on membrane performance*

The same poisoning experiments including the subsequent recoveries in pure $H_2$ were performed on membrane C-04 at other temperatures in order to investigate the effect of temperature on $H_2S$ poisoning. At each testing temperature, membrane C-04 was exposed to a 55 ppm $H_2S/H_2$ mixture for 4 hours followed by a recovery period in pure $H_2$ at the same temperature. After a steady state permeance recovery was reached, the temperature was then increased to 500°C to fully recover the permeance before the next poisoning/recovery test.

Figure 7.12 displays the relative permeance of membrane C-04 upon exposure to a 55 ppm $H_2S/H_2$ mixture and the subsequent recovery in $H_2$ (before the full recovery at 500°C) as a function of time in the temperature range of 350 - 500 °C. The instantaneous decline in permeance to a steady value after the $H_2S$ introduction during the 4 hours duration of exposure was observed at all testing temperatures with the only difference being in the percentage of the permeance decline. This indicated that the surface site blocking effect by the dissociative adsorption of $H_2S$ took place and accounted for the permeance loss in the entire testing temperature range. In addition, the similar permeance recovery phenomenon with the recovery rate changing in stages during the recovery

process was also observed at all testing temperatures. However, the recovery rate and degree of recovery were different at different temperatures, substantiating that the permeance recovery was associated with the sulfur desorption from the membrane surface.

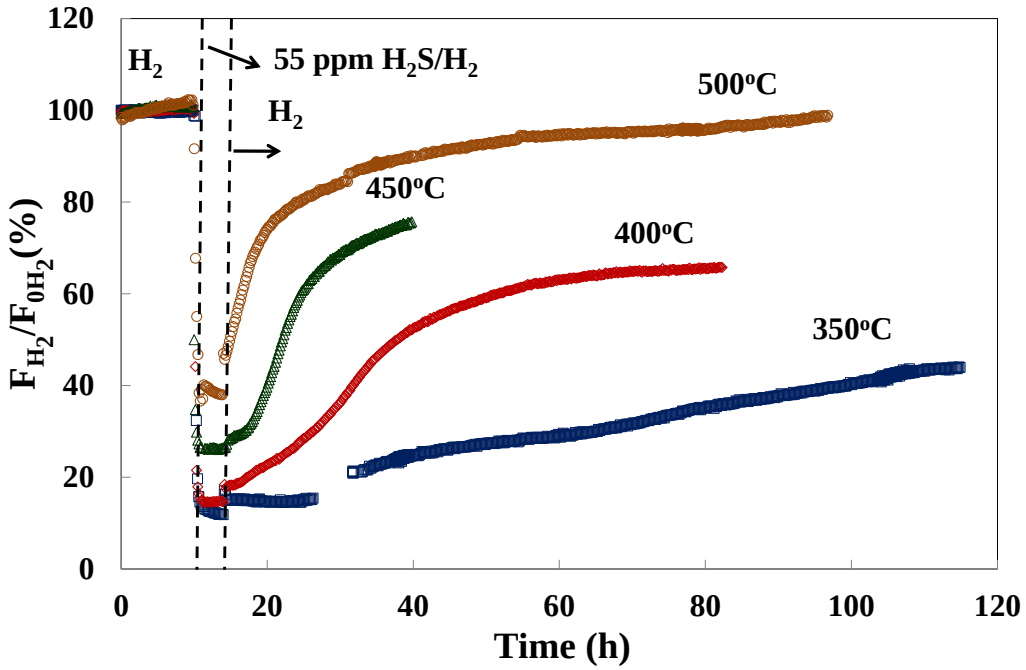


Figure 7.12. The poisoning and the recovery of membrane C-04 in a 55 ppm $H_2S/H_2$ mixture as a function of time at different temperatures. The temperature next to the curves indicates the poisoning and recovery temperature.

Figure 7.13 summarized the percentages of the permeance remained during the $H_2S$ poisoning and permeance recovered in $H_2$ at different temperatures. Not only did a higher percentage of permeance remain during the $H_2S$ exposure, but also a higher permeance recovery was observed at higher temperatures. The temperature dependence of the permeance remained/recovered once again substantiated the surface adsorption related poisoning effect due to the exothermic nature of the dissociative adsorption of

$H_2S$ on metals. The equilibrium of gas-solid adsorption of sulfur shifted toward gas phase at higher temperatures resulting in less permeance decline and more permeance recovery.

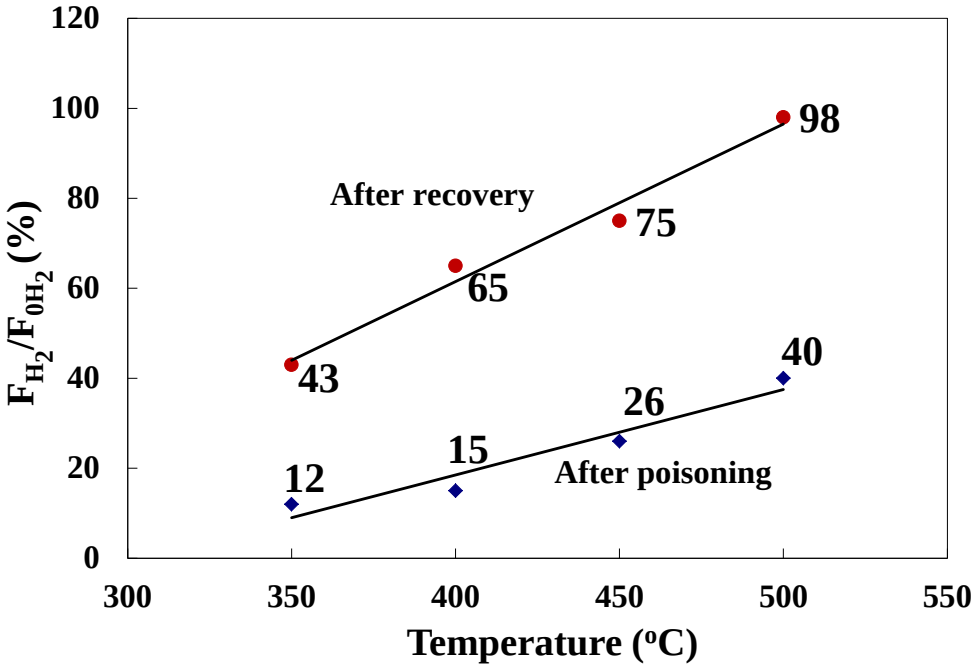


Figure 7.13. $H_2$ permeance after the poisoning (in a 55 ppm $H_2S/H_2$ mixture) and after the recovery (at the poisoning temperature) of membrane C-04 as a function of temperature.

Membrane C-04 showed a greater permeance decline in the presence of $H_2S$ when compared to work in the literature. Upon exposure to a 20 ppm $H_2S/H_2$ mixture at 350°C, McKinley (1967) reported a 56% decline in $H_2$ flux of the Pd/Au alloy foil with 40 wt% Au. Way et al. (2008) reported that a 38% decline in permeance was observed at 400°C when a $Pd_{85}Au_{15}$ alloy membrane was exposed to a 5 ppm $H_2S/H_2$ mixture. The higher $H_2S$ concentrations used in the current study accounted for the higher permeance loss due to the thermodynamic equilibrium of the $H_2S$ adsorption on the membrane surface. In addition, less Au content in membrane C-04 also resulted in more permeance decline since the stability of the bonding between sulfur and Pd/Au alloy decreased with

increasing Au content in the alloy (Alfonso, 2005; Way et al. 2008). Further discussion regarding the influence of $H_2S$ concentration and Au composition on the sulfur tolerance is provided in *Section 7.3.7*.

### *7.3.5 Effect of the length of $H_2S$ exposure time on membrane performance*

Figure 7.14 summarized the relative permeance of membrane C-04 upon exposures to a 55 ppm $H_2S/H_2$ mixture with the exposure durations of 4, 8, 12, and 24 hours and the subsequent recoveries in $H_2$ (before the full recovery at 500°C) as a function of time at 400°C. As shown in Figure 7.14, the similar instantaneous permeance drop to a steady state value upon the $H_2S$ introduction was observed on the tests with different exposure durations. In addition, the extents of permeance decline were nearly identical with 85 – 90% of the original permeance during the tests of different testing durations (i.e. the degree of the permeance decline did not increase as the exposure time was increased.). Similar phenomenon with exposure time showing no effect on the degree of permeance decline of the Pd/Cu alloy membranes while exposing to $H_2S$ have been reported in literature (Morreale et al., 2004; Kulprathipanja et al., 2005).

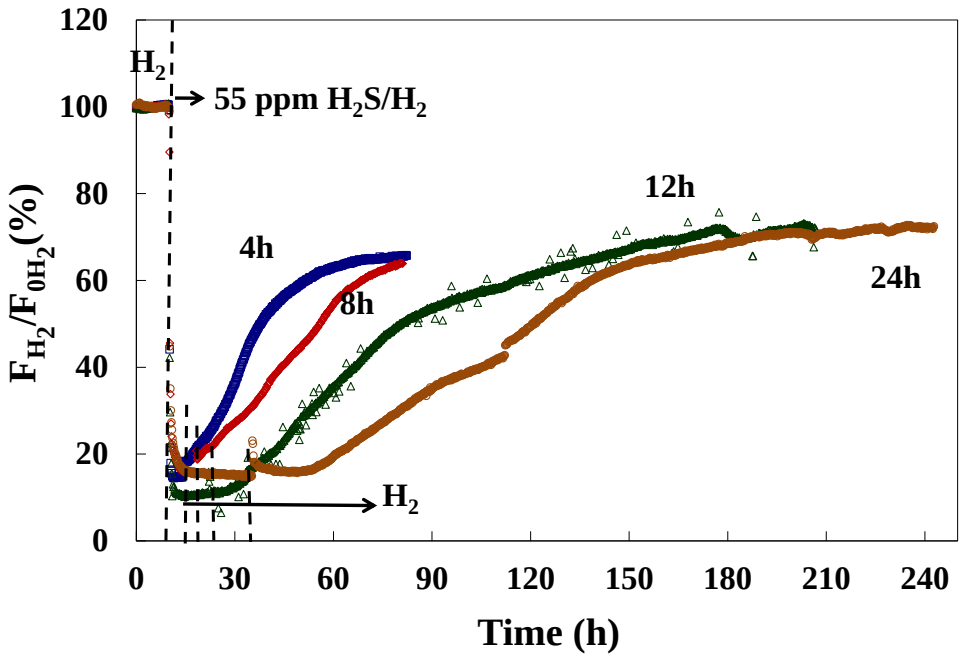


Figure 7.14. The poisoning and the recovery of membrane C-04 in a 55 ppm $H_2S/H_2$ mixture at 400°C as a function of $H_2S$ exposure time. The time next to the curves indicates the exposure duration.

No influences of the exposure time on the degree of the permeance loss once again substantiated the surface poisoning mechanism rather than the bulk sulfidation. Since the thermodynamic equilibrium of gas-solid adsorption of sulfur on the Pd/Au surface was fast (within a few minutes) and time independent, the percentage of surface adsorption sites occupied by the adsorbed sulfur was not affected by the exposure time.

Although increasing the exposure time did not increase the extent of the permeance decline, longer exposure time increased the time required to recover the permeance to the steady state values as observed in Figure 7.14. The slower recovery rates after the longer exposures suggested that the amount of adsorbed sulfur with higher binding energies increased with increasing exposure time. Previous theoretical calculations indicated that beyond a certain sulfur coverage (0.75 ML), the incorporation

of sulfur into the subsurface of Pd became more energetically favorable than continuous adsorption on the surface (Alfonso, 2006). The longer exposure time potentially increased the subsurface bonded sulfur with a higher binding energy without increasing the surface sulfur coverage. As a result, the permeance recovery after a longer $H_2S$ exposure time occurred with a slower rate.

Pomerantz and Ma (2009) investigated the effect of exposure time on the recovery of the Pd/Cu membranes. 65% of the original permeance was recovered in 500 hours in $H_2$ at 450°C after 125 hours exposure to a ~50 ppm $H_2S/H_2$ at the same temperature, while 80% of the original permeance was recovered within 95 hours after 2 hours exposure to the $H_2S$ under the same conditions. The authors reasoned that the amount of irreducible surface sulfides increased with increasing exposure time.

### *7.3.6 Effect of the $H_2S$ concentration of $H_2S$ exposure on membrane performance*

In this section, the influence of the $H_2S$ concentration in the $H_2S/H_2$ gas mixture on the performance of the Pd/Au membranes was discussed. The $H_2S$ concentration range studied was mainly within 0.2 – 5 ppm. This was due to the significant permeance decline (60 – 90% at 350 - 500°C) of the Pd/Au membrane (i.e. membrane C-04) in the presence of 55 ppm $H_2S$ as discussed in the previous sections. In order to better investigate the $H_2S$ concentration effect on the $H_2$ permeance decline, small increments of the $H_2S$ concentrations were used. Moreover, the understanding of the performance of the Pd/Au membranes in the presence of small $H_2S$ concentrations was also important for the practical applications and worth to be investigated.

Figure 7.15 shows the relative $H_2$ permeance ($F_{H2}/F_{0H2}$) of membrane C-09 (~4.2 wt% Au) as a function of time at 400°C upon exposure to a 2 ppm $H_2S/H_2$ mixture and

the subsequent recovery in $H_2$ at 450°C and 500°C. The $H_2S$ concentration in the retentate (at the outlet of the shell side) monitored by the GC during the testing and recovery was also plotted in Figure 7.15 (the right-hand side *y*-axis). Upon the $H_2S$ exposure, the hydrogen permeance decreased to 21% of the original value over a period of 24 hours. Since the sulfur poisoning effect on the Pd/Au membranes was resulted from the surface sulfur adsorption, this indicated that approximately 79% of the surface active sites for hydrogen dissociation were blocked by the adsorbed sulfur.

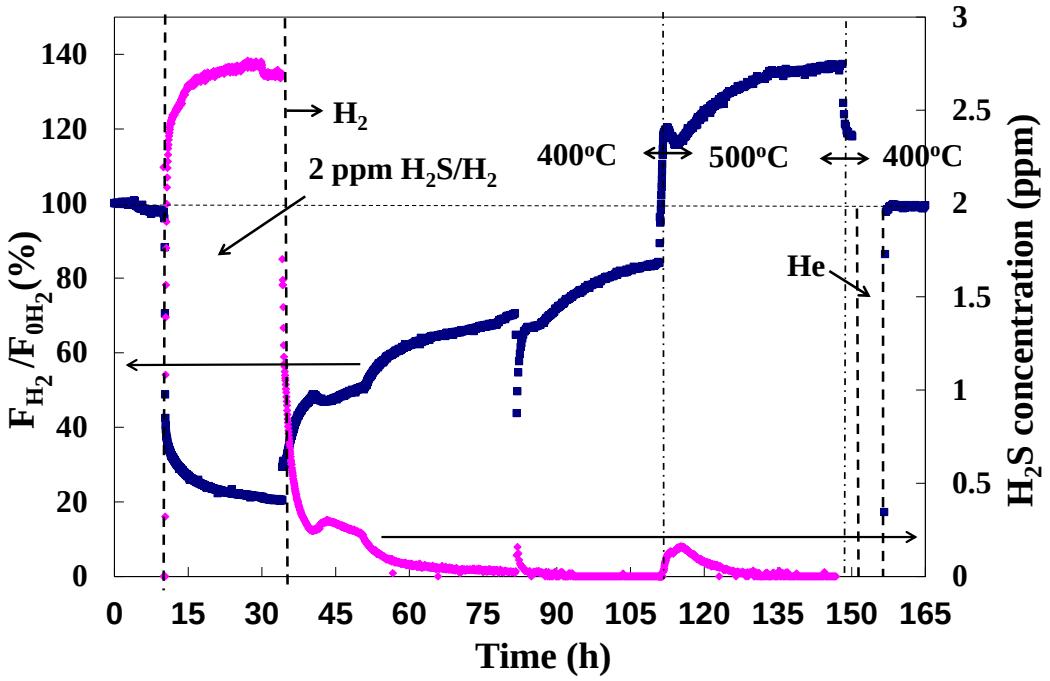


Figure 7.15. The poisoning of membrane C-09 at 400°C in a 2 ppm $H_2S/H_2$ mixture and the recovery in pure $H_2$ at 400°C and 500°C.

Based on the percentage of the permeance loss, the sulfur coverage on membrane C-09 was approximately between 0.06 – 0.20 ML (monolayer) assuming one sulfur atom effectively blocks 4 – 13 sites (Burke and Madix, 1990; Gravil and Toulhoat, 1999; Lang et al., 1985). The estimated sulfur coverage resulted from the exposure to the 2 ppm $H_2S$

was very close to the value (0.07 – 0.21 ML) caused by the exposure to the 55 ppm $H_2S$ as discussed in the previous section. This indicated that the gas-solid adsorption equilibrium between $H_2S$ and the Pd/Au surface was attained with a very small gaseous $H_2S$ concentration.

After the $H_2S$ exposure, pure $H_2$ was reintroduced to the system at the same temperature (400°C) for the permeance recovery. As shown in Figure 7.15, the permeance was recovered to 89% of the original value over 24 hours. The rate of permeance recovery decreased as the recovery progressed as expected due to the decrease of sulfur desorption rate as discussed in the previous section. The $H_2S$ concentration in the retentate during the recovery at 400°C substantiated the variation in $H_2S$ desorption rate. More $H_2S$ with a higher rate was desorbed initially and decreased as the recovery time increased (became un-detectable after ~ 14 hours). The results confirmed that the hydrogen permeance recovery was directly related to the $H_2S$ desorption, and the higher permeance recovery rate was resulted from the higher $H_2S$ desorption rate.

Figure 7.15 also shows that the full restoration of the permeance was possible after the further recovering at 500°C. This was resulted from more $H_2S$ desorption at the higher temperature due to the exothermal nature of the sulfur adsorption as mentioned earlier. Indeed, as observed in Figure 7.15, more $H_2S$ was desorbed from the membrane and detected by the GC at 500°C after the long un-detectable period at 400°C. Similar to recovering the Pd membrane as described earlier, the recovery of the Pd/Au membrane at 500°C was conducted until the $H_2S$ concentration became un-detectable along with the attainment of the stable $H_2$ permeance. The recovery time at 500°C was within 30 – 60 hours.

Finally, a slight permeance decline during the poisoning duration was observed in Figure 7.15, which was caused by the slight increase of the $H_2S$ concentration in the feed. As mentioned previously, this was because the $H_2S$ concentration in the mixed gas was diluted initially due to the sulfur adsorption of the system wall. In addition, the $H_2S$ concentration in the retentate increased to a higher value of 2.7 ppm than the desired feed concentration of 2 ppm since the $H_2$ in the retentate permeating through the membrane during the exposure. Nevertheless, the steady state permeance and the $H_2S$ concentration in the retentate were achieved in the latter stage of the exposure as shown in Figure 7.15.

Figure 7.16 is the relative permeance history of membrane C-09 during the testing with a 0.2 ppm $H_2S/H_2$ at 450°C and the subsequent recovery in pure $H_2$ at 450°C and 500°C. As seen in Figure 7.16, the permeance remained unchanged (i.e. 100%) for approximately 2 hours upon the $H_2S$ exposure along with the un-detectable $H_2S$ concentration in the retentate for approximately 3 hours. Once again, this was due to the dilution of the $H_2S$ in the feed resulted from the sulfur adsorption of the system walls. As expected, the phenomenon became more obvious while the feeding $H_2S$ concentrations were smaller. Compared to membrane C-10 which showed the permeance decline in the $H_2S$ concentration range below 0.2 ppm (as shown in Figure 7.5), the unchanged permeance of membrane C-09 in the initial exposure stage suggested the better sulfur tolerance of the Pd/Au membrane. In addition, due to the $H_2$ permeation through the membrane, the $H_2S$ concentration in the retentate was higher (0.22 ppm) than the feed concentration (0.2 ppm). The permeance of membrane C-09 was 60% of the original value over 24 hours in 0.2 ppm $H_2S$ at 450°C, and the permeance loss was fully recovered after the recovery at 500°C as expected (as shown in Figure 7.16). The He leak

of membrane C-09 at 500°C increased from 0.17 to 0.41 sccm (Δp = 1atm, $P_{feed}$ = 2 atm, $P_{permeate}$ = 1 atm), resulting in the ideal selectivity decreasing from 2700 to 1150 over the entire $H_2S$ testing (up to 5 ppm $H_2S$) of approximately 2600 hours. This indicated the insignificant impact of the $H_2S$ exposure on the membrane structure.

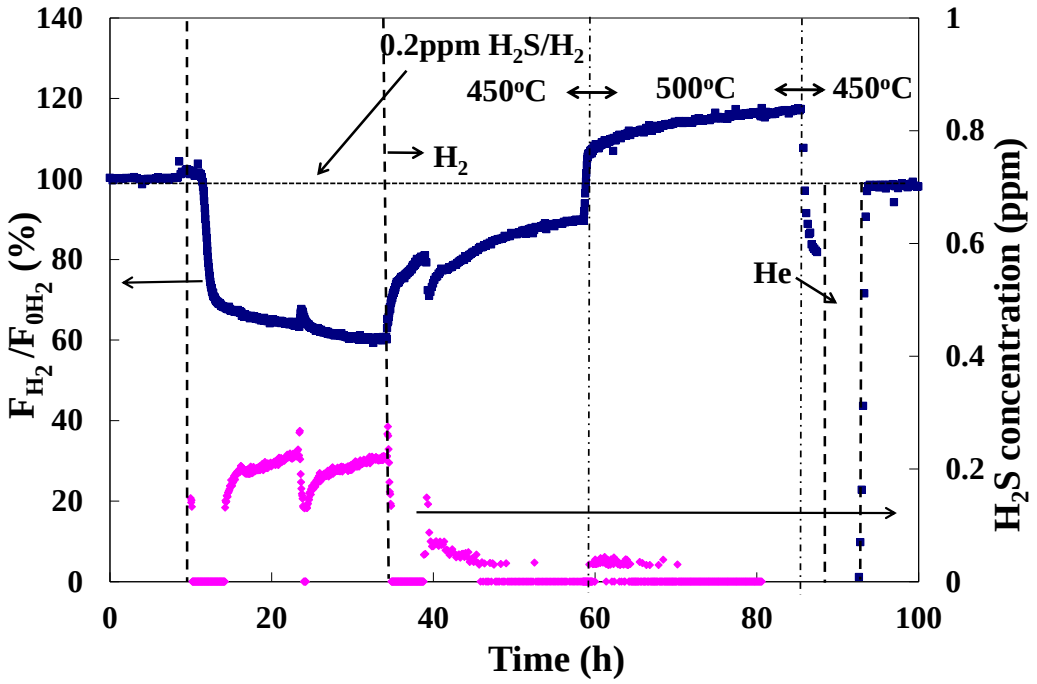


Figure 7.16. The poisoning of membrane C-09 at 450°C in a 0.2 ppm $H_2S/H_2$ mixture and the recovery in pure $H_2$ at 450°C and 500°C.

Figure 7.17 shows the relative permeance history of membrane C-09 during the $H_2S$ poisoning and the subsequent recovery in $H_2$ at 450ºC with the $H_2S$ concentration of 0.2 – 2 ppm. The result of the 55 ppm $H_2S$ exposure on membrane C-04 at the same temperature was also plotted in Figure 7.17. Similar permeance decline phenomenon was observed with all the $H_2S$ concentrations, indicating the same surface blocking mechanism caused by $H_2S$. As expected, higher $H_2S$ concentrations resulted in more permeance decline during the testing due to more surface active sites were blocked.

Figure 7.17 also shows that upon the permeance recovery, the permeance recovery rates as well as the extents of the permeance recovered after the poisonings with different $H_2S$ concentrations were very similar. This indicated that the desorption of $H_2S$ was mainly affected by temperature and independent of the $H_2S$ concentration.

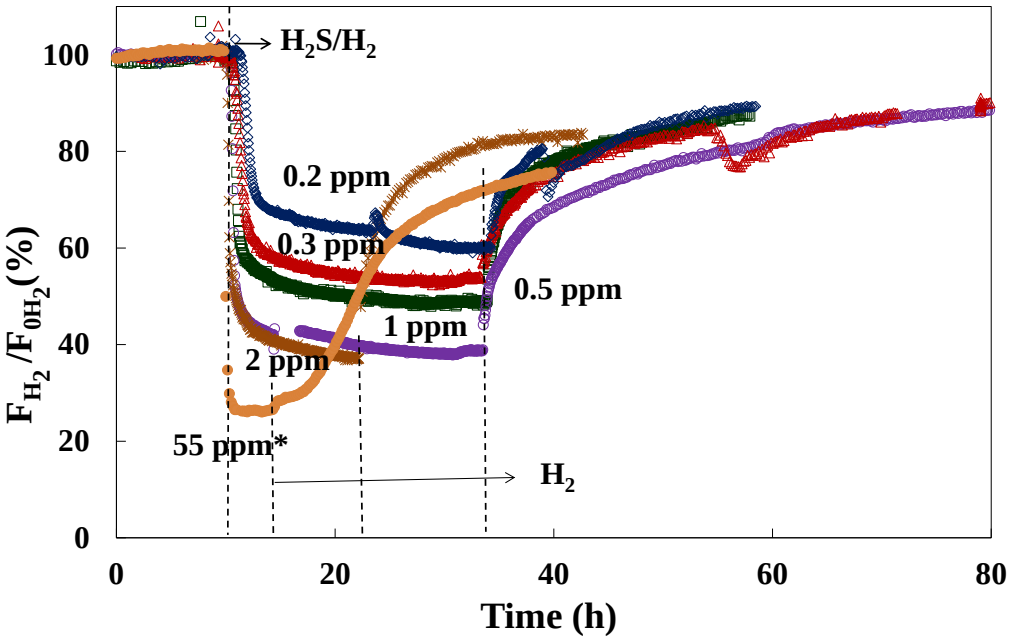


Figure 7.17. The poisoning and the recovery of membrane C-09 at 450°C as a function of time with different $H_2S$ concentrations. The concentration next to the curves indicates the $H_2S$ concentration used for the poisoning. * The 55ppm data were taken from the results of membrane C-04. The exposure time was 24 hours except for the 2 ppm (12 hours) and 55 ppm (4 hours) exposure.

Figure 7.18 summarized the percentages of the permeance loss $((F_{0H2} - F_{H2})/F_{0H2})$ of membrane C-09 as a function of $H_2S$ concentration at 400 - 500°C. The results of the 55 ppm $H_2S$ exposure on membrane C-04 were also included in Figure 7.18. As observed in Figure 7.18, the amount of the permeance loss increased with increasing $H_2S$ concentration at all the testing temperatures. This was due to more surface sites were

blocked with higher $H_2S$ concentration as described earlier. In addition, more permeance loss was observed at low exposure temperature with the same $H_2S$ concentration. Once again, this was due to that the adsorption was favored at lower temperatures.

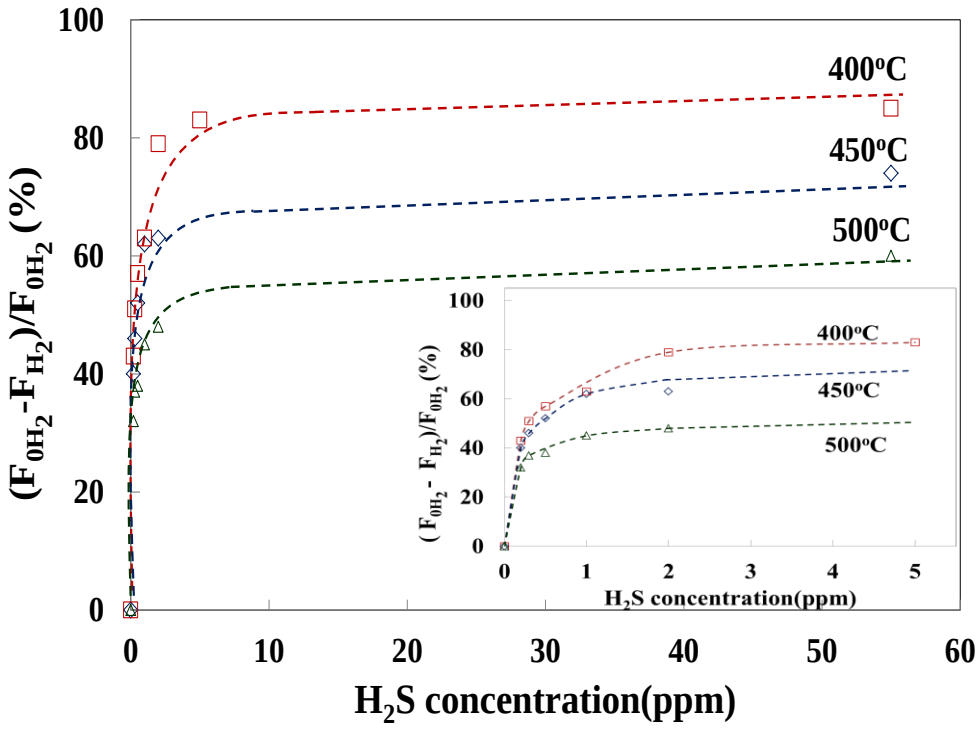


Figure 7.18. Permeance loss of membrane C-09 during the $H_2S$ exposure as a function of $H_2S$ concentration at 400 - 500°C (The 55ppm data was taken from the results of membrane C-04). The insert is the zoom in at the low concentration range.

However, the extent of the permeance loss decreased as the $H_2S$ concentration was increased (i.e. the slope of the curve decreased with increasing $H_2S$ concentration). As a result, the amount of permeance loss appeared to reach a constant value asymptotically. This was most likely due to that the gas-solid phase adsorption between the Pd/Au alloy surface and the gaseous $H_2S$ reached the saturation equilibrium capacity. The equilibrium permeance loss at 400, 450, 500°C were approximately 85, 74, 60% (measured with 55 ppm $H_2S$) which corresponded to sulfur coverages of 0.07 - 0.21, 0.06

- 0.19, 0.05 - 0.15 ML. In addition, the $H_2S$ concentration required to reach the saturation equilibrium capacity was small, roughly 5 – 10 ppm. The above estimation was based on the assumption that the permeance decline would not increase significantly beyond 55 ppm $H_2S$. Unfortunately, there was no testing with the $H_2S$ concentration greater than 55 ppm in the study. Another assumption made in the estimation was that the permeance loss was only resulted from the surface sulfur adsorption and no bulk sulfidation. In the concentration range where bulk sulfidation occurred and also accounted for the permeance loss, such an estimation would not be valid.

By assuming the permeance loss was only resulted from the surface sulfur adsorption without bulk sulfide formation, Figure 7.18 also represented the adsorption isotherms of $H_2S$ at 400 - 500°C on the Pd/Au alloy surface since the $H_2S$ concentration in the gaseous $H_2S/H_2$ mixture could be considered as the partial pressure of $H_2S$. Based on the shapes of the curves in Figure 7.18, these isotherms were most likely the Type I adsorption isotherm according to the classification proposed by Gregg and Sing (1967). Type I adsorption isotherm describes the monolayer adsorption with a limiting value of surface coverage with increasing adsorbate pressure. Type I adsorption isotherm was linear at low pressure range (Gasser, 1985). At the linear range, the adsorption followed Henry's law which described that the mole fraction in the condense phase of the component is proportional to the partial pressure of the component in the gaseous phase. The validity of the Henry's law at low pressure range was due to the interactions between the adsorbed molecules were negligible. Previous theoretical study by Alfonso (2005b) showed that significant S-S interactions took place at high coverages (> 0.5 ML) resulting in the strength of Pd-S bonding decreased.

The gas-solid equilibrium can be described by the Van't Hoff equation as shown in Equation 7.1 by assuming the heat of adsorption ($\Delta H$) is independent of temperature over modest temperature ranges (Gasser, 1985).

$$\left(\frac{d(\ln p)}{dT}\right)_{\theta} = \frac{\Delta H}{RT^2} \tag{7.1}$$

Where $T$ is the absolute temperature, $R$ is the universal gas constant, $\Delta H$ is the heat of the adsorption, and $p$ is the partial pressure of the adsorbate in gaseous phase. Integrating Equation 7.1 gave rise to Equation 7.2

$$\left(\ln(\frac{p_{H_2S}}{p_{H_2}})\right)_{\theta} = -\frac{\Delta H}{R}\left(\frac{1}{T}\right) \tag{7.2}$$

The heat of the adsorption ($\Delta H$) could, therefore, be estimated from the adsorption isotherm of $H_2S$ at different temperatures (i.e. from the semi-log plot where $\left(\ln(\frac{p_{H_2S}}{p_{H_2}})\right)_{\theta}$ is a function of $\left(\frac{1}{T}\right)$. It should be noted that the heat of adsorption is a function of surface sulfur coverage ($\theta$). Oudar et al. (1980a) have taken similar approach to calculate the heat of sulfur adsorption on different metals including Ag, Cu, Pt.

By the use of Equation 7.2 and the results shown in Figure 7.18, the heat of $H_2S$ adsorption on the Pd/Au surface at 400 – 500ºC was estimated. The heat of adsorption was estimated to be 72 kJ/mol with a fixed permeance loss of ~45% (corresponded to 0.03 – 0.11 ML sulfur coverage) at 400 – 500 ºC. The estimated heat of $H_2S$ adsorption on the Pd/Au alloy was within the range of the sulfur adsorption on metals reported in the literature (McCarty et al., 1983; Oudar et al., 1980a). However, no literature value of the heat of $H_2S$ adsorption on the Pd/Au alloy was available for comparison. It should be

noted that the estimation was based on the assumption that the permeance loss was only the result of the surface adsorption of sulfur and no bulk sulfidation. The heat of the adsorption is a function of surface sulfur coverage and increases with decreasing coverage due to the reduction of sulfur affinity at high coverage. McCarty et al. (1983) reported that the heat of the adsorption decreased from 122 to 26 kJ/mol while the sulfur coverage increased from 0.1 to 0.6 on Pt.

### *7.3.7 Effect of the Au composition on membrane performance during $H_2S$ exposure*

As discussed previously (*Section 7.3.3*), the Au content could also affect the performance of the Pd/Au membranes in the presence of $H_2S$. Therefore, the Pd/Au membranes of different Au compositions were characterized in the presence of $H_2S$ (up to 5 ppm).

Figure 7.19 shows the relative permeance history of membrane C-12 (12.3 wt% Au) during the exposure to a 2 ppm $H_2S/H_2$ gas mixture at 400°C and the subsequent recovery in pure $H_2$ at 400°C and 500°C. The $H_2S$ concentration in the retentate (at the outlet of the shell side) during the $H_2S$ exposure and the recovery was also plotted in Figure 7.19. Upon the $H_2S$ exposure, the $H_2$ permeance decreased immediately and reached a steady state value of 61% of the original value at the end of 24 hours exposure. Similar $H_2$ permeating characteristics in the presence of $H_2S$ were observed on membrane C-12 compared to membrane C-09, which had a smaller Au composition (See Figure 7.15). This indicated that the sulfur poisoning mechanism was still surface site blocking on the membrane with higher Au compositions. The result suggested that about 40% of the surface active sites were blocked by sulfur on membrane C-12 while exposing to 2 ppm $H_2S$ at 400°C.

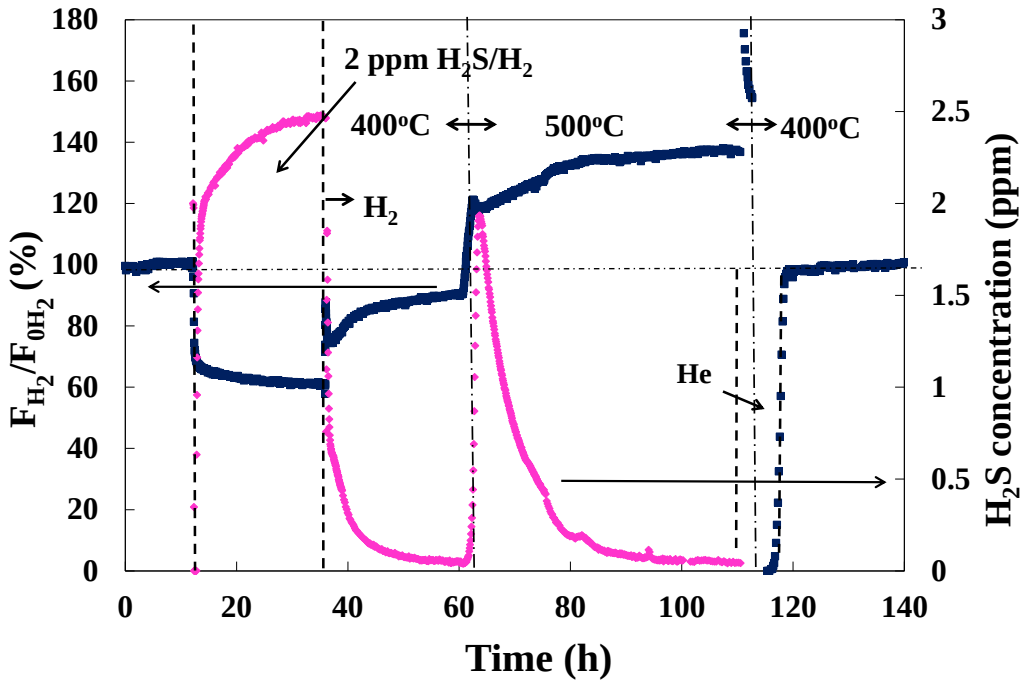


Figure 7.19. The poisoning of membrane C-12 at 400°C in a 2 ppm $H_2S/H_2$ mixture and the recovery in pure $H_2$ at 400°C and 500°C.

In addition, similar recovering pattern in $H_2$ was also observed on membrane C-12 after the $H_2S$ exposure as compared to membrane C-09. As shown in Figure 7.19, the permeance was recovered to a steady state value of 90% of the original value over a period of ~24 hours with a decreasing recovery rate as the recovery progressed. The additional recovery at 500°C caused a further permeance recovery resulting in the full restoration of the $H_2$ permeance to the value prior to the $H_2S$ exposure. The results substantiated that the $H_2$ permeance recovery was resulted from the sulfur desorption.

Although the poisoning and recovery characteristics were identical, the extents of permeance decline in the presence of $H_2S$ depended on the Au compositions. Figure 7.20 summarized the percentages of the remained permeance after the $H_2S$ exposures as a function of $H_2S$ concentration of membranes C-09, C-11, C-12, and C-16 at 400°C. It

should be noted that each $H_2S$ testing was performed for 24 hours in the presence of $H_2S$ (0.2 – 5 ppm) followed by the full recovery at 500°C. The performance of the Pd membrane, C-10 and the FCC Pd/Cu membrane in Pomerantz's work (2010) under the same exposure conditions were also included in Figure 7.20.

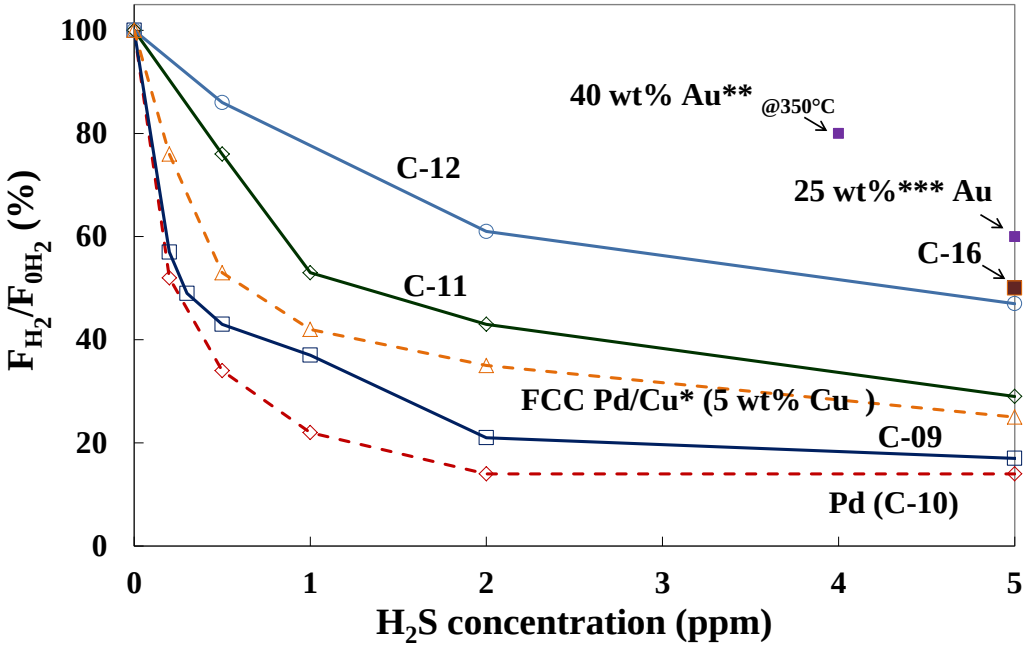


Figure 7.20. Remained permeance of membranes C-09, C-10 (Pd membrane), C-11, C-12, and C-16 during the $H_2S$ exposure as a function of $H_2S$ concentration at 400ºC. (*Pomerantz, 2010; **McKinley, 1967; ***Way et al. 2008).

As expected, all the membranes (including the Pd and the FCC Pd/Cu membrane) showed more permeance loss in the presence of the higher $H_2S$ concentrations because more surface sites were blocked by sulfur. In addition, the remained permeance (during the $H_2S$ exposure) of all the tested membranes appeared to reach a constant value asymptotically with increasing $H_2S$ concentration in the tested $H_2S$ concentration range. As explained in *Section 7.3.6*, the phenomenon was due to that the gas-solid adsorption between the Pd-Au alloy surface and the gaseous $H_2S$ approached the saturation

equilibrium. The $H_2S$ concentration required to reach the saturation adsorption increased with increasing Au composition. As shown in Figure 7.20, while membrane C-09 reached the saturation adsorption in approximately 5 ppm $H_2S$, membranes C-11 and C-12 of higher Au contents still showed noticeable permeance decline in 5 ppm $H_2S$ suggesting the saturation value have not yet reached. It should be noted that membrane C-10 (the Pd membrane) showed nearly identical permeance loss beyond roughly 2 ppm $H_2S$. The result suggested that higher $H_2S$ concentrations were required to reach the adsorption saturation on the membranes of higher Au contents, which implied the better sulfur toluene on the membranes with higher Au compositions.

Indeed, as shown in Figure 7.20, the membranes with higher Au compositions showed less permeance loss in the entire $H_2S$ concentration range tested, suggesting that the sulfur tolerance increased with increasing Au composition. It should be noted that the Pd membrane exhibited the lowest sulfur tolerance compared to all the alloyed membranes. The Pd/Au membrane of 8.5 wt% Au showed better sulfur tolerance compared to the FCC Pd/Cu membrane tested under the same conditions (Pomerantz, 2010).

Less permeance decline of the Pd-Au membrane with even higher Au compositions was reported in the literature. Way et al. (2008) reported a ~ 40% permeance decline of a $Pd_{85}Au_{15}$ (~25 wt% Au) after exposure to 5 ppm $H_2S$ at 400°C, while McKinley (1967) observed a 20% permeance decline of a 40 wt% Pd-Au membrane after exposure to 4 ppm $H_2S$ at 350°C. Figure 7.21 shows the relative permeance as a function of Au composition in the 5 ppm $H_2S$ at 400°C along with the results from the above-mentioned literature. It clearly showed that the relative permeance

remained increased almost linearly with the Au composition. The enhancement of the sulfur resistance with increasing Au composition was most likely due to the reduction of the thermal stability of the sulfides as the Au content was increased (Alfonso, 2005b; Way et al., 2008). Further discussion with respect to the effect of Au alloying on the sulfide formation will be given in *Chapter 8*.

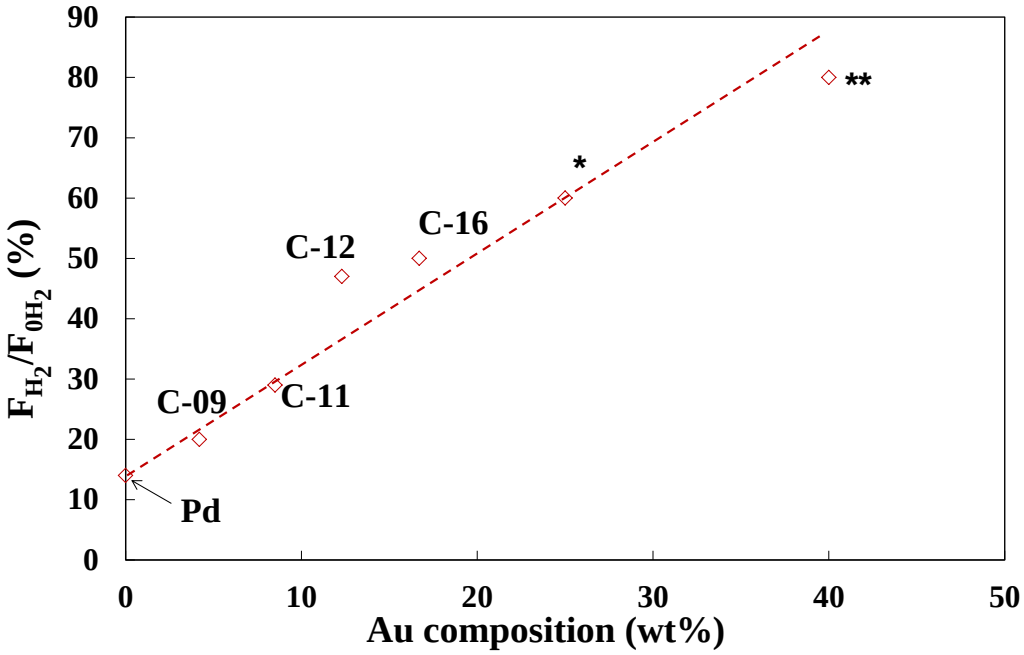


Figure 7.21. Relative permeance of the Pd/Au membrane in a 5 ppm $H_2S/H_2$ gas mixture at 400°C as a function of Au composition (*Way et al. 2008; ** McKinley, 1967).

Although increasing the Au weight fraction increased the sulfur resistance of the Pd/Au membrane with less relative permeance decline, the relative $H_2$ permeance of the Pd/Au alloy to Pd foil also decreased with increasing Au composition (See *Chapter 6*). Therefore, in order to determine the optimum Au composition with the highest relative $H_2$ permeance to Pd foil in the presence of $H_2S$, the relative $H_2$ permeance to Pd foil as a function of Au composition should also be taken into account. Figure 7.22(a) and (b)

displays respectively the relative permeance of Pd/Au with respect to Pd foil ($F_{HPd/Au}/F_{HPd}$) and the relative permeance ($F_{H2}/F_{0H2}$) of the Pd/Au membrane in the presence of a 5 ppm $H_2S$ as a function of Au composition at 400°C. The optimum Au composition to achieve the maximum performance (~40% of the Pd foil's permeance) in the presence of 5 ppm $H_2S$ at 400°C was determined to be in the range of 10 – 30 wt% as shown in Figure 7.22(c).

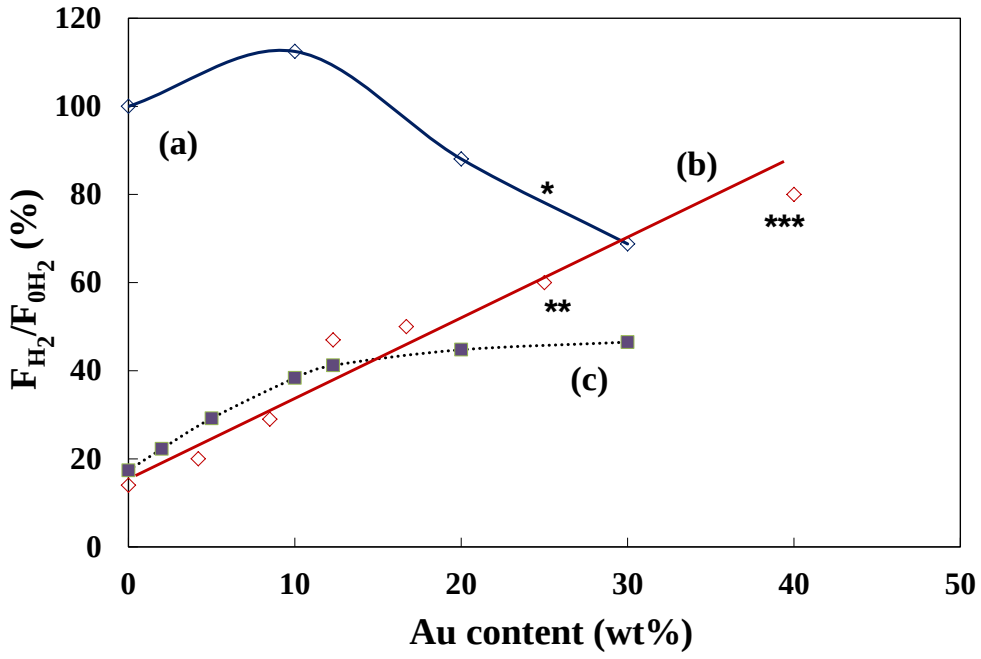


Figure 7.22. (a) Relative permeance of Pd/Au to Pd foil (in pure $H_2$), (b) relative permeance of the Pd/Au membranes in a 5 ppm $H_2S/H_2$ gas mixture, and (c) relative permeance of the Pd/Au membrane to Pd foil combined with the $H_2S$ tolerance as a function of Au composition at 400°C (*Un-published data from Catalano, 2011; **Way et al. 2008; ***McKinley, 1967).

Finally, the He leaks of membranes C-11, C-12, and C-16 during the $H_2S$ testing were monitored. The He leak of membrane C-11 at 500°C increased from 0.08 to 0.36 sccm ($\Delta p$ = 1atm, $P_{feed}$ = 2 atm, $P_{permeate}$ = 1 atm), resulting in the ideal selectivity

decreasing from 5200 to 1050 over the entire $H_2S$ testing (up to 5 ppm $H_2S$) of approximately 840 hours. The He leak of membrane C-12 at 400°C increased from 0.22 to 0.27 sccm with the ideal selectivity of 980 to 800 over the entire $H_2S$ testing (up to 5 ppm $H_2S$) of approximately 840 hours. Membranes C-11, C-12 showed notable He leak before the $H_2S$ testing possibly due to the defects on the supports. As a result, the relatively high He leak increase rate observed on membranes C-11 and C-12 was unlikely caused by the $H_2S$ exposure. A small He leak of 0.04 sccm was measured on membrane C-16 at 500°C, resulting in the selectivity of membrane C-16 remaining over 10000 after the 5 ppm $H_2S$ exposure at 400°C. It should be noted that the selectivity of membrane C-16 before the $H_2S$ exposure was theoretically infinite (i.e. no dateable He leak at $\Delta p$ = 1atm) before the $H_2S$ testing.

### *7.3.8 Performance of the membrane after the $H_2S$ test*

After the $H_2S$ poisoning/recovery tests, membranes C-09, C-10, C-11, C-12, and C-16 were characterized in pure $H_2$ again to examine the influence of the $H_2S$ exposure on the $H_2$ permeance as well as the $H_2$ transport mechanism. Membrane C-06R was not characterized due to the structural deterioration caused by the high extent of sulfide formation as described in *Section 7.3.2*.

Figure 7.23 shows the Sieverts' law regressions of membrane C-10 at 400ºC before and after the $H_2S$ testing under different concentrations (and recovery). The results showed that membrane C-10 still followed the Sieverts' law quite well after the $H_2S$ tests, indicating the hydrogen transport mechanism through the membrane was still the diffusion-controlled. The decrease of the $H_2$ permeance with increasing $H_2S$ concentration observed in Figure 7.23 was due to that the irreversible permeance loss

increased with increasing $H_2S$ concentration as described in *Section 7.3.2* (See Figure 7.8). Since the $H_2$ transport mechanism was essentially diffusion-controlled after the $H_2S$ tests, the decrease of the $H_2$ permeance was mainly caused by the decrease of the effective area (i.e. the number of surface adsorption sites) caused by the irreversibly adsorbed sulfur.

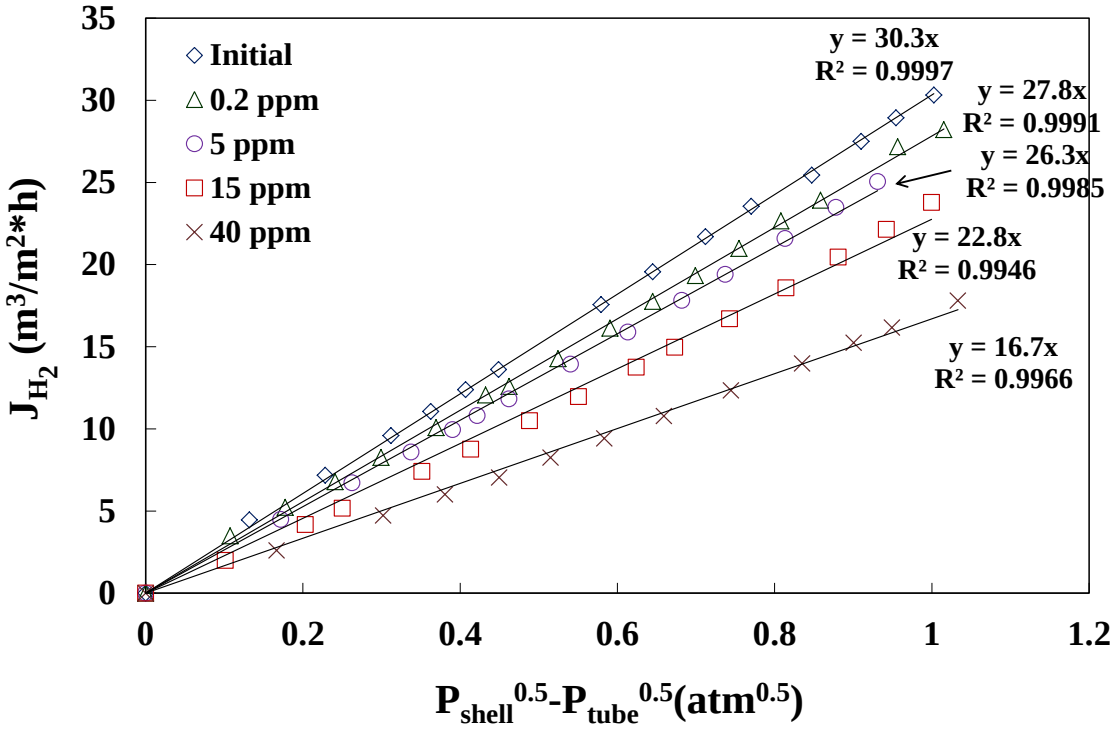


Figure 7.23. Sieverts' law regression for membrane C-10 at 400°C before and after the $H_2S$ tests (including the recovery) with different $H_2S$ concentrations.

As described in *Section 2.2*, the adsorption of the impurities not only reduced the active sites but also increased the energy barrier for hydrogen adsorption resulting in the increase of the *n*-value (Peden et al., 1986). Indeed, the *n*-values estimated by using non-linear regression of the flux data at 400°C increased with increasing $H_2S$ concentration from 0.47 before the $H_2S$ exposure to 0.7 after the 40 ppm $H_2S$ test. The result suggested

that the irreversibly adsorbed sulfur caused the increase of the energy barrier for the $H_2$ adsorption. The activation energies estimated by the $H_2$ permeance calculated from the Sieverts' regression at 350 – 450°C before and after the $H_2S$ tests also confirmed the increase of the energy barrier for the $H_2$ adsorption caused by the adsorbed sulfur.

As shown in Figure 7.24, the activation energy for the $H_2$ permeation increased with increasing $H_2S$ concentration from 11.7 to 16.4 kJ/mol. The increase of the activation energy for the $H_2$ permeation was believed to be the result of the increase in energy barrier for the $H_2$ adsorption by the adsorbed sulfur. Peden et al. (1986) reported that the $H_2$ transport mechanism would switch from diffusion-controlled ($n$ = 0.5) to surface adsorption-controlled ($n$ = 1) when the sulfur coverage on the Pd surface was greater than a critical coverage of 0.4 ML. The results showed that the energy barrier generated by the irreversibly adsorbed sulfur on membrane C-10 was high enough to alter the rate-limiting step for the $H_2$ transport.

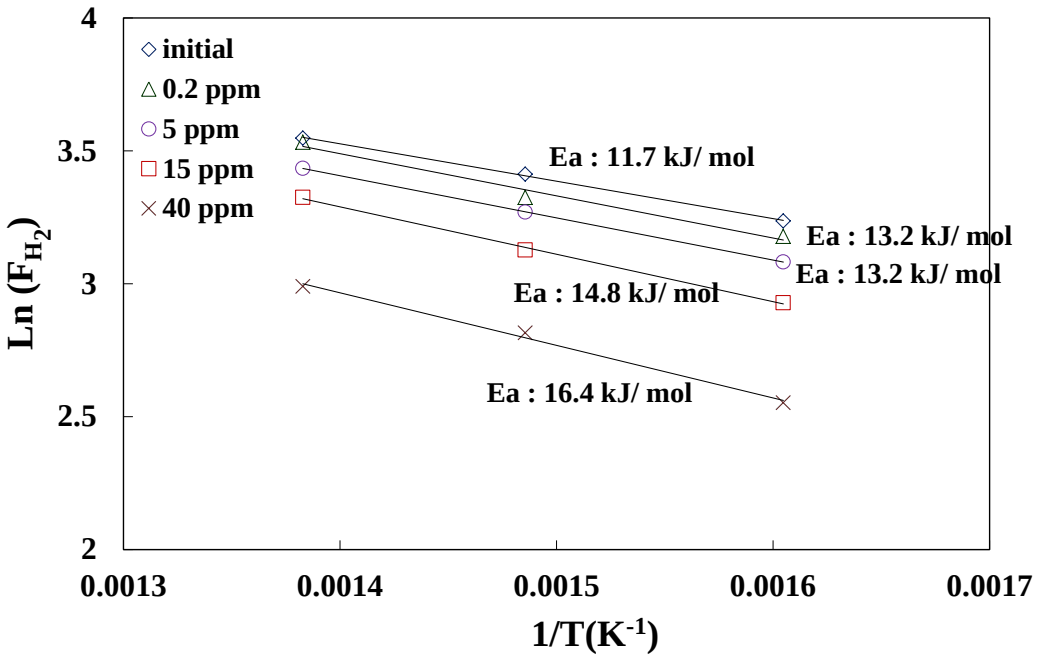


Figure 7.24. Arrhenius plot for $H_2$ permeance of membrane C-10 before and after the $H_2S$ tests (including the recovery) with different $H_2S$ concentrations. The estimated activation energies for $H_2$ permeation were also listed in the plot.

Figure 7.25 displays the Sieverts' law regressions of membranes C-09, C-11, C-12, and C-16 at 450ºC before and after the $H_2S$ testing. The flux data of all the tested membranes fit the Sieverts' equation quite well, indicating the hydrogen transport mechanism through the membrane remained diffusion-controlled after the $H_2S$ tests. Very small decrease in $H_2$ permeance (nearly negligible) of the membranes after the $H_2S$ as observed in Figure 7.25. As the decrease of the permeance was most likely due to the decrease of the effective area resulted from the irreversibly adsorbed sulfur, the amount of the irreversibly adsorbed sulfur on the membranes was negligible. The results were expected since the permeance of the membranes (the Pd/Au membranes) was recovered to nearly 100% in $H_2$ after each $H_2S$ test as described previously. In addition, the *n*-values estimated by using non-linear regression of the flux data of the membranes showed no

significant increases (~0.05) after the $H_2S$ tests, which also substantiated the insignificant property change of the membrane surfaces after the $H_2S$ exposures.

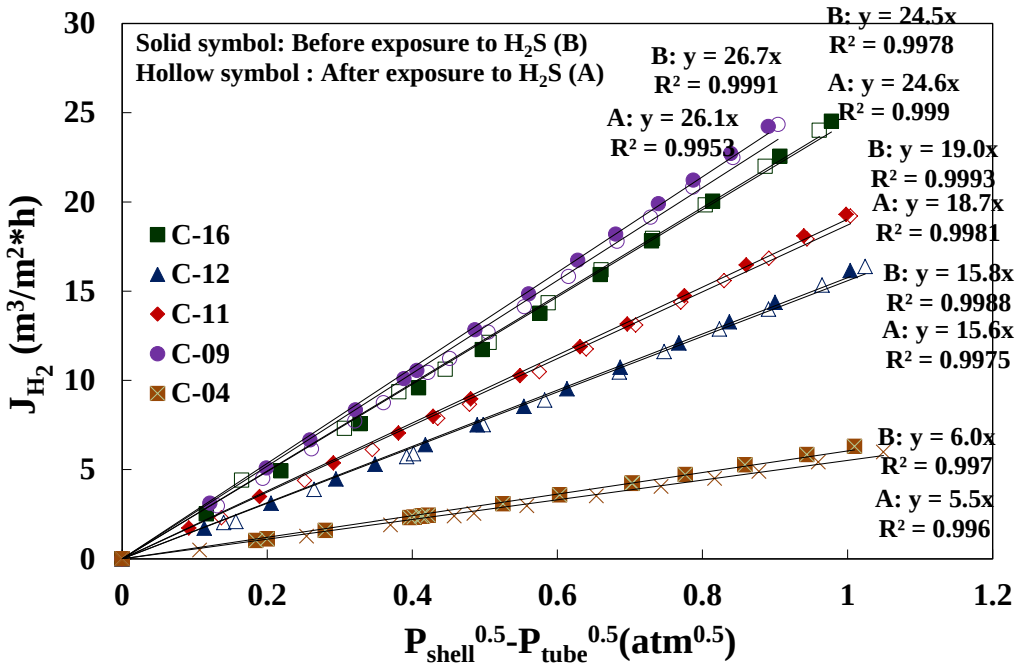


Figure 7.25. Sieverts' law regression for membranes C-09, C-11, C-12, and C-16 at 450°C before and after the $H_2S$ tests (including the recovery).

In fact, the $H_2$ transport mechanism through the Pd/Au membranes during the $H_2S$ exposure was found to be also diffusion-controlled. Figure 7.26 is the Sieverts' plot of membrane C-16 taken in the 5 ppm $H_2S/H_2$ gas mixture at 350 - 450°C. The good fit of the flux data to the Sieverts' equation indicated that membrane C-16 followed Sieverts' law in the presence of 5 ppm $H_2S$ although much lower permeance values were observed compared to the permeance values measured in pure $H_2$ (*Chapter 6*). The diffusion-controlled mechanism suggested that the loss of the permeance was resulted from the decrease of the effective area caused by the adsorbed sulfur.

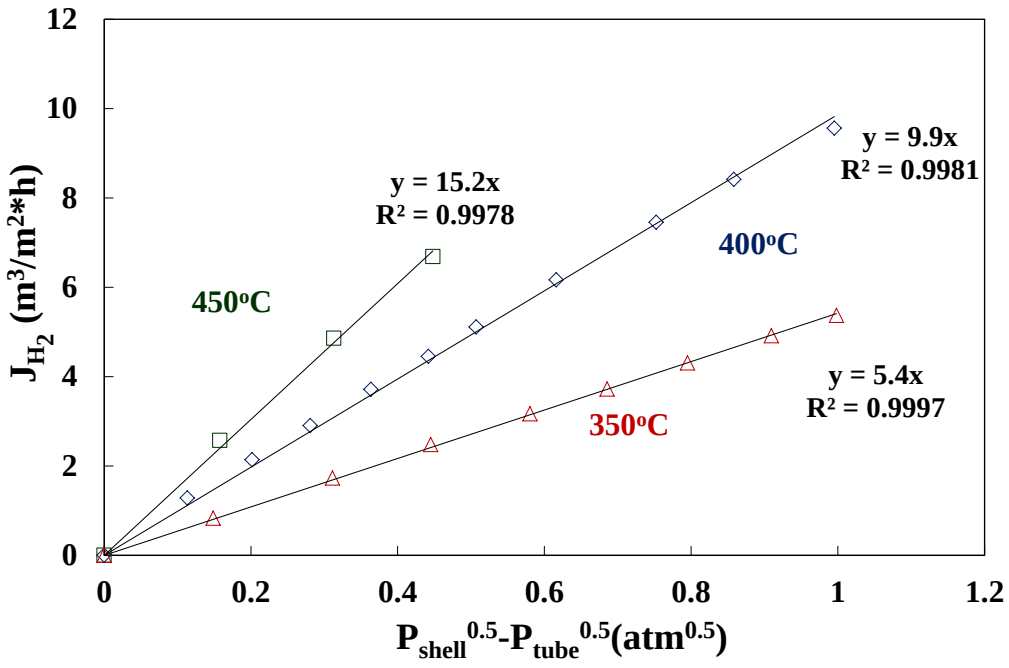


Figure 7.26. Sieverts' law regression for membranes C-16 at 350 - 450°C during the exposure to a 5 ppm $H_2S/H_2$ gas mixture.

Figure 7.27 is the Arrhenius plot for $H_2$ permeance of membranes C-09, C-11, C-12, and C-16 before and after the $H_2S$ tests. The activation energies of the membranes were estimated by the $H_2$ permeance calculated from the Sieverts' regression at 250 – 450°C. No noticeable change in activation energies (0.1 – 0.6 kJ/mol) of the membranes before and after the $H_2S$ test once again confirmed the insignificant property change of the Pd/Au alloy membranes caused by the sulfur adsorption.

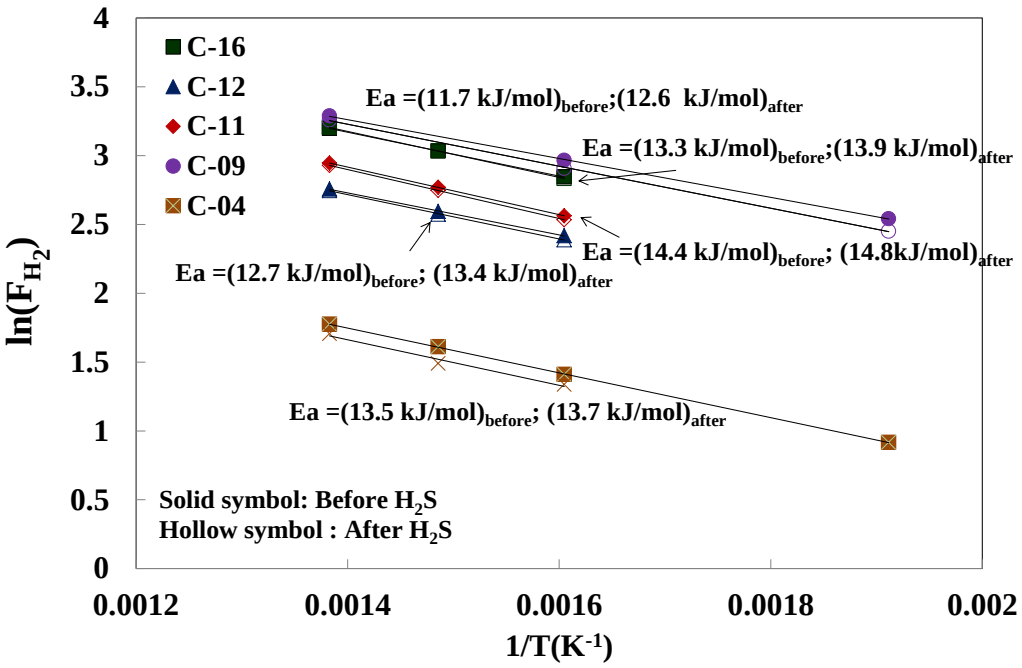


Figure 7.27. Arrhenius plot for $H_2$ permeance of membranes C-09, C-11, C-12, and C-16 before and after the $H_2S$ tests (including the recovery). The estimated activation energies for $H_2$ permeation were also listed in the plot.

### *7.3.9 Morphological and cross-sectional analysis*

Figure 7.28(a) shows the surface morphology in SEI micrograph of membrane C-06R after the $H_2S$ exposure tests. Membrane C-06R has been exposed to a 55 ppm $H_2S/H_2$ for 24 hours at 400ºC and recovered in $H_2$ for ~ 20 hours at the same poisoning temperature. Large nodules connecting to each other along with several pinholes were observed on the surface of membrane C-06R, which was most likely resulted from the formation of bulk $Pd_4S$. Indeed, the XRD analysis confirmed the $Pd_4S$ phase on membrane C-06R. As shown in Figure 7.28(b), $Pd_4S$ peaks (JCPDF-ICDD #10-355) were observed in addition to Pd peaks. In addition, the EDX area scans from the magnification of 1000x (as an example shown in Figure 7.28(e)) showed approximately 4 wt% sulfur on the membrane surface resulting in the Pd/S atomic ratio of roughly 7. The

microstructure of membrane C-06R after the $H_2S$ test were very close to that of the Pd coupon after the $H_2S$ exposure under the same conditions (*Chapter 8*). The pinholes observed on membrane C-06R (as shown in Figure 7.28(a)) due to the formation of $Pd_4S$ were considered to account for the large He leak measured after the $H_2S$ exposure as described in *Section 7.3.2*.

Figure 7.28(c) is the cross sectional SEI micrograph of membrane C-06R after the $H_2S$ testing. The thickness of the Pd layer was approximately 14 $\mu$m and pinholes could be seen in the Pd layer near the surface (to the resin side) which agreed with the result of the surface micrograph (Figure 7.28(a)). In addition, the dark contrast regions in the Pd layer near the surface were the $Pd_4S$ layers, as evidenced by the EDX spot scans with 6 – 8wt% sulfur detected in the dark contrast region and ~ 0wt% sulfur in the bottom of the Pd layer (to the support side). Figure 7.28(d) is the corresponding EDX line scan in Pd-S weight fraction of the cross-sectional micrograph in Figure 7.28(c). The results showed a sulfur gradient with highest sulfur composition of 8 - 9 wt% from the surface to approximately 5 $\mu$m deep beneath the surface, indicating that the adsorbed sulfur diffused into Pd layer up to 5 $\mu$m depth forming bulk sulfide. Mundschau et al. (2006) also observed the formation of a 5 - 10 $\mu$m thick $Pd_4S$ layer on a pure palladium foil after testing with a 20 ppm $H_2S$ 60 % $H_2$-He gas mixture at 320ºC for 5 days.

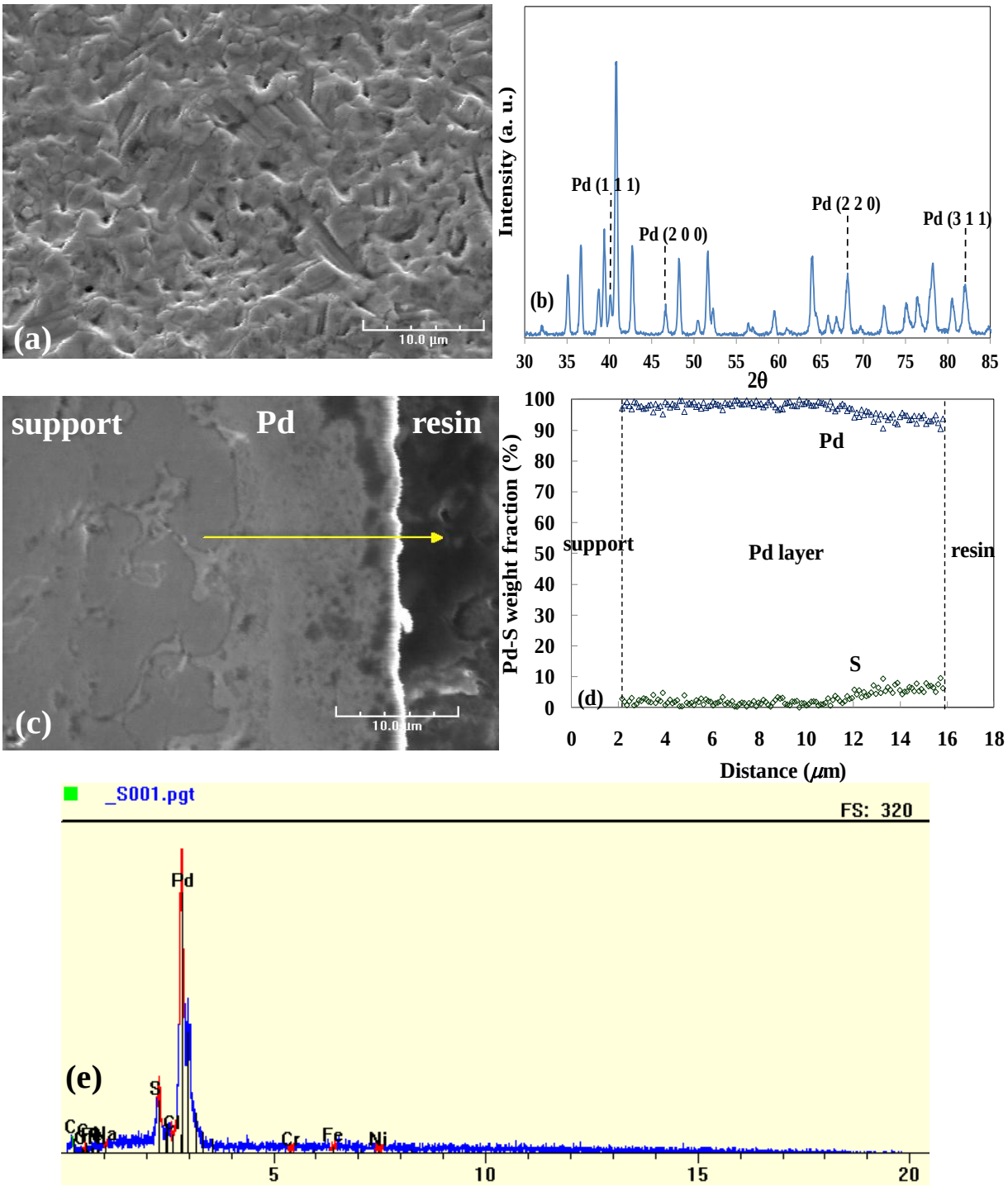


Figure 7.28. (a) Surface SEI micrograph, (b) XRD pattern, (c) cross-sectional SEI micrograph, (d) corresponding EDX line scan, and (e) surface EDX area scan of membrane C-06R after the $H_2S$ exposure tests.

Figure 7.29(a) shows the surface SEI micrographs of membrane C-10 after the $H_2S$ tests. Membrane C-10 has been exposed to the $H_2S/H_2$ mixtures (with $H_2S$ concentration of 0.2 – 40 ppm) at 400ºC followed by the recovery in $H_2$ at 400 and 500ºC for 10 testing cycles. Each test included the 24 hours' exposure duration in the $H_2S/H_2$ mixture and the approximately 100 hours' recovery in $H_2$. As observed in Figure 7.29(a), no nodule-like morphology caused by the sulfur incorporation was observed on the surface of membrane C-10, suggesting the nonexistence of the bulk $Pd_4S$. In addition, the EDX area scans (as an example shown in Figure 7.29(b)) also showed undetectable sulfur composition on the membrane surface. Although membrane C-10 has been exposed to the $H_2S$ under the stable sulfide conditions (Mundschau et al., 2006; Iyoha et al., 2007), the reverse reaction of the $Pd_4S$ formation during the recovery resulted in the disappearance of bulk $Pd_4S$. However, the muddy-like morphology along with a number of pinholes observed on the surface of membrane C-10 (Figure 7.29(a)) suggested the irrecoverable structural deformation caused by the sulfide formation. In addition, the nodule stack morphology as shown in the circle in Figure 7.29(a) was probably resulted from the sulfide formation although no sulfur composition was detected by the EDX spot scan on the area. The recovery of Pd phase from bulk $Pd_4S$ on the poisoned Pd after the recovery was also observed on the coupon study, which also showed the similar morphologies (*Chapter 8*). The pinholes observed on membrane C-10 (Figure 7.29(a)) accounted for the large He leak measured after the $H_2S$ exposure up to 40 ppm as shown in Figure 7.9.

Figure 7.29(c) shows the cross sectional SEI micrograph of membrane C-10 after the $H_2S$ exposure tests. The thickness of the Pd layer was approximately 17 $\mu$m. No

evidence for the existence of $Pd_4S$ layers was observed. In addition, the corresponding EDX line scan as shown in Figure 7.29(d) showed negligible sulfur composition throughout the Pd layer. However, porous structure in some area was seen in the Pd layer near the surface (e.g. in the circle in Figure 7.29(c)). The results agreed with the surface morphology (Figure 7.29(a)), and the porous structure was most likely caused by the $Pd_4S$ formation.

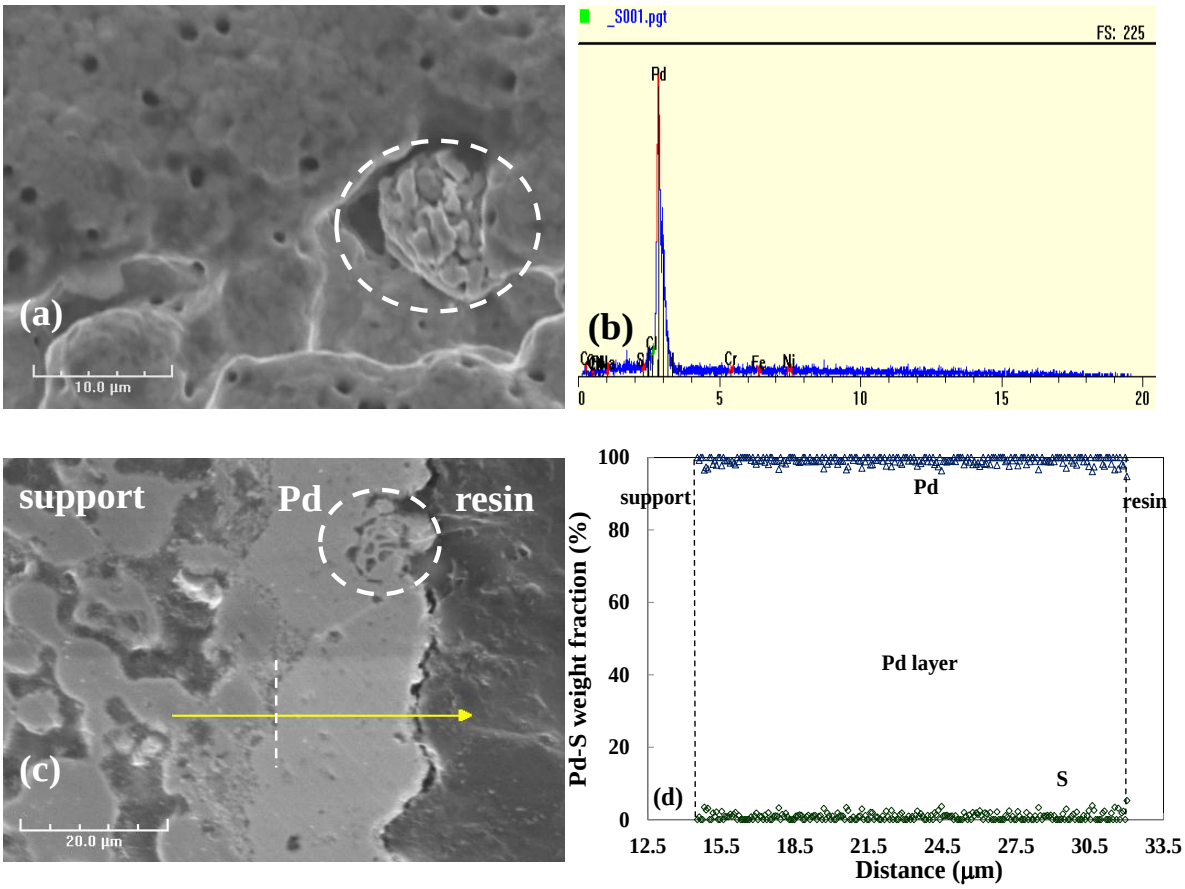


Figure 7.29. (a) Surface secondary electron image micrographs, (b) cross-sectional SEI micrographs, and (c) the corresponding EDX line scans of membrane C-10 after the $H_2S$ exposure tests.

Figure 7.30(a) displays the surface morphology of membrane C-04 after the $H_2S$ testing. Membrane C-04 has been tested and recovered in a 55 ppm $H_2S/H_2$ gas mixture and $H_2$ for several cycles in the temperature range of 350 – 500ºC. The total testing time (including recovery) for membrane C-04 was over 3000 hours with over 70 hours in the 55 ppm $H_2S/H_2$ mixture. As observed in Figure 7.30(a), the morphology of membrane C-04 was similar to that of the annealed Pd/Au bi-layer in hydrogen with the coarsened grains and a couple of pinholes on the surface (See *Chapter 5*). The pinholes were most likely resulted from the grain coarsening and the rearrangement at elevated temperatures as described in *Chapter 5*. The pinholes caused by the high temperature annealing were smaller compared to the pinholes caused by the sulfur incorporation. More discussion regarding the pinholes formed caused by the sulfur will be provided in *Chapter 8*. Nevertheless, no evidence of bulk sulfide formation was observed in the surface morphology of membrane C-04 after the $H_2S$ testing (Figure 7.30(a)). In addition, the EDX area scans (as an example shown in Figure 7.30(e)) were not able to detect the presence of sulfur, substantiating the absence of bulk sulfide on membrane C-04. As shown in Figure 7.30(b), the XRD results also confirmed that only Pd/Au alloy phase present in the membrane with no sulfide phase. Although the recovery in $H_2$ could cause the decomposition of the $Pd_4S$ as observed in the Pd samples, no bulk sulfide observed in membrane C-04 was due to that no bulk sulfide was formed in the first place during the poisoning as evidenced by the permeating characteristics of membrane C-04 described in *Section 7.3.3*. In addition, the coupon study also confirmed the lack of bulk sulfide formation during the exposure to the $H_2S$ under the similar exposure conditions with 55 ppm $H_2S$ at 350 – 500°C (*Chapter 8*).

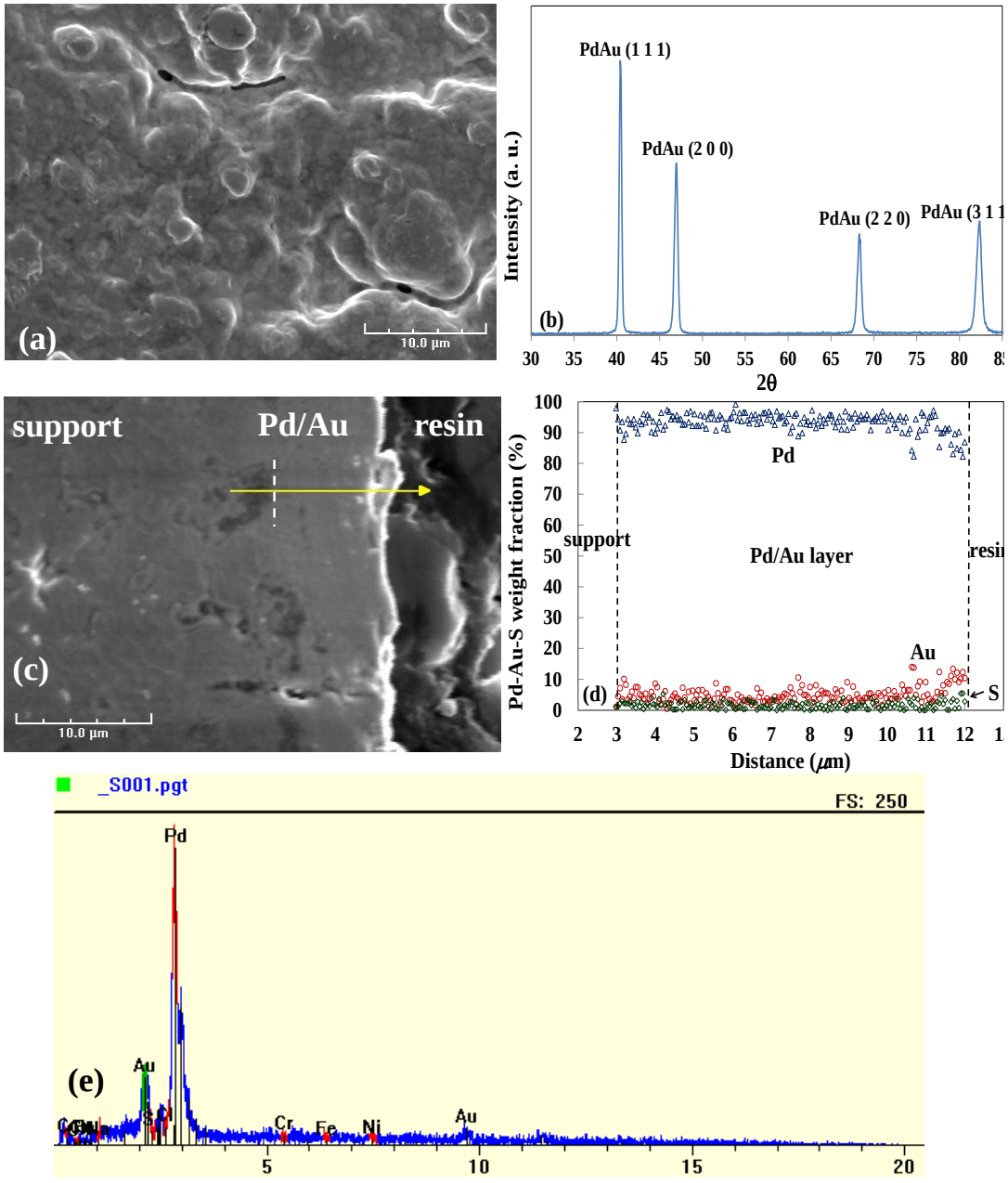


Figure 7.30. (a) Surface SEI micrograph, (b) XRD pattern, (c) cross-sectional SEI micrograph, (d) corresponding EDX line scan, and (e) surface EDX area scan of membrane C-04 after the $H_2S$ exposure tests.

Figure 7.30(c) and (d) show the cross-sectional SEI micrograph and the corresponding EDXS line scan of Pd/Au membrane C-04. The thickness of the Pd/Au selective layer was 7 – 9 $\mu$m according to the cross-sectional micrograph (Figure 7.30(c)). A gold gradient within 2 – 3 $\mu$m from the top surface of the Pd/Au layer with the highest Au content of approximately 15 wt% at the top surface was observed in the EDX line scan (Figure 7.30(d)). As expected, no noticeable pinholes and sulfur contents throughout the entire Pd/Au layer were seen in the cross-sectional SEI micrograph and EDX line scan, substantiating no dissolution of sulfur into the Pd/Au layer.

Figure 7.31(a) - (d) show respectively the surface morphologies of membranes C-09, C-11, C-12, and C-16 after the $H_2S$ testing. Membranes C-09 has been exposed to the 0.2 – 5 ppm $H_2S/H_2$ gas mixtures at 400 - 500ºC followed by the recovery in $H_2$ at the poisoning temperature and 500ºC for several testing cycles. Membranes C-11, C-12 have been exposed to the 0.5 – 5 ppm $H_2S/H_2$ gas mixtures at 400ºC followed by the recovery in $H_2$ at 400 and 500ºC for several testing cycles. Each test included the 24 hours' exposure duration in the $H_2S/H_2$ mixture and the approximately 100 hours recovery in $H_2$. The total $H_2S$ exposure time for membranes C-09, C-11, and C-12 was 360, 96, and 72 hours, respectively. Membrane C-16, on the other hand, was exposed to the 5 ppm $H_2S/H_2$ mixture for 80 hours at 400ºC followed by the recovery in $H_2$ at 400 and 500ºC for approximately 200 hours.

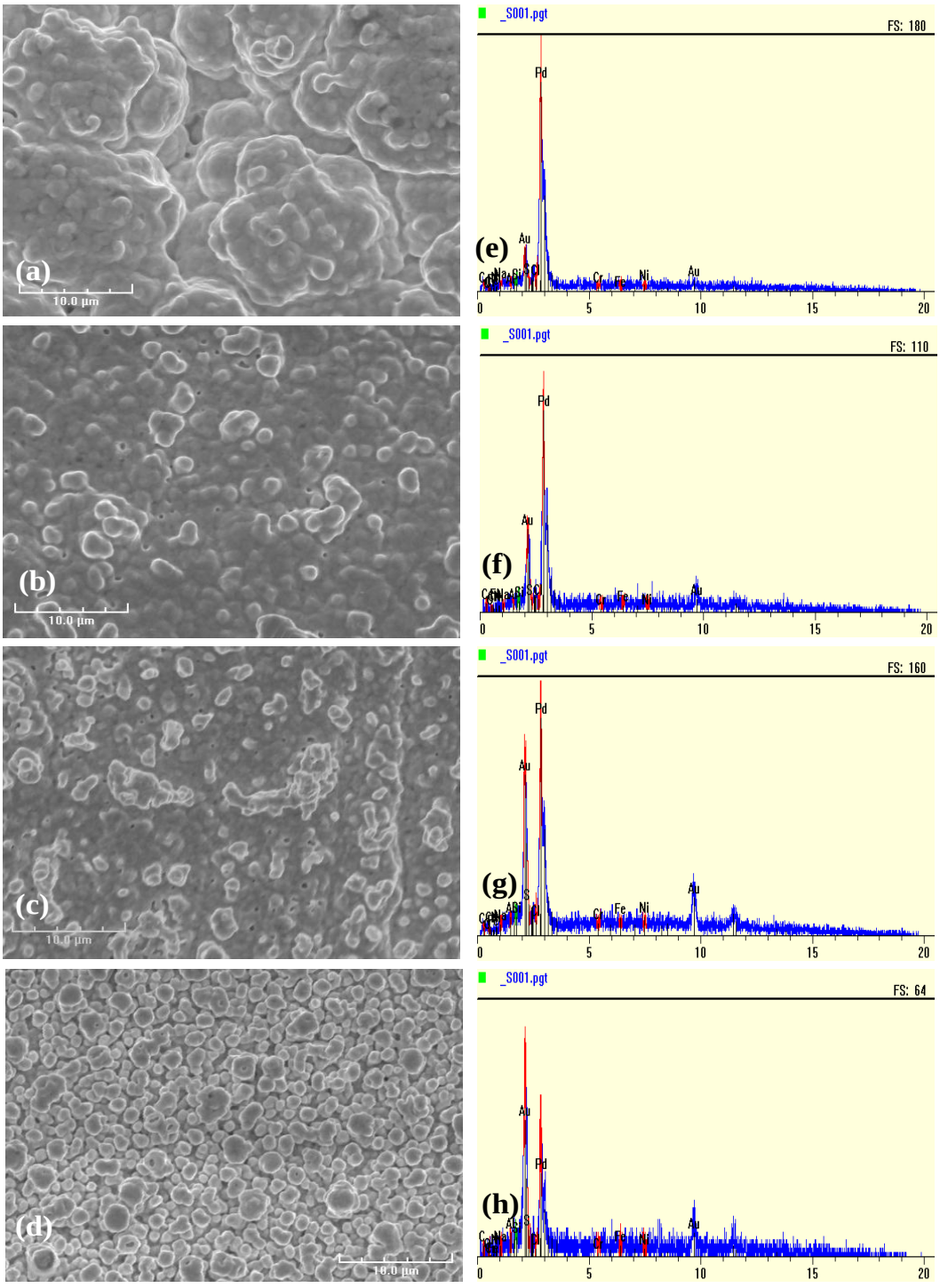


Figure 7.31. Surface SEI micrographs of membranes (a) C-09, (b) C-11, (c) C-12, (d) C-16, and the corresponding EDX area scans for membranes (e) C-09, (f) C-11, (g) C-12, and (h) C-16 after the $H_2S$ testing.

No evidence of bulk sulfide formation on the morphologies of the membranes could be seen (Figure 7.31(a)-(d)). The tiny pinholes observed on the morphologies were caused by the high temperature annealing rather than the sulfide formation as discussed previously (See Figure 7.30). The nodule-like morphologies observed on membranes C-11, C-12, and C-16 were most likely resulted from the relative high surface of Au weight fraction rather than the sulfide formation as evidenced by the EDX results, which will be discussed in the next paragraph. Since membrane C-16 was characterized in $H_2$ at low temperatures (down to 150°C) after the $H_2S$ testing, the unique surface morphology was also possibly resulted from the hydrogen embrittlement.

The EDX area scans shown in Figure 7.31(e) - (h) showed no detectable sulfur composition on all the membrane surfaces, which substantiated the lack of sulfide in the membranes. As also observed in Figure 7.31(e) - (h), the Au peak intensities in the EDX spectrums increased in the sequence from membranes C-09, C-11, C-12 to C16, indicating the increase of the Au compositions in the same order. This agreed with the gravimetric estimation during the membrane preparation. Indeed, the average Au compositions (Au-Pd weight fraction) detected by the EDX areas scans were 5, 15, 26, and 46 wt% for membranes C-09, C-11, C-12, and C-16, respectively.

Finally, the cross-sectional analysis of membranes C-09, C-11, C-12, and C-16 as shown in *Section 6.4.2* showed no porous structure caused by the buck sulfide formation in the dense Pd/Au layers, substantiating the lack of sulfur dissolution into the Pd/Au layers as expected.

## 7.4 Conclusions

The influence of the $H_2S$ exposure under different conditions on the hydrogen permeating characteristics of the Pd and the Pd/Au membranes were examined in this work. The exposure of the pure Pd membrane to a high $H_2S$ concentration (55 ppm $H_2S$) $H_2S/H_2$ mixture at 400°C resulted in two-stage of permeance decline due to (i) surface site blocking by the dissociative adsorption of $H_2S$, and (ii) bulk sulfidation of Pd with the formation of $Pd_4S$. On the other hand, while exposing to a $H_2S$ concentration below the equilibrium concentration (approximately 5 ppm 400°C) for $Pd_4S$ formation, the Pd membranes showed only the permeance decline caused by the sulfur site-blocking. The amount of irreversible sulfur (after the recovery in $H_2$) was a constant in the concentration range where only surface site-blocking took place, and increased with $H_2S$ concentration in the $H_2S$ concentration range where bulk sulfide start to form. Once the significant extent of bulk sulfidation occurred, the structure of the Pd membrane was deteriorated with the formation of pinholes even though the recovery of the Pd from the $Pd_4S$ was possible.

The Pd/Au membranes showed the resistance to bulk sulfidation upon exposure to the $H_2S/H_2$ mixtures up to 55 ppm in the temperature range of 350 – 500°C, and underwent no significant structural changes caused by the bulk sulfide formation after the exposures. The permeance decline of the Pd/Au alloy membrane upon the $H_2S$ exposures was mainly resulted from the surface site-blocking by adsorbed sulfur, which caused the decrease of the effective area for the $H_2$ adsorption without altering the $H_2$ transport mechanism. In addition, the permeance loss was essentially recoverable.

The permeance loss during the $H_2S$ exposure as well as the permeance recovery were temperature dependent with less permeance loss and more permeance recovery occurring at higher temperatures due to the exothermic nature of the $H_2S$ adsorption. The exposure duration of $H_2S$ showed no effect on the degree of permeance decline at a fixed temperature substantiating that the permeance loss was resulted from the equilibrium adsorption of $H_2S$ on the membrane surface. Increasing the $H_2S$ concentration increased the permeance loss due to more surface sites being blocked by the adsorbed sulfur. However, once the equilibrium adsorption capacity was attained, increasing $H_2S$ concentration showed no further significant permeance loss. Increasing the Au composition in the Pd/Au membranes increased the sulfur tolerance with less permeance decline in the presence of $H_2S$. However, by taking the effect of Au composition on the $H_2$ permeance into account, the optimum Au composition with the highest relative $H_2$ permeance (to Pd foil) in the presence of $H_2S$ was within 10 – 30 wt%.

# 8. The Effect of $H_2S$ exposure on the micro-structure of Pd and Pd/Au alloy

## 8.1 Introduction

As discussed in *Chapter 7*, the Pd and Pd/Au membranes showed different phenomena of $H_2$ permeance decline in the presence of $H_2S$. This was believed to be caused by the two poisoning mechanisms, which were the surface site blocking and the bulk sulfidation (Chen and Ma, 2010). While the first mechanism was resulted from the dissociative adsorption of $H_2S$ on the surface of the membranes reducing the $H_2$ adsorption sites (effective area), the second mechanism involved the dissolution of adsorbed sulfur forming bulk sulfides in the membranes. The surface sulfur adsorption caused a rapid but steady and finite permeance reduction while the bulk sulfidation resulted in a continuous permeance decline over time. The two different sulfur poisoning phenomena by sulfur (i.e. surface site blocking and sulfidation of the Pd layer) have been termed as "catalytic poisoning" (refer to the surface site blocking) and "corrosive decay" (refer to the bulk sulfidation), respectively in the previous study (Morreale et al., 2007).

In the case of the bulk sulfidation, the structure of the hydrogen-selective layers varied significantly due to the formation of a new phase in addition to the permeance decline. The incorporation of sulfur into the metal lattice also generated large stress and strain, which possibly caused the morphology of the membrane to change.

The main objective of this chapter was to investigate the exposure conditions that caused the formation of bulk sulfide on the Pd and Pd/Au films. The micro-structure and crystal phases of the Pd and the Pd/Au layers were examined after the $H_2S$ exposure under different conditions. The effects of exposure temperature, time, and the $H_2S$ concentration were investigated. In addition, the morphologies and crystal phases of the Pd and the Pd/Au layers after recovering in $H_2$ were also examined to study the recoverability of the structural change caused by the sulfidation.

## 8.2 Experimental

The Pd and Pd/Au coupon samples tested in this chapter were prepared on the 0.1 $\mu$m media grade PSS or porous Hastelloy C-22 coupons (1cm x 1cm or 1cm x 1.5cm). After oxidizing at 800°C for 12 hours in air, the porous coupons were deposited with approximately 10 μm thick Pd layers by the electroless deposition. For the preparation of the Pd/Au coupons, Pd-deposited coupons were plated with Au by the Au displacement deposition described in *Chapter 4* to have approximately 0.5 $\mu$m Au layers on top of the Pd layers. Following the Au deposition, the coupons were annealed at 550ºC for 24 hours in $H_2$ atmosphere to form Pd/Au alloy using the procedure described in *Chapter 5*. The prepared Pd/Au alloy coupons were estimated to have about 8 - 11 wt% Au.

Figure 8.1 shows the annealing module for the $H_2S$ exposure test of the coupon samples, which was consisted of stainless steel tubes and Swagelok fittings. The prepared Pd and Pd/Au alloy coupons were placed on the stainless steel sample holder and inserted into the module inside the furnace, which was a BLUE M tube furnace, model TF55035A with a programmable PID temperature control (maximum temperature of the furnace was

1100ºC). Pure helium was used to purge the housing during the heating stages. The $H_2S/H_2$ gas mixture of the desired concentration was switched to the system upon the attainment of the target temperature and flowed continuously to the vent. 30 minutes before cooling, the module was switched to pure helium again and continued to be purged with helium until the system cooled to the room temperature. The gas mixer was used to produce the $H_2S/H_2$ gas mixture of the desired concentrations (as described in *Section 3.2.2*). The prepared Pd and Pd/Au alloy coupons were exposed to the $H_2S/H_2$ gas mixtures of 0.2 – 55 ppm at the temperatures of 350 - 500°C for 2 – 96 hours. The recovery of the poisoned samples was performed at 500°C in $H_2$ for 48 hours.

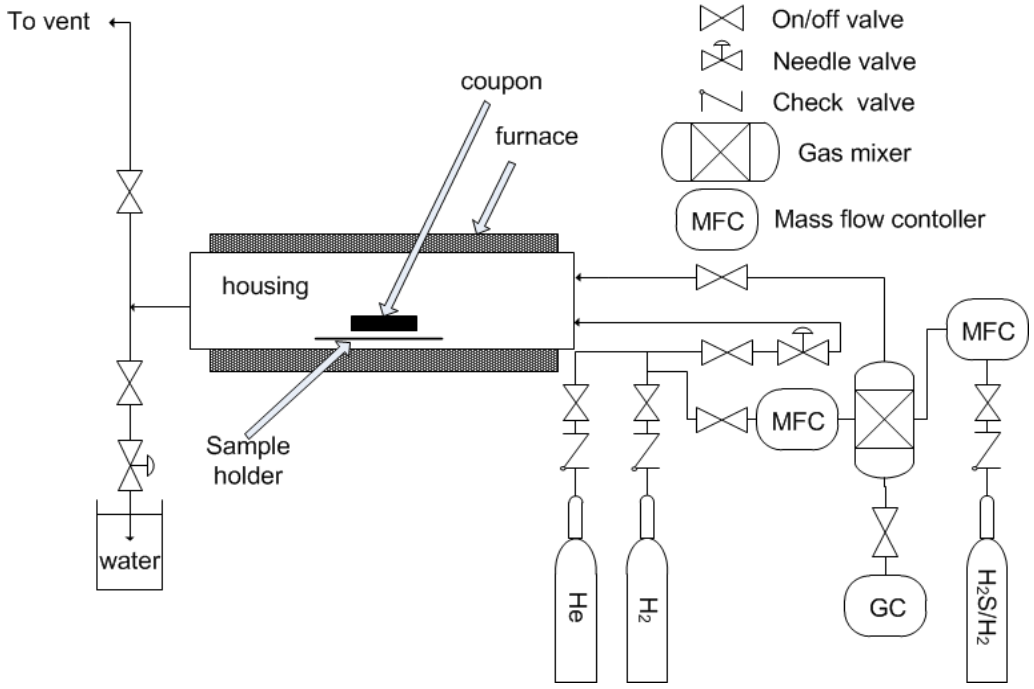


Figure 8.1. Schematic of the annealing module for the $H_2S$ exposure test.

## 8.3 Results and discussion

### *8.3.1 Poisoned Pd*

Figure 8.2 shows the X-ray diffraction patterns of the Pd samples before and after exposure to a 50 ppm $H_2S$/ $H_2$ mixture for 24 hours in the temperature range of 350 - 500ºC. Distinct FCC Pd peaks at $2\theta$ of 40.35°, 47.05°, 68.55°, and 82.25° diffracted from the plane (1 1 1) to (2 2 0) were observed in the XRD pattern before the $H_2S$ exposure (Figure 8.2(a)), indicating the existence of pure Pd phase on the sample. After exposing to the 50 ppm $H_2S$/ $H_2$ mixture at 350 to 450ºC (Figure 8.2(b) - (d)), the XRD patterns showed the appearance of apparent numerous new peaks along with the Pd peaks, indicating the formation of the sulfide phases caused by the $H_2S$ exposure. Based on the $2\theta$ positions of the peaks, the new phase formed was identified to be $Pd_4S$ (According to JCPDF-ICDD #10-355). Although several Pd sulfides including $Pd_4S$, $Pd_3S$, $Pd_{16}S_7$, and PdS were thermodynamic feasible in the testing temperature range, $Pd_4S$ was the most thermodynamically stable specie due to the highest magnitude of the Gibbs' free energy of formation (Taylor, 1985; Brain et. al. 1993).

As shown in Figure 8.2, the intensity of $Pd_4S$ peak decreased as the exposure temperature was decreased. Along with the higher Pd peak intensity observed at higher temperatures, the results suggested that the formation of $Pd_4S$ decreased with increasing temperature. No apparent $Pd_4S$ peaks were seen on the Pd samples after exposing to the $H_2S/H_2$ mixture at 500ºC (Figure 8.2(e)), indicating the insignificant formation of $Pd_4S$ at the temperature. The XRD results at different temperatures suggested that the sulfidation of palladium was a function of temperature. The extent of palladium sulfidation decreased with increasing temperature.

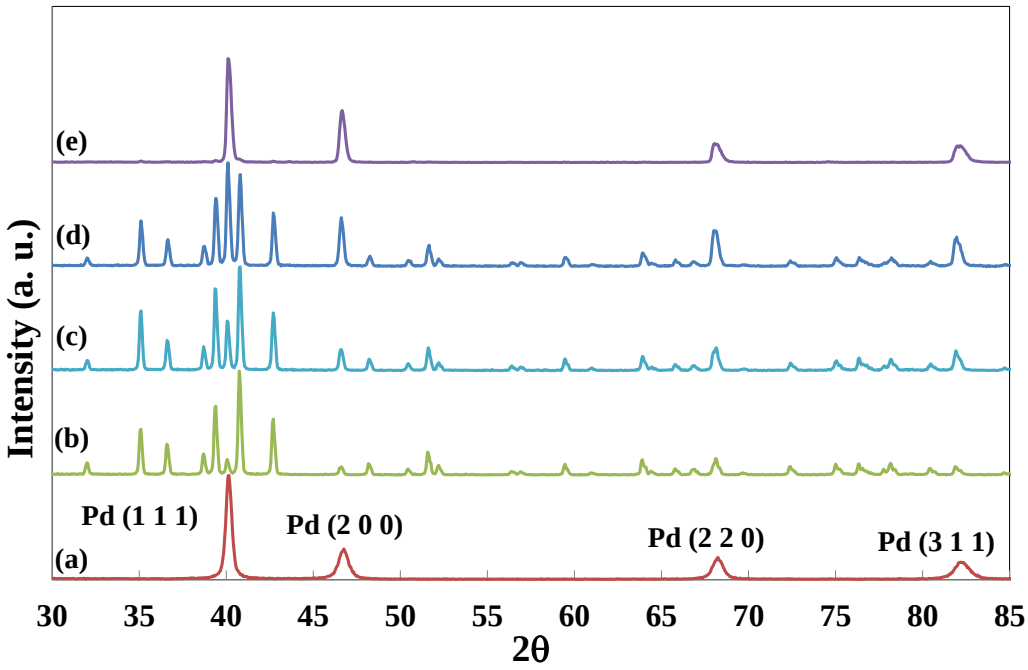


Figure 8.2. XRD patterns of the Pd coupons that were (a) as-deposited, (b) exposed to 50 ppm $H_2S/H_2$ for 24 h at 350ºC, (c) at 400ºC, (d) at 450ºC, and (e) at 500ºC.

The temperature-dependent sulfidation of Pd could be understood thermodynamically. Equation 8.4 shows the Gibbs' free energy expression for the $Pd_4S$ formation from $Pd_{(s)}$ and $H_2S_{(g)}$.

$$4Pd + H_2S \leftrightarrow Pd_4S + H_2 \qquad \Delta G^0 = -RT\ln K \tag{8.1}$$

In Equation 8.1, $K$ is the equilibrium constant for the reaction, and could be expressed as Equation 8.2.

$$K = \frac{a_{Pd_4S} P_{H_2}}{a_{Pd}^4 P_{H_2S}} \tag{8.2}$$

Where $a_i$ is the activity of the solids, $P_i$ is the partial pressure of the gases. The activity of the solids could be considered as 1 by assuming they are in their standard

states (i.e. pure and immiscible solids). As a result, the equilibrium constant was essentially a function of the ratio of the partial pressure of $H_2S$ to $H_2$ (i.e. concentration of $H_2S$). The smaller magnitude of Gibbs' free energy for the reaction shown in Equation 8.1 at higher temperatures suggested the less thermal stability of $Pd_4S$ at higher temperatures. As a result, the extent of sulfidation decreased with increasing temperature. According to Equation 8.1 and 8.2, higher concentrations of $H_2S$ were required to form $Pd_4S$ at higher temperatures.

In addition, the formation of $Pd_4S$ involved the adsorption of $H_2S$ gas molecules on the palladium surface as the first step. As a result, the exothermic nature of the dissociative adsorption of $H_2S$ on the metal resulted in less adsorption of $H_2S$ on palladium surface at higher temperatures, which also resulted in the less formation of $Pd_4S$. On the other hand, although the adsorption of $H_2S$ was favored at lower temperatures, the formation of bulk sulfides also required the dissolution and segregation of the adsorbed sulfur molecules, which required extra energy (i.e. at higher temperatures) to allow sufficient diffusion (Oudar et al., 1980b). As a result, there would be a minimum temperature for the formation of bulk sulfide, where the diffusion of the surface-adsorbed sulfur to the bulk was sufficient. Nevertheless, in the testing temperature range (i.e. 350 - 500°C), the extent of sulfidation increased with decreasing temperature.

Corresponding scanning electron micrographs of the Pd coupons after the $H_2S$ exposure at the temperature of 350 - 500ºC are shown in Figure 8.3. In comparison to the morphology before the $H_2S$ exposure as shown in Figure 8.3(a), significant morphology deformations were observed after the $H_2S$ exposure in the entire testing

temperature range (Figure 8.3(b) - (e)). Except for the one after exposing to the $H_2S$ at 500ºC (Figure 8.3(e)), the morphology deformations were caused by the formation of $Pd_4S$. Several surface nodule-like structures were observed on the surface after the $H_2S$ exposure at 450°C (Figure 8.3(d)). Similar sulfide nodules were also observed by Iyoha et al. (2007), who exposed the 125 $\mu$m Pd film to a 10 ppm $H_2S$-10% He-$H_2$ gas mixture at 450°C for 15 hours.

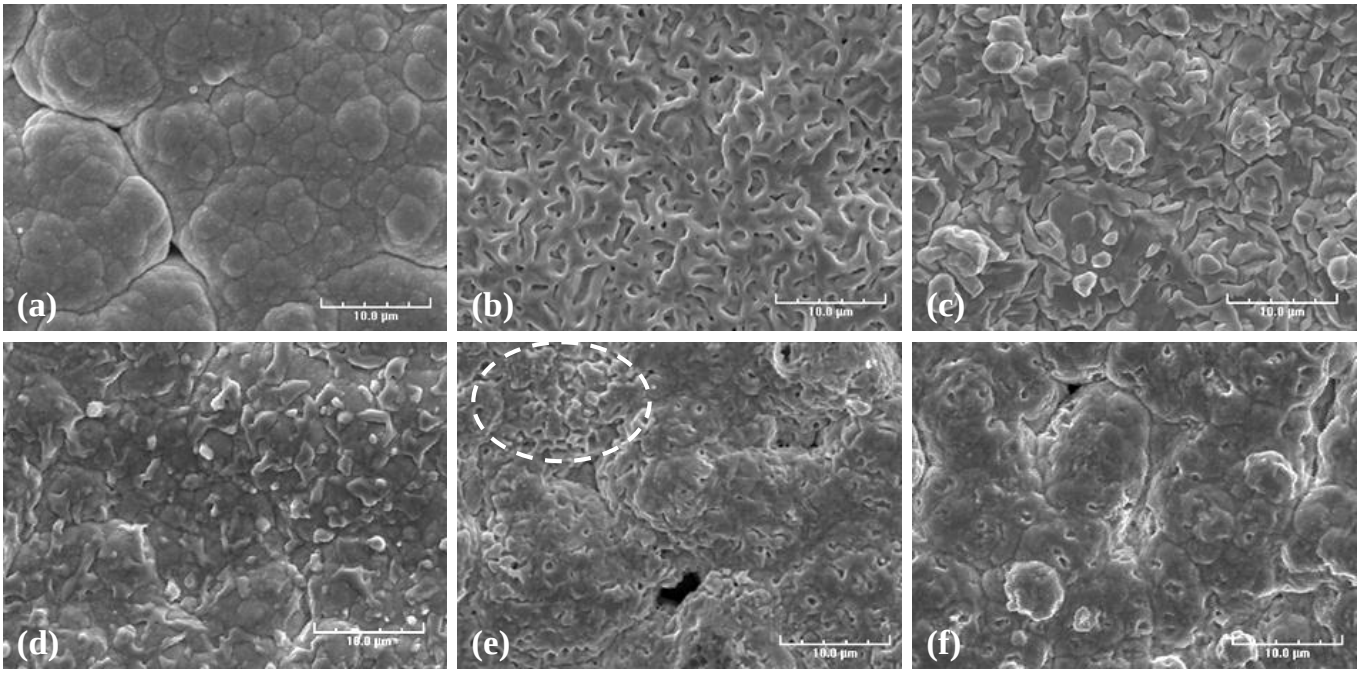


Figure 8.3. SEI micrographs of the Pd coupons that were (a) as-deposited, (b) exposed to 50 ppm $H_2S/H_2$ for 24 h at 350ºC, (c) at 400ºC, (d) at 450ºC, (e) at 500ºC, and (f) annealed in $H_2$ for 24 h at 500ºC.

The nodules were notably larger and connected to each other along with several pinholes formed at 400°C (Figure 8.3(c)). Even higher degree of the nodules connection with more pinholes formed resulting in a coral-reef-like porous morphology at 350°C (Figure 8.3(b)). The higher degree of the deformation in the surface morphology after exposing to the $H_2S$ indicated the higher extent of the sulfidation at lower temperatures

which agreed with the XRD analyses. The pinholes formed on the samples after exposing to the $H_2S$ at 350 and 400ºC had the diameters over 1 $\mu$m and were most likely resulted from the large difference of the lattice constant between pure Pd and $Pd_4S$. While Pd has cubic FCC crystal structure with the lattice constant of 3.891 Å, $Pd_4S$ has tetragonal structure with the lattice constants of 5.115 Å and 5.590 Å. The stress and strain increased inside the Pd lattice as $Pd_4S$ was formed by the dissolution of sulfur into the Pd lattice. The relaxation of the stress and strain caused the formation of pinholes due to the rearrangement of the structure.

Sulfur has been known as one of the main factors in the inter-granular embrittlement of many metals such as iron and nickel due to the segregation of sulfur to grain boundaries (Oudar, 1980a; Oudar and Wise, 1985). Several previous work (Kulprathipanja et al., 2005; Mundschau et. al., 2006; Morreale et. al., 2007) reported similar surface morphology with the formation of pinholes of the Pd foil membranes caused by the formation of bulk $Pd_4S$ after exposing to $H_2S$ under similar exposure conditions.

As shown in Figure 8.3(e), a number of pinholes were also observed on the Pd coupon after the $H_2S$ exposure at 500ºC. However, the majority of the pinhole formation was believed to be related to the Pd grain coarsening at high temperatures especially in $H_2$ atmosphere (Guazzone, 2006). This could be evidenced by the morphology of the Pd sample after annealing at 500ºC in pure $H_2$ for 24 hours as shown in Figure 8.3(f). The pinholes caused by the high temperature annealing were rounder and smaller compared to the pinholes caused by the sulfur incorporation. A small degree of deformation

possibly caused by the sulfur poisoning was observed in the surface morphology after the $H_2S$ exposure at 500ºC (e.g. in the circle at the left upper part in Figure 8.3(e)).

The EDX analyses of the surfaces provided another evidence of less $Pd_4S$ formation at higher temperatures with average 4.1 wt%, 3.7 wt%, 2.7wt%, and ~ 0 wt% sulfur detected on the Pd samples after exposing to the $H_2S$ at 350, 400, 450, and 500 ºC. The EDX elemental analysis was performed by several area scans at a magnification of 1000X. The atomic ratio of Pd to S (Pd/S) was determined to be 7.2, 7.9, and 10.8 on the Pd coupons after the exposure at the temperature from 350 - 450ºC. The atomic ratio of Pd to S should be 4 if $Pd_4S$ were formed on the surface. The observed higher Pd to S ratio was most likely due to the fact that the formed $Pd_4S$ layer was not thick enough so that the pure Pd layer underneath could also be detected by the EDS scan. In addition, the formed $Pd_4S$ layer was not dense enough and did not uniformly covered the entire Pd surface. Previous theoretical work by Alfonso (2006) pointed out that beyond the critical surface sulfur coverage of 0.75 ML (monolayer), the incorporation (dissolution) of sulfur into the subsurface of Pd became energetically favored rather than continuous adsorption on the surface. This suggested that the formation of bulk sulfide did not necessary mean that the entire palladium surface was covered by adsorbed sulfur. Although the slight deformation in the surface morphology implied that a certain degree of sulfidation took place as mentioned earlier, no sulfur was able to be detected by the EDX scans on the Pd sample after exposing to the $H_2S$ at 500ºC. This was because the X-ray penetration depth of the EDX technique was more than 1 $\mu$m, the small amount of sulfur at the top surface of the sample was below the detection limit of the EDX analysis.

Figure 8.4 displays the X-ray diffraction patterns of the Pd samples before and after the 24 hours exposure to the $H_2S/H_2$ mixture of 0.2, 2, 5, 10, 15, 30, and 50 ppm at 400ºC. No apparent $Pd_4S$ peaks were observed on the Pd samples exposed to the $H_2S$ of concentration up to 5 ppm $H_2S$ (Figure 8.4(b) - (d)). On the other hand, after exposing to the $H_2S$ of concentration above 10 ppm, apparent $Pd_4S$ peaks appeared in the XRD patterns (Figure 8.4(e) – (h)) indicating noticeable amount of $Pd_4S$ formed. The intensity of the $Pd_4S$ increased with the increasing $H_2S$ concentration as expected.

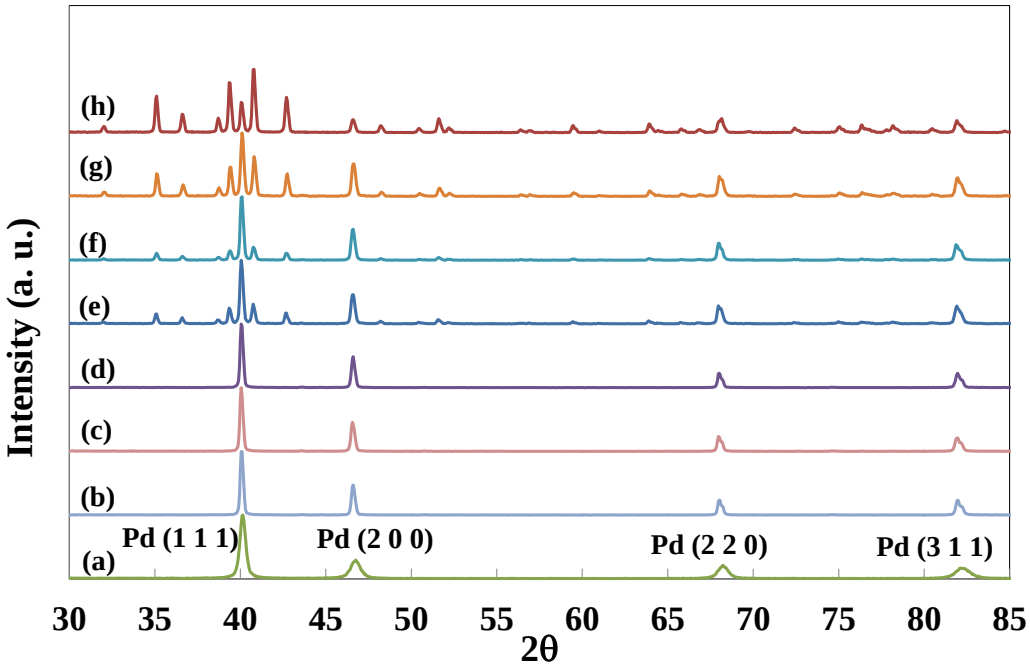


Figure 8.4. XRD patterns of the Pd coupons that were (a) as-deposited, (b) exposed to 0.2 ppm (c) 2 ppm, (d) 5 ppm, (e) 10 ppm, (f) 15 ppm, (g) 30 ppm, and (h) 50 ppm $H_2S/H_2$ at 400ºC for 24 h.

Figure 8.5 are the corresponding surface SEM micrographs of the Pd samples exposed to the $H_2S$ of different concentration for 24 hours at 400ºC. The morphologies of the Pd exposed to the $H_2S$ of concentration up to 5 ppm (Figure 8.5(a) – (c)) were very similar to the one before exposure (See Figure 8.3(a)) except for few tiny nodules

appearing on the surface. No sulfur composition was detected by the EDX due to the extremely small amount of sulfur adsorbed on the surface of the samples. As the $H_2S$ concentration was increased to more than 10 ppm, noticeable sulfide nodules were observed on the surface, and the size of the nodules increased with the increasing $H_2S$ concentrations (Figure 8.5(d) – (f) and Figure 8.3(c)). The EDX analysis showed 1.2, 1.3, 2.5 and 3.7 wt% sulfur on the Pd samples exposed to 10, 15, 30, and 50 ppm $H_2S$, respectively.

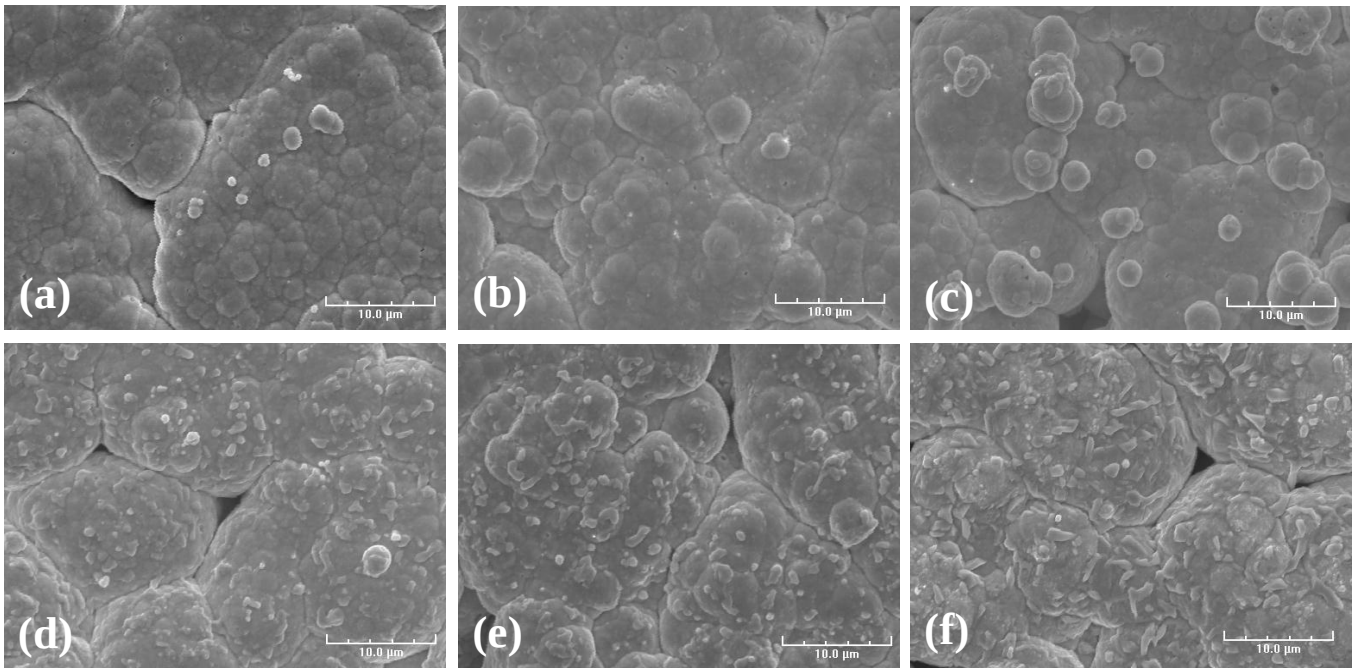


Figure 8.5. SEI micrographs of the Pd coupons that were exposed to (a) 0.2 ppm, (b) 2 ppm (c) 5 ppm, (d) 10 ppm, (e) 15 ppm, and (f) 30 ppm $H_2S/H_2$ at 400ºC for 24 h.

The thermodynamic calculations by the use of Equation 8.1 and 8.2 and the thermodynamic data (i.e. Gibb's free energy of formation for $Pd_4S$ and $H_2S$) gave the minimum $H_2S$ concentration required in the $H_2S$-$H_2$ gas mixture for the formation of $Pd_4S$. The aforementioned calculations reported in the literature were depicted in Figure

8.6 (Mundschau et. al., 2006; Iyoha et. al., 2007). A noticeable discrepancy was observed between the two reported results mainly due to the different thermodynamic data used.

The experimental results of the current study were also shown in Figure 8.6. Most of the experimental conditions performed in the current study were above the equilibrium values predicted for $Pd_4S$ formation, and showed the formation of $Pd_4S$ which agreed with the thermodynamic prediction. It should be noted that $Pd_4S$ was expected to form when exposed to the $P_{H2S}/P_{H2}$ value above the equilibrium value (the stable $Pd_4S$ region in Figure 8.6), while no sulfidation of Pd was expected below the equilibrium value (the unstable Pd4S region in Figure 8.6). However, there were experimental points (e.g. the one exposed to 50 ppm $H_2S$ at 500°C and the one exposed to 5 ppm $H_2S$ at 400°C) showed no apparent $Pd_4S$ formation when exposed to the $P_{H2S}/P_{H2}$ value above the equilibrium value. These points were very close to the equilibrium values. As a result, any slight temperature or $H_2S$ concentration gradient in the experimental system could possibly cause the slight discrepancy observed. In addition, although $Pd_4S$ was thermodynamically stable under the conditions, the exposure time (24 hours) could be insufficient for a noticeable amount of $Pd_4S$ formation especially when these conditions were very close to the equilibrium values. In fact, since $Pd_4S$ is a peritectic compound as shown in the Pd-S phase diagram (See Figure 2.6), the formation of $Pd_4S$ is expected to be a slow process which required the diffusion of Pd and S to the interface. Nevertheless, the experiment results obtained fitted fairly with the thermodynamic prediction.

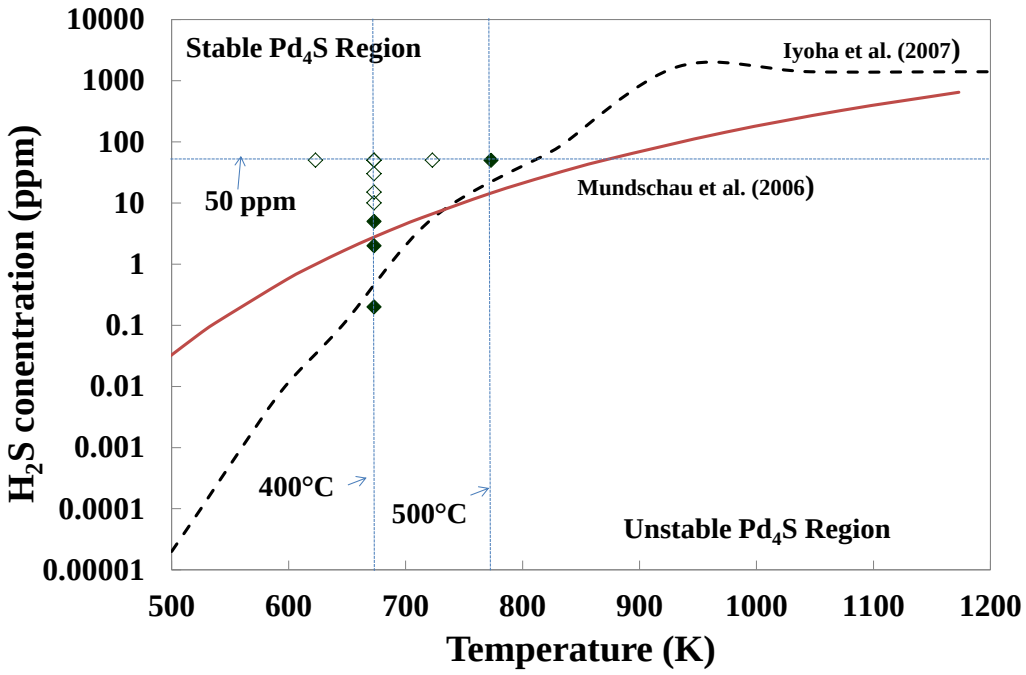


Figure 8.6. Minimum $H_2S$ concentration for forming $Pd_4S$ as a function of temperature according to the thermodynamic calculations. The solid line was established by Mundschau et. al (2006) and dashed lines were constructed by Iyoha et al. (2007), who used Taylor's thermodynamic data (1985).The diamond symbols represented the experimental data performed in the current study. The hollow diamonds represented the observation of apparent bulk $Pd_4S$ while the solid diamonds represented no apparent bulk $Pd_4S$ formation.

Figure 8.7 are the X-ray diffraction patterns of the Pd coupons after exposing to a 50 ppm $H_2S/H_2$ mixture at 400ºC for 2, 4, 8, 12, and 24 h along with the one before the $H_2S$ exposure. According to the thermodynamic calculation (See Figure 8.6), $Pd_4S$ was stable and should form when exposing Pd to a 50 ppm $H_2S/H_2$ mixture at 400ºC. However, as shown in Figure 8.7(b), the Pd sample after 2 hours exposure under the condition (i.e. 50 ppm $H_2S$ at 400ºC) showed no apparent $Pd_4S$ peaks, which was believed to be due to insufficient exposure time. As mentioned previously, the formation of $Pd_4S$ is a peritectic reaction and requires the diffusion of adsorbed sulfur and Pd atoms

to be contacted at the interface. The result suggested that the exposure time of 2 hours was not sufficient to form the noticeable amount of $Pd_4S$ under the exposure condition.

On the other hand, while the exposure time was more than 4 hours, apparent $Pd_4S$ peaks began to show along with the metallic palladium peaks in the XRD patterns (Figure 8.7(c) - (f)). This indicated that significant amount of bulk $Pd_4S$ formed within 4 hours of the exposure to a 50 ppm $H_2S$ at 400°C. As expected, the intensity of $Pd_4S$ peaks increased along with the decrease of the Pd peak intensity as the exposure time was increased due to thickening of the $Pd_4S$ layer with increasing exposure time.

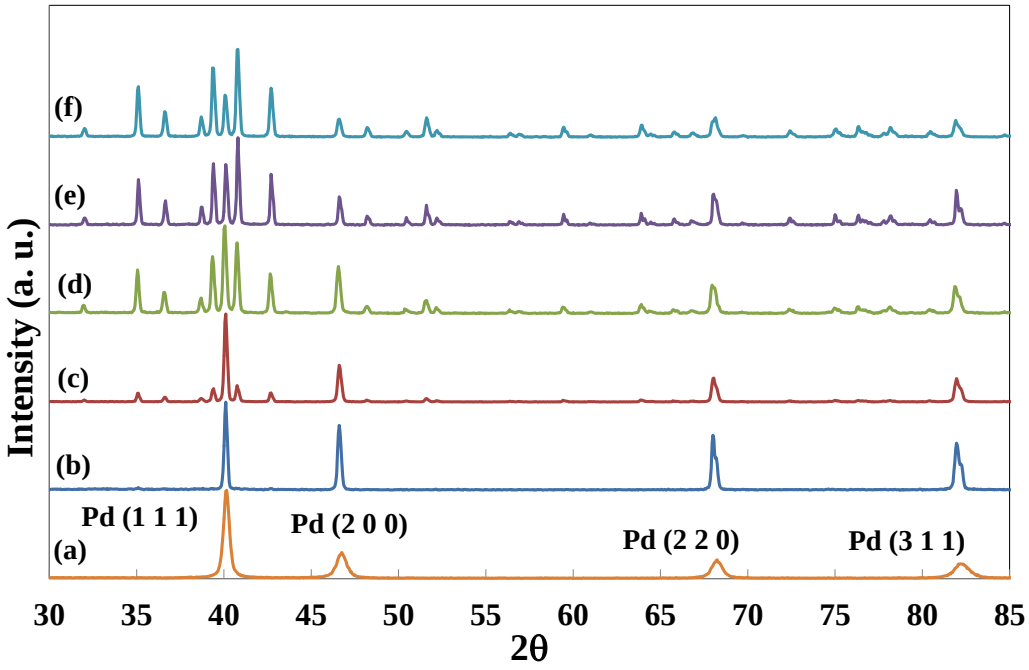


Figure 8.7. XRD patterns of the Pd coupons that were (a) as-deposited, (b) exposed to 50 ppm $H_2S/H_2$ at 400ºC for 2 h, (c) for 4 h, (d) for 8 h, (e) for 12 h, and (f) for 24 h.

The evolution of the surface morphology in SEM micrographs as a function of $H_2S$ exposure time at 400ºC is shown in Figure 8.8. After 2 hours $H_2S$ exposure (Figure 8.8(a)), the morphology was similar to the one before exposure (See Figure 8.6(a)) except

for a number of tiny nodules appearing on the surface. Those tiny nodules were most likely the nuclei of the bulk $Pd_4S$. In this stage, no significant amount of sulfur was adsorbed on Pd surface as the XRD and the EDX was not sensitive enough to detect the $Pd_4S$ phase and sulfur composition. As the exposure time was increased to more than 4 hours (Figure 8.8(b) – (e)), the formed nodules grew and started to connect to each other causing noticeable deformation in morphology. The amount of sulfur detected by the EDX was 1.8, 3.5, 3.6, and 3.7 wt% on the Pd samples after 4, 8, 12, and 24 hours exposure, respectively. The results suggested that the formation of bulk $Pd_4S$ layer was governed by nucleation-growth mechanism. After the adsorption of sulfur on the Pd surface, nuclei of $Pd_4S$ start to form on the Pd surface followed by the growth of $Pd_4S$ on those nuclei.

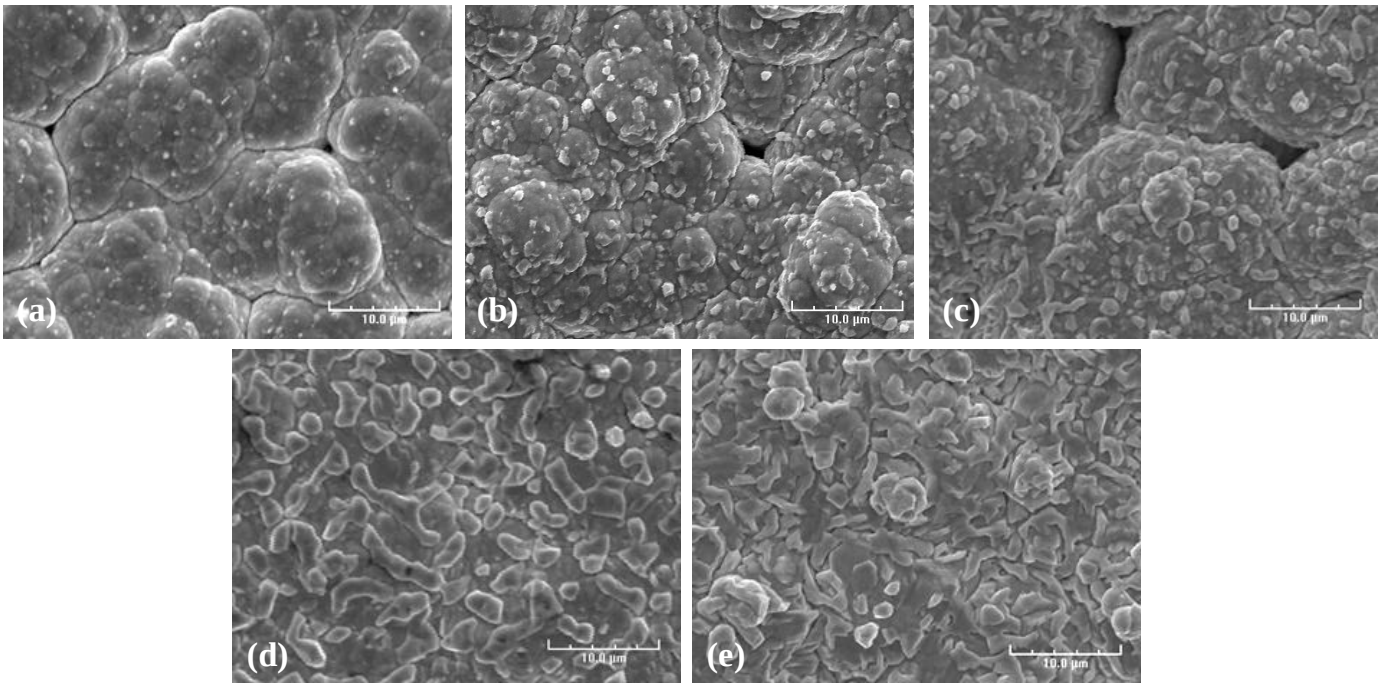


Figure 8.8. SEI micrographs of the Pd coupons that were exposed to 55 ppm $H_2S/H_2$ at 400ºC for (a) 2 h, (b) 4 h, (c) 8 h, (d) 12 h, and (e) 24 h.

As mentioned in *Chapter 5*, the isothermal solid-state phase transformation via the nuclei growth mechanism could be described by the Avrami model (See Equation 5.4). The weight fractions of Pd and $Pd_4S$ phases were estimated by the direct comparison method (Cullity and Stock, 2001) of the XRD data (See Figure 8.7) and are shown in Figure 8.9. By the use of the estimated $Pd_4S$ phase weight fractions and the linearized Avrami equation (Equation 5.5), the Avrami constant, *n*, and the rate constant, *k*, were estimated to be 1.04 and $5.27*10^{-5}$ $sec^{-1}$. The *n* value of 1 suggested that the $Pd_4S$ phase formation was most likely the one-dimensional phase boundary controlled mechanism with a zero nucleation rate, or saturation of the point sites (Hulbert, 1969). Figure 8.9 also showed the fit of the experimental data to the Avrami model. As seen in the plot, the weight fraction of $Pd_4S$ obtained from the XRD analysis and calculated by the Avrami model fit quite well.

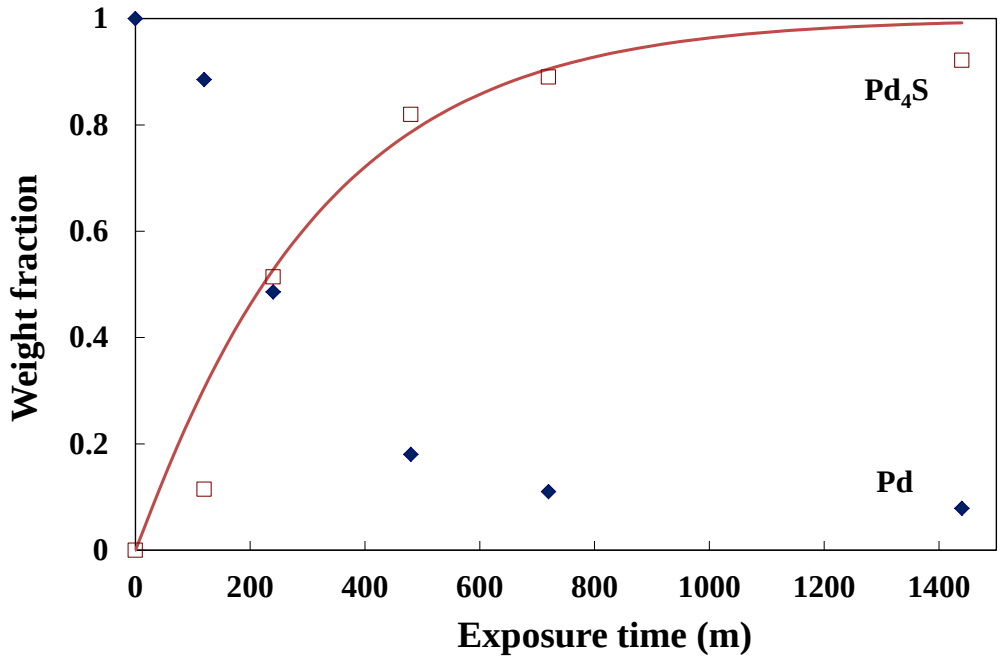


Figure 8.9. Weight fraction of Pd and $Pd_4S$ phase as a function of time at 400°C. The solid line corresponds to the Avrami model.

The growth rate of the $Pd_4S$ layer while exposing to a 50 ppm $H_2S/H_2$ mixture on a Pd film at 400°C was estimated by the power law equation as expressed in Equation 8.3, which was well represented the reacation curve in a solid state reaction (Bamford, 1969)

$$X_{Pd_4S} = kt^n \tag{8.3}$$

Where $X_{Pd4S}$ is the thickness of the $Pd_4S$ layer, $k$ is the rate constant, $t$ is the exposure time, and $n$ is the exponent constant. The thickness of the $Pd_4S$ layer was estimated by the weight fraction of Pd and $Pd_4S$ phase obtained from the XRD data (Figure 8.9) and the penetration depth of the X-ray. As mentioned in *Chapter 5*, the penetration depth of X-ray through the Pd film was approximately 6 $\mu$m (See Figure 5.3). The thicknesses of the $Pd_4S$ phase formed under the poisoning conditions were less than the penetration depth of the X-ray as evidenced by the distinct Pd peaks in the XRD

patterns as shown in Figure 8.7. Assuming that the weight fraction of $Pd_4S$ was resulted from the thickness fraction within the X-ray penetration depth (i.e. 6 $\mu$m), the thickness of the $Pd_4S$ layers were estimated and shown in Figure 8.10. By linearizing the Equation 8.3, the exponent constant, *n*, and the rate constant, *k*, were estimated to be 0.32 and 0.16 ($\mu m/sec^{0.32}$). As shown in Figure 8.10, a satisfactory fit between the experimental data (coupon study) and the values calculated by the model was observed. The deviation of the exponent constant from 0.5 indicated that the parabolic rate law could not successfully describe the formation of $Pd_4S$. This suggested that the formation of $Pd_4S$ was not through the simple one-dimensional diffusion-controlled mechanism with constant interface area. Morreale et al. (2007) studied the $Pd_4S$ growth rate by exposing Pd coupon to the 0.1% $H_2S$-10% He-$H_2$ gas mixture in the temperature range of 350 – 635°C. The authors also adopted the power law for the $Pd_4S$ growth rate expression and reported the exponent constants ranged from 0.28 – 0.39 in the studied temperature range.

For an independent check of the model, the thickness of the $Pd_4S$ layer measured by the cross-sectional SEM and EDX line scan of the Pd membrane C-06R after the 24 hours testing at 400°C in the presence of 55 ppm $H_2S$ was also shown in Figure 8.10 (the solid diamond symbol). Detailed $H_2S$ characterization of membrane C-06R including the cross-sectional morphology analysis can be found in *Chapter 7*. Approximately 5 $\mu$m of sulfide layer was measured by the SEM on membrane C-06R after the $H_2S$ exposure (See Figure 7.28), which showed a fair fit with the model prediction (Figure 8.10). The thickening of the bulk $Pd_4S$ layer with time caused the continuous permeance decline observed on membrane C-06R during the 55 ppm $H_2S$ exposure at 400°C due to the much lower hydrogen permeability of the $Pd_4S$ (Morreale, 2007). The large helium leak

measured on membrane C-06R after the $H_2S$ exposure was resulted from the formation of the pinholes as the significant $Pd_4S$ layer formed which generated the large stress inside the Pd lattice.

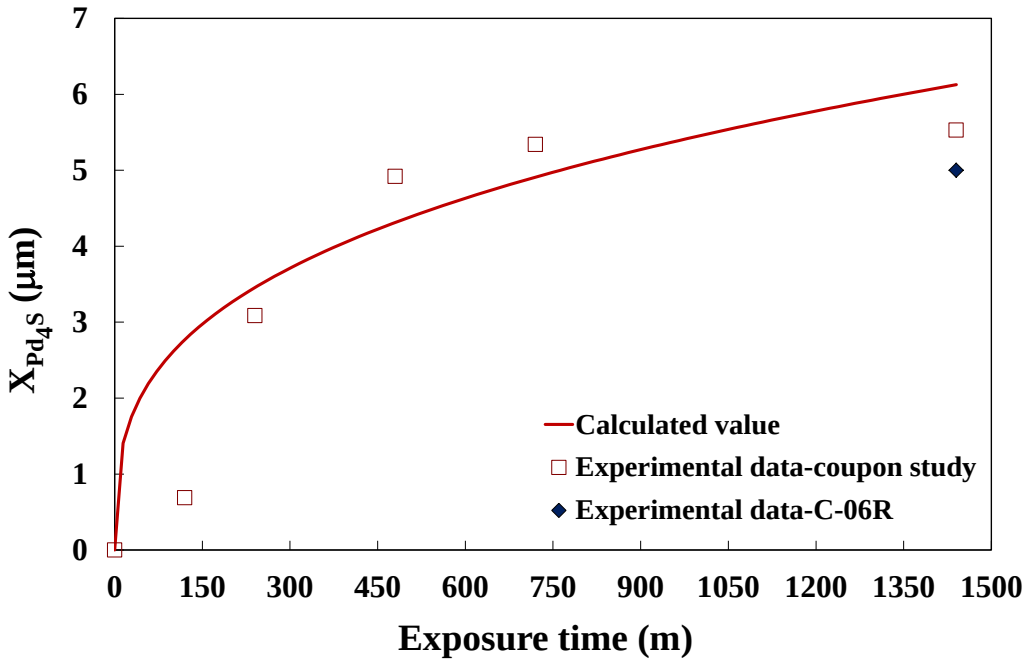


Figure 8.10. Estimated thickness of the $Pd_4S$ layer as a function of time in a 50 ppm $H_2S/H_2$ mixture at 400°C. The solid line was calculated according to Equation 8.3. The thickness of the sulfide layer of membrane C-06 was measured after 24 hours testing in a 55 ppm $H_2S/H_2$ mixture at 400°C.

### *8.3.2 Poisoned Pd/Au*

The similar $H_2S$ exposure testings were also performed on the Pd/Au alloy coupons with the $H_2S/H_2$ mixtures of 0.5 - 50 ppm in the temperatures range of 350 - 500ºC for as long as 96 hours, and the resultant X-ray diffraction patterns are shown in Figure 8.11. No formation of bulk sulfide phase on the Pd/Au alloy samples was observed in the XRD patterns after the $H_2S$ exposure in the entire testing temperature

range for as long as 96 hours. The XRD patterns after the $H_2S$ exposures were nearly identical to the one before the $H_2S$ exposure.

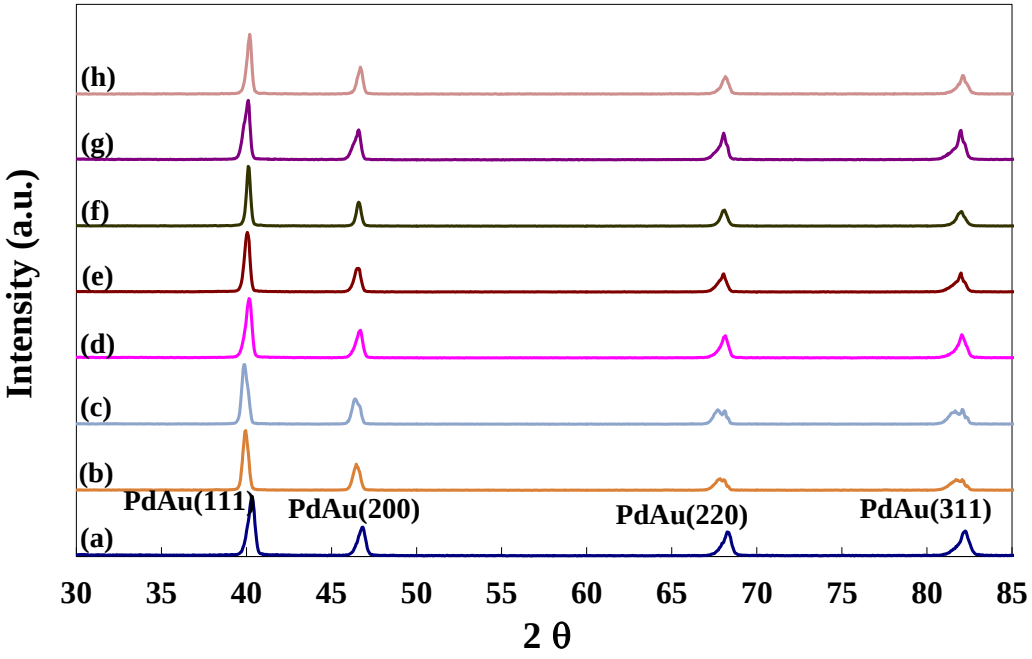


Figure 8.11. XRD patterns of the Pd/Au alloy samples that were (a) as-formed, exposed to (b) 0.5 ppm, (c) 5 ppm $H_2S/H_2$ for 24 h at 400ºC, (d) 50 ppm $H_2S/H_2$ for 24 h at 350ºC, (e) 400ºC, (f) 450ºC, (g) 500ºC, and (h) 50 ppm $H_2S/H_2$for 96 h at 350ºC.

Figure 8.12 are the corresponding SEM micrographs of the Pd/Au samples after the $H_2S$ exposures. Compared to the morphology before the $H_2S$ exposure (Figure 8.12(a)), the Pd/Au alloy samples after the $H_2S$ testings under all the testing conditions showed insignificant changes in morphology with no pinholes caused by the sulfur dissolution as observed on the poisoned Pd samples. This provided an additional indication of no bulk sulfide formation on the Pd/Au alloy samples. Moreover, no sulfur content was detected by the EDX area scans on the Pd/Au alloy samples after the $H_2S$ exposures. Figure 8.13 is a typical EDX spectrum for the Pd/Au samples after exposing to 50 ppm $H_2S$ at 350°C for 96 hours. The sulfur peak was not observed. The sulfur

content calculated according to the spectrum was 0.02 wt%, which was negligible. The granules structure observed on the Pd/Au morphologies (Figure 8.12(b) – (h)) were most likely due to the surface Au composition rather than the sulfide formation since the similar morphology was also observed on the sample before the $H_2S$ exposure (Figure 8.12(a)). The results of no bulk sulfide formation on the Pd/Au samples under the testing conditions substantiated that the sulfur poisoning effect of the Pd/Au membranes in the presence of $H_2S$ was mainly caused by the surface site blocking rather than the bulk sulfide formation as described in *Chapter 7*.

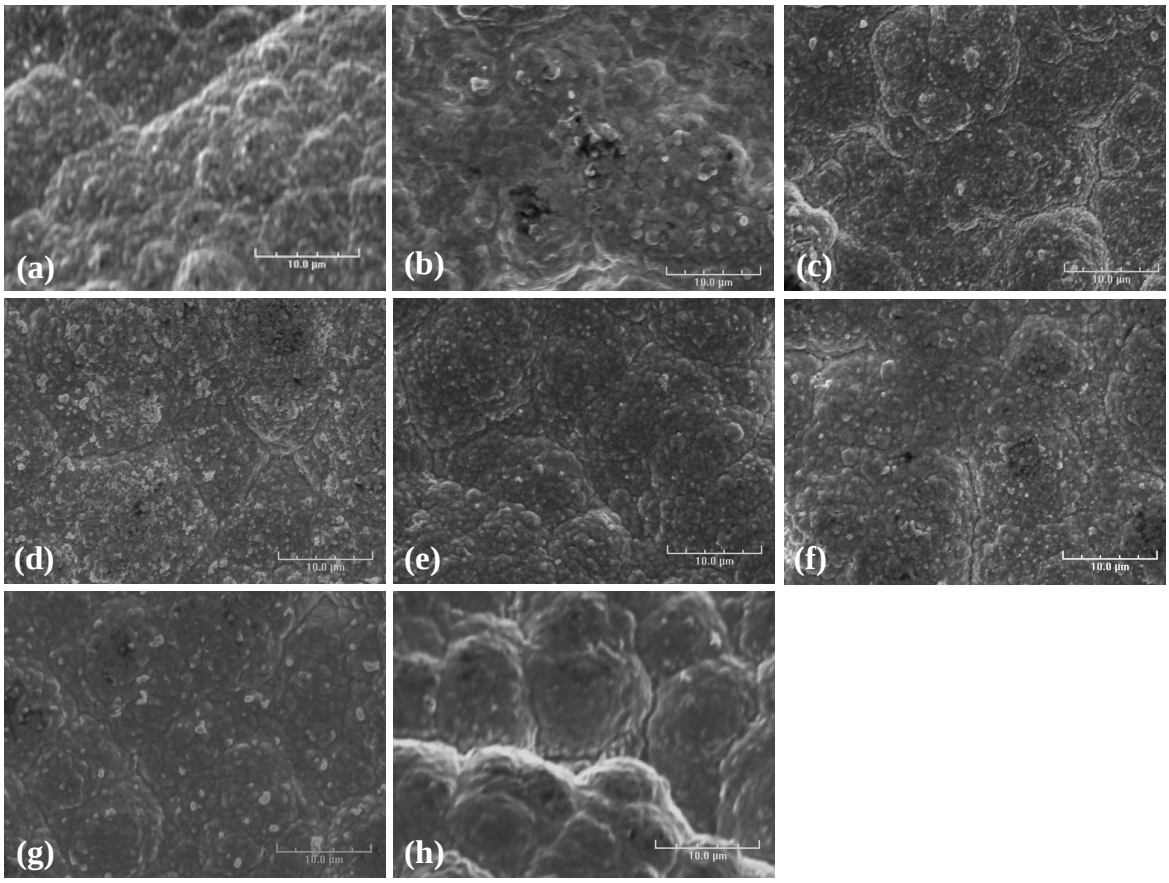


Figure 8.12. SEI micrographs of the Pd/Au alloy samples that were (a) as-formed, exposed to (b) 0.5 ppm, (c) 5 ppm $H_2S/H_2$ for 24 h at 400ºC, (d) 50 ppm $H_2S/H_2$ for 24 h at 350ºC, (e) 400ºC, (f) 450ºC, (g) 500ºC, and (h) 50 ppm $H_2S/H_2$for 96 h at 350ºC.

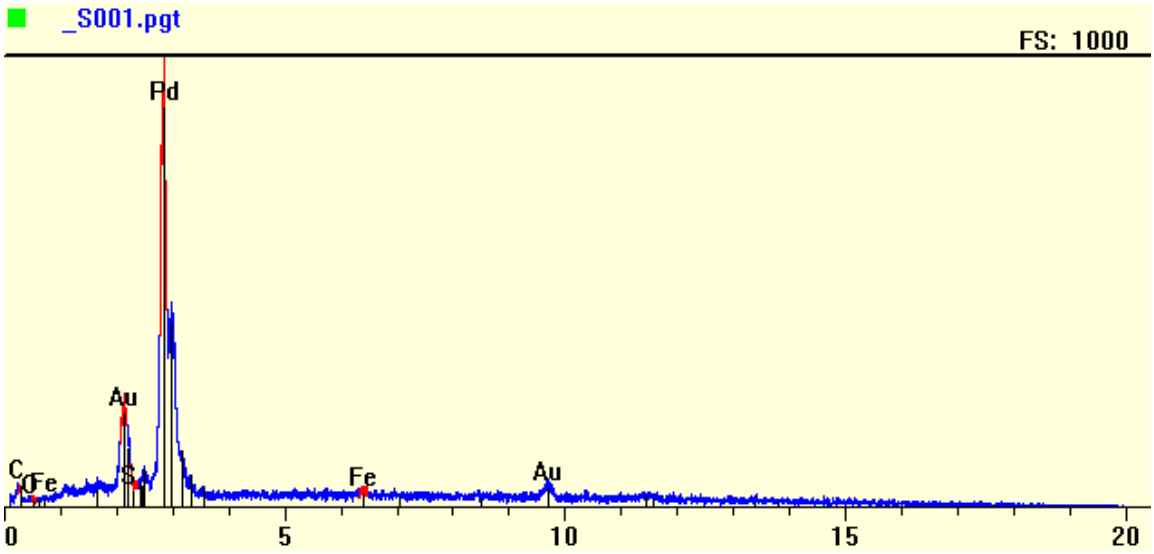


Figure 8.13. EDX spectrum of the Pd/Au coupon exposed to 50 ppm $H_2S/H_2$ mixture at 350°C for 96 hours.

The results of the $H_2S$ exposure tests on the Pd/Au alloy samples indicated that the Pd/Au alloy films exhibited the higher resistance to forming sulfide compared to pure Pd. The better sulfur resistance of Pd/Au alloy was most due to the less thermal stability of the Pd/Au alloy sulfides compared to Pd sulfides. Previous theoretical work by Alfonso (2005b) and Way et al. (2008) showed that the S-Pd binding energy was 5.07 ev/ S atom and S-50% Au Pd-Au alloy binding energy was 2.573 ev/ S atom, suggesting the less stability of S-50% Pd/Au alloy sulfide than Pd sulfide. It should be noted that higher binding energy of a compound means that the compound formed is more stable. Poor stability of the Pd/Au alloy sulfides potentially resulted in the resistance to forming sulfide of the Pd/Au alloy layers observed in the study.

In addition, the equilibrium $H_2S$ concentrations in the $H_2S$-$H_2$ mixture for forming $Pd_4S$ were increased after alloying (Iyoha et. al. 2007). In Equation 8.2, the activity of Pd, $a_{Pd}$ is not 1 in a Pd alloy. By assuming Pd and Au forming an ideal solution (i.e. followed

the Raoult's law), the activity of a component in the solution equals to the mole fraction of the component in the solution. As a result, the activity of Pd became less than 1 causing the increase of the minimum $H_2S$ concentration required to form $Pd_4S$.

Figure 8.14 shows the minimum $H_2S$ concentrations for forming $Pd_4S$ as a function of temperature (based on the work of Iyoha et al. 2007) with different values of Pd activity. 10 wt% Au in the Pd/Au alloys used in the study corresponded to approximately 6 mole% Au, resulting in a Pd activity of 0.94. However, according to the Pd/Au alloy formation study described in *Chapter 5*, an Au gradient with surface Au composition of 20 – 30 wt% existed in the alloyed Pd/Au film, which corresponded to 12 – 20 mole% Au. As indicated in Figure 8.14, the required $H_2S$ concentration for forming $Pd_4S$ increased with decreasing Pd activity. As an example, at 450°C, the $H_2S$ concentration required to form $Pd_4S$ increased from 5 ppm for Pd to 14 ppm for the Pd/Au alloy with 20 mole% Au. This provided another reason why the Pd/Au alloy samples exhibited higher resistance to forming sulfide compared to Pd. The result also suggested that by increasing the composition of Au, the sulfur resistance of the Pd/Au alloy potentially increased.

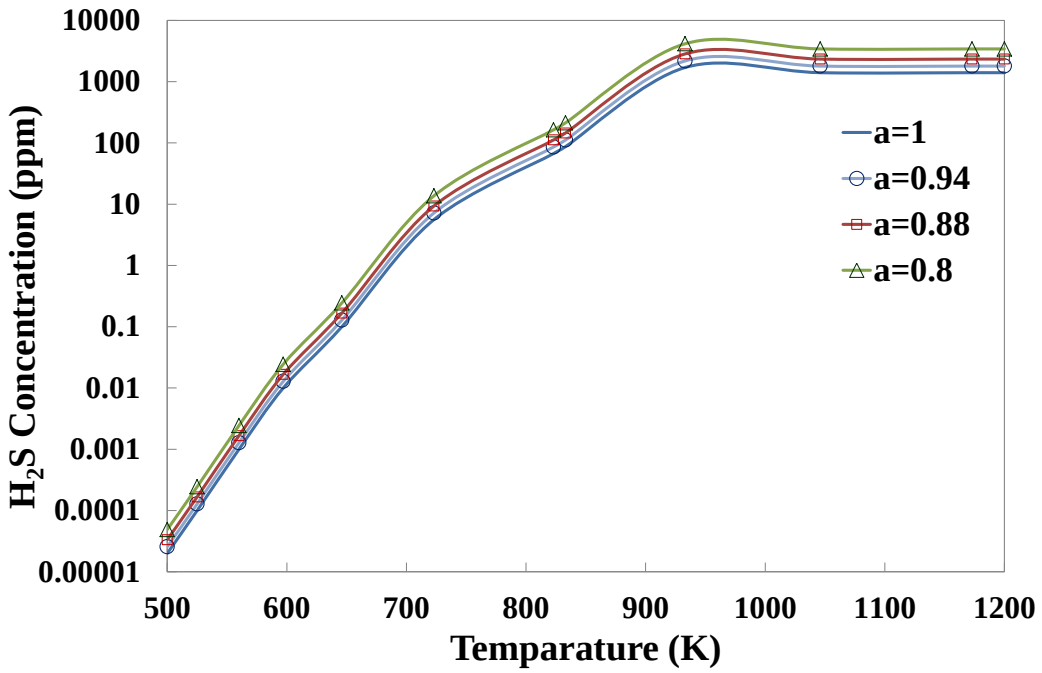


Figure 8.14. Minimum $H_2S$ concentration for forming $Pd_4S$ as a function of temperature with different Pd activity, *a*. The lines were constructed according to the work of Iyoha et al. (2007), who used Taylor's thermodynamic data (1985).

Similarly, the required $H_2S$ concentration was also increased for forming Au sulfide in the Pd/Au alloy since the activity of Au was also decreased. In the case of Pd-rich Pd/Au alloy, the activity of Au was largely decreased due to the small fraction of Au in the alloy, resulting in the large increase of $H_2S$ concentration for forming Au sulfides. Unfortunately, no thermodynamic data related to the formation of Au sulfide could be found in the literature. In fact, according to the phase diagram of Au-S as shown in Figure 8.15, Au and S are immiscible in the entire composition range. Generally, more noble metals (e.g. Au) required higher $H_2S$ concentrations to form stable sulfide compared to the less noble metals such as Pd, Ag, and Cu.

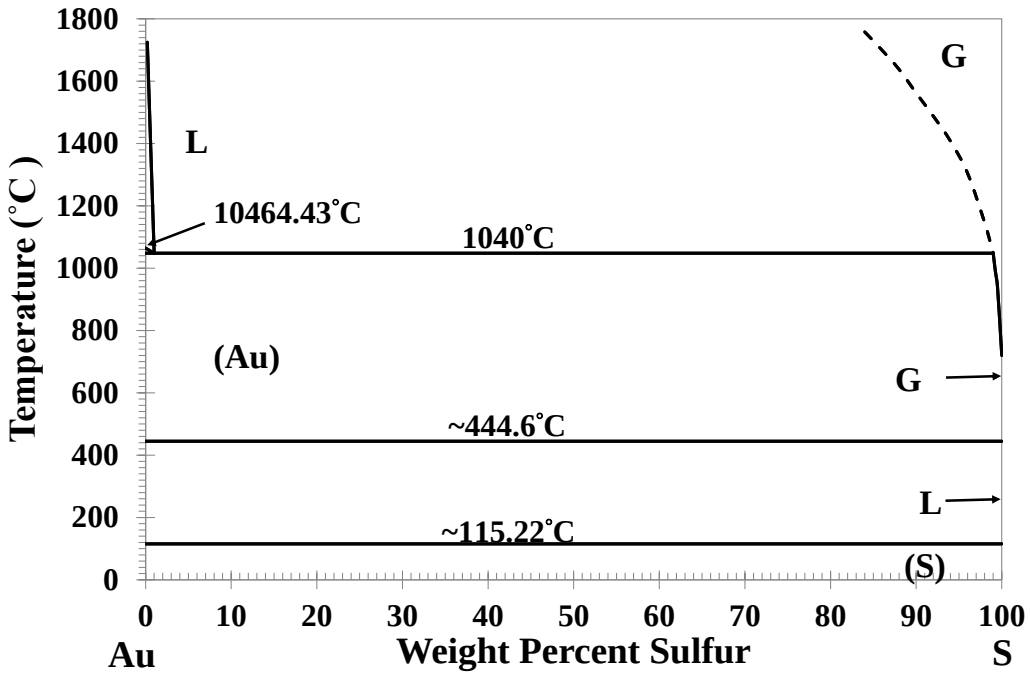


Figure 8.15. Au-S phase diagram (Okamoto and Massalski, 1985)

Pd/Au alloy foils have been reported to exhibit the resistance to forming sulfide in the stable $Pd_4S$ region according to the thermodynamic calculation (based on Iyoha et. al.'s work, 2007). McKinley reported no sulfide formation on the 74 mol% Pd-Au membranes after exposure to $H_2S/H_2$ mixtures of 4 – 6600 ppm at 350°C. Higher surface Au compositions due to the Au segregation possibly accounted for the phenomenon observed. Several researchers (Anton et. al., 1993; Way et. al. 2008) have reported the segregation of Au to the surface due to the reduction of surface energy by Au. In addition, the assumption of Pd/Au forming ideal solution might not be valid. In the case of non-ideal solution, the activities of Pd and Au varied with composition and temperature, which potentially resulted in the even lower activity of Pd and Au than the predicted values by using merely the composition.

The results confirmed the benefits of alloying Pd with Au with respect to sulfur resistance. In fact, similar enhancement of sulfur resistance by alloying Au was also observed in the catalyst field. Research on the Pd/Au catalysts (Vnerzia et al., 2003; Pawelec et. al., 2004) have shown the enhanced sulfur resistance and consequently the improved catalysts performance in the presence of $H_2S$ by alloying Au into Pd as mentioned in *Section 2.6*.

Finally, although no bulk sulfide was observed on the Pd/Au alloy samples after the $H_2S$ exposures, there was most certainly surface sulfide presented on the surface of the Pd/Au alloy samples. As described in *Section 2.6*, the $H_2S$ concentration required to form surface sulfide (caused by the $H_2S$ adsorption) was much lower than forming bulk sulfide, and surface sulfide was stable under the conditions where bulk sulfide was not. The permeance decline of the Pd/Au membranes was resulted from the surface sulfide as discussed in *Chapter 7*. For analyzing the small amount of adsorb sulfur on the top surface of the Pd/Au samples, the surface sensitive instrument, X-ray Photoemission Spectroscopy (XPS) was used in cooperation with High Temperature Material Laboratory at Oak Ridge National Laboratory, Tennessee. The comprehensive XPS analyses of the poisoned Pd and Pd/Au samples are given in next chapter for a better understanding of the interaction between sulfur and Pd and Pd/Au alloy.

### *8.3.3 Recovery of the poisoned Pd and Pd/Au*

Permeance recovery in $H_2$ after the $H_2S$ exposures of the Pd/Au and the Pd membranes under the testing conditions used in the study have been observed as described in *Chapter 7*. The desorption of the adsorbed sulfur in the reducing atmosphere (i.e. $H_2$) was considered to account for the restoration of the $H_2$ permeance. In order to

investigate the influence of recovery on the micro-structures of the Pd and Pd/Au layers, the poisoned Pd and Pd/Au coupons were recovered at 500°C in flowing $H_2$ for 48 hours. The recovery condition was chosen since that most of $H_2$ permeance recovery of the membranes was accomplished within 48 hours at 500°C as discussed in *Chapter 7*.

Figure 8.16 shows the XRD patterns of the poisoned Pd samples before and after the recovery under the conditions described previously. The Pd samples after exposing to 50 ppm $H_2S/H_2$ mixture at 400°C for 24 hours showed the formation of $Pd_4S$ as shown in Figure 8.16(b). The XRD pattern after the recovery became nearly identical to the as-deposited Pd film before the $H_2S$ exposure with the disappearance of the $Pd_4S$ phase (Figure 8.16(a) and (c)). Narrower peaks were observed after the recovery compared to the as-deposited Pd due to the larger gain size caused by the grain growth at elevated temperatures. The result indicted that the most of adsorbed sulfur desorbed under the recovery condition, which resulted in the restoration of the Pd phase from the Pd sulfide phase on the poisoned Pd layer.

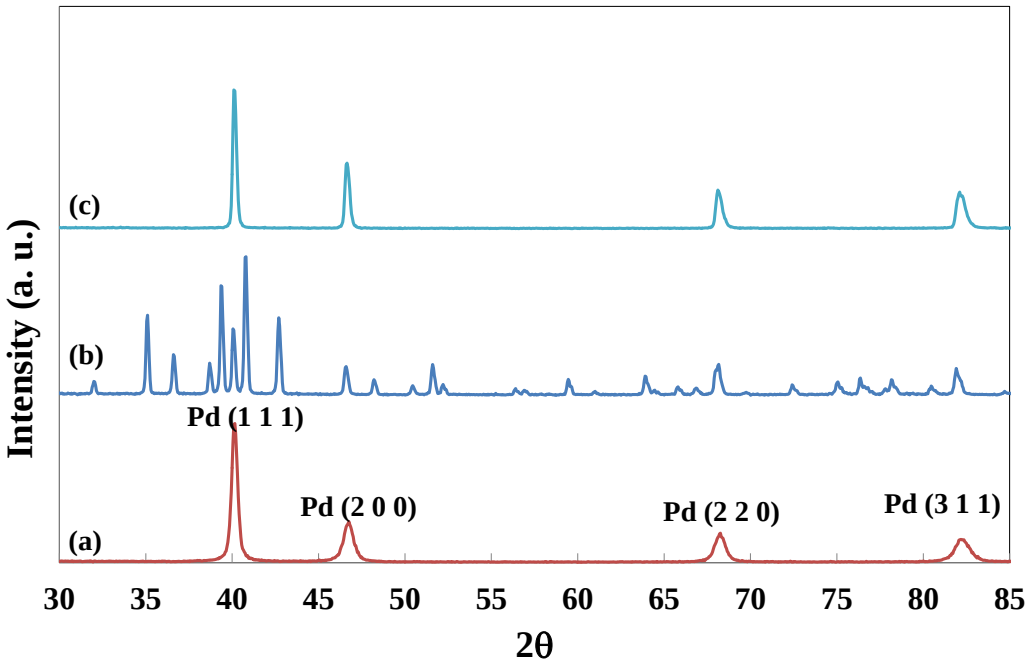


Figure 8.16. XRD patterns of thePd samples that were (a) as-deposited, (b) exposed to a 50 ppm $H_2S/H_2$ at 400ºC for 24 hours, (c) recovered at 500°C in $H_2$ for 48 hours after the $H_2S$ exposure.

Similar restoration of the Pd phase from the Pd sulfide phase on the Pd samples poisoned under different conditions was also observed. Figure 8.17 are the XRD patterns of the recovered Pd samples that were previously poisoned in a 50 ppm $H_2S/H_2$ for 24 hours at 350 - 500°C. As seen in Figure 8.17, only the Pd peaks were observed on all the previously poisoned Pd samples and after the recovery no $Pd_4S$ peaks were seen. Compared to the XRD patterns after poisoning (See Figure 8.2), the disappearance of $Pd_4S$ peaks suggested the restoration of the Pd phase due to the desorption of the adsorbed sulfur. The Pd samples poisoned under milder conditions (i.e. $H_2S$ concentration below 50 ppm and the exposure time less than 24 hours) that also formed $Pd_4S$ (See Figure 8.4 and Figure 8.7) also showed the restoration of the Pd phase after the recovery as expected.

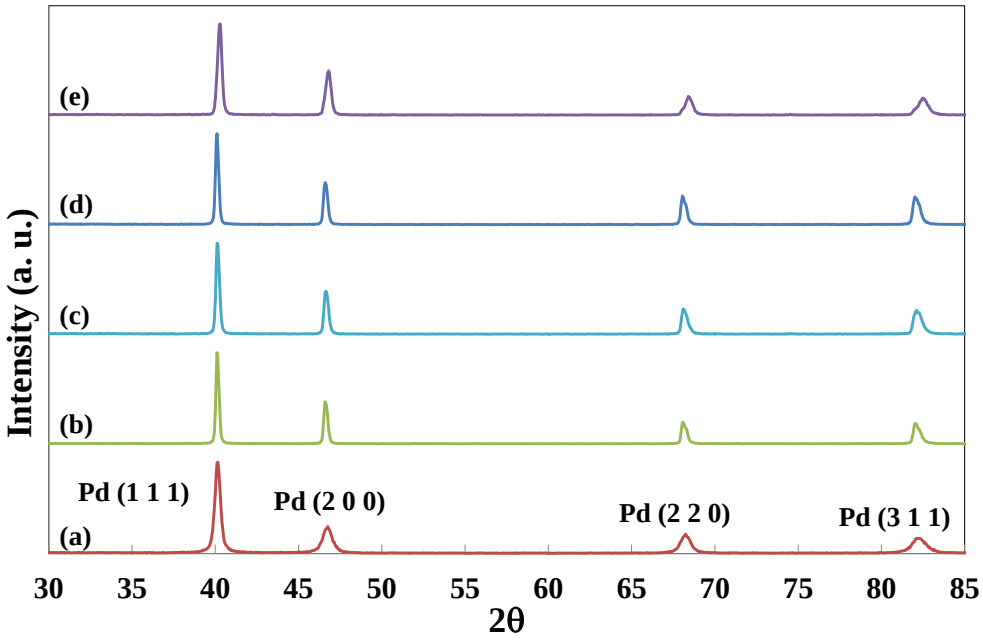


Figure 8.17. XRD patterns of thePd samples that were (a) as-deposited, and recovered at 500°C in $H_2$ for 48 hours after the 24 hours to a 50 ppm $H_2S/H_2$ at (b) 350ºC, (c) 400ºC, (d) 450ºC, and (e) 500ºC.

EDX scans also provided evidential results for desorption of adsorbed sulfur from the Pd layers after recovering. Figure 8.18 is the EDX spectrum of the recovered Pd samples that was previously poisoned in the 50 ppm $H_2S/H_2$ mixture at 350°C for 24 hours. No sulfur composition was detected as indicated by the negligible sulfur peak observed in the EDX spectrum (Figure 8.18). Other recovered Pd samples that were previously poisoned under other conditions also showed un-detectable sulfur composition (by the EDX).

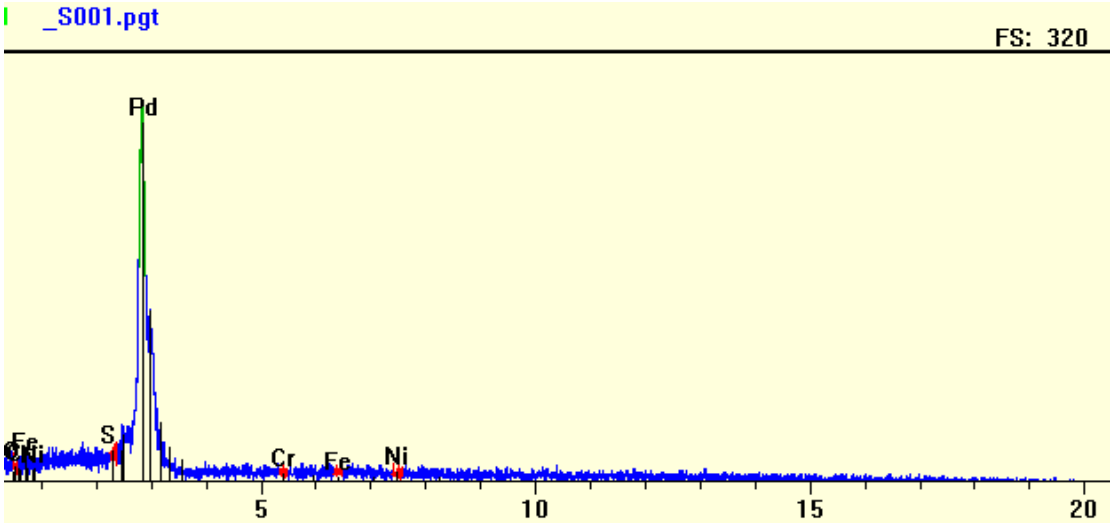


Figure 8.18. EDX spectrum of the Pd coupon after recovering at 500C in $H_2$ for 48 hours that was previously exposed to a 50 ppm $H_2S/H_2$ mixture at 350°C for 24 hours.

The results suggested that the bulk sulfidation of Pd and the transition between $Pd_4S$ and Pd phase was reversible. The restoration of the Pd phase from the $Pd_4S$ phase in $H_2$ was mainly due to that the $H_2S$ concentration became below the equilibrium concentration required to sustain the stable Pd sulfide according to the thermodynamic calculations (See Figure 8.6). As a result, the reduction of the Pd sulfide back to pure Pd was favored and took place in $H_2$ environment (Iyoha et. al. 2007).

In addition, the tendency for sulfur to segregate to the Pd surface also resulted in the removal of the sulfur in the bulk. The segregation of sulfur from the bulk has been confirmed in the literature (Matsumoto et. al., 1980). The authors observed that sulfur segregated to the surface from the bulk while heating the PdS sample at 773K. It should be noted that the surface of the PdS sample used by the authors was pre-treated with oxygen of several micro-torrs ($10^{-6}$ torr) at 673K followed by flashing to 1000K for a few

second under vacuum. The surface of the sample was confirmed by the Auger Electron Spectroscopy to be pure Pd before the experiments. The authors reasoned the tendency for the sulfur segregation to the Pd surface was due to the lower sublimation heat of sulfur compared to Pd according to the thermodynamics.

In spite of the fact that $Pd_4S$ formed during the poisoning was able to be reduced to Pd after recovering as shown by the previous evidential results, there was still irreversible change in the micro-structure of the Pd layer caused by the sulfide formation. Figure 8.19 is the SEM micrographs of the recovered Pd samples previously poisoned under different conditions. Although the sulfide nodules that were seen on the poisoned Pd samples (See Figure 8.3, Figure 8.5, and Figure 8.8) were barely seen after the recovery, the muddy surface morphologies still indicated some extent of the irreversible structural damage caused by the incorporated sulfur. In addition, the pores generated during the poisoning under some conditions (e.g. 24 hour at 350 and 400°C with 50 ppm $H_2S$; shown in Figure 8.3) remained on the surface (Figure 8.19(k) and (i)). As expected, the higher extent of the structural damage was observed on the samples that were previously poisoned under more severe poisoning conditions with large amounts of sulfide formed. The result indicated that although desorption of adsorbed sulfur was possible on the poisoned Pd, the structural change caused by the sulfide formation (i.e. sulfur incorporation) was permanent.

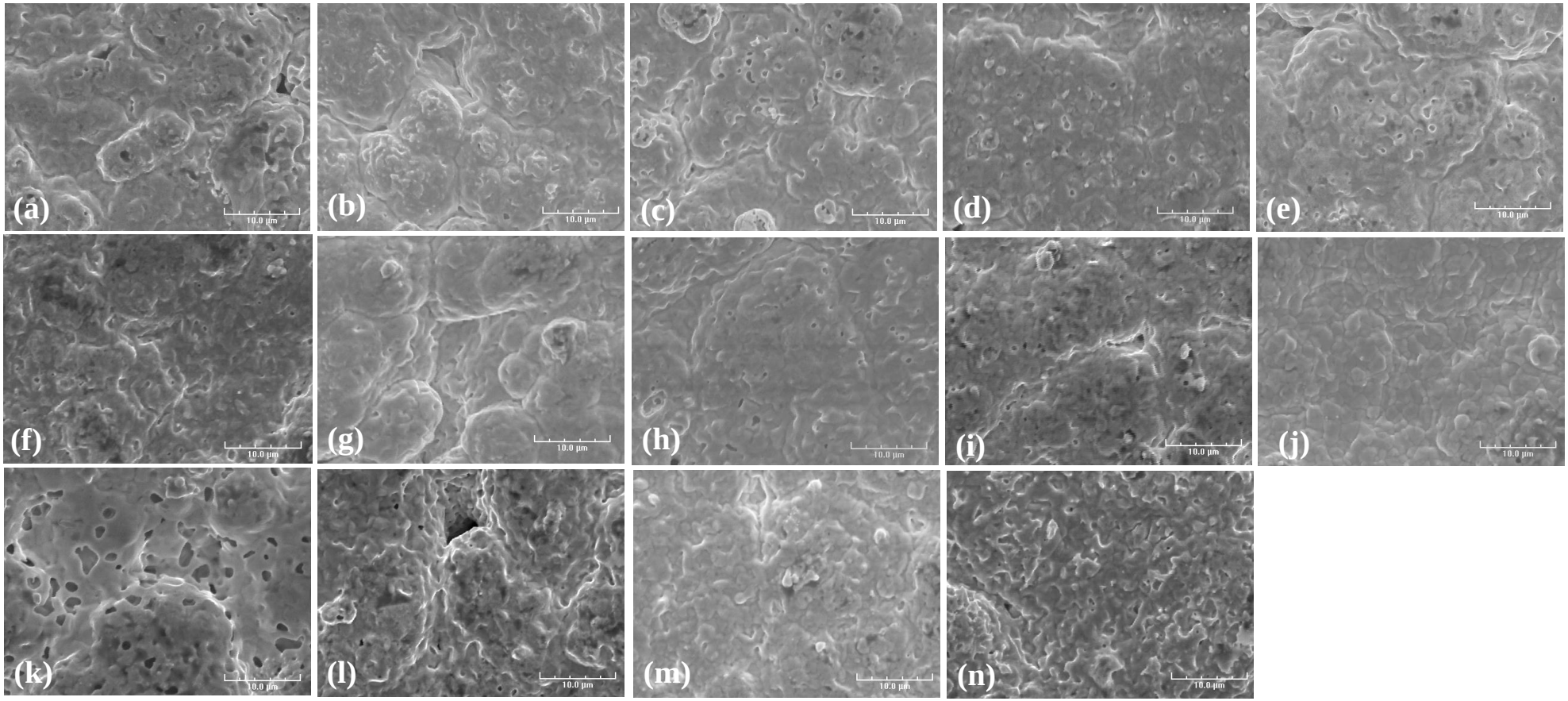


Figure 8.19. SEI micrographs of the Pd samples that were recovered at 500°C in $H_2$ for 48 hours after the exposure to a (a) 0.2 ppm, (b) 2 ppm, (c) 5 ppm, (d) 10 ppm, (e) 15ppm, (f) 30ppm at 400ºC for 24 hours, (g) 50 ppm at 400ºC for 2 hours, (h) 4 hours, (i) 8 hours, (j) 12 hours, (k) 50 ppm for 24 hours at 350ºC, (l) 400ºC, (m) 450ºC, and (n) 500ºC.

Although most of the adsorbed sulfur could be desorbed resulting in that no bulk sulfide was observed after the recovery, there was most likely surface sulfide remaining on the surface of the Pd samples due to the high stability of the surface sulfide. Such un-recoverable surface sulfide caused the irreversible permeance loss of the Pd membranes after the recovery as discussed in *Chapter 7*. The surface sensitive instrument, XPS was used for analyzing the surface adsorbed sulfur as mentioned earlier, and the XPS results of the recovered Pd samples are given and discussed in *Chapter 9*.

Figure 8.20 shows the XRD patterns of the recovered Pd/Au samples that were previously poisoned in a 50 ppm $H_2S/H_2$ for 24 hours at 350 - 500°C. As expected, only the Pd/Au peaks in the XRD patterns were observed on the recovered Pd/Au samples since no bulk sulfide peaks appeared even after the poisoning (See Figure 8.11). In addition, no sulfur content was detected on the recovered Pd/Au samples by the EDX technique. Due to the small amount of sulfur adsorption on the Pd/Au surfaces during the poisoning, the influence of the recovery on the sulfur content on the Pd/Au surfaces were not detectable by the XRD and the EDX, and the XPS study regarding the recovery of the Pd/Au samples is given in *Chapter 9*.

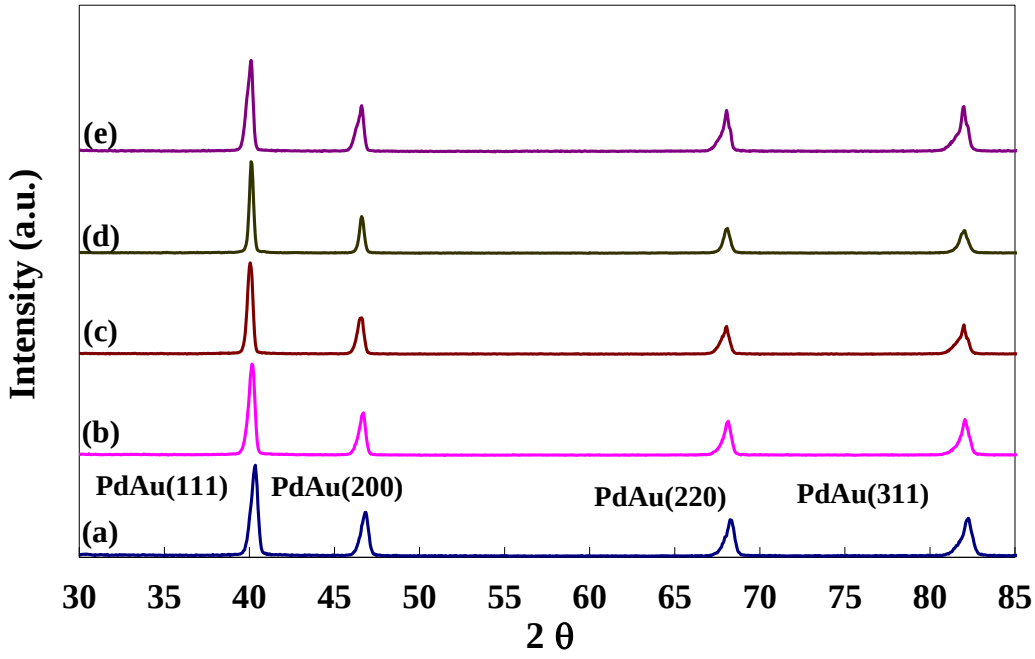


Figure 8.20. XRD patterns of the Pd/Au samples that were (a) as-formed, and recovered at 500°C in $H_2$ for 48 hours after the 24 hours exposure to a 50 ppm $H_2S/H_2$ at (b) 350ºC, (c) 400ºC, (d) 450ºC, and (e) 500ºC.

Figure 8.21 shows the surface morphologies of the recovered Pd/Au samples that were previously poisoned under different conditions. Contrary to the results of the recovered Pd, the morphologies of the recovered Pd/Au samples were nearly identical compared to the ones before recovering and poisoning (See Figure 8.12). This was expected since the morphological changes of the Pd/Au samples were minimum after the sulfur exposure due to the negligible sulfur incorporation into the lattice of the Pd/Au alloy.

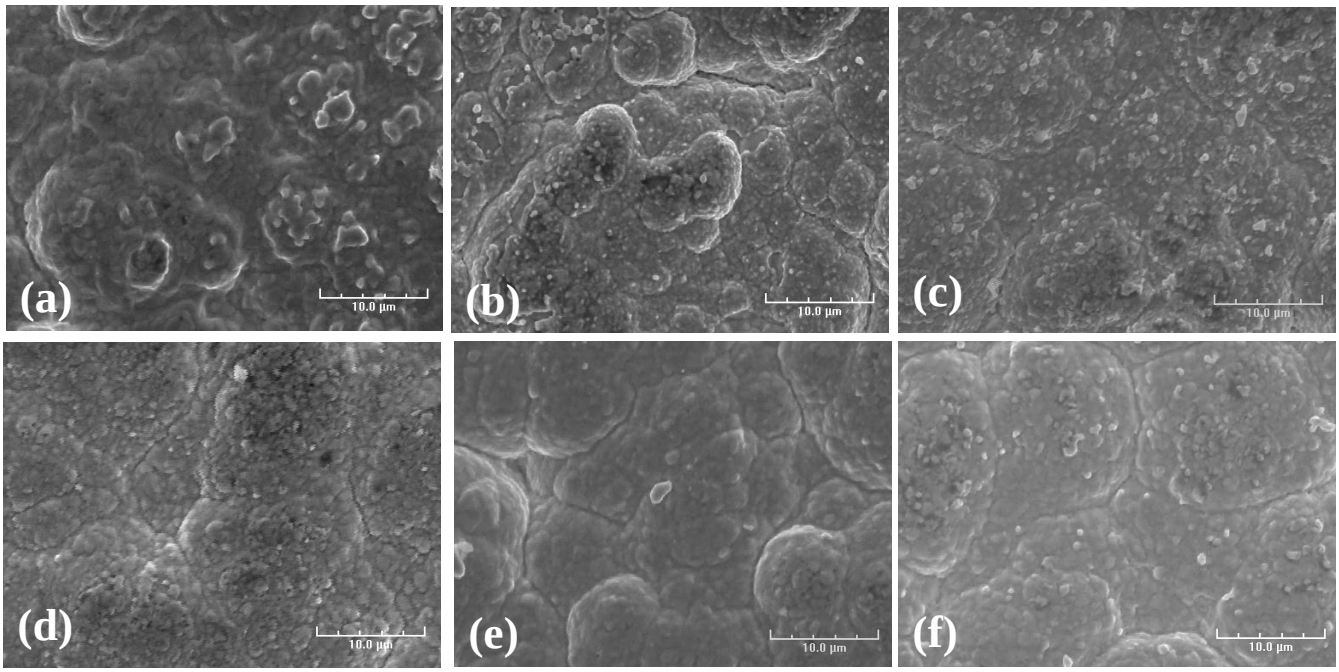


Figure 8.21. SEI micrographs of the Pd/Au samples that were recovered at 500°C in $H_2$ for 48 hours after the 24 hours exposure to a (a) 0.5 ppm $H_2S/H_2$, (b) 5 ppm $H_2S/H_2$ at 400ºC, (c) 50 ppm $H_2S/H_2$ at 350ºC, (d) 400ºC, (e) 450ºC, and (f) 500ºC.

## 8.4 Conclusions

By performing the coupon study, the influence of $H_2S$ exposures on the micro structure of the Pd and the Pd/Au films were investigated. The sulfidation of Pd with the formation of bulk $Pd_4S$ in the temperature range of 350 - 500ºC with the exposure to the $H_2S/H_2$ gas mixtures was confirmed.

The exposure conditions for forming stable $Pd_4S$ observed in the study agreed with the thermodynamic prediction. The sulfidation of Pd was temperature dependent and more $Pd_4S$ was formed at lower temperatures in the temperature range studied due to the less thermodynamic stability of $Pd_4S$ at higher temperatures. The growth of the $Pd_4S$ layer was one-dimensional phase boundary controlled according to the fit of Avrami model with $Pd_4S$ layer increased with exposure time. The dissolution of sulfur into the Pd lattice while forming $Pd_4S$ caused the pore formation on the Pd layers. Pinholes were formed due to the large stress in the Pd lattice caused by the incorporation of sulfur as $Pd_4S$ was formed. On the other hand, the Pd/Au alloy samples showed the resistance to forming bulk sulfide under the same poisoning conditions for as long as 96 hours as evidenced by that no sulfide phase was detected and the insignificant morphology change after the $H_2S$ poisoning.

The recovery tests of the poisoned Pd samples indicated that the formation of bulk $Pd_4S$ was reversible. The restoration of Pd from $Pd_4S$ in $H_2$ was resulted from the favored backward reaction of the $Pd_4S$ formation due to the equilibrium condition. However, the structural change caused by the bulk sulfide formation (e.g. pinhole formation) was irreversible. On the other hand, since no bulk sulfidation occurred on the Pd/Au samples resulting in the minimum micro-structural change after the sulfur tests,

the compositional and morphological changes of the Pd/Au samples after the recovery tests were also negligible from the XRD and SEM (EDX) analysis.

# 9. Surface chemical analysis of the $H_2S$-exposed/$H_2$-recovered Pd and Pd/Au alloy

## 9.1 Introduction

Although the microstructure analysis has confirmed the lack of bulk sulfide formation on the Pd/Au layers after the $H_2S$ exposure as described in *Chapter 8*, the permeance decline of the Pd/Au membranes in the presence of $H_2S$ (*Chapter 7*) suggested the presence of surface sulfide. In addition, the restoration of Pd phase from the $Pd_4S$ after the recovery in $H_2$ has also been discussed in *Chapter 8*. However, the irrecoverable permeance loss of the Pd membrane after the recovery (*Chapter 7*) indicated the irreversibly adsorbed sulfur on the Pd surface. Indeed, surface sulfide species were much more thermally stable than bulk sulfide species as described in *Section 2.6*.

In order to study the surface sulfide which mainly accounted for the permeance loss of the Pd/Au and Pd membranes, the surface chemical analysis of the sulfur-poisoned Pd and Pd/Au layers was required. One of the most powerful and suitable characterization methods for the surface chemical analysis is the X-ray Photoemission Spectroscopy (XPS). However, very few research have been reported regarding the surface chemical analysis of the sulfur-poisoned Pd-based layers (Pomerantz, 2010; Miller et. al. 2008b). As the cited work was focused on the Pd/Cu alloys, none has been

reported regarding the Pd/Au layers. In addition, the surface chemical analysis of the recovered Pd-based layers was even rarely reported in the literature.

As a result, the main objective of this chapter was to analyze the surface sulfur on the sulfur-poisoned Pd and Pd/Au alloys by the use of XPS. The effects of exposure temperature, time and the $H_2S$ concentration on the surface sulfide formation were investigated. In addition, the surface sulfur characterization of the Pd and Pd/Au alloys after the recovery in $H_2$ was also performed.

## 9.2 Experimental

The Pd and Pd/Au (8 – 11 wt% Au) coupon samples characterized in this chapter were prepared on the 0.1 $\mu$m media grade PSS or porous Hastelloy C-22 coupons (1cm x 1cm or 1cm x 1.5cm). The $H_2S$ poisoning and the recovery of the Pd and Pd/Au coupons were conducted in the annealing module inside a BLUE M tube furnace. The detailed preparation of the coupons as well as the experimental setup and procedure were described in *Section 8.2*. The exposure conditions for the Pd and Pd/Au alloy coupons were with the $H_2S$ concentrations of 0.2 – 55 ppm at the temperatures of 350 - 500°C for 2 – 24 hours. The recovery of the poisoned samples was performed at 500°C in $H_2$ for 48 hours.

The XPS instrument used for the surface chemical analysis was the Thermo Scientific K-alpha at the High Temperature Material Laboratory at Oak Ridge National Laboratory, Tennessee. The detailed description of the instrument as well as the operation conditions was provided in *Section 3.3.3*.

## 9.3 Results and Discussion

### *9.3.1 Poisoned Pd*

Figure 9.1 shows the XPS survey spectra for the Pd samples before and after the $H_2S$ exposures under the different conditions. The spectrum for the Pd sample before the $H_2S$ exposure (Figure 9.1(a)) shows not only the Pd peaks, but also the carbon 1s peak, nitrogen 1s peak, oxygen 1s[13] and Auger KLL peak, sodium 1s and KL1 peak, and chlorine 2p peak. In addition, although not apparent, the S 2s and 2p peaks were also observed in the spectrum. The presence of sodium along with chlorine was most likely from the hands (NaCl) during the sample handling. On the other hand, carbon, oxygen, nitrogen, and sulfur usually came from the environment due to the unavoidable adsorption of the gaseous contaminants during the sample storage.

Similar spectra compared to the un-poisoned one were observed for the samples after the exposures to the $H_2S$ under the different conditions (Figure 9.1(b)-(e)). Although it's not obvious in the plot, the intensities of the sulfur 2s and 2p peaks increased after the poisoning even under the mildest exposure conditions. These conditions included 0.2 ppm $H_2S$/400°C/24 hours (Figure 9.1(b)), 50 ppm $H_2S$/400°C/2 hours (Figure 9.1(c)), and 50 ppm $H_2S$/500°C/24 hours (Figure 9.1(d)), where no $Pd_4S$ phase was detected after the poisoning as described in *Chapter 8*. The spectrum of the Pd sample after the $H_2S$ exposure under the condition that generated the highest extent of the sulfidation (i.e. 50 ppm $H_2S$/350°C/24 hours) showed the most intense sulfur 2s and 2p peaks as expected

[13] O 1s peak overlaps with Pd 3p peak at ~530 eV, the presence of the O Auger KLL feature (shown at ~1000 eV) confirmed the presence of O 1s peak as well as oxygen.

(Figure 9.1(e)). The relative atomic fractions of Pd and S on the Pd samples before and after the $H_2S$ exposure under the different conditions were summarized in Table 9.1.

It should be noted that the sulfur fraction was calculated based on the sulfur 2p and Pd 3d peak in the survey scans. Noticeable increases in the sulfur atomic fraction were observed on the poisoned samples compared to the un-poisoned one even under the mildest exposure conditions. The results showed that sulfur had indeed adsorbed on the Pd surfaces following the exposure to the $H_2S/H_2$ mixture.

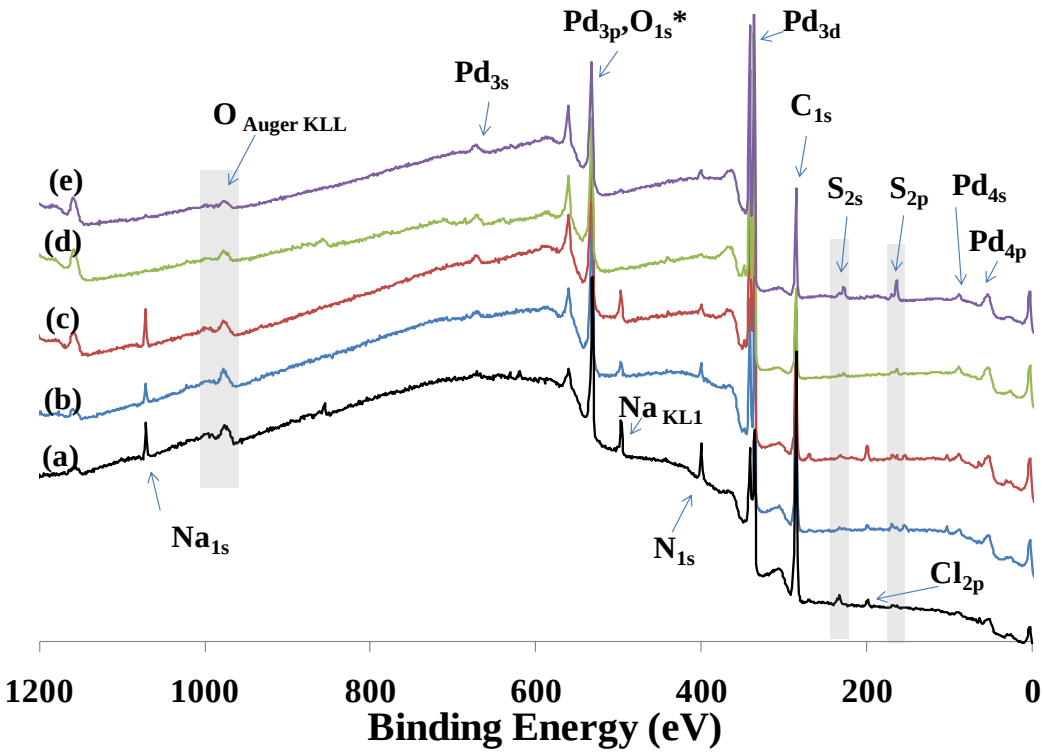


Figure 9.1. XPS survey spectra of (a) un-poisoned Pd, after exposing to (b) a 0.2 ppm $H_2S/H_2$ at 400°C for 24 hours; to a 50 ppm $H_2S/H_2$ (c) at 400°C for 2 hours, (d) at 500°C for 24 hours, and (e) 350°C for 24 hours.

Table 9.1. The composition of the poisoned Pd samples.

| Sample conditions | Pd (at%) | S (at%) |
|---|---|---|
| Un-poisoned | 90.5 | 9.5 |
| 0.2 ppm $H_2S$/400°C/24 hours | 77.1 | 22.9 |
| 50 ppm $H_2S$/400°C/2 hours | 79.6 | 20.4 |
| 50 ppm $H_2S$/500°C/24 hours | 80.4 | 19.6 |
| 50 ppm $H_2S$/350°C/24 hours | 62.2 | 37.8 |

High resolution (narrow) scans of the elements interested including Pd, S, C, and O were performed on the poisoned Pd samples for more accurate quantitative analysis and the chemical status of the elements. The analysis of the high resolution sulfur peak was especially emphasized in the study since the quantity and the bonding status of sulfur was the major interest of the work. Figure 9.2 shows the high resolution core level spectrum of S 2p of the Pd sample exposed to the 50 ppm $H_2S/H_2$ mixture for 24 hours at 400°C. The peak fitting of the spectrum was also shown in Figure 9.2. Two separate S-species are apparent from the data shown: the feature at ~162 - 165 eV is attributed to a sulfide and the feature at ~168 eV to a sulfate. The presence of the sulfide species confirmed the bonding between Pd and sulfur, which caused the permeance decline of the membranes in the presence of $H_2S$ (*Chapter 7*). On the other hand, the presence of sulfate species which contained the bonding with oxygen was most likely resulted from the adsorption of the environment contaminants and the partial oxidation of the sulfide on the surfaces during the storage.

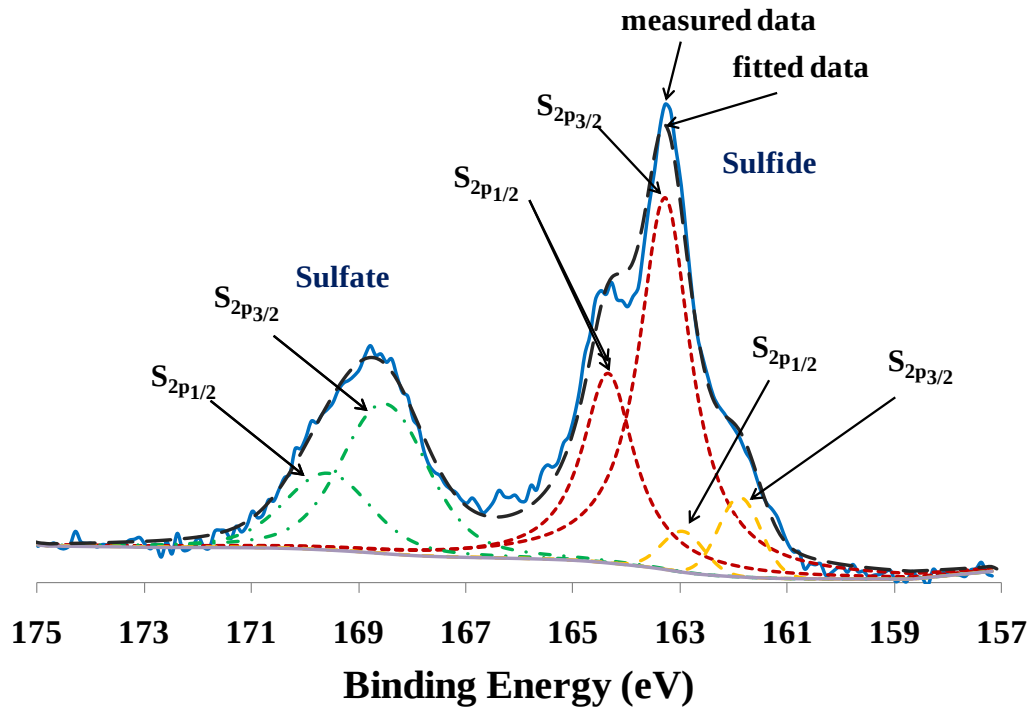


Figure 9.2. High resolution XPS scan and peak fitting of the S 2p peak of the Pd sample after the $H_2S$ exposure of 50 ppm at 400°C for 24 hours.

As shown in Figure 9.2, the broad and non-descript shape of the sulfate peak indicated a number of sulfate bonding chemistries. The deconvolution of the sulfate peak, therefore, became extremely difficult due to the lack of knowledge of how many bonding chemistries that comprised the peak and their corresponding standard binding energies. In fact, to quantify the amount was more important rather than differentiating the bonding chemistries of sulfate since the bonding chemistries of sulfate would not provide the information regarding the bonding chemistry between Pd and sulfur, which was major concern in the study. As a result, only a set of sulfur double peak with S $2p_{3/2}$ at ~168.8 eV was used to fit the sulfate peaks for quantifying the sulfate fraction. It should be noted that sulfur possesses a doublet peak structure in the 2p orbitals (Moulder et al., 1993). For the peak fitting conditions used in the study for both the Pd and Pd/Au samples, the full-

width, half-maximum (FWHM) values were constrained between 0.5 – 3.5 and the Lorentzian/Gaussian (L/G) ratio was constrained 0 - 50%. The distance of the 2p orbital split was also 1.16 eV. All S $2p_{1/2}$ peaks were equal to half the area of the corresponding $2p_{3/2}$ peak, and the FWHM and L/G ratios of the doublets were kept equal.

On the other hand, the well-defined doublet sulfide peaks observed indicated a predominant Pd-sulfide species with the S $2p_{3/2}$ peak at ~163.2 eV (Figure 9.2). However, a small shoulder at lower binding energies of ~ 162 eV indicated a small fraction of another sulfide species. Since the only metal on the sample surface was Pd as evidenced by the survey scans (See Figure 9.1). The results suggested that there was possibly more than one Pd-sulfide species formed caused by the poisoning.

In fact, the sulfide species of the lower binding energy (~162 eV) became more apparent under the milder poisoning conditions where the bulk $Pd_4S$ was not detected after the exposures (e.g. 500°C/24 hours/55 ppm $H_2S$). Figure 9.3 shows the high resolution spectra of S 2p of the Pd samples exposed to the 50 ppm $H_2S/H_2$ for 24 hours at 350 - 500°C. While the spectra of the Pd samples after the $H_2S$ exposures at 350 - 450°C were similar with the predominant Pd sulfide species (S $2p_{3/2}$ at ~163.2 eV) appearing in the spectra, the spectrum after the exposure at 500°C showed the broad and non-descript sulfide peak with the summit of the peak shifting towards the lower binding energy. The less-defined sulfide peak indicated that more than one sulfide species was presented on the samples and none of them was predominant, which was due mainly to much smaller sulfide peak at 163.2 eV compared to other poisoning temperatures. In fact, the intensity of the sulfide peak at 500°C was much smaller compared to other spectra at lower temperatures, suggesting that much smaller amount of sulfur was presented on the sample.

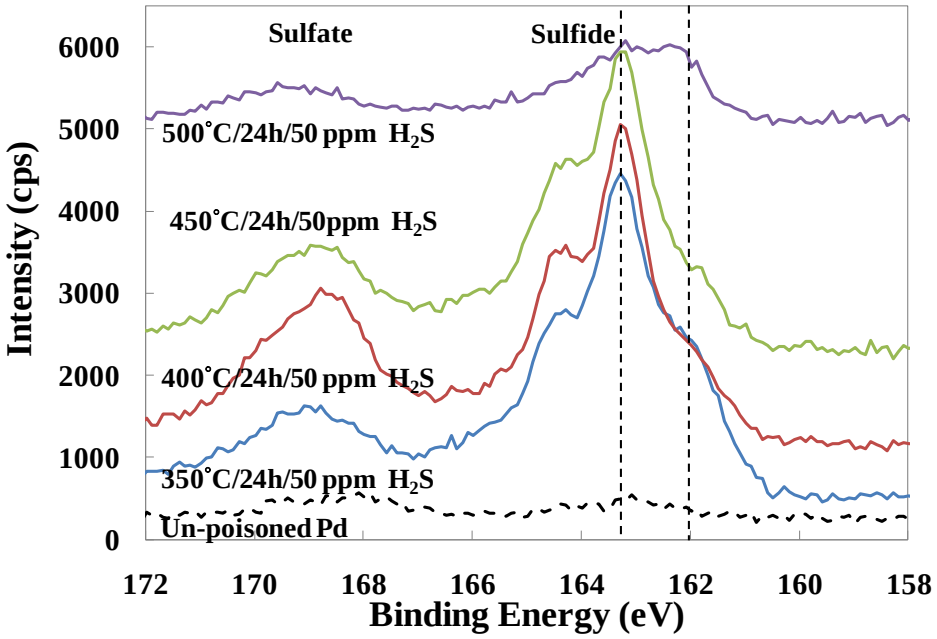


Figure 9.3. High resolution XPS scans of the S 2p peak of the Pd samples after the $H_2S$ exposure of 50 ppm for 24 hours at 350 - 500°C.

Similar broad and non-descript sulfide peaks with much smaller peak intensities and the shift of the peak summit toward the lower binding energy were also observed on the samples after the exposures under the conditions that did not generate the bulk $Pd_4S$ formation, such as below 5 ppm $H_2S$ at 400°C for 24 hours, or 2 hours exposure at 400°C with a 50 ppm $H_2S/H_2$ mixture (*Chapter 8*). The results appeared to suggest that the sulfide of the lower binding energy (~162 eV) was most likely resulted from the Pd-S bonding at top surface, while the sulfide of higher binding energy (~163.2 eV) was caused by the Pd-S bonding in the sub-layers. In the literature, Forbes et al. (1992) has proposed the structural model for the sulfur-adsorbed Pd (1 1 1) surface with one sulfur atom on the top surface and two sulfur atoms in the sub-layers exposing to 4 Pd atoms per unit cell. The model has been substantiated by the authors with the results of the

atomic resolution scanning tunneling microscope (STM) and the low energy electron diffraction (LEED) analysis of the $(7^{0.5}*7^{0.5})R19^{o}$ sulfur over-layer lattices formed on the Pd (1 1 1) surface. The Pd-S bonding in the sub-layers was considered to be the precursor for the bulk sulfide. Since the bulk $Pd_4S$ phase has been confirmed by the XRD on the poisoned Pd samples that exhibited the sub-layer Pd-S bonding (*Chapter 8*), the Pd-S bonding in the sub-layer (~163.2 eV) was most likely resulted from the $Pd_4S$.

In addition, the binding energy of the sulfide S 2p peak was found to increase with increasing surface sulfur coverage on the Pd surface (Matsumoto et. al., 1980). As shown in Figure 9.3, the results obtained agreed with the trend. It should be noted that after the exposure under the milder condition (e.g. 500°C/24 hours/55 ppm $H_2S$), the sulfur coverage was also smaller. The binding energy for the S 2p peak of PdS was reported to be $161.5 \pm 0.3$eV (Matsumoto et. al., 1980). As a result, the sulfide with the binding energy of ~162 eV was probably PdS. However, according to the thermodynamics, PdS is less stable compared to other possible sulfides such as $Pd_3S$ or $Pd_{16}S_7$ and required much higher $H_2S$ concentration to form (Taylor, 1985). Therefore, further characterization is still needed to confirm the type of the Pd-S bonding formed on the Pd surface (at ~ 162 eV).

Figure 9.4 shows the high resolution core level spectra of Pd 3d orbitals of the Pd samples before and after the exposure to the 50 ppm $H_2S/H_2$ for 24 hours at 350 - 500°C. The position of the Pd $3d_{5/2}$ peak before poisoning was at 335.38 eV, while the binding energy of the Pd-Pd bonding was 335.1 eV (Moulder et al., 1993). The slight peak shift to a higher binding energy was possibly due to the slight surface oxidation. The formation

of PdO at 298K was confirmed in the literature (Su et. al., 1998). The presence of the oxygen was also confirmed by the survey spectra (See Figure 9.1).

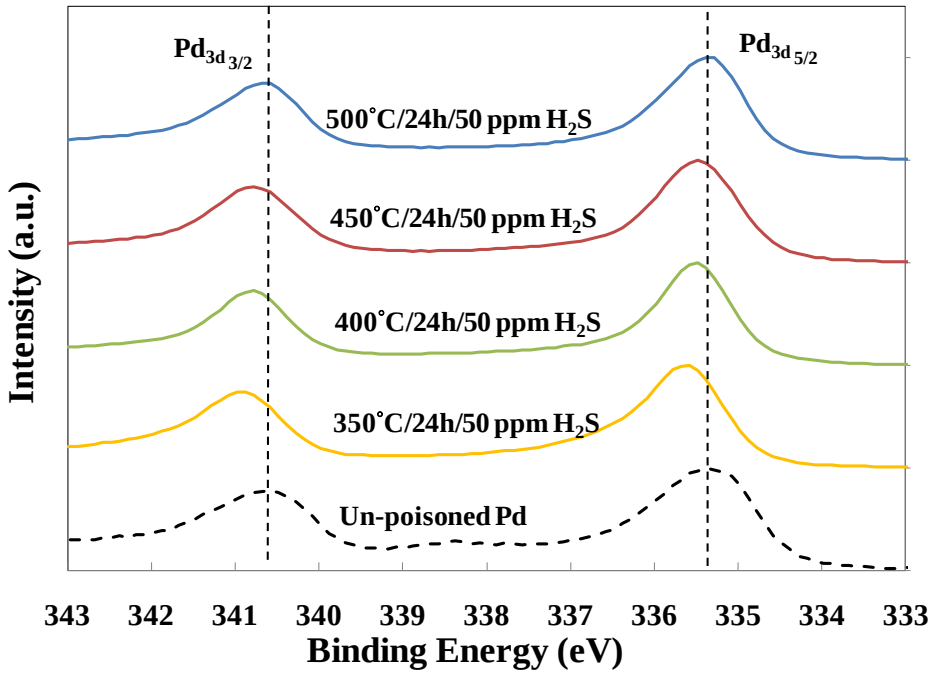


Figure 9.4. High resolution XPS scans of the Pd 3d peak of the Pd samples after the $H_2S$ exposure of 50 ppm for 24 hours at 350 - 500°C.

The shifts of the Pd 3d peaks to the higher binding energy after the poisoning were observed in Figure 9.4, especially at lower poisoning temperatures. When Pd and S form a bonding, the electrons in Pd transfer to sulfur due to the higher electron affinity of sulfur. This resulted in the binding energy shift to a lower value for sulfur compared to S-S bonding and to a higher value for Pd compared to Pd-Pd. Along with the binding energy of sulfide observed (~163.2 eV, Figure 9.3), the shift of the Pd 3d peaks to the higher binding energy substantiated the Pd-S bonding. It should be noted that the S-S bonding has the binding energy of 164 eV for the S 2p peak (Moulder et al., 1993).

As shown in Figure 9.4, the shift of the Pd 3d peak increased with the decreasing poisoning temperatures, which suggested the increase of the Pd-S bonding with decreasing temperature. Higher extents of the sulfur poisoning on the Pd samples at lower temperatures were confirmed in the XRD and SEM study (*Chapter 8*). Chaplin et al. (2007) has also reported that the shift of the Pd 3d peak increased with increasing sulfur fouling (poisoning) of the Pd-based catalysts. Similarly, the shifts of the Pd 3d peaks to the higher binding energy after poisoning under other conditions tested in the study (i.e. 0.2 – 50 ppm $H_2S$ for 2 – 24 hours at 400°C) were also observed with the only difference being the extent of the peaks shift. Once again, the higher extents of the peak shift due to more Pd-S bonding were observed on the samples under the conditions which caused the higher extent of sulfur poisoning.

Figure 9.5(a) shows the composition as a function of depth of the Pd sample exposed to the 50 ppm $H_2S$ at 450°C for 24 hours. The depth was determined by using a known sputter rate (5 *n*m/min) calibrated with a standard $SiO_2$ film. The S 2p signal was deconvoluted into a sulfide species and a sulfate species. Due to the small signal strength, both sulfide and sulfate signals are increased by a factor of 5 for plotting in order to obtain a better observation. The carbon signal decreased largely since the sputtering began, which confirm that the carbon came from the environments. Both Pd and the sulfide signals increased as the adventitious carbon was removed by sputtering. While Pd increased to a leveled value of approximately 70 at%, the sulfide increased initially to ~11 at% then decreased to a value of ~8 at%. The constant sulfide fraction (~8 at%) throughout the investigated depth profile (of ~12 *n*m) suggested that the sulfur was bonded with Pd deep into the Pd layer. Indeed, bulk sulfide ($Pd_4S$) was confirmed on the

sample after the $H_2S$ exposure under the condition as discussed in *Section 8.3.1*. On the other hand, the sulfate decreased at all sputter increments from ~4 at% initially to ~2 at%. This indicated that the sulfate species was most likely only present on the surface. The narrow (high resolution) scans of the S 2p at each sputter increment (Figure 9.5(b)) show that the sulfide peak still noticeable deep into the Pd layer (up to 12 *n*m deep) while the sulfate peak became negligible in the sub-surface layer. The results substantiated that the sulfide was still present deep into the Pd layer while the sulfate was only present on the surface. It should be noted that the leveled values for both the adventitious carbon and sulfate signals may be due to shadowing of the supporting Ar-ion beam because of high surface roughness of the porous coupon samples.

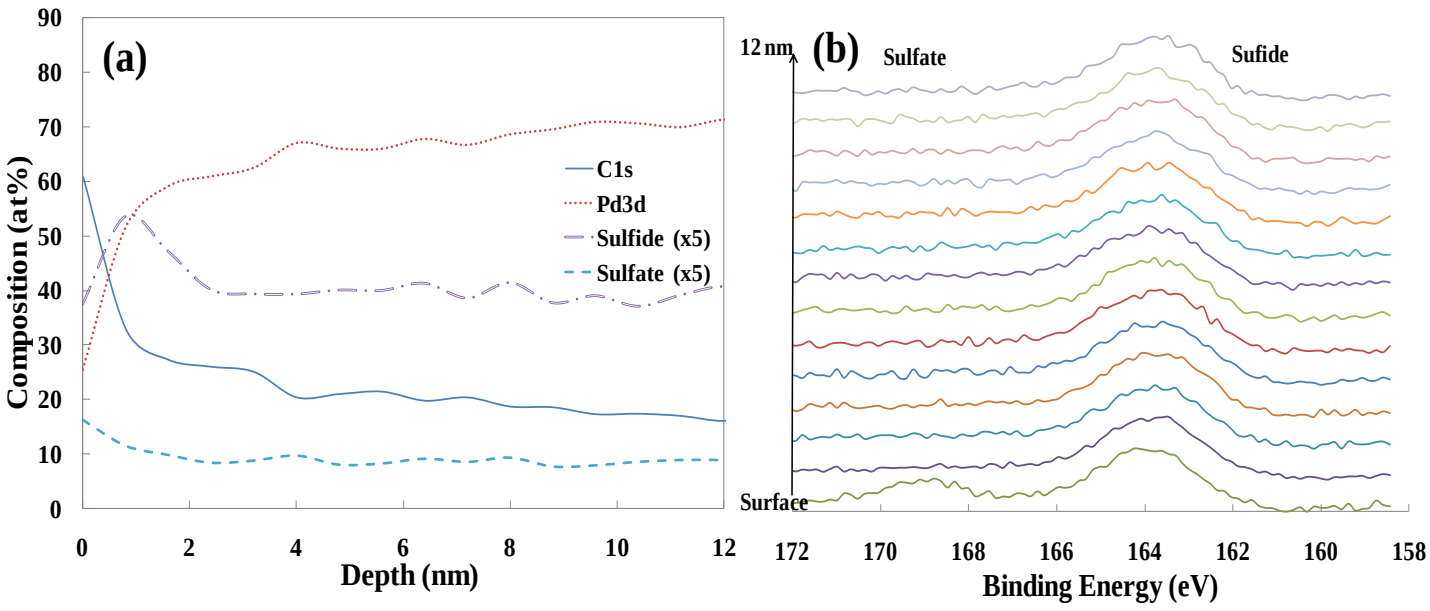


Figure 9.5. (a) Composition as a function of depth of the Pd sample after the exposure to the 50 ppm $H_2S$ at 450°C for 24 hours, and (b) corresponding narrow scans of the S 2 p peak at each sputtering increment.

Figure 9.6(a) shows the composition as a function of depth of the Pd sample exposed to the 50 ppm $H_2S$ at 500°C for 24 hours. Similarly, the S 2p signal was

deconvoluted into a sulfide species and a sulfate species. Both sulfide and sulfate signals are increased by a factor of 10 for plotting due to the extremely small signal strength. While Pd increased to approximately 70 at%, the sulfide increased initially to ~4 at% as carbon was removed then decreased with continued sputtering to ~2.5 at%. The sulfate decreased at all sputter increments from ~3 at% initially to < 1 at%. The narrow scans of the S 2p peak at each sputter increment are shown in Figure 9.6(b). In addition to sulfate, sulfide also decreased with increasing supporting increments although the decreasing rate was smaller compared to the sulfate. The result suggested that the sulfide formed on the condition (50 ppm $H_2S$/500°C/24 hours) was only in the near surface area and did not penetrate too deep into the Pd layer. The formation of the thinner sulfide layer at 500ºC (Figure 9.6) than at 350ºC (Figure 9.5) agreed with the results of the XRD and SEM (EDX) analysis (*Section 8.3.1*). The less (thinner) sulfide formed at higher temperatures was due to the decrease of the sulfide stability with increasing temperature as discussed in *Section 8.3.1*.

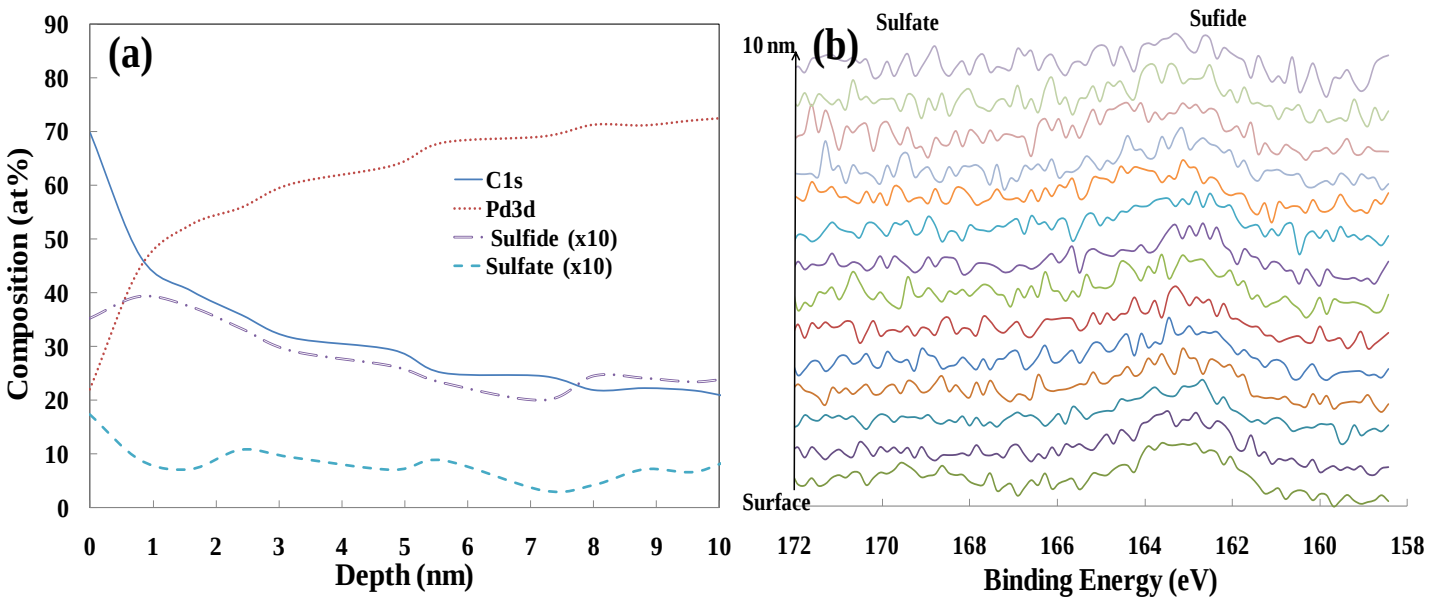


Figure 9.6. (a) Composition as a function of depth of the Pd sample after the exposure to the 50 ppm $H_2S$ at 500°C for 24 hours, and (b) corresponding narrow scans of the S 2 p peak at each sputtering increment.

In addition to the poisoning, the recovery of the poisoned Pd samples was also characterized for further understanding the Pd-S interactions. Figure 9.7 compares the high resolution spectra of Pd 3d orbitals of the Pd sample after being poisoned in the 50 ppm $H_2S/H_2$ for 24 hours at 350°C and after the recovery at 500°C in $H_2$ for 48 hours. The spectrum of the un-poisoned sample was also included in Figure 9.7 as the reference. The spectrum of the Pd sample after poisoning showed a shift of the Pd peaks to a higher binding energy compared to the un-poisoned Pd sample due to the Pd-S bonding as discussed previously. After the recovery, the Pd peaks shift back to almost the original positions before the poisoning indicating the reduction of the most Pd-S bonding formed during the $H_2S$ exposure. Similar shift of the Pd 3d peaks back to the original positions after the recovery was also observed on the Pd samples poisoned under other conditions tested in the study. However, based merely on the high resolution spectra of Pd 3d peaks,

it was insufficient to determine if there was still Pd-S bonding presented on the surface after the recovery.

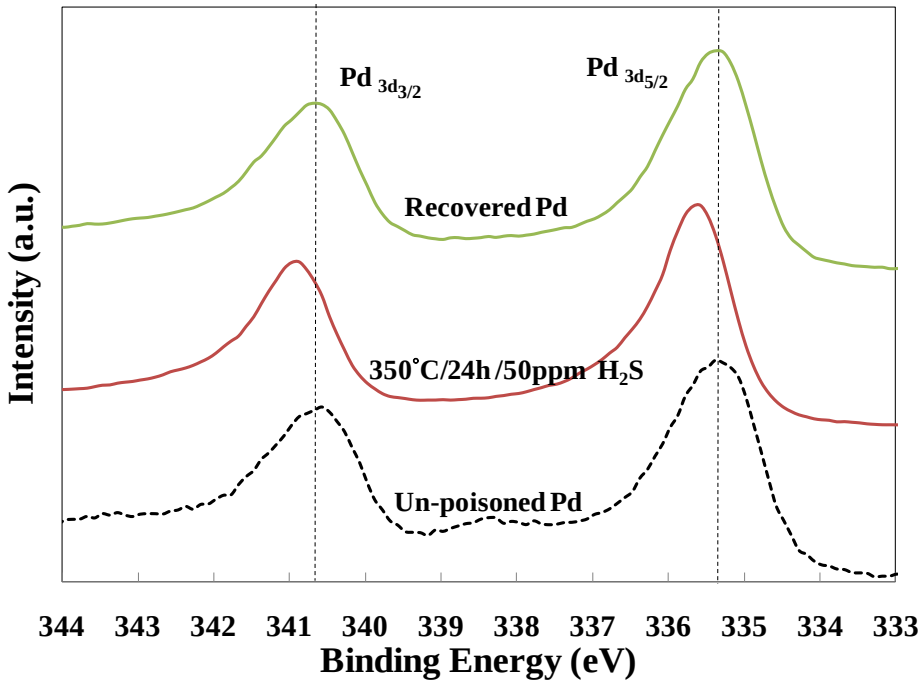


Figure 9.7. High resolution XPS scans of the Pd 3d peak of the Pd samples before, after the $H_2S$ exposure of 50 ppm for 24 hours at 350°C, and after recovery in $H_2$ at 500°C for 48 hours.

Figure 9.8 displays the high resolution spectra of S 2p orbitals of the Pd sample after poisoning in the 50 ppm $H_2S/H_2$ for 24 hours at 350°C and after the recovery at 500°C in $H_2$ for 48 hours. As shown in Figure 9.8, the significant decrease of the sulfide peak intensity after the recovery substantiated once again the reduction of the Pd-S bonding. In addition, the shape of the sulfide peak became broad and lost its apparent doublet peak feature with the summit of the peak shifting toward lower binding energy (~162eV). Since the well-define sulfide peak at the higher binding energy (~163.2eV) was resulted from the Pd-S bonding in the bulk as mentioned earlier, the result suggested that the most of the sub-layer bonded sulfur was removed from the Pd sample after the

recovery. Indeed, the disappearance of the $Pd_4S$ phase was observed on the Pd sample after the recovery as discussed in *Section 8.3.3*. However, there was still noticeable amount of sulfur on the sample (mostly on the surface) after the recovery under the recovering condition.

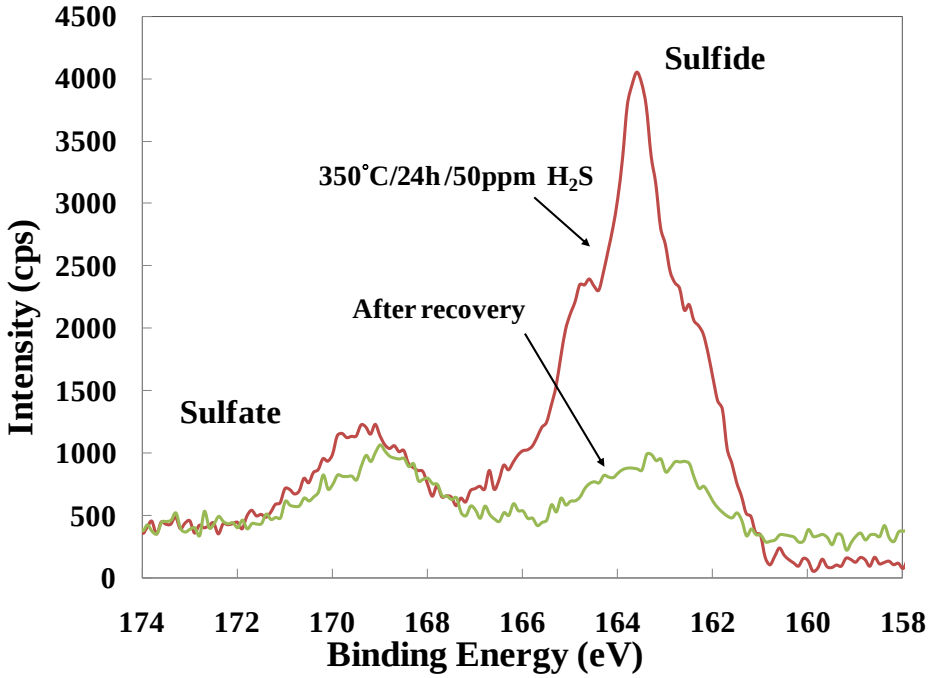


Figure 9.8. High resolution XPS scans of the S 2p peak of the Pd samples before, after the $H_2S$ exposure of 50 ppm for 24 hours at 350°C, and after recovery in $H_2$ at 500°C for 48 hours.

Figure 9.9 exhibits the high resolution spectra of S 2p orbitals of the Pd sample after poisoning in the 50 ppm $H_2S/H_2$ for 24 hours at 500°C and after the recovery. A decrease of the sulfide peak intensity after the recovery was observed in Figure 9.9 due to reduction of the Pd-S bonding. However, the decrease was not as noticeable as the one as observed in the case of poisoning at 350°C (See Figure 9.8) due to the fact that the sulfide formed was much less and only near the surface under the condition. Although the amount of the sulfide was smaller during the poisoning, there was still noticeable amount

of sulfide remained on the Pd surface after the recovery. This indicated that a certain amount of the sulfur was bonded with Pd with higher binding energies and it was difficult to remove those sulfur under the recovery condition. Further discussion on the recovery of the Pd samples that were previously poisoned under different conditions is given later in this section.

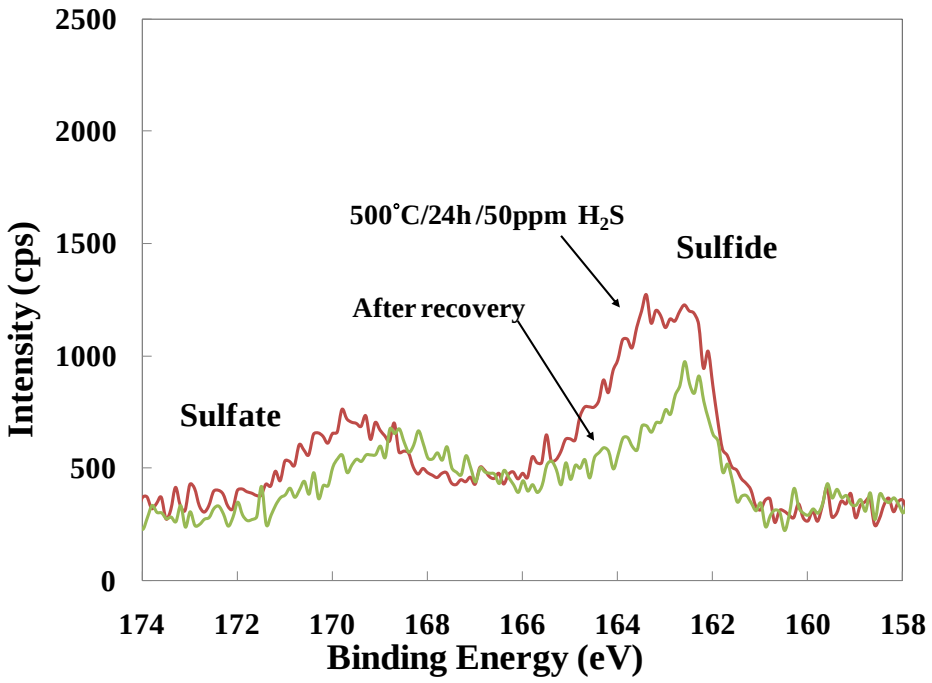


Figure 9.9. High resolution XPS scans of the S 2p peak of the Pd samples before, after the $H_2S$ exposure of 50 ppm for 24 hours at 500°C, and after recovery in $H_2$ at 500°C for 48 hours.

Figure 9.10(a) shows the composition as a function of depth of the Pd sample after the recovery that was previously exposed to the 50 ppm $H_2S$ at 450°C for 24 hours. The sulfide and sulfate signals deconvoluted from the S 2p signal are increased by a factor of 10 for plotting due to the extremely small signal strength. Once again, the increase of Pd to approximately 75 at% due to the removal of the adventitious carbon signal was observed. Both the sulfide and the sulfate decreased with continued sputtering

from ~ 2 at% to <1 at%. The narrow scans of the S 2p at each sputter increment shown in Figure 9.10(b) also confirmed the decrease of both sulfide and sulfate signal with increasing supporting increments. Since the sample after poisoning showed the sulfide presence deep into the Pd layer as shown in Figure 9.5, the result suggested that most of the Pd-S bonding in the bulk was removed and only Pd-S bonding near the surface remained after the recovery.

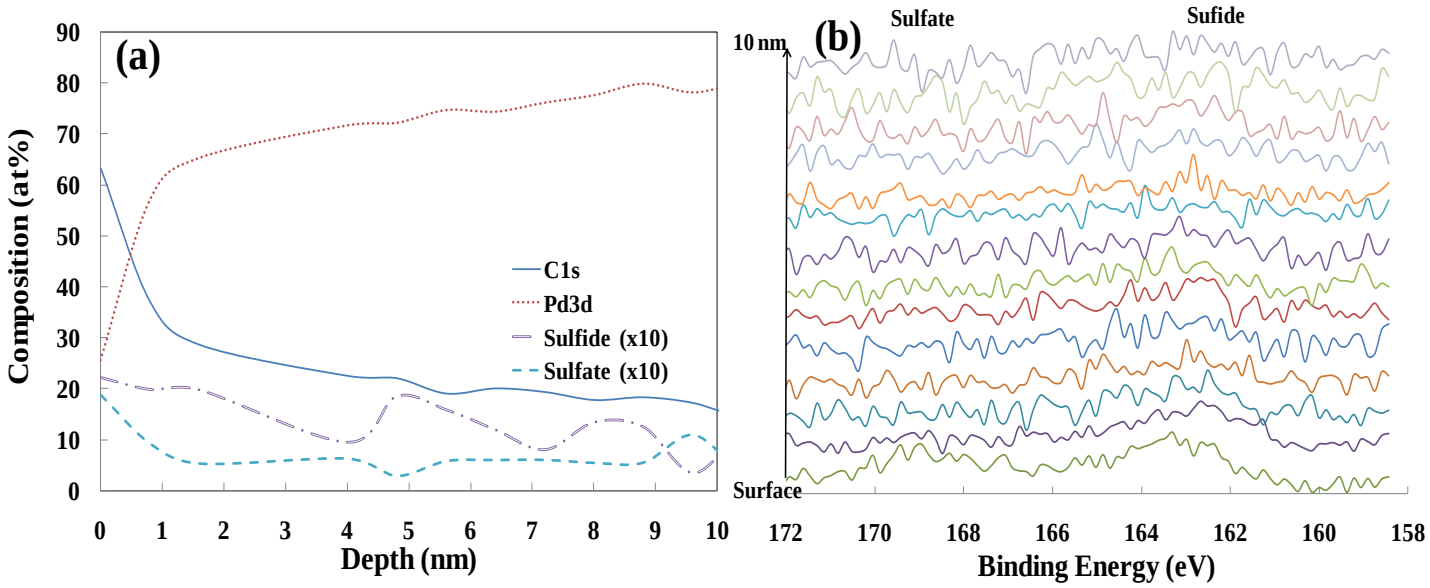


Figure 9.10. (a) Composition as a function of depth of the Pd sample after the exposure to the 50 ppm $H_2S$ at 450°C for 24 hours, and (b) corresponding narrow scans of the S 2 p peak at each sputtering increment.

Figure 9.11 shows the sulfur atomic fraction (relative to Pd) on the Pd samples after poisoning with the 50 ppm $H_2S$ for 24 hours at 350 – 400°C and the recovery. The sulfur and palladium content were calculated from the high resolution XPS S 2 p peak and Pd 3d peak. As observed in Figure 9.11, the sulfur content after the poisoning decreased with increasing temperature from approximately 36 at% at 350°C to ~18 at% at 500°C. More sulfur presented on the Pd sample at lower temperature agreed with the

results from the SEM and XRD studies, which was due to the exothermal adsorption of the $H_2S$ on the Pd as discussed in detailed in *Chapter 8*.

After the recovery, the decrease of the sulfur contents were observed on the Pd samples that were previously poisoned at all the temperatures (Figure 9.11). This substantiated the removal of sulfur by the recovery. The sulfur contents after recovery were within 12 – 18 at% with higher sulfur on the sample that was previously poisoned at lower temperatures.

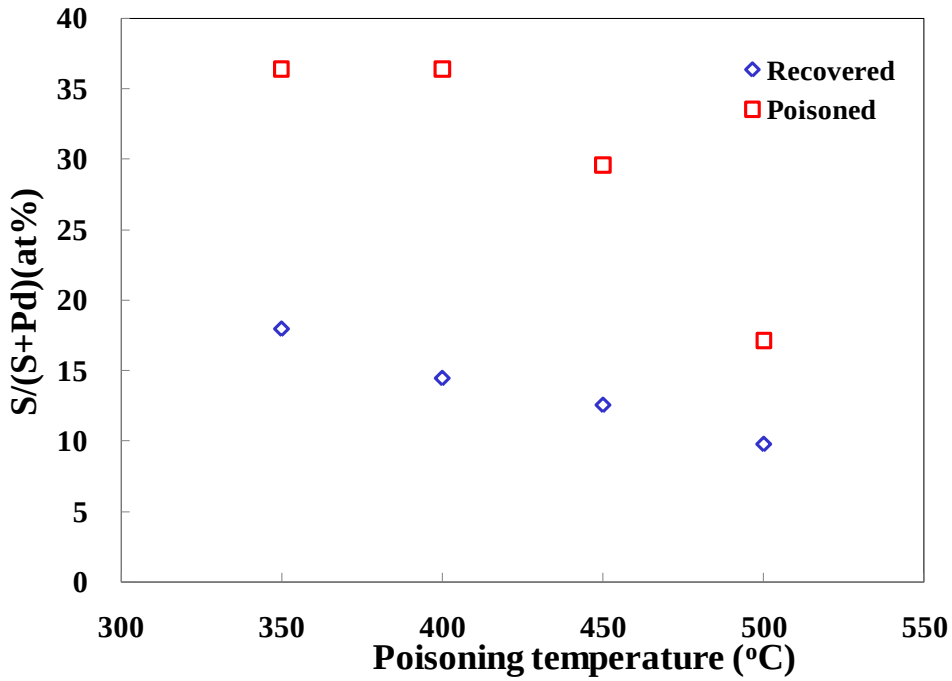


Figure 9.11. Total sulfur on the Pd surfaces after the poisoning and the recovery as a function of temperature. The poisoning was performed with the 50 ppm $H_2S/H_2$ mixture for 24 hours at 350 – 500°C and the recovery condition was fixed at 500°C in $H_2$ for 48 hours.

The sulfur fraction shown in Figure 9.11 included both sulfide and sulfate. Since sulfide, which was the sulfur-metal bonding, was the cause for the permeance loss observed during the membrane characterization in the presence of $H_2S$ (*Chapter 7*), the

sulfide fraction was quantified. Figure 9.12 shows the sulfide fraction (relative to Pd, at%) on the Pd samples after the poisoning with the 50 ppm $H_2S$ for 24 hours at 350 – 400°C and the recovery. It should be noted that the sulfide fraction estimated included both sulfide species (the S 2p peak at 163.2eV and 162eV, respectively) shown in Figure 9.2. The fraction of sulfide after the poisoning decreased with increasing temperature from roughly 32 at% at 350°C to ~13 at% at 500°C. The slight difference between the total sulfur (See Figure 9.11) and the sulfide fraction (Figure 9.12) indicated the relative high percentage of sulfide to sulfate. Indeed, the sulfide was roughly 80 at% relative to sulfate in the total sulfur content. Less sulfide formed at lower temperatures was due to the less stability of the sulfide at higher temperatures according to thermodynamics as discussed in *Chapter 8*.

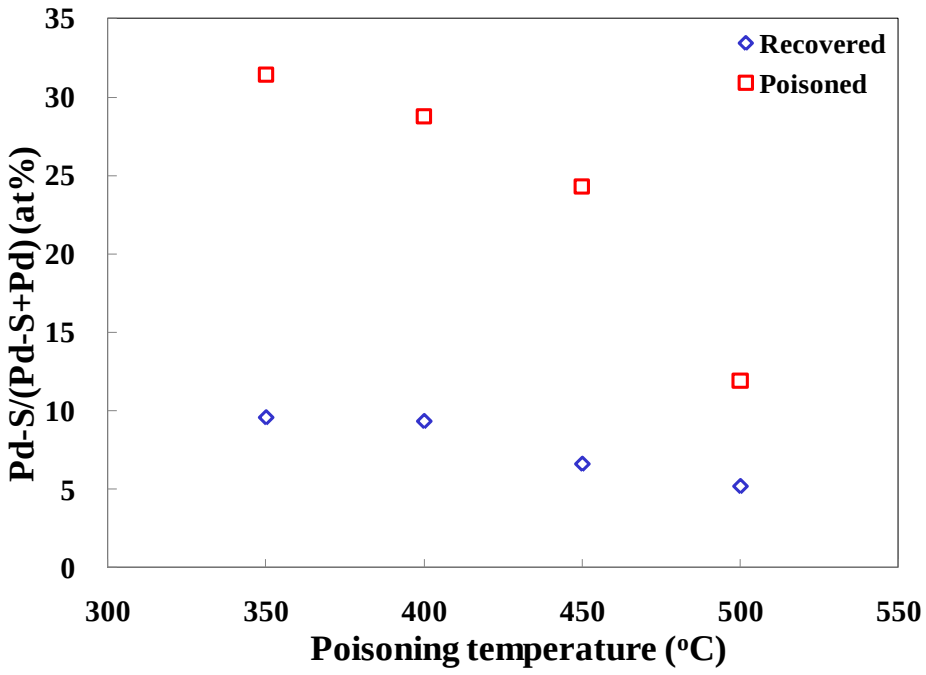


Figure 9.12. Total Pd sulfide on the Pd surfaces after the poisoning and the recovery as a function of temperature. The poisoning was performed with the 50 ppm $H_2S/H_2$ mixture for 24 hours at 350 – 500°C and the recovery condition was fixed at 500°C in $H_2$ for 48 hours.

Figure 9.12 also shows that the sulfide fraction decreased to 7 – 10 at% after the recovery. A slightly higher sulfide fraction was observed on the sample that was previously poisoned at lower temperatures with more sulfides formed. The noticeable amount of sulfide remained on the samples after the recovery indicated that a fixed number of the Pd-S bonding were irreversible under the recovery condition. Much more sulfide reduction was observed at 350 – 450°C compared to 500°C. Since poisoning at 350 – 450°C formed bulk sulfide while poisoning at 500°C formed only the surface sulfide as evidenced by SEM, XRD, and XPS, the result suggested that most Pd-S bonding in the bulk was reduced to pure Pd-Pd bonding. On the other hand, the surface sulfide contained a higher percentage of irreversible Pd-S bonding. Indeed, as mentioned

in *Section 2.6.1,* surface sulfide was much more stable compared to bulk sulfide and could be present under the conditions where bulk sulfide was not stable according to the thermodynamics. As a result, it was much more difficult to break the surface Pd-S bonding. In addition, the binding energy of sulfur to Pd increased as the sulfur coverage was decreased (Alfonso, 2005b). This caused the Pd-S bonding being more difficult to break at low sulfur coverage.

Figure 9.13 shows the sulfide atomic fraction on the Pd samples poisoned with the 50 ppm $H_2S$ at 400°C for 2 - 24 hours along with the sulfide fraction after the recovery. After poisoning, the sulfide fraction appeared to increase asymptotically with increasing exposure time from ~ 7 at% after 2 hours exposure to a plateau value of ~ 28 at% after 24 hours exposure. This indicated that the amount of sulfide formed increased with increasing exposure time, and the sulfide formed near the surface reached the saturation value as the exposure time was increased. After the recovery, significant reduction of the sulfide fraction on the samples was observed indicating the removal of sulfur. The amount of sulfide reduced after 4 – 24 hours exposures that caused the bulk sulfide to form was much more significant compared to that after 2 hours exposure which did not form the bulk sulfide. Once again, this was due to the higher stability of surface sulfide than bulk sulfide and the low surface coverage as mentioned earlier.

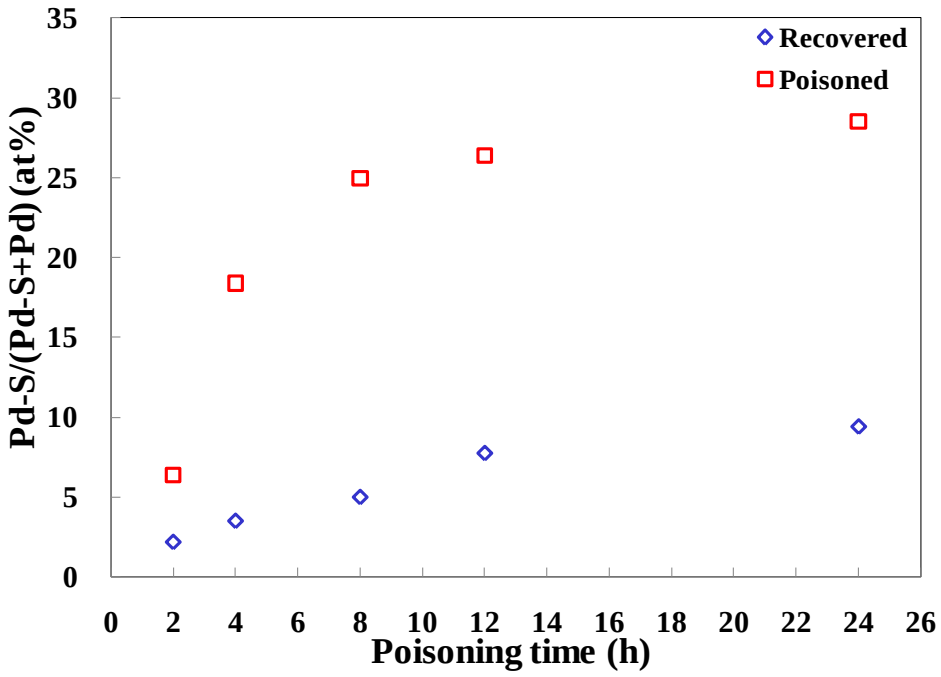


Figure 9.13. Total Pd sulfide on the Pd surfaces after the poisoning and the recovery as a function of exposure time. The poisoning was performed with the 50 ppm $H_2S/H_2$ mixture for 2 - 24 hours at 400°C and the recovery condition was fixed at 500°C in $H_2$ for 48 hours.

Figure 9.14 shows the sulfide atomic fraction on the Pd samples after poisoning with the 0.2 - 50 ppm $H_2S$ at 400°C for 24 hours along with the sulfide fraction after the recovery. As expected, the sulfide fraction increased with increasing $H_2S$ concentration. Approximately 9 at% sulfide presented on the surface with the 0.2 ppm $H_2S$ exposure and increased to 28 at% with the 50 ppm $H_2S$ exposure. A sudden increase was observed above 5 ppm $H_2S$, which was due to that the bulk sulfide started to form above the concentration. A large increase in the intensity of the sulfide peak was seen on the samples with the presence of bulk sulfide (See Figure 9.3). In fact, such step increase in the sulfide fraction due to the formation of bulk sulfide was also observed between 2 and 4 hours exposure (See Figure 9.13) and between the exposures at 500 and 450°C (See

Figure 9.12). Once again, the reduction of the sulfide fraction on the samples was observed after the recovery. In addition, due to the higher stability of surface sulfide than bulk sulfide and the higher sulfur coverage, more significant reduction of sulfide under the conditions that formed the bulk sulfide (i.e. > 10 ppm $H_2S$) was observed. The noticeable amount of irreversible sulfide remained on the samples after the recovery confirmed that the irrecoverable permeance loss of the Pd membrane (i.e. C-10) after the $H_2S$ exposure was caused by the un-recovered sulfur as discussed in *Section 7.3.2*.

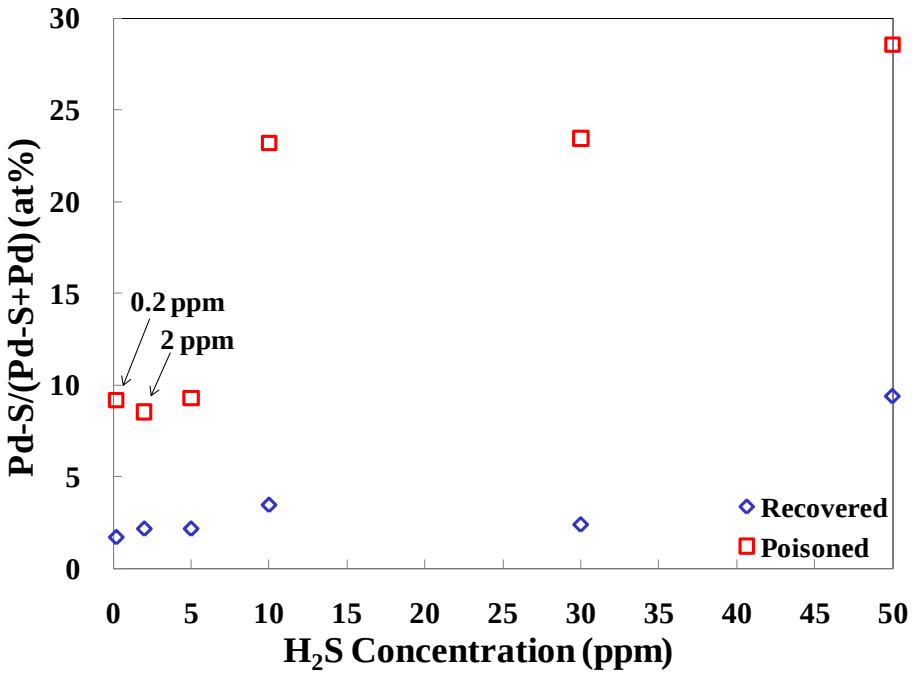


Figure 9.14. Total Pd sulfide on the Pd surfaces after the poisoning and the recovery as a function of $H_2S$ concentration. The poisoning was performed with the 0.2 - 50 ppm $H_2S/H_2$ mixture for 24 hours at 400°C and the recovery condition was fixed at 500°C in $H_2$ for 48 hours.

### *9.3.2 Poisoned Pd/Au alloys*

Figure 9.15 shows the XPS survey spectra for the Pd/Au samples before and after the 24 hours exposures with the 50 ppm $H_2S/H_2$ mixture at 350 – 500°C. The presences

of palladium and gold (Au 4f, ~84 eV) on the samples were confirmed by the spectra before and after the $H_2S$ exposures. In addition, carbon (C 1s), nitrogen (N 1s), oxygen (O 1s, O KLL), sodium (Na 1s, Na KL1), chlorine (Cl 2p) along with small amount of sulfur (S 2s and 2p) were also present on the samples randomly. As mentioned in *Section 9.3.1*, sodium, chlorine, carbon, oxygen, nitrogen were most likely resulted from the sample handling and storage due to the contact with the contaminants from the environments. Gaseous sulfur containing compounds from the environments could also be adsorbed on the sample surface during the sample storage as evidenced by the small S peak in the spectrum of the un-poisoned sample (Figure 9.15).

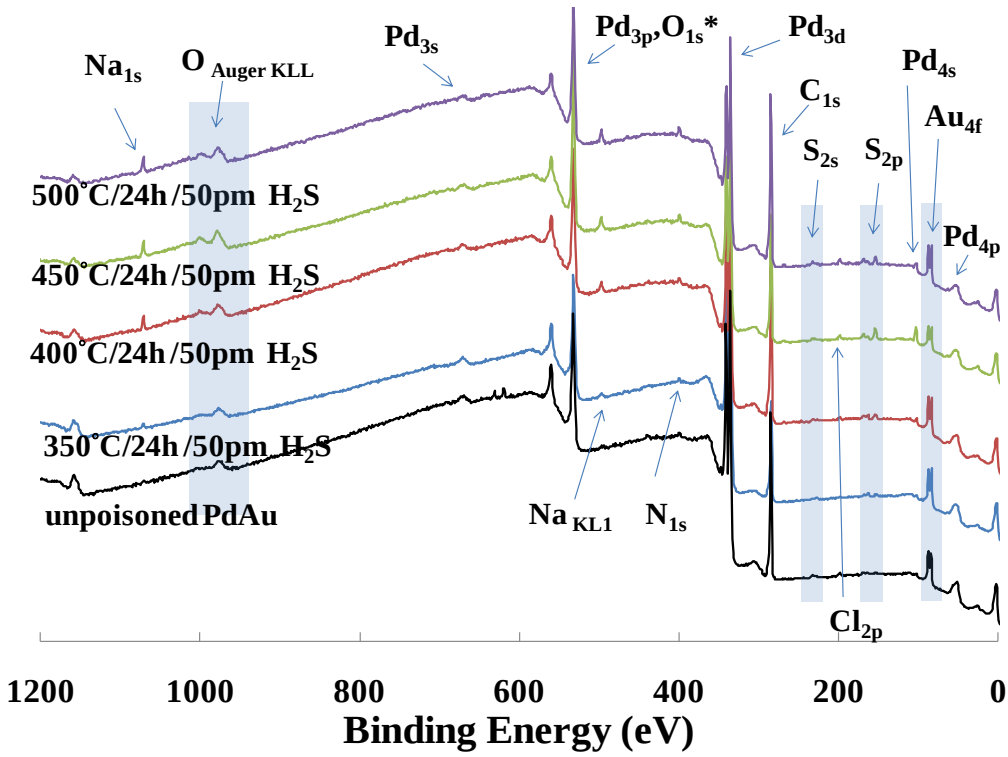


Figure 9.15. XPS survey spectra of the Pd/Au samples before and after the 24 hours exposures with the 50 ppm $H_2S/H_2$ mixture at 350 – 500°C.

The spectra of the samples after the poisoning showed the slight increase in intensity of the S peaks (Figure 9.15), which indicated the sulfur adsorption caused by the $H_2S$ exposures did occur. The relative atomic fractions of the interested elements, including Pd, Au, and S on the Pd/Au samples before and after the $H_2S$ exposures were summarized in Table 9.2. The elemental fractions were calculated based on the S 2p, Pd 3d, and the Au 4f peak in the survey scans. Noticeable increases in sulfur atomic fraction were observed on the poisoned samples.

Table 9.2. The composition of the poisoned Pd/Au samples.

| Sample conditions | Pd (at%) | Au (at%) | S (at%) |
|---|---|---|---|
| Un-poisoned | 78.1 | 14.8 | 7.1 |
| 50 ppm $H_2S$/350°C/24 hours | 70.8 | 15.5 | 13.5 |
| 50 ppm $H_2S$/400°C/2 hours | 66.8 | 15.5 | 17.7 |
| 50 ppm $H_2S$/450°C/24 hours | 66.2 | 11.3 | 22.5 |
| 50 ppm $H_2S$/500°C/24 hours | 61.5 | 17 | 21.5 |

Figure 9.16 shows the high resolution core level spectra of Pd 3d orbitals of both the as-prepared Pd and Pd/Au samples (before the $H_2S$ testing). The position of the Pd $3d_{5/2}$ peak was at 335.38 eV on the un-poisoned Pd sample and shifted to the lower binding energies of 335.2 eV after alloying on the Pd/Au sample. It should be noted that the position for the Pd $3d_{5/2}$ peak of the Pd-Pd bonding was at 335.1 eV (Moulder et al., 1993). As mentioned in *Section 9.3.1*, the slight peak shift to a higher binding energy of the Pd sample was due to the slight surface oxidation. Nevertheless, the result showed a noticeable binding energy decrease of the $3d_{5/2}$ peak after alloying with Au.

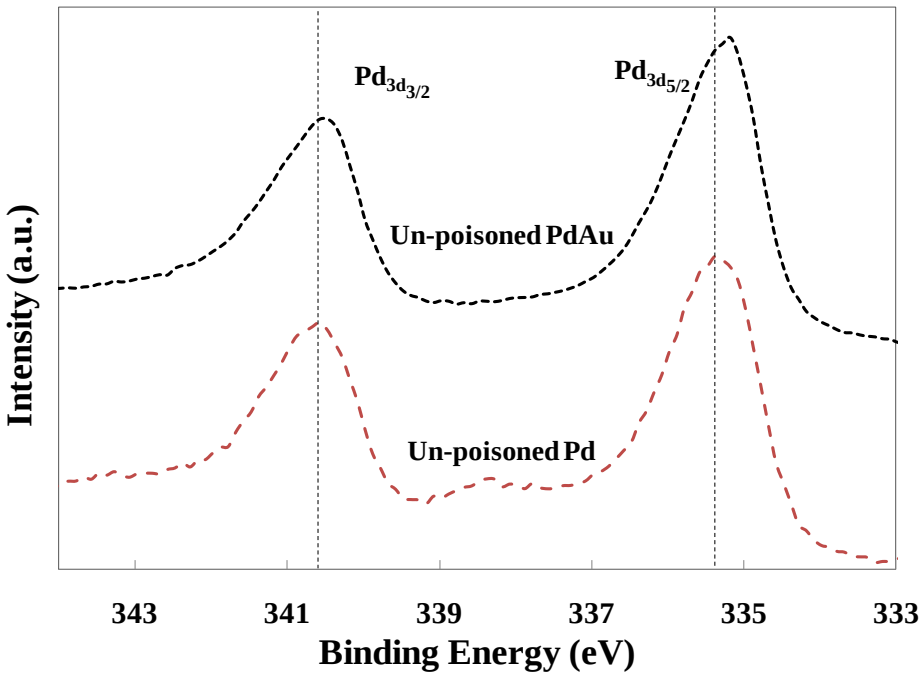


Figure 9.16. High resolution XPS scans of the Pd 3d peaks of the as-prepared Pd and Pd/Au samples.

In addition, the binding energy of the Au $4f_{7/2}$ peak on the un-poisoned Pd/Au sample was also lower (83.6 eV) compared to the Au-Au bonding of 84.0 eV (Moulder et al., 1993) as shown in Figure 9.17, which was the high resolution XPS Au 4f spectrum of the as-prepared Pd/Au sample. Similar shifts to lower binding energies of both core level Pd (3d) and Au (4f) peaks after forming Pd/Au were reported in the literature (Yi et. al, 2005; Lee et al., 2000; Sohn et al., 2010). Yi et al. (2005) reported that the Au $4f_{7/2}$ and Pd $3d_{3/2}$ peak positions shift to lower binding energies by ~0.45 eV and ~0.15 eV, respectively, relative to bulk Au and Pd while annealing the Pd/Au sample to 800K. The binding energy shifts in Au 4f and Pd 3d peak observed in the current study (0.4eV for Au $4f_{7/2}$ and 0.18 eV for Pd $d_{5/2}$) was very close to the values reported by Yi et al. (2005). The shifts of the binding energies for both core level Pd and Au peak after alloying could

be explained by the charge compensation model proposed by Lee et al. (2000), who augured that while forming Pd/Au alloy, Au gained sp-type electrons while losing d-electrons whereas Pd lost sp-electrons and gained d-electrons. Nevertheless, the results confirmed that the presence of Pd/Au alloy on the Pd/Au samples.

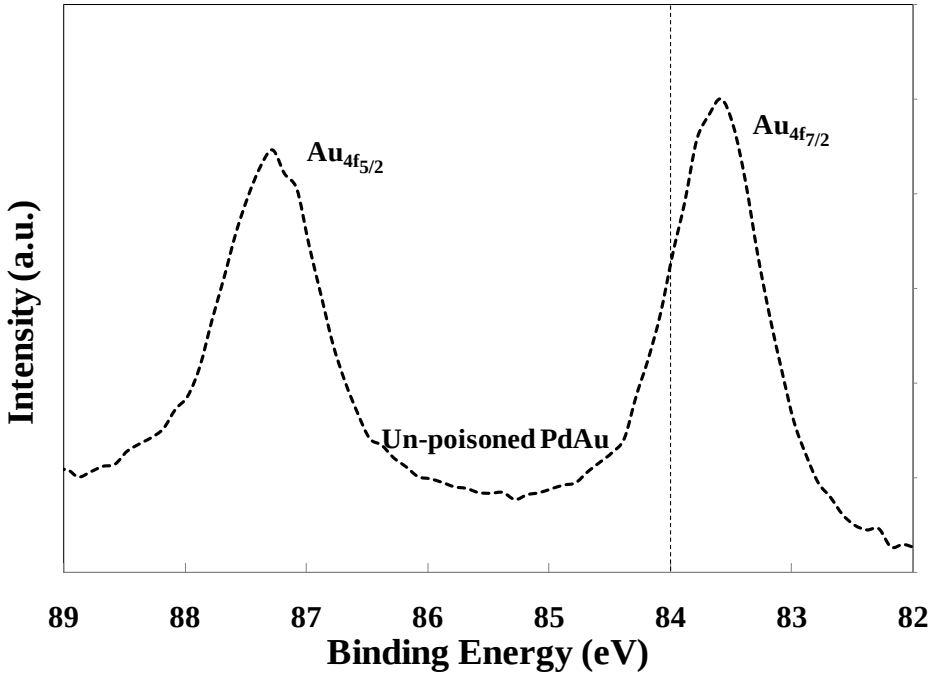


Figure 9.17. High resolution XPS scans of the Au 4f peak of the as-prepared Pd/Au samples. (The dotted line showed the Au-Au bonding of 84.0 eV (Moulder et al., 1993))

Figure 9.18(a) and (b) respectively shows the high resolution core level spectra of Pd 3d and Au 4f orbitals of the Pd/Au samples before and after the exposure to the 55 ppm $H_2S/H_2$ for 24 hours at 350 - 500°C. The positions of the Pd $3d_{5/2}$ and Au $4f_{7/2}$ peaks before poisoning were at 335.2 and 83.6 eV. The slight position shifts of both Pd and Au peaks compared to the Pd-Pd and Au-Au bonding was due to the Pd/Au alloying and the slight oxidation as mentioned earlier.

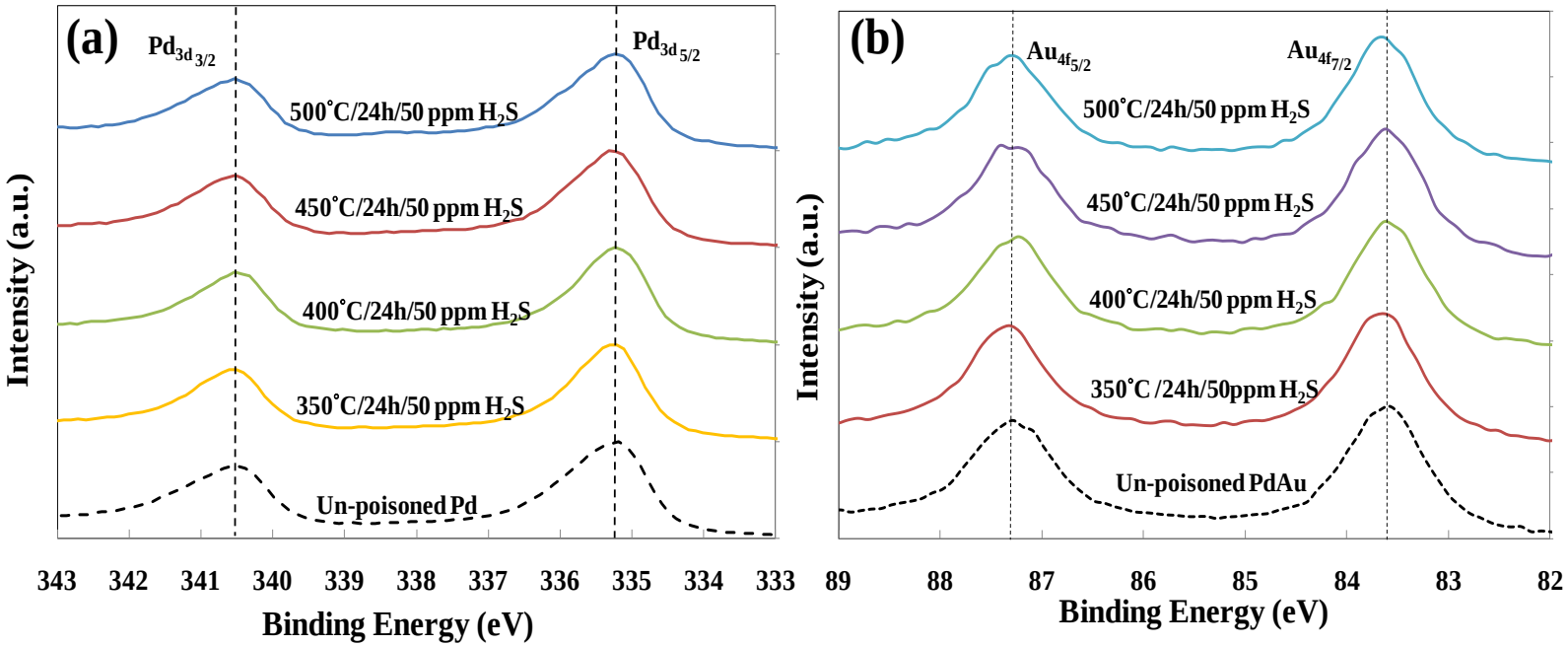


Figure 9.18. High resolution XPS scans of (a) Pd 3d and (b) Au 4f peak of the Pd/Au samples after the $H_2S$ exposure of 55 ppm for 24 hours at 350 - 500°C.

In contrary to poisoned Pd (See Figure 9.4), the shifts of the Pd 3d and Au 4f peaks after the poisoning were negligible as shown in Figure 9.18 although the presence of the sulfides (i.e. Pd-S, Au-S, or $Pd_xAu_y$-S) on the Pd/Au samples was confirmed by the high resolution scans of the S 2p peak (See Figure 9.19). Usually, shifts of the metal bonding (e.g. Pd, Au) to higher binding energies when metal sulfide (e.g. Pd sulfide, Au sulfide) formed were observed (Pomerantz, 2010; Chaplin et al. 2007; Lustemberg et. al. 2008; Widler et. al., 2002) due to the electrons transfer from the metal to sulfur. The insignificant shifts of the Pd 3d and Au 4f peak observed could possibly due to the extremely small sulfide formed. Chaplin et al. (2007) reported that the shift of the Pd 3d peak increased with increasing sulfur poisoning extent of the Pd-based catalysts. Indeed, the sulfide fractions on the Pd/Au samples were much smaller compared to the poisoned Pd (See Figure 9.19), which will be discussed shortly.

In addition, Morris et al., 2002; Kuo and Huang, 2008 have shown that the Au 4f peak position of the $Au_2S$ nano-structures was identical to that of metal Au. The lack of Au peak shifting observed on the $Au_2S$ was reasoned to be due to the covalent characteristic of the Au-S bonding due to the small electron affinity between S and Au (Morris et. al., 2002). As a result, it was possible that the negligible shift of the Pd and Au peaks observed on the poisoned Pd/Au samples was resulted from the enhancement of the covalent characteristic of the sulfide bonding by Au alloying.

The negligible shifts in both Pd 3d and Au 4f peaks of the poisoned Pd/Au samples (Figure 9.18) made the peak deconvolution with different bonding chemistries (including the Pd-S and Au-S) extremely difficult. In addition, a number of possible

bonding including Pd-Pd, Pd-O, Pd-S, Pd-Au for the Pd peak and the lack of standards of Au-Au, Au-S, Au-O, and Au-Pd increased the difficulty for the peak deconvolution.

Figure 9.19 shows the high resolution core level spectrum of S 2p of the Pd/Au sample exposed to the 50 ppm $H_2S/H_2$ for 24 hours at 350°C. The deconvolution of the peak was also shown in Figure 9.19. Similar to the poisoned Pd (See Figure 9.2), both sulfide (at ~162 – 165 eV) and sulfate (at ~ 168eV) were present on the surface. As mentioned in *Section 9.3.1*, while the sulfide species was resulted from the metal-sulfur bonding (i.e. Pd-S, Au-S, or $Pd_xAu_y$-S), the sulfate species was resulted from the adsorption of the environmental contaminants and the partial oxidation of sulfide on the surface. In addition, Figure 9.19 also showed that the intensity of the peak was very small as evidenced by the rough (zigzag) outline of the peak. This indicated that the amount of sulfide formed on the Pd/Au surface was extremely small.

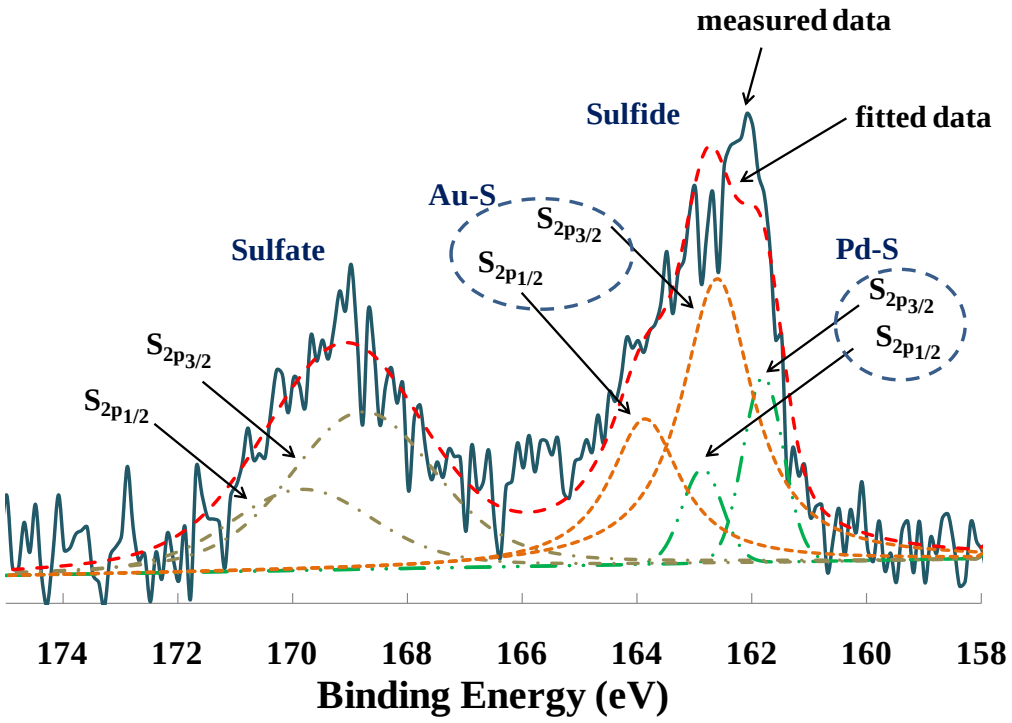


Figure 9.19. High resolution XPS scan of the S 2p peak and the peak fitting of the Pd/Au sample after the $H_2S$ exposure of 50 ppm at 350°C for 24 hours.

In contrary to the poisoned Pd (See Figure 9.2), Figure 9.19 also shows that the sulfide peak of the poisoned Pd/Au was broad and non-descript. This indicated the sulfide peak was composed of a number of sulfide bonding chemistries. Indeed, in addition to the two possible Pd-S bonding chemistries (at ~162 and 163.2 eV) as mentioned in *Section 9.3.1*, Au-S (more than one), and $Pd_xAu_y$-S bonding chemistries also possibly existed on the sample. In order to simply the peak fitting, it was assumed that only one predominant Pd and Au sulfide species existed and no alloy sulfide was present in the samples. Since no bulk sulfide formed on the Pd/Au samples, the Pd sulfide peak at 162 eV was chosen. For the Au sulfide, the predominant Au sulfide ($Au_2S$) peak at 162.6 eV reported in the literature was chosen (Morris et. al., 2002; Kuo and Huang, 2008; Mikhlin et. al. 2010). Since Au had a higher electronic affinity than Pd (therefore, closer to the value of sulfur), the Au sulfide peak at

higher binding energy than Pd sulfide was quite reasonable due to the less negative charge of sulfur.

Figure 9.20(a) shows the composition as a function of depth of the Pd/Au sample exposed to the 50 ppm $H_2S$ at 350°C for 48 hours. As mentioned in *Section 9.3.1*, the depth was determined by using a known sputter rate calibrated with a standard $SiO_2$ film. The S 2p signal was deconvoluted into a sulfide species and a sulfate species. Both sulfide and sulfate signals were increased by a factor of 10 for plotting due to the extremely small signal strength. The significant decrease of the adventitious carbon fraction removed by the sputtering resulted in the increases in both Pd and Au fractions to ~75 and 7 at%, respectively. The total sulfide fraction decreased from ~2.3 at the surface to ~0.5 at% at the depth of 10 nm. The sulfate also decreased at all sputter increments from ~1.1 at% initially to ~0.2 at%. The narrow scans of the S 2p at each sputter increment were shown in Figure 9.20(b). Both sulfate and sulfide decreased with increasing sputtering increments although the sulfate decreased much faster than the sulfides. The results confirmed that the sulfide formed on the Pd/Au sample during the $H_2S$ exposure was essentially on the surface even with the $H_2S$ concentration as high as 55 ppm at 350°C for as long as 48 hours. The results of the XRD and SEM characterization also suggested the lack of bulk sulfide formation on the Pd/Au samples under the similar testing conditions (*Section 8.3.2).* As mentioned in *Section 8.3.2*, the resistance for forming bulk sulfide was due to the reduction of the bulk sulfide (i.e. bulk Pd and Au sulfide) thermal stability after alloying.

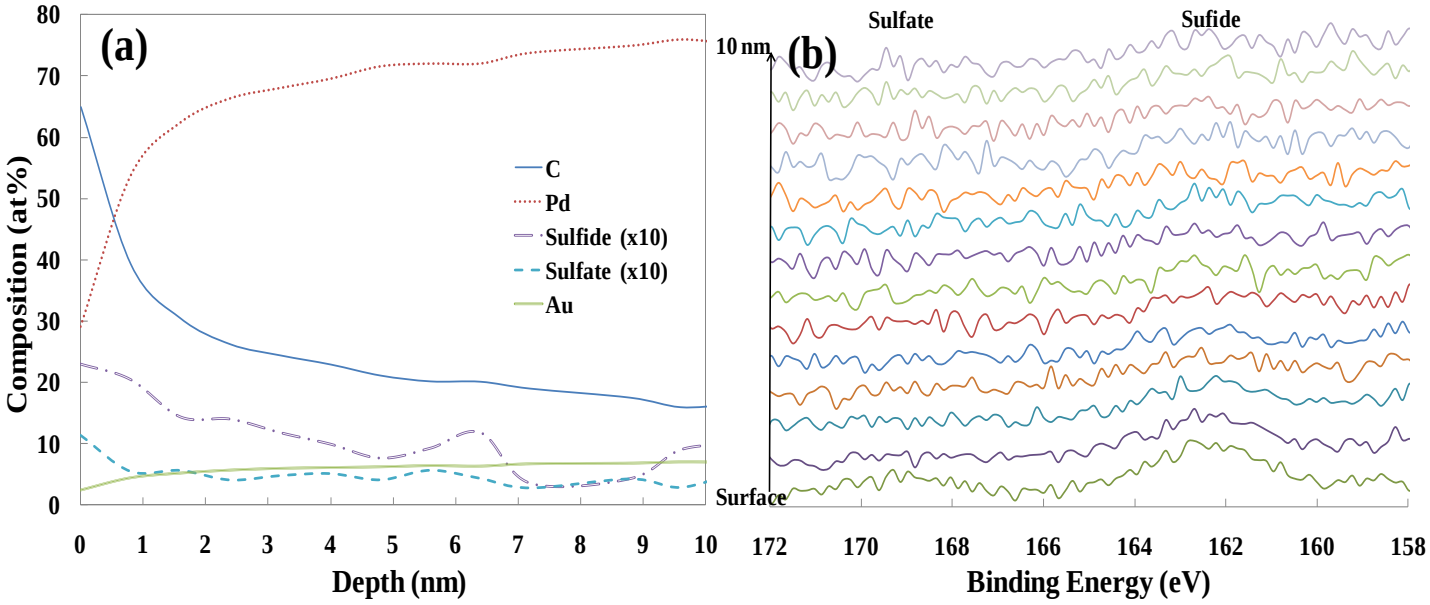


Figure 9.20. (a) Composition as a function of depth of the Pd/Au sample after the exposure to the 50 ppm $H_2S$ at 350°C for 48 hours, and (b) corresponding narrow scans of the S 2 p peak at each sputtering increment.

Figure 9.21(a) and (b) shows respectively the high resolution spectra of Pd 3d and Au 4f orbitals of the Pd/Au samples before and after the 50 ppm $H_2S$ exposure for 24 hours at 350°C, and after the recovery at 500°C in $H_2$ for 48 hours. No observable shifts of both Pd 3d and Au 4f peaks after the poisoning due to the small amount of sulfide formation was observed. Therefore, the peak positions of both Pd 3d and Au 4f peaks remained unchanged as expected (Figure 9.21(a), (b)). Due to the negligible peak shifts, it was difficult to conclude whether the sulfide bonding on the Pd/Au samples were recovered or not based on the narrow scans of Pd 3d and Au 4f peaks.

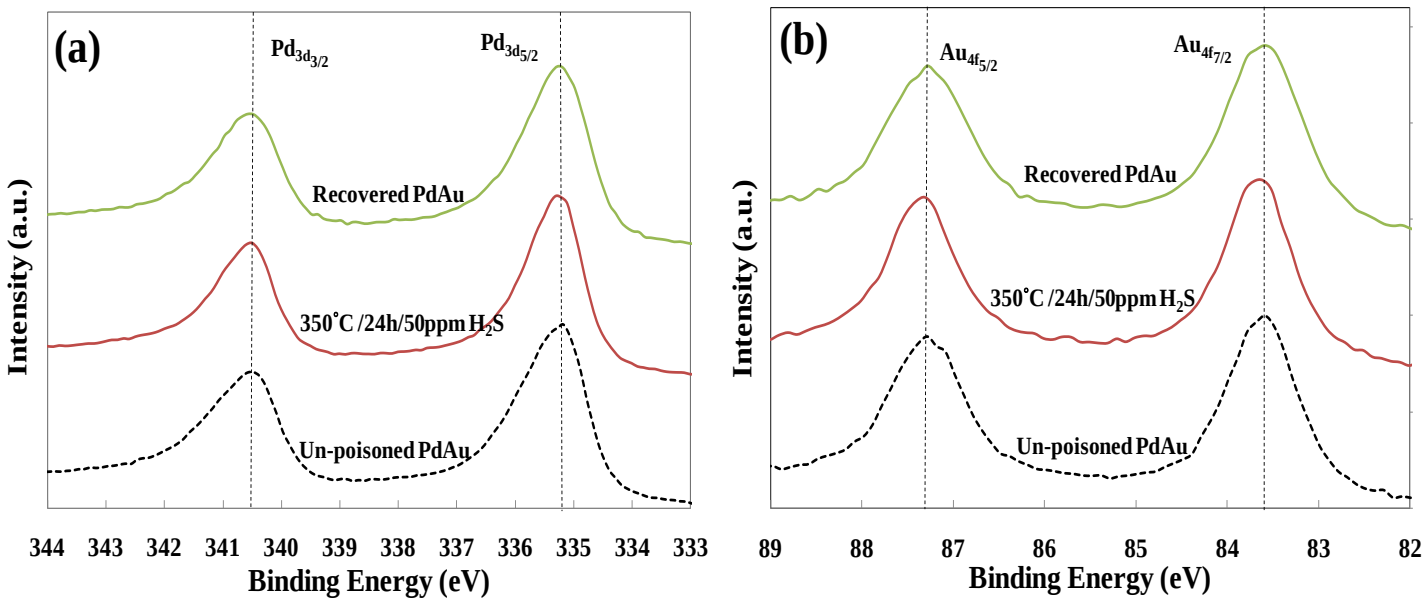


Figure 9.21. High resolution XPS scans of (a) Pd 3d and (b) Au 4f peak of the Pd/Au samples before and after the $H_2S$ exposure of 50 ppm for 24 hours at 350°C, and after recovery in $H_2$ at 500°C for 48 hours.

Figure 9.22 exhibits the high resolution spectra of S 2p orbitals of the Pd/Au sample after poisoning in the 50 ppm $H_2S/H_2$ for 24 hours at 350°C and after the recovery. A decrease of the sulfide peak intensity after the recovery was observed, indicating the reduction of sulfide on the sample. Since, the sulfide formed was much less on the Pd/Au sample, the decrease was less noticeable compared to the recovered Pd. As seen in Figure 9.22, both sulfide and sulfide peaks were still present after the recovery indicating the presence of the sulfur on the Pd/Au sample. However, the shift of the peak summit position suggested that the fractions of Au and Pd sulfide changed after the recovery.

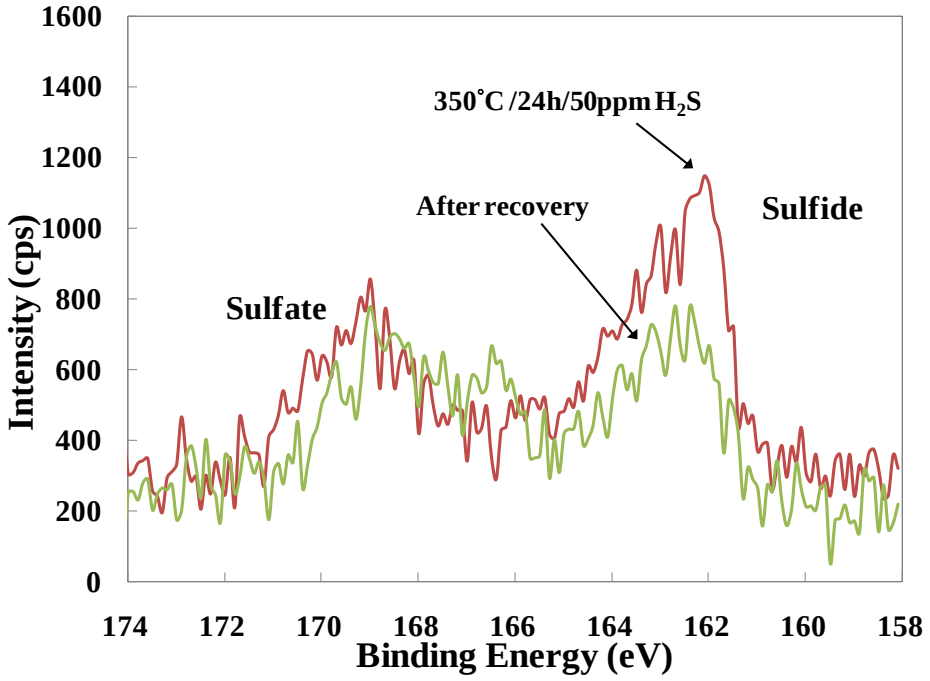


Figure 9.22. High resolution XPS scans of the S 2p peak of the Pd/Au sample before and after the $H_2S$ exposure of 50 ppm for 24 hours at 350°C, and after recovery in $H_2$ at 500°C for 48 hours.

Figure 9.23 shows the total sulfur (including sulfide and sulfate) fraction on the Pd/Au samples after poisoning with the 50 ppm $H_2S$ for 24 hours at 350 – 400°C. The total sulfide fraction to total sulfur (i.e. (Au-S+Pd-S)/S) was also depicted in Figure 9.23. in the right *y*-axis. As observed in Figure 9.23, while the total sulfur increased with increasing temperature from approximately 12 at% at 350°C to 18 at% at 500°C, the sulfide fraction to total sulfur decreased with increasing temperature from 60 to 30% (350 to 500°C). This resulted in the total sulfide formed on the Pd/Au samples slightly increased with the decreasing temperature within 6 - 8 at% ((Au-S+Pd-S)/(Au-S+Pd-S+Au+Pd)). The much smaller amount of sulfide formed on the Pd/Au sample compared to the Pd samples substantiated the better sulfur resistance of the Pd/Au than Pd. The better sulfur resistance observed on the Pd/Au samples was due to the reduction of

thermal stability of the sulfide after alloying. In addition, since the sulfide bonding was the major cause for the permeance loss in the presence of $H_2S$, the trend agreed with the observation that more permeance decline of the Pd/Au membranes at lower poisoning temperatures (*Chapter 7*). Less thermal stability of the sulfide species at lower higher temperatures as well as the exothermal adsorption accounted for the observed phenomenon. The higher total sulfur observed at higher temperature was mainly due to that more sulfate was present on the surface possibly due to the more contaminant adsorption during the sample storage.

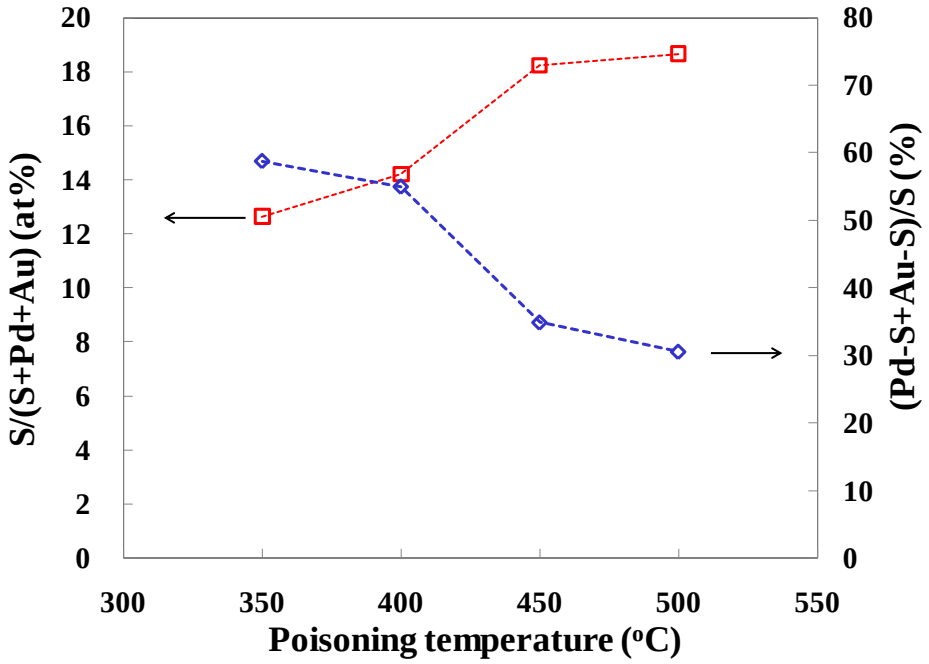


Figure 9.23. The total sulfur fraction and the total sulfide (Pd-S+Au-S) percentage in total sulfur on the Pd/Au samples as a function of temperature after poisoning with the 55 ppm $H_2S/H_2$ mixture for 24 hours at 350 – 500°C.

Figure 9.24 displays the atomic fractions of Au and Pd sulfides relative to the film composition (i.e. Pd+Au) after poisoning with the 50 ppm $H_2S$ for 24 hours at 350 – 400°C and the recovery. The right *y*-axis in Figure 9.24 shows the percentage of the Au-S

in the total sulfide after poisoning and after the recovery. Surprisingly, most of the sulfide species formed after the poisoning was the Au sulfide (80 – 97%). Since the Au fraction on the Pd/Au samples was within 11.3 – 17 at % (as shown in Table 9.2), the result that most sulfide formed was Au sulfide suggested that the Au-S bonding was more preferential than the Pd-S bonding.

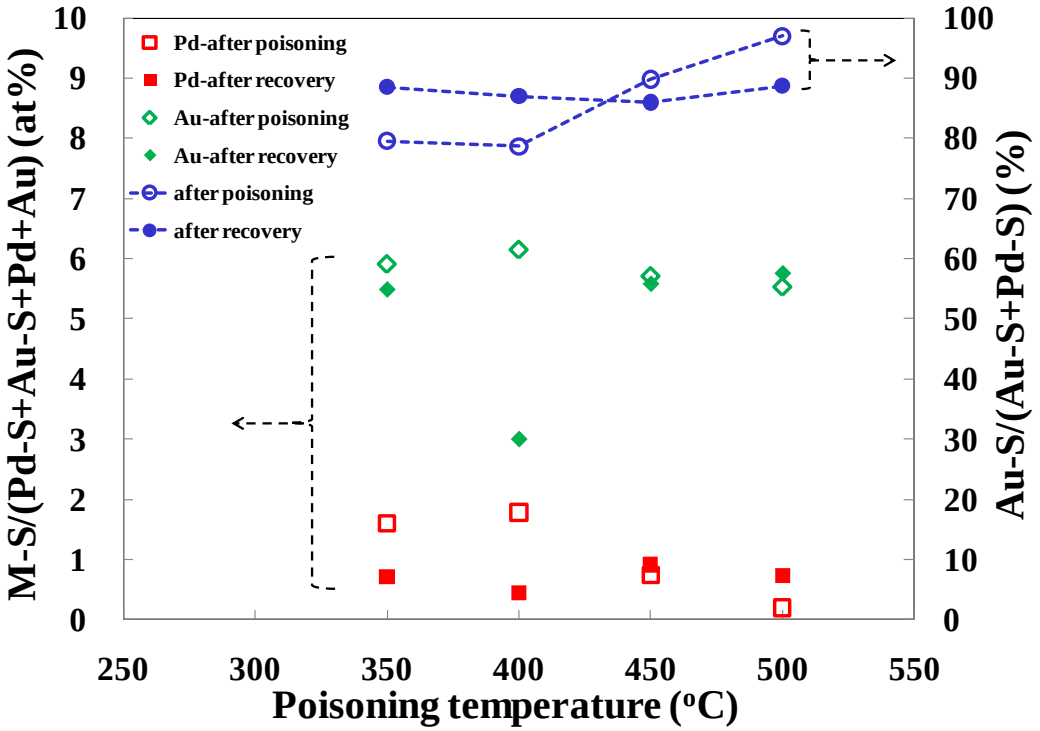


Figure 9.24. The Pd sulfide (Pd-S) and the Au sulfide (Au-S) formed and the percentage of Au-S in total sulfide on the Pd/Au surfaces as a function of temperature after the poisoning and the recovery. The poisoning was performed with the 55 ppm $H_2S/H_2$ mixture for 24 hours at 350 - 500°C and the recovery condition was fixed at 500°C in $H_2$ for 48 hours. (M in the left *y*-axis is Pd or Au)

Due to the fact that the sulfide (bulk) formed with more noble metals (e.g. Au) generally were less stable and required higher $H_2S$ concentrations to form compared to the less noble metals such as Pd, one would expect more preferential bonding between Pd

and sulfur than Au and sulfur. However, the thermodynamics (i.e. the Gibbs' free energy of formation) for forming bulk sulfide and surface sulfide was significantly different as mentioned in *Section 2.6.1*. In addition, the adsorption characteristics between sulfur and metals also altered the surface metal-sulfur bonding largely from bulk metal sulfide bonding, resulting in different sulfide species formed on the surface and in the bulk. As a result, the prediction for the preference of the surface sulfide formation by the bulk sulfide thermodynamics was insufficient. In fact, Pomerantz (2010) reported similar contradiction between the thermodynamic prediction and the experimental observation of the surface sulfide species formed on the sulfur poisoned Pd/Cu alloys. The author also attributed the contradiction to the difference between the bulk sulfide and surface sulfide thermodynamics. In any case, the preferential bonding between Au and S possibly resulted in the less permeance decline of the Pd/Au membranes compared to the Pd membranes observed in the presence of $H_2S$ (*Chapter 7*) since the Pd-S bonding was largely reduced, resulting in more Pd sites for $H_2$ dissociation.

In addition, Figure 9.24 also shows that while the amount of the Pd sulfide formed after the poisoning decreased with increasing temperature from ~2 at% at 350°C to ~0.5 at% at 500°C, the amount of the Au sulfide were nearly identical of approximately 6 at% in the entire range of the testing temperatures. The decrease of the Pd sulfide formation with increasing temperature agreed with the observation on the pure Pd samples discussed previously (See Figure 9.12). On the other hand, the almost identical amount of the Au sulfide formed at different temperatures suggested that the formation of the Au sulfide was much less sensitive to temperature compared to Pd in the tested temperature range.

The amount of the Au sulfide formed was also found to be insensitive to the $H_2S$ exposure time as shown in Figure 9.25, which shows the Au and Pd sulfides fractions after poisoning with the 50 ppm $H_2S$ at 350°C for 2 - 48 hours. As seen in Figure 9.25, while Pd sulfide increased with increasing time from ~ 1 at% after 2 hours to ~ 2 at % after 48 hours, the Au sulfide remain roughly 5.2 at % for as long as 48 hours. The increase of the Pd sulfide with increasing time was consistent with the results of the Pd samples (See Figure 9.13). No apparent increase of the Au sulfide fraction with increasing exposure time suggested that the formation of the surface Au-S bonding reached the saturation value rapidly, and no significant Au-S could further form once the saturation Au-S bonding was attained. The preferential Au-S bonding largely reduced the Pd-S bonding so that the bulk Pd sulfide did not form, while the Au-S bonding itself showed the limited saturation value. The results of the XPS analysis provided the possible reasons why the Pd/Au alloys did not form bulk sulfide under the testing conditions as described in *Chapter 8*.

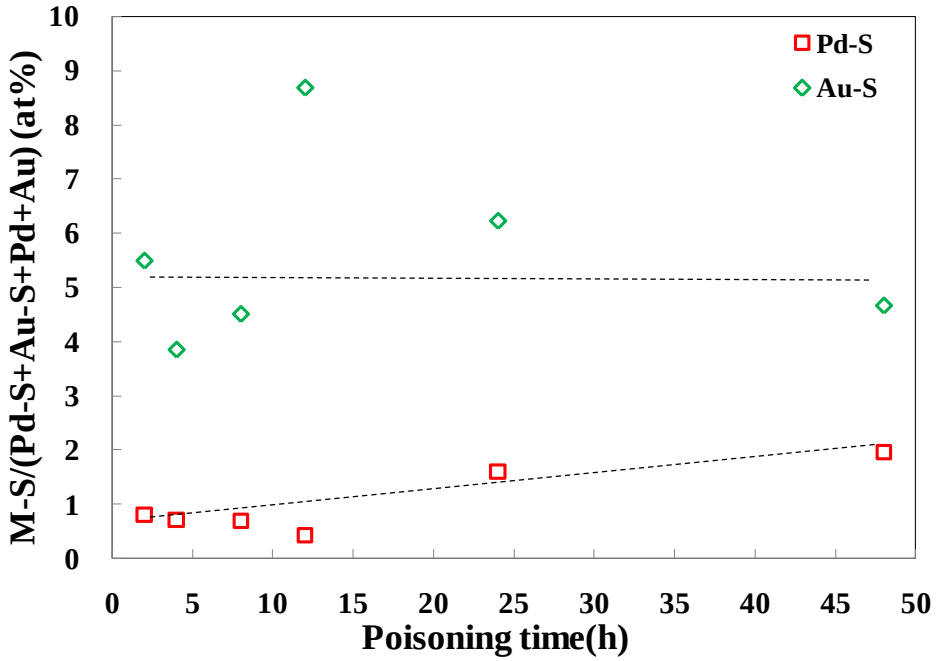


Figure 9.25. The Pd sulfide (Pd-S) and the Au sulfide (Au-S) formed on the Pd/Au surfaces as a function of time after poisoning with the 55 ppm $H_2S/H_2$ mixture at 350°C for 2 – 48 hours. (M in the left *y*-axis is Pd or Au).

As also observed in Figure 9.24, in spite of the scatter of the date points, the result appeared to show that more Pd-sulfide was reduced compared to the Au sulfide after the recovery suggesting that the Pd-S bonding was easier to be broken than the Au-S bonding. This indicated that the Au-S bonding formed on the Pd/Au alloy samples during the $H_2S$ exposure was more energetically stable as compared to the Pd-S bonding. The breaking of the most Pd-S bonding accounted for the near full permeance restoration of the Pd/Au membranes observed after the recovery described in *Chapter 7*. It should be noted that the presence of adventitious sulfur on the Pd/Au samples (See Table 9.1 and Table 9.2) potentially increased the error during the quantification of sulfur, causing the scatter of the data, since the sulfur amount was extremely small on the Pd/Au samples.

As discussed in *Section 9.3.1*, due to the increase of the Pd-S binding energy with decreasing sulfur coverage (Alfonso 2005b), it was difficult to break all the Pd-S bonding (See Figure 9.12) especially at low sulfur coverage. As a result, the permeance loss of the Pd membranes was not fully restored as described in *Chapter 7*. In the case of the Pd/Au alloy, however, the nearly irreversible Au-S bonding kept the relative high overall sulfur coverage on the surface, which potentially prevented the Pd-S binding energy to increase even when the Pd-S fraction became very small. As a result, most Pd-S bonding could be reduced during the recovery causing the near 100% permeance recovery of the Pd/Au membranes as observed in *Chapter 7*. The results also implied that the majority of the $H_2$ dissociation occurred only on the Pd sites rather than the Au sites on the surface of the Pd/Au alloy membranes.

## 9.4 Conclusions

The surface chemistries of the Pd and the Pd/Au alloy layers after the $H_2S$ poisoning and the recovery were investigated by conducting the XPS analysis. The presence of sulfur bonded with Pd surface was confirmed even under the exposure conditions that were not favorable for the Pd (bulk) sulfide formation. The deconvolution of the high resolution sulfur peak (S 2p) suggested the two potential Pd sulfide species, PdS and $Pd_4S$ that possibly bonded on the top surface and in the sub-layers of Pd respectively. The depth profile analysis substantiated the sulfide presence deep into the Pd layer on the Pd samples poisoned under the condition that generated the bulk sulfide.

The reduction of the sulfide fraction on the Pd samples after the recovery was confirmed. The absence of the sulfide in the sub-surface as evidenced by the depth profile analysis indicated the breaking of the bulk Pd-S bonding by the recovery. However, a fixed amount of surface sulfide was still present on the Pd after the recovery. More sulfide formed on the Pd samples at lower poisoning temperatures, after longer exposure time, and with higher $H_2S$ concentrations were observed by the XPS analysis, which agreed with the results from the SEM and XRD analysis described in *Chapter 8*.

Although the presence of surface sulfide was also observed on the Pd/Au alloy surface, the sulfide fraction was much smaller compared to Pd indicating much less sulfide formation on the Pd/Au surfaces. The negligible shifting of the core level Au and Pd binding energies also substantiated the extremely small sulfide formation. Depth profile analysis confirmed that only surface sulfide was present on the Pd/Au surface. Two sulfide species, Au sulfide and Pd sulfide, were used to deconvolute the sulfur peak

on the Pd/Au samples. The preferential Au-S bonding with the limited saturation value was confirmed on the poisoned Pd/Au alloys which resulted in the significant reduction of the Pd-S bonding compared to the poisoned Pd, causing no bulk sulfide formation under the testing conditions. More reduction of the Pd-S bonding was observed compared to Au-S bonding on the recovered samples. The un-recovered Au-S bonding increased the overall surface coverage resulting in the nearly complete reduction of the Pd-S bonding possibly due to the decrease of the Pd-S binding energy at high overall sulfur coverage.

# 10. Conclusions

- Pd/Au alloy (non-homogeneous) composite membranes were successfully fabricated by the Pd electroless deposition and the Au displacement deposition method followed by the heat treatment in the moderate temperature range (500 - 550ºC) within reasonable annealing time (24 – 48 hours). The Au weight fraction in the Pd/Au alloy membranes could be controlled by the number of Au displacement deposition loops with the multi-layer structure.
- Pre-treating the Pd surface with acid to remove the non-conducting contaminants was found to be important for the Au displacement reaction, which had an empirical reaction order of 3.2 with respect to Au ion concentration. Approximately 0.5 – 0.6 $\mu$m thick Au layer was deposited before the termination of the reaction. Increasing the Au ion concentration, acidity, and temperature of the displacement bath resulted in a faster Au displacement deposition rate.
- The Pd/Au inter-diffusion occurred at the temperature as low as 322°C according to the *in-situ* non-isothermal HTXRD study. However, the inter-diffusion rate decreased significantly as the annealing proceeded due to the strongly composition-dependent diffusion rate of Pd and Au, resulting in the formation of thermally stable non-homogenous Pd/Au alloy layers. For forming a stable Pd/Au alloy top layer with a sufficient thickness to obtain potentially higher $H_2$ permeance and sulfur resistance, annealing the Pd/Au bi-layers (~10 wt% Au) at above 500°C for ~ 48 hours was sufficient.

- By performing the *in-situ* time-resolved HTXRD analysis, the isothermal Pd/Au alloy formation at 450 - 600ºC was studied. The kinetics of the Pd/Au alloy formation was obtained by the quantitative analyses of the HTXRD data based on the Avrami model, which indicated that the transformation was a one-dimensional diffusion controlled process. The estimated activation energy for the Pd/Au alloy formation was 248 kJ/mol, and in good agreement with the literature value for Pd-Au inter-diffusion.
- The results of the $H_2$ permeation characterization showed that the non-homogenous Pd/Au composite membranes (the bulk Au wt% up to 16.7 wt%, ~ 46 wt% Au at surface) followed Sieverts' law at 250 – 450°C with the $H_2$ feed pressure up to 4 atmospheres.
- The Pd/Au alloy layers formed were thermally stable and the $H_2$ permeance of the Pd/Au membranes was stable at elevated temperatures up to 500ºC.
- The $H_2$ permeability of the Pd/Au membranes was enhanced at low Au weight fraction but further increasing the Au composition showed no beneficial effect.
- The influence of the $H_2S$ exposure on the hydrogen permeating characteristics of the Pd and the Pd/Au membranes were examined, and two different poisoning phenomena were observed on Pd and Pd/Au alloy membranes.
- The exposure of the pure Pd membrane to a 55 ppm $H_2S/H_2$ mixture at 400°C resulted in two-stage of permeance decline due to (i) surface site blocking by the dissociative adsorption of $H_2S$, and (ii) bulk sulfidation of Pd with the formation of $Pd_4S$.
- The bulk sulfidation of Pd with the formation of bulk $Pd_4S$ at 350 - 500ºC with the exposure to the $H_2S/H_2$ gas mixtures was confirmed by the micro-structural (XRD and SEM) analysis, and the exposure conditions for forming $Pd_4S$ observed in the

study agreed with the thermodynamic prediction. The extent of the Pd sulfidation increased with decreasing temperature and the growth of the $Pd_4S$ layer were one-dimensional phase boundary controlled based on the Avrami analysis.

- By conducting the XPS analysis, the presence of Pd-S bonding on the poisoned Pd surface was confirmed even under the exposure conditions that were not favorable for the Pd (bulk) sulfide formation. The deconvolution of the high resolution sulfur peak (S 2p) suggested the two potential Pd sulfide species, PdS and $Pd_4S$ that possibly bonded on the top surface and in the sub-layers of Pd, respectively.
- The permeance loss of Pd membranes was found to be partially recoverable in $H_2$ with the restoration of Pd from $Pd_4S$ confirmed by the SEM and XRD analysis.
- The reduction of the sulfide fraction on the Pd samples after the recovery was confirmed by the XPS. The absence of the sulfide in the sub-surface as evidenced by the XPS depth profile analysis indicated the breaking of the bulk Pd-S bonding by the recovery. However, a fixed amount of surface sulfide was still present on the Pd after the recovery.
- Once the significant extent of the bulk sulfidation occurred, the structure of the Pd membrane was deteriorated with the formation of pinholes due to the large stress in the Pd lattice caused by the incorporation of sulfur as $Pd_4S$ was formed even though the recovery of the Pd from the $Pd_4S$ was possible.
- The Pd/Au membranes showed the resistance to bulk sulfidation upon exposure to the $H_2S/H_2$ mixtures up to 55 ppm in the temperature range of 350 – 500$^{\circ}$C, and underwent no significant structural changes caused by the bulk sulfide formation after the exposures evidenced by the micro-structural analysis.

- The permeance decline of the Pd/Au alloy membrane upon the $H_2S$ exposures resulted mainly from the surface site-blocking by adsorbed sulfur, which caused the decrease of the effective area for the $H_2$ adsorption without altering the $H_2$ transport mechanism. In addition, the permeance loss was essentially fully recoverable.
- The surface chemistries of the sulfur-poisoned Pd/Au alloy layers were investigated by conducting the XPS analysis, and the presence of surface sulfide was confirmed on the Pd/Au alloy surface. However, the sulfide fraction was much smaller compared to the poisoned Pd membranes.
- The deconvolution of the sulfur peak on the Pd/Au samples with the presence of Pd sulfide and Au sulfide species suggested the preferential Au-S bonding, which resulted in the significant reduction of the Pd-S bonding compared to the poisoned Pd in the pure Pd membranes.
- More reduction of the Pd-S bonding was observed compared to Au-S bonding after recovering in $H_2$. The un-recovered Au-S bonding increased the overall surface coverage enabling the nearly complete reduction of the Pd-S bonding due to the decrease of the Pd-S binding energy at high overall sulfur coverage.
- Less permeance loss and more permeance recovery of the Pd/Au membranes occurred at higher temperatures due to the exothermic nature of the $H_2S$ adsorption. The exposure duration of $H_2S$ showed no effect on the degree of permeance decline at a fixed temperature indicated that the permeance loss was resulted from the $H_2S$ adsorption on the membrane surface.

- The permeance loss of the Pd/Au membranes as a function of $H_2S$ concentration indicated that the adsorption of sulfur on the Pd/Au surface was monolayer adsorption with limited surface coverage.
- Increasing the Au composition in the Pd/Au membranes reduced the permeance loss in the presence of $H_2S$. However, by taking the effect of the Au composition on the $H_2$ permeance into account, the optimum Au composition with the highest relative $H_2$ permeance (to Pd foil) in the presence of $H_2S$ was within 10 – 30 wt%.

# 11. Recommendations

- In order to obtain further understanding of the sulfur tolerance of Pd/Au alloys, further research should focus on:
  - Sulfur poisoning tests with high $H_2S$ concentration (> 55 ppm) mixtures. The relation between the Au weight fraction and the highest $H_2S$ concentration that the Pd/Au would not form bulk sulfide should be investigated.
  - Sulfur resistance characterization of the Pd/Au alloy membranes in the presence of other WGS gaseous components (i.e. CO, $CO_2$, and $H_2O$). The influence of other gaseous components on the sulfur tolerance of the Pd/Au alloy membranes should be studied.
- In order to utilize the Pd/Au membranes as membrane reactors for $H_2$ production in WGS, the influence of other gaseous components (i.e. CO, $CO_2$, and $H_2O$) on the $H_2$ permeation of the Pd/Au alloy membranes should also be investigated.
- In order to further enhance the sulfur tolerance of Pd membranes, further research should focus on:
  - Fabricate non-homogenous Pd/Au alloy membranes with a thin Pd/Au alloy layer of high Au composition (>50 wt%). While high Au content on the surface enhance the sulfur resistance, the small thickness of the Pd/Au alloy layer would keep the permeance of the Pd/Au alloy membrane comparable to Pd membrane and decrease the usage of Au at the same time.

- ✧ Dope Pd with non-metal elements to form interstitial Pd alloys (i.e. insert boron, phosphate…etc. into the interstitial sites of the Pd lattice). Due to the unavoidable high sulfur affinity to metals, alloy Pd with metals (forming substutional alloys) limits the enhancement of sulfur resistance. On the other hand, dope Pd with non-metal elements potentially enhances the sulfur resistance due to the potential intrinsic change of sulfur adsorption affinity.

# 12. Nomenclature

| | **Latin letters** | |
|---|---|---|
| A | area | $cm^2$ |
| A | absorbance, pre-exponential factor | |
| a | activity | |
| b | path length of the sample | cm |
| C | concentration | mol/L or $mol/m^3$ |
| D | diffusion coefficient | $m^2/h$ |
| D | dissociation energy | kJ/mol |
| E | electrode potential | eV |
| E | activation energy | kJ/mol |
| $E_D$ | activation energy for diffusion | kJ/mol |
| $E_Q$ | activation energy for permeation | kJ/mol |
| $E_a$ | activation energy of adsorption | kJ/mol |
| $E_d$ | activation energy of desorption | kJ/mol |
| F | Faraday constant | 96,500coulombs/mol |
| F | permeance | $mol/(m^2*h*atm^{0.5})$ or $m^3/(m^2*h*atm^{0.5})$ |
| F | structure factor | |
| $F_k$ | permeance from Knudsen diffusion | $mol/(m^2*h*atm^{0.5})$ or $m^3/(m^2*h*atm)$ |
| $F_v$ | permeance from viscous flow | $mol/(m^2*h*atm^{0.5})$ or $m^3/(m^2*h*atm)$ |
| f | form factor | |
| G | Gibb's free energy | kJ/mol |
| $G_x$ | fraction of diffracted intensity | |
| H | enthalpy | kJ/mol |
| I | intensity of X-ray diffraction line | |

| | | |
|---|---|---|
| J | flux | $m^3/(m^2*h)$ |
| $K_s$ | Sieverts' constant | $atm^{0.5}$ |
| K | equilibrium constant | |
| K | Avrami rate constant, reaction rate constant | |
| $k_a$ | adsorption rate constant | $m^3/(m^2*h*atm)$ |
| $k_d$ | desorption rate constant | $m^3/(m^2*h)$ |
| $k_i$ | rate constant into Pd lattice | $m^3/(m^2*h)$ |
| $k_o$ | rate constant exiting Pd lattice | $m^3/(m^2*h)$ |
| l | membrane thickness | m |
| M | molecular weight | g/mol |
| m | mass | g |
| $n_{H/Pd}$ | atomic H/Pd ratio | |
| N | density of nuclei | $1/cm^2$ |
| n | n-value exponent, Avrami exponent | |
| P | pressure | atm |
| Q | permeability | $mol/(m*h*atm^{0.5})$ or $m^3/(m*h*atm^{0.5})$ |
| R | universal gas constant | J/(mol*K) |
| $R_i$ | resistance of component i of composite membrane | $(h*atm^{0.5})/m$ |
| $R_{tot}$ | resistance of composite membrane | $(h*atm^{0.5})/m$ |
| r | reaction rate | mM/min |
| r | tube radius | m |
| S | solubility | $mol/(m^3*atm^{0.5})$ |
| S | entropy | kJ/(mol*K) |
| s(θ) | sticking coefficient | |
| T | temperature | °C or K |
| t | time | h or min |
| X | volume adsorbed/volume of krypton in monolayer | |
| X | Binding energy | kJ/mol |
| X | thickness of new phase | µm |

| | | |
|---|---|---|
| x | penetration depth | μm |
| x | conversion | |
| Z | atomic number | |
| z | gravimetric thickness | μ |

**Greek letters**

| | | |
|---|---|---|
| α | fraction of new phase | |
| α | reaction order for $Au^{3+}$ | |
| α | Knudsen coefficient | $m^3/(m^2*h*atm^2)$ |
| β | viscous coefficient | $m^3/(m^2*h*atm^2)$ |
| Γ | rate of molecular bombardment | $mol/(m^2*h)$ |
| θ | fractional surface coverage | |
| θ | half of the diffra tion angle | |
| κ | hydrogen solubility constant | $mol/m^3$ |
| ε | porosity | |
| ε | molar absorptivity | L/(mol*cm) |
| μ | linear absorption coefficient | 1/m |
| $\mu_k$ | geometric factor for Knudsen diffusion | |
| $\mu_v$ | geometric factor for viscous flow | |
| η | viscosity | kg/(sec*m) |
| π | pi constant | |
| ρ | density | $g/cm^3$, $kg/m^3$ |

# 13. References


Abys, J. A. “Electroless palladium process.” US Patent 4424241, 1984.

Acoya, A.; Cortes, A.; Fierro, J. L. G. and Seoane, X. L. Bartholomew, C. H.; Butt, J. B. Eds. Catalytic Deactivation. Elsevier, Amsterdam., 1991.

Agnew, W.G., ed. The Hydrogen Economy: Opportunities, Costs, Barriers, and Research and Development Needs. National Academies Press, Washington D.C., 2004.

Al-Kassab, T.; Macht, M. and Wollenberger, H. “FIM/AP analysis of Cu-Pd multilayers.” *Appied Surface Science.* **87 - 88** (1995) 329-336

Alefeld, G. and Volkl, J., eds. Hydrogen in Metals. Springer – Verlag, Berlin, 1978.

Alfonso, D.R.; Cugini, A.V. and Sorescu, D.C. “Adsorption and decomposition of $H_2S$ on Pd(1 1 1) surface: a first-principles study.” *Catalysis Today.* **99** (2005a) 315 – 322.

Alfonso, D.R. “First-principles study of sulfur over-layers on Pd(111) surface.” *Surface Science.* **596** (2005b) 229 – 241.

Alfonso, D.R. “Initial incorporation of sulfur into the Pd(1 1 1) surface: a theoretical study.” *Surface Science.* **600** (2006) 4508 – 4516.

Anton, R.; Eggers, H.; Veletas, J. “Auger electron spectroscopy investigations of segregation in gold-palladium and silver-palladium alloy thin films.” *Thin Solid Films*, **226**(1) (1993) 39-47.

Antoniazzi, A.B.; Haasz, A.A. and Stangeby, P.C. “The effect of adsorbed carbon and sulfur on hydrogen permeation through palladium.” *Journal of Nuclear Materials.* **162 – 164** (1989) 1065 – 1070.

Athayde A.L.; Baker, R.W. and Nguyen, P. "Metal composite membranes for hydrogen separation." *Journal of Materials Science*. **94** (1994) 299 – 311.

Avrami, M. “Kinetics of phase change. I. General theory.” *Journal of Chemical Physics*. **7** (1939) 1103 – 1112.

Avrami, M. “Kinetics of phase change. II. Transformation-time relations for random distribution of nuclei.” *Journal of Chemical Physics*. **8** (1940) 212 – 224.

Avrami, M. “Granulation, phase change and microstructure. Kinetics of phase change. III.” *Journal of Chemical Physics*. **9** (1941) 177 – 184

Ayturk, M.E.; Mardilovich, I.P.; Engwall, E.E. and Ma, Y.H. “Synthesis of composite Pd-porous stainless steel (PSS) membranes with a Pd/Ag intermetallic diffusion barrier.” *Journal of Membrane Science*. **285** (2006) 385 – 394

Ayturk, M.E. “Synthesis, annealing strategies and in-situ characterization of thermally stable composite thin Pd/Ag alloy membranes for $H_2$ separation.” PhD thesis, Worcester Polytechnic Institute, 2007.

Ayturk, M.E.; Payzant, E.A.; Speakman, S.A. and Ma, Y.H. “Isothermal nucleation and growth kinetics of Pd/Ag alloy phase via *in situ* time-resolved high-temperature X-ray diffraction (HTXRD) analysis.” *Journal of Membrane Science*. **316** (2008) 97 – 111.

A.Criscuoli, A. Basile, and E. Drioli, An analysis of the performance of membrane reactors for the water-gas shift reaction using gas feed mixtures, Catal. Today, 56 (2000) 53.

Bamford, C. H. and Tipper, C.F.H., Comprehensive Chemical Kinetics, Elsevier Publishing Company, Amsterdam, Netherlands, 1969

Barbier, J.; Lamy-Pitara, E.; Marecot, P.; Boitiaux, J.P.; Cosyns, J. and Verna, F. “Role of sulfur in catalytic hydrogenation reactions.” *Advances in Catalysis*. **39** (1990) 279 – 318.

Barbier, J; Marecot, P.; Tifouti, L.; Guenin, M. and Frety, R. “Thioresistance of supported metal catalysts: structure sensitivity of hydrogen sulfide adsorption on platinum/alumina, iridium/alumina, and platinum-iridium/alumina catalysts.” *Applied Catalysis*. **19** (1985) 375 – 385.

Barin, I., ed. Thermochemical data of pure substances. VCH, New York, USA, 1993.

G. Barbieri, A. Brunetti, T. Granato, P. Bernardo, and E. Drioli, Engineering Evaluations of a Catalytic Membrane Reactor for the Water Gas Shift Reaction, Ind. Eng. Chem. Res., 44 (2005) 7676.

Bard, A. J.: Parsons, R.: and Jordan, J. Standard Potentials in Aqueous Solution, Marcell Dekker INC., New York, USA, 1985

Bartholomew, C.H.; Agrawal, P.K. and Katzer, J.R. “Sulfur poisoning of Metals.” *Advances in Catalysis.* **31** (1982) 135 – 242.

Biswas, J.; Bickle, G.M. and Gray, P.G. “The role of deposited poisons and crystallite surface structure in the activity and selectivity of reforming catalysts.” *Catalysis Reviews – Science and Engineering.* **30** (1988) 161 – 247.

Bitler, W.R.; Pickering, H.W. and Kaja, S. “Interdiffusion kinetics of copper with palladium.” *Platinum Surface Finishings*. **72** (1985) 60 - 63.

Bomermann, J.; Huck, M.; Kuntze, J.; Rauch, T.; Speller, S. and Heiland, W. “An STM, AES and LEED study of the segregated sulfur on Pd(111).” *Surface Science.* **357 – 358** (1996) 849 – 854.

Boyko, B.T., Palatnik, L.S. and Lebedeva, M.V., *Fiz. Met. Metalloved.,* **25** (1968) 845.

Bryden, K.J. and Ying, J.Y. "Nanostructured palladium membrane synthesis by magnetron sputtering." *Materials Science and Engineering*. **A204** (1995) 140 – 145.

Bryden, K.J. and Ying, J.Y. "Pulsed electrodeposition synthesis and hydrogen adsorption properties of nanostructured palladium-iron alloy films." *Journal of electrochemical soc*. ***4*5** (1998) 3339 – 3346.

Bryden, K.J. and Ying, J.Y. "Nanostructured palladium-iron membranes for hydrogen separation and membrane hydrogenation reactions." *Journal of Membrane Science*. **203** (2002) 29 – 42

Bredesen, R.; Jordal, K. and Bolland, O. “High-temperature membranes in power generation with $CO_2$ capture.” *Chemical Engineering and Processing.* **43** (2004) 1129 – 1158

Butt, J. B. and Petersen, E. E., Activation, deactivation, and poisoning of catalysts, Academic Press, Inc., San Diego, USA, 1988.

M.L. Burke, R.J. Madix, Hydrogen on palladium(100)-sulfur: the effect of sulfur on precursor mediated adsorption and desorption, Surf Sci, 237 (1990) 1.

Burke, M.L. and Madix, R.J. “Hydrogen on Pd (100) – S: the effect of sulfur on precursor mediated adsorption and desorption.” *Surface Science.* **237** (1990) 1 – 19.

Buxbaum, R.E. and Kinney, A.B. “Hydrogen Transport through Tubular Membranes of Palladium-Coated Tantalum and Niobium.” *Industrial and Engineering Chemistry Research*. **35** (1996) 530 – 537.

Catalano, J.: Baschetti, M.G. and Sarti, G.C. “Hydrogen permeation in palladium-based membranes in the presence of carbon monoxide.” *Journal of Membrane Science*. **362** (2010) 221-233.

Chaplin,B.P.: Shapley,J.R. and Werth,C.J. “Regeneration of Sulfur-Fouled Bimerallic Pd-Based Catalysts.” *Environ. Sci.*, **41** (2007) 5491-5497

Chen, H. I.; Chu, C. Y. and Huang, T. C. “Characterization of $PdAg/Al_2O_3$ composite membrane by electroless co-deposition.” *Thin Solid Films*. **460** (2004) 62 – 71.

Chen , C.H. and Y.H. Ma,, "The effect of $H_2S$ on the performance of Pd and Pd/Au composite membrane." *Journal of Membrane Science.* **362** (2010) 535-544.

Cheng, Y.S. and Yeung, K.L. "Palladium-silver membranes by electroless plating technique." *Journal of Membrane Science*. **158** (1999) 127 - 141.

Cheng, Y.S. and Yeung, K.L. "Effects of electroless plating chemistry on the synthesis of palladium membranes." *Journal of Membrane Science*. **182** (2001) 195 - 203.

Choi, S. Y.: Mamak, M., :Speakman, S.:Chopra, N. and Ozin, G. A. "Evolution of Nanocrystallinity in Periodic Mesoporous Anatase Thin Films." *Small,* **1** (2005) 226-232.

Christian, J.W. The theory of transformations in metals and alloys; an advanced textbook in physical metallurgy,. Pergamon, New York, USA, 1965.

Chow, K.M.; Ng, W.Y. and Yeung, L.K. "Barrier properties of Ni, Pd and Pd-Fe for Cu diffusion." *Surface Coating Technology*. **105** (1998) 56-64.

Collins, J.P. and Way, J.D. "Preparation and Characterization of a Composite Palladium - Ceramic Membrane." *Industrial and Engineering Chemistry Research*. **32** (1993) 3006 - 3013.

Cottam, M.G. and Tilley, D. R. eds. Introduction to Surface and Superlattice Excitations. Cambridge University Press, Cambridge, 1989.

Coutts, M. D. and Revesz, A. G. "Decoration of semiconductor surfaces for electron microscopy by displacement deposition of gold." *Journal of Applied Physics*. **37** (1966) 3280 - 3286.

Cullity, B. D. and Stock, S. R. Elements of X-ray Diffraction. Prentice Hall: New Jersey, USA, 2001.

DeBonte, W. J.; Poate, J. M.; Melliar-Smith, C. M. and Levesque, R. A.; Picraux, S. T.(ed.); Eernise, E. P.(ed.) and Vook, F. L.(ed.), Applications of ion beans to metals. Plenum Press, New York, USA, 1974.

DeBonte, W. J. and Poate, J. M. " Low temperature interdiffusion in the Au-Pd and Au-Rh thin film couples." *Thin Solid Films*, **25** (1975) 441-448.

DeBonte, W. J.; Poate, J. M.; Melliar-Smith, C. M. and Levesque, R. A.; Picraux, S. T.(ed.); Eernise, E. P.(ed.) and Vook, F. L.(ed.), Applications of ion beans to metals. Plenum Press, New York, USA, 1974.

Deville, H. St C. *C.r. hebd. Seanc. Acad. Sci.,* Paris **59** (1864) 965 – 967.

Dhanak, V. R.; Shard, A. G.; Cowie, B. C. C. and Santoni, A. “The structures of sulphur on Pd (111) studied by X-ray standing wavefield absorption and surface EXAFS.” *Surface Science*. **410** (1998) 321 – 329.

Edlund, D.J. and McCarthy, J. "The relationship between intermetallic diffusion and flux decline in composite-metal membranes: implications for achieving long membrane lifetime." *Journal of Membrane Science*. **107** (1995) 147 – 153.

Edlund, D.J. and Pledger, W.A. "Thermolysis of hydrogen sulfide in a metal-membrane reactor." *Journal of Membrane Science*. **77** (1993) 255 – 264.

Edlund, D.J. and Pledger, W.A. "Catalytic platinum-based membrane reactor for removal of $H_2S$ from natural gas streams." *Journal of Membrane Science*. **94** (1994) 111 – 119.

El-Shazly, M. F. and Baker, K. D. “High build electroless gold process.” *proceeding of First AES electroless plating Symposia, St Louis, 1982*.

Engwall, E. E.; Mardilovich, I P.; Ma, Y. H. “Transport resistance for oxide diffusion barriers on porous metal supports used in composite Pd and Pd-alloy membranes.” *Preprints of Symposia - American Chemical Society, Division of Fuel Chemistry.* **48(1)** (2003) 390-391.

Feuerriegel, U. and Klose,W., “Investigations into the Mechanism of the Deactivation of a Palladium-Supported Catalyst by Hydrogen Sulfide Poisoning.” *Chem. Eng. Technol*. **2**1 (1998) 7,562-562.

Forbes, Jeffrey G.; Gellman, Andrew J.; Dunphy, James C.; Salmeron, Miquel. “Imaging of sulfur overlayer structures on the palladium (111) surface.” *Surface Science*, **279**(1-2), (1992), 68-78.

Frieske, H. and Wicke, E. “Magnetic susceptibility and equilibrium diagram of palladium hydride.” *Berichte der Bunsen-Gesellschaft.* **77** (1973) 48-52.

Gade, S.K., Coulter K.E. andWay, J.D., “Effects of fabrication technique upon material properties and permeation characteristics of palladium-gold alloy membranes for hydrogen separations.” *Gold Bulletin,* **43** (2010) 287-297.

Gao, H.; Lin, Y.S.; Li, Y. and Zhang, B. "Chemical stability and its improvement of palladium-based metallic membranes." *Industrial and Engineering Chemistry Research*. **43** (2004) 6920 - 6930.

Gao, H.; Lin, Y.S.; Li, Y. and Zhang, B. "Electroless plating synthesis, characterization and permeation properties of Pd-Cu membranes supported on $ZrO_2$ modified porous stainless steel." *Journal of Membrane Science*. **265** (2005) 142 – 152.

Gasser, R. P. H. An introduction to chemisorption and catalysis by metals. Clarendon Press, Oxford, 1985

Geilin, P.; Urfels, L.; Primet, M. and Tena, E. "Complete oxidation of methane at low temperature over Pt and Pd catalysts for the abatement of lean-burn natural gas fuelled vehicles emissions: influence of water and sulfur containing compounds." *Catalysis Today*. **83** (2003) 45 – 57.

Gleiter, H., "Diffusion in nanostructured metals." *Physica Status Solidi B: Basic Research*, **172** (1992) 41-51.

Graham, T. "On the adsorption and dialytic separation of gases by colloid septa." *Philosophical Transactions of the Royal Society of London.* **156** (1866) 399 – 439.

Grashoff, G. J.; Pilkington, C. E. and Corti, C. W. "The purification of hydrogen." *Platinum metals review.* **27** (1983) 157 – 169.

Gravil, P. A. and Toulhoat, H. " Hydrogen sulphur and chlorine coadsorption on Pd(111): a theoretical study of poisoning and promotion." *Surface Science.* **430** (1999) 176 – 191.

Gregg, S. J. and Sing, K. S. W., Adsorption, surface area, and porosity. Academic Press, New York, USA, 1967.

Gryaznov, V.M.; Serebryannikova, O.S.; Serov, Y.M.; Ermilova, M.M.; Karavanov, A.N.; Mischenko, A.P. and Orekhova, N.V. "Preparation and catalysis over palladium composite membranes." *Applied Catalysis A: General.* **96** (1993) 15 – 23.

Gryaznov, V.M. "Metal containing membranes for the production of ultrapure hydrogen and the recovery of hydrogen isotopes." *Separation and Purification Methods*. **29**(2) (2000) 171 – 187.

Guazzone, Federico. "Engineering of substrate surface for the synthesis of ultra-thin composite Pd and Pd-Cu membranes for $H_2$ separation." PhD thesis. Worcester Polytechnic Institute, 2005.

Guazzone, F. "Engineering of substrate surface for the synthesis of ultra-thin composite Pd and Pd-Cu membranes for $H_2$ separation." PhD thesis. Worcester Polytechnic Institute, 2006.

Han, J.; Kim, I. S. and Choi, K. S. "High purity hydrogen generator for on-site hydrogen production." *Int. Journal of Hydrogen Energy.* **27** (2002) 1043 – 1047.

Hancock, J. D. and Sharp, J. H. " Method of comparing solid state kinetic data and its application to the decomposition of Kaolinite, Brucite, and $BaCO_3$." *Journal of the American Ceramic Society*. **55** (1972) 74-77.

Henis, J.M.S. and Tripodi, M.K. “Composite hollow fiber membranes for gas separation: the resistance model approach.” *Journal of Membrane Science.* **8** (1981) 233 – 246.

Holleck, G. L. “Diffusion and solubility of hydrogen in palladium and palladium-silver alloys.” *The journal of physical chemistry.* **74** (1970) 503 – 511.

Honma, H. and Watanabe, H. : Schultze, W.J. (ed.). , Osaka, Tetsuya (ed.), and Datta, Madhav (ed.). Ch. 8 Advanced plating technology for electronics packaging in Electrochemical Microsystem Technologies, Taylor and Francis, New York, USA, 2002.

Hough, W. V.; Little, J. L. and Warheit, K. E. “Method for the electroless deposition of palladium.” US patent 4279951, 1981; “Palladium alloy baths for the electroless deposition.” US Patent 4255194, 1981.

Hughes, R. Deactivation of Catalysts, Academic Press Inc., Orlando, USA, 1984.

Hunter, J. B. “A new hydrogen purification process.” *Platinum metals review*. **4**(1960) 130 – 131.

Hulbert, S.F. “Models for solid-state reactions in powdered compacts.” *Journal of the British Ceramic Society.* **6** (1969) 11-20.

Hurlbert, R.C. and Konecny, J.O. “Diffusion of hydrogen through palladium.” *The Journal of Chemical Physics.* **34**(2) (1961) 655 – 658.

Ilias, S. and Islam, M. “Effect of surfactants in fabrication of palladium thin-film composite membrane by electroless plating.” *Proceeding of North American Membrane Society Annual meeting, Orlando, FL, 2007.*

Itoh, N.; Wu, T. and Haraya, K. “Two and three dimensional analysis of diffusion through a dense membrane supported on a porous material.” *Journal of Membrane Science.* **99** (1995) 175 – 183.

Itoh, N.; Xu, W. C.; Hara, S.; Kimura, H. M. and Masumoto, T. “Permeability of hydrogen in amorphous $Pd_{(1-x)}Si_x$ alloys at elevated temperatures.” *Journal of Membrane Science.* **139** (1998) 29 – 35.

Itoh, N.; Akiha, T.; Sato, T. “Preparation of thin palladium composite membrane tube by a CVD technique and its hydrogen permselectivity.” *Catalysis Today*, **104** (2005) 231-237.

Iyoha, O.; Enick, R.; Killmeyer, R. and Morreale, B. “The influence of hydrogen sulfide-to-hydrogen partial pressure ratio on the sulfidation of Pd and 70 mol% Pd-Cu membranes.” *Journal of Membrane Science*. **305** (2007) 77 - 92.

Jayaramam, V.; Lin, Y.S.; Pakala, M.; Lin, R.Y. “Fabrication of ultrathin metallic membranes on ceramic supports by sputter deposition.” *Journal of Membrane Science.* **99** (1995a) 89 – 100.

Johnson, W. and Mehl, R. “ Reaction kinetics in processes of nucleation and growth.” *Trans. AIME*, **135** (1939) 416-458.
Li, Z.Y.; Maeda, H.; Kusakabe, K.; Morooka, S.; Anzai, A. and Akiyama, S. "Preparation of palladium-silver alloy membranes for hydrogen separation by the spray pyrolysis method." *Journal of Membrane Science*. **78** (1993) 247 - 254.

Lustemberg, P. G.; Vericat, C.; Benitez, G. A.; Vela, M. E.; Tognalli, N.; Fainstein, A.; Martiarena, M. L.; Salvarezza, R. C. , “Spontaneously Formed Sulfur Adlayers on Gold in Electrolyte Solutions: Adsorbed Sulfur or Gold Sulfide?”, *Journal of Physical Chemistry C*, **112** (2008) 11394-11402.

Jayaramam, V. and Lin, Y.S “Synthesis and hydrogen permeation properties of ultrathin palladium-silver alloy membranes.” *Journal of Membrane Science.* **104** (1995b) 251 – 262.

Kajiwara, M.; Uemiya, S. and Kojima, T. "Stability and hydrogen permeation behavior of supported platinum membranes in the presence of hydrogen sulfide." *International Journal of Hydrogen Energy*. **24** (1999) 839 - 844.

Kamakoti, P and Sholl, D. S. “A comparison of hydrogen diffusivities in Pd and CuPd alloys using density functional theory.” *Journal of Membrane Science.* **225** (2003) 145 – 154.

Kamakoti, P.; Morreale, B.D.; Ciocco, M.V.; Howard, B.H.; Killmeyer, R.P.; Cugini, A.V.; and Sholl, D.S. "Prediction of Hydrogen Flux Through Sulfur-Tolerant Binary Alloy Membranes." Science. 307 (2005) 569 - 573.

Karpova, R. A. and Tverdovskii, I. P. “Hydrogen sorption in the dispersed palladium-copper alloys.” *Inst. Appl. Chem., Leningrad.* **33** (1959) 1393-1400.

Kawagoshi, S. Japanese patent (Kokai Tokyo Koho) (1977) 77-733.

Keuler, J. N.; Lorenzen, L., Sanderson, R. D., Prozesky, R. D. and Pryzbylowicz, W. J. “Characterization of electroless plated palladium-silver alloy membranes.” *Thin Solid Film*. **347** (1999) 91 – 98.

Kim, S. : Kim, W. K.: Payzant, E. A.: Acher, R.: Kaczynski, R.: Yoon, S. :Anderson, T.J.: Crisalle, O. D.: and Li, S. S. “Reaction Kinetics and Pathways of $CuInSe_2$ Growth from Bilayer Precursor Films: Time-resolved High Temperature X-ray Diffusion Analysis,” *J. Vac. Sci. Technol. A,* **23** (2) (2005) 310-315

Kim, W.K. : Payzant, E.A. : Kim, S. : Speakman, S.A. : Crisalle, O.D. : Anderson. T.J., "Reaction Kinetics of $CuGaSe_2$ Formation from a GaSe/CuSe Bilayer Precursor Film." *Journal of Crystal Growth* **310** (2008) 2987-2994

King, H. W.; Payzant, E. A. and Caughlin, T. A.," Temperature discrepancies in high temperature diffractometery." *Advances in X-Ray Analysis*, **40** (1997-1998) 679.

Klette, H. and Bredesen, R. "Sputtering of very thin palladium-alloy hydrogen separation membranes." *Membrane Technology.* May 2005, 7 – 9.

Knapton, A.G. "Palladium alloys for hydrogen diffusion membranes: A review of high permeability materials." *Platinum Metal Reviews*. **21** (1977) 44 – 50.

Kolmogorov, A." A statistical theory for the recrystallization of metals." *Akad. Nauk. SSSR, Izv., Ser. Matem.*, **1** (1937) 355.

Kulprathipanja, A.; Alptekin, G.O.; Falconer, J.L. and Way, J.D. "Pd and Pd-Cu membranes: inhibition of $H_2$ permeation by $H_2S$." *Journal of Membrane Science*. **254** (2005) 49 – 62

Kuo, C.L. and Huang, M.H "Hydrothermal Synthesis of Free Floating $Au_2S$ Nanoparticle Superstructures." *J. Phys. Chem. C*, **112** (2008) 11661-11666.

Lam, Y. L.; Boudart, M., "Oxidation of small palladium particles*." Journal of Catalysis*, **47** (1977) 393-398.

Lang, N. D.; Holloway, S and Norskov, J. K. "Electrostatic adsorbate-adsorbate interactions: the poisoning and promotion of the molecular adsorption reaction." *Surface Science*. **150** (1985) 24 – 38

Latyshev, V.V. and Gur'yanov, V.G. "The interaction of hydrogen with palladium-based alloy membranes." *Russian Journal of Physical Chemistry*. **62**(2) (1988) 220 – 224.

Lee, D. W.; Lee, Y. G.; Nam, S. E.; Ihm, S. K. and Lee, K. H. "Study on the variation of morphology and separation behavior of the stainless steel supported membranes at high temperature." *Journal of Membrane Science*. **220** (2003) 137– 153.

Lee, Y.S. : Chung, Y.D. " Lim, K.Y. : Whang C.N. " Kim, J.H. :Kang, H.J. and Woo, J.J. "Electron excited Auger line shape study of ion-beam-mixed Pd-Au alloys." *Journal of Electron Spectroscopy and Related Phenomena*, **105** (1999) 77-84

Lewis, F. A., The Palladium-hydrogen system. Academic, New York, USA, 1967.

Li, Z.Y.; Maeda, H.; Kusakabe, K.; Morooka, S.; Anzai, A. and Akiyama, S. "Preparation of palladium-silver alloy membranes for hydrogen separation by the spray pyrolysis method." *Journal of Membrane Science*. **78** (1993) 247 - 254.

Li, A.; Xiong, G.; Gu, J.; Zheng, L. " Preparation of Pd/ceramic composite membrane 1. Improvement of the conventional preparation technique." *Journal of Membrane Science*. **110** (1996) 257 - 260.

Li, A.; Liang, W. and Hughes, R. "Characterization and permeation of palladium/stainless steel composite membranes." *Journal of Membrane Science*. **149** (1998) 259 - 268.

Li, A.; Liang, W. and Hughes, R. "Repair of Pd/□-$Al_2O_3$ composite membrane containing defects." *Separation and Purification Technology*. **15** (1999) 113 - 119.

Li, A.; Liang, W. and Hughes, R. "Fabrication of dense palladium composite membranes for hydrogen separation." *Catalysis Today*. **56** (2000a) 45 - 51.

Lin, W. H. and Chang, H. F. "A study of ethanol dehydrogenation reaction in a palladium membrane reactor." *Catalysis Today*. **97** (2004) 181 - 188.

Ma, Y.H.; Mardilovich, P.P. and She, Y. "Hydrogen gas-extraction module and method of fabrication." US Patent 6,152,987, 2000.

Ma, Y.H.; Akis, B.C.; Ayturk, M.E.; Guazzone, F.; Engwall, E.E. and Mardilovich, I.P. "Characterization of intermetallic diffusion barrier and alloy formation for Pd/Cu and Pd/Ag porous stainless steel composite membranes." *Industrial Engineering and Chemistry Research.* **43** (2004) 2936 – 2945.

Ma, Y.H.; Mardilovich, I.P. and Engwall, E.E. "Thin composite palladium and palladium/alloy membranes for hydrogen separation." *Annals of the New York Academy of Sciences*. **984** (2003) 346 – 360.

Ma, Y.H.; Mardilovich, I.P. and Engwall, E.E. "Composite gas separation modules having intermediate porous metal layers." US Patent 7,175,694, 2007.

Maca, F.; Scheffler, M. and Berndt, W. " The adsorption of sulfur on palladium(111). I. A LEED analysis of the ($2^{0.5}$*$3^{0.5}$)R30$^{o}$ sulfur adsorbate structure." *Surface Science.* **160** (1985) 467 - 474.

Maeland, A. and Flanagan, T. B. "Lattice Spacings of Gold-Palladium Alloys." *Canadian Journal of Physics* **42** (1964) 2364-2366.

Maeland, A. and Flanagan, T. B. "X-Ray and Thermodynamic Studies of the Absorption of Hydrogen by Gold-Palladium Alloys" *The Journal of Physical Chemistry*, **69** (1965), 3575-3581.

Mealand, A. and Flanagan, T. B. “Comparison of Hydrogen and Deuterium Solubility in Palladium-Rich Alloys Gold-Palladium.” *The Journal of Physical Chemistry*, **71** (1967), 1950-1952.

Maestas, S. and Flanagan, T. B. „Diffusion of Hydrogen in Gold-Palladium Alloys.“ *The Journal of Physical Chemistry*, **77** (1973) 850-854.

Makin, S. M.: Rowe, A. H. : and LeClaire, A. D. “Self-Diffusion in Gold.” *Proc. Phys. Soc. B,* **70** (1957) 545-552.

Mallory, G.O. and Hajdu, J.B., ed. Electroless Plating: Fundamentals and Applications. American Electroplaters and Surface Finishers Society, Orlando, 1990.

Mardilovich, P.P.; She, Y.; Ma, Y.H. and Rei, M. "Defect free palladium membranes on porous stainless steel support." *AiChE Journal*. **44**(2) (1998) 310 - 322.

Mardilovich, I.P.; Engwall, E. and Ma, Y.H. "Dependence of hydrogen flux on the pore size and plating surface topology of asymmetric Pd-porous stainless steel membranes." *Desalination.* **144** (2002) 85 - 89.

Mason, E.A. and Malinauskas, A.P. Gas Transport in Porous Media: The Dusty-gas Model. Elsevier, Amsterdam, 1983.

Mathieu, M. and Primet, M. “Sulfurization and Regeneration of Platinum.” *Applied Catalysis*, **9** (1984) 360-370.

Matsumoto,Y.: Soma,M. :Onishi,T. and Tamaru, K., “State of Sulphur on the Palladium Surface Studied by Auger Electron Spectroscopy, Electron Energy Loss Spectroscopy, Ultraviolet Photoelectron Spectroscopy and X-ray Photoelectron Spectroscopy.” *J. Chem. Soc.*, Faraday Trans. 1, **76** (1980) 1122-1130

Mazzone, G.; Rivalta, I.; Russo, N. and Sicilia, E. “Interaction of CO with PdAu(111) and PdAu(100) Bimetallic surfaces: a theoretical cluster model study.” *Journal of Physical Chemistry (c).* (2008).

McCarty, J. G. and Wise, H. J. “Thermodynamics of sulfur chemisorption on metals. 1. Alumina supported nickel.” *Journal of chemical physics.* **72** (1980) 6332 - 6337.

McCarty, J. G.; Sancier. K. M. and Wise, H. J. “Thermodynamics of sulfur chemisorption on metals. 4. Alumina supported platinum.” *Journal of catalysis.* **82** (1983) 92 - 97.

McKinley, D.L. "Method for hydrogen separation and purification." US Patent 3,247,648, 1966.

McKinley, D.L. and Nitro, W. "Metal Alloy for Hydrogen Separation and Purification." US Patent 3,350,845, 1967.

McKinley, D.L. and Nitro, W. "Method for Hydrogen Separation and Purification." US Patent 3,439,474, 1969.

Mikhlin, Y. : Likhatski, M. : Tomashevich, Y. Romanchenko, A. : Erenburg, S. and Trubina, S., "XAS and XPS examination of the Au-S nanostructures produced via the reduction of aqueous gold (III )by sulfide ions." *Journal of Electron Spectroscopy and Related Phenomena*, **177** (2010) 24-29.

Miller, J.B.; Morreale, B.D. and Gellman, A.J. "The effect of adsorbed sulfur on surface segregation in a polycrystalline $Pd_{70}Cu_{30}$ alloy." *Surface Science*. **602**(10) (2008b) 1819.

Mori, H.; Komatsu, M.; Takeda, K.; Fujita, H. "Spontaneous alloying of copper into gold atom clusters." *Philosophical Magazine Letters*, **63** (1991) 173-178.

Morris,T. : Copeland, H. and Szulczewski G. "Synthesis and Characterization of Gold Sulfide Nanoparticles." *Langmuir*, **18** (2002) 535-539.

Morreale, B.D.; Howard, B.H.; Iyoha, O.; Enick, R.M.; Ling, C. and Sholl, D.S. "Experimental and computational prediction of the hydrogen transport properties of $Pd_4S$." *Industrial Engineering and Chemistry Research*. **46**(19) (2007) 6313.

Morreale, B.D.; Ciocco, M.V.; Howard, B.H.; Killmeyer, R.P.; Cugini, A.V. and Enick, R.M. "Effect of hydrogen-sulfide on the hydrogen permeance of palladium-copper alloys at elevated temperatures." *Journal of Membrane Science*. **241** (2004) 219 – 224.

Moulder, J.F, :Stickle, W.F.: Sobol, P.E. and Bomben, K.D. Handbook of X-ray Photoelectron Spectroscopy, Physical Electronic Inc., Minnesota, 1993.

Mundschau, M.V.; Xie, X.; Evenson IV, C.R.; and Sammells, A.F. "Dense inorganic membranes for production of hydrogen from methane and coal with carbon dioxide sequestration." *Catalysis Today*. **118** (2006) 12 – 23.

Murakami, M. : deFontaime, D.: and Fodor, J. "X-ray diffraction study of interdiffusion in bimetallic Au/Pd films." *Journal of Applied Physics* **47** (7) (1976) 2850-2856.

Nam, S. E. and Lee, S. H. and Lee, K. H." Preparation of a palladium alloy composite membrane supported in a porous stainless steel by vacuum electrodeposition." *Journal of Membrane Science*. **153** (1999) 163 – 173.

Nam, S. E. and Lee, K. H." A study on the palladium/nickel composite membrane by vacuum electrodeposition." *Journal of Membrane Science*. **170**(2000) 91 – 99.

Nam, S. E. and Lee, K. H." Hydrogen separation by Pd composite membranes: Introduction of diffusion barrier." *Journal of Membrane Science*. **192** (2001) 163 – 173.

Neukam, O., "Diffusion coatings." *Galvanotechnik*, **61** (8) (1970) 626-33.

O'Brien, C.P.; Howard, B.H.; Miller, J.B.; Morreale, B.D. and Gellman, A.J. "Inhibition of hydrogen transport through Pd and $Pd_{47}Cu_{53}$ membranes by $H_2S$ at 350°C." *Journal of Membrane Science*. **349** (2010) 380 – 384.

Okamoto, H. and Massalski, T.B. "The Au-Pd (Gold-Palladium) System" Bulletin of Alloy Phase Diagram.", **6**(3) (1985) 229-235

Okamoto, H. and Massalski, T.B. Phase diagrams of binary gold alloys. ASM International, Metal Park, Ohio, 1987.

Okinaka, Y.; Mallory, G.O.(ed.) and Hajdu, J.B., (ed.). Chapter 15 Electroless plating of gold and gold alloys in Electroless Plating: Fundamentals and Applications. American Electroplaters and Surface Finishers Society, Orlando, 1990.

Okkerse, B. "Self-Diffusion of Gold." *Physical Review*. **103** (1956) 1246-1249.

Oudar, J. "Sulfur-metal interactions." *Materials Science and Engineering.* **42** (1980a) 101 – 109.

Oudar, J. "Sulfur adsorption and poisoning of metallic catalysts." *Catalysis Reviews – Science and Engineering*. **22** (1980b) 171 – 195.

Oudar, J. (ed.) and Wise, H.(ed.), Deactivation and Poisoning of Catalysts. Marcel Dekker, Inc., New York, USA, 1985.

Paglieri, S.N.; Foo, K.Y.; Way, J.D.; Collins, J.P. and Harper-Nixon, D.L. "A new preparation technique for Pd/alumina membrane with enhanced high-temperature stability." *Industrial Engineering and Chemistry Research*. **38** (1999) 1925 – 1936.

Parker, E. A.; Reid, F. H.(ed.) and Goldie, E.(ed.) Chapter 10 in Gold Plating Technology. *Electrochemical Publications limited*, Ayr, Scotland, 1974.

Patterson, C. H. and Lambert, R. M. "Structure and properties of the palladium/ sulphur interface: $S_2$ chemisorption on Pd (111)." *Surface Science.* **187** (1987) 339 – 358.

Peterson, N.L. "Isotope Effect in Self-Diffusion in Palladium." **Physical Review**, **136**, 2A (1964) 568-574.

Pawelec, B.; Cano-Serrano, E.; Campos-Martin, J.M.; Navarro, R.M.; Thomas, S. and Fierro, J.L.G. "Deep aromatics hydrogenation in the presence of DBT over Au-Pd/γ-alumina catalysts." *Applied Catalysis A: General*. **275** (2004) 127 - 139.

Pearlstein, F. and Weightman, R. F. "Electroless palladium deposition." *Plating*. **56** (1969) 1158 - 1161.

Pearlstein, F. and Lowenheim, F. A. eds. Modern Electroplating (3rd Edition). Wiley, New York, 1974.

Peden, C.H.F.; Kay B.D. and Goodman, D.W. "Kinetics of hydrogen adsorption by chemically modified Pd(1 1 0)." *Surface Science.* **175** (1986) 215 – 225.
Peterson, N. L. "Isotope Effect in Self-Diffusion in Palladium." *Physical Review*. **136** (1964) A568-A574.

Pollock, D. D. Physical properties of materials for engineers. CRC Press INC.Boca Raton, FL, USA 1993

Pomerantz, N. "Sulfur tolerant palladium membranes for hydrogen separation from coal gas." Ph. D. proposal, Worcester Polytechnic Institute, 2007.

Pomerantz, N. and Ma, Y. H. "Effect of $H_2S$ on the performance and long-term stability of Pd/Cu membranes", *Ind. Eng. Chem. Res*., **48** (2009) 4030.

Pomerantz, N "Sulfur poisoning and tolerance of Pd/Cu Alloy membranes for hydrogen separation from coal gas" PhD thesis, Worcester Polytechnic Institute, 2010.

Pomerantz, N. and Ma, Y. H., "Novel method for producing high $H_2$ permeability Pd membranes with a thin layer of the sulfur tolerant Pd/Cu fcc phase", *Journal of Membrane Science*, **370** (2011) 97-108.

Rhoda, R.N. and Madison, A. "Palladium Plating by Chemical Reduction" US Patent 2,915,406, 1959.; Rhoda, R.N. " Electroless palladium plating." *Trans. Inst. Metal Finish.* **36** (1959) 82 – 85

Roa, F. and Way, J.D. "Influence of alloy composition and membrane fabrication on the pressure dependence of the hydrogen flux of palladium-copper membranes." *Industrial Engineering and Chemistry Research.* **42** (2003) 5827 – 5835.

Rodriguez, J.A. and Kuhn, M. "Electronic and chemical properties of Pd in bimetallic systems: interaction of Pd with Rh(111)." *Surface Science.* **365** (1996) L669 – L675.;

Rodriguez, J.A. " Physical and chemical properties of bimetallic surfaces." *Surface Science Reports.* **24** (1996) 223 – 287.;

Rodriguez, J.A. " Electronic and chemical properties of Pt, Pd and Ni in bimetallic surfaces." *Surface Science.* **345** (1996) 347 – 362.

Rodriguez, J.A.; Chaturvedi, S. and Jirsak, T. "The bonding of sulfur to Pd surfaces: photoemission and molecular-orbital studies." *Chemical Physics Letters.* **296** (1998) 421 – 428.

Rosenqvist, T. “A thermodynamic study of iron, cobalt, and nickel sulfides.” *Journal of the Iron and Steel Institute.* **176** (1954) 37 – 57.

Ryu, C.K.; Ryoo, M.W.; Ryu, I.S. and Kang, S.K. "Catalytic combustion of methane over supported bimetallic palladium catalysts: Effects of Ru or Rh addition." *Catalysis Today.* **47** (1999) 141 – 147.

Saleh, J.M.; Kemball, C. and Roberts, M.W. “Interaction of hydrogen sulfide with nickel, tungsten and silver films.” *Transactions of the Faraday Society.* **57** (1961) 1771 – 1780.

Saleh, J.M. “Interaction of sulfur compounds with palladium.” *Transactions of the Faraday Society.* **66**(1) (1970) 242 – 250.

Sarkany, A.; Horvath, A. and Beck, A. “Hydrogenation of acetylene over low loaded Pd and Pd-Au/$SiO_2$ catalysts.” *Applied Catalysis A: General.* **229** (2002) 117 – 125.

Sergoenko, A. “Hypophosphite solutions for chemical plating of palladium stabilized by ethylenediamine compounds.” US Patent 3418143, 1968.

Shi, L.: Goldbach, A.: Zeng, G.: and Xu, H. “Preparation and performance of thin-layered PdAu/ceramic composite membranes.” *International Journal of Hydrogen Energy*, **35** (2010) 4201-4208.

Shu, J.; Grandjean, B.P.A.; Van Neste, A. and Kaliaguine, S. “Catalytic Palladium -based Membrane Reactors: A Review.” *The Canadian Journal of Chemical Engineering.* **69** (1991) 1036 – 1060.

Shu, J.; Grandjean, B.P.A. and Kaliaguine, S. "Simultaneous deposition of Pd and Ag on porous stainless steel by electroless plating." *Journal of membrane science*. **77** (1993a) 181-195.

Shu, J.; Grandjean, B.P.A. and Kaliaguine, S. "Asymmetric Pd-Ag/stainless steel catalytic membranes for methane steam reforming.” *Catalysis Today.* **25** (1995) 327 -332.

Shu, J.; Adnot, A.; Grandjean, B.P.A.; Kaliaguine, S. "Structurally stable composite Pd-Ag alloy membranes: Introduction of a diffusion barrier." *Thin solid films*. 286 (1996) 72 - 79.

Sieverts, A.; Jurisch, E. and Metz, A. “solubility of hydrogen in the solid alloys of palladium with gold, silver and platinum. “ *Z. anorg. Allg. Chem.* **92**(1915) 322-362.

Sohn, Y. : Pradgan, D. and Leung K.T. “Electrochemical Pd Nanodeposits on a Au Nanoisland Template Supported on Si(100) : Formation of Pd-Au Alloy and Interfacial Electronic Structures.” *ACSNANO*, **4** (2010) 9, 5111-5120.

Souleimanova, R.S.; Mukasyan, A.S. and Varma, A. "Study of structure formation during electroless plating of thin metal-composite membranes." *Chemical Engineering Science*. **54** (1999) 3369 – 3377.

Souleimanova, R.S.; Mukasyan, A.S. and Varma, A. "Effects of osmosis on microstructure of Pd-composite membranes synthesized by electroless plating technique." *Journal of Membrane Science*. **166** (2000) 249 – 257.

Souleimanova, R.S.; Mukasyan, A.S. and Varma, A. "Pd-composite membranes prepared by electroless plating and osmosis: synthesis, characterization and properties." *Separation and Purification Technology*. **25**(2001) 79 – 86.

Souleimanova, R.S.; Mukasyan, A.S. and Varma, A. "Pd membranes formed by electroless plating with osmosis: Hydrogen permeation studies." *AIChE Journal*. **48**(2) (2002) 262 – 268.

Sonwane, C. G.; Wilcox, J.; Ma, Y. H. "Solubility of hydrogen in PdAg and PdAu binary alloys using density functional theory." *Journal of physical chemistry (B).* **110** (2006a) 24549 – 24558.

Sonwane, C. G.; Wilcox, J.; Ma, Y. H. "Achieving optimum hydrogen permeability in PdAg and PdAu alloys." *The Journal of chemical physics.* **125** (2006b) 184714.

Speller, S.; Rauch, T.; Bomermann, J.; Borrmann, P.; and Heiland, W. "Surface structures of S on Pd (111)." *Surface Science.* **441** (1999) 107 – 116.

Starkov, V.; Vyatkin, A.; Volkov, V.; Presting, H.; Konle, J. and Konig, U. " Highly efficient to hydrogen permeability palladium membranes supported in porous silicon." *Physica status solidi(c).* **2** (2005) 3457 – 3460.

Su, S.C., Carstens, J.N. and Bell, A.T., "Study of the dynamics of Pd oxidation and PdO reduction by $H_2$ and $CH_4$", *J. Catal*., **176** (1998) 125.

Subramanian, P.R. and Laughlin, D.E. "Copper-Palladium." *Journal of Phase Equilibria.* **12**(2) (1991) 231 – 243.

Taylor, J.R. "Phase relationships and thermodynamic properties of the Pd-S system." *Metallurgical Transactions B.* **16B** (1985) 143 – 148.

Teng, X.; Wang, Q.; Liu, P.; Han, W.; Frenkel, A. I.; Wen, W.; Marinkovic, N.; Hanson, J. C. and Rodriguez, J. A., "Formation of Pd/Au nanostructures from Pd nanowires via galvanic replacement reaction." *J. Am. Soc.*, **130** (2008) 1093-1101.

Tong, J. and Matsumura, Y. "Thin Pd membrane prepared on macroporous stainless steel tube filter by an in-situ multi-dimensional plating mechanism." *Chemical Communications*. (2004) 2460 – 2461.

Tong, H.D.; Hoang, H.T.; Gielens, F.C.; Jansen, H.V. and Elwenspoek, M.C. “Fabrication and characterization of dual sputtered Pd-Cu alloy films for hydrogen separation membranes.” *Material Letters.* **58** (2004a) 525 – 528.

Tong, H.D.; Gielens, F.C.; Gardeniers, J.G.E.; Jansen, H.V.; Rijn, C.J.M.; Elwenspoek, M.C. and Nijdam, W. “Microfabricated palladium-silver alloy membranes and their application in hydrogen separation.” *Industrial Engineering and Chemical Research.* **43** (2004b) 4182 – 4187.

Tong, J.; Kashima, Y.; Shirai, R.; Suda, H. and Matsumura, Y. “Thin defect-free Pd membrane deposited on asymmetric porous stainless steel substrate.” *Industrial Engineering and Chemical Research.* **44** (2005a) 8025 – 8032.

Tong, H.D.; Vanden Berg, A.H.J.; Gardeniers, J.G.E.; Jansen, H.V.; Gielens, F.C and Elwenspoek, M.C. “Preparation of palladium-silver alloy films by a dual-sputtering technique and its application in hydrogen separation membrane.” *Thin Solid Films.* **479** (2005b) 89 – 94.

Uemiya, S.; Sato, N.; Ando, H.; Kude, Y.; Matsuda, T. and Kikuchi, E. “Separation of hydrogen through palladium thin film supported on a porous glass tube.” *Journal of Membrane Science*. **56** (1991a) 303 - 313.

Uemiya, S.; Matsuda, T.; Kikuchi, E., “Hydrogen permeable palladium-silver membrane supported on porous ceramics.” *Journal of Membrane Science*. **56** (1991b) 315 – 325.

Uemiya, S.; Kajiwara, M. and Kojima, T. "Composite Membranes of Group VIII Metal Supported on Porous Alumina." *AIChE Journal*. **43** (1997) 2715 – 2723.

Van Dal, M. J. H.; Pleumeekers, M. C. L. P.; Kodentsov, A. A. and Van Loo, F. J. J.,” Intrinsic diffusion and Kirkendall effect in Ni-Pd and Fe-Pd solid solutions.” Acta Materialia, **48** (2000) 385.

Venezia, A. M.; La Parola, V.; Deganello, G.; Pawelec, B. and Fierro, J. L. G. “Synergetic effect of gold in Au/Pd catalysts during hydrodesulfurization reactions of model compounds.” *Journal of Catalysis*. **215** (2003) 317 – 325.

Wang, D.; Tong, J.; Xu, H. and Matsumura, Y. “Preparation of palladium membrane over porous stainless steel tube modified with zirconium oxide.” *Catalysis Today.* **93 – 95** (2004) 689 – 693.

Ward, T.L.; and Dao, T. "Model of hydrogen permeation behavior in palladium membranes." *Journal of Membrane Science*. **153** (1999) 211 - 231.

Way, J. D.; Lusk, M and Thoen, P. “Sulfur-resistance composite metal membranes.” US Patent 20080038567, 2008.

Wicke, E. and Nernst, G. “Phase diagram and thermodynamic behavior of the system $Pd/H_2$ and $Pd/D_2$ at normal temperatures; H/D separations effects.” *Berichte der Bunsen-Gesellschaft fur Physikalische Chemie*. **68** (1964) 224 – 235

Widler, A. M.; Seward, T. M., “The adsorption of gold(I) hydrosulphide complexes by iron sulphide surfaces*.”, Geochimica et Cosmochimica Acta* **66** (2002) 383-402.
Wilke, S. and Scheffler, M. “Poisoning of Pd(1 0 0) for the dissociation of $H_2$: a theoretical study of co-adsorption of hydrogen and sulfur.” *Surface Science.* **329** (1995) L605 – L610.

Wu, L.; Xu, N. and Shi, J. "Preparation of a Palladium Composite Membrane by an Improved Electroless Plating Technique." *Industrial Engineering and Chemistry Research*. **39** (2000) 342 – 348

Xomeritakis, G. and Lin, Y.S. “Fabrication of a thin palladium membrane supported in a porous ceramic substrate by chemical vapor deposition.” *Journal of Membrane Science*. **120** (1996) 261 - 272.

Yan, S.; Maeda, H., Kusakabe, K and Morooka, S. “Thin palladium membrane formed in support pores by metal-organic chemical vapor deposition method and application to hydrogen separation.” *Ind. Eng. Chem. Res.* **33** (1994) 616 - 622.

Yeung, K. L.; Sebastian, J.M. and Varma, A. “Novel preparation of Pd/Vycor composite membranes.” *Catalysis Today.* **25** (1995) 231 - 236.

Yeung, K.L.; Christiansen, S.C. and Varma, A. "Palladium composite membranes by electroless plating technique: Relationships between plating kinetics, film microstructure and membrane performance." *Journal of Membrane Science*. **159** (1999) 107 - 122.

Yi, C.W. : Luo, K. : Wei, T. and Goodman, D.W. “The Composition and Structure of Pd-Au Surface.” *J. Phys. Chem. B*, **109** (2005) 18535-18540.

Zayats, A. I.; Stepanova, I. A. and Gorodyskii, A. V. ”Chemical reduction of palladium by sodium hypophosphite.“ *Zahch Metals.* **9** (1973) 116 - 117.

Zhao, H.B.; Pflanz, K.; Gu, J.H.; Li, A.W.; Stroh, N.; Brunner, H. and Xiong, G.X. "Preparation of palladium composite membranes by modified electroless plating procedure." *Journal of Membrane Science*. **142** (1998) 147 - 157.

Zhao, H.B.; Xiong, G.X. and Baron, G.V. "Preparation of palladium-based composite membrane by electroless plating and magnetron sputtering." *Catalysis Today*. **56** (2000) 89 - 96.

# Appendix A: GC calibration

As mentioned in *Chapter 3*, the GC signal (peak area) should be maximized before the characterization for the maximum sensitivity. The pressure of both air and hydrogen used for fueling the FPD detector affected the peak area. Figure A.1 shows the dependence of the peak area on the hydrogen pressure with the feed gas of a 5 ppm $H_2S/H_2$ gas mixture. The peak area increased with increasing hydrogen pressure up to 35 psia. Figure A.2 shows the dependence of the peak area on the air pressure while running a 5 ppm $H_2S/H_2$ gas mixture. The peak area increased with decreasing air pressure linearly within 2 – 5 psia. The results suggested that the GC signal was higher in a hydrogen richer flame. It should be noted that the flame extinguished when the air pressure went below 2 psia. On the other hand, the pressure of the carrier gas, He, showed no influence on the peak area. The flow rate of the sample to the GC also showed influence on the peak. As shown in Figure A.3 (Pomerantz, 2010), the peak area increased as the flow rate of a 50 ppm $H_2S/H_2$ gas mixture to the GC was increased. This is due to that the loop was not completely filled at lower flow rates which resulted in a false peak area. As indicated in Figure A.3, the peak area stabilized above 30 sccm.

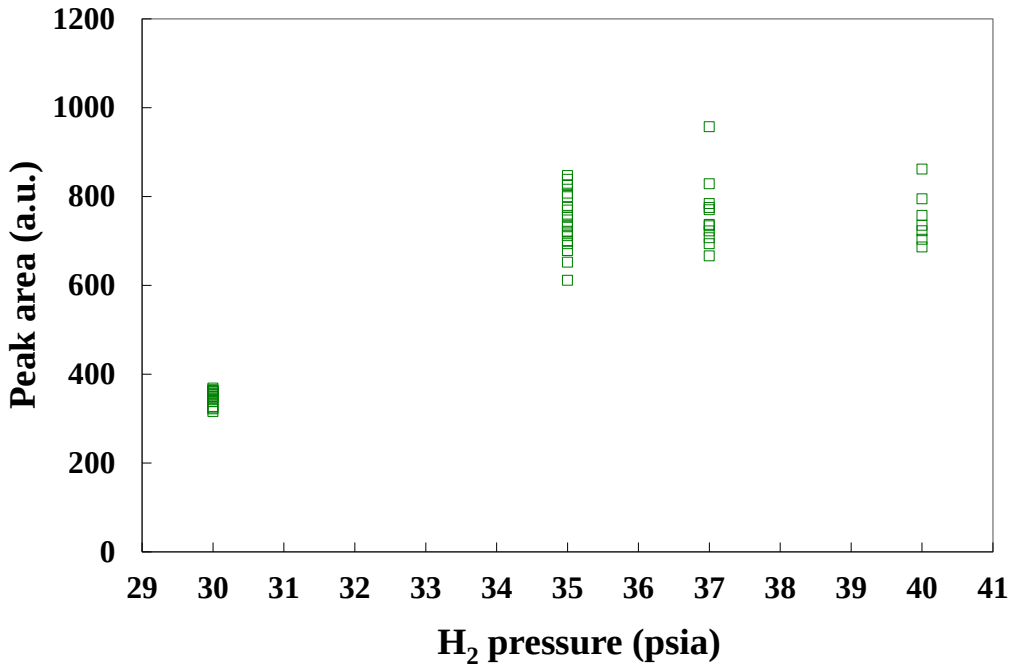


Figure A.1. Dependence of the GC signal on the fueling $H_2$ pressure.

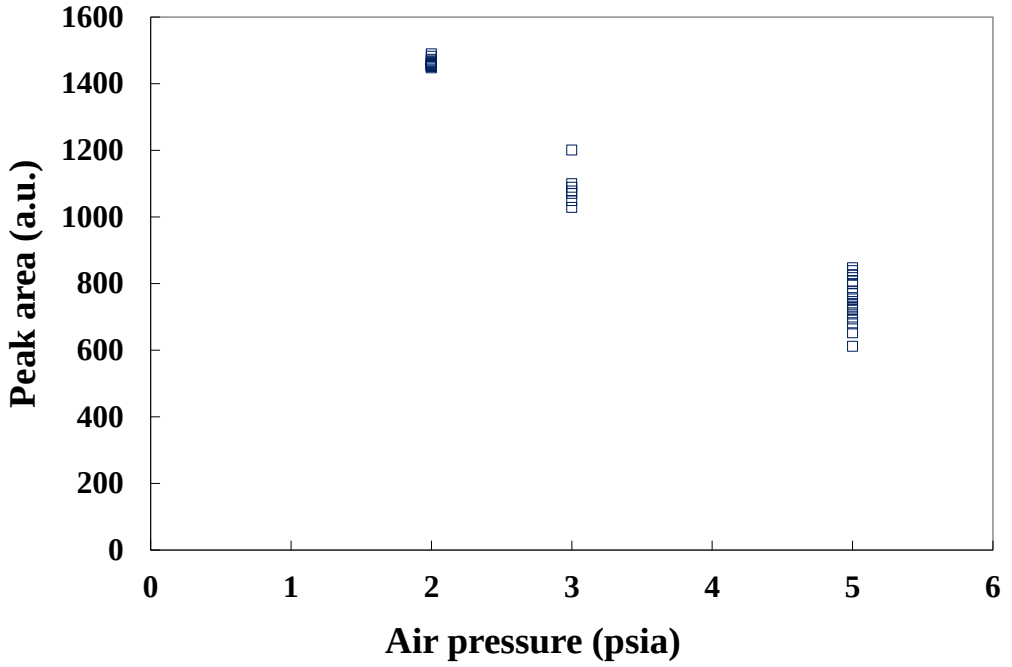


Figure A.2. Dependence of the GC signal on the fueling air pressure.

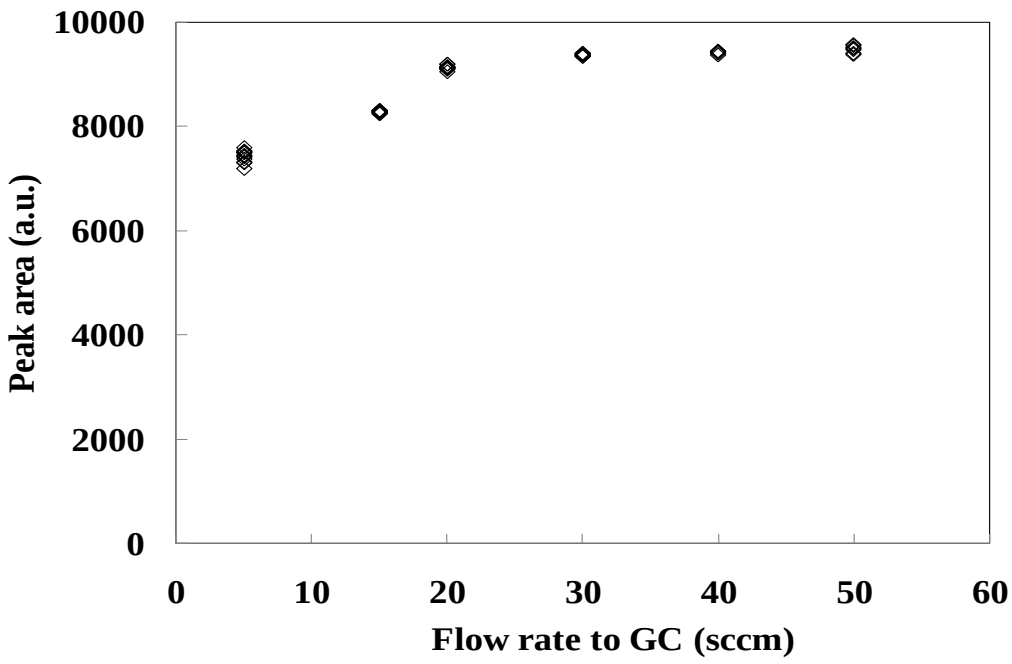


Figure A.3. Dependence of the GC signal on the flow rate (Pomerantz, 2010).

The GC was calibrated for detecting concentrations of 0.2 – 50 ppm. Figure A.4 shows the calibration curve for the GC in the range of 0.2 - 5 ppm $H_2S$. The air and hydrogen gases used for fueling the FPD were flowed at pressures of 2 and 35 psia, respectively with all other operation condition remaining the same as described in *Section 3.3.4*. The gain was set to high and a sampling loop of 500 $\mu$l was used. The calibration was carried out by diluting the 5 ppm $H_2S/H_2$ mix with $H_2$ in the specific ratios with the mixer (see Figure 3.3). A second order polynomial regression was used to fit the calibration curve.

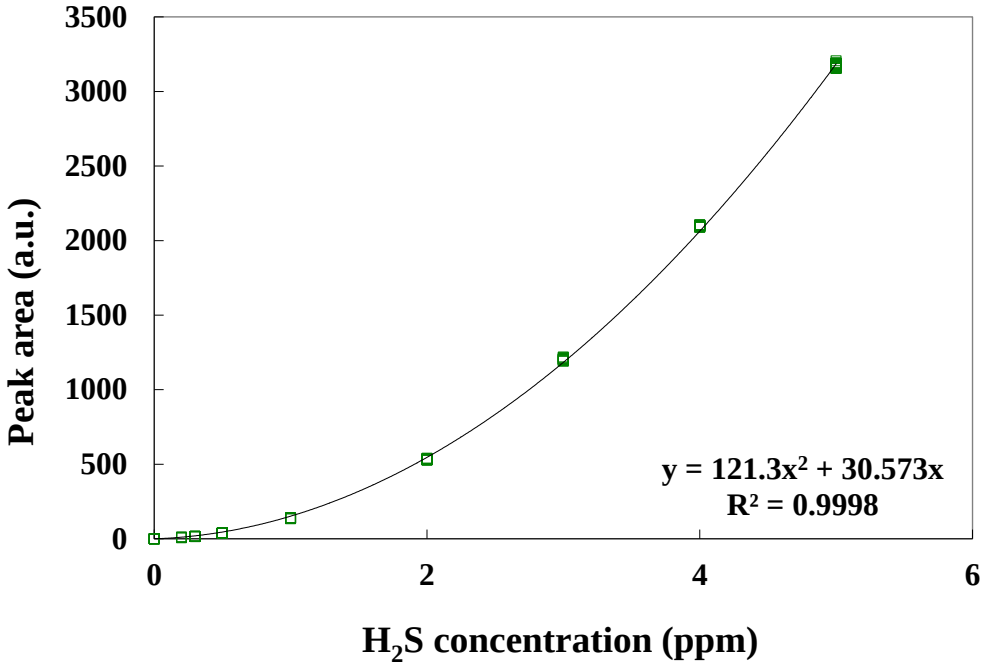


Figure A.4. Typical calibration curve for the GC in the range of 0 - 5 ppm $H_2S$.

Figure A.5 shows the calibration curve for the GC running up to 50 ppm $H_2S$. Although larger peak area was preferred as mentioned earlier, the peak area of the GC could not exceed 10,000 (a.u.). As a result, the pressures of air and hydrogen used for running 50 ppm $H_2S/H_2$ gas mixture were 4 and 30 psia, respectively and the gain was set to medium. The same sampling loop of 500 $\mu$l and calibration approach was used. The calibration curve also fitted well with a second order polynomial regression.

For running the characterization, the GC was firstly attenuated by adjusting the voltage of the PMT until the signal of the $H_2S/H_2$ mixture of known concentration feed fall on the calibration curve. After the attenuation, the GC then started to take to sample from the permeation system continuously for analysis.

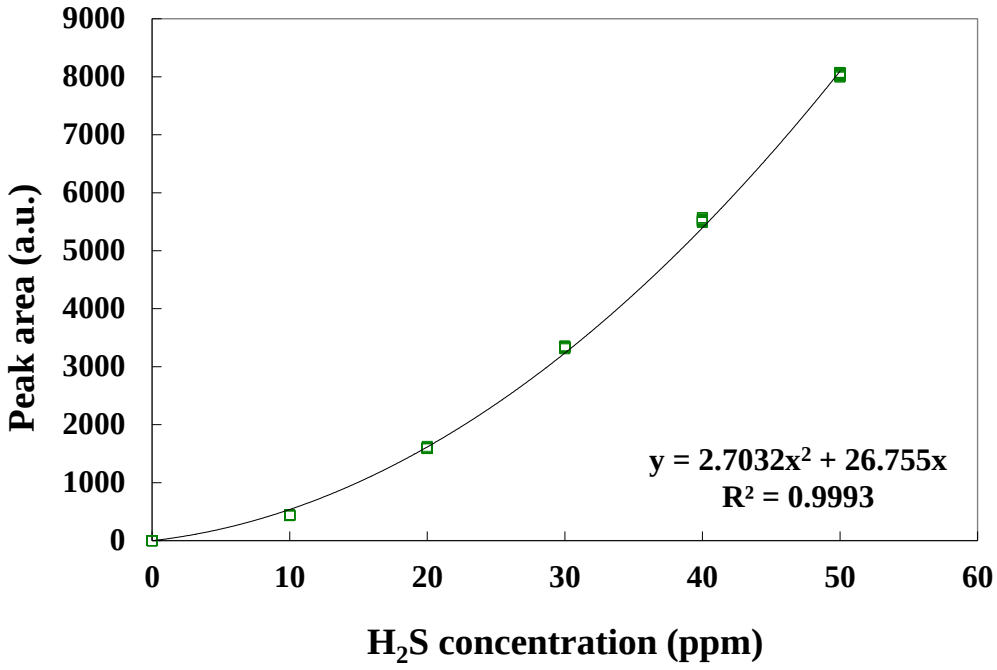


Figure A.5. Typical calibration curve for the GC in the range of 0 - 50 ppm $H_2S$.

# Appendix B: AAS calibration

According to the Beer-Lambert law (or Beer's law), the absorbance depends on the concentration of an absorbing species linearly. Equation B.1 is the expression of the Beer's law, where A is the absorbance of the sample, $\varepsilon$ is the molar absorptivity in L/(mol*cm), $b$ is the path length of the sample in cm and $C$ is the concentration of the sample in mol/L. In the absence of interference, linear dependences are usually observed for low concentrations. The concentration range for Au to have the linear dependence was 0 – 50 mg/l (at the wavelength of 242.8 *n*m), and that for Pd was 0 – 10 mg/l (at the wavelength of 244.8 *n*m).

$$A = \varepsilon \cdot b \cdot C \tag{B.1}$$

Figure B.1 shows the calibration curve for Au in the Au displacement solution. The calibration was carried out with four different concentrations of 0.5, 3, 6, and15 mg/l. The Au stock standard solutions of 1000 ± 4 mg/l purchased from Fluka Analytical was diluted with the 5 wt% HCl for preparing different Au concentration solutions. The absorbance increased linearly with the increasing Au concentrations up to 15 mg/l was observed as expected since it was within the linear dependence range. It should be noted that the error in the absorbance from a single sample was negligible and only two repeats of each sample were performed in the calibration curves. The method for determining the error for the AAS can be found in the work of Pomerantz (2010).

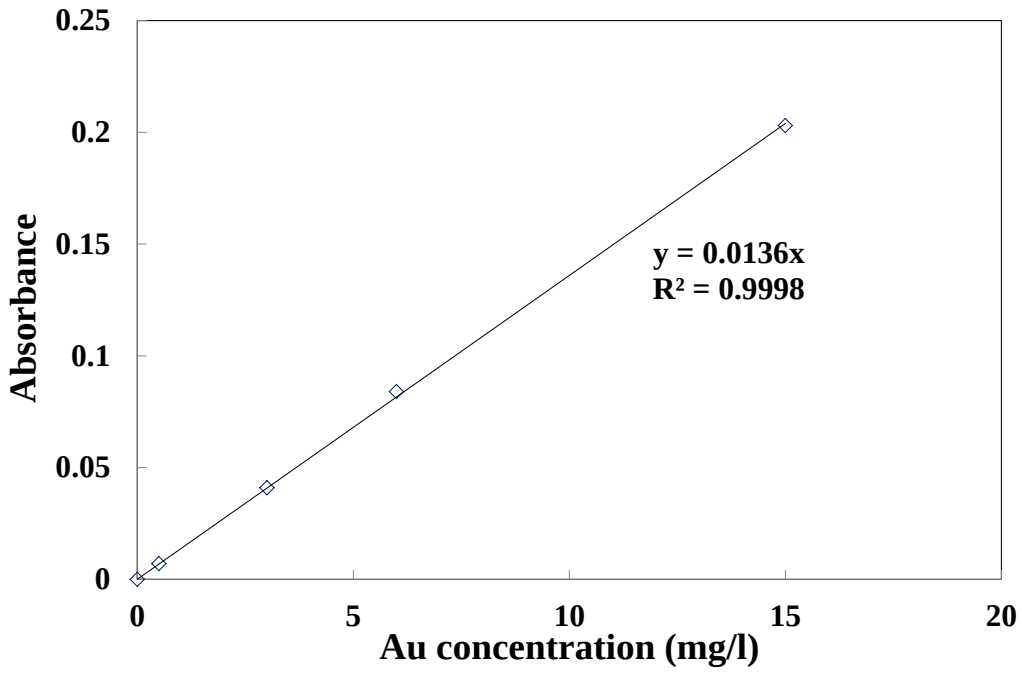


Figure B.1. Typical calibration curves for the Au plating solution.

A typical calibration curve for Pd in the displacement solution is shown in Figure B.2. The concentrations of 0.2, 0.5, 1, 3 mg/l were used for constructing the calibration curve. The Pd stock standard solutions of 1000 ± 4 mg/l purchased from Fluka Analytical was diluted with the 1 % v/v $HNO_3$ for preparing different Pd concentration solutions. Once again, since the Pd concentrations used were within the linear concentration dependence range, the absorbance increased linearly with increasing Pd concentrations.

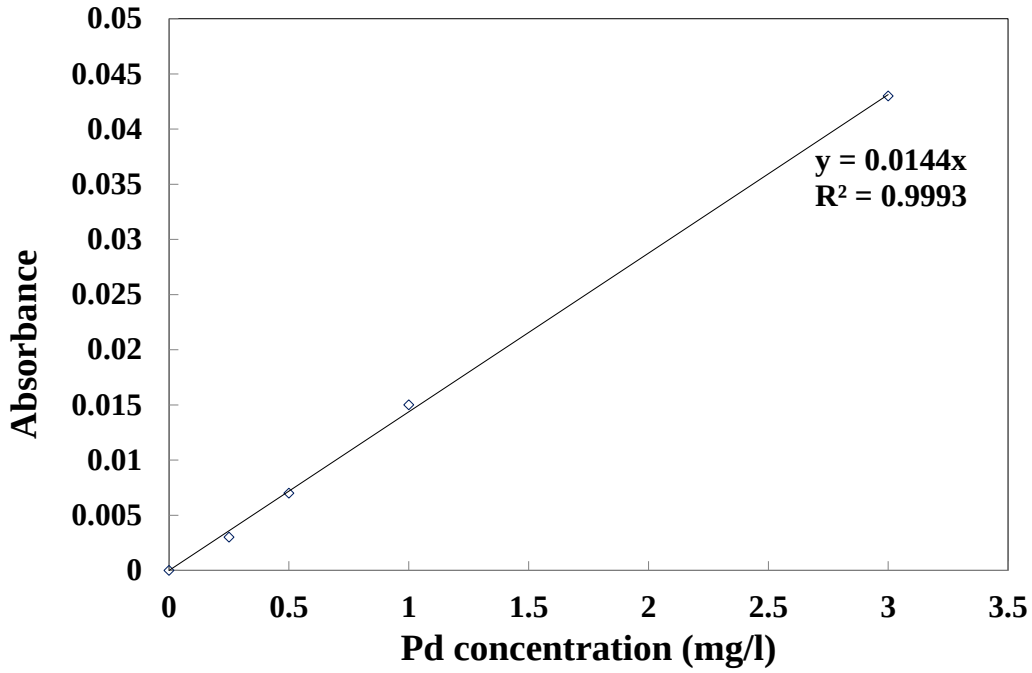


Figure B.2. Typical calibration curve for the Pd displacement solution.

# Appendix C: The estimation of the $H_2$ permeance of the selective layer of the composite Pd/Au membranes

The hydrogen permeance of the dense selective layer (Pd or Pd/Au) of the composite membranes discussed in *Section 6.4.3* was estimated by the following approach.

The approach was essentially to estimate the pressure drop between the selective layer from the known pressure drop between the entire composite membrane (including the selective layer and the porous support) and the known pressure drop between the porous support. As shown in Figure C.1, the pressure drop between the entire composite membrane, which is the difference of the shell side pressure ($P_s$, high pressure) and tube pressure ($P_t$, low pressure), can be manipulated and measured. In the case, the pressure drop between the entire composite membrane was 1 atmosphere ($P_s$ = 2 atm. and $P_t$ = 1 atm.). For estimating the pressure drop between the porous supports, the dusty-gas model (Mason and Malinauskas, 1983, see Equation 2.16) was used, which described that the permeating gas flux was the summation of the Knudsen diffusion and viscous flow. A simplified equation as expressed in Equation C.1 (Mardilovich et al., 1998) was applied for the calculation.

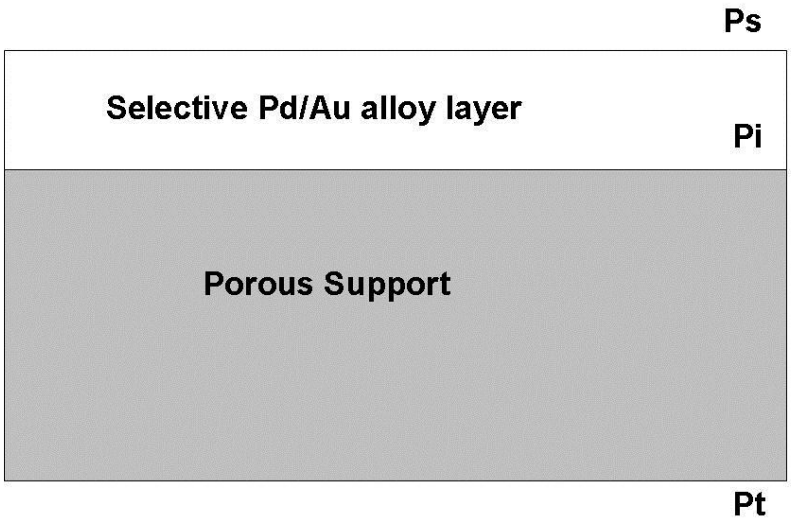


Figure C.1. Schematic representation of the composite membrane.

$$\frac{J_{gas}}{\Delta p} = \alpha + \beta P_{average} \tag{C.1}$$

In Equation C.1, $\alpha$ is the Knudsen coefficient in $m^3/m^2*h*atm$ and $\beta$ is the viscous coefficient in $m^3/m^2*h*atm^2$. In the study, the He fluxes under different pressure difference (up to 1 atm) of all the tested composite membranes discussed in *Chapter 6* were measured at room temperature (~25$^o$C) before any metal deposition (i.e. after the grading with the $Al_2O_3$ slurries). As a result, the Knudsen ($\alpha$) and viscous coefficients ($\beta$) for He permeation of the composite membranes at room temperature were then estimated as summarized in Table C.1.

Table C.1. Knudsen and viscous coefficient for the tested composite membranes at room temperature.

| Membrane | α | β |
|---|---|---|
| C-07 | 108.0 | 69.0 |
| C-09 | 255.3 | 37.7 |
| C-11 | 314.8 | -18.1 |
| C-12 | 213.4 | 6.0 |
| C-16 | 1290.7 | -247.0 |

The Knudsen and viscous coefficients for $H_2$ permeation at elevated temperatures were then estimated from those coefficients for He permeation at room temperature by the use of the Equation C.2, C.3, C.4, and C.5.

$$\frac{\alpha_{H2}}{\alpha_{He}} = \left( \frac{M_{He}}{M_{H2}} \right)^{0.5} \tag{C.2}$$

$$\frac{\beta_{H2}}{\beta_{He}} = \frac{\eta_{He}}{\eta_{H2}} \tag{C.3}$$

$$\alpha(T) = \alpha(T_0) \left( \frac{T_0}{T} \right)^{0.5} \tag{C.4}$$

$$\beta(T) = \beta(T_0) \left( \frac{\eta_0 * T_0}{\eta * T} \right) \tag{C.5}$$

At the steady state, the permeating hydrogen flux through the entire composite membrane equals to that permeating through the selective layer and that permeating

through the porous supports. Combining the Knudsen and viscous coefficients calculated for the hydrogen permeation at the elevated temperatures and the stable hydrogen flux of the entire composite membrane measured at the same temperature with pressure difference of 1 atmosphere (2 atm. to 1 atm.), the pressure drop between the porous support was then estimated by the use of Equation C.1. The pressure drop between the selective layer was then calculated by the known pressure drop between the entire composite membrane and that between the porous support. The pressure drop between the selective layer calculated was then used to calculate the $H_2$ permeance rather than that between the entire composite membranes. The estimated pressure at the interface of the selective layer and porous support and the $H_2$ permeances of the selective layer of the composite membranes at elevated temperatures were summarized in Table C.2.

Table C.2. The estimated pressure at the interface of the selective layer and porous support and the $H_2$ permeances of the selective layer of the composite membranes.

| Membrane | T(°C) | $P_{H2}$(membrane) | $P_i$(atm) | $P_{H2}$(film) |
|---|---|---|---|---|
| C-07 | 450 | 29.61 | 1.09 | 33.38 |
| | 350 | 23.11 | 1.07 | 25.05 |
| | 250 | 13.19 | 1.03 | 13.72 |
| C-09 | 450 | 26.8 | 1.04 | 28.27 |
| | 350 | 19.4 | 1.03 | 20.12 |
| | 250 | 12.7 | 1.02 | 12.97 |
| C-11 | 450 | 19.03 | 1.03 | 19.70 |
| | 400 | 15.95 | 1.02 | 16.40 |
| | 350 | 12.97 | 1.02 | 13.26 |
| C-12 | 450 | 15.76 | 1.03 | 16.41 |
| | 400 | 13.38 | 1.03 | 13.83 |
| | 350 | 11.22 | 1.02 | 11.53 |
| C-16 | 450 | 24.46 | 1.01 | 24.67 |
| | 400 | 20.74 | 1.01 | 20.93 |
| | 350 | 17.17 | 1.01 | 17.27 |